

Lecture Notes in Electrical Engineering 929

Pradip Kumar Jain
Yatindra Nath Singh
Ravi Paul Gollapalli
S. P. Singh *Editors*

Advances in Signal Processing and Communication Engineering

Select Proceedings of ICASPACE 2021

 Springer

Lecture Notes in Electrical Engineering

Volume 929

Series Editors

Leopoldo Angrisani, Department of Electrical and Information Technologies Engineering, University of Napoli Federico II, Naples, Italy

Marco Arteaga, Departament de Control y Robótica, Universidad Nacional Autónoma de México, Coyoacán, Mexico

Bijaya Ketan Panigrahi, Electrical Engineering, Indian Institute of Technology Delhi, New Delhi, Delhi, India

Samarjit Chakraborty, Fakultät für Elektrotechnik und Informationstechnik, TU München, Munich, Germany

Jiming Chen, Zhejiang University, Hangzhou, Zhejiang, China

Shanben Chen, Materials Science and Engineering, Shanghai Jiao Tong University, Shanghai, China

Tan Kay Chen, Department of Electrical and Computer Engineering, National University of Singapore, Singapore, Singapore

Rüdiger Dillmann, Humanoids and Intelligent Systems Laboratory, Karlsruhe Institute for Technology, Karlsruhe, Germany

Haibin Duan, Beijing University of Aeronautics and Astronautics, Beijing, China

Gianluigi Ferrari, Università di Parma, Parma, Italy

Manuel Ferre, Centre for Automation and Robotics CAR (UPM-CSIC), Universidad Politécnica de Madrid, Madrid, Spain

Sandra Hirche, Department of Electrical Engineering and Information Science, Technische Universität München, Munich, Germany

Faryar Jabbari, Department of Mechanical and Aerospace Engineering, University of California, Irvine, CA, USA

Limin Jia, State Key Laboratory of Rail Traffic Control and Safety, Beijing Jiaotong University, Beijing, China

Janusz Kacprzyk, Systems Research Institute, Polish Academy of Sciences, Warsaw, Poland

Alaa Khamis, German University in Egypt El Tagamoa El Khames, New Cairo City, Egypt

Torsten Kroeger, Stanford University, Stanford, CA, USA

Yong Li, Hunan University, Changsha, Hunan, China

Qilian Liang, Department of Electrical Engineering, University of Texas at Arlington, Arlington, TX, USA

Ferran Martín, Departament d'Enginyeria Electrònica, Universitat Autònoma de Barcelona, Bellaterra, Barcelona, Spain

Tan Cher Ming, College of Engineering, Nanyang Technological University, Singapore, Singapore

Wolfgang Minker, Institute of Information Technology, University of Ulm, Ulm, Germany

Pradeep Misra, Department of Electrical Engineering, Wright State University, Dayton, OH, USA

Sebastian Möller, Quality and Usability Laboratory, TU Berlin, Berlin, Germany

Subhas Mukhopadhyay, School of Engineering and Advanced Technology, Massey University, Palmerston North, Manawatu-Wanganui, New Zealand

Cun-Zheng Ning, Electrical Engineering, Arizona State University, Tempe, AZ, USA

Toyooki Nishida, Graduate School of Informatics, Kyoto University, Kyoto, Japan

Luca Oneto, Department of Informatics, Bioengineering, Robotics, University of Genova, Genova, Genova, Italy

Federica Pascucci, Dipartimento di Ingegneria, Università degli Studi "Roma Tre", Rome, Italy

Yong Qin, State Key Laboratory of Rail Traffic Control and Safety, Beijing Jiaotong University, Beijing, China

Gan Woon Seng, School of Electrical and Electronic Engineering, Nanyang Technological University, Singapore, Singapore

Joachim Speidel, Institute of Telecommunications, Universität Stuttgart, Stuttgart, Germany

Germano Veiga, Campus da FEUP, INESC Porto, Porto, Portugal

Haitao Wu, Academy of Opto-electronics, Chinese Academy of Sciences, Beijing, China

Walter Zamboni, DIEM - Università degli studi di Salerno, Fisciano, Salerno, Italy

Junjie James Zhang, Charlotte, NC, USA

The book series *Lecture Notes in Electrical Engineering* (LNEE) publishes the latest developments in Electrical Engineering—quickly, informally and in high quality. While original research reported in proceedings and monographs has traditionally formed the core of LNEE, we also encourage authors to submit books devoted to supporting student education and professional training in the various fields and applications areas of electrical engineering. The series cover classical and emerging topics concerning:

- Communication Engineering, Information Theory and Networks
- Electronics Engineering and Microelectronics
- Signal, Image and Speech Processing
- Wireless and Mobile Communication
- Circuits and Systems
- Energy Systems, Power Electronics and Electrical Machines
- Electro-optical Engineering
- Instrumentation Engineering
- Avionics Engineering
- Control Systems
- Internet-of-Things and Cybersecurity
- Biomedical Devices, MEMS and NEMS

For general information about this book series, comments or suggestions, please contact leontina.dicecco@springer.com.

To submit a proposal or request further information, please contact the Publishing Editor in your country:

China

Jasmine Dou, Editor (jasmine.dou@springer.com)

India, Japan, Rest of Asia

Swati Meherishi, Editorial Director (Swati.Meherishi@springer.com)

Southeast Asia, Australia, New Zealand

Ramesh Nath Premnath, Editor (ramesh.premnath@springernature.com)

USA, Canada

Michael Luby, Senior Editor (michael.luby@springer.com)

All other Countries

Leontina Di Cecco, Senior Editor (leontina.dicecco@springer.com)

**** This series is indexed by EI Compendex and Scopus databases. ****

Pradip Kumar Jain · Yatindra Nath Singh ·
Ravi Paul Gollapalli · S. P. Singh
Editors

Advances in Signal Processing and Communication Engineering

Select Proceedings of ICASPACE 2021

 Springer

Editors

Pradip Kumar Jain
National Institute of Technology Patna
Patna, Bihar, India

Ravi Paul Gollapalli
Department of Engineering and Technology
University of North Alabama
Florence, SC, USA

Yatindra Nath Singh
Department of Electrical and Electronics
Engineering
Indian Institute of Technology Kanpur
Kanpur, India

S. P. Singh
Department of Electronics
and Communication Engineering
Mahatma Gandhi Institute of Technology
Gandipet, India

ISSN 1876-1100

ISSN 1876-1119 (electronic)

Lecture Notes in Electrical Engineering

ISBN 978-981-19-5549-5

ISBN 978-981-19-5550-1 (eBook)

<https://doi.org/10.1007/978-981-19-5550-1>

© The Editor(s) (if applicable) and The Author(s), under exclusive license to Springer Nature Singapore Pte Ltd. 2022

This work is subject to copyright. All rights are solely and exclusively licensed by the Publisher, whether the whole or part of the material is concerned, specifically the rights of translation, reprinting, reuse of illustrations, recitation, broadcasting, reproduction on microfilms or in any other physical way, and transmission or information storage and retrieval, electronic adaptation, computer software, or by similar or dissimilar methodology now known or hereafter developed.

The use of general descriptive names, registered names, trademarks, service marks, etc. in this publication does not imply, even in the absence of a specific statement, that such names are exempt from the relevant protective laws and regulations and therefore free for general use.

The publisher, the authors, and the editors are safe to assume that the advice and information in this book are believed to be true and accurate at the date of publication. Neither the publisher nor the authors or the editors give a warranty, expressed or implied, with respect to the material contained herein or for any errors or omissions that may have been made. The publisher remains neutral with regard to jurisdictional claims in published maps and institutional affiliations.

This Springer imprint is published by the registered company Springer Nature Singapore Pte Ltd. The registered company address is: 152 Beach Road, #21-01/04 Gateway East, Singapore 189721, Singapore

ICASPACE 2021—Organising Committee

Conference Chair

Sudarshan Rao Nelatury, Penn State University, Erie, PA, 16563, USA

Conference Co-chairs

K. Jaya Sankar, Mahatma Gandhi Institute of Technology, Hyderabad, India

S. P. Singh, Mahatma Gandhi Institute of Technology, Hyderabad, India

Conveners

D. Venkat Reddy, Mahatma Gandhi Institute of Technology, Hyderabad, India

T. D. Bhatt, Mahatma Gandhi Institute of Technology, Hyderabad, India

Ch. Raja, Mahatma Gandhi Institute of Technology, Hyderabad, India

Co-conveners

V. S. N. Kumar Devaraju, Mahatma Gandhi Institute of Technology, Hyderabad, India

T. R. Vijayalakshmi, Mahatma Gandhi Institute of Technology, Hyderabad, India

Y. Praveen K. Reddy, Mahatma Gandhi Institute of Technology, Hyderabad, India

Advisory Board-International

David Benton, Aston University, Birmingham, England
 Ravi Paul Gollapalli, UNA, Florence, Alabama, USA
 Arokiaswami Alphones, NTU, Singapore
 Mahadevan Iyer, University of Texas, USA
 David Benton, Aston University, Birmingham, England
 Mahender Kumbham, Valeo, Cork, Ireland
 T. G. Thomas, BITS Pilani, Dubai, UAE
 Siva Nagireddy, RF Pixels, California, USA
 Yoshiki Maekawa, Kyocera Asia Pacific, Thailand
 Kamesh Namuduri, University of North Texas, USA
 Jagadish Nayak, BITS Pilani, Dubai, UAE
 M. Prashant Reddy, Khalifa University, Abu Dhabi, UAE
 Sattar B. Sadakhan, University of Babylon, Iraq
 M. A. Burhanuddin, Universiti Teknikal Malaysia Melaka, Malaysia

Advisory Board-National

N. V. S. N. Sarma, IIIT Trichy, Tamil Nadu
 Y. N. Singh, IIT Kanpur, Uttar Pradesh
 Chandan Chakraborty, NITTTR, Kolkata, West Bengal
 Brajesh K. Kaushik, IIT Roorkee, Uttarakhand
 M. Zafar Ali Khan, IIT Hyderabad, Telangana
 S. Bapiraju, IIIT Hyderabad, Telangana
 Anupam Sharma, DSP, DRDO, Hyderabad, Telangana
 K. S. Udgata, University of Hyderabad, Telangana
 Atul Negi, University of Hyderabad, Telangana
 L. Anjaneyulu, NIT Warangal, Telangana
 L. Pratap Reddy, JNTU Hyderabad, Telangana
 A. K. Singh, DLRL, Hyderabad, Telangana
 N. Balaji, JNTU Kakinada, Andhra Pradesh
 V. Sumalatha, JNTU Anantapur, Andhra Pradesh
 P. Chandra Shekar, Osmania University, Hyderabad, Telangana
 N. P. Rath, VSS University of Technology, Odisha
 Aravind Kumar, NIT Kurukshetra, Haryana
 M. Chinnasamy, Semiconductor Fabless Accelerator Laboratory, Karnataka

Steering Committee

P. V. Ramana, MGIT, Hyderabad, India
M. Fayazur Rahaman, MGIT, Hyderabad, India
S. Praveena, MGIT, Hyderabad, India

Program Committee

S. Srinivasa Rao, MGIT, Hyderabad, India
G. Madhavi, MGIT, Hyderabad, India
V. Saidulu, MGIT, Hyderabad, India
K. Raghu, MGIT, Hyderabad, India
M. Chandrakala, MGIT, Hyderabad, India
A. Veerabhadra Rao, MGIT, Hyderabad, India
J. Sneha Latha, MGIT, Hyderabad, India
P. Durga Devi, MGIT, Hyderabad, India
D. Subhasini, MGIT, Hyderabad, India
B. Kesava Rao, MGIT, Hyderabad, India
G. Usha Rani, MGIT, Hyderabad, India
A. Navaneetha, MGIT, Hyderabad, India
A. Bala Raju, MGIT, Hyderabad, India
P. Usha Rani, MGIT, Hyderabad, India
G. Ravi Kumar, MGIT, Hyderabad, India
S. Swetha, MGIT, Hyderabad, India
M. Sanjeev Kumar, MGIT, Hyderabad, India
B. Roopa, MGIT, Hyderabad, India
G. Srilatha, MGIT, Hyderabad, India
D. Anji Reddy, MGIT, Hyderabad, India
D. Sudhakar, MGIT, Hyderabad, India
Divya A. Sagar, MGIT, Hyderabad, India
K. N. Mallesh, MGIT, Hyderabad, India
Archana Yadav, MGIT, Hyderabad, India
M. Naga Sitaram, MGIT, Hyderabad, India
P. Shirisha, MGIT, Hyderabad, India
P. Vinod Reddy, MGIT, Hyderabad, India
M. Vishwaja, MGIT, Hyderabad, India
K. Bapayya, MGIT, Hyderabad, India

Reviewers

Vilas H. Gaidhane
Prashanth Reddy Marpu
Raj Kumar Patro
C. Satish Kumar
D. D. Ebnizer
Kanhira Kadavath Mujeeb Rahman
Jagadish Nayak
Ahmed Faheem Zobaa
Akhtar Kalam
Afredo vaccaro
Dimitri Vinnikov
Gorazad Stumberger
Lausiong Hoe
Hussian shareef
Murad Al-Shibli Emmet
Nesimi Ertugrul
Richarad Blanchard
Shashi Paul
Zhao Xu
Ahmed Zobaa
Adel Nasiri
P. N. Sugunathan
Hiroya Fuji Saki
Fawnizu Azmadi Hussin
Ganesh R. Naik
Shamimul Qamar
M. Mukunda Rao
E. S. R. Rajgopal
U. Chandrasekhar
Viod Kumar P.
N. V. L. Narasimha Murthy
M. Ravi Babu
Mellashwar Rao
Pamila Chawala
Ravindra Kumar Yadav
Maneesh Kumar Singh
Rohit Raja
Imran Ahmed Khan
Jugul Kishor
Neeta Awasthy
Lakshmanan M.
Ashish Gupta

Deepak Batra
B. Thiyaneswaran
N. Malmurugan
R. Maheswar
Korlapati Keerti Kumar
Prabha Selvaraj
D. Jackuline Moni
Suresh Merugu
Chaitanya Duggineni
Pushpa Mala
K. V. Ramprasad
Jithin Kumar M. V.
M. Aravind Kumar
M. Nizamuddin
S. Arul Jothi
Sathish Kumar Nagarajan
Deepika Ghai
Kirti Rawal
V. A. Sankar Ponnappalli
Hemlata Dalmia
Rahul Hooda
Anuj Singal
P. Venkateswara Rao
D. Jayanthi
Agha Asim Husain
K. Jaya Sankar
P. Venkata Ramana
D. Venkat Reddy
T. D. Bhatt
Ch. Raja
S. S. Rao
V. Saidulu
S. Praveena
Fayazur Rahaman Mohammad
T. R. Vijaya Lakshmi
Y. Praveen Kumar Reddy

Preface

This book contains the proceedings of papers presented in the 1st International Conference on Advances in Signal Processing and Communication Engineering (ICASPACE-21), held in July 2021, in the Department of Electronics and Communication Engineering, Mahatma Gandhi Institute of Technology, Hyderabad, India. The conference invited papers from research scholars, academicians, industry professionals and scientists. It provided them with a platform to discuss and put forward their ideas and research findings with their peers worldwide. Further, ICASPACE-21 organized six invited talks delivered by (i) Dr. N. Sudarshan Rao, Professor, Penn State Behrend, Erie, USA; (ii) Dr. Mahendar Kumbham, Valeo, Ireland Photonics; (iii) Dr. T. G. Thomas, Professor, BITS Pilani, UAE; (iv) Mr. Swapnil Bora, Founder and CEO, MeshTek Labs, Texas, USA; (v) Dr. Yatindra Nath Singh, Professor (HAG), Electrical Engineering Department, IIIT Kanpur, India; and (vi) Dr. Anupam Sharma, Associate Director, DSP, DRDO, Hyderabad, India. This provided an opportunity for the participants to listen to the eminent speakers in the areas of signal processing and communication engineering.

ICASPACE-21 received a total of 220 papers in the areas of signal processing, communication, VLSI, IoT and machine learning applications in these areas, across four countries. Works submitted to the conference underwent a rigorous single-blind peer review each by three experts (among which two are from external Institutions) selected by the conference committee. To ensure a quality review process, each subject expert was not assigned more than five papers. Subsequently, the authors were given an opportunity to incorporate the review comments given by the reviewers. After comprehensive verification of technical content, plagiarism and grammar, the conference committee recommended 44 papers be published in this proceedings book.

This book covers several theoretical and mathematical approaches that address different challenges in signal, image, speech processing and communication systems. It primarily focuses on effective mathematical methods, algorithms and models that enhance the performance of existing systems. The areas include advances in signal processing (radar and biomedical), image processing (satellite, medical and general optical images), speech processing (speech signal compression, conversion

and audio mixing). Further, the contents of this book address technical and environmental challenges in 5G technology, strategies for optimal utilization of resources to improve the efficacy of the communication systems in terms of bandwidth and radiating power, some innovative IoT applications, mathematical, theoretical and algorithmic aspects of evolutionary computation models that support hybrid intelligence in machine learning/deep learning problems with applications focused in signal processing; exploratory research in electromagnetics, microwave and radar signal processing.

Through this book, we aim to unify the latest achievements of the authors in the research projects and practices across several areas of signal processing and communication engineering. We further expect this book will act as a catalyst for research in related areas, future collaborations and international cooperation.

We would like to express our appreciation and heartfelt thanks to every individual who has directly or indirectly contributed toward the content quality improvement of this conference proceedings and consistently assisted us in consolidating and bringing the works submitted to the ICASPACE-21 into good shape.

Florence, USA
Patna, India
Kanpur, India
Gandipet, India
January 2022

Ravi Paul Gollapalli
Pradip Kumar Jain
Yatindra Nath Singh
S. P. Singh

Acknowledgements

At the outset, we, the Department of Electronics and Communication Engineering at Mahatma Gandhi Institute of Technology, Hyderabad, thank the management of Chaitanya Bharathi Educational Society for their acquiescence and constant support to the first International Conference on Advances in Signal Processing and Communication Engineering (ICASPACE-2021). Further, our deep sense of gratitude to Conference Chair Dr. Sudarshan R. Nelatury, Co-chair and Principal Dr. K. Jaya Sankar, for their invaluable administrative and technical inputs. In addition, the organizing committee is indebted to all the expert reviewers who have spared their valuable time for reviewing the papers and helping us to maintain the quality of the content publishing in the proceedings. We thank the keynote speakers, session chairs, technical committee and advisory board members for their cooperation in different ways for the success of the ICASPACE-21. Furthermore, we are thankful to the authors of the contributed papers who submitted their quality works to the conference and rendered their cooperation in the preparation of the camera-ready documents. Finally, we highly appreciate the conveners and co-conveners of ICASPACE-21 for maintaining the submissions, plagiarism checking, communication with the authors and other invitees and consistent support to the preparation of the conference proceedings.

Contents

Lumped Circuit Modeling at Nanoscale (Part-I: Dielectric Anisotropy)	1
Sudarshan R. Nelatury	
Lumped Circuit Modeling at Nanoscale (Part-II: Coupling Between Two Nanospheres)	15
Sudarshan R. Nelatury	
Deep Learning Model for Multiclass Classification of Diabetic Retinal Fundus Images Using Gradient Descent Optimization	27
Ram Krishn Mishra	
Configuration of the Communication Radius for Partial Coverage in WSN	37
Rameshwar Nath Tripathi, Kumar Gaurav, and Yatindra Nath Singh	
Bandwidth Enhancement of Two Element Closely Spaced MIMO Antenna for WLAN Applications	47
Pendli Pradeep, K. Jaya Sankar, and P. Chandra Sekhar	
Early Prediction of Sepsis Using Convolutional and Recurrent Neural Networks	55
S. K. Chaya Devi, Y. Varun Reddy, K. Sai Sri Vasthav, and G. Praneeth	
Content-Based Nonlinear Filter for the Removal of Impulsively Modeled Artifacts from Images and Videos	63
D. V. N. Kameswari, M. Divya, K. Vasanth, S. Pradeep Kumar Reddy, and S. Nagaraj	
Hardware Implementation of Epidermis Segmentation in Skin Histopathological Images	75
Raju Machupalli, Luiz Antonio de Oliveira Junior, Masum Hossain, and Mrinal Mandal	

Dual-Band MIMO Antenna with Enhanced Isolation Using Fractal Isolators	83
Akanksha Singh, Arvind Kumar, and Binod Kumar Kanaujia	
Sub-graph p-Cycle Formation for Span Failures in All-Optical Networks	95
Varsha Lohani, Anjali Sharma, and Yatindra Nath Singh	
Single-Precision Floating-Point Multiplier Design Using Quantum-Dot Cellular Automata with Power Dissipation Analysis	103
A. Arunkumar Gudivada and Gnanou Florence Sudha	
Compression Techniques for Low Power Hardware Accelerator Design: Case Studies	117
Govinda Rao Locharla, Pogiri Revathi, and M. V. Nageswara Rao	
Sequence Set Design for Radar System	129
P. Shravan Kumar, S. P. Singh, T. D. Bhatt, and D. V. S. Nagendra Kumar	
Design of an All Digital Phase-Locked Loop Using Cordic Algorithm	143
Mohd Ziauddin Jahangir, Chandra Sekhar Paidimarry, Md. Sikander, and M. V. Shravanthi	
Analysis of Deep Learning Algorithms for Image Denoising	151
Nikita Choudhary and Rakesh Sharma	
An Extensive Survey on Assessment of Multicore Processors for Embedded Systems	161
P. Yasasri Uma, M. V. Kala Sindhuja, A. Kishore Reddy, N. Arun Vignesh, and Asisa Kumar Panigrahy	
Image Segmentation Techniques and Optimization Algorithms for Lung Cancer Detection	171
B. Sucharitha, Damiseti Savitri Devi, and Jakku Sushmitha	
Handwritten to Text Document Converter	187
S. Aruna Deepthi, E. Sreenivasa Raol, and M. D. Shadab farhan	
An Efficient Energy Aware for Reliable Route Discovery Using Energy with Movement Detection Technique in MANET	197
Kamlesh Chandravanshi, Gaurav Soni, and Durgesh Kumar Mishra	
Design and Implementation of Imprecise Adders for Low-Power Applications	205
N. Aivelu Manga and Varala Pasula Nikhila	

Speech Processed Public Addressing System 215
 Vijaya Kumar Gurrala, Y. Padma Sai, Nikhitha Karennagari,
 and K. Yashwanth Reddy

**An Approach Towards Data Privacy Issues in Distributed Cyber
 Physical System** 223
 Shubham Joshi, Radhika Joshi, and Durgesh Mishra

**Classification of LPI Radar Signals Using Multilayer Perceptron
 (MLP) Neural Networks** 233
 Metuku Shyamsunder and Kakarla Subba Rao

**A Systematic Review on Screening of Diabetic Retinopathy
 and Maculopathy Using Artificial Intelligence** 249
 Aida Jones, Thulasi Bai Vijayan, Sadasivam Subbarayan,
 and Sheila John

**Area Efficient and High-Throughput Radix-4 1024-Point FFT
 Processor for DSP Applications** 259
 Mohan Rao Thokala

Air Quality Monitoring System Based on Artificial Intelligence 267
 Vattam Sowmya and Shravya Ragiphani

**An Improved Technique for Identification of Forgery Image
 Detection Using Clustering Method** 275
 S. Jeevetha, Deepa Jose, P. Nirmal Kumar, and H. Kareemullah

**EEG Signal Analysis During Stroop Task for Checking the Effect
 of Sleep Deprivation** 287
 Bhagyashree Narkhede, Sai Kate, Vaishnavi Malkapure,
 and Revati Shriram

**UWB Localization Procedures with Range Control
 Methods—A Review** 295
 Y. VenkataLakshmi and Parulpreet Singh

**Multilevel Authentication to Wireless Sensor Networks Against
 Malicious Attacks Using Butterfly Method** 317
 Ishrath Unissa, Ch. Raja, and Syed Jalal Ahmad

**Advanced 18 nm FinFET Node-Based Energy Efficient
 and High-Speed Data Comparator Using SR Latch** 327
 M. Lavanya, Malla Jyothsna Priya, Ponukumatla Janet,
 Kavuluri Pavan Kalyan, and Vijay Vallabhuni

A Novel Fault Diagnosis and Recovery Mechanism Based on Events Prediction in Distributed Network 335
M. Srinivasa Rao, D. Nagendra Rao, P. Chandrashekhara Reddy, and V. Usha Shree

Medical Image Fusion by Using Different Wavelet Transforms 349
M. N. Narsaiah, D. Venkat Reddy, and T. Bhaskar

Two-State Hybrid Learning Approaches for Energy Reduction Estimation on Wireless Sensor Networks 359
V. Sivasankara Reddy and G. Sundari

Design of IoT-Based Transmission Line Fault Monitoring System 373
N. Dhanalakshmi, Chanikya Mamindlapalli, Dinesh Reddy Sunkari, and Rohith Reddy Salguti

Optimized VLSI Design of Squaring Multiplier Using Yavadunam Sutra Through Deficiency Bits Reduction 387
J. Sravana, K. S. Indrani, Sankeerth Mahurkar, M. Pranathi, D. Rakesh Reddy, and Vijay Vallabhuni

Design and Simulation of High Performance Hybrid Full Adder Using CMOS 45 nm Technology 401
S. Jayamangala, T. Pullaiah, J. Sunilkumar, and M. Sivakumar

Techniques for Designing Efficient ELINT Digital Receiver 413
A. K. Singh

Robust Deep Learning Approach for Brain Tumor Classification and Detection 427
J. Hima Bindu, Appidi Meghana, Sravani Kommula, and Jagu Abhishek Varma

Impact of Distance Measure on Kriging Interpolation on Natural Images Corrupted by Drop-Out Noise 439
J. Sridevi, Ch. Raghava Prasad, and K. Vasanth

Implementation of Reed–Solomon Coder and Decoder Using Raspberry PI for Image Applications 451
Kallepalli Bapayya and Bagadi Kesava Rao

Software Defined Radio-Based ELINT System for Geolocation of RF Emitters 471
D. Mallikarjuna Reddy, S. Rani Surender, and Nikhitha Karenagari

Performance Analysis of TDOA Localization Algorithm Based on PSO with Formation Flying	483
Amar Singh, P. Naveen Kumar, and Anupam Sharma	
Intruder Detection and Tracking Using Computer Vision and IoT	499
Devarakonda Abhinay, Krishna Chaitanya, and Prakki Sathwik Ram	

About the Editors

Pradip Kumar Jain is a Professor in Electronics Engineering, and he is the Director of the National Institute of Technology Patna. Dr. Jain has immense experience both in research and administration. He made a significant contribution to the analysis, modeling, and development of high-power microwave tubes and gyrotron devices. Prof. Jain guided 20 Doctoral theses and has 100 peer-reviewed articles published in indexed journals, 200 conference proceedings, a patent, and authored six book/monograph chapters, to his credit. He served in various administrative positions as Dean-R&D at IIT (BHU), Varanasi; Coordinator of Microwave Tubes Research Centre and Centre of Advanced Studies; Head of the Department of Electronics Engineering, IIT (BHU). Prof. Jain did extensive R&D activities in collaboration with CEERI (CSIR, Pilani), DRDO, IPR (DAE, Gandhi Nagar), and successfully executed numerous sponsored research projects.

Yatindra Nath Singh is currently the Dean of Infrastructure and Planning at IIT Kanpur. Prof. Singh has led a team of researchers and academicians across India to develop Brihaspati, a project that aims at developing a platform-independent highly scalable content delivery system for a web-based e-learning system. He pursued his under graduation in electrical engineering from REC Hamirpur (present National Institute of Technology Hamirpur), a master's with a specialization in optoelectronics and optical communications, and a Ph.D. in optical communication networks from IIT Delhi. He supervised 15 Ph.D. theses, published several journal articles, and conference proceedings, and completed several sponsored projects besides Brihaspati.

Ravi Paul Gollapalli is an Associate Professor in the Department of Engineering Technology at the University of North Alabama. He has an electrical engineering background with a specialization in optics and has research experience in signal and image processing, pattern recognition analysis for remote sensing, and applications of femtosecond lasers. Dr. Gollapalli received his Ph.D. from the University of Alabama, Huntsville, and was a Post-Doctoral Research Associate at the University of South Alabama, USA. He has published his works in peer-reviewed Journals,

Conferences, and a book chapter. Besides, Dr. Gollapalli is actively involved in experimental works, numerical simulations, simulation of femtosecond laser pulse propagation in materials, fabrication of nanostructures on glass and silicon substrates using micro/nanofabrication processes, and designing RF circuits for noise analysis. Further, he built an optical amplifier (EDFA) and supported the processing of signals from an impedance probe equipped on-board the NASA SOUND rocket.

S. P. Singh is a Professor and Head of the Electronics and Communication Engineering Department at Mahatma Gandhi Institute of Technology, Hyderabad. He worked for 18 years in the Indian Army Corps of EME. During his service in the Indian Army, he was in radar maintenance activities. Dr. Singh has developed a synchro-based training model for defense application, received several cash rewards for his indigenization work on the radar Schilka and did several modifications in radar SFM to reduce the error rate. Later he chose his career as an academician. Dr. Singh received his Ph.D. from Osmania University, Hyderabad, in 2007. He supervised three doctoral theses so far, and four are in progress. He has over 96 publications in journals and conference proceedings and completed several funded projects from AICTE.

Lumped Circuit Modeling at Nanoscale (Part-I: Dielectric Anisotropy)



Sudarshan R. Nelatury 

Abstract The past decade has witnessed a growing interest in pushing the limits of lumped circuit theory to the analysis and design of nanocircuits at infrared and visible frequencies. Just as how a relentless pursuit of microminiaturization of electronic devices has resulted in the very large-scale integration (VLSI) technology today, an even more aggressive research activity in the field of metamaterials and complex media opened roadmaps for subwavelength nanostructures. The motive for this urge is to break free from the diffraction limit and pitch into all new frontiers of plasmonics and nano-technology, whereby information processing and transmission are projected to happen at a greater speed and lower power levels. In order for nanocircuits and systems to develop, it is imperative that electromagnetic interaction with nanoparticles made of diverse media types be studied not only using full wave analysis, but also with the aid of quasi-static approach. Numerous papers have appeared that considered dielectric and plasmonic particles possessing isotropy, but dielectric anisotropy and bianisotropy have yet to garner their rightful attention. This paper aims to carry out this in case of anisotropic nanospheres. In a companion paper, we shall consider the equivalent circuits of nanospheres. We shall outline quasi-static analysis and derive fields both inside and outside a nanosphere and obtain equivalent circuit that takes into account coupling between two nanospheres.

Keywords Anisotropic medium · Nanocircuits · Quasi-static model · Lumped circuits

1 Introduction

With growing demand for nanomaterials and nanocircuitry, there is a greater need to characterize complex material media and nanoparticles and develop equivalent circuits that serve as reasonably accurate models as far as terminal behavior is con-

S. R. Nelatury (✉)
Penn State University, Erie, PA 16563, USA
e-mail: srn3@psu.edu
URL: <https://behrend.psu.edu/person/sudarshan-rao-nelatury>

© The Author(s), under exclusive license to Springer Nature Singapore Pte Ltd. 2022
P. Kumar Jain et al. (eds.), *Advances in Signal Processing and Communication Engineering*, Lecture Notes in Electrical Engineering 929,
https://doi.org/10.1007/978-981-19-5550-1_1

cerned. If the size of a nanoparticle is too small, quantum effects play their role, but if it is small enough at optical and infrared wavelengths to render quasi-static analysis applicable, it is possible to develop a lumped circuit model for these particles. Today, the traditional techniques that were prevalent at microwave and millimeter wave are being scaled down to optical systems. Examples include lidar for detection of stationary or moving objects submerged under water, measurement of turbulence in airways and malignant tumors in biological tissues. Optical signals modulated at few GHz of frequencies as in lidar–radar promise superior performance in many ways compared to lidar. Examples of research works are, for instance [1], surfaces in the design and development of very complex tunable high-speed laser for frequency-chirped lidar–radar systems and other sophisticated applications.

Optical nanocircuits at subwavelength operations are being devised at a faster pace without the aid of mechanical steering, but solely incorporating electrical tuning. Typical functions include coupling mechanisms of various kinds, splitting and redirecting of power and so on [2].

We know that scattering from conducting spheres and multiply stratified media can be formulated and solved using the Mie formulation [3], which lays down a strong mathematical basis. Several authors succeeded in the use of full-wave analysis to determine scattering in case of a general anisotropic sphere possessing a radius of arbitrary magnitude. Although their work is quite exact, it is too rigorous to be understood by a common designer. There are quite a few numerical software tools commercially available; they prove to be an overkill for the simple object of circuit modeling or elucidating the terminal characteristics that reasonably represent interaction between an em wave and a nanoparticle. Expediency calls for simple closed-form expressions in terms of integrated quantities like terminal voltages and currents.

A quasi-static approach may well be adopted in case of a nanoparticle whose physical presence occupies smaller space compared to the wavelength of operation. Solution of Maxwell field equations, which in general is more complicated could be held in abeyance, and one might employ the stopgap of the lumped circuit theory [4]. The more exact solution involves dipole moments of higher order. But if we ignore all of them and pick just the dominant single dipole term, the resulting expressions have an accuracy that would be acceptable for majority of scenarios and applications. It permits lumped circuit formulation.

In this paper, we shall present the quasi-static field analysis considering an *anisotropic* dielectric particle in the form of a sphere of small radius. It is assumed that the sphere is exposed to a plane electromagnetic wave. First, we shall set up field vectors both inside and outside the sphere. The average effects of these fields obtained by integration from the bottom pole to the top pole of the nanosphere and also around the horizontal section of the sphere are used in defining terminal voltages and currents. These expressions constitute the basis for circuit modeling of nanospheres [4, 5].

When a dielectric nanosphere is illuminated by an incoming wave, dipole formation occurs described as dielectric polarization. It is reasonable to assume that the electric field inside the sphere is almost invariant and may be viewed as the field

averaged over the volume and arising from the bound charge inside the sphere. As for the region outside the sphere, in addition to the incident field, we might consider the bound charge as a single dipole placed at the center, and the field resulting from this can be added to the former.

The average dipole moment per unit volume determines the average induced field strength inside. The field of the incident uniform plane wave brings about almost constant polarization whose density might be assumed to arise from its dyadic transformation. Imposition of boundary conditions permits the determination of this dyadic. This transformation dyadic after all the mathematical simplification appears to be a straightforward generalization of the scalar value it has in case of a simple isotropic sphere.

Two simple numerical examples are included showing the angle of refraction suffered by the electric field vector. Assuming that the particle is made of a gyrotropic material in a static magnetic field, angles of refraction of field vector in the particle are shown to vary with the angle made by the magnetic field with the incident electric field vector. Just as how an isotropic nanosphere acts as a fixed resistor–capacitor or resistor–inductor nanocircuit depending on whether it is non-plasmonic or plasmonic [4, 5], an anisotropic nanosphere can be used to realize a multi-port or tunable circuit element [6, 7].

As for the notation, we shall employ an overbar to denote a vector, a hat for a unit vector, a double overbar to denote a dyadic and the identity dyadic by $\overline{\overline{I}}$.

2 Dielectric Anisotropy

Before we obtain expressions for the fields in case of a nanoparticle, let us provide a brief overview of dielectric anisotropy. This helps the reader to gain some physical insights. The constitutive properties of an isotropic medium do not depend on spatial direction, but that of an anisotropic medium do. In an isotropic medium, the electric flux density vector and the field intensity vector and, likewise, the magnetic flux density vector and magnetic field intensity are co-directional. On the other hand, there is an angle between these pairs of vectors in an anisotropic medium. Accordingly, their Cartesian components are related by dyadics. The Tellegen constitutive relations for an anisotropic medium are

$$\overline{D} = \overline{\overline{\epsilon}} \cdot \overline{E} \quad (1)$$

$$\overline{B} = \overline{\overline{\mu}} \cdot \overline{H} \quad (2)$$

In this work, let us consider only electric anisotropy and assume that $\overline{\overline{\mu}} = \mu \overline{\overline{I}}$. Dielectric anisotropy arises naturally on account of crystalline structure of materials, and depending on the values of the elements of the permittivity tensor $\overline{\overline{\epsilon}}$, it is said to be one of the hexagonal, isotropic, monoclinic, orthorhombic, tetragonal, triclinic,

trigonal systems [8–10]. The global properties of a materials can be represented in terms of the local properties with the aid of rotation dyadics. The permittivity dyadic has a general form given by

$$\bar{\bar{\epsilon}} = \epsilon_0 \bar{\bar{R}} \cdot (\epsilon_a \hat{x}\hat{x} + \epsilon_b \hat{y}\hat{y} + \epsilon_c \hat{z}\hat{z}) \cdot \bar{\bar{R}}^T \quad (3)$$

where the superscript T stands for transpose and

$$\bar{\bar{R}} = \bar{\bar{R}}_x \cdot \bar{\bar{R}}_y \cdot \bar{\bar{R}}_z \quad (4)$$

$$\bar{\bar{R}}_u = \left(\bar{\bar{I}} - \hat{u}\hat{u} \right) \cos(\theta_u) + \hat{u} \times \bar{\bar{I}} \sin(\theta_u) + \hat{u}\hat{u} \quad (5)$$

for $u = x, y, z$.

In the general case when $\epsilon_a \neq \epsilon_b \neq \epsilon_c$, $\bar{\bar{\epsilon}}$ is said to be biaxial. If $\epsilon_a = \epsilon_b$, it is uniaxial. A special case of anisotropy arises when the permittivity dyadic is uniaxial and also has an antisymmetric part. Such materials are said to be gyrotropic. Examples of gyrotropic media include ferrites such as Yttrium iron garnet (YIG) with chemical composition $Y_3Fe_2(FeO_4)_3$ or $Y_3Fe_5O_{12}$ [11] and magnetized plasmas [12]. In an unmagnetized plasma, the permittivity as a function of frequency is given by [10]

$$\epsilon(\omega) = \epsilon_0 \left(1 - \frac{\omega_p^2}{\omega(\omega - i\nu_c)} \right) \quad (6)$$

where $\omega_p = e \sqrt{\frac{n}{m\epsilon_0}}$ is the plasma frequency related to the electron charge e , mass m and the electron density n . The collision parameter ν_c arises due to damping and takes into account losses in the medium. If the average electron density is sparse, this number can be neglected. Suppose the plasma is subjected to a steady biasing magnetic field $\bar{B} = B \hat{g}$, the electrons suffer Lorentz force and begin to rotate about the magnetic field vector. The plasma then becomes uniaxial and nonreciprocal with antisymmetric components manifesting themselves. The permittivity dyad can be represented as:

$$\bar{\bar{\epsilon}} = \epsilon_0 \left(\epsilon_a \hat{g}\hat{g} + \epsilon_t (\bar{\bar{I}} - \hat{g}\hat{g}) - i\delta \hat{g} \times \bar{\bar{I}} \right). \quad (7)$$

where ϵ_a has the same expression as in (6) but ϵ_t and δ are now given by

$$\epsilon_t(\omega) = \epsilon_0 \left(1 - \frac{(\omega/\omega_p)^2 [1 + i\nu_c/\omega]}{[1 + i\nu_c/\omega]^2 - (\omega_b/\omega)^2} \right) \quad (8)$$

$$\delta = \epsilon_0 \left(\frac{(\omega/\omega_p)^2 (\omega_b/\omega)}{[1 + i\nu_c/\omega]^2 - (\omega_b/\omega)^2} \right) \quad (9)$$

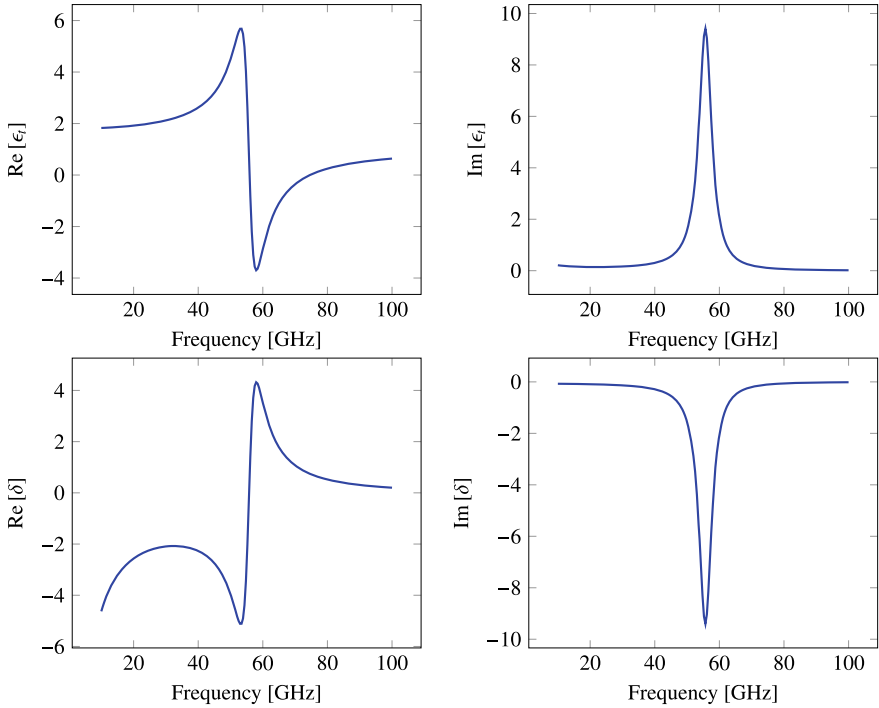


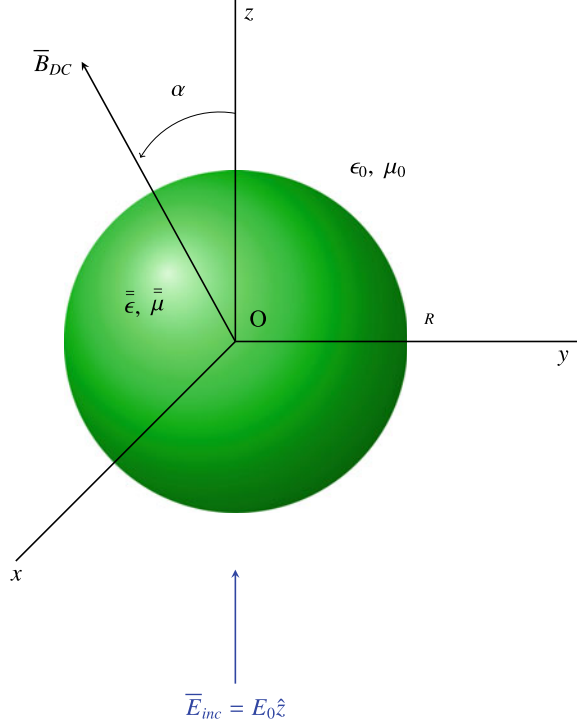
Fig. 1 Real and imaginary parts of ϵ_t and δ for $\omega_p = 2\pi \times 50 \times 10^9$ rad/s, $\omega_b = 3.5 \times 10^{11}$ rad/s, $\nu_c = 1.5 \times 10^{10}$

where $\omega_b = eB/m$, called the gyrofrequency. To illustrate the dispersive characteristics of elements of the permittivity dyadic, suppose we take the typical values: $\omega_p = 2\pi \times 50 \times 10^9$ rad/s, $\omega_b = 3.5 \times 10^{11}$ rad/s, $\nu_c = 1.5 \times 10^{10}$ and plot the real and imaginary parts of ϵ_t and δ , they appear to vary as shown in Fig. 1. Electromagnetic interaction of anisotropic nanoparticles at optical frequencies permits us to take lumped circuit theory to a whole new realm. Tunable circuit elements using gyrotropic particles was reported in [6]. In [13], we shall attempt to extend the ideas in [6] to general anisotropic dielectrics and show how coupling between two particles can be characterized.

3 Fields Internal and External to the Sphere

This section is adapted from the author's previous work [7]. Consider a nanosphere of radius R placed in free space with origin of coordinates at its center as shown in Fig. 2. Assume that the particle is illuminated by a time harmonic wave ($e^{-i\omega t}$ notation) with the electric field $\vec{E}_{\text{inc}} = \vec{E}_0 = E_0 \hat{z}$. Let the permittivity and permeability tensors of

Fig. 2 Anisotropic nanoparticle exposed to an incident wave $\vec{E}_{inc} = E_0 \hat{z}$. R is the radius of the sphere. Medium parameters of the sphere are shown as dyadics. The static magnetic field imparts gyroelectric behavior to the particle, and by varying the orientation angle α , the medium parameters can be varied



the particle be $\vec{\epsilon}$ and $\vec{\mu}$, respectively. As mentioned before, let us assume that $\vec{\mu} = \mu \vec{I}$. As a special case, the anisotropy might arise due to the gyrotropic characteristic of the nanosphere in the presence of a static magnetic field of density \vec{B} shown in Fig. 2 oriented at an elevation angle α .

The incident field causes dielectric polarization in the sphere. Let the polarization vector be \vec{P} . This is directly proportional to \vec{E}_0 , and we can use a scalar to represent the proportionality in case of an isotropic medium. But in an anisotropic medium, we are required to have a tensor. So for convenience, let

$$\vec{P} = 3\epsilon_0 \vec{\gamma} \cdot \vec{E}_0. \quad (10)$$

where $\vec{\gamma}$ is as yet unknown. If the volume of the sphere is $\tau = \frac{4}{3}\pi R^3$, the average dipole moment acting in the sphere is

$$\vec{p} = \tau \vec{P} \quad (11)$$

$$= 3\epsilon_0 \tau \vec{\gamma} \cdot \vec{E}_0 \quad (12)$$

$$= 4\pi\epsilon_0 R^3 \vec{\gamma} \cdot \vec{E}_0. \quad (13)$$

The electric field due to the dielectric polarization, averaged over the volume inside the sphere, can be obtained using the quasi-static model as long as the size of the nanosphere is smaller than the wavelength. Our derivation follows the analysis in [14] for an isotropic sphere, but considerably differs in the sense that we are considering an *anisotropic* sphere in this paper.

Let $\Phi(\bar{r})$ be the quasi-electrostatic potential arising due to a charge distribution $\rho(\bar{r}')$ given by

$$\Phi(\bar{r}) = \frac{1}{4\pi\epsilon_0} \iiint_{0 < r' < R} \frac{\rho(\bar{r}')}{|\bar{r} - \bar{r}'|} dv' \quad (14)$$

The volume averaged electric field due to the dielectric polarization \bar{E}_P is

$$\bar{E}_P = \frac{1}{\tau} \iiint_{0 < r < R} -\nabla\Phi(\bar{r}) dv \quad (15)$$

$$= \frac{-1}{\tau} \iint_{r=R} R^2\Phi(\bar{r}) \hat{r} d\Omega \quad (16)$$

$$= \frac{-R^2}{4\pi\epsilon_0\tau} \iiint_{0 < r' < R} \rho(\bar{r}') dv' \iint_{r=R} \frac{\hat{r} d\Omega}{|\bar{r} - \bar{r}'|} \quad (17)$$

where dv and $d\Omega$ denote differential volume and differential solid angle, respectively. In the case of a sphere, there exists azimuthal symmetry, and the reciprocal distance in (17) can be expressed as

$$\frac{1}{|\bar{r} - \bar{r}'|} = \sum_{\ell=0}^{\infty} \frac{r_{<}^{\ell}}{r_{>}^{1+\ell}} P_{\ell}(\hat{r} \cdot \hat{r}') \quad (18)$$

$$= 4\pi \sum_{\ell=0}^{\infty} \sum_{m=-\ell}^{\ell} \frac{1}{2\ell+1} \frac{r_{<}^{\ell}}{r_{>}^{1+\ell}} Y_{\ell m}^*(\theta', \phi') Y_{\ell m}(\theta, \phi) \quad (19)$$

where $P_{\ell}(\cdot)$ is the Legendre polynomial of order ℓ , $Y_{\ell m}(\theta, \phi)$ are spherical harmonics, $r_{<}$ is smaller of r and r' and likewise $r_{>}$ is the greater of them. When the surface integral in (17) is taken over the surface of the sphere, $r_{<} = r'$ and $r_{>} = R$. Further, expanding \hat{r} in rectangular components, we observe that orthogonality strikes off all the terms in the summation of (18) except the one corresponding to $\ell = 1$. This permits us to rewrite (17) as

$$\bar{E}_P = \frac{-R^2}{4\pi\epsilon_0\tau} \iiint_{0 < r' < R} \rho(\bar{r}') dv' \iint_{r=R} \frac{r'}{R^2} \bar{R} \cdot \hat{r}' d\Omega \quad (20)$$

where $\bar{\bar{R}} = \hat{r}\hat{r}$. Also, since

$$\iiint_{r=R} r' \bar{\bar{R}} \cdot \hat{r}' d\Omega = \frac{4\pi}{3} \bar{r}' \quad (21)$$

we can modify (20) as

$$\bar{E}_P = \frac{-1}{3\epsilon_0\tau} \iiint_{0 < r' < R} \bar{r}' \rho(\bar{r}') dv' \quad (22)$$

$$= -\frac{1}{3\epsilon_0} \bar{P} \quad (23)$$

$$= -\bar{\gamma} \cdot \bar{E}_0. \quad (24)$$

The polarization as seen from outside the sphere seems as if it were the field of a dipole, which from (13) is given by

$$\bar{E}_{\text{dip}} = \frac{3 \bar{\bar{R}} \cdot \bar{p} - \bar{p}}{4\pi\epsilon_0 r^3} \quad (25)$$

$$= \left(3 \bar{\bar{R}} \cdot \bar{\gamma} \cdot \bar{E}_0 - \bar{\gamma} \cdot \bar{E}_0 \right) \frac{R^3}{r^3}. \quad (26)$$

So now the total fields internal and external to the sphere are given by

$$\bar{E}_{\text{int}} = \bar{E}_0 + \bar{E}_P \quad (27)$$

$$= \bar{E}_0 - \bar{\gamma} \cdot \bar{E}_0 \quad (28)$$

$$\bar{E}_{\text{ext}} = \bar{E}_0 + \left(3 \bar{\bar{R}} \cdot \bar{\gamma} \cdot \bar{E}_0 - \bar{\gamma} \cdot \bar{E}_0 \right) \frac{R^3}{r^3}. \quad (29)$$

We can find $\bar{\gamma}$ using the boundary conditions. One might verify that the tangential component in the $\hat{\theta}$ direction is satisfied independent of $\bar{\gamma}$, but in order to meet the boundary condition on the normal component of the electric displacement density in the \hat{r} direction we require that

$$\hat{r} \cdot \bar{\epsilon} \cdot \bar{E}_{\text{int}} \Big|_{r=R} = \hat{r} \cdot \epsilon_0 \bar{I} \cdot \bar{E}_{\text{ext}} \Big|_{r=R} \quad (30)$$

where \bar{I} stands for the identity dyadic as mentioned at first. Using (28) and (29),

$$\hat{r} \cdot \bar{\epsilon} \cdot \left(\bar{E}_0 - \bar{\gamma} \cdot \bar{E}_0 \right) = \hat{r} \cdot \epsilon_0 \left(\bar{I} + 3 \bar{\bar{R}} \cdot \bar{\gamma} - \bar{\gamma} \right) \cdot \bar{E}_0 \quad (31)$$

$$= \hat{r} \cdot \left(\epsilon_0 \bar{I} + 2\epsilon_0 \bar{I} \cdot \bar{\gamma} \right) \cdot \bar{E}_0 \quad (32)$$

and rearranging terms,

$$\hat{r} \cdot \left\{ (\bar{\epsilon} - \epsilon_0 \bar{I}) - (\bar{\epsilon} + 2\epsilon_0 \bar{I}) \cdot \bar{\gamma} \right\} \cdot \bar{E}_0 = 0. \quad (33)$$

In the above, \hat{r} can be anywhere on the sphere and is arbitrary whereas, \bar{E}_0 is impressed from outside and does not depend on the medium. So it requires that

$$(\bar{\epsilon} - \epsilon_0 \bar{I}) - (\bar{\epsilon} + 2\epsilon_0 \bar{I}) \cdot \bar{\gamma} = \bar{\emptyset} \quad (34)$$

or

$$\bar{\gamma} = (\bar{\epsilon} + 2\epsilon_0 \bar{I})^{-1} \cdot (\bar{\epsilon} - \epsilon_0 \bar{I}) \quad (35)$$

where $\bar{\emptyset}$, needless to say, is the null dyadic. This is the *generalized Clausius–Mossotti transformation dyadic*. Next using the identity

$$(\bar{A} + \alpha \bar{I})^{-1} \equiv \left(\alpha^2 \bar{I} + \alpha(\bar{A}_t \bar{I} - \bar{A}) + \text{adj } \bar{A} \right) / |\bar{A}| \quad (36)$$

where the subscript t stands for the trace, one might readily verify that the members taking part in the dot product in (35) commute, so we might as well write equivalently,

$$\bar{\gamma} = (\bar{\epsilon} - \epsilon_0 \bar{I}) \cdot (\bar{\epsilon} + 2\epsilon_0 \bar{I})^{-1} \quad (37)$$

Equations (35) and (37) were earlier derived in another excellent paper [15] starting from Hall effect in an alternative manner. They can be equivalently expressed in terms of double products [16] as,

$$\bar{\gamma} = \frac{3(\bar{\epsilon} - \epsilon_0 \bar{I}) \cdot \left((\bar{\epsilon} + 2\epsilon_0 \bar{I}) \times (\bar{\epsilon} + 2\epsilon_0 \bar{I}) \right)^T}{\left((\bar{\epsilon} + 2\epsilon_0 \bar{I}) \times (\bar{\epsilon} + 2\epsilon_0 \bar{I}) \right) : (\bar{\epsilon} + 2\epsilon_0 \bar{I})} \quad (38)$$

where the superscript T denotes transpose. The symbols $:$ and \times stand for double dot and double crossproducts respectively. For the dyads $\bar{p}\bar{q}$ and $\bar{r}\bar{s}$, they can be written [16, 17] as

$$\bar{p}\bar{q} : \bar{r}\bar{s} = (\bar{p} \cdot \bar{r})(\bar{q} \cdot \bar{s}) \quad (39)$$

$$\bar{p}\bar{q} \times \bar{r}\bar{s} = (\bar{p} \times \bar{r})(\bar{q} \times \bar{s}) \quad (40)$$

$$\begin{aligned} &= (\bar{p} \times \bar{r}) \cdot (\bar{q} \times \bar{s}) \bar{I} + (\bar{p} \cdot \bar{s})\bar{q}\bar{r} + (\bar{r} \cdot \bar{q})\bar{s}\bar{p} \\ &\quad - (\bar{p} \cdot \bar{q})\bar{s}\bar{r} - (\bar{r} \cdot \bar{s})\bar{q}\bar{p} \end{aligned} \quad (41)$$

Substituting (35) or (37) in (28) and (29), we can obtain the quasi-static electric fields internal and external to the sphere. When specialized to ordinary isotropic case, all the expressions derived so far tally with those found in [14]. The associated magnetic fields can be found in a like manner. Suppose the sphere is magnetically isotropic with a permeability μ , in the present $e^{-i\omega t}$ notation, the magnetic fields are given by

$$\overline{H}_{\text{int}} = \frac{1}{i\omega} \mu^{-1} \cdot \nabla \times \overline{E}_{\text{int}} \quad (42)$$

$$\overline{H}_{\text{ext}} = \frac{1}{i\omega} \mu_0^{-1} \nabla \times \overline{E}_{\text{ext}}. \quad (43)$$

4 Angle(s) of Refraction

Now, we shall find the angle between the incident electric field $\overline{E}_{\text{inc}}$ and the field vector inside the sphere $\overline{E}_{\text{int}}$. The incident electric field vector $\overline{E}_{\text{inc}}$ is in the \hat{z} direction. Let the orientation of the field internal to the sphere be given in spherical coordinate system by the elevation and azimuthal angles (ϑ, φ) . Using Eq. (28), we can find these angles as

$$\vartheta = \cos^{-1} \left\{ \frac{1 - \gamma_{zz}}{\sqrt{\gamma_{xz}^2 + \gamma_{yz}^2 + (1 - \gamma_{zz})^2}} \right\} \quad (44)$$

$$\varphi = \tan^{-1} \left(\frac{\gamma_{yz}}{\gamma_{xz}} \right). \quad (45)$$

Next, we shall offer two simple numerical examples. The permeability is assumed to be μ_0 and the magnetic fields are not computed.

5 Numerical Examples

Example 1 Suppose the nanosphere is made of an anisotropic material whose permittivity dyadic has a general form given by (3)–(5). For the choice of values $\epsilon_a = 6$, $\epsilon_b = 4$, $\epsilon_c = 2$, $\theta_x = 60^\circ$, $\theta_y = 30^\circ$, $\theta_z = 45^\circ$, we get $\vartheta = 13.52^\circ$ and $\varphi = -4.1^\circ$. This choice is arbitrary and is meant to provide a numerical example. A yttrium iron garnet (YIG)-based particle has been used to realize a tunable lumped circuit element, and the variation of capacitance was reported by the author in [6].

Example 2 For a second example, let us consider a nanosphere made of gyroelectric material biased with a static magnetic field of flux density $\overline{B}_{DC} = B_{DC} \hat{g}$, where α

is the elevation angle. From Fig. 2, we note that $(\sin \alpha \hat{x} + \cos \alpha \hat{z})$ describes the orientation of the biasing field, so we shall write

$$(\sin \alpha \hat{x} + \cos \alpha \hat{z}) = \hat{g} \quad (46)$$

The permittivity dyadic of a gyrotropic particle has been expressed in (7) which, when substituted either in (35) or (37) or even in (38), we can obtain

$$\begin{aligned} \bar{\bar{\gamma}} = & [(\epsilon_t + 2\epsilon_0 + \epsilon_a - \epsilon_t) \{(\epsilon_t + 2\epsilon_0)(\epsilon_t - \epsilon_0) - \delta^2\} \bar{\bar{I}} \\ & - 3i\delta\epsilon_0(\epsilon_t + 2\epsilon_0 + \epsilon_a - \epsilon_t)\hat{g} \times \bar{\bar{I}} \\ & + 3\epsilon_0 \{ \delta^2 - (\epsilon_t + 2\epsilon_0)(\epsilon_a - \epsilon_t) \} \hat{g}\hat{g}] / \\ & [(\epsilon_t + 2\epsilon_0 + \epsilon_a - \epsilon_t) ((\epsilon_t + 2\epsilon_0)^2 - \delta^2)] \end{aligned} \quad (47)$$

Substituting (47) in (28) and performing significant simplification, we can get the field vector inside the sphere. For a choice of numerical values $E_0 = 1$, $B_{DC} = 1$, $\epsilon_a = 8$, $\epsilon_t = 1.5$, which are reasonably typical in a magnetized plasma or in some ferrite materials, we get

$$\bar{E}_{\text{int}} = -0.2786 \sin 2\alpha \hat{x} + 0.08571(3.5 + 6.5 \sin^2 \alpha) \hat{z}. \quad (48)$$

Note that δ is small in magnitude relatively; but in this numerical example for the purpose of plotting results, we set $\delta = 0$. For a visual display, the orientation of the total field inside the sphere and the incident field (which is in \hat{z} direction) are displaced in Fig. 3 as α is varied from 0 to π radians.

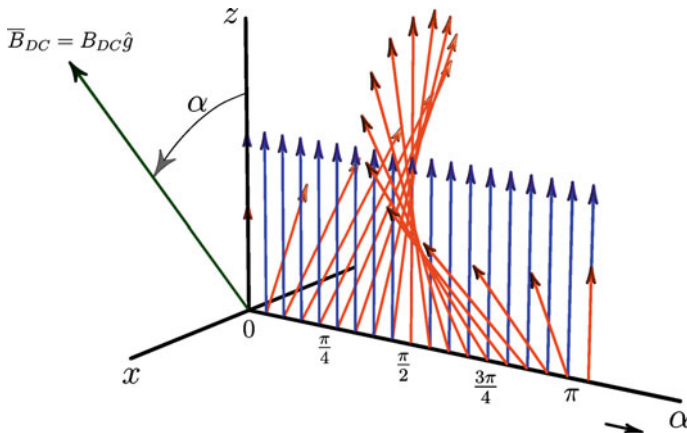


Fig. 3 Change in polarization inside the sphere compared to that of the incident wave as the DC biasing magnetic field is rotated from 0 to π . Magnitude of incident field vector is altered by a scale factor for clarity

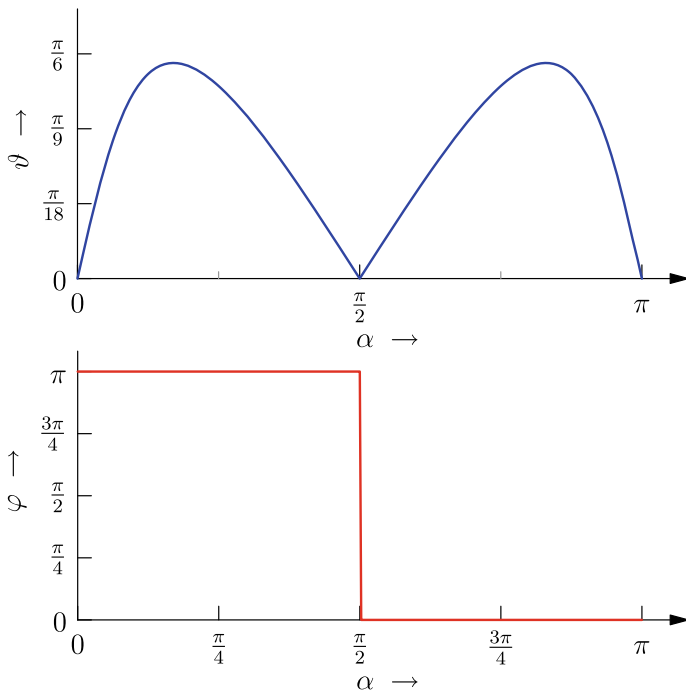


Fig. 4 Angles ϑ and φ as functions of α

For this example, we note that

$$\vartheta = \tan^{-1} \left[\left| \frac{3.2505 \sin 2\alpha}{(3.5 + 6.5 \sin^2 \alpha)} \right| \right] \quad (49)$$

$$\varphi = \begin{cases} \pi & \text{for } 0 < \alpha < \pi/2 \\ 0 & \text{for } \pi/2 < \alpha < \pi \end{cases} \quad (50)$$

and they vary as shown in Fig.4.

6 Conclusions

Nanoparticles and their interaction with em waves at infrared and optical frequencies have gained significant attention. Adequate research was done in case of isotropic nanospheres, but dielectric anisotropy did not receive the same degree of focus. This paper extended quasi-static analysis to anisotropic nanospheres.

A quasi-static analysis is made to find the fields inside and outside of an anisotropic nanosphere exposed to a plane wave. The radius of the sphere is assumed to be so

small compared to the wavelength of the incident wave that application of quasi-static modeling is permitted, but not exceedingly small in which case quantum effects kick in and invalidate the present analysis. The field vector undergoes refraction, and the angle(s) of refraction in spherical coordinates are given. In case of a gyrotropic sphere, how the angle of refraction changes with the orientation of biasing DC magnetic field is also plotted. The expressions for fields are useful for finding average voltage across, current through the nanosphere and impedance offered thereby. This is further discussed in the companion paper [13]. These are useful in nanocircuit modeling. While plasmonic and non-plasmonic isotropic nanospheres and combination(s) of nanohemispheres permit the nanocircuit design involving fixed circuit elements, multi-ports and tunable elements can be envisioned using anisotropic and gyrotropic nanospheres [6]. It is forecast that such nanocircuit elements would be useful to build adaptive nanosystems for smart applications including lidar–radar. Study of interaction of anisotropic particles with an incoming plane wave also helps in biological and agricultural research. The present paper attempted to apply the quasi-static approach that can yield reasonably accurate results.

Acknowledgements The author is grateful to Dr. N. Engheta for his guidance, support and kind hospitality at the Moore School of Electrical Engineering, University of Pennsylvania, Philadelphia. Also, he thanks Dr. A. Alù for his constructive feedback. A part of this paper is adapted from the author's previous publication [7], and permission was kindly granted by IEEE copyright clearance center's RightsLink service vide order# 5123350381408.

References

1. Li Y, Vieira AJC, Goldwasser SM, Herczfeld PR (2001) Rapidly tunable millimeter-wave optical transmitter for lidar-radar. *IEEE Trans Microw Theory Tech* 49:2048–2054
2. Huang KCY, Seo M-K, Sarmiento T, Huo Y, Harris JS, Brongersma ML (2014) Electrically driven subwavelength optical nanocircuits. *Nat Photon* 8:244–249
3. Stratton JA (1941) *Electromagnetic theory*. Wiley
4. Engheta N, Salandrino A, Alù A (2005) Circuit elements at optical frequencies: nanoinductors, nanocapacitors, and nanoresistors. *Phys Rev Lett* 95:095504-1–095504-4
5. Engheta N (2007) Circuits with light at nanoscales: optical nanocircuits inspired by metamaterials. *Science* 317:1698–1702
6. Nelatury S (2012) Tunable circuit elements at optical frequencies using gyro-electric nanoparticles. *JOSA B* 29:2685–2690
7. Nelatury S (2014) An anisotropic nanosphere in a uniform field. In: *Proceedings of IEEE Benjamin Franklin symposium on microwave and Antenna sub-systems for radar, telecommunications, and biomedical applications (BenMas)*, 26 Sept 2014
8. Nye JF (1985) *Physical properties of crystals*. Oxford University Press, Oxford
9. Fedorov FI (1968) *Theory of elastic waves in crystals*. Plenum Press, New York
10. Born M, Wolf E (1999) *Principles of optics*, 7th edn. Cambridge University Press, Cambridge
11. Gillies JR, Hlawiczka P (1976) TE and TM modes in gyrotropic waveguides. *J Phys D Appl Phys* 9:1315–1322
12. Hunsberger F, Luebbers R, Kunz K (1992) Finite-difference time-domain analysis of gyrotropic media-I: magnetized plasma. *IEEE Trans Antennas Propagat* 40(12):1489–1495

13. Nelatury S, Lumped Circuit Modeling at Nanoscale (Part-II: Coupling Between Two Nanospheres). In: Kumar Jain P et al. (eds) *Advances in Signal Processing and Communication Engineering, Lecture Notes in Electrical Engineering* 929. pp. 15–26. https://doi.org/10.1007/978-981-19-5550-1_2
14. Jackson JD (1999) *Classical electrodynamics*, 3rd edn. Wiley
15. Lakhtakia A, Varadan VK, Varadan VV (1991) Low-frequency scattering by an imperfectly conducting sphere immersed in a dc magnetic field. *Int J Infrared Millim Waves* 12:1253
16. Lindell IV (1992) *Methods for electromagnetic field analysis*. IEEE Press (Chapter 2)
17. Chen HC (1992) *Theory of electromagnetic waves—a coordinate-free approach*. McGraw-Hill (Chapter 1)

Lumped Circuit Modeling at Nanoscale (Part-II: Coupling Between Two Nanospheres)



Sudarshan R. Nelatury 

Abstract The equivalent circuit of a nanosphere illuminated by an em wave at optical frequencies can be obtained using the quasi-static analysis. In the companion paper fields, external and internal to a nanosphere were provided in case of a general anisotropic nanosphere as well as a gyroelectric nanosphere biased by a dc magnetic field. In this part, we shall first review how one might derive an equivalent circuit for an isolated nanosphere of small radius and extend the discussion to determine the coupling between two nanospheres in general made of anisotropic materials and provide an equivalent circuit for this arrangement. Note that the derivation in an earlier paper by Alu et al. involving isotropic nanospheres had a minor mathematical oversight, which is fixed in the present paper, and the correct expressions for the fields internal and external to the nanospheres and those coupling from one nanosphere to the other are provided. Further note that the present paper assumes anisotropic materials for the two nanospheres used to determine the coupling. As such, the expressions for currents induced comprise dyadic terms. These models are acceptable if quantum effects are not significant.

Keywords Anisotropic medium · Quasi-static model · Nanocircuits · Coupling between two nanospheres

1 Introduction

The mathematical and computational difficulties underlying the full-wave analysis of scattering by nanoparticles exposed to electromagnetic waves at optical and infrared frequencies have led to the development of lumped circuit theory. Under the assumptions that are valid for their physical size, modeling the nano particles using the well established circuit theory has been found to be effective. Engheta et al. [1,

S. R. Nelatury (✉)

Penn State University, Erie, PA 16563, USA

e-mail: srn3@psu.edu

URL: <https://behrend.psu.edu/person/sudarshan-rao-nelatury>

© The Author(s), under exclusive license to Springer Nature Singapore Pte Ltd. 2022
P. Kumar Jain et al. (eds.), *Advances in Signal Processing and Communication Engineering*, Lecture Notes in Electrical Engineering 929,
https://doi.org/10.1007/978-981-19-5550-1_2

15

2] have developed such circuit models and showed a new paradigm that has potential applications in diverse areas like, bio-photonics, nano-optics, biochemical signaling, optical data storage, etc. The validity of their circuit postulates was established when certain landmark parameters like plasmon resonances and filtering characteristics coincided with those obtained using rigorous theory [3]. In so far as the terminal behavior is concerned, by properly defining voltages and currents, the impedance values of these nanoparticles help us to predict the wave particle interaction with reasonable accuracy. Limitations of this approach arise when the size of the particle is extremely small compared to the wavelength and when quantum effects become significant.

In this paper, we shall review Engheta's equivalent circuit of a nanosphere of small radius illuminated by a plane electromagnetic wave. If a sphere is made up of two halves, such as one plasmonic and another nonplasmonic, it is possible to simulate series or parallel resonant circuits. The normal to the plane of intersection with reference to the orientation of incident electric field determines the topology. In the equivalent circuit proposed in [1] for series and parallel arrangement of hemispheres, loss element was ignored. In the present paper, we shall include it. Next, we shall extend to study the coupling between two nanospheres that are in general anisotropic. We find that the inter-particle separation influences the dependent sources forming the equivalent circuit.

Vectors are denoted by either boldface letters or a single overbar. A hat is used to indicate a unit vector, a double overbar to denote a dyadic. The identity dyadic is shown by $\overline{\overline{I}}$.

2 A Nanosphere in a Uniform Field

In this section, we shall review the lumped circuit formulation of Engheta et al. [1] for an isotropic sphere of radius R . Let it be placed at the origin of coordinate system and illuminated by an incident EM wave with a field $\overline{\overline{E}}_0 = E_0 \hat{z}$. Let us assume a time harmonic variation of $e^{-i\omega t}$. Let the sphere be isotropic and homogeneous for now and is characterized by a permittivity ϵ and permeability μ . Outside the sphere, we have free space. See Fig. 1 for the geometry.

The incident field polarizes the sphere and if we apply quasi-static analysis, we can assume that this polarization is due to a single dipole of moment \mathbf{p} . This is a reasonable approximation. Then, the fields outside the sphere would be the field due to this dipole $\overline{\overline{E}}_{\text{dip}}$ plus the incident field $\overline{\overline{E}}_0$; whereas, the fields inside the sphere would be a residual field $\overline{\overline{E}}_{\text{res}}$ plus the incident field $\overline{\overline{E}}_0$.

Following [4], we can express these fields as

$$\overline{\overline{E}}_{\text{int}} = \overline{\overline{E}}_0 + \overline{\overline{E}}_{\text{res}} \quad r < R \quad (1)$$

$$\overline{\overline{E}}_{\text{ext}} = \overline{\overline{E}}_0 + \overline{\overline{E}}_{\text{dip}} \quad r > R \quad (2)$$

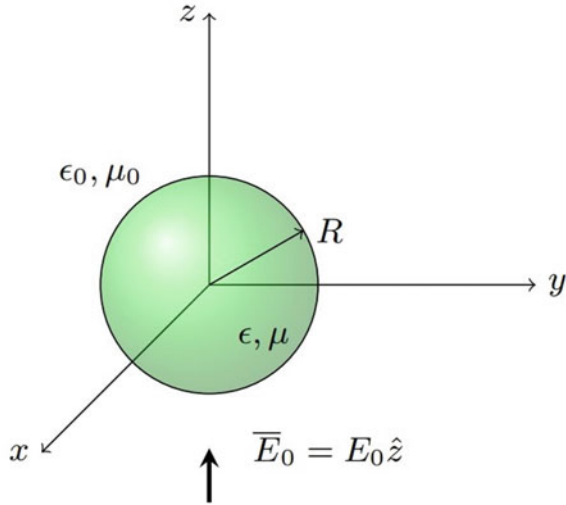


Fig. 1 A nanosphere illuminated by a plane wave

Substituting expressions for residual and the dipole fields,

$$\bar{E}_{\text{int}} = \bar{E}_0 + \left(\frac{\epsilon_0 - \epsilon}{2\epsilon_0 + \epsilon} \right) \bar{E}_0 \quad (3)$$

$$\bar{E}_{\text{ext}} = \bar{E}_0 + \frac{\left(3 \bar{R} \cdot \mathbf{p} - \mathbf{p} \right)}{4\pi\epsilon_0 r^3} \quad (4)$$

where

$$\mathbf{p} = \left(\frac{\epsilon - \epsilon_0}{\epsilon + 2\epsilon_0} \right) 4\pi\epsilon_0 R^3 \bar{E}_0 \quad (5)$$

$$\bar{R} = \hat{r} \quad (6)$$

Boundary condition on the normal component of the electric flux density yields

$$-i\omega(\epsilon - \epsilon_0)\bar{E}_0 \cdot \hat{n} = i\omega\epsilon\bar{E}_{\text{res}} \cdot \hat{n} - i\omega\epsilon_0\bar{E}_{\text{dip}} \cdot \hat{n} \quad (7)$$

Integrating the above over the upper hemisphere, we get terms which can be interpreted as currents that might be attributed as follows. The first term on the right is the current flowing in the sphere, and the second term represents the current fringing

out of the sphere due to the dipole formation. Thirdly, the term on the left is the impressed current due to the incoming wave. These are given below:

$$\underbrace{-i\omega(\epsilon - \epsilon_0)\pi R^2 E_0}_{I_{\text{imp}}} = \underbrace{-i\omega\epsilon\pi R^2 \left(\frac{\epsilon - \epsilon_0}{\epsilon + 2\epsilon_0}\right) E_0}_{I_{\text{sph}}} \underbrace{-i\omega\epsilon_0 2\pi R^2 \left(\frac{\epsilon - \epsilon_0}{\epsilon + 2\epsilon_0}\right) E_0}_{I_{\text{fringe}}} \quad (8)$$

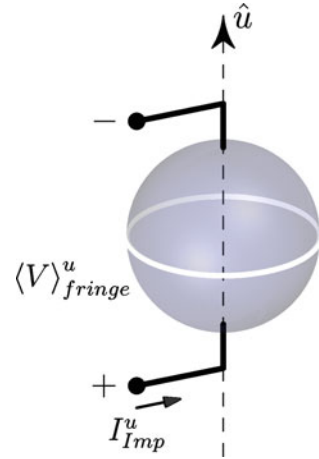
3 Terminal Behavior

In order to obtain the lumped equivalent circuit, we need to select two points on the sphere and designate the ports in a chosen direction [1]. This is shown in Fig. 2 in the direction \hat{u} , which in our case is \hat{z} . The terminal voltage is the average of integral of the electric field, and the current is the total displacement current from the lower hemisphere to the upper hemisphere.

Integrating \bar{E}_{res} along the vertical lines inside the sphere, we get the average voltage. Further, taking the ratio of voltage to current, we get the impedance. From the real and imaginary parts of the impedance, we can get the expressions for the lumped components forming the equivalent circuit.

$$\langle V \rangle_{\text{sph}} = \langle V \rangle_{\text{fringe}} = \left(\frac{\epsilon - \epsilon_0}{\epsilon + 2\epsilon_0}\right) R E_0 \quad (9)$$

Fig. 2 Port designation and terminal voltage and currents. Adapted from [5] with kind permission



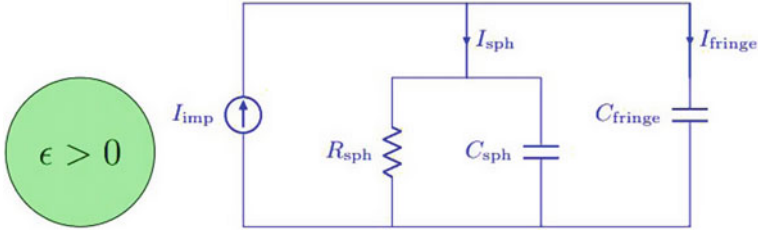


Fig. 3 Equivalent circuit of a nonplasmonic nanosphere ($\epsilon > 0$)

Taking the ratio of $\langle V \rangle_{\text{sph}}$ and I_{sph} , we get Z_{sph} and likewise, taking the ratio of $\langle V \rangle_{\text{sph}}$ and I_{fringe} , and we get Z_{fringe} . From the impedances, we can figure out the expressions for the circuit elements. Thus,

$$Z_{\text{sph}} = (-i\omega\epsilon\pi R)^{-1} \quad (10)$$

$$Z_{\text{fringe}} = (-i\omega 2\pi\epsilon_0 R)^{-1} \quad (11)$$

$$C_{\text{sph}} = \pi R \Re\{\epsilon\} \quad (12)$$

$$G_{\text{sph}} = \pi\omega R \Im\{\epsilon\} \quad (13)$$

$$C_{\text{fringe}} = 2\pi\epsilon_0 R \quad (14)$$

We can specialize the above for various cases. If the nanosphere is made of a nonplasmonic material, i.e., $\epsilon > 0$ as shown in Fig. 3, the equivalent circuit consists of C_{sph} , whereas, if it is made of plasmonic material in which case $\epsilon < 0$, as shown in Fig. 4, the equivalent circuit consists of L_{sph} . Further, we can construct parallel and series LC circuits by combining plasmonic and nonplasmonic hemispheres as shown in Figs. 5 and 6. Note that the components in these two cases have to be understood as those arising from hemispherical particles and more emphatically, we need to observe that these are lumped approximations to be validated by performing full-wave analysis. It is to be noted that the loss element R_{sph} is ignored in [1], but in this paper, we like to keep its presence as shown in Figs. 5 and 6.

It is worth mentioning a numerical example provided in [1]. If the nanosphere has a radius $R = 30$ nm, at a wavelength $\lambda_0 = 633$ nm, it is known that $\epsilon = (-19 + j0.53)\epsilon_0$. From (10) and (11), we can determine the lumped circuit component values as $L_{\text{sph}} = 7.12 \times 10^{-15}$ H = 7.12 femtoH, $G_{\text{sph}} = 1.32$ mS, $C_{\text{fringe}} = 1.67 \times 10^{-18}$ F = 1.67 attoF. On the other hand, if it is made of gold sulfide Au_2S , again with $R = 30$ nm, $\lambda_0 = 633$ nm, $\epsilon = 5.44\epsilon_0$, we find that $C_{\text{sph}} = 2.89$ attoF.

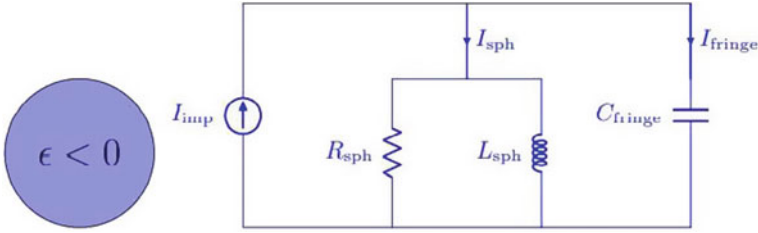


Fig. 4 Equivalent circuit of a plasmonic nanosphere ($\epsilon < 0$)

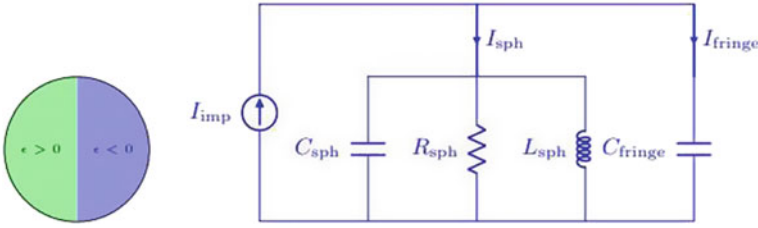


Fig. 5 Two hemispheres, nonplasmonic, and plasmonic, joined in parallel and their equivalent circuit

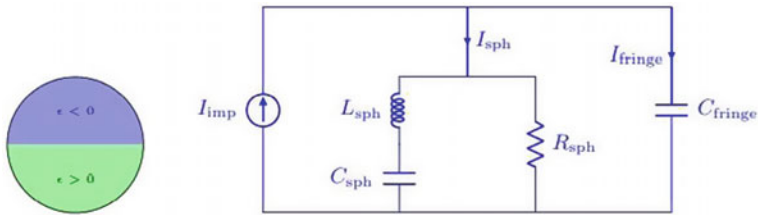


Fig. 6 Two hemispheres, nonplasmonic, and plasmonic, joined in series and their equivalent circuit

4 Coupling Between Two Anisotropic Nanospheres

Let us draw our attention to [5–7] for a brief review of fields obtained based on quasi-static analysis in case of a single anisotropic nanosphere. The paper by Lakhtakia [8] provides ideas based on Hall effect to obtain Clausius-Mossotti dyadic. Also relevant in this context are Refs. [4, 9, 10]. As an extension to the single isotropic nanosphere, in order to study the coupling between two general nanospheres, let us consider two different anisotropic nanospheres a and b of radii R_a and R_b , and permittivity tensors $\bar{\bar{\epsilon}}_a$ and $\bar{\bar{\epsilon}}_b$, respectively. Assume that their centers are separated by d meters. Let \hat{d} be a unit vector from the center of sphere a to that of sphere b . If an incident wave traveling in the xy -plane, excites these two spheres as shown in Fig. 7, we can express the fields and derive the coupling between the two. This problem for isotropic spheres was addressed by Alù et al. in [11]. Here, we shall extend

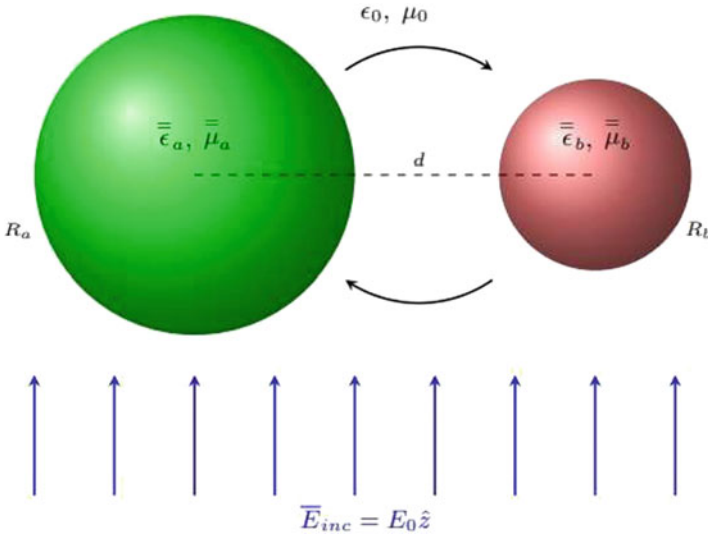


Fig. 7 Two nanospheres electromagnetically coupled. The incident wave $\bar{E}_{inc} = E_0 \hat{z}$

it for anisotropic case. Also, the authors did not provide mathematically accurate expressions due to a minor oversight. This paper fixes that.

Toward this, let us start with the generalized Clausius-Mossotti transformation dyadics corresponding to spheres a and b . Please refer to part I of this paper, i.e., [7] wherein the following make sense.

$$\bar{\gamma}_a = (\bar{\epsilon}_a + 2\epsilon_0 \bar{I})^{-1} \cdot (\bar{\epsilon}_a - \epsilon_0 \bar{I}) \quad (15)$$

$$\bar{\gamma}_b = (\bar{\epsilon}_b + 2\epsilon_0 \bar{I})^{-1} \cdot (\bar{\epsilon}_b - \epsilon_0 \bar{I}) \quad (16)$$

In terms of these, let us first express the fields internal and external to each sphere:

$$\bar{E}_{a \text{ int}} = 3\epsilon_0 (\bar{\epsilon}_a + 2\epsilon_0 \bar{I})^{-1} \cdot (\bar{E}_0 + \bar{E}_{ab}) \quad (17)$$

$$\bar{E}_{a \text{ ext}} = \bar{I} \cdot \bar{E}_0 + \frac{R_a^3}{r^3} (3 \bar{R} \cdot \bar{\gamma}_a - \bar{\gamma}_a) \cdot (\bar{E}_0 + \bar{E}_{ab}) \quad (18)$$

$$\bar{E}_{b \text{ int}} = 3\epsilon_0 (\bar{\epsilon}_b + 2\epsilon_0 \bar{I})^{-1} \cdot (\bar{E}_0 + \bar{E}_{ba}) \quad (19)$$

$$\bar{E}_{b \text{ ext}} = \bar{I} \cdot \bar{E}_0 + \frac{R_b^3}{r^3} (3 \bar{S} \cdot \bar{\gamma}_b - \bar{\gamma}_b) \cdot (\bar{E}_0 + \bar{E}_{ba}) \quad (20)$$

where

$$\bar{\bar{S}} = \hat{s}\hat{s} \quad (21)$$

$$\hat{s} = \frac{\bar{r} - \bar{d}}{|\bar{r} - \bar{d}|} \quad (22)$$

Here, the field vectors \bar{E}_{ab} and \bar{E}_{ba} are components coupling from a to b and vice versa. Denoting $\bar{\bar{D}} = \hat{d}\hat{d}$, we can write

$$\bar{E}_{ab} = \bar{E}_{b\text{ext}}|_{r=0} = \bar{\bar{I}} \cdot \bar{E}_0 + \frac{R_b^3}{d^3} \left(3 \bar{\bar{D}} \cdot \bar{\gamma}_b - \bar{\gamma}_b \right) \cdot (\bar{E}_0 + \bar{E}_{ba}) \quad (23)$$

which yields

$$\begin{aligned} d^3 \bar{\bar{I}} \cdot \bar{E}_{ab} - R_b^3 \left(3 \bar{\bar{D}} \cdot \bar{\gamma}_b - \bar{\gamma}_b \right) \cdot \bar{E}_{ba} \\ = \left[d^3 \bar{\bar{I}} + R_b^3 \left(3 \bar{\bar{D}} \cdot \bar{\gamma}_b - \bar{\gamma}_b \right) \right] \cdot \bar{E}_0 \end{aligned} \quad (24)$$

Likewise,

$$\bar{E}_{ba} = \bar{E}_{a\text{ext}}|_{r=d} = \bar{\bar{I}} \cdot \bar{E}_0 + \frac{R_a^3}{d^3} \left(3 \bar{\bar{D}} \cdot \bar{\gamma}_a - \bar{\gamma}_a \right) \cdot (\bar{E}_0 + \bar{E}_{ab}) \quad (25)$$

which yields

$$\begin{aligned} -R_a^3 \left(3 \bar{\bar{D}} \cdot \bar{\gamma}_a - \bar{\gamma}_a \right) \cdot \bar{E}_{ab} + d^3 \bar{\bar{I}} \cdot \bar{E}_{ba} \\ = \left[d^3 \bar{\bar{I}} + R_a^3 \left(3 \bar{\bar{D}} \cdot \bar{\gamma}_a - \bar{\gamma}_a \right) \right] \cdot \bar{E}_0 \end{aligned} \quad (26)$$

In order to obtain \bar{E}_{ab} and \bar{E}_{ba} , we need to solve the system,

$$\begin{bmatrix} \bar{E}_{ab} \\ \bar{E}_{ba} \end{bmatrix} = \begin{bmatrix} \bar{\bar{T}}_{aa} & \bar{\bar{T}}_{ab} \\ \bar{\bar{T}}_{ba} & \bar{\bar{T}}_{bb} \end{bmatrix}^{-1} \begin{bmatrix} \bar{U}_a \\ \bar{U}_b \end{bmatrix} \quad (27)$$

where

$$\bar{\bar{T}}_{aa} = d^3 \bar{\bar{I}} \quad (28)$$

$$\bar{\bar{T}}_{ab} = -R_b^3 \left(3 \bar{\bar{D}} \cdot \bar{\gamma}_b - \bar{\gamma}_b \right) \quad (29)$$

$$\bar{\bar{T}}_{ba} = -R_a^3 \left(3 \bar{\bar{D}} \cdot \bar{\gamma}_a - \bar{\gamma}_a \right) \quad (30)$$

$$\bar{\bar{T}}_{bb} = d^3 \bar{\bar{I}} \quad (31)$$

$$\bar{U}_a = \left[d^3 \bar{I} + R_b^3 \left(3 \bar{D} \cdot \bar{\gamma}_b - \bar{\gamma}_b \right) \right] \cdot \bar{E}_0 \quad (32)$$

$$\bar{U}_b = \left[d^3 \bar{I} + R_a^3 \left(3 \bar{D} \cdot \bar{\gamma}_a - \bar{\gamma}_a \right) \right] \cdot \bar{E}_0 \quad (33)$$

and one obtains

$$\bar{E}_{ab} = \left(\bar{T}_{ab}^{-1} \bar{T}_{aa} - \bar{T}_{bb}^{-1} \bar{T}_{ba} \right)^{-1} \cdot \left(\bar{T}_{ab}^{-1} \cdot \bar{U}_a - \bar{T}_{bb}^{-1} \cdot \bar{U}_b \right) \quad (34)$$

$$\bar{E}_{ba} = \left(\bar{T}_{aa}^{-1} \bar{T}_{ab} - \bar{T}_{ba}^{-1} \bar{T}_{bb} \right)^{-1} \cdot \left(\bar{T}_{aa}^{-1} \cdot \bar{U}_a - \bar{T}_{ba}^{-1} \cdot \bar{U}_b \right) \quad (35)$$

Equivalent circuit representing an isolated sphere placed in an incident field was described in [1]. The incident field forces an impressed current in the sphere. Part of this is found to flow in the sphere while the remaining fringes into the space as dipolar current. When there are two spheres placed a small distance apart, the coupling between them is accounted for by placing dependent current sources due to the coupling fields, in parallel to the impressed currents that are due to the incident field. Equivalent circuit representing two spheres placed a small distance apart was shown in [11]. The circuit is generalized in this paper and is re-depicted in Fig. 8. As mentioned earlier in this paper about the designation of ports for the nanoparticle, one might select the ports in various directions. Accordingly, the terminal voltages and currents are found. The paper by Alù et al. [11] has an oversight in the simplification of field expressions and also it does not consider anisotropy of the nanoparticles. But from the details furnished in [5, 6], we can obtain the equivalent circuit elemental values, which may be specialized in a straight forward manner. For the present choice of port designations, the terminal voltages and currents can be obtained in the following way. Voltage across the nanosphere a is

$$\langle \bar{V} \rangle_{a \text{ fr}} = \bar{\gamma} \cdot \bar{E}_0 R_a \quad (36)$$

and that across the nanosphere b is

$$\langle \bar{V} \rangle_{b \text{ fr}} = \bar{\gamma} \cdot \bar{E}_0 R_b \quad (37)$$

The impressed current $I_{a \text{ imp}}$ is given by

$$I_{a, \text{imp}} = -i\omega \left(\bar{\epsilon}_a + 2\epsilon_0 \bar{I} \right) \cdot \int_{\phi=0}^{2\pi} \int_{\theta=0}^{\pi/2} \bar{\gamma}_a \cdot \bar{E}_0 \cdot \hat{r} R_a^2 d\Omega \quad (38)$$

and $I_{b \text{ imp}}$ is given by

$$I_{b,\text{imp}} = -i\omega \left(\bar{\epsilon}_b + 2\epsilon_0 \bar{I} \right) \cdot \int_{\phi=0}^{2\pi} \int_{\theta=0}^{\pi/2} \bar{\gamma}_b \cdot \bar{E}_0 \cdot \hat{r} R_b^2 d\Omega \quad (39)$$

where $d\Omega = \sin \theta d\theta d\phi$ is the differential solid angle. Likewise the fringe currents are given by

$$I_{a\text{ fr}} = (-i\omega\epsilon_0) \int_{\phi=0}^{2\pi} \int_{\theta=0}^{\pi/2} 2 \bar{\gamma}_a \cdot \bar{E}_0 \cdot \hat{r} R_a^2 d\Omega \quad (40)$$

$$I_{b\text{ fr}} = (-i\omega\epsilon_0) \int_{\phi=0}^{2\pi} \int_{\theta=0}^{\pi/2} 2 \bar{\gamma}_b \cdot \bar{E}_0 \cdot \hat{r} R_b^2 d\Omega \quad (41)$$

Next, the currents in each sphere become

$$I_{a\text{ sph}} = (-i\omega \bar{\epsilon}_a) \int_{\phi=0}^{2\pi} \int_{\theta=0}^{\pi/2} \bar{\gamma}_a \cdot \bar{E}_0 \cdot \hat{r} R_a^2 d\Omega \quad (42)$$

$$I_{b\text{ sph}} = (-i\omega \bar{\epsilon}_b) \int_{\phi=0}^{2\pi} \int_{\theta=0}^{\pi/2} \bar{\gamma}_b \cdot \bar{E}_0 \cdot \hat{r} R_b^2 d\Omega \quad (43)$$

The effect of coupling is denoted by dependent current sources. They are similar to the impressed currents shown earlier but with the electric fields replaced accordingly. They are given by

$$I_{ab,\text{imp}} = -i\omega \left(\bar{\epsilon}_a + 2\epsilon_0 \bar{I} \right) \cdot \int_{\phi=0}^{2\pi} \int_{\theta=0}^{\pi/2} \bar{\gamma}_a \cdot \bar{E}_{ab} \cdot \hat{r} R_a^2 d\Omega \quad (44)$$

and $I_{b\text{ imp}}$ is given by

$$I_{ba,\text{imp}} = -i\omega \left(\bar{\epsilon}_b + 2\epsilon_0 \bar{I} \right) \cdot \int_{\phi=0}^{2\pi} \int_{\theta=0}^{\pi/2} \bar{\gamma}_b \cdot \bar{E}_{ba} \cdot \hat{r} R_b^2 d\Omega \quad (45)$$

Evaluating the above integrals and taking the ratios of currents to the corresponding voltages yield values of admittance components in the equivalent circuits. We have not given any numerical values, but from the material data pertaining to each nanosphere, this calculation is straight forward.

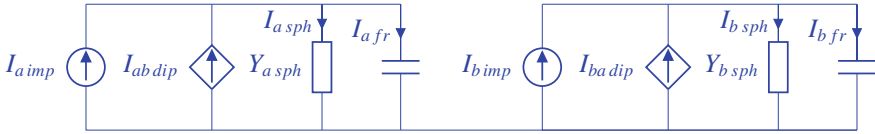


Fig. 8 Equivalent circuit representing the coupling between two anisotropic nanospheres

The elements $Y_{a\ sph}$ and $Y_{b\ sph}$ are rather general and have directional interpretation [5]. More interestingly, they are subject to variation in the presence of a static magnetic field if the particles exhibit gyrotropy. When the spheres have anisotropy, expressions for the coupled fields appear too formidable. However, the foregoing expression for (34) and (35) and those of the dyadic members involved therein might be numerically evaluated to determine the internal polarization and obtain the equivalent circuit parameters quantitatively. More work is necessary to undertake such computations and to verify the same experimentally.

5 Conclusions

Lumped circuit formulation of nanoparticles as introduced by Engheta for an isolated isotropic nanosphere has been reviewed. The ideas used in case of isotropic nanospheres can be extended to anisotropic media. We have shown that the use of a dyadic transformation of the electric field helps us to generalize this. Variable circuit elements can be realized using gyrotropic materials. Analysis of quasi-static fields and of the coupling between nanospheres in close proximity is discussed. An equivalent circuit that models them is obtained. These are useful in nanocircuit modeling. While plasmonic and non-plasmonic isotropic nanospheres and combination(s) of nanohemispheres permit the nanocircuit design involving fixed circuit elements, multi-ports and tunable elements can be envisioned using anisotropic and gyrotropic nanospheres. It is forecast that such nanocircuit elements would be useful to build adaptive nanosystems for smart applications including lidar-radar. Study of interaction of anisotropic particles with an incoming plane wave also helps in biological and agricultural research.

References

1. Engheta N, Salandrino A, Alù A (2005) Circuit elements at optical frequencies: nanoinductors, nanocapacitors, and nanoresistors. *Phys Rev Lett* 95:095504-1–095504-4
2. Engheta N (2007) Circuits with light at nanoscales: optical nanocircuits inspired by metamaterials. *Science* 317:1698–1702
3. Bohren CF, Huffman DR (1983) Absorption and scattering of light by small particles. Wiley, New York

4. Jackson JD (1999) Classical electrodynamics, 3rd edn. Wiley
5. Nelatury S (2012) Tunable circuit elements at optical frequencies using gyro-electric nanoparticles. *JOSA B* 29:2685–2690
6. Nelatury S (2014) An anisotropic nanosphere in a uniform field. In: Proceedings of IEEE Benjamin Franklin symposium on microwave and antenna sub-systems for radar, telecommunications, and biomedical applications (BenMas)
7. Nelatury S, Lumped circuit modeling at nanoscale (part-I: dielectric anisotropy). In: Kumar Jain P et al. (eds) *Advances in signal processing and communication engineering, lecture notes in electrical engineering* 929, pp1–14. https://doi.org/10.1007/978-981-19-5550-1_1
8. Lakhtakia A, Varadan VK, Varadan VV (1991) Low-frequency scattering by an imperfectly conducting sphere immersed in a dc magnetic field. *Int J Infrared Millim Waves* 12:1253
9. Lindell IV (1992) *Methods for electromagnetic field analysis*. IEEE Press (Chapter 2)
10. Chen HC (1992) *Theory of electromagnetic waves—a coordinate-free approach*. McGraw-Hill (Chapter 1)
11. Alù A, Salandrino A, Engheta N (2007) Coupling of optical lumped nanocircuit elements and effects of substrates. *Opt Express* 15:13865–13876

Deep Learning Model for Multiclass Classification of Diabetic Retinal Fundus Images Using Gradient Descent Optimization



Ram Krishn Mishra

Abstract Multiclass classification of diabetic retinal fundus images is a challenging task for classical methods due to presence of non-linear patterns in the images. Non-linearity in the shape and structure of blood vessels causes loss of crucial information used in accurate diagnosis of the disease. Hence, machine learning models became more prominent with high accuracy and speed of disease diagnosis. However, the efficacy of these methods largely depends on the feature extraction models. Convolutional neural networks (CNNs) provide solution to these difficulties by incorporating both feature extraction and classification in a single architecture. This work presents a gradient-descent (GD)-based optimization in CNN classifier that improves both speed and accuracy of classification. Experiments conducted on Kaggle, DRIVE, and STARE datasets, and the results are compared to the existing methods. The proposed approach shows a false positive rate (FPR) of 0.00075, specificity of 100%, precision of 99.9%, recall rate of 99.75%, and F_1 -score of 99.99%.

Keywords Diabetic retinopathy · Medical image classification · Gradient descent · Convolutional neural networks · Optimization

1 Introduction

1.1 Motivation

Diabetic retinopathy (DR) is a chronic medical disorder usually appear in patients with diabetes. According to the World health organization (WHO) [11], up to 80% of population over 20 years who have diabetes are more prone to DR and are responsible for 4.8% of blindness globally. Also, in at least 90% newly affected cases, the DR could be cured thorough proper monitoring and treatment of eyes. Fundus imaging is a non-invasive, and safer optical imaging mechanism gives high-resolution images

R. K. Mishra (✉)

Department of Computer Science, BITS Pilani Dubai Campus, Dubai International Academic City, Dubai 345055, UAE

e-mail: rkmishra@dubai.bits-pilani.ac.in

© The Author(s), under exclusive license to Springer Nature Singapore Pte Ltd. 2022

P. Kumar Jain et al. (eds.), *Advances in Signal Processing and Communication Engineering*, Lecture Notes in Electrical Engineering 929,

https://doi.org/10.1007/978-981-19-5550-1_3

of eye retina and widely using by ophthalmologists across the world to diagnose DR [7]. Manual analysis of these images is time consuming, sometimes difficult for a physician to understand certain tissues due to similarity in nature.

Feature extraction methods reduce the dimensionality of data present in the high-resolution images and gives the best features in the image. These features used as bio-markers to train the artificial neural networks (ANNs) classifiers to segment the data either into binary classification (positive/negative) or multiclass classification. In general, DR images can be classified into non-proliferative DR (NPDR) and proliferative DR (PDR). NPDR is a condition which can be reduced without the need of a surgery through early detection and proper medication. On the other hand, proliferative DR (PDR) is a severe stage of the disease and cannot be recovered even by surgery, if delayed. This makes the early detection of the disease as a preventive measure. However, early diagnosis is a tough task for the physicians to estimate the exact cause of certain lesions present in the patient's eye. To overcome these difficulties, authors proposed various classical, ANNs, and deep learning models and attained better accuracy across datasets available at various sources.

1.2 Related Works

Multiclass classification methods basically use the blood vessels, micro-aneurysms (MAs), haemorrhage, and exudates as bio-markers. Yelampalli et al. presented a gradient operator and morphological processing based blood vessel segmentation approach to classify the retinal fundus images using statistical models. The experimentation is conducted by taking blood vessel area and circumference of the optic disc as bio-markers. In another ANN-based approach, the same features of the retinal images are used for classification and attained better accuracy. Every ANN-based approach requires the feature extraction, and these features are used train, evaluate, and test the classifier. Extracting robust features with low-dimensionality is a challenging task due to the fear of loss of crucial information. Among the various models proposed, k -nearest neighbours (k -NN), Gaussian mixture model (GMM), AdaBoost, and support vector machines are more popular and widely accepted by the research community.

With the introduction of deep learning models, where the CNNs do not require any feature extraction before being applied data to the classifier. CNNs obtained better accuracy and speed compared to classical ANNs that has driven the researchers to work on these models. Lesions such as exudate area, blood vessel area, entropy, and texture histograms are used as features in [6]. Even though this work attained better accuracy than the existing ANNs and other CNN models, the classifier was more complex and time consuming. Pratt et al. performed diagnosis and severity classification using a CNN model by validating 5000 images. This method attained the accuracy of 75% but displayed better speed [8]. Further, Huang et al. have used a multilayer perceptron (MLP) feed forward network that consists of one input, hidden, and out layers each. Usage of single perceptron layer drastically reduced the complexity of

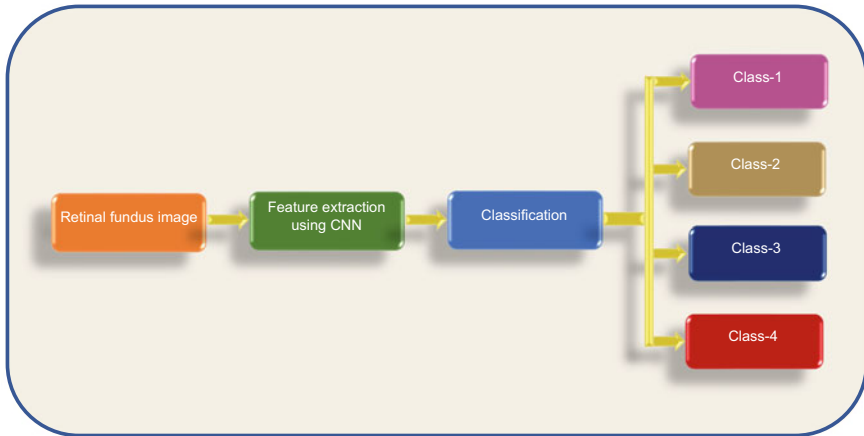


Fig. 1 Overview of the proposed work

the model, but the efficiency has declined significantly [5]. Gavin [2] addressed the problem of curve-fitting in non-linear least squares using the Levenberg-Marquardt algorithm. He had simulated various non-linear problems and the MATLAB[®] sources available on his Web page.

A complete pack of machine learning (ML) project titled diabetic retinopathy analysis using machine learning (DREAM) was proposed and publicly released by [9] in 2014. This had paved a path to many prospective researchers to work on ML approaches to DR-related applications. Support vector machines proven to be effective for low-dimensional data problems and used for multiclass classification of retinopathy images by [10]. SVMs provide an accuracy of 95% with datasets of lower dimension and lesser efficacy with all other high-resolution images data. Yang et al. [12] have used two-stage CNNs for the segmentation and diagnosis of DR images and obtained an accuracy of 97.2%. Further, Gayathri et al. [3] proposed a light-weight model whose major focus was on computational speed and attained better results across various datasets. In a recent work of Yaqoob et al., [13] used a random forest model and ResNet-based deep features are taken into consideration for classifying multiple fundus images. This work is partly based on the algorithms proposed by Fokas et al. [1] for the prediction of number of individuals are to be affected by SARS-Cov-2. However, these methods have practical implications such as dimensionality problem, curve-fitting for non-linear models, computational speed, and accuracy. These limitations in the existing works are the primary focus of the current method and verified with retinal fundus images of various databases and obtained better results in terms of accuracy, FPR, specificity, and F_1 -score.

The subsequent sections of the article organized as follows. Next section discusses the materials and methodologies used in the present work, followed by portrayal of results and discussions on various models. A concise analysis of the methods used in the manuscript presented in conclusion with a possible extension to this work.

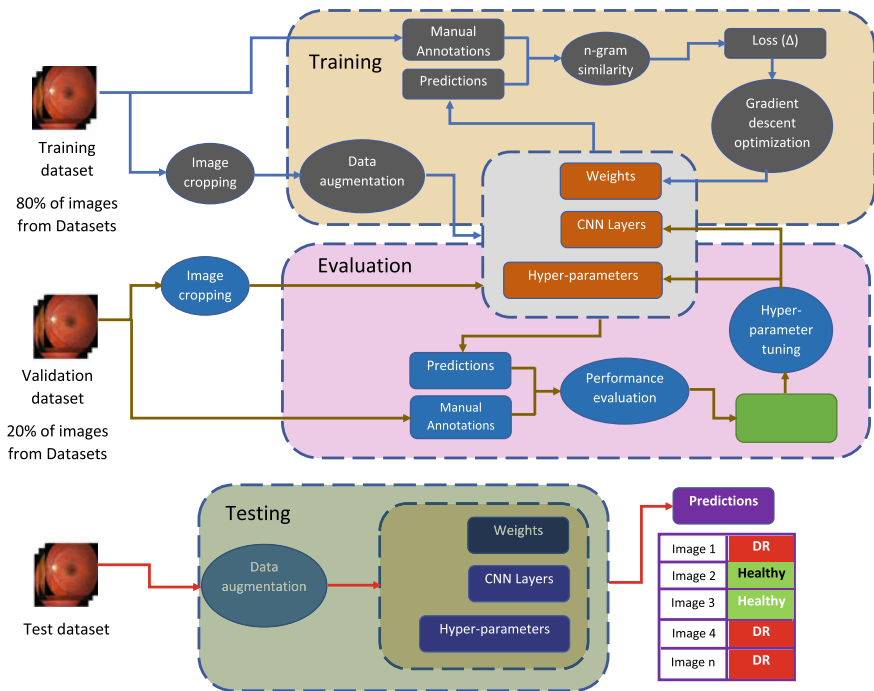


Fig. 2 Schematic workflow used in the proposed method

2 Materials and Methodology

An outline of the steps involved in the proposed work is shown in Fig. 1. As discussed in earlier section, the image datasets are directly fed to a CNN network, that has multiple layers, such as input layer, convolutional layer, hidden layers, and output layer. Figure 2 illustrates a detailed work flow of the methods used in our methodology. It consists of 3-tier analysis, namely training, evaluation, and testing. As shown in Fig. 2, 80% of available images in the dataset are used for training the CNN classifier, 20% used for evaluation of the accuracy of the training process, and several random images from different datasets are applied to the classifier for the classification. This work categorizes each given image into any of normal, mild, moderate, or severe. A gradient descent optimizer is used to generate the strong features from the applied image and verified with the features which are annotated manually by the expert physicians. Errors, if any, will be propagated back to the input to adjust the weights.

Gradient Descent Gill and Murry [4] proposed effective algorithms to minimize the sum of squares of non-linear functions

$$F(x) = \sum_{i=1}^m [f_i(x)]^2, \quad x \in E^n, \quad m \geq n. \quad (1)$$

The Hessian matrix $G(x)$ of $F(x)$ and the gradient vector $g(x)$ can be written as $2(J(x)^T J(x) + B(x))$ and $2J(x)^T f(x)$, respectively. Here, $J(x)$ is the $m \times n$ Jacobian matrix of $f(x)$, the i th row of $f(x)$ is $\nabla f_i(x) = (\partial f_i / \partial x_1, \partial f_i / \partial x_2, \dots, \partial f_i / \partial x_n)$ and $B(x) = \sum_{i=1}^m f_i(x) G_i(x)$, and $G_i(x)$ is the Hessian matrix of $f_i(x)$.

Hidden Layer Single hidden layer is used of the form

$$m_i(n_i) = (1 + e^{-n_i})^{-1} \quad (2)$$

m_i is the output of the node i , and n_i is the weighted sum of the input synapses. The error at any node can be computed using

$$\Delta_j(n) = a_j(n) - m_j(n) \quad (3)$$

where $a_j(n)$ and $m_j(n)$ are the actual and predicted values as depicted in Fig. 2. In order to minimize the error $\Delta_j(n)$, the weights have to be adjusted, and new weight at each node is

$$\sigma(n) = \frac{1}{2} \sum_j [e_j^2(n)] \quad (4)$$

and new weights are

$$\omega_{ji}(n) = -\gamma \frac{\partial \sigma(n)}{\partial_j(n)} m_i(n) \quad (5)$$

3 Results and Discussion

Retinal fundus images have been collected from various publicly available databases as listed below.

- **Kaggle**: Consists of 88,702 high-resolution images ranging from 433×289 pixels to 5184×3456 pixels, captured from different cameras, and the images are manually classified into five DR stages.
- **DRIVE**: DRIVE is openly available to public consisting of 40 images acquired at a 45° FOV with 565×584 pixels resolution.
- **STARE**: This is also open to public includes 20 images acquired at a 35° FOV. The size of each image is 700×605 pixels.

In this paper, the comparison tables are not included for STARE and DRIVE datasets due to insufficient availability of images on each dataset. Nonetheless, the numerical values are presented below (Table 1).

The MLP method shown comparatively better performance on DRIVE and STARE datasets since the sample size is too small in addition, these images are

Table 1 Confusion matrices of all the algorithms on Kaggle dataset

	Normal	Mild_NPDR	Mod_NPDR	Seve_NPDR	PDR
<i>(a) SVM</i>					
Normal	25,716	0	71	23	0
Mild_NPDR	0	2365	78	0	0
Mod_NPDR	75	71	5146	0	0
Seve_NPDR	421	0	0	447	5
PDR	52	0	0	634	22
<i>(b) Random forest</i>					
Normal	25,810	0	0	0	0
Mild_NPDR	0	2440	3	0	0
Mod_NPDR	1	0	5291	0	0
Seve_NPDR	29	0	0	840	4
PDR	10	0	0	12	686
<i>(c) MLP</i>					
Normal	25,772	0	38	0	0
Mild_NPDR	0	2380	63	0	0
Mod_NPDR	47	51	5194	0	0
Seve_NPDR	873	0	0	0	0
PDR	708	0	0	0	0
<i>(d) J48</i>					
Normal	25,809	0	0	1	0
Mild_NPDR	0	2442	1	0	0
Mod_NPDR	1	0	5291	0	0
Seve_NPDR	0	0	0	872	1
PDR	0	0	0	0	708
<i>(e) GD</i>					
Normal	25,810	0	0	0	0
Mild_NPDR	1	2442	0	0	0
Mod_NPDR	0	0	5292	0	0
Seve_NPDR	0	0	0	873	0
PDR	0	0	0	0	708

of low-resolution. MLP achieved FPR of 0.73% and 1.22%, specificity of 99% and 94.5%, precision of 97.8% and 94.1%, and F_1 -score of 98% and 98.6%, respectively. But, from Table 2, it is evident that any single hidden layer models are unfit for large datasets and seldom result in poor performance.

In Table 1, except J48 and the proposed models, rest of the methods have poor accuracy in classifying the images into five categories. It can be observed, most the positive cases have falsely recognized as NORMAL, that affects the false negative rate (FNR) of the algorithm. It is also observed that both J48 and GD have shown

Table 2 Evaluation metrics comparison on Kaggle dataset

Classifier	FPR (%)	Specificity (%)	Accuracy (%)	F_1-score (%)	Class
SVM	5.9	94.1	97.9	98.8	Normal
	0.2	99.8	97.1	96.9	Mild_NPDR
	0.5	99.5	97.2	97.2	Mod_NPDR
	1.9	98.1	51.2	45.2	Seve_NPDR
	0	100	3.1	6	PDR
Random forest	0.4	99.6	99.8	99.9	Normal
	0	100	100	99.9	Mild_NPDR
	0	100	99.9	100	Mod_NPDR
	0	100	98.6	97.4	Seve_NPDR
	0	100	99.4	98.1	PDR
MLP	17.5	82.5	94.1	96.9	Normal
	0.2	99.8	97.9	97.7	Mild_NPDR
	0.3	99.7	98.1	98.1	Mod_NPDR
	0	100	–	–	Seve_NPDR
	0	100	–	–	PDR
J48	0	100	100	100	Normal
	0	100	100	100	Mild_NPDR
	0	100	100	100	Mod_NPDR
	0	100	99.9	99.9	Seve_NPDR
	0	100	99.9	99.9	PDR
GD	0	100	100	100	Normal
	0	100	99.9	99.9	Mild_NPDR
	0	100	100	100	Mod_NPDR
	0	100	100	100	Seve_NPDR
	0	100	100	100	PDR

remarkable performance in multiclass classification. This is due to both methods have incorporated non-linear gradients to extract the features. On the other hand, training performance of these two has dramatic gap. The proposed model has converged just before 50 iterations and one can notice there is no improvement in error. Whereas, the J48 method is still unsettled even after 200 iterations, and also the error is more compared to GD method. This performance of GD with respect to the training speed leads to grater difference in performance when a large pool of data is being applied. Another limitation with J48 is, in Fig. 3, at 19th iteration, the error has increased and continued for some more iterations. If we reduce the epoch count in order to save, the classification performance results in significant trade-off. So when the outcomes of these two methods are evaluated in far more metrics, the gap would definitely be large between the two.

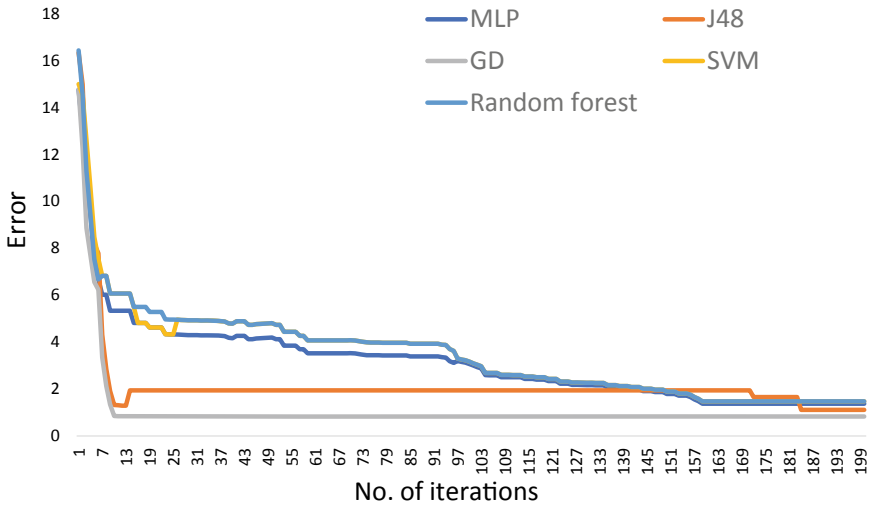


Fig. 3 Error and convergence comparison of CNN models

4 Conclusion

In this article, a gradient descent-based CNN classifier is presented for multiclass classification of diabetic retinopathy images of DRIVE, STARE, and Kaggle datasets. Experiments have been conducted, and the results have been evaluated using statistical metrics such as FPR, specificity, accuracy, and F_1 -score. All the metrics have compared with the existing prominent deep learning models such as SVM, random forest, MLP, and J48 and show significant improvement in all the parameter metrics. There is a narrow gap between the proposed model and J48 in terms of accuracy; but as shown in Fig. 3, the time taken to converge by later is more, and also, the error is higher after 200 iterations. Further, this approach can be improved by incorporating better loss function that limits the weight adjustments, hence by reducing the training and evaluation times.

References

1. Fokas AS, Dikaios N, Kastis GA (2020) Mathematical models and deep learning for predicting the number of individuals reported to be infected with SARS-CoV-2. *J R Soc Interface* 17(20200494)
2. Gavin HP (2021) The Levenberg-Marquardt algorithm for nonlinear least squares curve-fitting problems. <https://people.duke.edu/~hpgavin/ce281/lm.pdf>. Online; accessed 25 July 2021
3. Gayathri S, Gopi VP, Palanisamy P (2020) A lightweight CNN for diabetic retinopathy classification from fundus images. *Biomed Sig Process Control* 62(102115)

4. Gill PE, Murry W (1978) Algorithms for the solution of the nonlinear least-squares problem. *SIAM J Numer Anal* 15(5):977–992
5. Huang GB, Chen YQ, Babri HA (2000) Classification ability of single hidden layer feed forward neural networks. *IEEE Trans Neural Netw* 11(3):799–801
6. Mookiah M, Acharya U, Martis R, Chua C, Lim C, Ng E, Laude A (2013) Evolutionary algorithm based classifier parameter tuning for automatic diabetic retinopathy grading: a hybrid feature extraction approach. *Knowl Based Syst* 39:09–22
7. Pasquel FJ, Hendrick AM, Ryan M, Cason E, Ali MK, Narayan KMV (2015) Cost-effectiveness of different diabetic retinopathy screening modalities. *J Diab Sci Technol* 10(2):301–307
8. Pratt H, Coenen F, Broadbent D, Harding S, Zheng Y (2016) Convolutional neural networks for diabetic retinopathy. *Proc Comput Sci* 200–205
9. Roychowdhury S, Koozekanani D, Parhi K (2014) Dream: diabetic retinopathy analysis using machine learning. *IEEE J Biomed Health Inform* 18:1717–1728
10. Sidibe D, Sadek I, Meriaudeau F (2015) Discrimination of retinal images containing bright lesions using sparse coded features and SVM. *Comput Biol Med* 62:175–184
11. World Health Organization (2021) World report on vision. <https://www.who.int/news/item/08-10-2019-who-launches-first-world-report-on-vision>. Online; accessed 25 July 2021
12. Yang Y, Li T, Li W, Wu H, Fan W, Zhang W (2017) Lesion detection and grading of diabetic retinopathy via two-stages deep convolutional neural networks. In: International conference on medical image computing and computer-assisted intervention-MICCAI, pp 533–540
13. Yaqoob MK, Ali SF, Bilal M, Hanif MS, Al-Saggaf UM (2021) Resnet based deep features and random forest classifier for diabetic retinopathy detection. *Sensors* 21:01–14

Configuration of the Communication Radius for Partial Coverage in WSN



Rameshwar Nath Tripathi^{ID}, Kumar Gaurav^{ID}, and Yatindra Nath Singh^{ID}

Abstract The Wireless Sensor Network is primarily an information gathering network which collects the information through deployed sensors and sends it back to a central authority for further processing and necessary actions. To perform sensing task properly, the two network properties coverage and connectivity, must be maintained above a desired threshold. Coverage is the cumulative measure of the sensed area, and connectivity is the measure of existence of the node to node communication paths and nodes to base station communication paths. We focus on the coverage and connectivity properties simultaneously in this work. There must be a relationship between sensing radius and communication radius due to expected dependency between coverage and connectivity. This relationship has been studied in the past only in the context of the full coverage. However, there are many applications not requiring full coverage but can function with partial coverage. Therefore, we investigate the dependency of coverage and connectivity in the context of partial coverage. We establish this novel relationship for partial coverage and derive the closed form relation among communication radius, sensing radius and partial coverage, to achieve the desired coverage and connectivity. Our relationship/condition is more generic because it reduces to well-known relationship for full coverage, i.e. communication radius must be at least twice the sensing radius. This condition will facilitate the network designers to configure the communication radius for the desired coverage fraction to get a connected network.

Keywords Partial coverage · Connectivity · Communication radius

R. N. Tripathi (✉) · Y. N. Singh
Indian Institute of Technology, Kanpur, India
e-mail: rameshn@iitk.a.c.in

Y. N. Singh
e-mail: ynsingh@iitk.ac.in

Kumar Gaurav
Harcourt Butler Technical University, Kanpur, India
e-mail: gauravet@hbtu.ac.in

1 Introduction

A single node can sense only in a small region. Hence, to monitor large area, a network of sensor nodes is needed. If these sensor nodes can communicate wirelessly, the network is called Wireless Sensor Networks (WSNs). In the WSN, generally, there will be a base station which collects measurements from all the nodes. As the nodes can communicate over short distances due to the limited capabilities, multi-hop communication is used for transferring measurements to base station. Thus, sensing as well as connectivity are the important features in a WSN.

Coverage of a sensor network represents how well the sensors monitor a field of interest (FoI) where they are deployed. It is the performance measure of the network sensing capability. Connectivity represents how well the nodes can communicate. It is the performance measure of the network communication capability. Characterization of these two measures helps in the better design of sensor networks for different applications. The coverage problem can be formulated as an optimization problem, i.e. to maximize lifetime subject to minimum coverage guarantee while maintaining the connectivity.

Coverage is broadly classified into three categories: (a) area coverage, (b) target coverage and (c) barrier coverage. Area coverage concerns how well the sensor nodes monitor an area of interest (AOI). Target coverage requires monitoring of a set of targets instead of the whole sensing field. The problem of preventing an intruder from entering a boundary of interest (BOI) is referred to as the barrier coverage.

The coverage characterizes the performance of a sensing network. It is represented by coverage fraction α where every point in the covered area = $\alpha \times$ total area is sensed by at least one sensor. Here, $0 < \alpha \leq 1$. If coverage fraction $\alpha = 1$, then, we have full coverage. In the present paper, we focus on partial coverage, i.e. $\alpha < 1$. Since full coverage is stringent condition and expensive, it should be used only if necessary. Most of the applications may work satisfactorily with partial coverage. For example, one such scenario is a sensor network for weather forecast [1]. Instead of knowing the humidity at every location in the field, measurement of certain fraction of the area might prove sufficient for the humidity profile of the whole field. Therefore, applications may require network configurations with different degree of coverage and connectivity. We can classify the connectivity and coverage (CC) requirements as follows: connected full coverage (CFC) and connected partial coverage (CPC) [2, 3].

While solving the connected coverage (CC) optimization problem, the least possible number of constraints should be used to reduce the design complexity. The need for constraints reduction gives rise to two critical research questions concerning the design of wireless sensor networks:

1. Are coverage and connectivity constraints independent?
2. If not, does coverage imply connectivity or vice versa so that a sensor network only needs to be configured to satisfy the stronger of the two conditions?

Answering these questions qualitatively and quantitatively would greatly facilitate the design of WSNs. It will lead to insights into how to utilize minimum number of

nodes to achieve a desired coverage degree and coverage fraction while maintaining the required system connectivity. When number of nodes are more than needed, it will also tell us about increase in lifetime of WSN.

Most of the research work on sensing coverage in the literature has focused on the connected full coverage (CFC). Researchers in [4, 5] contributed to achieve full coverage as well as connectivity. However, the above two research questions have not been explored in the context of partial coverage.

In this paper, we report an investigation on this relationship for deterministic deployment and the conditions which guarantee connectivity while configuring the desired coverage fraction. We discuss the network connectivity and coverage problem. We find the lower bound as well as the upper bound on communication radius and also derive an exact expression for communication radius in terms of coverage fraction.

The paper is organized as follows: In Sect. 2, the notion of coverage and connectivity is introduced. Section 3 discusses the relationship between partial coverage and the connectivity problem in WSN. Finally, in Sect. 4, we conclude the outcome of this work along with the future research directions and some open problems.

2 System Model

In this section, we present the network model along with its various components, i.e. monitored space, sensing region, coverage of a space point, network coverage, node communication region and measure of network connectivity. The network consists of uniformly deployed sensor nodes over a rectangular field of interest (FoI), Ψ . Though, we have taken rectangular field, our results will hold true for any arbitrary field of interest. The events of interest (EOI) can take place randomly at any location in the sensing field. The events are represented as space points. A node can detect events within a certain distance, called sensing radius R_S . Let us consider a space point z and a set of sensors $\Omega = \{s_1, s_2, \dots, s_N\}$ deployed in the sensing field. The $d(s, z)$ denotes the distance between a sensor s and a space point z . Let (s_x, s_y) and (z_x, z_y) be the coordinates of the sensor s and the space point z , respectively.

The coverage function of a space point z relative to a sensor node i is given by a binary value

$$f(d(s_i, z)) = \begin{cases} 1 & d(s_i, z) \leq R_S \\ 0 & \text{otherwise.} \end{cases} \quad (1)$$

The value 1 implies that the sensor can monitor the point z .

A point might be covered by multiple sensors at the same time. The set of these multiple sensors is represented by $\Omega_z \subset \Omega$. The coverage function of a space point relative to a set of sensors can be the addition of the coverage function of the point relative to each individual sensor. Thus, coverage function $F(z)$ of a space point z is defined as

$$F(z) = \sum_{i=1}^k f(d(s_i, z)). \quad (2)$$

If $F(z) = k$, then we can say that the point z is k -covered.

The coverage of the sensing field relative to the deployed sensor nodes can be computed using Eq. (2), and is called the network coverage. The network coverage function F_N is defined as the minimum value of $F(z)$ among all the possible values of z in the entire network, i.e.

$$F_N = \min_{\forall z \in \mathcal{P}} F(z). \quad (3)$$

We assume that each node s_i is able to communicate only up to a certain distance from itself, called the communication radius R_C . The two nodes s_i and s_j are said to be connected if they are able to communicate directly with each other. In other words, the Euclidean distance between them must be less than or equal to their communication radius, i.e. $d(s_i, s_j) \leq R_C$. The communication network of the set of nodes S is modeled as a communication graph. A network is said to be connected if there is at least a path between any pair of nodes as well as a path from every node to the base station.

3 Relationship Between Partial Coverage and Full Connectivity

In this section, we focus on understanding the relationship between partial coverage and full connectivity. We also find the conditions when partial coverage implies full connectivity.

There exist two possibilities—(i) coverage implies connectivity and (ii) connectivity implies coverage. A connected network cannot guarantee coverage, because coverage is concerned with whether every point of FoI is covered or not, while connectivity only requires all locations of active nodes to be connected. A covered network may guarantee connectivity, as coverage requires majority locations of the sensing field to be covered. The connectivity for a certain coverage depends upon the ratio of communication radius to sensing radius. Zhang and Hou [2] explored and established a connected full coverage(CFC) condition. It states that:

Assuming the monitored region to be a convex set, the condition of $R_C \geq 2R_S$ is both necessary and sufficient to ensure that the complete coverage of a convex region implies connectivity in an arbitrary network.

The above condition is stated to be true for convex region, but we found that, this condition is also true for any arbitrary monitored region which may not be the convex region. The statement can be restated as:

For a given arbitrary monitored region, the condition of $R_C \geq 2R_S$ is both necessary and sufficient to ensure that complete coverage of the region implies connectivity.

The condition $R_C \geq 2R_S$ will also suffice as the connectivity criteria in contiguous partial coverage. In this paper, we will find a tighter bound on R_C in terms of α .

The goal in planning a WSN is to maximize coverage with a minimum number of sensors. Thereby achieving least cost for the network. To realize this goal, the deployment process of the sensors plays an important role. A deployment is characterized by a deployment strategy and a deployment pattern. On the basis of the deployment strategy, the networks can be classified as structured or unstructured. In an structured sensor network, the nodes are placed at the specific locations, while in an unstructured sensor network, the nodes are placed randomly. Based on the area of the sensing field, area covered by deployed sensors, and overlapped sensing area among the nodes, the coverage can be classified as: exact coverage, over coverage and under coverage. The exact coverage means sensing field is covered without any overlap among the sensing regions of the nodes. If sensing field is covered and there exists some overlap among nodes, it is called over coverage. To achieve exact coverage, which is not possible for circular sensing range. Only the possibilities of over-coverage and under-coverage exists. Formally, over coverage is called full coverage. Here, each point is covered by at least one sensor. Under coverage is called partial coverage where some points are not covered. In a deterministic deployment to cover a plane, optimal placement pattern is equilateral triangle lattice where sensor nodes are placed on the vertices of equilateral triangles [6].

In this work, we study the partial coverage for the deterministic deployment strategies in the field of interest. We consider full coverage as the baseline to study partial coverage. Sensor nodes in triangular lattice pattern provides optimal full coverage when side length of the basic triangle pattern is $\sqrt{3}R_S$. This side length represents the maximum inter-node distance while ensuring 100% coverage. If the inter-node distance is less than or equal to $\sqrt{3}R_S$, then coverage is full otherwise the FoI is under covered. Therefore, partial coverage can only happen if $d \geq \sqrt{3}R_S$. If we keep on increasing the spacing between nodes, overlap area just becomes zero at $d = 2R_S$. For $d \geq 2R_S$, there is no overlap area. Therefore, for study of partial area coverage, the region of interest is $d \geq \sqrt{3}R_S$. we can divide this region into two sub-regions, i.e. $\sqrt{3}R_S \leq d \leq 2R_S$ and $d \geq 2R_S$. We compute the spacing between nodes in triangular mesh to achieve desired α . We refer to this spacing d_α . To make our discussion precise, we will derive d_α .

Lemma 1 *Given that the nodes with sensing radius R_S are deployed in the triangular mesh configuration in the sensing field Ψ , the coverage fraction of the sensing field varies nonlinearly with spacing between two adjacent nodes, in the range $\sqrt{3}R_S \leq d \leq 2R_S$.*

Proof The nodes are deployed in a rectangular region of size $L \times L$. Consider the simple scenario, where any two nodes s_i and s_j are neighbor and s_j lies on either side of s_i . The inter-node distance between neighboring nodes s_i and s_j is given by $d = d(s_i, s_j)$. With large number of nodes, the sensor placement is shown in Fig. 1a. It is just a regular pattern of the configuration as shown in Fig. 1b. The common sensing area of two nodes is denoted by I_{ij} . It is given by

$$I_{ij} = R_S^2 \left[2 \arccos \left(\frac{d}{2R_S} \right) - \frac{d}{R_S} \sqrt{1 - \left(\frac{d}{2R_S} \right)^2} \right].$$

The overall coverage ratio, α , of the sensing field Ψ in Fig. 1a will be equal to the coverage ratio of triangular pattern in Fig. 1b.

$$\alpha = \frac{R_S^2 \left[\frac{\pi}{2} - 3 \arccos \left(\frac{d}{2R_S} \right) + \frac{3d}{2R_S} \sqrt{1 - \left(\frac{d}{2R_S} \right)^2} \right]}{\frac{\sqrt{3}}{4} d^2}.$$

We define inter-node distance relative to $2R_S$ as $\beta = d/2R_S$, and putting this value in α , we get

$$\alpha = \frac{1}{\sqrt{3}\beta^2} \left[\frac{\pi}{2} - 3 \arccos(\beta) + 3\beta \sqrt{1 - (\beta)^2} \right]. \quad (4)$$

Equation (4) represents the relationship between α and β in the triangular mesh. We can set the spacing between triangle vertices to meet desired α -coverage. We denote this spacing by d_α . Thus, for a given α , one can compute the d_α . For $\alpha = 0.906$, the d_α is $2R_S$. The $d_\alpha = 2R_S$ represents a special configuration where the overlap among adjacent nodes just becomes zero. We refer to this d_α as d_p which denotes the point overlap. The mere knowledge of relative inter-node distance with respect to d_p can be used to define bounds on α . For given arbitrary d , bounds on α can be given as.

$$\alpha = \begin{cases} <90.6\% & d > d_p \\ 90.6\% & d = d_p \\ >90.6\% & d < d_p. \end{cases} \quad (5)$$

Lemma 2 *The coverage ratio of a sensing field is inversely proportional to the square of inter-node distance d when $d \geq 2R_S$.*

Proof From Lemma 1, one can compute d_α for coverage ratio α , where $\alpha < 0.9068$. The nodes are placed as shown in Fig. 2a. One can observe that the pattern in Fig. 2b can be repeated to get the configuration shown in Fig. 2a. The α for the sensing field, Ψ is equal to

$$\begin{aligned} \alpha &= \frac{\text{Area covered by circular region in } \triangle ABC}{\text{Area of } \triangle ABC} \\ &= \frac{2\pi R_S^2}{\sqrt{3}d^2}. \end{aligned} \quad (6)$$

Thus, for a given sensing radius, the coverage ratio depends only on the spacing between two adjacent nodes and follows the inverse square law.

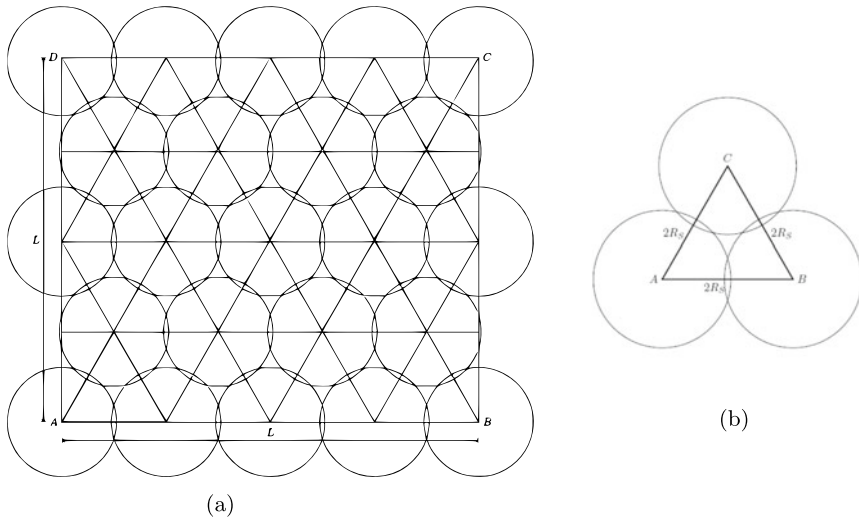


Fig. 1 Triangular deployment coverage with nodes' sensing region overlap in the sensing field: **a** Deployment in sensing field and **b** basic unit of the pattern

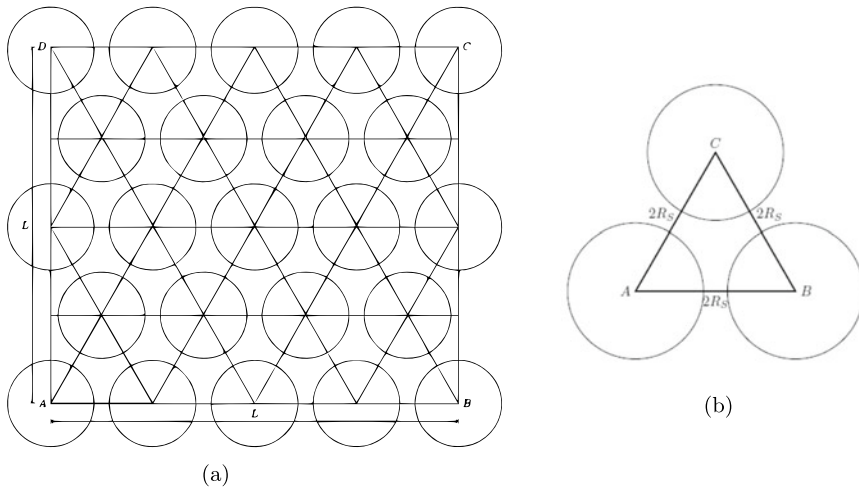


Fig. 2 Triangular deployment for arbitrary partial coverage without any overlap in nodes' sensing regions: **a** Deployment in sensing field and **b** basic unit of the pattern

In this case also, we can set the spacing between triangle vertices to meet desired α -coverage. So far in this work, we have focused on the coverage problem, which ensures that an event happening at any point in FoI is detected. In order to transfer sensed information, network must be connected. The following theorem provides the condition on the communication range to ensure connected network for the required α .

Theorem 1 For a given coverage fraction, $\alpha \in (0.906, 1)$, we will have $R_C^{\min} \in (\sqrt{3}R_S, 2R_S)$. Having $R_C \geq R_C^{\min}$ is both necessary and sufficient condition to ensure that α -coverage implies connectivity.

Proof For the considered deterministic deployment, the sensing network is connected if minimum communication range of nodes is greater than or equal to the maximum separation between any two adjacent nodes for a given α , i.e. $R_C^{\min} \geq d_\alpha$. For an $\alpha \in (0.906, 1)$, corresponding d_α can be obtained in two ways: direct computation using Eq. (4) and retrieval of data-pair (α, d_α) from a look up table. The inter-node distances corresponding to 0.906 and 1 are $2R_S$ and $\sqrt{3}R_S$, respectively. Therefore for $\alpha \in (0.906, 1)$, the R_C^{\min} must be in the range $(\sqrt{3}R_S, 2R_S)$.

Theorem 2 For a given α in the range $\alpha \leq 0.906$, the condition $D_\Psi \leq R_C^{\min} \leq (\sqrt{\frac{2\pi}{\sqrt{3}\alpha}}) \times R_S$ is both necessary and sufficient to ensure that α -coverage implies connectivity. Here, D_Ψ is sensing field diameter.

Proof To maintain connectivity in the any sensing field, communication radius R_C must be $\geq d$. We can compute the value of d from Eq. (6) to get R_C as a function of α and R_S , i.e.

$$R_C \geq \left(\sqrt{\frac{2\pi}{\sqrt{3}\alpha}} \right) \times R_S. \quad (7)$$

Above expression gives the lower bound on R_C . To get upper bound on the required communication radius, we consider the worst-case scenario of a two-node network. To create the worst-case scenario, we place the nodes at the farthest possible points in the sensing field. In this scenario, the distance between two nodes is equal to the sensing field diameter. The diameter of a shape is the upper bound on the set of all pairwise distances between all points in the area Ψ . It is given by

$$D_\Psi = \sup\{d(z_1, z_2) \mid z_1, z_2 \in \Psi\}. \quad (8)$$

In other words, maximum inter-node distance is D_Ψ . To form a connected network, these nodes would need to set their minimum communication radius equal to the sensing field diameter. The communication radius need not to be set greater than the diameter of the sensing field as it gives no additional advantage and leads to waste of energy.

Although the relationship $R_C^{\min} \geq 2R_S$ is necessary to guarantee network connectivity provided that the required coverage is ensured. We have computed the lower and the upper bounds on the minimum communication radius for the various ranges of α as

$$R_C^{\min} = \begin{cases} f(\alpha)R_S & \alpha < 90.6\% \\ 2R_S & \alpha = 90.6\% \\ \in (\sqrt{3}R_S, 2R_S) & \alpha \in (90.6\%, 100\%). \end{cases} \quad (9)$$

Here, $f(\alpha) = \sqrt{\frac{2\pi}{\sqrt{3}\alpha}}$ and for $\alpha \in (90.6\%, 100\%)$ the exact value of R_C^{\min} can be computed using Eq. (4), as an implicit function of d_α . These bounds help to reduce the communication energy. This could be exploited by the designers to conserve the energy in the network.

4 Conclusion

This work explored the problem of maintaining both the desired partial coverage and full connectivity in deterministically deployed wireless sensor networks. We proved that α -coverage can imply full network connectivity and computed the tighter lower and upper bounds on the minimum communication radius for various ranges of α . At a high-level, our analysis of α -coverage advocates the use of our results because of the potential energy savings. This work can be extended in several directions. The first extension can be to find the exact or approximate partial coverage condition for the random deployment. Second possible extension is to consider probabilistic sensing model and probabilistic communication model and third extension could be to use these results in the design of topology control for WSNs.

References

1. Yetgin H, Cheung KTK, El-Hajjar M, Hanzo LH (2017) A survey of network lifetime maximization techniques in wireless sensor networks. *IEEE Commun Surv Tutor* 19(2):828–854
2. Zhang H, Hou JC (2005) Maintaining sensing coverage and connectivity in large sensor networks. *Ad Hoc Wirel Sens Netw* 1:89–124
3. Xing G, Wang X, Zhang Y, Lu C, Pless R, Gill C (2005) Integrated coverage and connectivity configuration for energy conservation in sensor networks. *ACM Trans Sens Netw (TOSN)* 1(1):36–72
4. Li Y, Vu C, Ai C, Chen G, Zhao Y (2011) Transforming complete coverage algorithms to partial coverage algorithms for wireless sensor networks. *IEEE Trans Parall Distrib Syst* 22(4):695–703
5. Ammari HM, Das SK (2009) Critical density for coverage and connectivity in three-dimensional wireless sensor networks using continuum percolation. *IEEE Trans Parall Distrib Syst* 20(6):872–885
6. Cheng W, Li Y, Jiang Y, Yin X (2016) Regular deployment of wireless sensors to achieve connectivity and information coverage. *Sensors* 16(8)

Bandwidth Enhancement of Two Element Closely Spaced MIMO Antenna for WLAN Applications



Pendli Pradeep , K. Jaya Sankar, and P. Chandra Sekhar

Abstract In this paper, a compact s-shaped slot (SSS) two element MIMO antenna is proposed for WLAN applications with enhanced bandwidth and isolation. The proposed antenna placed side by side with edge to edge distance 2mm. The mutual coupling is reduced by incorporating a neutralization line between the radiating elements. A $50\ \Omega$ microstrip line is used to feed the radiating elements. The occupied area of the proposed s-shaped slot MIMO antenna is $20\text{ mm} \times 26\text{ mm} \times 1.6\text{ mm}$. A low cost substrate FR4 is used with dielectric constant value is $\epsilon_r = 4.4$ and loss tangent value is $\tan \delta = 0.02$. The proposed compact MIMO antenna designed and simulated using HFS Simulator at 5.2 GHz with isolation greater than 18 dB. The proposed antenna covers impedance bandwidth from 4.25 to 5.81 GHz (impedance bandwidth of 30%) with return loss of -35 dB . The MIMO antenna parameters are ECC, DG and channel capacity are within the limit for the proposed antenna. This compact MIMO antenna suitable for all 5.2 GHz WLAN applications.

Keywords S-shaped slot antenna · Two element MIMO antenna · Decoupling network · Microstrip feed line

1 Introduction

Today's wireless system requires higher data rates to enhance multimedia applications. According to channel capacity formula, channel capacity can't be improved by increasing the power and bandwidth due to certain limitations [1]. MIMO technology

Sreenidhi Institute of Science and Technology and Osmania University.

P. Pradeep (✉)

Sreenidhi Institute of Science and Technology, Hyderabad, India
e-mail: pradeependli@gmail.com

K. Jaya Sankar
Mahatma Gandhi Institute of Technology, Hyderabad, India

P. Chandra Sekhar
University College of Engineering, Osmania University, Hyderabad, India

© The Author(s), under exclusive license to Springer Nature Singapore Pte Ltd. 2022
P. Kumar Jain et al. (eds.), *Advances in Signal Processing and Communication Engineering*, Lecture Notes in Electrical Engineering 929,
https://doi.org/10.1007/978-981-19-5550-1_5

is one used to improve higher data rates and throughput. Multiple-input-multiple-output (MIMO) wireless system has N -number of antennas at transmitter and receiver to improve the channel capacity in multipath channels [2]. In MIMO antenna system, N -number of antennas are placed with minimum distance due to space constrain. Such issue leads to mutual coupling between N -number of antennas, the performance of MIMO antenna degraded ultimately. Mutual coupling reduction with compact size antenna is really a challenging task for researchers.

In literature, various kind of methods are proposed to reduce the mutual coupling between MIMO antenna elements. Two Nested U ring resonators are placed between MIMO antenna elements [3]. In [4], without any decoupling structure two element MIMO antenna was presented. The isolation between closely placed antennas elements in MIMO system is must require in WLAN application [5], H-shape Defective Ground Structure in ground plane is used [6]. Four parasitic parallel coupled line are placed between radiating elements [7] and a four port compact MIMO antenna was designed with a slot at the center of the proposed antenna ground plane in [8]. H-shaped conducting wall is used as decoupling structure [9]. In paper [10], an isolation is improved using interdigital lines.

In this letter, we propose a compact s-shaped slot (SSS) two element MIMO antenna is proposed for WLAN applications with enhanced bandwidth and isolation. A high isolation achieved by incorporating a neutralization line (NL) between closely spaced antenna elements. This NL is used to cancel the reactive coupling between antenna elements. Bandwidth of the proposed antenna is enhanced by etching edges of the radiating elements. Section 2 presents the proposed single SSS antenna design, evaluation and construction. In Sect. 2, a compact two port SSS MIMO antenna and decoupling structure are presented. In Sect. 3, the proposed SSS MIMO antenna results are given and finally Sect. 4 gives over all conclusion of the proposed antenna followed by references and acknowledgement.

2 Design and Geometry of S-Shaped Slot MIMO Antenna

A compact SSS two port MIMO antenna proposed for WLAN applications with enhanced bandwidth and isolation with overall dimension of MIMO antenna is $20 \text{ mm} \times 26 \text{ mm} \times 1.6 \text{ mm}$. A low cost substrate FR4 is used with dielectric constant value is $\epsilon_r = 4.4$ and loss tangent value is $\tan \delta = 0.02$. The radius of inner and outer circles are 5 mm and 4 mm, respectively. The design and evolution process of the proposed two element s-shaped Slot MIMO antenna illustrated in the following sections.

2.1 Design of SSS Unit Antenna Element

The proposed s-shaped slot (SSS) unit antenna element is illustrated in Fig. 1. The initial stage of a compact SSS antenna at 5.2 GHz frequency is shown in Fig. 1a.

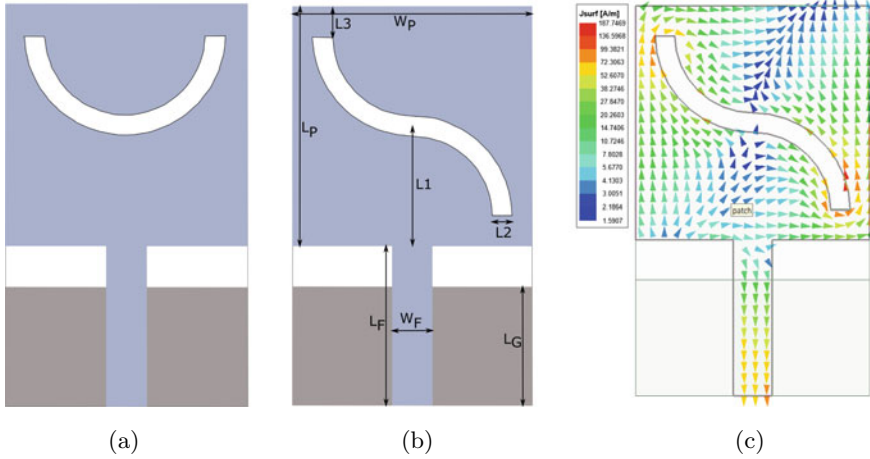


Fig. 1 Proposed s-shaped slot single element. **a** Antenna 1, **b** Antenna 2 (proposed element) and **c** Current distribution at 5.2 GHz

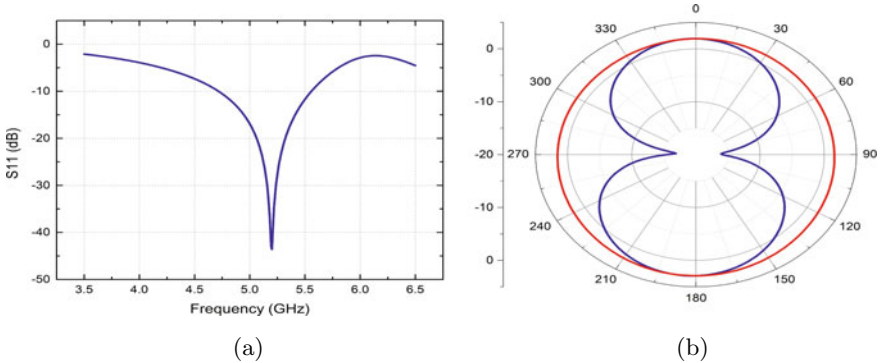


Fig. 2 Proposed single element antenna. **a** Return loss plot and **b** radiation pattern at 5.2 GHz

Figure 1b is a proposed s-shaped slot (SSS) unit antenna element. The s-shaped slot in the patch acts as a radiator. The arc length of the SSS is approximately equal to half wavelength, i.e. 14.03 mm ($\approx \frac{\lambda_g}{2}$) and width of the slot is 1 mm. The impedance bandwidth of SSS antenna is 840 MHz, and it covers frequency band from 4.72 to 5.56 GHz with return loss of -43.6 dB at frequency 5.2 GHz. The surface currents are densely populated and flowing around the edges of the SSS antenna shown in Fig. 1c. The return loss plot and radiation pattern plot (gain 2.9 dBi) of the SSS unit element is shown in Fig. 2a, b, respectively.

The proposed antenna SSS unit element antenna operates at 5.2 GHz with detailed dimensions $L_P = 12$ mm, $W_P = 12$ mm, $L_F = 8$ mm, $W_F = 2$ mm, h (thickness of the substrate) = 1.6 mm, $L_1 = 6$ mm, $L_2 = 1$ mm and $L_3 = 1.55$ mm.

2.2 Two Element S-Shaped Slot MIMO Antenna

A compact two element SSS MIMO antenna represented in Fig. 3. The proposed compact s-shaped slot (SSS) two element MIMO antenna without a decoupling structure and with a decoupling structure is shown in Fig. 3a, b, respectively. Two SSS unit antenna elements are spaced very closely with edge to edge distance 2 mm ($\approx 0.035\lambda_0$). The gap between patch elements could be thought of capacitance. A metallic strip is added between the radiating elements at suitable position, this strip could be thought of inductance. Which produces balanced inductive-capacitive effect. Here the metallic strip acts as a neutralization line, which is used to cancel the radiated fields and induced fields, when current flows in opposite direction. Hence, mutual coupling between antennas improved greatly. The edges of the MIMO antenna elements are etched to improve the antenna bandwidth. L_7 value is 3 mm and its value is 2 mm before etching the edge of patch and L_8 value is 1 mm. The two element MIMO antenna radiates at 5.2 GHz with impedance bandwidth of 1560 MHz covers frequency from 5.25 to 5.81 GHz with return loss of -35 dB. The mutual coupling is more than -18.5 dB over the frequency band. The proposed MIMO antenna operate at frequency 5.2 GHz with dimensions $L_4 = 2$ mm, $L_5 = 0.5$ mm, $L_6 = 6.5$ mm, $L_2 = 7$ mm and $L_8 = 1$ mm.

3 Results and Discussion of SSS MIMO Antenna

The proposed two element SSS MIMO antenna designed and simulated by using Ansys HFSS EM tool. A high isolation is obtained by adding a neutralization line between the radiating patches. Figure 4a, b shows the current distribution around slots without and with a neutralization line. The results clearly show mutual reduction when element1 excited and element 2 terminated with $50\ \Omega$ load. The radiated and induced fields are cancelled when current flows through a neutralization line in both

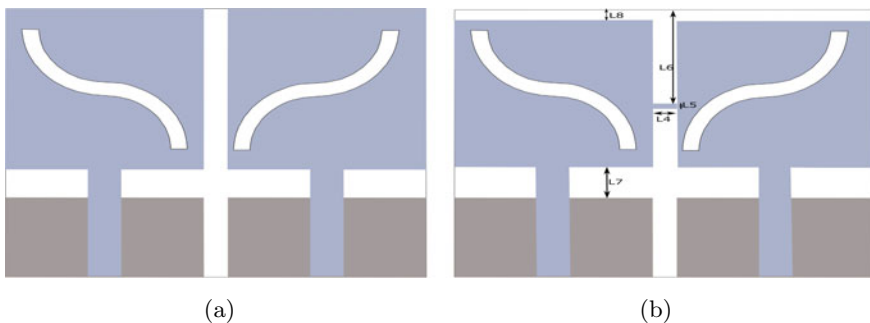


Fig. 3 Proposed SSS MIMO antenna **a** without decoupling and **b** with decoupling

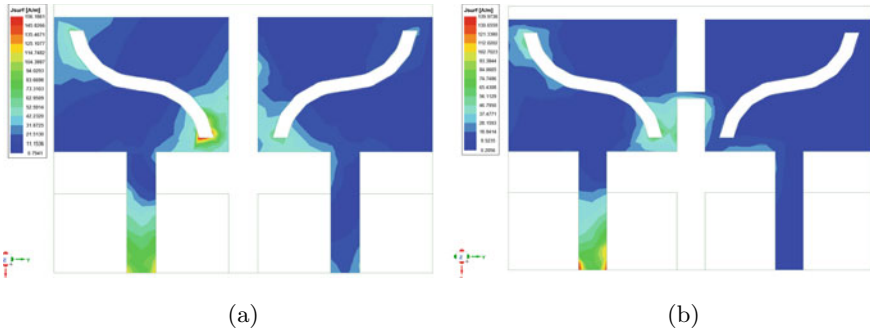


Fig. 4 Current distribution between two antenna elements **a** without decoupling and **b** with decoupling

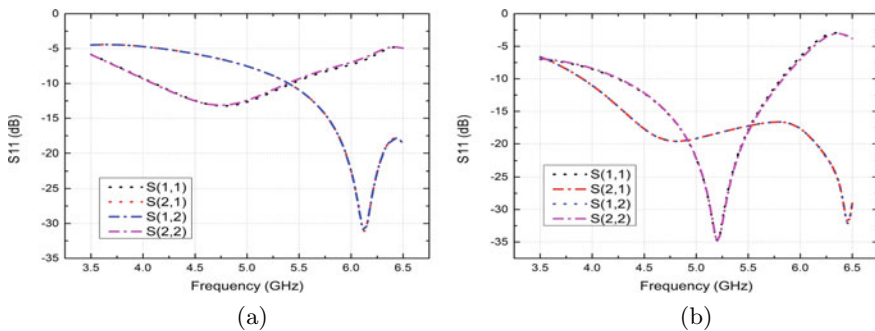


Fig. 5 Return loss of proposed s-shaped slot MIMO antenna **a** without decoupling structure and **b** with decoupling structure

directions with equal magnitude and out of phase. The isolation is improved and achieved more than 18 dB between the radiating elements over the operating band. Figure 5a, b shows the simulated S-parameter results of s-shaped Slot MIMO antenna without and with a neutralization line. The bandwidth SSS MIMO antenna enhanced by etching the edges of the radiating elements. The two element SSS MIMO antenna radiates at 5.2 GHz with impedance bandwidth of 1560 MHz covers frequency from 5.25 to 5.81 GHz with return loss of -35 dB. The two element SSS MIMO antenna gain is 2.9 dBi.

The proposed MIMO antenna has certain advantages as compared with recent literature tabulated in Table 1.

Envelope Correlation Efficient (ECC) and Channel Capacity Loss (CCL) are two important parameters required to characterize MIMO antennas along with regular parameters.

Table 1 Proposed SSS MIMO antenna characteristics comparison with recent literature

References	fr (GHZ)	BW (MHZ)	Isolation (dB)	Spaced	ECC	Dimensions (mm ³)
[4]	5.2	600	11.5	NA	0.01	37.5 × 17 × 1.524
[6]	5.3	NA	41	NA	0.007	60 × 50 × 1.46
[7]	5.7	220	25	3.5	0.01	57 × 32 × 1.57
[9]	5.2	NA	51	3	NA	50 × 30 × 1.57
Proposed	5.2	1560	18	2	0.0001	20 × 26 × 1.6

3.1 Envelope Correlation Efficient (ECC)

In a MIMO antenna diversity system, correlation between antenna elements can be evaluated by ECC parameter. In fact, lowest ECC gives highest diversity gain. The ECC parameter can be obtained by following Eq. (1).

$$\rho = \frac{|S_{11}^* S_{12} + S_{21}^* S_{22}|^2}{(1 - |S_{11}|^2 - |S_{12}|^2)(1 - |S_{21}|^2 - |S_{22}|^2)} \quad (1)$$

Here S_{11} , S_{22} are return loss scattering parameters and S_{12} , S_{21} are isolation scattering parameters. The ECC parameter plot for the designed SSS MIMO antenna is shown Fig. 6a and its ECC value is less than 0.0001 for the operating band. The ECC value should be below 0.5 to obtain better performance from any MIMO antenna. Hence, this design ensures that performance of spatial multiplexing is good, i.e. improved data rate.

3.2 Channel Capacity Loss (CCL)

The CCL parameter is one which is used to find the transmission rate through the communication channel in terms of number of data bits per second per Hertz. The CCL parameter is a useful parameter in MIMO system, its value should be less than 0.4bps/Hz to get good performance of MIMO antenna system. The CCL parameter is calculated by following Eq. (2). For the proposed antenna, CCL parameter value is 0.043bps/Hz at frequency 5.2GHz and CCL plot is shown in Fig. 6b.

$$C_{\text{loss}} = -\log_2^{|\Psi|^R} \quad (2)$$

where $\Psi^R = [\rho_{ij}]$, $(i, j) \in (1, 2, 3, 4)$ is a correlation matrix at receiver antenna end, with

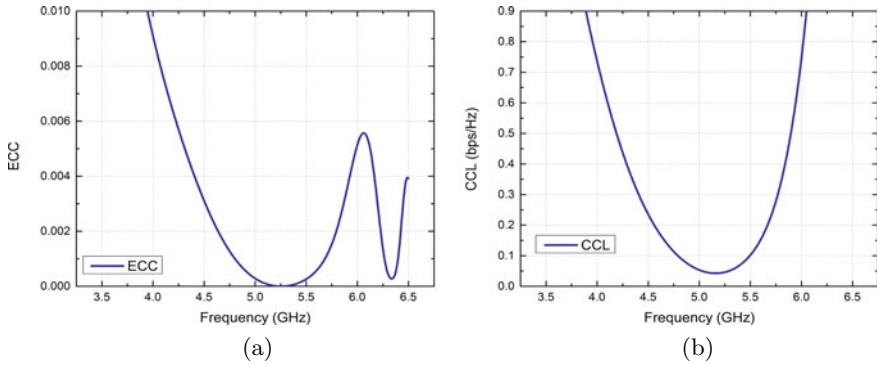


Fig. 6 Proposed MIMO antenna parameters **a** ECC **b** CCL

$$\rho_{11} = (1 - |S_{11}|^2 - |S_{12}|^2) \quad (3a)$$

$$\rho_{22} = (1 - |S_{21}|^2 - |S_{22}|^2) \quad (3b)$$

$$\rho_{12} = -(S_{11}^* S_{12} - S_{21}^* S_{22}) \quad (3c)$$

$$\rho_{21} = -(S_{22}^* S_{21} - S_{12}^* S_{11}) \quad (3d)$$

4 Conclusion

A compact two element s-shaped slot (SSS) MIMO antenna is presented for WLAN applications with enhanced bandwidth and high isolation. An half wavelength s-shaped slots are incorporated in the patches to radiate at frequency 5.2 GHz. The proposed two element SSS antenna elements are spaced very closely with 2mm edge to edge distance. A metallic strip connected between patch elements which acts as a neutralization line. The neutralization line is used to cancel the radiated fields and induced fields, when current flow in opposite direction. Hence, mutual coupling between antennas improved greatly. The edges of the MIMO antenna elements are etched to improve the antenna bandwidth. The SSS MIMO antenna has been proposed, modelled, simulated and analysed by using Finite Element Method-based Ansys HFSS EM tool. The proposed antenna parameters ECC and CCL values are within the standard limits of the MIMO antenna system. This compact, high gain and simple structured SSS MIMO antenna suitable for all WLAN applications.

References

1. Sharawi MS (2013) Printed MIMO antenna systems: performance metrics, implementations and challenges. *J Forum Electromagn Res Methods Appl Technol (FERMAT)* 55(1)
2. Jensen MA, Wallace JW (2004) A review of antennas and propagation for MIMO wireless communications. *IEEE Trans Antennas Propag* 52(11):2810–2824. <https://doi.org/10.1109/TAP.2004.835272>
3. Aouadi B, Tahar JB (2015) Requirements analysis of dual band MIMO antenna. *Wirel Pers Commun* 82(1):35–45. <https://doi.org/10.1007/s11277-014-2190-4>
4. Chouhan S, Malviya L (2019) Two element folded meander line MIMO antenna for wireless applications. *Electronics* 23(1):11–17. <https://doi.org/10.7251/ELS1923011C>
5. Gong Y-Y, Wang L, Zhang Z (2018) The novel Y shaped fractal defected ground structure for the mutual coupling reduction. *Prog Electromagnet Res* 72:13–21. <https://doi.org/10.2528/PIERM18062301>
6. Khan A, Geng S, Zhao X, Shah Z, Jan MU, Abdelbaky MA (2020) Design of MIMO antenna with an enhanced isolation technique. *Electron Multi Digit Publ Inst* 9(8):1–7. <https://doi.org/10.3390/electronics9081217>
7. Mark R, Singh HV, Mandal K, Das S (2019) Reduced edge-to-edge spaced MIMO antenna using parallel coupled line resonator for WLAN applications. *Microw Opt Technol Lett* 61(10):2374–2380. <https://doi.org/10.1002/mop.31911>
8. Pandit S, Mohan A, Ray P (2018) A compact four-element MIMO antenna for WLAN applications. *Microw Opt Technol Lett* 60(2):289–295. <https://doi.org/10.1002/mop.30961>
9. Park C-H, Son H-W (2016) Mutual coupling reduction between closely spaced microstrip antennas by means of H-shaped conducting wall. *Electron Lett* 52(13):1093–1094. <https://doi.org/10.1049/el.2016.1339>
10. Qi H, Yin X, Liu L, Rong Y, Qian H (2015) Improving isolation between closely spaced patch antennas using interdigital lines. *IEEE Antennas Wirel Propag Lett* 15:286–289. <https://doi.org/10.1109/LAWP.2015.2441739>

Early Prediction of Sepsis Using Convolutional and Recurrent Neural Networks



S. K. Chaya Devi, Y. Varun Reddy, K. Sai Sri Vasthav, and G. Praneeth

Abstract The body's severe reaction to an infection is called sepsis. It is a medical emergency that could put your life at risk. When an existing infection sets off a series of events in the human body, sepsis develops. Sepsis can rapidly prompt tissue harm, organ disappointment, and death if not treated immediately. Physicians use the sequential organ failure assessment (SOFA) score to detect organ failure as soon as possible. Any hour that sepsis is diagnosed and treated with antibiotics reduces mortality. The earliest possible detection of patients should be done to decrease the mortality rate as the traditional laboratory process of detection is time-consuming for physicians. As part of building an efficient algorithm, a count of 40,336 ICU patient records were taken from PhysioNet/Computing in Cardiology Challenge 2019. Recurrent neural network (RNN), convolutional neural network (CNN), K-fold cross validation to the CNN classifiers have gained an accuracy of 95.8%, 96.3%, and 97.7%, respectively. Sepsis is the body's extreme response to an infection. It is a life-threatening medical emergency. Sepsis happens when an infection you already have triggers a chain reaction throughout your body. Without timely treatment, sepsis can rapidly lead to tissue damage, organ failure and death. Doctors use the sequential organ failure assessment score for the earliest possible recognition. This is a disease with high mortality and expensive cost of treatment. Mortality decreases with every hour that sepsis is detected and treated with antibiotics. Earliest possible detection of patients should be done to improve the outcomes of patients. A total of 40,336 ICU patients data was taken from PhysioNet/Computing in Cardiology Challenge 2019. By the total data available and using the supplied biomedical data, we reduced the original 41 attributes to 12 attributes. These 12 attributes of data are then fed into a neural network classifier implemented in TensorFlow. Implemented convolutional neural network (CNN) and also done K-fold cross validation for CNN to increase the accuracy. Implemented recurrent neural network (RNN) for serially ordered data. Gained an accuracy of 96.98 % for CNN and 95.35% for RNN.

S. K. Chaya Devi · Y. Varun Reddy · K. Sai Sri Vasthav (✉) · G. Praneeth
Vasavi College of Engineering, Hyderabad, Telangana, India
e-mail: vasthav1729@gmail.com

© The Author(s), under exclusive license to Springer Nature Singapore Pte Ltd. 2022
P. Kumar Jain et al. (eds.), *Advances in Signal Processing and Communication Engineering*, Lecture Notes in Electrical Engineering 929,
https://doi.org/10.1007/978-981-19-5550-1_6

55

Keywords Sepsis · Convolutional neural network (CNN) · Recurrent neural network (RNN) · Deep learning · Classification · Long short-term memory (LSTM)

1 Introduction

A serious illness brought by the human body's reactions to combat infections is called sepsis. The immune system protects the human body from many illnesses and infections but sometimes immune systems response may be counterproductive. When the chemicals are released into the blood by the immune system to combat an infection, it induces inflammation in the body, when a person is infected with sepsis. Small blood clots might form throughout the human body which blocks the flow of blood to other parts of the body which results in organ failure and extreme cases this might lead to death. Sequential organ failure assessment (SOFA) score is used as medical standards for diagnosing in the laboratory. The SOFA score is a risk grouping metric used to recognize patients at increased risk of death [1]. Sepsis affects over 30 million people worldwide each year, with approximately 6 million people losing their lives as a result [2].

It has been observed that detecting sepsis early and treating it with antibiotics are very important for improving results, where each hour of treatment delay might result in a 4–8% increase in mortality rate [3, 4]. The fundamental need to identify and provide early treatment for sepsis persists, and basic concerns regarding early detection's limits remain unanswered because of erroneous and incomplete electronic clinical records, as well as the intricacy of sepsis.

The use of deep learning from hereby referred to as DL for the analysis and diagnosis of many healthcare problems has received unprecedented attention from the previous decade. These DL algorithms have recorded many achievements and accomplished many tasks that are difficult to solve by regular methods and human experts. Under artificial intelligence, DL is a function that emulates the functioning of the human brain in processing data and patterns used in decision making. Among the available DL algorithms, convolutional neural networks from hereby referred to as CNN and recurrent neural networks from hereby referred to as RNN have gained more popularity in recent years in providing solutions to medicare problems and providing extremely accurate results. This paper aims to develop and experiment with the DL models based on CNN and RNN techniques to predict the disease sepsis 6h before clinical onset which helps healthcare organizations.

2 Related Work

The recent years have provided several advancements in understanding and managing sepsis. To perform the detection, firstly preprocessing needs to be done. RNN and CNN models were combined using bagging which gained an accuracy of 90.6% [5] due to the imbalance in the data has considered only 11 attributes out of 41 attributes. The models implemented were CNN, RNN, and ensemble with the accuracy of 89%, 87.5%, and 92.7%, respectively. Also, an ensemble technique that incorporates bagging and boosting tree model (random forest, xgboost, and lightgbm) was developed. The performance achieved by this is the accuracy of 72.7% [6]. Also, a long short-term memory network was developed which got a utility score of 0.29 in a fully hidden test set [7]. Considering the above works which are already available in the literature, we aim to increase the accuracy by preprocessing the data efficiently and by developing an effective multi-layered convolution neural network and recurrent neural network model.

3 Data

3.1 Dataset

The dataset consists of hourly data of 40,336 patients who are admitted to the hospital which consists of 42 features including the sepsis label. This dataset is provided as part of the PhysioNet challenge 2019. The patient records are unbalanced; there are many positive samples (patients with no sepsis) compared to negative samples (patients with sepsis).

3.2 Data Preprocessing

This dataset is incomplete; many features in the 42 features contain NAN values. So, the challenge is to handle these null values. We have checked how many missing values are there for each attribute. After calculating them, we have removed the attributes which are having missing values greater than 90%. So the remaining attributes are O2Sat, Temp, HR, SBP, DBP, MAP, Resp, glucose, Unit1, Unit2, gender, and age. Missing values of these selected attributes are handled using ffill and bfill method. Hourly data of each patient is concatenated into a single row; thus, for 40,336 patients, we have 40,336 rows. But the problem here is ICULOS i.e the length of stay varies from patient to patient. After concatenating the hourly data of each patient, we observed that the length of the record (row) is not constant for all the patients.

4 Methodology

4.1 Convolution Neural Network

Data Preparation To set the size of a row constant, we found out the row with the smallest length, i.e., 96 and all the other rows which have a length greater than 96 are resized by considering only the last 96 elements because that data is the latest data of the patient. Thus, we made the length of the record size constant.

Architecture The data which is prepared from the above step is fed into the CNN model which is developed using Keras API which runs on top of TensorFlow. An embedding layer is the architecture’s first layer. The data is fed to an embedding layer that represents the data using a dense vector representation into a continuous vector space. The data is then fed into three Conv1D layers with which are followed by MaxPooling1D layers. By taking the maximum value over the window specified by pool(size), the MaxPooling1D layer downsamples the input representation. In the next step, data is fed to a flatten layer which flattens the input. The output of flatten layer is fed to two dense layers where the activation functions are relu and softmax, respectively. The dense layer implements the activation function on the dot product of input to the dense layer and kernel which is a weight matrix. The output will be a 2D vector (probabilities) specifying sepsis or not. The maximum of them will be set to 1 and will be considered as a result. The cost function used for this model is categorical cross-entropy combined with adam as optimizer and accuracy as a metric. We used the same architecture and same data to train both CNN and K-fold CNN models (Figs. 1 and 2).

Fig. 1 CNN model architecture

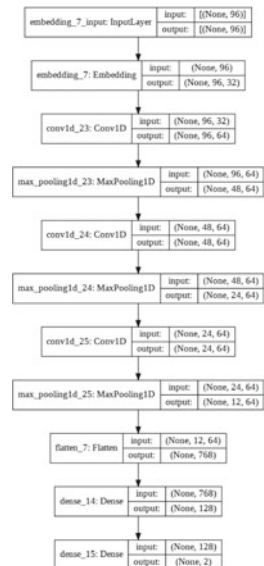
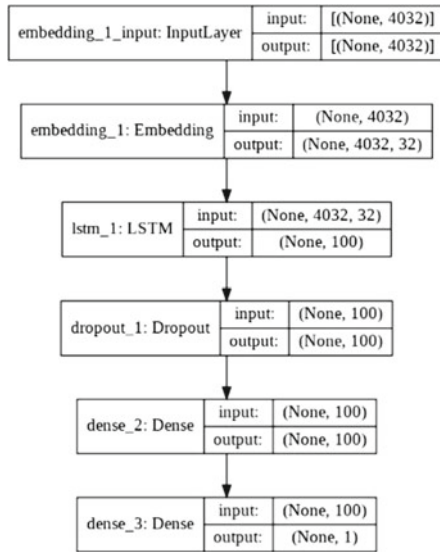


Fig. 2 RNN model architecture



4.2 Recurrent Neural Network

Data Preparation To set the size of a row constant unlike data preparation for CNN, we did not prune the data so that all the rows have the same length but in this scenario instead of pruning we have pre-padded the data because RNN’s work better on sequential (temporal) data. We have pre-padded the data with zeroes such that all the rows have the same length, i.e., maximum length of rows before padding. It is observed that after concatenating the hourly data, the maximum length of the record is 4032. So all the rows are pre-padded with zeroes as mentioned earlier to 4032 for each patient. Pre-padding is done because the latest data does not get disturbed. Thus, we made the length of the record size constant and is ready for training.

Architecture The data which is prepared from the above step is fed into the RNN model which is developed using Keras API which runs on top of TensorFlow. An embedding layer is the architecture’s first layer. The data is fed to an embedding layer which represents the data using a dense vector representation into a continuous vector space. The data which is the output of the embedding layer is fed into long short-term memory hereby referred to as LSTM. Given delays of varying length, LSTM is appropriate to recognize, analyze, and predict time series. The output is fed to a dropout layer. The dropout layer’s output is fed into two dense layers where the activation functions are relu and softmax, respectively. The sigmoid function is a logistic function where the input to the function is converted into a value between 0.0 and 1.0. The output will be a single value specifying the probability of whether the person got infected with sepsis or not. The maximum of them will be set to 1 and will be considered as a result. The loss function used for this model is binary cross-entropy combined with adam as optimizer and accuracy as the metric.

5 Results

In this approach, we used the PhysioNet Computing in Cardiology Challenge 2019 dataset for detection of sepsis where three models are implemented; CNN, CNN with K-fold, and RNN. K used in this case is 4, and it is used for 4 iterations. For each iteration, train data size to validation data size will be in the ratio of 3:1. CNN has shown validation accuracy of 96.3%, CNN with K-fold has shown an average validation accuracy of 97.7% and RNN has shown validation accuracy of 95.5%. Table 1 sums up the exhibition of all the three models including the training loss and validation loss (Figs. 3, 4 and 5).

6 Conclusions and Future Work

Our proposed neural network model has pretty much performed well in predicting sepsis disease. The model’s hyperparameters have been tweaked a lot to improve performance. The main challenge that is faced here is handling the imbalanced and incomplete dataset that has been prevailed over by removing some of the attributes and filling in other missing values. The model’s performance can be upgraded further if the number of missing values is less in the dataset present which is used for training the model. From the results, CNN with K-fold has performed better and produced a better outcome. This model can be used by healthcare organizations for providing treatment to the patients by not depending completely on the lab reports which are

Table 1 Results obtained from RNN and CNN models

Model	Train accuracy	Train loss	Validation accuracy	Validation loss
RNN	0.9531	0.1559	0.9525	0.1587
CNN	0.9860	0.0419	0.9603	0.2112
CNN K-fold	0.9965	0.1080	0.9772	0.6080

Fig. 3 RNN CF

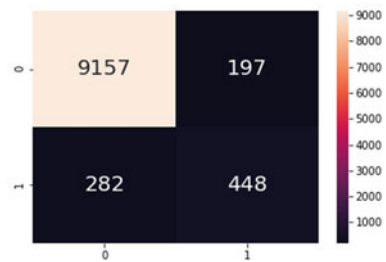
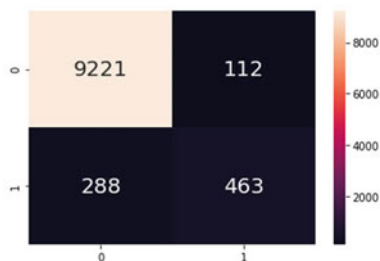


Fig. 4 CNN CF**Fig. 5** K-fold CNN CF

time-consuming for testing. Since the prediction task is extremely sensitive to even slight changes in study parameters, if we get a complete dataset, the results can get improved further.

References

1. Singer M et al (2016) The third international consensus definitions for sepsis and septic shock (Sepsis-3). *JAMA* 315(8):801–810. <https://doi.org/10.1001/jama.2016.0287>
2. Paoli CJ et al (2018) Epidemiology and costs of sepsis in the United States—an analysis based on timing of diagnosis and severity level. *Crit Care Med* 46(12):1889–1897. <https://doi.org/10.1097/CCM.0000000000003342>
3. Kumar A et al (2006) Duration of hypotension before initiation of effective antimicrobial therapy is the critical determinant of survival in human septic shock. *Crit Care Med* 34(6):1589–1596. <https://doi.org/10.1097/01.CCM.0000217961.75225.E9>
4. Seymour CW et al (2017) Time to treatment and mortality during mandated emergency care for sepsis. *New Engl J Med* 376(23):2235–2244. <https://doi.org/10.1056/NEJMoa1703058>
5. Li X, Ng GA, Schlindwein FS (2019) Convolutional and recurrent neural networks for early detection of sepsis using hourly physiological data from patients in intensive care unit. In: 2019 computing in cardiology (CinC), pp 1–4. <https://doi.org/10.23919/CinC49843.2019.9005765>
6. Fu M, Yuan J, Lu M, Hong P, Zeng M (2019) An ensemble machine learning model for the early detection of sepsis from clinical data. In: 2019 computing in cardiology (CinC), pp 1–4. <https://doi.org/10.23919/CinC49843.2019.9005710>
7. Schellenberger S, Shi K, Wiedemann JP, Lurz F, Weigel R, Koelpin A (2019) An ensemble LSTM architecture for clinical sepsis detection. In: 2019 computing in cardiology (CinC), pp 1–4. <https://doi.org/10.23919/CinC49843.2019.9005457>

Content-Based Nonlinear Filter for the Removal of Impulsively Modeled Artifacts from Images and Videos



D. V. N. Kameswari, M. Divya, K. Vasanth, S. Pradeep Kumar Reddy, and S. Nagaraj

Abstract A content-based nonlinear filter capable of eliminating impulsively modeled artifacts from images and videos is proposed. The algorithm is a nonlinear filter that chooses median of the array or modified trimmed winsorized median of the array as the threshold to estimate the pixel is noisy or not. The median or modified winsorized median will act as a measure of central tendency to estimate the pixel is noisy or not. There are two demarcation levels used to conclude the estimated pixel is noisy or not. The first demarcation is named as TH1 which holds value between (20 and 35). The second demarcation level is called TH2 which holds value between (0 and 15). The first delimiter says that the processed pixel is noisy or not and the second delimiter says that the median of the array is faulty or not. The proposed algorithm is applied on different defaced images and found to give very good visual results.

Keywords Blotches · Strip lines · Streaks · Black band missing

1 Introduction

Old images and videos are often corrupted by artifacts due to aging, defaced video tapes, etc. These artifacts are blotches, black band missing, stripes, streaks, etc. Stripes and scratches occur due to physical disturbance caused by the cassette reader to the tape. Blotches occur in images and videos due to the transmission error to the display device. Blotches are uniform pixels occur in a vicinity of the image. Band missing happens due to the faulty illumination or camera sensor which is captured. This is modeled as a line interaction that exist for three rows of pixels.

D. V. N. Kameswari · M. Divya · K. Vasanth (✉) · S. Pradeep Kumar Reddy
Department of Electronics and Communication Engineering, Vidya Jyothi Institute of Technology, Hyderabad, India
e-mail: vasanthecek@gmail.com

S. Nagaraj
Department of Electronics and Communication Engineering, SVCET (Autonomous), Chittoor, Andhra Pradesh, India

Stripes and scratches occur in old images as lines objecting the video content. Many filters are presented over the years for the removal of these impulsive burst. A filter that perceives faulty pels with rank ordered absolute difference value followed by median filter that is variable in nature in subsequent stage [1]. A basic 3 elements of chain are considered: they are digital encoder which converts analog sequence to digital and artifact generator which allows the qualitative tests for the restoration and last the artifact detector for finding the degraded region in the image and it marks [2]. A decision rule is applied to identify the faulty pels with an estimated value that uses a 5×5 window sizes to avoid blurring [3]. In this filter, without adverse edge elimination of artifacts is done [4]. A new technique for detecting and removing line starches by 2D autoregressive model [5]. A new method for removing of ringing and blur artifact. Gaussian filter is used to remove the blurring in the images with the less time and good performance. Ringing artifacts eliminate the value of the iterations [6]. A progressive iterative algorithm that uses a outlier detection rule is proposed [7]. Modified TANH function-based process is used for evaluating error paths for FXLMS. This method gives the weights to the different samples of large value and they remain to be constant [8]. A switching rank ordered filter is used to detect the static outliers [9]. An intermediate rank ordering-based filter replaces the damaged pels at complex noise densities with good edge preservation. It removes both the blurring in the large window and the poor noise in the small window [10]. In the first stage after the standard median filter, the intensity of the pixels decreases, then noisy intensity identification is performed for two different switching median filter. In the second stage, noise is detected [11]. This paper shows how to eradicate outlier from digital images in a effective way. Initially, the pels are categorized into two groups: “noise-free pixel” and “noise pixel.” The noisy category is subsequently eliminated [12]. Image noise may come from a variety of places, including the image sensor and electronic components. A difference-based median filter for efficiently locating dynamic outliers was suggested and it offered very good results [13]. This work proposes a new median filter that captures natural pixels for restoration using prior knowledge. The proposed filter restores corrupted images based on two dissimilar sets of veiled pels for median finding [14]. The adaptive median filter detects noisy pixels and arranges them as if they were original pixels without noise. It can detect images at higher densities as well, but the process takes longer to complete. For removing static outliers from images without modifying the retained edges, median filter algorithms are well established [15]. We suggest an iterative method for eliminating random-valued impulse noise based on a two-phase median filter. The adaptive center-weighted median filter is used in the first step to distinguish pixels that are likely to be affected by noise. These noises are restored using an iterative median filter approach that preserves edges and noise-free pixels [16]. All the artifacts discussed in this paper are assumed to be impulsive and noise model has been formulated. Each of the algorithms discussed in this section removes either only one type of noise. A generic algorithm that removes all impulsive noise artifacts is to be proposed. Section 2 of the work gives the targeted noise model. Section 3 illustrates the flow of proposed algorithm. Section 4 gives the case by case

discussion of the proposed algorithm. Section 5 gives the experiment and discussion about the work. Section 6 concludes the work.

2 Noise Model for All the Degradation

The modified trimmed winsorized median of the array as the threshold algorithm maps for the model specified in Eq. 1. This noise model gives the mathematical model that has many noise corrupts the pixels of the image. In this work, noise is assumed to be impulsive in nature. The proposed noise model is given by few proportions of static and dynamic outliers, zero mean Gaussian noise with variance 0.001 (white noise), image artifacts such as blotches, scratches and band missing.

$$C(i, j) = O(i, j) * \delta\delta(i, j) * (1 - D(i, j)) + (D(i, j) G(i, j)) + \gamma(i, j) \quad (1)$$

where $C(k, l)$ is the corrupted pixel, $O(k, l)$ is the uncorrupted pixel, $\delta(k, l)$ is the fixed valued impulse noise, $\beta(k, l)$ is the dynamic outlier noise, $\gamma(k, l)$ is white noise. A revealing parameter $D(k, l)$ is made to 1 if the pels are faulty and made 0 otherwise. $G(k, l)$ is the observed intensity in the corrupted region. k and l are the pixel locations.

3 Proposed Algorithm

The proposed algorithm employs a fixed 3×3 window for the elimination of impulsive artifacts. The algorithm is a nonlinear filter that chooses median of the array or modified trimmed winsorized median of the array as the threshold to estimate the pixel is noisy or not. The median or modified winsorized median will act as a measure of central tendency to estimate the pixel is noisy or not. There are two demarcation levels used to conclude the estimated pixel is noisy or not. The first demarcation is named ad TH1 which holds value between (20 and 35). The second demarcation level is called TH2 which holds value between (0 and 15). The first delimiter says that the processed pixel is noisy or not and the second delimiter says that the median of the array is faulty or not. Figure 1 gives the flowchart of the multiple threshold-based nonlinear filter a.k.a proposed algorithm. In case of videos, the algorithm splits the videos into different frames. The algorithm is applied to individual frames and subsequently to other frames. Finally, concatenating the restored frames results in the de-noised image.

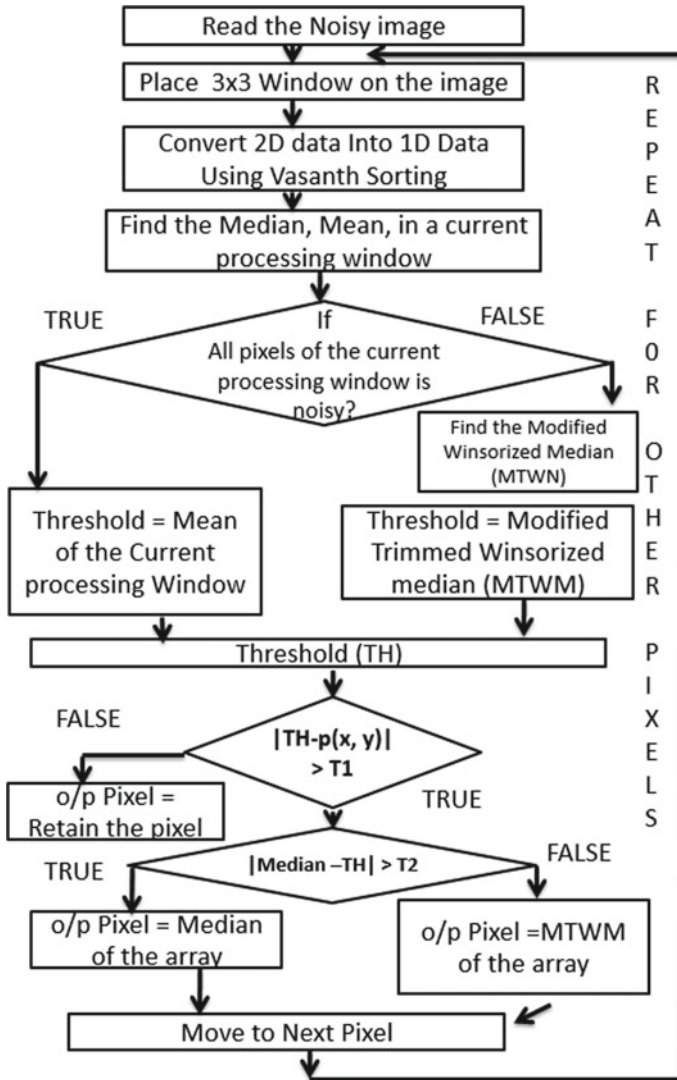


Fig. 1 Flowchart of the multiple threshold-based nonlinear filter

4 Insight of the Proposed Methodology

To illustrate the working of the multiple threshold-based nonlinear filter, we have broken the working of algorithm as different operating cases. The larger segment of matrix to the left is considered as defamed image segment, and the one in the right denotes the de-noised image segment. The pixel value encircled is the pixel processed. The smaller rectangle is the fixed 3×3 window visualization.

Case 1:

Window information is converted into the group information as specified:

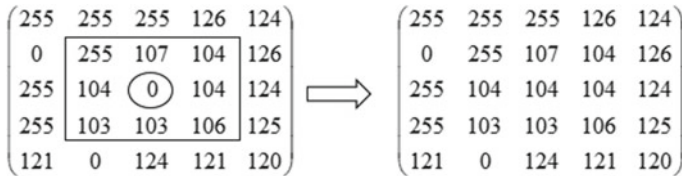
255 104 103 107 0 103 104 104 106

Organize the group information from smallest pixel value to largest values

0 103 103 104 104 104 106 107 255

Attain the average of the group information

$$(0 + 103 + 103 + 104 + 104 + 104 + 106 + 107 + 255)/9 = 109$$



Now attain middle value from the group information (0 103 103 104 104 104 106 107 255) = 105. From this case, it is observed that not all pixels of the processed window are faulty. Hence, find the modified winsorized median.

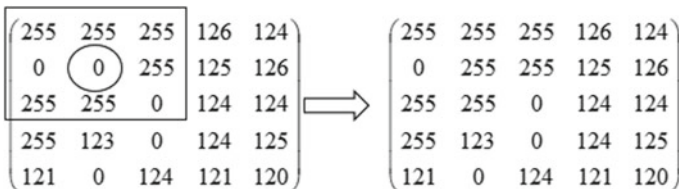
Modified Winsorized Median:

Consider the 1D data: (0 103 103 104 104 104 106 107 255)

Eliminate 0 and 255 from the given array. Also replicate the first and last value of the array and find the median (103 103 103 104 104 104 106 107 107) = 104. This is the process to find the modified winsorized median. Now, the threshold of the given algorithm holds 104 (which is modified winsorized median). The encircled pixel is processed currently which holds 0. The detector uses the absolute value of the modified winsorized median (which acts as threshold in this case) and processed pixel greater than a specific value. $|0 - 104| > 30$ the condition returns true. The program control enters the next loop now the absolute value of the threshold (104 in this case) and median array is evaluated and compared with a specific value 2. $|105 - 104| > 15$ this condition is false, and hence, the processed pixel is declared as faulty and the modified winsorized median of the array is replaced in the defaced pixel.

Case 2:

Window information is converted into the group information as specified:



255 0 255 255 0 255 255 255 0

Organize the group information from smallest pixel value to largest values

0 0 0 255 255 255 255 255 255

Attain the average of the group information

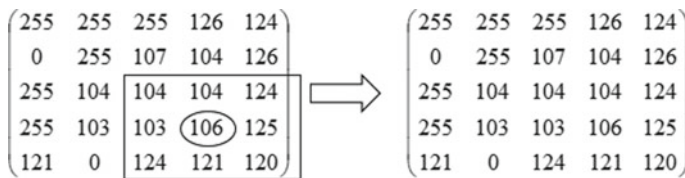
$$(0 + 0 + 0 + 255 + 255 + 255 + 255 + 255 + 255)/9 = 170$$

Now, attain middle value from the group information (0 0 0 255 255 255 255 255 255) = 255. All the pixels in the considered window have either 0 or 255. Hence, the entire window is deemed noisy.

The threshold of the given algorithm holds the mean of the array, i.e., 170. The encircled pixel is processed currently which holds 0. The detector uses the absolute value of the mean of the array (which acts as threshold in this case) and processed pixel greater than a specific value. $|0 - 170| > 30$ the condition returns true. The program control enters the next loop; now, the absolute value of the threshold (170 in this case) and median array is evaluated and compared with a specific value 2. $|255 - 170| > 15$ this condition is true, and hence, the processed pixel is declared as faulty and the median of the array is replaced in the defaced pixel.

Case 3:

Window information is converted into the group information as specified



104 103 124 104 106 121 124 125 120

Organize the group information from smallest pixel value to largest values

103 104 104 106 120 121 124 124 125

Attain the average of the group information

$$(103 + 104 + 104 + 106 + 120 + 121 + 124 + 124 + 125)/9 = 114$$

Now, attain middle value from the group information (103 104 104 106 120 121 124 124 125) = 120. From this case, it is observed that not all pixels of the processed window are faulty. Hence, find the modified winsorized median.

Modified Winsorized Median:

Consider the 1D data: (103 104 104 106 120 121 124 124 125)

Eliminate 0 and 255 from the given array. Also replicate the first and last value of the array and find the median. Median (103 103 104 104 106 120 121 124 124 125) = 120. Now, the threshold of the given algorithm holds 120 (which is modified winsorized median). The encircled pixel is processed currently which holds 106. The detector uses the absolute value of the modified winsorized median (which acts as threshold in this case) and processed pixel greater than a specific value. $|106 - 120| > 30$ the condition returns false. Hence, the processed pixel is declared as non-faulty and the pixel is retained.

5 Simulation Results and Discussions

The initial aim was to design a filter that eliminates different impulsive image artifacts. Hence, images hosted by signal and image processing institute of University of South California is used for the work. The impulsive artifacts are induced artificially to the image. Black band noise induced by damaging three column of pixels with "0." Blotches were created by adding random 0 and 255 arbitrarily in a confined vicinity. Streaks are added to the image replacing three column values with 255. Stripes are created by replacing 1 column of pixels with 0. White stripes are also created by replacing one column of 255 both horizontally and vertically. All the degradation is employed on an image (30% salt and pepper noise, 5% random-valued impulse noise, zero mean 0.001 variance Gaussian noise, blotches, black band missing, blotches, streaks, white stripes and stripes) by adding all the above composition of noises. Once the images are corrupted, the algorithms are employed on the corrupted images and images were taken. Figures 2, 3, 4, 5, 6 and 7 give the visual performance of different algorithms corrupted by black band missing, blotches, streaks, stripes, white stripes and all degradations, respectively. It was observed from Figs. 2 and 3 that proposed filter is good in restoring pixels corrupted by black band noise and blotches. The performance of the proposed algorithm is moderate while removing streaks. A part of the streaks is removed from the image as seen in Fig. 4. It is obvious from Fig. 5 that the developed filter is worthy in eliminating black stripes fully from the image. The algorithm very faintly removes white stripes from the image. When it comes to the elimination of all degradation, the proposed algorithm removes static and dynamic outliers, few traces of zero mean Gaussian noise, blotches, stripes and black band missing.

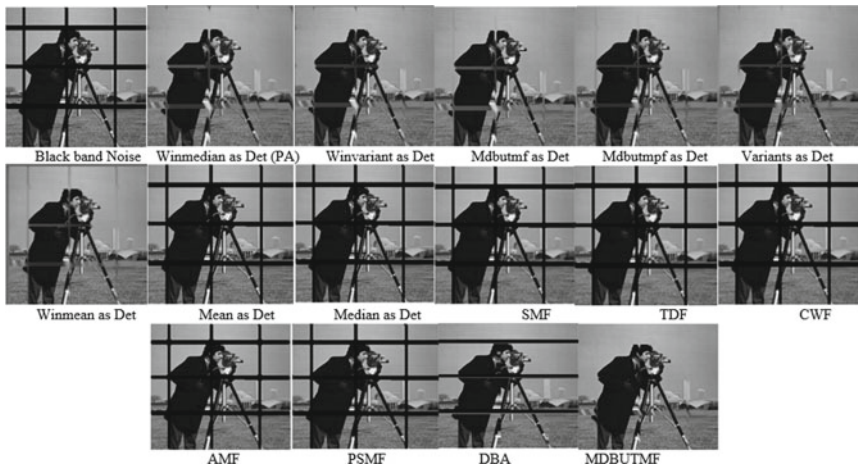


Fig. 2 Black band missing artifact and its elimination by different filters on cameraman images

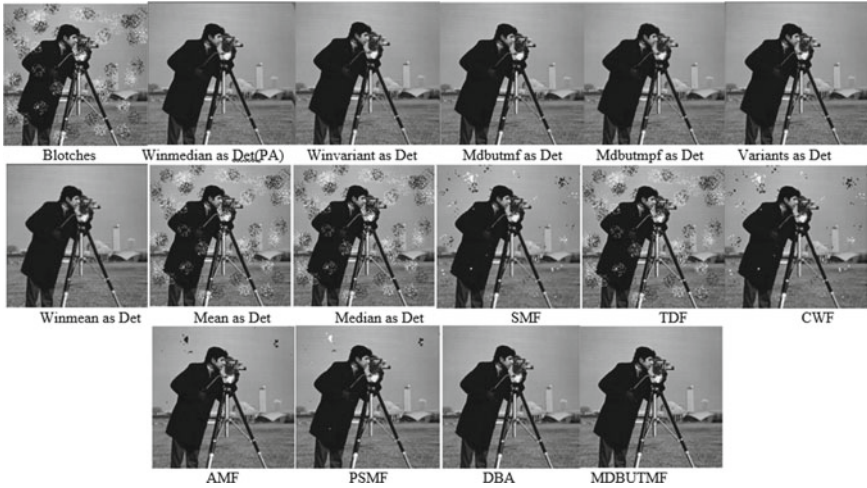


Fig. 3 Blotches artifact and its elimination by different filters on cameraman image

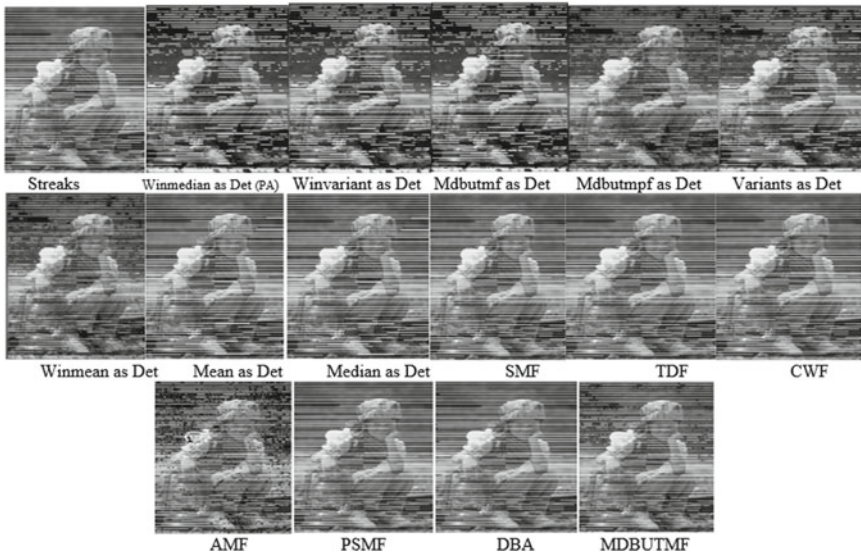


Fig. 4 Streaks artifact and its elimination by different filters on girl image

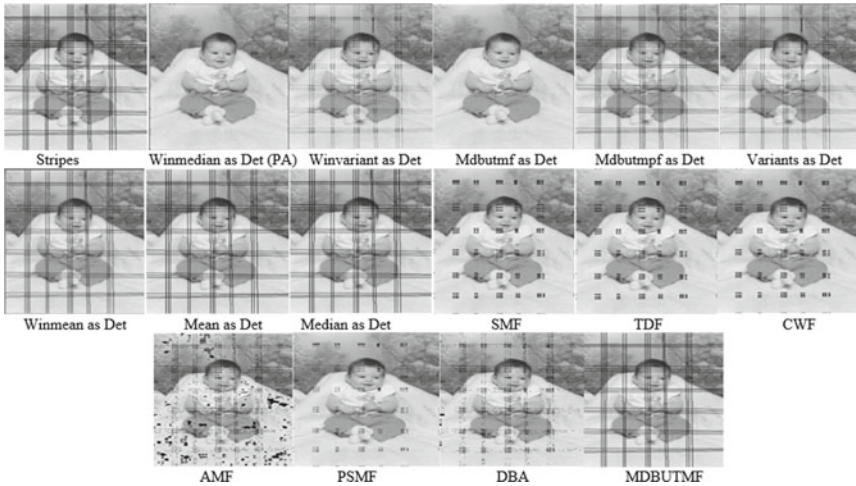


Fig. 5 Stripes artifact and its elimination by different filters on baby image

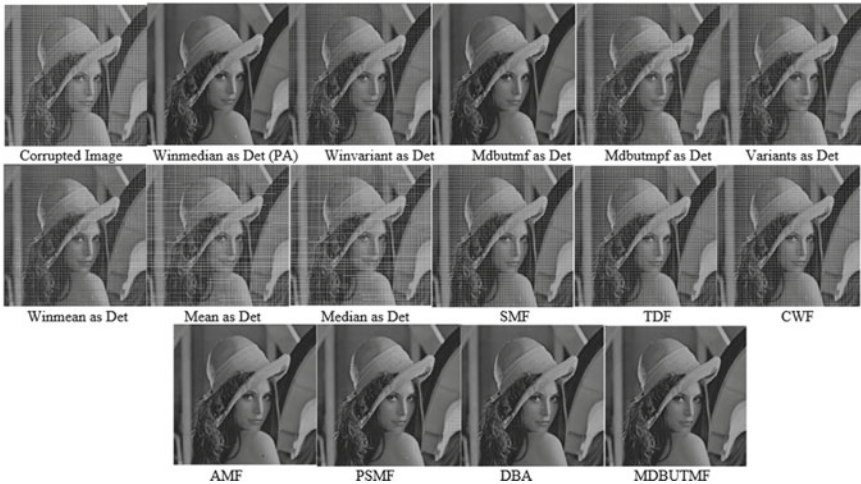


Fig. 6 White stripes artifact and its elimination by different filters on Lena image

But few traces of white stripes and streaks were removed in the image. Adding to the curiosity, the proposed algorithm was applied on old videos which were converted from VHS tapes to digital media. It was found that the proposed algorithm eliminates low-tailed impulsive artifacts better than long-tailed impulsive artifacts. The original and restored frames are shown in Fig. 8. The algorithm is capable of eliminating image impulsive artifacts such as blotches, black band missing, streaks and white stripes and composition of all degradation. The main reason for the good

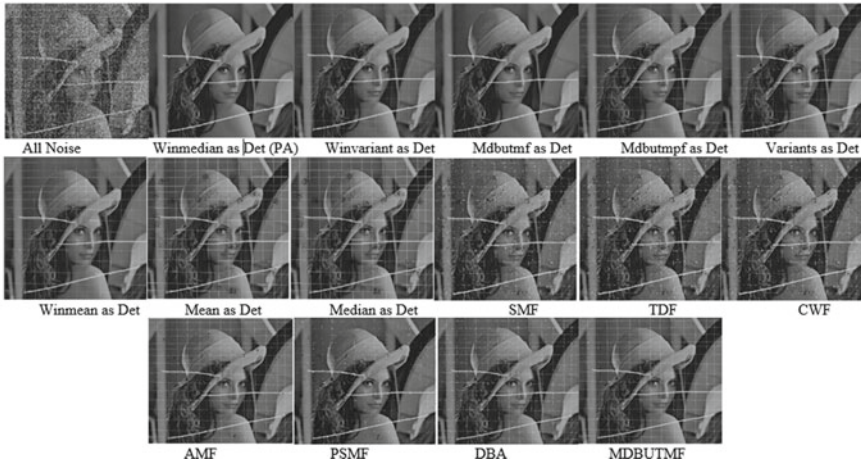


Fig. 7 All degradation artifact and its elimination by different filters on Lena image

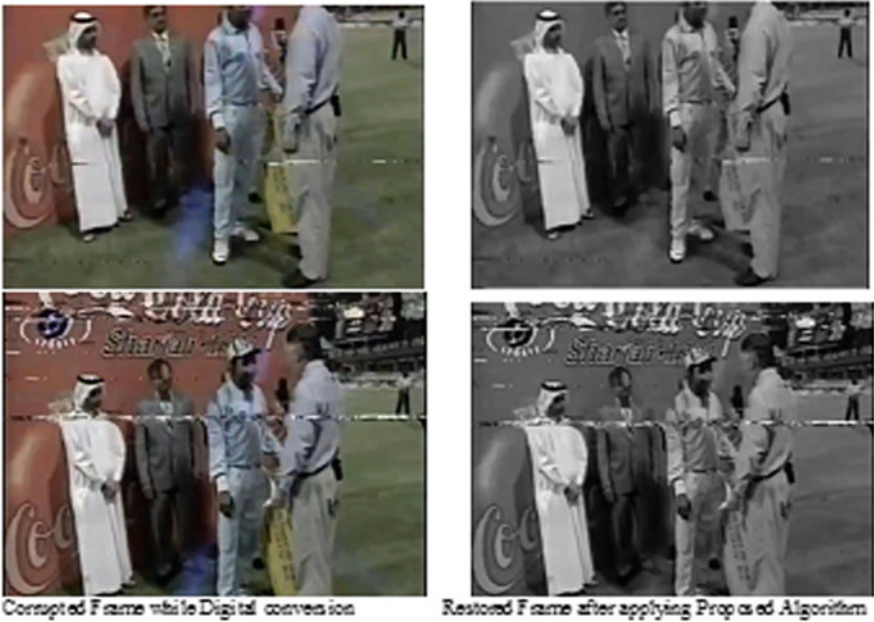


Fig. 8 Real-time corrupted frame and restored frames (Courtesy Doordarshan, India)

restoring capability is mainly the use of median or modified unsymmetrical trimmed winsorized median as a threshold to estimate the noisy pixel with two delimiters.

6 Conclusion

An algorithm capable of eliminating different impulsive noise is proposed. This algorithm shows excellent noise elimination capabilities up to the pixel corrupted by three column levels. The filter also uses multiple threshold making it content-based decision-making to identify the faulty pixel and replace it subsequently. This makes the noise suitable for elimination of black band missing, blotches, stripes, streaks, white stripes and all degradation.

References

1. Vijaykumar VR, Jothibasu P (2010) Decision based adaptive median filter to remove blotches, starches, streaks, stripes and impulsive noise in images. In: International conference on image processing, pp 117–120
2. Silva AU, Corte-Real L (1999) Removal of blotches and line scratches from film and video sequences using a digital restoration chain. In: Workshop on nonlinear signal and image, pp 826–829
3. Hanji G, Latte MV, Shweta NM (2012) An improved nonlinear decision based algorithm for removal of blotches and impulses in gray scale images. In: International conference on advanced computing and communication technologies, pp 240–244
4. Manikandhan S, Ebenezer D (2008) A nonlinear decision based algorithm for removal of strip lines, drop lines, blotches, band missing and impulses in images and videos. *EURASIP J Image Video Process* 485921:1–10
5. Kokaram A (1996) Detection and removal of line starches in the degraded motion pictures sequences. In: European signal processing conference, pp 5–8
6. Kaushik MK, Chandrakala GC, Abhinay R (2018) Ringing and blur artifact removal in image processing applications. In: International conference on intelligent computing and control systems (ICICCS), pp 260–264
7. Wang Z, Zhang D (1999) Progressive switching median filter for the removal of impulse noise from highly corrupted images. *IEEE Trans Circ Syst* 46:78–80
8. Akhtar M (2018) An adaptive algorithm based on modified tanh nonlinear and fractional processing for impulsive active noise control system. *Sage J* 37:495–508
9. Pandey R (2008) An improved switching median filter for uniformly distributed impulse noise removal. *Int J Commun Eng* 2(2):240–242
10. Srinivasan KS, Ebenezer D (2007) A new fast and efficient decision based algorithm for removal of high density impulse noises. *IEEE Trans Sig Process* 14:189–192
11. Xia J, Xiong J, Zhang Q (2010) An efficient two state switching median filter for the reduction of impulse noises with different distributions. In: 3rd international congress on image and signal processing, pp 639–644
12. Ibrahim H, Kong NSP, Ng TF (2008) Simple adaptive median filter for the removal of impulse noise from highly corrupted images. *IEEE Trans Consum Electron* 54(4):1920–1927
13. Ma C, Lv X, Ao J (2019) Difference based median filter for removal of random value impulse noise in images. *Multimed Tools Appl* 78:1131–1148

14. Hsieh MH, Cheng FC, Shie MC, Ruan SJ (2013) Fast and efficient median filter for removing 1–99% levels of salt-and-pepper noise in images. *Eng Appl Artif Intell* 26(4):1333–1338
15. Abhishek R, Srinivas N (2013) Removal of salt and pepper noise in image through weighted median filter. *Int J Eng Res Technol* 2(10):3587–3592
16. Zhang J (2010) An efficient median filter based method for removing random valued impulse noise. *Digital Sig Process* 20(4):1010–1018

Hardware Implementation of Epidermis Segmentation in Skin Histopathological Images



Raju Machupalli, Luiz Antonio de Oliveira Junior, Masum Hossain, and Mrinal Mandal

Abstract The histopathological analysis of tissue specimens is the gold standard to diagnose many kinds of cancer. Recently, a few computer-aided diagnosis (CAD) techniques have been proposed for the automated diagnosis of a skin cancer type, known as melanoma, by analyzing whole slide images (i.e., biopsy slides). The first step in the automated melanoma diagnosis is the epidermis segmentation of the biopsy images. The whole slide images are typically very large and hence require a significant amount of processing time. In this paper, we propose a hardware accelerator for the epidermis segmentation in a skin whole slide image. Experimental results show that the proposed system provides a significant speedup over a software-only implementation.

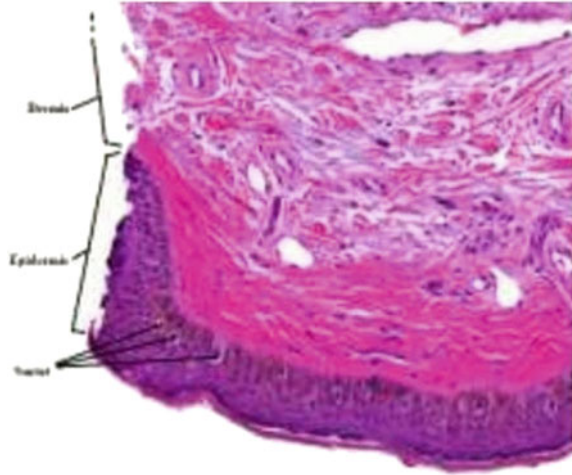
Keywords Whole slide image analysis · Melanoma diagnosis · Epidermis segmentation · Image processing · FPGA accelerator

1 Introduction

Skin cancer is among the most frequent types of cancer around the world and melanoma is the most aggressive type of skin cancer [1]. The gold standard used by the pathologists to diagnose melanoma is the histopathological analysis of tissue specimen (i.e., biopsy slides) as these slides provide a cellular level view of the disease [2]. The anatomy of skin tissue with different skin layers such as dermis, and epidermis, as well as the nuclei of the skin cells, are shown in Fig. 1. Diagnosis of melanoma can be made based on the architectural and morphological features of atypical cells in the epidermis and dermis-epidermis junctional area. Therefore, segmentation of the epidermis layer in a whole slide image (WSI) is the first step for automated diagnosis of melanoma. Lu and Mandal [1] proposed a computer-aided diagnosis (CAD) technique for epidermis segmentation which uses red channel of a

R. Machupalli (✉) · L. A. de Oliveira Junior · M. Hossain · M. Mandal
Department of Electrical and Computer Engineering, University of Alberta, Edmonton, AB
T6G2R3, Canada
e-mail: machupal@ualberta.ca

Fig. 1 Anatomy of skin tissue in a WSI



WSI as the input. The CAD technique has five major modules, namely image thresholding, complement, image dilation, connected component analysis and epidermis extraction [1].

The WSI images are typically acquired by using digital scanners at high magnification. A WSI may have several billion color pixels. For example, at $40\times$ magnification (with $0.11625\ \mu\text{m}$ pixel resolution), a $30\ \text{mm}^2$ glass slide tissue can generate about 2.2×10^9 color pixels [3]. Processing such images on a general purpose processor (GPP) takes a significant amount of time. Therefore, to increase the speed of analysis and diagnosis, it is desirable to develop hardware accelerators.

With advancements in CMOS and fabrication technology, Field Programmable Gate Array (FPGA) and Graphical Processing Unit (GPU) are being used as a High-Performance Computing (HPC) solution to overcome the GPP limitations. GPUs are efficient for data parallel applications with high memory bandwidth requirement. GPUs are programmed using high-level languages. FPGAs have more flexibility than GPUs but takes more time to implement a technique. FPGAs are efficient for both data and task parallel applications. Hence, FPGA is chosen to implement in this paper.

Ankit and Mandal [3] proposed a solution for speeding up epidermis segmentation (proposed in [1]) on a MATLAB-FPGA-based hybrid hardware simulator platform. In [3], four modules image thresholding, complement, dilation, and epidermis mask extraction were implemented in HDL to simulate on the FPGA platform. The connected component analysis (CCA) module was implemented on MATLAB as implementation of CCA involves scanning the image multiple times and does not offer much speedup on the hardware over software. An overall speedup (simulated) of 2.9 over MATLAB was reported in [2]. As implementation on a simulation platform imposes fewer restrictions on available resources and memory management, the reported speedup may not be obtained for actual implementation on a specific

FPGA hardware. In this paper, we propose an FPGA-based accelerator architecture for the epidermis segmentation. The accelerator has been implemented on the DE2i-150 FPGA development board [4]. The organization of the paper is as follows. Section 2 presents the implementation details of each module. Section 3 presents the performance of the proposed accelerator, followed by the conclusion in Sect. 4.

2 Proposed Hardware Implementation

A hardware accelerator for the epidermis segmentation using FPGA is presented in this paper. The DE2i-150 FPGA development board used for the implementation. The board is an embedded platform with Intel N2600 Atom Dual core processor coupled with Altera's Cyclone IV GX FPGA. The Atom processor has 64-bit Instruction set, 1M cache running at 1.6 GHz clock speed. The Atom paired with Intel[®] NM10 Express Chipset through Direct Media Interface (DMI) to provide rich I/O capabilities and flexibility via high-bandwidth interfaces, such as PCI Express, Serial ATA, and USB 2.0. The Cyclone IV FPGA is connected to the Atom processor through the PCI Express (PCIe) bus. The PCI Express protocol developed by Jacobsen et al. [5] under open library a Reusable Integration Framework for FPGA Accelerators (RIFFA) is used to establish 64-bit communication between the Atom processor and FPGA through PCIe. The schematic of the proposed architecture is shown in Fig. 2. The threshold value (τ) is calculated using Otsu's method [6] on the Atom processor using C++. The red channel image (R) and the threshold value (τ) are then sent to the FPGA through the PCI Express bus. At each clock cycle, 64-bits, i.e., 8-pixel values (i1 to i8), are received at the FPGA and processed in parallel as shown in Fig. 2.

2.1 Image Threshold and Complement (T&C)

Image thresholding converts a monochrome image into a binary image of foreground and background pixels using a threshold value τ . In the red channel WSI image, the epidermis layer looks darker than the dermis layer, as shown in Fig. 1. Therefore, after thresholding, the epidermis and dermis layers are segmented as background pixels and foreground pixels, respectively. However, in the diagnosis of melanoma, the epidermis is a major region of interest, and therefore, the epidermis pixels should be classified as the foreground pixels for further analysis. This can be done by applying the 'complement' operation on the binary image. The thresholding and complement operations (T&C) are combined and implemented using an 8-bit comparator as follows

$$\bar{p} = \begin{cases} 0 \text{ (background or dermis),} & \text{if } i \geq \tau \\ 1 \text{ (foreground or epidermis),} & \text{otherwise} \end{cases} \quad (1)$$

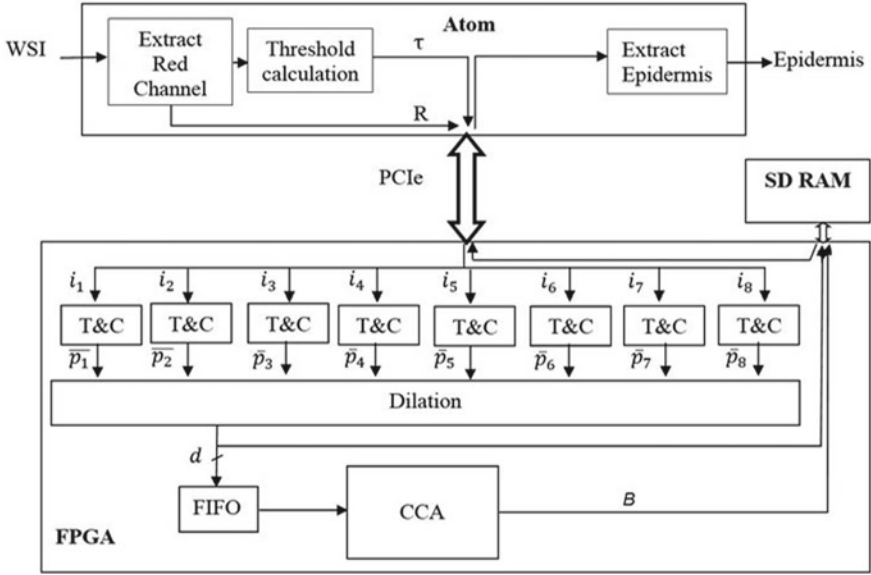


Fig. 2 Illustration of proposed architecture

2.2 Image Dilation

An example of a binary image generated by the T&C module is shown in Fig. 3c. Figure 4a shows a magnified version of the square region in Fig. 3c. It is observed that, the epidermis boundary in the binary image is not smooth. Therefore, the image dilation operation is applied on the binary image. Note that, image dilation is a fundamental morphological operation that enhances objects and smoothens the boundary of objects in an image. The effect of dilation on a binary image can be seen in Fig. 4. It is observed that the boundary gets smoothed and noise inside the objects is reduced.

In dilation, a structuring element S is superimposed on top of the image with the center of S coinciding with an input pixel. The dilation operation corresponding to an input pixel $I(p, q)$, with a binary structuring element S , can be formulated as follows:

$$d_{p,q} = \max\{I_{p+m,q+n} \times S_{m,n}; \quad -M/2 \leq m \leq M/2, -N/2 \leq n \leq N/2\} \quad (2)$$

where $S_{m,n}$ is the coefficient in S at (m, n) , $M \times N$ is the size of S , and $d_{p,q}$ is the dilated output pixel. Based on the size of the S , a few previous rows of image, data need to be stored to avoid memory read and write for each pixel dilation. For an $M \times N$ structuring element, $M - 1$ previous rows of data need to be stored in the registers. In this work, a 3×3 structuring element is used. Hence, two previous rows of image data are stored in two register arrays. Eight pixels from T&C and two rows of image in register array can generate eight 3×3 windows of image data. Therefore,

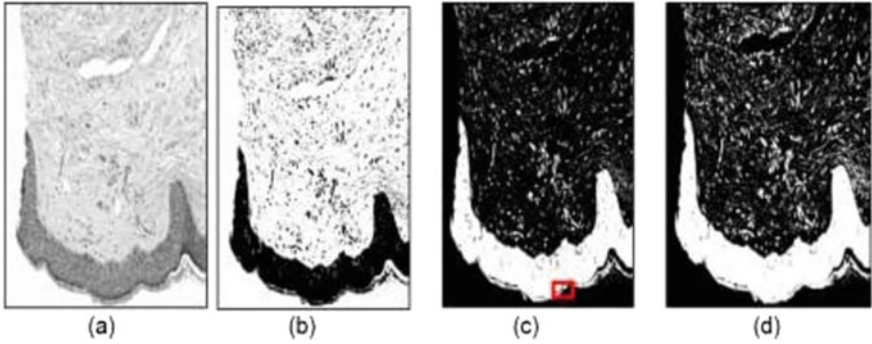


Fig. 3 **a** Red channel image (i) from WSI, **b** threshold binary image (p), **c** complemented binary image (\bar{p}), and **d** dilated binary image (d)

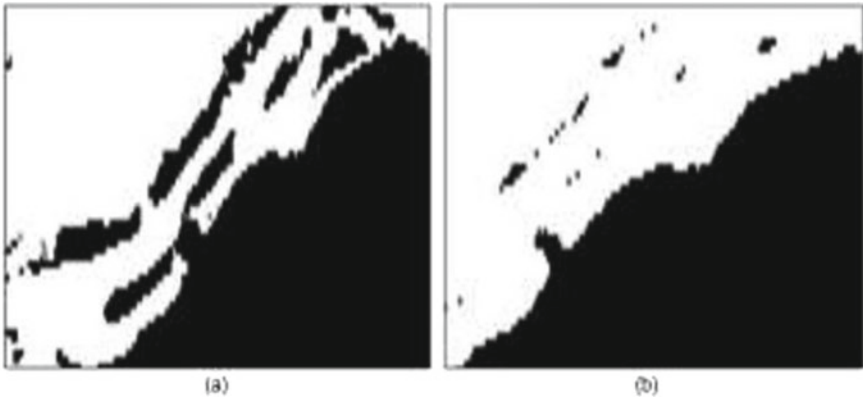


Fig. 4 A magnified area of the binary image, **a** binary image before dilation and **b** binary image after dilation

dilation on 8-pixels can be done in parallel. The circuit for binary dilation can be implemented using the simple AND and OR logic gates. In the implementation, first the AND operation is performed between individual elements in S and image data, and then the OR operation. In the proposed architecture, eight single-pixel dilation circuits are implemented in parallel to process 8 pixels at a time. Therefore, the implemented dilation module gives a throughput of 8-pixels per clock.

2.3 Connected Component Analysis

A dilated binary image can have thousands of foreground objects (for larger images). Epidermis should be identified among these foreground objects to generate the epi-

dermis mask. This can be done by connected component analysis (CCA). The conventional CCA requires multiple raster scans of the whole image to complete the process. Reading the whole image multiple times consume a significant amount of time on the hardware. Tang et al. [7] proposed a run-length-based single-pass CCA algorithm to eliminate multiple read of image and improve the throughput. In this work, we implemented a run-length-based single-pass CCA algorithm [7]. The relation among the equivalent labels (labels belonging to the same objects) is constructed in the equivalence resolver using linked list structure. NEXT, HEAD, and TAIL tables are used to store the equivalence information. The object features are accumulated using temporary data cache and DATA table in the feature accumulation process. DATA table is constantly updated with new data of each object at the end of each row scan.

In general, the epidermis has a long and narrow shape. All other objects in the dilated binary image are much smaller. With the help of bounding box information, the epidermis region can be identified among other objects by using the area criteria as follows:

$$B_i = \begin{cases} \text{epidermis,} & \text{if } A(B_i) \geq T_{\text{area}} \text{ and } \frac{l_{i1}}{l_{i2}} \geq T_S \text{ or } \frac{l_{i1}}{l_{i2}} \geq \frac{1}{T_S} \\ \text{others,} & \text{otherwise} \end{cases} \quad (3)$$

where B_i denotes the bounding box of the object i and $A(B_i)$ is the area of the B_i . T_{area} and T_S are, respectively, the threshold values for area and axes ratio to identify the epidermis region. l_{i1} and l_{i2} are the width and height of the object BI, respectively, from the bonding box information. In this implementation, T_{area} is set to 1% of input image size, T_S is set to 2 (as width is higher than height for a narrow shape horizontal epidermis). The identified epidermis bounding box information is sent to SDRAM.

2.4 Epidermis Mask Extraction

The cropped epidermis area has epidermis and noise. To remove the noise, hole filling should be applied on the cropped binary image. Reading the cropped epidermis data from SDRAM, performing hole filling and generating a mask consume more time in FPGA than the Atom processor. Hence, the dilated image and the bounding box information are sent to the Atom processor. Mask generation is implemented using C++ with the help of OpenCV library in the Atom processor.

3 Experimental Result

Epidermis segmentation results are shown in Fig. 5. Figure 5 (a) is the input WSI image, (b) is the segmentation result from MATLAB, and (c) is segmentation result

from the proposed hardware. Segmented region boundary is highlighted with color. Both MATLAB and FPGA implementation provide same accuracy. Generally, the WSI images are large. To perform segmentation on a full WSI image using proposed hardware, a WSI image is divided into several slices of size 4096×8192 with some overlap, and then processed one slice at a time.

Different WSI images are tested on the hardware and the execution time is compared with existing works. Table 2 gives the comparison between software [1], hybrid [3], and proposed hardware. The MATLAB is running on the CPU with AMD Athlon II processor working at 2.90 GHz clock speed, with 4 GB RAM. It is observed that the proposed architecture provides a speedup of over 300% [3]. The FPGA implementation of the proposed architecture is showing a moderate speedup of 9 since it is running at 100 MHz clock. The ASIC implementation can provide a significantly higher speedup.

4 Conclusion

A software implementation of CAD technique takes a significant amount of processing time. To assist the pathologists for real-time diagnosis, this processing time should be reduced. In this paper, an FPGA-based hardware accelerator for the epidermis seg-

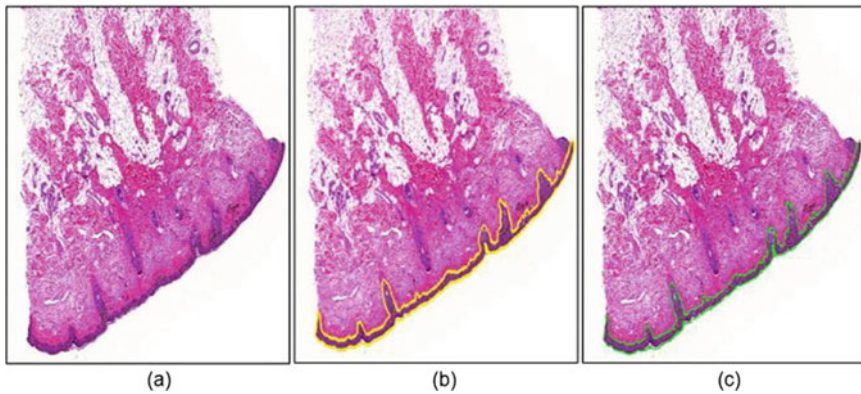


Fig. 5 Segmentation performed on a WSI image, **a** input image, **b** output from MATLAB, and **c** output from proposed implementation

Table 1 Hardware utilization on FPGA for an image size of 4096×8192

Resources	Utilized/available
Logic elements	22,617/149,760 (14%)
Memory bits	1,958,775/6,635,520 (30%)
PLLs	3/8

Table 2 Comparison with existing techniques

Resources	Clock frequency	Speedup
MATLAB (on CPU) [1]	2.9GHz	1 (reference)
Hybrid implementation	143 MHz	2.9
Proposed implementation	100 MHz	9

mentation has been proposed, and its performance is evaluated by implementing on DE2i-150 FPGA development board. The hardware accelerator shows a significant performance improvement, approximately 9:1 over a MATLAB, even though it is running at a much lower clock frequency. The achieved speedup is limited by the SDRAM memory bandwidth. Further performance improvement can be achieved by implementing the proposed accelerator on a high-end FPGA development board with higher memory bandwidth or ASIC implementation.

References

1. Lu C, Mandal M (2012) Automated segmentation and analysis of the epidermis area in skin histopathological images. In: 2012 annual international conference of the IEEE engineering in Medicine and Biology Society, 2012 Aug 28. IEEE, pp 5355–5359
2. Kumar V, Abbas AK, Fausto N, Aster JC (2014) Robbins and Cotran pathologic basis of disease. Professional edition e-book, Elsevier Health Sciences
3. Ankit A, Mandal M (2015) Novel hybrid hardware architecture for nuclei detection in skin histopathological images. In: 2015 IEEE international conference on signal processing, informatics, communication and energy systems (SPICES), 2015 Feb 19, pp 1–6
4. DE2i-150 FPGA development board specifications and architecture. <https://www.terasic.com.tw/cgi-bin/page/archive.pl?Language=English&CategoryNo=11&No=529&PartNo=1>, last accessed 2021/05/21
5. Jacobsen M, Richmond D, Hogains M, Kastner R (2015) RIFFA 2.1: a reusable integration framework for FPGA accelerators. ACM Trans Reconfigurable Technol Syst (TRETs) 8(4):1–23
6. Otsu N (1979) A threshold selection method from gray-level histograms. IEEE Trans Syst Man Cybern 9(1):62–66
7. Tang JW, Shaikh-Husin N, Sheikh UU, Marsono MN (2018) A linked list run-length-based single-pass connected component analysis for real-time embedded hardware. J Real-Time Image Process 15(1):197–215

Dual-Band MIMO Antenna with Enhanced Isolation Using Fractal Isolators



Akanksha Singh, Arvind Kumar, and Binod Kumar Kanaujia

Abstract This paper illustrates the outcome of novel fractal-based geometry of the low-profile multi-input multi-output (MIMO) antenna system with enhanced isolation for 5G mm wave, satellite and defense applications. Four identical fractal-shaped isolators are acquired to lower the coupling between each elements. Each fractal structure is responsible for isolation enhancement between adjacent antenna elements. The proposed four-port MIMO antenna works for 12.1–18.9 GHz for satellite and defense applications and 20.1–30 GHz for the 5G mm wave application allocated by FCC. The simulations are done on the HFSS version 13. The simulation results of different parameters like S parameters, mutual coupling, and gain and radiation pattern are presented. A maximum improvement of 26.6 dB isolation is achieved in the desired frequency band (20.1–30 GHz). The gain of around 4.8 dB and 6.1 dB in 12.4–18.9 GHz and 26 GHz frequency bands, respectively, which gives the proposed antenna excellent diverse performance, and hence, it is suitable for the MIMO applications.

Keywords Fractal structure · 5G mm wave · MIMO · Decouple

1 Introduction

With the increase in the mobile communication and IOT, the need for high data rate is increasing dramatically which need high amount of information interchange and high

A. Singh (✉) · A. Kumar
Department of Electronics and Communication Engineering, National Institute of Technology,
Kurukshetra, Haryana 136119, India
e-mail: akankshasingh5614@gmail.com

A. Kumar
e-mail: arvind_sharma@ntkkr.ac.in

B. K. Kanaujia
School of Computational and Integrative Sciences, Jawaharlal Nehru University, New
Delhi 110067, India
e-mail: bkkanaujia@ieee.org

© The Author(s), under exclusive license to Springer Nature Singapore Pte Ltd. 2022
P. Kumar Jain et al. (eds.), *Advances in Signal Processing and Communication Engineering*, Lecture Notes in Electrical Engineering 929,
https://doi.org/10.1007/978-981-19-5550-1_9

system reliability. This demand of increase in reliability is satisfied by multi-input multi-output antenna systems. The increasing data rate explosion in the communication system grabs the attention to the 5G mm frequency bands. Various researchers are doing research to design the 5G mm wave antennas. Various antennas are used for the millimeter wave communication. An innovative ultra-wideband MIMO antenna with very low degree of mutual coupling is presented in [1]. A unique fractal slot antenna is suggested as a MIMO antenna with four ports in [2] which are used for 5G frequency bands.

In present days, fractal-shaped structure can be applied to enhance the performance of MIMO antenna. As a result, new unique characteristics of the fractal-shaped structure, antenna elements with compact size and multiband performance, can be introduced. By using fractal-based isolation, structure can restrain the current flow path which results in low mutual coupling. Fractal structure results in compact size of the MIMO antenna. When more than two antenna elements are placed in the close vicinity, performance of the system decreases because of the poor isolation [3]. In the past decades, lot of methods are used to increase MIMO diversity performance between the dense antenna elements. Normally, there are so many techniques to remove the interference between closely packed elements. One technique is to diminish the surface current flow path. This is usually done by using metamaterial [4, 5] EBG structures and the defected ground surface. In [6] and [7], decoupling networks are introduced to lessen the interference. Neutralization lines are used for lowering the mutual coupling in [8]. F-shaped defected ground structure is also used in [9] for the suppression of mutual coupling. Extensive research has been done to reduce the mutual coupling in MIMO antenna systems. Recently, fractal structure has been introduced in contemporary MIMO antenna design for compactness, high isolation, leakage suppression, and in filter e-application. A novel decoupling technique is acquired which is based on a tapered slot to upgrade the MIMO performance of the antenna in [10].

In this present work, fractal structure was used for enhancement of isolation between each element which is working in the MIMO environment. Fractal structure has the very unique property of compactness with long current path. A 4×4 MIMO antenna is designed with fractal-shaped isolator. Compared to the previous antennas in [11, 12], the suggested antenna design not only attains the dual-band operation but also have simple structure. Furthermore, the proposed antenna is also compact in size, and proposed antenna offers high MIMO diversity in terms of high gain and better efficiency in addition to compact size. Other parameter study such as radiation pattern, gain is presented in other section of the paper. A comparison between the measure and simulated is also present in the section. Section 2 illustrates the geometry and structure of the suggested MIMO antenna. In Sect. 3, study of newly developed fractal structure is shown. Section 4 presents the result and discussion. Section 5 provides the conclusions.

2 Antenna Designing and Structure

The evolution of the MIMO antenna working in 5G mm wave application is shown in Fig. 3. Reference antenna consists of a rectangular patch. It can be noticed that this conventional antenna works in single band for the frequency range of 18.9–25.5 GHz. In ant 2, a u-shaped slot is engraved from the rectangular shape radiator and a rectangular shaped slot is etched in the bottom plane to enhance bandwidth from single band to dual-band resonating at 19 and 24.5 GHz (Fig. 1). Figure 2 show the return loss of ant1, ant2 and ant3. The design of the MIMO antenna is commenced from the rectangular patch. The lower surface of the antenna consists of a ground plane of size 10 mm × 20 mm; to achieve the better isolation characteristics, orthogonal orientation is used of antenna elements [1]. The suggested antenna consists of a rectangular shaped radiator with size of 10 mm × 8 mm, and it is fed with 50 Ω micro-strip feed line. The proposed structure is printed on the Roger 5800 substrate with the dimension of 40 mm × 40 mm × 1.6 mm with the ξ of 4.4 and δ of 2.2. For the simulation purpose, HFSS is used. Finally, MIMO antenna is fabricated using this conventional antenna.

The fabricated antenna is working in the 24 GHz band with very high mutual coupling in this band. On the top of the substrate, rectangular patch is designed, and on the lower side of the substrate, ground is placed with a rectangular slot on the bottom plane. Figure 4 shows the simulated S_{11} of 4 × 4 MIMO systems. For the isolation purpose, newly developed fractal design is introduced in the four port MIMO antenna. In the first iteration, a rectangular shape is taken of the size 4 mm × 12 mm. In the second iteration, rectangular shape is of the size 0.5 mm × 1.7 mm. The size of the fractal design isolator is 4 mm × 12 mm. Rectangular-shaped portions are etched in the design to make the shape fractal. Size of the etched rectangles is 0.5 mm × 1.7 mm by using this fractal-based geometry isolation is improved in the desired band.

It can be observed that the antenna is resonating at 12.6 GHz, 15.2 and 26 GHz. Antenna 3 shows very high mutual coupling in the desired band. Since there is very high interference in between mounted elements, there is a need to develop separately and should be introduced in the proposed antenna system. To obtained high degree of isolation, a newly designed fractal based designed is introduced in the proposed antenna. Since proposed MIMO antenna is having four element so the decoupling

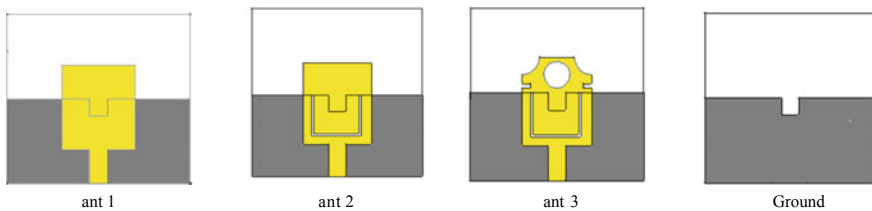


Fig. 1 Evolution of reference antenna

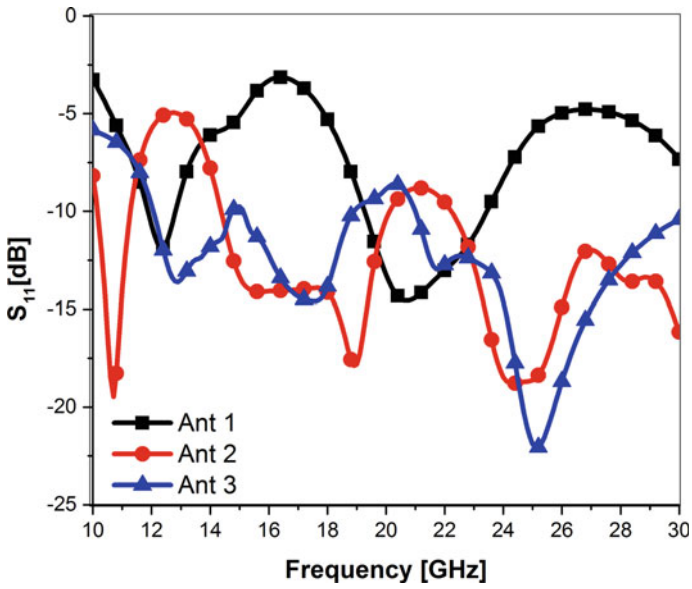


Fig. 2 S_{11} of the single antenna

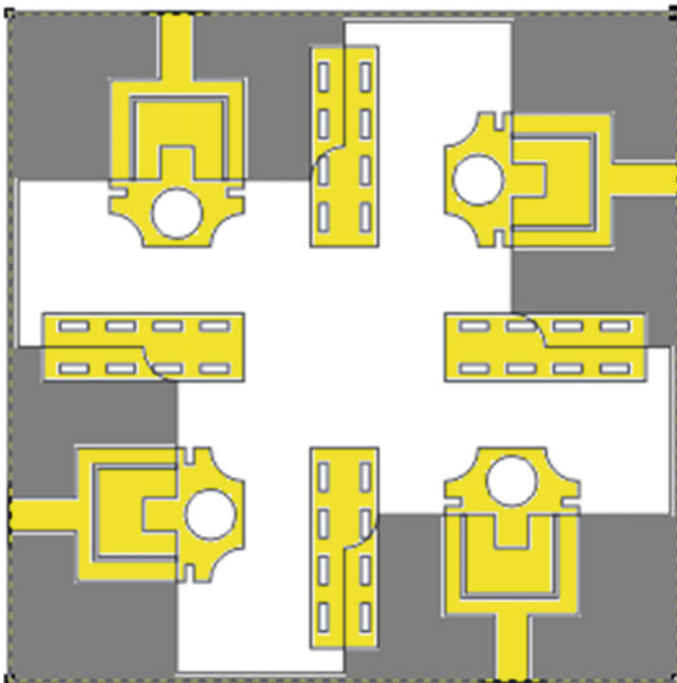


Fig. 3 Proposed MIMO antenna

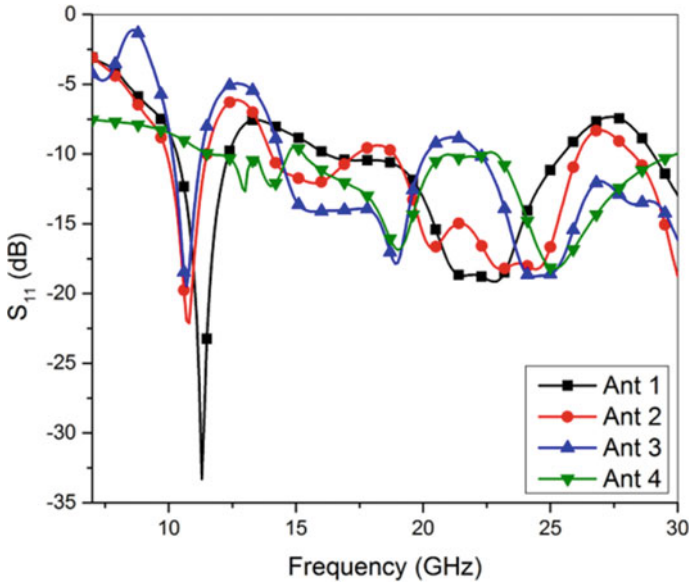


Fig. 4 S_{11} of the offered MIMO antenna structure

network introduced are 4 in number. Each single decoupling network is used to improve the isolation between adjacent elements.

The isolation is improved by these fractal-shaped isolators by suppressing the surface current from adjacent antenna elements. Figure 3 shows the design and dimensions of the new designed fractal-shaped isolator. By using this fractal design isolator, the isolation is further enhanced above 16 dB in the operating frequency range. Measurements of the designed MIMO antenna are given in Table 1. This fractal-shaped design works as a decoupling network in between designed antenna elements. Furthermore, arc-shaped slots are introduced to further introduced in the desired frequency band. Further, a circle shape is etched from the radiator to enhance the operating bandwidth by introducing he circle shaped slot bandwidth is increased to 12.1–18.9 GHz and 20.1–30 GHz.

3 Result and Discussion

3.1 Bandwidth

The suggested MIMO system is simulated. The simulated S_{11} , S_{12} , S_{13} , S_{14} are deliberated because of the mirror-like arrangement of each antenna element in antenna geometry. It can be noticed that the working bandwidth is from 12.1 to

Table 1 XXX

$L_1 = 40$ mm
$W_2 = 8$ mm
$L_2 = 40$ mm
$W_3 = 1$ mm
$L_3 = 4$ mm
$W_4 = 24$ mm
$L_4 = 10$ mm
$A = 0.5$ mm
$L_5 = 6$ mm
$H = 1.6$ mm
$L_6 = 13$ mm
$L_7 = 0.5$ mm
$W_1 = 12$ mm

18.9 GHz and 20.1 to 30 GHz. There is acceptable change in theoretical and simulated results; this is due the fabrication losses, soldering and the losses because of the SMA connectors. In Fig. 4, it is apparent that interference is less than -17 dB in frequency band 12.1–18.9 GHz and less than -26.6 dB in the 28 GHz band. So, the simulated results are in strong concurrence with the theoretical results.

Gain on the suggested antenna is around 4.8 dB in frequency band 12.1–18.9 GHz and 6.5 dB in 28 GHz band. The band for the military applications and defense application is obtained by etching rectangular slot in the ground plane. Length of rectangular slot is deliberated by the formula

$$L = \frac{c}{2f_{\text{notch}}\sqrt{\epsilon_{\text{eff}}}} \approx 2L_2 + 2L_3 - L_4$$

C in the speed of light. ϵ_{eff} is the as evaluated in [13], f_{notch} is the notch frequency, and L is length of slot. The determined length of the slot is 2 mm. Figure 7 illustrates the current flow of the MIMO antenna at the desired notch frequency with and without rectangular slot.

Figure 7 shows the surface current distribution at 12.4, 15.2 and 28 GHz. Cutting the C-shaped slot and arcs on the corner of the ground plane introduces the new path for the current to be flow which leads the two resonant modes. From the figure, it is discernible that surface current is higher at the edges.

The simulated results of the S parameters are elaborated in Fig. 5. It has been seen that there is an acceptable agreement. The simulated -10 dB bandwidths are (12.1–18.9 GHz) and (20.9–30 GHz). Within the desired operating band, both the measured and simulated isolation are around 26.6 dB in the 28 GHz band. Differentiation between the simulated S parameters of the suggested MIMO antenna is obtained by HFSS software.

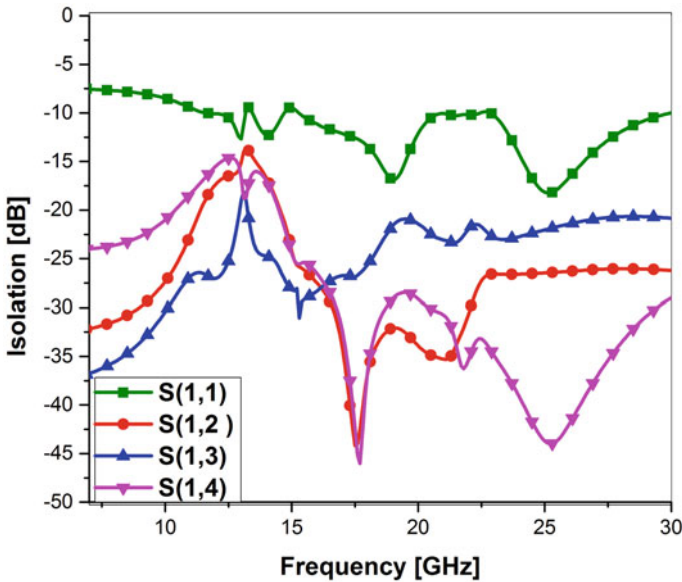


Fig. 5 S parameters of the proposed MIMO design

3.2 Radiation Characteristic

Figure 8 manifests the radiation characteristic of the offered MIMO structure at the 12.4, 15.2 and 28 GHz frequencies. When 1 port S excited, rest of all other ports are ended with 50Ω load. It is shown in Fig. 8 that each elements is polarized in the $+_x$ -direction. Value of polarization is enhanced by increasing the desired resonant frequency. The arcs in the patch are cause of alteration in the surface current path which is useful in enhancing the radiation characteristics of the suggested antenna, and hence, improvement in radiation characteristic leads to upgrade in the overall gain of the suggested antenna system. It is apparent in Fig. 6 that the peak gain of the MIMO structure is around 4.8 dB in the desired bandwidth.

4 MIMO Performance Analysis

The characteristics of the MIMO systems are depicted by parameters like ECC, diversity gain DG and TARC. By calculating these parameters we can have the idea about the correlation between adjacent antenna elements S how much correlated to adjacent antenna elements. Value of ECC can be deliberated using the S parameters of antenna. The envelope correlation coefficient (ECC) of the suggested MIMO antenna is evaluated using the following formula.

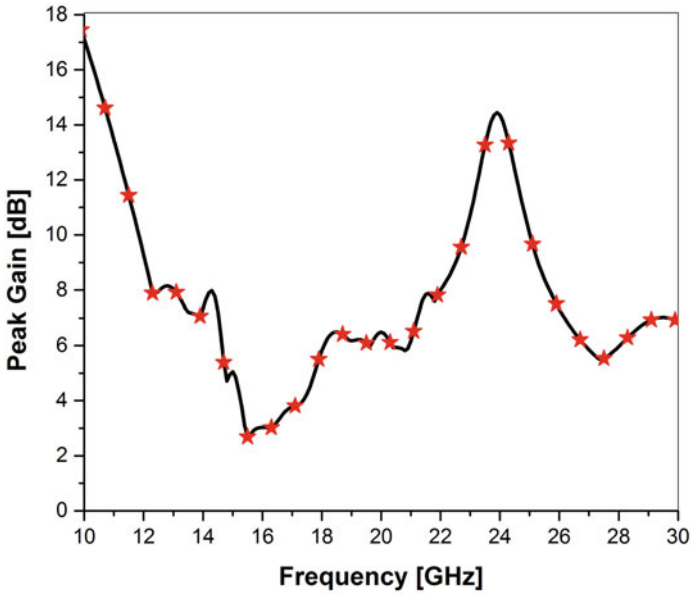


Fig. 6 Peak gain of the proposed MIMO antenna structure

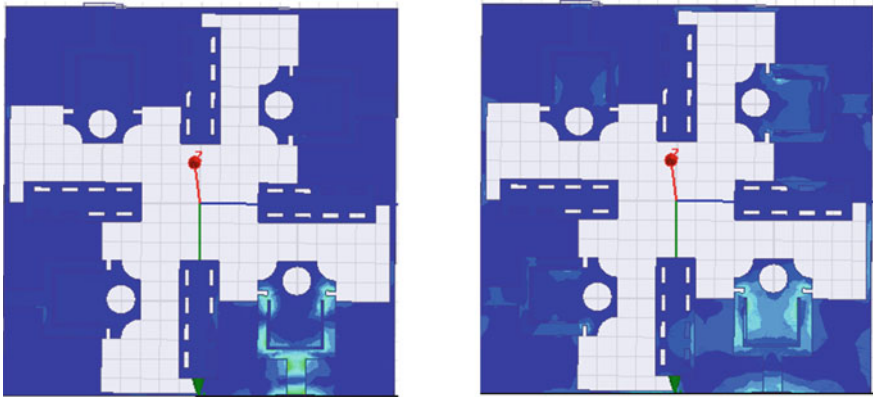


Fig. 7 Current distribution of proposed MIMO antenna

ECC is the evaluation of the correlation between the individual elements. The acceptable limit of ECC in MIMO system is, it should be < 0.5 and ideally value of ECC is zero. If the value of ECC is < 0.5 , then it is the accepted limit. Suggested antenna value of ECC is 0.002 which shows the excellent diversity performance of the proposed antenna system. The diversity gain (DG) of the MIMO antenna is calculated after the evaluation of the ECC.

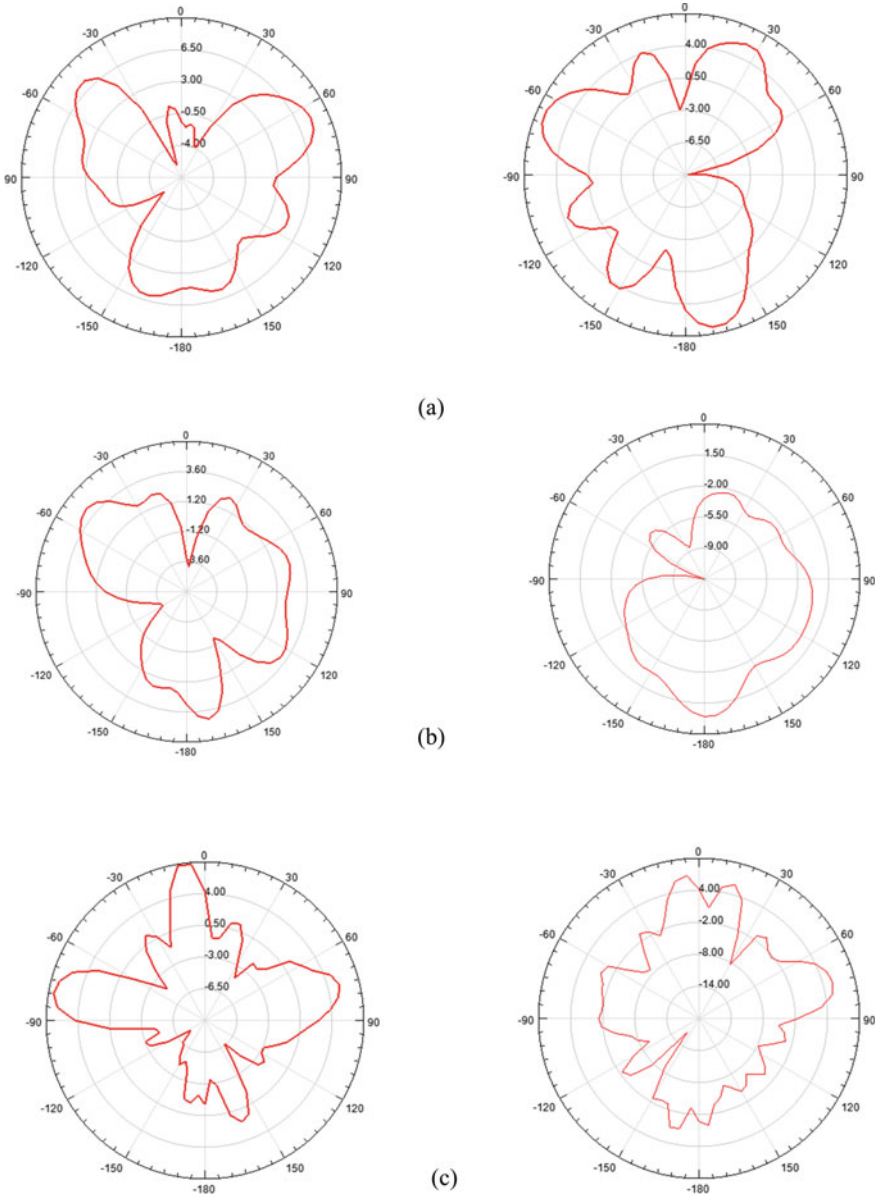


Fig. 8 Radiation pattern of the suggested MIMO structure at **a** at 12.4 GHz E and H plane **b** at 15.2 GHz E and H plane **c** at 26 GHz E and H plane

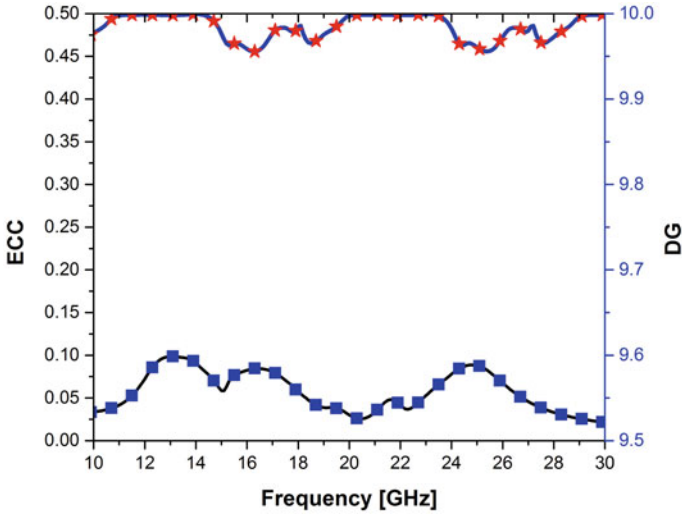


Fig. 9 ECC and DG of the proposed MIMO antenna

Figure 9 expresses the value of ECC and DG. From the figure, it can be seen that the diversity gain of the proposed system is around 9.99. Another parameter for evaluating the diversity characteristic of the MIMO system is obtained after calculating TRAC. The TARC of the proposed MIMO structure is manifested in Fig. 10.

It is apparent from Fig. 10 that TARC of the suggested antenna is less than -15 dB for the entire bandwidth which is good enough for the high performance of the MIMO system. Therefore, the suggested antenna satisfies the diversity performance, and hence, it is suitable for the MIMO application.

5 Conclusion

A closely packed four-port fractal MIMO antenna with good isolation characteristic between adjacent elements is proposed. To overcome the interference between closely packed elements, a fractal-shaped design is introduced. Proposed MIMO antenna has very compact dimension of $40\text{ mm} \times 40\text{ mm}$. The dual band covers 12.4 broadcast satellites, 15.2 GHz for defense application and 28 GHz for millimeter wave application. All of these bands play a very significant role in industry. There is a very strong agreement in simulated results. This closely packed antenna has significantly high gain and efficiency in the desired band. The measured ECC is 0.002, and DG is less than -15 dB. Value of TARC is also in the acceptable limit which provides the very high diversity performance of the suggested MIMO structure which is appropriate for the wireless communication.

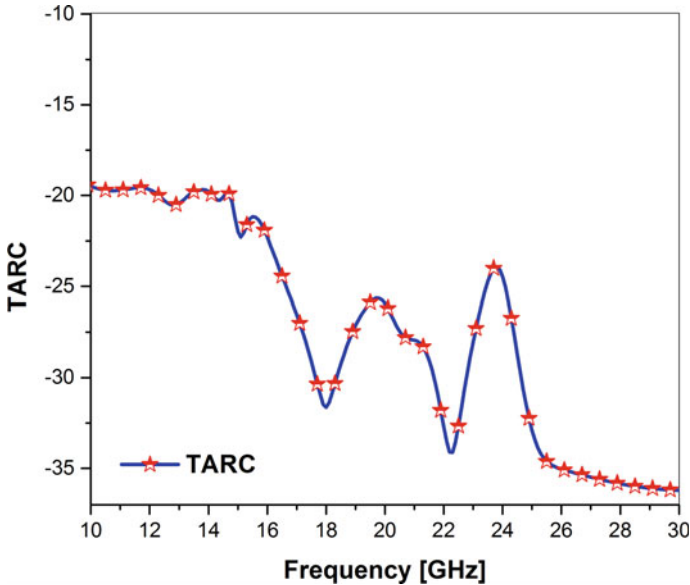


Fig. 10 TARC of the proposed MIMO structure

References

1. Kim T, Park J, Seol J-Y, Jeong S, Cho J, Roh W (2013) Tens of Gbps support with mmWave beamforming systems for next generation communications. In: 2013 IEEE global communications conference (GLOBECOM). Atlanta, pp 3685–3690
2. Murdock JN, Ben-Dor E, Qiao Y, Tamir JI, Rappaport TS (2012) A 38 GHz cellular outage study for an urban outdoor campus environment. In: 2012 IEEE wireless communications and networking conference (WCNC). Shanghai, pp 3085–3090
3. Zhao et al H (2013) 28 GHz millimeter wave cellular communication measurements for reflection and penetration loss in and around buildings in New York city. In: 2013 IEEE international conference on communications (ICC), Budapest, pp 5163–5167
4. Hasan M, Faruque MR, Islam MT (2018) Dual band metamaterial antenna for LTE/bluetooth/WiMAX system. *Sci Rep* 8:1240. <https://doi.org/10.1038/s41598-018-19705-3>
5. Shen X et al (2019) A miniaturized microstrip antenna array at 5G millimeter wave band. *IEEE Antennas Wirel Propag Lett*
6. Tan X, Wang W (2018) Enhancing isolation in dual-band meander-line multiple antenna by employing split EBG structure. *IEEE Trans Antennas Propag*
7. Pandit S, Mohan A, Ray P (2018) A compact four-element MIMO antenna for WLAN applications. Wiley, India 60(2)
8. Sahu NK, Das G, Sharma A, Gangwar RK (2017) Design of a dual-polarized triple-band hybrid MIMO antenna for WLAN/WiMAX applications. In: IEEE conference on antenna measurements and applications (CAMA), 4–6 Dec 2017
9. Das G, Sharma A, Gangwar RK (2018) Wideband self-complementary hybrid ring dielectric resonator antenna for MIMO applications. *12(1)*:108–114
10. Joozdani MZ, Amirhosseini MK, Abdolali A (2016) Wideband radar cross-section reduction of patch array antenna with miniaturised hexagonal loop frequency selective surface. *Electron Lett* 52(9):767–768

11. Baskey HB, Johari E, Akhtar MJ (2017) Metamaterial structure integrated with a dielectric absorber for wideband reduction of antennas radar cross-section. *IEEE Trans Electromagn Compat* 59(4):1060–1069
12. Yang P, Yan F, Yang F, Dong T (2016) Microstrip phased-array in-band RCS reduction with a random element rotation technique. *IEEE Trans Antennas Propag* 64(6):2513–2518
13. Liu T, Cao X, Gao J, Zheng Q, Li W, Yang H (2012) RCS reduction of waveguide slot antenna with metamaterial absorber. *IEEE Trans Antennas Propag* 61(3):1479–1484

Sub-graph p-Cycle Formation for Span Failures in All-Optical Networks



Varsha Lohani, Anjali Sharma, and Yatindra Nath Singh

Abstract p-Cycles offer ring-like switching speed and mesh-like spare capacity efficiency for protecting the network against link failures. This makes them extremely efficient and effective protection techniques. p-Cycles can also protect all the links in a network against simultaneous failures of multiple links. For large networks, the use of p-cycles is difficult because their optimization requires an excessive amount of time as the number of variables in the corresponding Integer Linear Program (ILP) increases with the increase in the network size. In a real-time network situation, setting up highly efficient protection in a short time is essential. Thus, we introduce a network sub-graphing approach in which a network is segmented into smaller parts based on certain network attributes. We achieved better computational efficiency at the expense of marginal spare capacity increases with this approach.

Keywords Graph clustering · p-Cycles · Protection · Restoration · Survivability

1 Introduction

Optical networks need to carry an enormous amount of traffic while maintaining service continuity even in the presence of faults. Failure of even a single link¹ will result in loss of a substantial amount of data if not protected automatically and restored in a very short time after the failure. Therefore, survivability against link or path failures is an essential design requirement for the high-speed optical networks.

¹span, link and edges are used interchangeably in this paper.

V. Lohani (✉) · A. Sharma · Y. N. Singh
Indian Institute of Technology Kanpur, Kanpur, India
e-mail: lohani.varsha7@gmail.com

Y. N. Singh
e-mail: ynsingh@iitk.ac.in

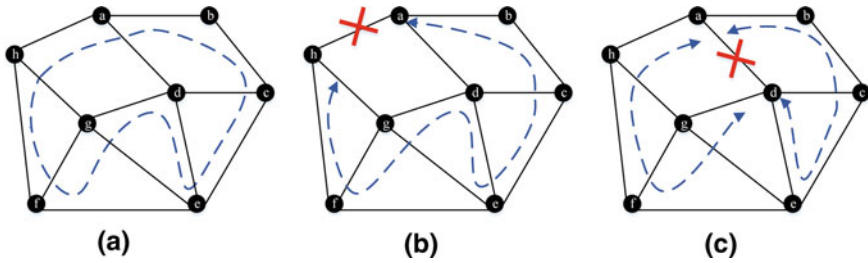


Fig. 1 **a** A p-Cycle, p ($a-b-c-e-d-g-f-h-a$), **b** a failed on-cycle link i ($a-h$), p-cycle p provides single unit of backup path ($a-b-c-e-d-g-f-h-a$) and **c** a failed straddling link i ($a-d$), p-cycle p provides two units of backup path ($a-h-f-g-d$) and ($a-b-c-e-d$)

The goal of a survivability scheme is to offer reliable services for large volume of traffic even on the occurrence of failures² as well as abnormal operating conditions [1].

p-Cycles are one of the best methods to provide protection and achieve much faster restoration speeds in case of failures. But as the network size becomes large, finding an optimum solution for p-cycle-based protection becomes a time-consuming task. We are trying to resolve this problem by breaking a bigger problem into smaller sub-problems which can be solved in parallel on different machines. But we need to find out the best strategy of partitioning, the network graph into sub-graphs with optimum size, to minimize the computation time without much increase in the spare capacity requirement (i.e. minimizing sub-optimality).

In this paper, Sect. 2 discusses related research done on p-cycles and graph partitioning. In Sect. 3, we present our proposed method to reduce compute time using graph partitioning methods, and in Sect. 4, we present resulting p-cycles and spare capacity requirement after partitioning. These are compared with the results for the formation of p-cycles in the whole network without any partitioning. In Sect. 4, results for different topologies are compared. Finally, the conclusions are presented in the last section.

2 p-Cycles and Related Works

p-Cycles in an optical mesh network provide the same switching speed as the ring-based protection ($<50\text{ms}$)³ and capacity efficiency as in mesh networks [2, 3] as explained in Fig. 1.

A good amount of work has been done in the past that highlights the advantages of p-cycles for the protection and restoration of traffic [2, 3]. The p-cycles can also be used for protecting nodes [4], paths [5, 6] and path-segments [7] in addition to

² Fiber cut, human-made errors or natural disasters such as earthquakes, hurricanes, etc.

³ Bi-directional Line Switched Ring.

links in an optical mesh network. For 100% single link protection, optimum required p-cycles can be computed using an ILP. The main objective of the ILP is to choose the number of p-cycles to provide 100% protection while minimizing the spare capacity to be used.

The p-cycle protection in large networks have also been explored using multi-domain approach [8–12]. The idea is to partition the whole network into multiple domains using graph clustering algorithms. For protecting the links connecting different domains, separate inter-domain p-cycles are computed. Normally, each domain is an independently administered entity, and hence, they are clearly defined by using some parameters like hop-length.

We would like to take clue from multi-domain protection and use partitioning of large-sized optical networks to find the near-optimal solutions using p-cycles in each partition independently. We can allow the node and links to be shared across two partitions to avoid inter-domain p-cycles.

In this paper, we are using clustering of the graph for resolving the problem of survivability in the optical networks with lesser computation. For large networks, graph partitioning can be very helpful in finding the near-optimal solution. Faster convergence (i.e. smaller run-time) of ILP can be achieved by running the algorithm in parallel to find a solution for all the sub-graphs.

3 Proposed Method: Sub-graphing Using Minimum Cut-Set Algorithm

The method proposed in this section is for both WDM-based optical networks and elastic optical networks [13]. Here, we consider that routing and resource⁴ allocation is done a priori. The method is only dependent on the working capacity traversing through the network.

Algorithm 1 Sub-Graphing Algorithm

- | | |
|--|-------------------------------------|
| 1: $p_{org} = \text{PCYCLE}(G(V, E));$ | ▷ original graph p-cycle count |
| 2: $P = [p_{org}];$ | ▷ p-cycle count for each partition |
| 3: $P_s = [];$ | ▷ contains sub-graphs p-cycle count |
| 4: $\text{PCYCLESUB}(G(V, E), P, P_s)$ | |
-

The Algorithm 2, is used for finding the sub-graphs by further subdivisions. In this method, the entire graph is divided into two parts based on minimum cut-set algorithm. The pairs of nodes which are endpoints of links in the cut-set, are used to form sub-graphs, after performing the partitioning on the super-graph using the minimum cut-set algorithm. One of the sub-graph contains both the nodes in all such

⁴ Resource can be either Wavelength or Spectrum Slots.

pairs. The other sub-graph contains only those nodes from the pairs, which already belong to it. Spectral partitioning method [14] is used for finding minimum cut-set as explained in Algorithm 3.

Algorithm 2 Function for Sub-Graphing using p-cycle

```

1: function PCYCLESUB( $G(V, E), P, P_s$ )
2:   Call [ $g^{(1)}, g^{(2)}$ ] = SPF( $G(V, E)$ )
3:   [ $p_{g^{(1)}}, p_{g^{(2)}}$ ] = PCYCLE( $g^{(1)}, g^{(2)}$ );
4:   if  $p_{g^{(1)}} \geq 1$  &&  $p_{g^{(2)}} \geq 1$  then
5:      $P_s$ .APPEND( $[g^{(1)}, p_{g^{(1)}}]$ );
6:      $P_s$ .APPEND( $[g^{(2)}, p_{g^{(2)}}]$ );
7:      $Sum_p$  = null;
8:      $Sum_p$  = SUM( $P_s$ );           ▷ SUM function is to find out the sum of pycles (not graph)
9:      $P$ .APPEND( $Sum_p$ );
10:     $max P_s$  = MAX( $P_s$ );       ▷ MAX function is to find out the element( $[graph, pcycle]$ ) with
    maximum  $p_{g^{(i)}}$  value from  $P_s$ 
11:     $P_s$ .REMOVE( $max P_s$ );
12:  end if
13:  PCYCLESUB( $max P_s[0], P, P_s$ ) ▷ input argument takes sub-graph with highest number of
    p-cycles
14: end function

```

Every time out of all sub-graphs, the one with most number of p-cycles is taken up for further partitioning thereby increasing the number of sub-graphs by one. The process iterates until we obtain fundamental cycles.⁵

In Algorithms 1 and 2, PCYCLE() function is used to calculate the number of p-cycles within a graph. Algorithm 2 is a recursive function used for the sub-graphing of a graph based on the p-cycles count. In each recursion, the sub-graphs with the maximum number of p-cycles is separated from the list and further partitioned into two using Algorithm 3, i.e. Spectral Partitioning Function (SPF). The partitioning continues until all the sub-graphs are simply fundamental p-cycles. Algorithm 1 gives the list of p-cycles for every partition. This list is used in subsequent section for spare capacity optimization and computes time analysis.

The Sub-Graphing Algorithm 1 returns the partitioned graph with the p-cycle count for each partition. The ILP are used for calculating spare capacity requirement and analyzing compute time for each partition. The set of candidate p-cycles are used as an input to the ILP.

⁵ Fundamental cycles are those cycles which does not have straddling links.

Algorithm 3 Spectral Partitioning Function (SPF)

```

1: function SPF( $G(V, E)$ ) ▷  $v \in V, e \in E$ 
2:    $A = \text{ADJ}(G(V, E));$  ▷ ADJ is used to find Adjacency Matrix(A) of the G(V,E)
3:    $D = \text{DIAG}(G(V, E));$  ▷ DIAG is used to find Diagonal Matrix(D) of the G(V,E)
4:    $L = D - A;$  ▷ Laplacian Matrix (L)
5:   Compute eigenvector( $ei_v$ ) of the vertices using  $L$  matrix;
6:   for each vertices  $v$  do
7:     if  $ei_v < 0$  then
8:       place vertex  $v$  to  $V^{(1)}$ 
9:     else
10:      place vertex  $v$  to  $V^{(2)}$ 
11:    end if
12:  end for
13:  Using  $V^{(1)}$  and  $V^{(2)}$  find Minimum cut-set;
14:  Mark Minimum cut-set as Slider;
15:  return  $g^{(1)}, g^{(2)}$  ▷  $g^{(i)} = g^{(i)}(V^{(i)}, E^{(i)})$  where  $i = 1, 2$ .
16: end function

```

4 Results for Different Topology

We consider the four network topologies as given in Table 1 and also displays the amount of total working capacity assigned to all links in each network. SCILAB 5.5.2 and CPLEX 12.9.0 are used for network parameters calculation and optimization, respectively. For different partitions of network topologies, different attributes (Number of p-cycles, spare capacity, and compute time) are computed and plotted in Fig. 2a–d. We estimated two compute times—the overall computation time in Fig. 2c and the maximum computation time in Fig. 2d. The overall computation time is the sum of all sub-graphs' computation time in the i th iteration of partitioning. If we run the optimization on all the sub-graphs in parallel, then the maximum computation time is selected from the times taken by each of them.

The working capacity distribution between the common links of the two partitions is $0:k$ or $k:0$ (Type I) based on spare capacity minimization, where k is the working capacity on the common link. But the spare capacity for this sort of distribution turns out to be very high. So, we chose equal distribution of working capacity on the common link to the two partitions, i.e. $k/2:k/2$ (Type II). As we can see from Fig. 2b, the value of spare capacity is high when less number of partitions are made

Table 1 Assigned capacities for various network topologies

Networks	Total capacity	Working capacity	Spare capacity
Net1: N6L10	880	300	580
Net2: N8L18	1120	390	730
Net3: NSFNET	1680	510	1170
Net4: COST239	1760	550	1210

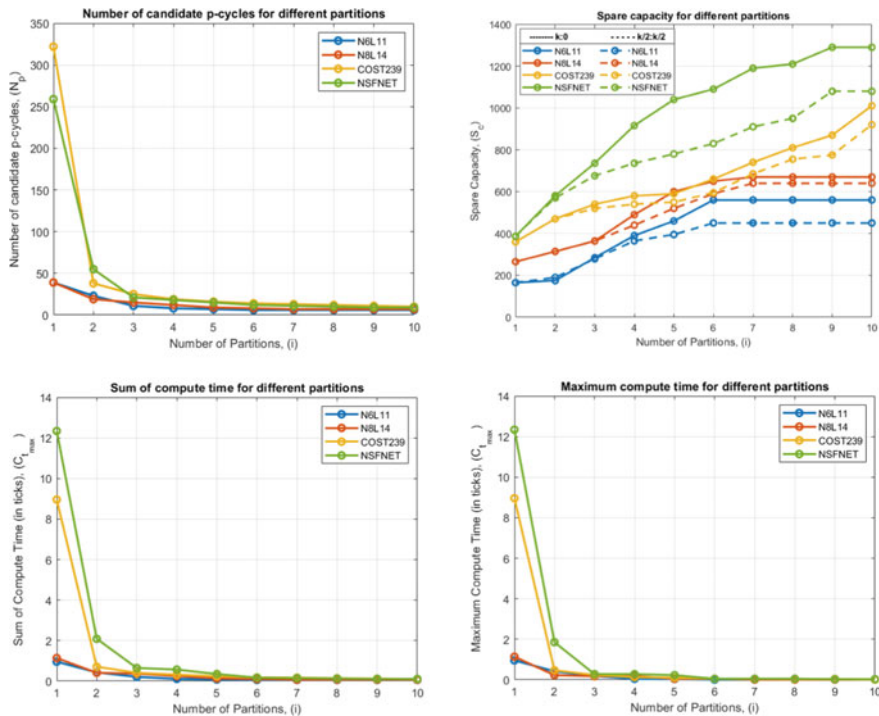


Fig. 2 Different network parameters for various network topologies

for both Type I and Type II working capacity distributions. But with the increasing number of partitions, the spare capacity requirement reduces for Type II. So, opting for $k/2:k/2$ working capacity distribution is better. The dynamic partitioning is also possible $k/i:k/j$ ⁶ but the results are almost same as $k/2:k/2$ for less partitions. Since the spare capacity values are much higher for more partitions, we are ignoring them.

Here, we are partitioning the networks to get faster configuration of protection, which is desirable for large networks as well as real-time scenarios. As we can see in Fig. 2a, c, d, that after fourth partitioning iteration, the results are almost constant for all the network topologies. But, here we seek to keep partitioning as minimal as possible so that the spare capacity used is not high and the remaining capacity can be used for another failed link which is disjoint to the protection of first failed link. We can see in Fig. 2a that the number of candidate p-cycles are significantly reduced for all the network topologies. As the candidate p-cycles are reduced, the number of variables in the ILP, and hence, the compute time also decreases. So, we can go for partitions starting from 2 until the results are almost constant (i.e. the near-optimal partition, in our case four partitions).

⁶ i and j are the whole numbers.

Sub-graphing method reduces the compute time for finding p-cycle-based protection configuration in real-time scenario. p-Cycles have not found practical use only due to large compute time for finding optimal strategy for big networks. But now, the protection configuration can be determined quickly as a consequence of sub-graphing. The partitioning methods used [8–12] considers inter-domain and intra-domain. Each intra-domain is provisioned with different sets of p-cycle, whereas for inter-domain either FIPP p-cycles are used or different approach is used to provision protection. This increases the compute time for ILP.

5 Conclusion

We have formulated sub-graphing method that splits the network graph into several partitions, so that optimization for each partition can be made in parallel. But, with this, the key issue is the increase in the amount of spare capacity needed. So, we have tried to find out near-optimal partitions with which the both the requirement of minimum compute time and spare capacity can be met. The results indicate that this method holds promise in making p-cycles practically feasible.

References

1. Asthana R et al (2004) Protection and restoration in optical networks. *IETE J Res* 50(5):319–329
2. Grover WB et al (1998) Cycle-oriented distributed pre-configuration: ring-like speed with mesh-like capacity for self-planning network restoration. In: *Proceedings of IEEE ICC'98*, vol 54(17), pp 537–543
3. Asthana R et al (2010) p-Cycles: an overview. *IEEE Commun Surv Tutor* 12(1):97–111
4. Stamatelakis D et al (2000) IP layer restoration and network planning based on virtual protection cycles. *IEEE J Sel Areas Commun* 18(10):1938–1949
5. Grover WD et al (2005) Failure-independent path protection with p-cycles: efficient, fast and simple protection for transparent optical networks. In: *Proceedings of the 7th international conference on transparent optical networks (ICTON'05)*, Barcelona, Spain, pp 3–7
6. Kodian A et al (2005) Failure independent path-protecting p-cycles: efficient and simple fully pre-connected optical-path protection. *IEEE J Lightw Technol (JLT)* 23(10)
7. Shen G et al (2003) Extending the p-cycle concept to path segment protection for span and node failure recovery. *IEEE J Sel Areas Commun* 21:1306–1319
8. Szigeti J et al (2009) p-Cycle protection in multi-domain optical networks. *Photon Netw Commun* 35–47
9. Drid H et al (2009) A topology aggregation model for survivability in multi-domain optical networks using p-cycles. In: *IEEE international conference on network and parallel computing*, pp 211–218
10. Drid H et al (2010) Graph partitioning for survivability in multi-domain optical networks. *IEEE Commun Lett* 1–5
11. Jaumard B et al (2012) A distributed p-cycle protection scheme in multi-domain optical networks. In: *Globecom 2012—optical networks and systems symposium*, pp 3019–3025

12. Jaumard B et al (2012) p-Cycle based protection mechanisms in multi-domain optical networks. In: Fourth international conference on communications and electronics (ICCE). Hue, Vietnam, pp 19–24
13. Wei Y et al (2014) Applying p-cycle technique to elastic optical networks. In: 2014 international conference on optical network design and modeling. Stockholm, pp 1–6
14. Leskovec J et al, Coursera course: mining massive datasets. Stanford University

Single-Precision Floating-Point Multiplier Design Using Quantum-Dot Cellular Automata with Power Dissipation Analysis



A. Arunkumar Gudivada and Gnanou Florence Sudha

Abstract Addition and multiplication are the two essential operations of any computational device. They, in fact, decide the performance of the overall system. Such adders and multipliers have been developed on fixed-point numbers using CMOS technology. It is very much necessary to implement low-power architectures for floating-point multiplication as well. In any large-scale application, arithmetical operations on floating-point numbers may lag the system's performance. CMOS technology at a very high data rate with lesser transistor dimensions has its limitations when the technology of the transistor goes down the nanometer scale. Hence, a fast and latest transistor-less nanotechnology like quantum-dot cellular automata has to be used to design low-power VLSI architectures at nanometer scales. In this paper, low power and less area-occupied floating-point multiplier have been implemented using a new paradigm like quantum-dot cellular automata on QCA Designer 2.0.3. The proposed model has noticeable response characteristics in terms of area, power, and delay, viz., $10.45 \mu\text{m}^2$, 2.91 nW , and 62 ns , respectively.

Keywords Quantum-dot cellular automata · Floating-point multiplier · Power dissipation analysis

1 Introduction

In large computational applications, arithmetical and logical operations play a crucial role. These operations decide the overall performance of the system. Hence, the core part, which deals with the arithmetical and logical operations, must be chosen, which satisfies the latest requirements of the novel designs in the market. Multiplication is one of the major operations performed by the arithmetical unit. As it is a time and power-consuming operation, it is necessary to build optimized, fast, and low-power

A. A. Gudivada (✉) · G. F. Sudha
Electronics and Communication Engineering, Pondicherry Engineering College, Puducherry
605014, India
e-mail: aarunkumar.g@pec.edu

© The Author(s), under exclusive license to Springer Nature Singapore Pte Ltd. 2022
P. Kumar Jain et al. (eds.), *Advances in Signal Processing and Communication Engineering*, Lecture Notes in Electrical Engineering 929,
https://doi.org/10.1007/978-981-19-5550-1_11

103

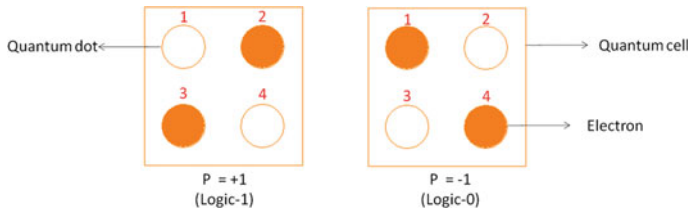
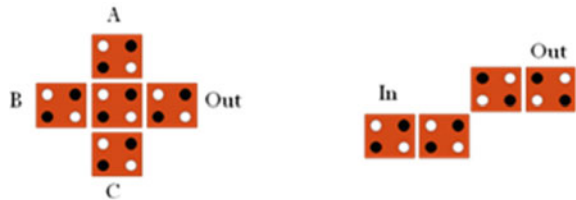


Fig. 1 Basic QCA cell and polarization [1]

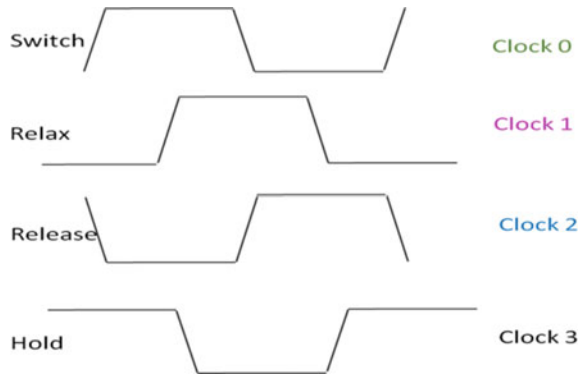
Fig. 2 a Majority voter gate.

b Inverter gate [2]



architecture for multiplication. Besides, the multiplication of floating-point numbers with less delay and low power consumption attracts the attention of the researchers. In this paper, a novel architecture has been built for the multiplication of floating-point numbers using quantum-dot cellular automata. Nowadays, there is a huge demand for circuits with low power, high speed, and less area. In VLSI circuit designing, the CMOS technology has better characteristics compared to other logic families. However, when the scaling of the MOS transistor goes beyond nanometers, the CMOS technology has some pitfalls like leakage currents and short-channel effects. To design the VLSI circuits by minimizing these problems, the solution is to go for nanotechnology. One of the best nanotechnologies is quantum-dot cellular automata (QCA). The logical circuits developed using QCA have high packing density, ultra-low power, and high operating frequency.

The main element of the quantum-dot cellular automata is a quantum cell. A quantum cell is nothing but a thin silicon wafer that is made to hold four quantum dots [1]. Quantum dot is a 5 nm area used to keep an electron. A quantum cell is designed in such a way that it can hold two electrons. These two electrons change their position based on excitation or polarization. In digital systems, the data are transmitted in the form of logic 0 and logic 1. In QCA technology, logic 0 and logic 1 are represented by the polarization of electrons inside the quantum cell, as shown in Fig. 1. The input cells are indicated by blue color, and the yellow color indicates output cells. The first symbol in Fig. 2 is the majority voter gate, which is a generalized gate to accomplish AND and OR operations by making any one of the inputs 0 and 1, respectively [2]. The expression for the output logic is given as $Out = AB + BC + AC$. In Fig. 2, next to the majority gate is the inverter gate that complements the input bit. The data are complemented by diagonally connecting the cells; this happens due to the Coulombic repulsion of electrons.

Fig. 3 Clocking in QCA [2]

As there is no wiring involved in the design of QCA layouts, the flow of data in a forward or backward direction depends on a clocking technique. Normally, there are four phases in a clock that are discriminated by four different colors. The colors are green (representing clock 0), pink (representing clock 1), blue (representing clock 2), and white (representing clock 3). As seen in Fig. 2, the clocking scheme used in the QCA design has four stages/phases like clock0, clock1, clock2, and clock3, with respective colors. These four phases are in different states like a switch, hold, release, and relax.

Further, the paper is organized as follows. Section 2 gives a brief introduction of past works on floating-point multipliers. Section 3 deals with the floating-point multipliers. The proposed QCA layout of the floating-point multiplier has been discussed in Sect. 4. Section 5 illustrates the simulation result of the proposed design. Section 6 describes the power dissipation analysis of the proposed floating-point multiplier. The conclusion of the paper is discussed in Sect. 7.

2 Literature Survey

Research on floating-point arithmetic unit has been carried out by few authors [3–8]. However, the design and implementation of the architectures were available with front-end designs like Xilinx in Verilog or VHDL languages. Some of the authors have also been implemented using CMOS using 90nm and 45nm technologies. In 2013, Gonzalez-Navarro et al. [3] have implemented a decimal-based binary implementation. The authors have multiplied floating-point numbers using a technique BID multiplication. In this BID algorithm, the input numbers were decoded first into the sign, exponent, and mantissa bits. Again at the end, the result was fed back to the encoder to get the final product. Using this technique, the area of the schematic was 50.37 mm² and a delay of 1.04 ns. Later in 2014, Kodali et al. [4] have designed a floating-point multiplier using two different multipliers. The authors have first separated the sign, exponent, and mantissa, and further, the mantissas have been

multiplied with booth and karatsuba multipliers. Through the use of these two multipliers, the delay and area were 72.122 ns and 3.28 nm², respectively. In 2015, Anjana et al. [5] have proposed a floating-point arithmetic unit using the Vedic mathematics algorithm. The power dissipation and delay of this model were 1.042 W and 56.481 ns, respectively. Jitesh R. Shinde and S. S. Suresh in 2015 have proposed floating-point arithmetic units [6]. The authors have implemented the schematic diagrams using CMOS 90 and 45 nm technologies. The power dissipation, delay, and area in 90 nm technology were 0.5913 mW, 19.89 ns, and 20,677 nm², respectively. The power dissipation, delay, and area at 45 nm technology were 6.3856 mW, 1.93 ns and 19.68 nm² μm², respectively.

Arish and Sharma [7] in 2015 have proposed a single-precision floating-point arithmetic unit. The authors have used the Vedic mathematical approach with algorithms like the Karatsuba algorithm and the Urdhva-Tiryagbhyam algorithm. The area and delay of the proposed model were 1073 μm² and 16.182 ns. Later, in the year 2020, Jha et al. [8] have designed a temporal approximation for floating-point units. The area, delay, and power dissipation of the proposed model were 3104 μm², 0.55 ns, and 3.11 mw, respectively.

By studying the existing designs, one can understand that the parameters area, delay, and power dissipation were not optimized using coding or CMOS technology. Hence, in this paper, the floating-point multiplier unit has been implemented using novel nanotechnology like quantum-dot cellular automata, which was never designed before.

3 Floating-Point Multiplier

A floating-point number is a simple way to represent large decimal numbers using sign, exponent, and mantissa. The difference in fixed and floating-point multiplication is that, in fixed-point numbers multiplication, there is a need for a multiplier alone. On the other hand, in floating-point number multiplication, three modules are needed. They are a multiplier to multiply the mantissas, adder to add the exponents and an XOR gate to obtain the resultant sign bit. Hence, when performing the multiplication of floating-point numbers, it is necessary to separate the sign, exponent, and mantissa of the input numbers [9].

Let N be the real number that can be represented in floating-point IEEE-754 standard format [10] as

$$N = \left(\pm \sum_{k=0}^{n-1} b_k 2^{-k} \right) * 2^E \quad (1)$$

where b is the binary representation of the mantissa, which is $b = b_0 b_1 b_2 \dots b_{n-1}$. Here, the exponent is given as E with a bias value. The real number N can be represented as a floating-point number as

Fig. 4 IEEE-754 format of a single-precision floating-point number

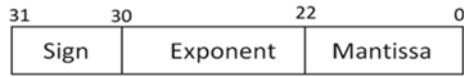
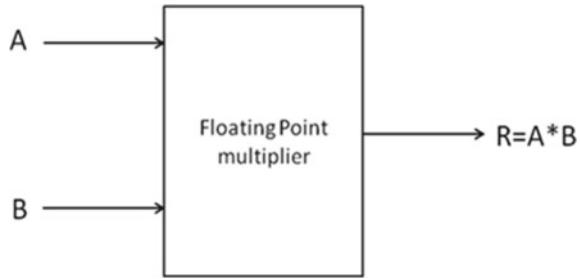


Fig. 5 Floating-point multiplier



$$N = (-1)^S \times (1.M) \times 2^{E-bias} \tag{2}$$

A single-precision floating-point number format is represented in Fig. 3. The sign bit is 0 for positive numbers and 1 for negative numbers. When exponent is represented in IEEE-754 format, a bias value should be added. The type of precision decides the bias value. For a single-precision floating-point number, the size of the exponent is 8-bits. Then, the bias = $2^7 - 1 = 127$. For double-precision floating-point numbers, the size of the exponent is 11-bits. Then, the bias = $2^{10} - 1 = 1023$.

For example, in the single-precision floating-point number format, the exponent value is 10. Then, in IEEE-754 format, it should be represented as $127 + 10 = 137$, and its binary value will be 10001001. If there is no exponent in the given number that is 0, then in IEEE-754 format, the exponent is 127 only. That is 01111111 in binary.

A multiplier is an arithmetical circuit used to multiply two numbers of any size. Figure 4 shows the general floating-point multiplier with n-bit size. A single-precision floating-point number has 32 bits. When two floating-point numbers are multiplied, then the mantissas of the numbers are multiplied, and exponents are to be added up. The sign of the resultant number is obtained by just XORing the input sign bits.

Figure 5 depicts the internal block diagram of a floating-point multiplier. It has two inputs A and B, with a size of n-bit each. The result of multiplication R should also have a length of n-bit. If any excess data occur during mantissa multiplication that can be adjusted in the exponent number. The input numbers A and B are separated in their respective sign, exponent, and mantissa. The sign of the result is positive if both input number signs are positive or negative. And the sign of the product is negative if any one of the inputs is negative. Hence, to perform this task, an XOR gate with 2-inputs is required. The exponent of both numbers must be added up with a bias of 127 (for single-precision floating-point number). And later, both biased numbers are to be added together. Hence, there is a need for three 8-bit adders, as shown in Fig. 4. Later, for the multiplication of two mantissas, a 23-bit multiplier is to be used.

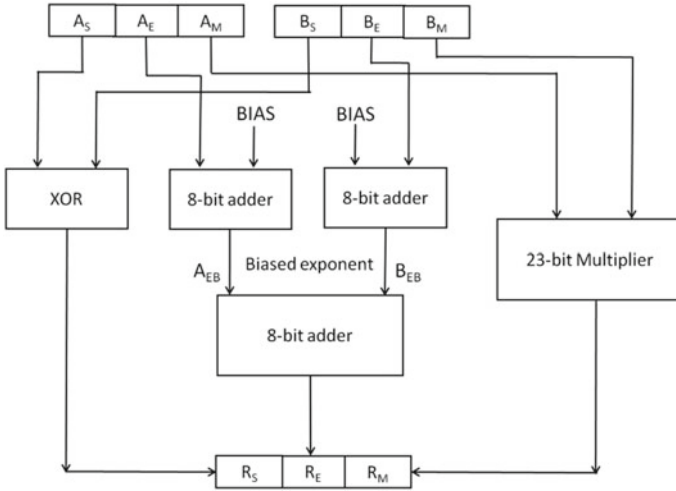


Fig. 6 Internal block diagram of Floating-point multiplier

Let us consider a single-precision floating-point multiplication with input numbers A and B .

$$A = (-1)^{A_S} \times (1.A_M) \times 2^{A_E - \text{BIAS}} \tag{3}$$

$$B = (-1)^{B_S} \times (1.B_M) \times 2^{B_E - \text{BIAS}} \tag{4}$$

and assume the representation of biased exponents as A_{EB} and B_{EB} as $A_{EB} = A_E + 127$ and $B_{EB} = B_E + 127$. Multiplication of these two numbers is as follows:

$$\begin{aligned} R &= A \times B \\ &= (-1)^{A_S} \times (1.A_M) \times 2^{A_{EB}} \times (-1)^{B_S} \times (1.B_M) \times 2^{B_{EB}} \\ &= (-1)^{A_S \oplus B_S} \times (1.A_M) \times (1.B_M) \times 2^{A_{EB} + B_{EB}} \\ &= (-1)^{A_S \oplus B_S} \times (1.A_M \times B_M) \times 2^{A_{EB} + B_{EB}} \\ &= (-1)^{R_S} \times (1.R_M) \times 2^{R_E} \end{aligned}$$

3.1 Calculation of Sign Bit

XOR gate is used to find the sign of the result. Table 1 describes how the XOR gate is used to be a sign identifier from its truth table. When both inputs are positive or negative, the result is positive. If any one of the inputs is negative, the resultant data are also negative. This can be accomplished using the XOR gate, as shown in Table 1.

Table 1 XOR gate truth table

AS	BS	RS
0 (Positive)	0 (Positive)	0 (Positive)
0 (Positive)	1 (Negative)	1 (Negative)
1 (Negative)	0 (Positive)	1 (Negative)
1 (Negative)	1 (Negative)	0 (Positive)

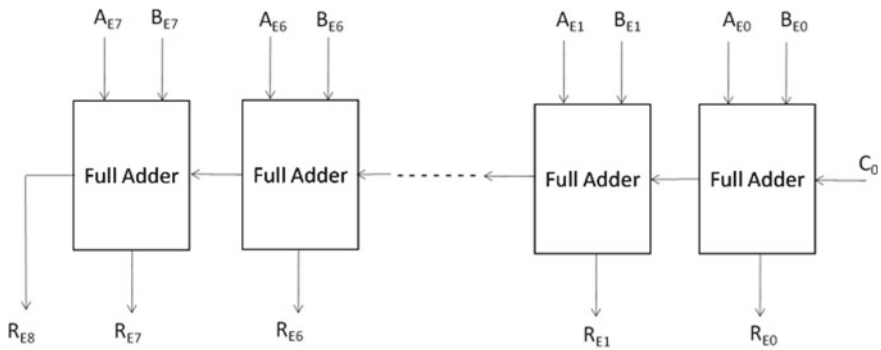


Fig. 7 8-bit full adder block diagram

3.2 Calculation of Exponent

In floating-point multiplication, the exponents should be added. Once the exponents have been biased, they need to be applied to the adders [11]. For single-precision floating-point numbers, the size of the exponent is 8-bit. Hence, we need an 8-bit adder, as shown in Fig. 6, to add the exponents AE and BE of two numbers A and B . The inputs of the adder are AE_7 to AE_0 and BE_7 to BE_0 . The result is stored in R_E .

3.3 Calculation of Mantissa

Let the input numbers A and B have their mantissas A_M and B_M , respectively. For instance, consider the mantissas from A_{m7} to A_{m0} and B_{m7} to B_{m0} . The array multiplication between these two numbers is as shown in Fig. 7. It needs 38 full adders and 8 half adders along with additional gates to implement this multiplication algorithm. The purpose of other gates is to produce the product terms at each stage.

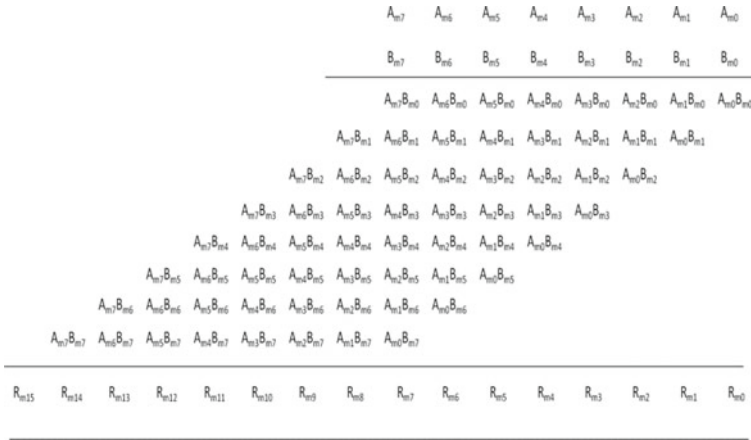


Fig. 8 Array multiplication of mantissas

4 Proposed QCA Layout of Floating-Point Multiplier

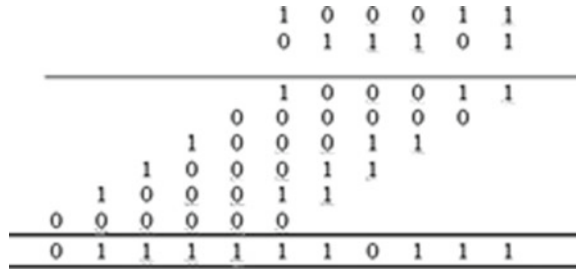
An IEEE-754 floating-point multiplier was designed so far using Xilinx with VHDL, Verilog, and dumped on FPGAs [12, 13]. However, the multiplier power dissipation and area were too high, which have to be optimized. These parameters of the floating-point multiplier can have better characteristics if implemented using nanotechnology like quantum-dot cellular automata.

Figure 10 shows the QCA layout of the floating-point multiplier. The two input numbers must be separated in terms of sign, exponent, and mantissa. The sign bits AS and BS are applied to the XOR gate, as shown in Fig. 10. In floating-point multiplication, the exponents of the two input numbers must be added to each other. Hence, we need an 8-bit adder. The 8-bit adder has been designed for this purpose with the inputs A_{E7} to A_{E0} and B_{E7} to B_{E0} . The result is stored as S_7-S_0 with a carry C_y . Later, to multiply the mantissa, an array multiplier has been designed for 8-bits of mantissa. This can be expanded up to 23-bit for single-precision floating-point multiplication.

5 Simulation Results of Proposed Layout

The proposed QCA layout has been simulated on QCA Designer 2.0.3 [14], a powerful tool to simulate the layouts made up of quantum cells. The proposed architecture consists of three different layouts designed for sign, exponent, and mantissa separately. The delay involved in the multiplication of the mantissa is 15.5 clock cycles, as shown in Fig. 11. However, the delay in the generation of sign and exponents is very less. To get these three simultaneously, quantum cells are needed to be added

Fig. 9 Multiplication of Mantissa in case-1



to increase the delay associated with the sign and exponent operation. Hence, to implement a floating-point multiplier, there is a need for 8696 quantum cells in an optimized area of $10.5 \mu\text{m}^2$. The simulation results of the proposed floating-point multiplier have been shown in Fig. 11. Different cases have been studied, and they can be calculated manually as follows.

Case-1:

Let $A = 8.75$ and $B = 7.25$. The binary equivalents of these numbers are $A = 1000.11$ and $B = 111.01$. Now, let us separate the sign, exponent, and mantissa from the given numbers as below.

$$\begin{aligned}
 A &= 1000.11 = 0.100011 \times 2^4 \\
 \text{Hence, Sign of } A, A_S &= 0 \\
 \text{Mantissa of } A, A_M &= 100011 \\
 \text{Exponent of } A, A_E &= 4 \\
 \text{and } B &= 111.01 = 0.11101 \times 2^3 \\
 \text{Hence, Sign of } B, B_S &= 0, \\
 \text{Mantissa of } B, B_M &= 100011 \\
 \text{Exponent of } B, B_E &= 3.
 \end{aligned}$$

As both signs are positives (0s), resultant number is also a positive. And multiplication of the two mantissas is $R_M = A_M \times B_M = 100011 \times 11101$.

From Fig. 8, the resultant mantissa is $R_M = 01111110111$ (i.e., 1015 as shown in Fig. 11). Exponents of the result should be added that is $R_E = A_E + B_E = 3 + 4 = 7$.

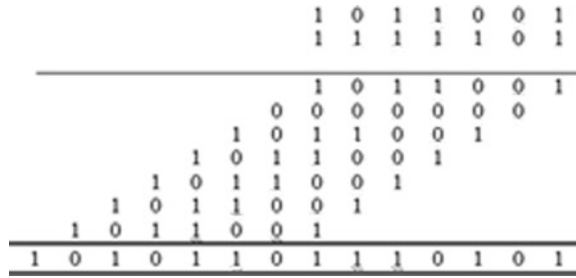
Hence, the result is $R = (-1)^{R_S} \times 0.01111110111 \times 2^7 = (-1)^0 \times 0.01111110111 \times 2^7$.
 $R = 63.4375$.

Case-2:

Let $A = 11.125$ and $B = -15.625$. The binary equivalents of these numbers are $A = 1011.001$ and $B = 1111.101$. Now, let us separate the sign, exponent, and mantissa from the given numbers as below.

$$\begin{aligned}
 A &= 1011.001 = 0.1011001 \times 2^4 \\
 \text{Hence, sign of } A, A_S &= 0 \\
 \text{Mantissa of } A, A_M &= 1011001 \\
 \text{Exponent of } A, A_E &= 4 \\
 \text{and } B &= 1111.101 = 0.1111101 \times 2^4
 \end{aligned}$$

Fig. 10 Multiplication of Mantissa in case-2



Hence, sign of B , $B_S = 1$
 Mantissa of B , $B_M = 1111101$
 Exponent of B , $B_E = 4$.

As one of the input numbers B is having a negative sign, the result is a negative number, thus $R_s = 1$. And multiplication of the two mantissas is

$$R_M = A_M \times B_M = 1011001 \times 1111101$$

From Fig. 9, the resultant mantissa is $R_M = 10101101110101$ (i.e., 11125 as shown in Fig. 11). Exponents of the result should be added that is $R_E = A_E + B_E = 4 + 4 = 8$.

Hence, the result is

$$\begin{aligned} R &= (-1)^{R_s} \times 0.10101101110101 \times 2^8 \\ &= (-1)^{R_s} \times 10101101.110101 \\ R &= -173.828125. \end{aligned}$$

6 Power Dissipation of Floating-Point Multiplier

The power dissipation of the proposed layout of the floating-point multiplier can be evaluated from the energy dissipation of the XOR gate, 8-bit adder, and array multiplier. The tool QD-E can be utilized to calculate the energy dissipation of individual blocks [15, 16]. The energy dissipations of the three modules are shown in Table 2. The total energy dissipation of the proposed floating-point multiplier is

$$E = 11.85 \times e^{-001} \text{ eV.}$$

To find the power dissipation, convert the eV into joules. This is obtained by multiplying the value in eV with the charge of an electron.

$$\text{Charge of an electron} = 1.607 \times 10^{-19} \text{ J.}$$

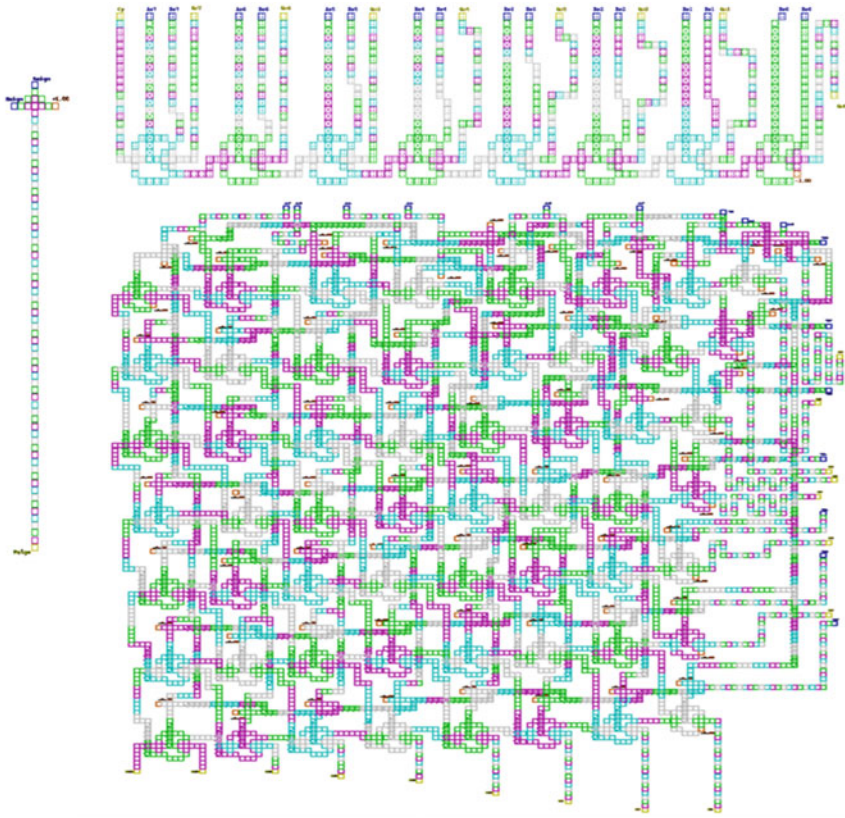


Fig. 11 Layout of the proposed floating-point multiplier

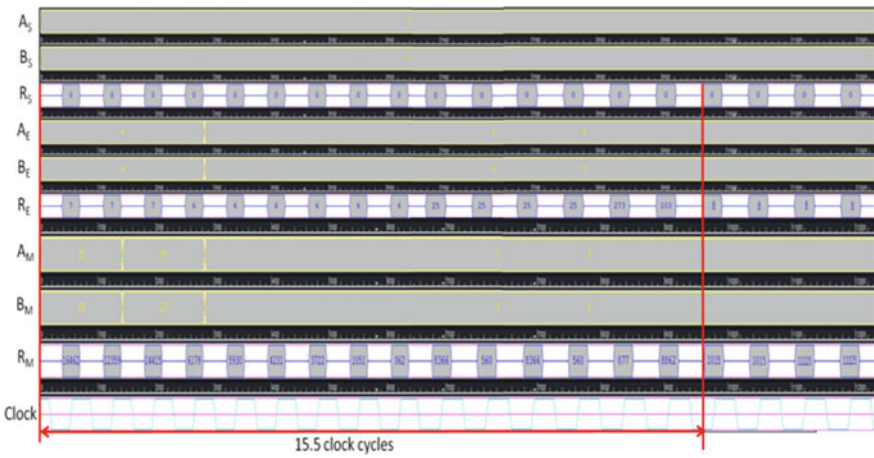


Fig. 12 Simulation results of the proposed floating-point multiplier

Table 2 Energy dissipation of various blocks in eV

Module	Sum _Ebath (eV)	Avg _ Ebath (eV)
XOR gate	1.90E-02	1.73E-03
8-bit adder	2.18E-01	1.98E-02
Array multiplier (8 × 8)	9.48E-01	8.62E-02
Total energy dissipation	1.19E+00	1.08E-01

Table 3 Comparison of area, power, and delay

Multipliers	Area (μm^2)	Power (mW)	Delay (ns)
FP multiplier [3]	50,369	–	121.04
FP multiplier [4]	3280	–	71.122
FP multiplier [5]	–	1042	56.481
FP multiplier [6]—45 nm	19.67	6.385	–
FP multiplier [6]—90 nm	20.67	0.591	–
FP multiplier [7]	1073	–	16.182

Hence, the energy dissipation is

$$\begin{aligned} E &= 11.85 \times 10^{-1} \times 1.607 \times 10^{-19} \text{ J} \\ &= 1.807 \times 10^{-19} \text{ J}. \end{aligned}$$

Using the basic relation between energy and power, the power dissipation can be calculated as Power dissipation, $P_d = \text{Energy } (E)/\text{Time } (T)$

The time is nothing but the clock period used for the simulation of the floating-point adder. This clock has a period of 4 ps. The delay incurred to generate the output is 15 clock cycles from Fig. 11. Then the total delay is $4 \text{ ps} \times 15.5 = 62 \text{ ps}$ (Fig. 12).

$$P_d = 1.807 \times 10^{-19} / 62 \times 10^{-12} = 2.91 \text{ nW}.$$

Therefore, the power dissipation of the proposed floating-point multiplier for single-precision QCA layout is 2.91 nW. Table 3 shows the comparative study of area, power, and delay of existing and proposed floating-point multipliers. When we use quantum-dot cellular automata technology, the area is $10.45 \mu\text{m}^2$; power is just 2.91 nW; and delay is of 15.5 clock cycles that is 62 ps. Hence, the proposed architecture is used in large-scale applications rather than CMOS technology; it improves the performance of the design in all aspects.

7 Conclusion

In this paper, we have designed a fast and efficient floating-point multiplier for several large applications work based on mathematical operations. The proposed model could overcome the problems identified by the CMOS technology as it is implemented with the latest novel technology like quantum-dot cellular automata. The parameters like area, delay, and power dissipation are calculated for the proposed model, which has proved that the proposed floating-point multiplier has better performance characteristics. The size of the floating-point multiplier is just $10.25 \mu\text{m}^2$. The power dissipation is calculated from energy dissipation with the latest tool that is QCA Designer-E. The proposed floating-point multiplier has the power dissipation of 2.91 nW only.

References

1. Porod W, Lent CS, Bernstein GH (1994) Quantum cellular automata. *Nanotechnology* 4:49–57
2. Tougraw PD, Lent CS (1994) Logical devices implemented using quantum cellular automata. *J Appl Phys* 46556:1818–1825
3. Gonzalez-Navarro S, Tsen C, Schulte MJ (2012) Binary integer decimal-based floating-point multiplication. *IEEE Trans Comput* 62(7):1460–1466
4. Kodali RK, Gundabathula SK, Boppana L (2014) FPGA implementation of IEEE-754 floating-point Karatsuba multiplier. In: 2014 international conference on control, instrumentation, communication and computational technologies (ICCICCT). IEEE, pp 300–304
5. Anjana S, Pradeep C, Samuel P (2015) Synthesize of high-speed floating-point multipliers based on Vedic mathematics. *Proc Comput Sci* 46:1294–1302
6. Shinde JR, Salankar SS (2015) VLSI implementation of bit-serial architecture based multiplier in floating-point arithmetic. In: 2015 international conference on advances in computing, communications and informatics (ICACCI). IEEE, pp 1672–1677
7. Arish S, Sharma RK (2015) An efficient floating-point multiplier design for high-speed applications using Karatsuba algorithm and Urdhva-Tiryagbhyam algorithm. In: 2015 international conference on signal processing and communication (ICSC). IEEE, pp 303–308
8. Jha CK, Doshi I, Mekie J (2020) Analysis of worst-case data-dependent temporal approximation in floating-point units. *IEEE Trans Circ Syst II Exp Briefs*
9. Zuras D, Cowlshaw M, Aiken A, Applegate M, Bailey D, Bass S, Bhandarkar D, Bhat M, Bindel D, Boldo S, Canon S (2008) IEEE standard for floating-point arithmetic. *IEEE Std* 754:1–70
10. Kravev J (2019) Design of floating-point arithmetic unit for FPGA with Simulink ®. In: IEEE EUROCON 2019-18th international conference on smart technologies. IEEE, pp 1–5
11. Al-Ashraf M, Salem A, Anis W (2011) An efficient implementation of the floating-point multiplier. In: 2011 Saudi international electronics, communications and photonics conference (SIEPC). IEEE, pp 1–5
12. Palekar S, Narkhede N (2016) High speed and area-efficient single-precision floating-point arithmetic unit. In: 2016 IEEE international conference on recent trends in electronics, information and communication technology (RTEICT). IEEE, pp 1950–1954
13. Wahba AA, Fahmy HAH (2016) Area efficient and fast combined binary/decimal floating-point fused multiply-add unit. *IEEE Trans Comput* 66(2):226–239
14. Walus K, Dysart TJ, Jullien GA, Budiman RA (2004) QCA Designer: a rapid design and simulation tool for quantum-dot cellular automata. *IEEE Trans Nanotechnol* 3(1):26–31

15. Gudivada AA, Sudha GF (2020) Design of Baugh-Wooley multiplier in quantum-dot cellular automata using a novel 1-bit full adder with power dissipation analysis. *SN Appl Sci* 2(5):1–13
16. Gudivada AA, Sudha GF (2021) Novel optimized tree-based stack-type architecture for 2 n-bit comparator at nanoscale with energy dissipation analysis. *J Supercomput* 77(5):4659–4680

Compression Techniques for Low Power Hardware Accelerator Design: Case Studies



Govinda Rao Locharla, Pogiri Revathi, and M. V. Nageswara Rao

Abstract Deep learning algorithms are playing a vital role in wide range of Artificial Intelligence-based applications. Since the CPU/GPU-based solutions are not suitable for low power applications like IoT due to their high-power requirements, a dedicated hardware called hardware accelerator is needed for a given AI-based processing. Further, the hardware accelerators are essential in reducing the inference-time latency. The FPGA/ASIC-based CNN accelerator implementations are in research focus now a days owing to their high performance per Watt in variety of domains such as vision, voice, text. In this paper, the k -means algorithm based technique for the CNN model compression and Winograd based techniques for reducing the number of multiplications reported in the literature are discussed as case studies for model compression, and hardware optimization.

Keywords Convolutional neural network · Deep learning neural network · Field programmable gate array · Hardware accelerator

1 Introduction

Many deep learning systems employ Convolutional Neural Networks (CNNs). CNNs are widely adopted in a number of applications such as object detection [1–3], image classification [4–6], and speech recognition [7, 8]. The Graphics Processing Unit (GPU) is normally opted for CNN processing due to its excellent performance and flexibility but consumes power up to hundreds of Watts. This makes GPU not suitable for the low-power applications like wearable gadgets, IoT devices, etc. During the recent decades, researchers are focusing on increased parallelism and reduced bus widths through quantization, with fixed points arithmetic to reduce memory bandwidth requirements [9, 10]. CNN processing is computationally complex and it

G. R. Locharla (✉) · M. V. N. Rao
Department of ECE, GMR Institute of Technology, Rajam, Andhra Pradesh, India
e-mail: govindarao.l@gmrit.edu.in

P. Revathi
Department of ECE, SVCET, Etcherla, Srikakulam, Andhra Pradesh, India

© The Author(s), under exclusive license to Springer Nature Singapore Pte Ltd. 2022
P. Kumar Jain et al. (eds.), *Advances in Signal Processing and Communication Engineering*, Lecture Notes in Electrical Engineering 929,
https://doi.org/10.1007/978-981-19-5550-1_12

117

requires a large number of multiplications. Cloud-based GPU services can be used for offline training for low-power trained neural processors which deployed in high throughput power-constrained applications. FPGAs and ASICs offer good performance per Watt compared to GPUs for deep CNN-based system implementations. Though the FPGAs are more energy efficient than GPUs, their on-chip memory is limited to meet the overall system performance requirements. However, such bottlenecks can overcome through design mitigations. The compression methods reported in the literature related to configuring the CNN-based models are broadly in two categories: The first is model compression, and second is hardware optimization. In the first category, pre-trained models are exclusively at software level to reduce their memory footprint [11–14]. The techniques adopted in this line includes network pruning, weight matrix decomposition, weight quantization, etc. The second category of compression methods focus on hardware components with a particular emphasis on high speed, power efficient CNN accelerators [15–17].

Juan Yopez et.al. reported Winograd algorithm-based techniques to reduce the number of multiplications required [18]. The Winograd minimal filtering algorithms (WMFAs) can be used for different stride sizes [19]. In this method, the number of multiplications required for overlapping computations between adjacent windows are reduced by substituting addition in place of the multiplication. Jain et al. [20] reported strided convolutions techniques to replace the pooling layers for down sampling [21], where stride taken as a kernel's displacement element-wise along a particular axis [22]. The k -means algorithm-based technique for the CNN model compression [20] and Winograd-based techniques for reducing the number of multiplications [18] are discussed in this paper as case studies for model compression, and hardware optimization. The hardware and performance reported in [18, 20] are also discussed.

This paper is organized as follows. In Sect. 2, network compression design methods are presented. Hardware Design using compression Techniques in Sect. 3. Performance comparison discussions are brought in Sect. 4 and Conclusions are given in Sect. 5.

2 Network Compression and Hardware Design Methods

The compression methods reported in the literature for the design of low power hardware accelerators can be classified broadly in to two categories: The first is model compression, and second is hardware optimization. Case studies [18, 20] of these two categories are brought in this section.

2.1 *Quantization Using Simple k -Means*

The compress of CNN model is achieved through weight partition, quantization, and rounding the final weights to powers of two [14]. Instead, a model-aware method

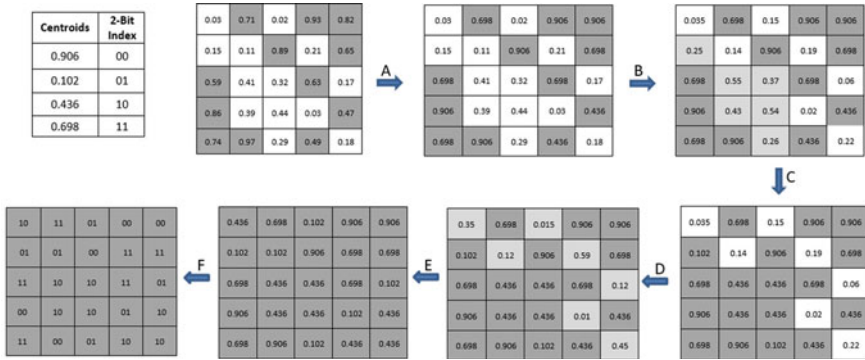


Fig. 1 Illustration of the kernel optimization using k -means method

reported in [20], final weights are calculated using k -means. As the procedure is depicted in Fig. 1, the pre-trained weights of each layer are used to calculate k centroids. The each of k -centroids are assigned with an index of a size of $\log_2(k)$ bits as shown in a lookup table. The predefined partition boundaries of $[0.5, 0.75, 1]$ are used for network quantization in this example as shown in Fig. 1. In each step half of the available weights with values higher than the rest in the kernel are quantized such that the network's precision is maintained. In step-A, possibly half of the available weights with values higher than the rest in the kernel taken into one partition and are quantized to the nearest centroid listed in the LUT. The rest of the weights are taken into other partition. The quantized partition is frozen and the other partition of lower value weights is trained to compensate the loss of precision caused by the clustering of the weights in step-B. The weights quantized at step-A will not be altered in further stages of quantization. A mask prevents the gradient back-propagation from updating the clustered weights during retraining. This weight partition, weight quantization and retaining steps are repeated during the step-C to step-E until all weights are quantized to the cluster centers. On completion of the training period, the total number unique valued weights in the kernel equals to k where k is much smaller than the total number of weights in the kernel prior to the quantization. This quantization method leads to a reduced complexity and enables the use of sum accumulators instead of MACs. Finally, the quantized weights are encoded with the respective bit-index from as the lookup table shown in Fig. 1.

Replacing MACs by Accumulators: Convolution is the process of multiplying the kernel weights with a part of the input feature map and accumulating the products at each step by repeating the same while moving the kernel window across the feature map with a given stride size. Since there are only k specific weights per layer, by the distributive property, replacing the actually required MACs with k accumulators results in reduced hardware complexity. MAC operations involved in the traditional method is illustrated in Fig. 2 and the reduction of MAC operations using k -mean method is shown in Fig. 3. To calculate one output value using the traditional method, nine multiplications and eight additions are needed. Since there are only two unique

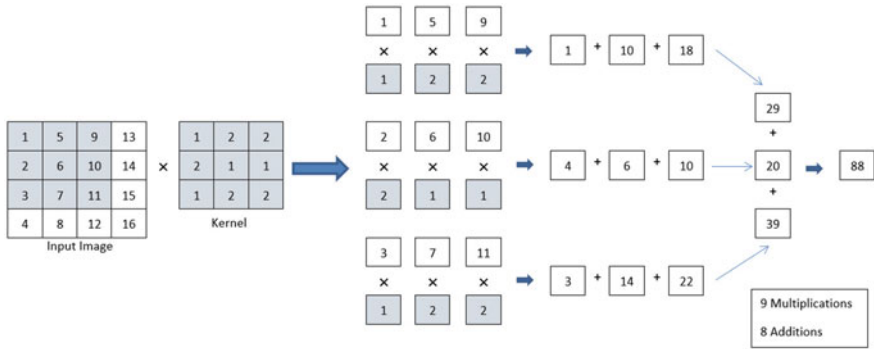


Fig. 2 Illustration of the MAC operations involved in the traditional method

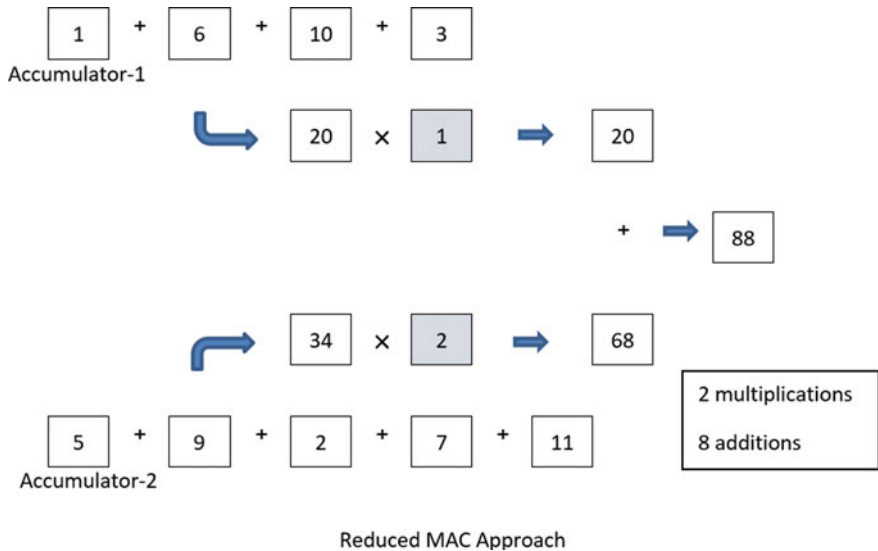


Fig. 3 Illustrating the reduction of MAC operations using k -mean method

weights in the compression method, only two multiplications and eight additions are enough to perform the same task. While this illustration only shows a two-dimensional kernel and input. In practice, the inputs are three-dimensional and there will be several convolution 3D kernels therefore, great saving in terms of the hardware can be achieved. Since the mapped centroid is referred to by their indices with a word length of $\log_2(k)$, the final output value is calculated by k MAC operations.

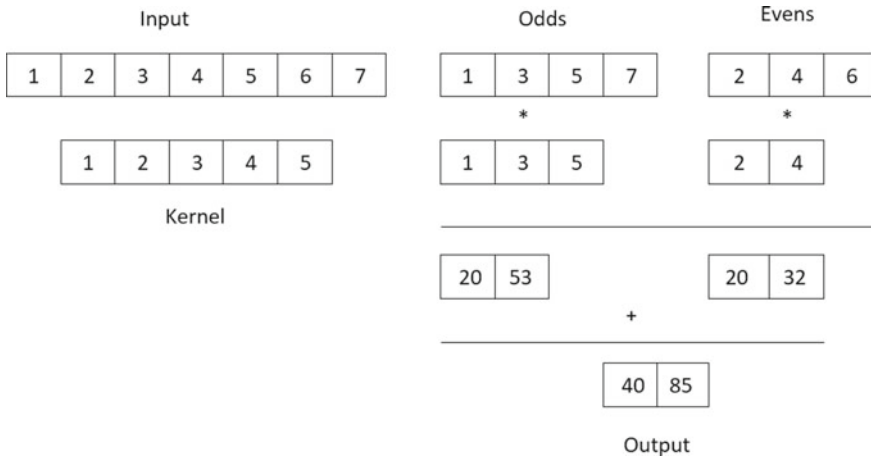


Fig. 4 Convolution process with stride size of 2 for kernel = 5

2.2 Winograd Algorithm for Hardware Compression

The number of multiplications required can be reduced by using Winograd algorithm-based techniques. In 1D WA with stride-2 approach, odd-positioned input elements and kernel elements are multiplied and even-positioned input elements and kernel elements are multiplied. The even and odd groupings can be used to split a stride-2 convolution into two stride-1 convolutions. This method is demonstrated for an input of size 5 and a kernel vector of size 3. The convolution process with stride size of 2 is shown in Fig. 4. The convolution process with stride size of 2 and kernel of 5 and 3×3 are shown in Figs. 4 and 5, respectively. One element for the kernel and two elements for the input make up the even group. On the other hand, the odd group has two kernel elements and three input elements, which are determined through WAF(2, 2). The Multiplications required for WMFA with p -outputs and an q -tap kernel $F(p, q)$ is represented in Eq. (1).

$$m(F(p, q)) = p + q - 1 \tag{1}$$

To adopt the Winograd for a two dimension case with stride size of 2, the kernel and input elements should be divided into four classes: the odd row-odd column; odd row-even column; even row-odd column positioned elements of the input and kernel and the residual four elements of the input and residual one element of the kernel. These classes are demonstrated as shown in Fig. 5. The first class is made up of 2×2 kernel elements and 3×3 input elements. In the second and third classes, two consecutive WAF(2, 2) operations are applied. The fourth class uses regular multiplications. The convolution of each group generates a 2×2 matrix, and results in sum of the intermediate matrices. The first group involves 9 multiply operations,

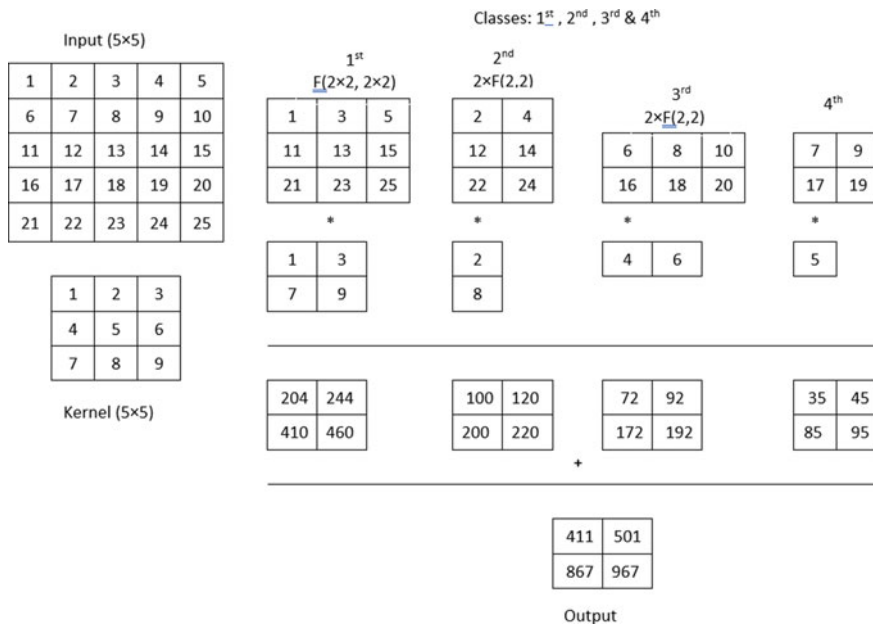


Fig. 5 Convolution process for stride size of 2 for kernel = 3 × 3

the second involves 6 multiply operations, the third has 6 multiplications; and the fourth has 4 multiplications. The total number of multiply operations is 25, while regular convolution uses 36.

3 Hardware Design Using Compression Techniques

Block diagrams of the architectures [18, 20] for the compression methods discussed in the earlier section are presented in this section.

k-means-based CNN Architecture The top-level diagram of the hardware architecture is shown in Fig. 6. The ARM core, Configurable logic, and external memory (DDR) make up the majority of the Zynq-based SoC architecture. The kernels and the input image for each layer during model initialization and convolutional layers’ input–output feature maps are stored in the external memory (DDR RAM). The BRAMs on the FPGA are used as on-chip buffers comes under the second stage. Since the size of the BRAMs on the FPGA is insufficient for storing complete function maps, entire function map is divided into several blocks through loop tiling. Since the external memory is expensive terms of latency and energy usage compared to BRAMs, on-chip memory is preferred for accessing the external memory. Convolution is performed in the computation Unit. The ARM core controls the entire

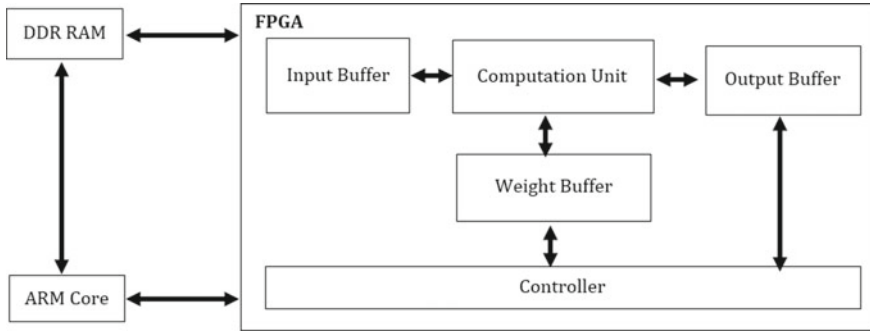


Fig. 6 Block diagram of the architecture for CNN using *k*-means method

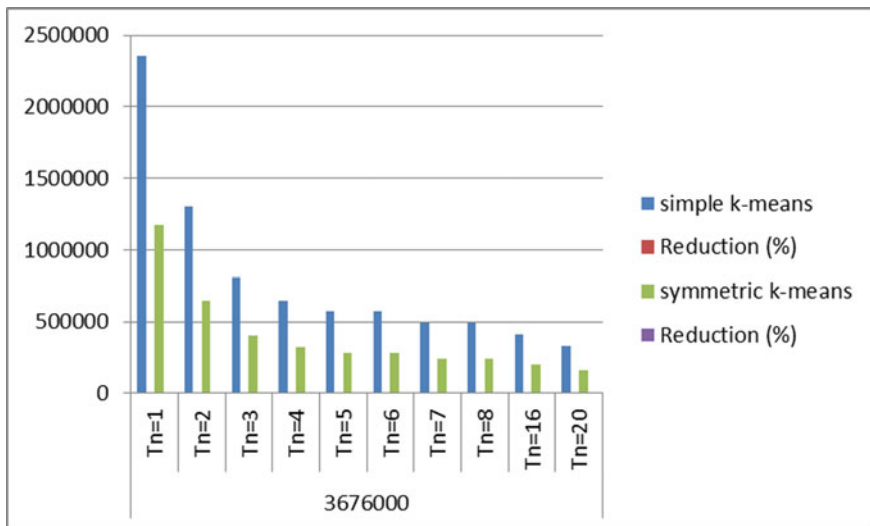


Fig. 7 The architecture of PE based on the modified Winograd for the hardware compression

process including off-chip data access. A portion of the input function map and weights retrieved from RAM are stored in the on-chip buffers. The convolution, biases addition and the activation are performed in the Computation Unit. Finally, the outputs are fetched from RAM and dense layer computations are performed in the ARM to obtain the final predictions.

Winograd-Based PE Architecture The architecture of PE based on the modified Winograd for the hardware compression is shown in Fig. 7. This PE can compute Two WAF($2 \times 2, 3 \times 3$) stride-1 operations in a clock and it employs 32 multipliers as each WA requires a 16 multiplications. The input tile size for Input registers block is 5×6 to compute one WA stride-2 or two WA stride-1 in one clock where the parallel processing of two Winograd strides 1 is possible. The Splitter Block is used

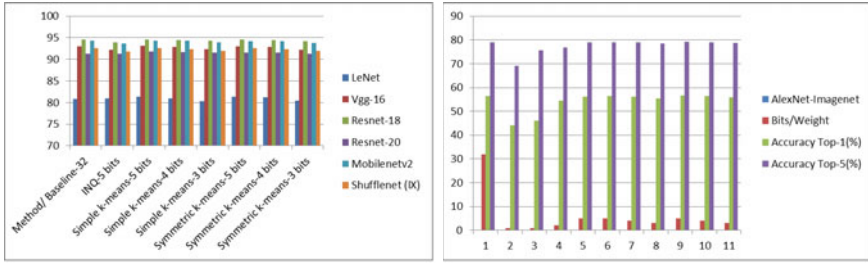
to break the input data according to the stride size. The Class-1 data feeds the input transform block, while rest of the classes data is rearranged to feed the input transform block. The Input Transform Block consists of are two parts which process the data of four groups. Filter Transform Block is controlled by “stride” signal to control the filter transform block. Multiplication block perform the multiplication of input transforms and the respective kernel transform to perform the convolution operations. Inverse Transform block performs the inverse Winograd. Accumulator Block adds the inverse transform results together for each group before sending to the register. Block diagram of the Winograd-based PE design with compressed/reduced hardware shown in Fig. 7. Since the algorithm requires 16-multiplications, input tiles are stored in input registers. Splitter block splits the input data according to the stride size of either 1 or 2. Input transform block performs the 2D or 1D transform of Winograd. Filter transform Block process the 2D Winograd transform into the kernel and passed it to the multiplication block. Multiplication block perform the convolution between input and the kernel. Inverse transform block performs the 2D or 1D transform of Winograd followed by the accumulation by accumulator and result is stored in the output registers.

4 Results and Analysis

Performance comparison of the compression methods [18, 20] discussed in the earlier section are presented in this section. Network compression using the k -mean centroids is evaluated by deploying in different CNN models using the CIFAR-10 dataset for the classification, while one (AlexNet2) [23] is evaluated on the Imagenet data set. The accuracy of the quantized CNN with clustered weights are recorded. The savings gained in terms of MAC operations are estimated for different values of k and the number of iterations (T_n).

4.1 Accuracy

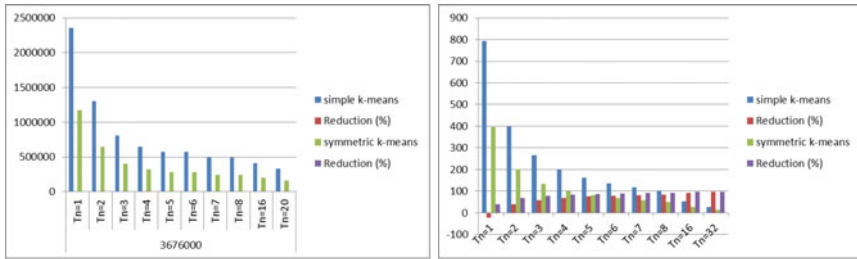
LeNet, ResNet-18 and ResNet-20 [24], VGG-16 [25], MobileNetV2 [26], and ShuffleNet ($1\times$) [27] with the CIFAR-10 dataset are used to evaluate task and accuracy comparison [20] is shown in Fig. 8a. For all CNN models, the quantization is expanded up to 3 bits with a marginal (0.65%) reduction in accuracy. The traditional CNN models LeNet and VGG-16 use simple convolutional filters. The principle of residual connections is introduced by the ResNet architecture. MobileNetV2 and ShuffleNet use less memory and are more effective in terms of computation. Channel shuffling and point-wise group convolution are used in the ShuffleNet, while MobileNetV2 uses depth-wise separable convolutions. Figure 8b shows the accuracy of AlexNet with the Imagenet dataset. The quantized network outperforms the pre-trained network in terms of 5-bit quantization accuracy.



(a) Accuracy comparison for CNN model with CIFAR-10 data set

(b) Accuracy of AlexNet with ImageNet dataset

Fig. 8 Accuracy comparison



(a) MAC Requirements for all convolutional layers in LeNet with $k=16$

(b) MAC Requirements for all convolutional layers in AlexNet with $k=16$

Fig. 9 Comparison of the MAC requirements

4.2 MAC Reductions

Figure 9a, b [20] show the results for a fixed k value and different T_n values. MAC requirements for LeNet with $k = 16$ are shown in Fig. 9. More input channels are processed simultaneously with a higher value of T_n , resulting in higher MAC count savings. The AlexNet MAC requirements are shown in Fig. 9b to demonstrates how these counts can be decreased using the Quantization Technique.

Hardware Resources and Latency [18] observed for $T_r = T_c = 16$ and $T_m = T_n = 8$ are shown in Table.1 for the k -means design with 4-bits weights.

Table 1 Resource utilization and clock latency

Resource	LUTs	Registers
Winograd stride-2	584	304
Two Winograd stride-1	930	487
Winograd based architecture	1076	587

5 Conclusion

In this paper CNN model compression and hardware optimization methods are discussed. As case studies, the k -means algorithm based technique for the CNN model compression and Winograd-based techniques for reducing the number of multiplications reported in the literature are discussed. Reduction of MAC operations using k -means algorithm and optimization of the multiplication requirements using Winograd-based algorithm are demonstrated. Block diagrams of the Winograd and k -mean-based algorithms are illustrated. Performance of the compression techniques is also discussed and compared.

References

1. Yu Y, Guan H, Ji Z (2015) Rotation-invariant object detection in high-resolution satellite imagery using superpixel-based deep hough forests. *IEEE Geosci Rem Sens Lett* 12(11):2183–2187
2. Le T-N, Sugimoto A (2018) Video salient object detection using spatiotemporal deep features. *IEEE Trans Image Process* 27(10):5002–5015
3. Han J, Zhang D, Hu X, Guo L, Ren J, Wu F (2014) Background prior-based salient object detection via deep reconstruction residual. *IEEE Trans Circ Syst Video Technol* 25(8):1309–1321
4. Romero A, Gatta C, Camps-Valls G (2015) Unsupervised deep feature extraction for remote sensing image classification. *IEEE Trans Geosci Rem Sens* 54(3):1349–1362
5. Chen S-W, Tao C-S (2018) Polarsar image classification using polarimetric-feature-driven deep convolutional neural network. *IEEE Geosci Rem Sens Lett* 15(4):627–631
6. Jiao L, Liu F (2016) Wishart deep stacking network for fast polarsar image classification. *IEEE Trans Image Process* 25(7):3273–3286
7. Wu B, Li K, Ge F, Huang Z, Yang M, Siniscalchi SM, Lee C-H (2017) An end-to-end deep learning approach to simultaneous speech dereverberation and acoustic modeling for robust speech recognition. *IEEE J Sel Top Sig Process* 11(8):1289–1300
8. Zhou P, Jiang H, Dai L-R, Hu Y, Liu Q-F (2015) State-clustering based multiple deep neural networks modeling approach for speech recognition. *IEEE/ACM Trans Audio Speech Lang Process* 23(4):631–642
9. Park S-W, Park J, Bong K, Shin D, Lee J, Choi S, Yoo H-J (2015) An energy-efficient and scalable deep learning/inference processor with tetra-parallel MIMD architecture for big data applications. *IEEE Trans Biomed Circ Syst* 9(6):838–848
10. Alam M, Vidyaratne LS, Iftekharuddin KM (2018) Sparse simultaneous recurrent deep learning for robust facial expression recognition. *IEEE Trans Neural Netw Learn Syst* 29(10):4905–4916
11. Han S, Mao H, Dally WJ (2015) Deep compression: compressing deep neural networks with pruning, trained quantization and Huffman coding. arXiv preprint [arXiv:1510.00149](https://arxiv.org/abs/1510.00149)
12. Han S, Pool J, Tran J, Dally WJ (2015) Learning both weights and connections for efficient neural networks. arXiv preprint [arXiv:1506.02626](https://arxiv.org/abs/1506.02626)
13. Chen W, Wilson J, Tyree S, Weinberger K, Chen Y (2015) Compressing neural networks with the hashing trick. In: International conference on machine learning. PMLR, pp 2285–2294
14. Zhou A, Yao A, Guo Y, Xu L, Chen Y (2017) Incremental network quantization: towards lossless CNNs with low-precision weights. arXiv preprint [arXiv:1702.03044](https://arxiv.org/abs/1702.03044)
15. Du Z, Fasthuber R, Chen T, Jenne P, Li L, Luo T, Feng X, Chen Y, Temam O (2015) Shidiannao: shifting vision processing closer to the sensor. In: Proceedings of the 42nd annual international symposium on computer architecture, pp 92–104

16. Han S, Liu X, Mao H, Pu J, Pedram A, Horowitz MA, Dally WJ (2016) EIE: efficient inference engine on compressed deep neural network. *ACM SIGARCH Comput Archit News* 44(3):243–254
17. Chen Y-H, Emer J, Sze V (2016) Eyeriss: a spatial architecture for energy-efficient dataflow for convolutional neural networks. *ACM SIGARCH Comput Archit News* 44(3):367–379
18. Yepez J, Ko S-B (2020) Stride 2 1-d, 2-d, and 3-d winograd for convolutional neural networks. *IEEE Trans Very Large Scale Integr (VLSI) Syst* 28(4):853–863
19. Winograd S (1980) *Arithmetic complexity of computations*, vol 33. SIAM
20. Jain A, Goel P, Aggarwal S, Fell A, Anand S (2020) Symmetric k -means for deep neural network compression and hardware acceleration on FPGAs. *IEEE J Sel Top Sig Process* 14(4):737–749
21. Springenberg JT, Dosovitskiy A, Brox T, Riedmiller M (2014) Striving for simplicity: the all convolutional net. *arXiv preprint [arXiv:1412.6806](https://arxiv.org/abs/1412.6806)*
22. Hannink J, Kautz T, Pasluosta CF, Barth J, Schülein S, Gaßmann K-G, Klucken J, Eskofier BM (2017) Mobile stride length estimation with deep convolutional neural networks. *IEEE J Biomed Health Inf* 22(2):354–362
23. Krizhevsky A, Sutskever I, Hinton GE (2012) ImageNet classification with deep convolutional neural networks. *Adv Neural Inf Process Syst* 25:1097–1105
24. He K, Zhang X, Ren S, Sun J (2016) Deep residual learning for image recognition. In: *Proceedings of the IEEE conference on computer vision and pattern recognition*, pp 770–778
25. Simonyan K, Zisserman A (2014) Very deep convolutional networks for large-scale image recognition. *arXiv preprint [arXiv:1409.1556](https://arxiv.org/abs/1409.1556)*
26. Sandler M, Howard A, Zhu M, Zhmoginov A, Chen L-C (2018) Mobilenetv2: inverted residuals and linear bottlenecks. In: *Proceedings of the IEEE conference on computer vision and pattern recognition*, pp 4510–4520
27. Zhang X, Zhou X, Lin M, Sun J (2018) Shufflenet: an extremely efficient convolutional neural network for mobile devices. In: *Proceedings of the IEEE conference on computer vision and pattern recognition*, pp 6848–6856

Sequence Set Design for Radar System



P. Shravan Kumar, S. P. Singh, T. D. Bhatt, and D. V. S. Nagendra Kumar

Abstract This paper proposes the design of near optimal orthogonal sequence sets for Radar applications. Proposed sequences demonstrate better performance in range and Doppler delays. These orthogonal sequence sets are generated by using Hadamard recursive method and minimizing its weighted sum of peak side lobe (PSL). To minimize PSL of the N -dimensional orthogonal sequence sets, coordinate descent (CD) optimization algorithm is used. The optimized polyphase sequences exhibit approximately orthogonal properties.

Keywords Orthogonal sequences · Hadamard recursive method · Peak side lobe coordinate descent · Radar · Aperiodic auto-correlation · Waveform design

1 Introduction

Waveform with orthogonal properties has significant role in the multiple input and multiple output (MIMO) radar systems. Orthogonal waveforms transmitted by the transmitting antennas are received after reflecting from the target. At the receiver, the corresponding matched filter detects the signal [1]. To enhance the performance of the MIMO radar, each antenna must transmit distinct set of waveforms which are orthogonal to each other. In general, orthogonal waveforms can be achieved by using the techniques such as time division multiplexing (TDM), frequency division multiplexing (FDM), Doppler division multiplexing (DDM) and Code division multiplexing (CDM). Among these techniques, CDM performs better in terms of Doppler frequency and detection of target in shorter range. The CDM-MIMO system needs set of sequences or waveforms, which demonstrate good auto and cross-correlation properties. Most of the modern radar systems use pulse compression technique for improving the range resolution and low probability of intercept (LPI). The wave-

P. Shravan Kumar · S. P. Singh (✉) · T. D. Bhatt · D. V. S. Nagendra Kumar
Department of Electronics and Communication Engineering, Mahatma Gandhi Institute of
Technology, Hyderabad, Telangana 500075, India
e-mail: spsingh@mgit.ac.in

© The Author(s), under exclusive license to Springer Nature Singapore Pte Ltd. 2022
P. Kumar Jain et al. (eds.), *Advances in Signal Processing and Communication
Engineering*, Lecture Notes in Electrical Engineering 929,
https://doi.org/10.1007/978-981-19-5550-1_13

129

forms used in such radar systems must have small PSL at the output of the matched filter. Sequences coded with appropriate phase and frequency can provide minimum PSL. In pulse compression, the entire pulse is divided in N sub-pulses, and each sub-pulse is coded either in phase or frequency. In case of phase coding, it can be binary or polyphase [2].

2 Waveform Design

The waveform design constrain for minimum phase transition is to improve spectrum efficiency. Set of sequences with continuous phases and minimum auto and cross-correlation sidelobes provide better detection probability at the output of matched filter [3–11].

Let us consider MIMO radar with N_T transmitting antennas and each antenna transmits N sub-pulses.

$$S = \begin{bmatrix} x_{11} & x_{12} & \dots & x_{1N} \\ x_{21} & x_{22} & \dots & x_{2N} \\ \vdots & \ddots & & \vdots \\ x_{N_T 1} & x_{N_T 2} & \dots & x_{N_T N} \end{bmatrix} \quad (1)$$

To achieve orthogonality, orthogonal phase coded matrix is overlaid with signal pulse [3]. Let Hadamard matrix H be a 2×2 orthogonal matrix given in Eq. (2). Through recursion one can construct 8×8 matrix or 16×16 matrix.

$$O = \begin{bmatrix} H & H \\ H & -H \end{bmatrix} \quad (2)$$

From matrix S , the aperiodic cross-correlation function at K -lag is given by,

$$CC_{ap}(k) = \sum_{n=1}^{N-k} \chi_{m_T}(n) \chi_{l_T}^*(n-k) \quad (3)$$

For aperiodic auto-correlation $m_T = l_T$, commonly approached parameter for detection of good auto-correlation properties of the given code. The peak side lobe (PSL) of matrix S is defined as:

$$\text{PSL} = \text{Max} \left\{ \max_{m_T} \max_{k \neq 0} |AC_{ap}(k)|, \max_{m_T, l_T (m_T \neq l_T)} \max_k |CC_{ap}(k)| \right\} \quad (4)$$

where $AC_{ap}(k)$ is an aperiodic auto-correlation function.

Many orthogonal binary sequences like Baker codes, maximum length sequences, gold sequences, Kasami sequences and Legendre sequences have been introduced in the wireless communications for simultaneous access for users without interference.

In radar systems, these sequences cannot be used as they are optimal as per the requirements. Correlation property has a significant role in design of sequence sets. Auto-correlation property is correlation between time shifted version of the same sequence.

Achieving Doppler resolution in radar usually requires a coherent processing of train of N pulses. In most of the cases, the train is constructed by repeating the same compressed pulse. In this context, it will be first observed that overlaying the N identical pulses with an orthogonal set of N sequences, each one is constructed with M elements, will remove completely the sidelobes of the auto-correlation function (ACF) over the delay range (t_s, T) , where t_s is the duration of one element of the sequence, which is referred to as a slice, and $T = M t_s$, is the pulse duration.

2.1 Orthogonal Phase Overlay

Orthogonal phase coded overlay uses phase matrix to generate orthogonal set matrix. This orthogonal set is overlaid on a pulse by simply multiplying with the signal. The orthogonal sequence set matrix of length 8 is generated using Hadamard matrix through recursion method given by (2). Orthogonal set for phase overlay using phase modulation given in [3] for 8×8 is described as

$$\varphi_{p,m} = \{\varphi_{8,8}\} \begin{bmatrix} 0 & 0 & 0 & 0 & 0 & 0 & 0 & 0 \\ 0 & 0 & 1 & 1 & 1 & 1 & 0 & 0 \\ 0 & 1 & 1 & 0 & 0 & 1 & 1 & 0 \\ 0 & 0 & 0 & 0 & 1 & 1 & 1 & 1 \\ 0 & 1 & 0 & 1 & 0 & 1 & 0 & 1 \\ 0 & 0 & 1 & 1 & 0 & 0 & 1 & 1 \\ 0 & 1 & 0 & 1 & 1 & 0 & 1 & 0 \\ 0 & 1 & 1 & 0 & 1 & 0 & 0 & 1 \end{bmatrix} \quad (5)$$

Orthogonal matrix set is given by formula $M = \{a_{p,m}\} = \{e^{j\varphi_{p,m}}\}$.

Phase modulation of p th pulse with p th row is the implementation of overlay method. Orthogonality among rows in matrix M is only possible when columns (m) \leq rows (p). Spectrum of orthogonal phase overlay is shown in Fig. 1. The drawback of adding binary-phase-coded overlay is spectrum broadening.

2.2 Derivative Phase Overlay

To overcome the effect of spectrum broadening, derivative phase (DP) overlay is used. It nullifies phase change in a single slice and hence gives better spectrum results. One can convert the orthogonal set into a DP set by using the split slice, in which

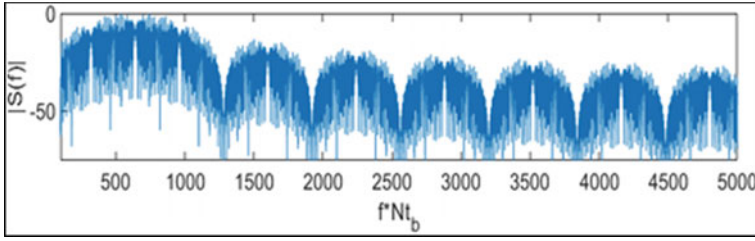


Fig. 1 Spectrum of orthogonal overlay

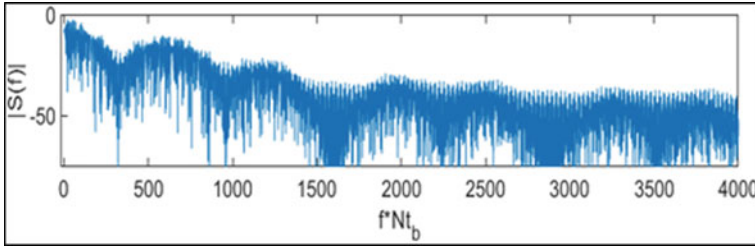


Fig. 2 Spectrum of derivative phase overlay

the frequency modulation (FM) is $\{\Delta f, -\Delta f\}$, in the first slice when current slice is identical to the previous slice, else $\{-\Delta f, -\Delta f\}$ is used. DP overlay provides better spectrum characteristics as shown in Fig. 2. Here single slice t_s is divided into 2 bits as $t_s = 1t_b$, there are many types of derivative phase overlays. In every slice, duration t_s accumulated phase change is 0 or π . During first bit duration t_b frequency step is $\Delta f = 1/4tb$ achieving accumulated phase as $2\pi \Delta f t_b = \pi/2$, in next duration bit frequency step is $-\Delta f$ and phase accumulation is of $-\pi/2$.

$$R = \begin{pmatrix} 1 & 1 \\ 1 & -1 \end{pmatrix}, \text{ for this } R \text{ matrix, DP matrix is } DP = \begin{bmatrix} 1 & -1 & 1 & -1 \\ 1 & -1 & -1 & -1 \end{bmatrix}.$$

2.3 Prometheus Ortho-Normal Sets Overlay

Prometheus Ortho-Normal Sets overlay, first, uses the basic set of PONS matrix and defines its rows as $s1$ and $s2$. Substitute these rows in the PONS construction matrix.

$$\begin{pmatrix} s1 \\ s2 \end{pmatrix} = \begin{pmatrix} 1 & 1 \\ 1 & -1 \end{pmatrix}, \text{ PONS matrix is } PONS = \begin{bmatrix} s1 & s2 \\ s1 & -s2 \\ s2 & s1 \\ -s2 & s1 \end{bmatrix}.$$

It provides better results than orthogonal phase matrix and simple DP overlay matrix. By using the 8 and 16 pulses, the auto-correlation side lobes are around -17.02 dB and -13 dB, respectively. Figures 3 and 4 shows the ACF for two different length sequences with PONS overlay.

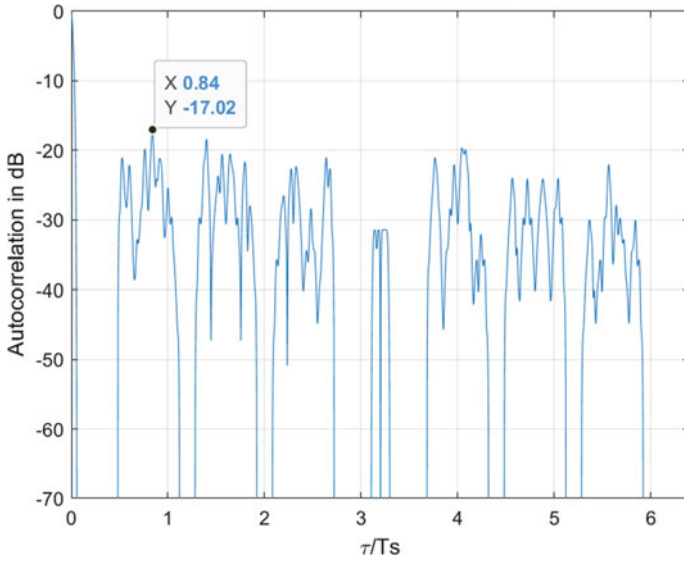


Fig. 3 ACF of PONS overlay for 8 pulses and sequence length $N=8$

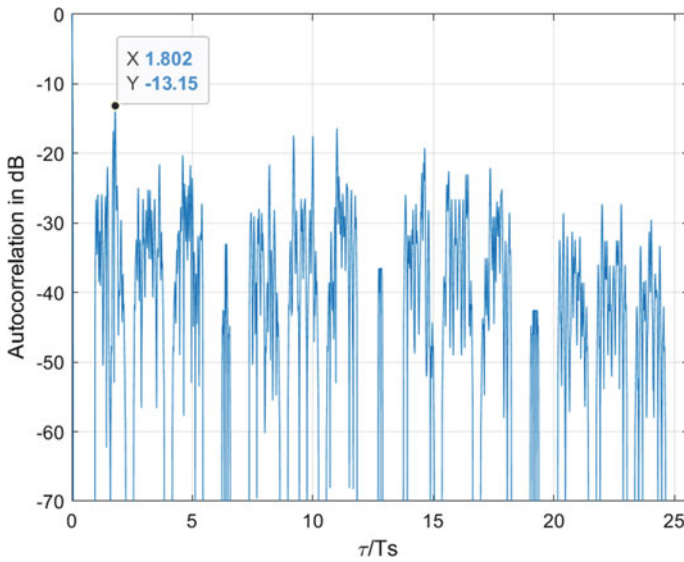


Fig. 4 ACF of PONS overlay for 8 pulses and sequence length $N=16$

3 Implementation of CD Algorithm

This section deals with the design of code to obtain sequences and discrete phases:

Let $f_1(S) = \max_{m_T} \max_{k \neq 0} |AC_{ap}(k)|$, $f_2(S) = \max_{m_i, l_i (m_i \neq l_i)} \max_k |CC_{ap}(k)|$ be the maximum sidelobe values for auto and cross-correlation values of N_T sequences. Aim is to design good set of sequences of S through minimizing $\{f_i(S)\}_{i=1}^2$.

The n -th sub-pulse of m -th antennas is,

$$x_m(n) = e^{j\theta_m(n)}, \quad m = 1, 2, \dots, N_T \quad \text{and} \quad n = 1, 2, \dots, N \quad (6)$$

$\theta_m(n)$ is phase of n -th sub-pulse and can be assigned only from the given set:

$$\theta_m(n) \in \{0, 2\pi/L, \dots, (L-1)2\pi/L\} \quad (7)$$

where L is number of discrete phase values. Let $\omega = e^{j2\pi/L}$ and $\varphi_L = \{1, \omega, \dots, \omega^{L-1}\}$, then feasibility region for constrain code problem is given by

$$\alpha_L = \{x_m | x_m(n) \in \varphi_L, n = 1, 2, \dots, N\} \quad (8)$$

Hence, design problem can be given by

$$P_S = \begin{cases} \min_S & f_1(S), f_2(S) \\ \text{s.t.} & x_{m,l} \in m, \quad l = 1, \dots, N_T \end{cases} \quad (9)$$

Minimization of all objective functions in multi-objective optimization problem does not exist [4]. Using scalarization technique to these types of problems, the specific weighted sum between them (Pareto-optimization) is given by

$$f_w(S) = w \max \{f_1(S), f_2(S)\} \quad (10)$$

Weighted coefficient w may vary 0–1 (9) is the linear function of depicts straight line with w as a slope. This scalarization leads to design problem,

$$P_S^w = \begin{cases} \min_S & f_w(S) \\ \text{s.t.} & x_{m,l} \in m, \quad l = 1, \dots, N_T \end{cases} \quad (11)$$

The different values of w lead to various set of orthogonal sequences. Let S^* be optimized set of sequences obtained after design problem. The polyphase matrix extracted from sequences after optimization is given by,

$$\text{polyphase matrix} = \tan^{-1} \left(\frac{\text{imag}(S^*)}{\text{Real}(S^*)} \right) \quad (12)$$

3.1 Optimized Polyphase Overlay

The input matrix with orthogonal sets O generated using recursion by using Eq. (2). $S = O$. In this paper, coordinate decent optimization algorithm is implemented by using iterative derivative method. This algorithm updates one or few blocks at a time instead of updating whole blocks [5]. Two loops, that is outer loop and inner loop, represent the coordinate of rows and columns, respectively. Optimization Procedure: Outer loop: Let in a row at t coordinate of the given orthogonal matrix S , where t varies from 1, 2, \dots , N_T and assign code vector of this row as x_t keeping remaining rows unchanged.

Inner loop: Pick a sub-coordinate from the x_t as scalar variable $x_t(d)$ where d varies from 1, 2, 3 \dots N , keeping the other sub-coordinates of x_t is unchanged.

By solving simple optimization technique, one can obtain desired matrix S^* . The implementing of optimization procedure is given below: Pick a coordinate t from 1 to N_T .

$$\text{Set } x_t^{i+1} = \arg \min_{x_t} f_w(x_t, S_{-t}^{(i)}) \quad (13)$$

where $S_{-t}^{(i)}$ indicates all the row coordinates kept unchanged during $i + 1$ -th iteration of outer loop.

$$S_{-t}^{(i)} = [x_1^{(i)}, x_2^{(i)}, \dots, x_{t-1}^{(i)}, x_{t+1}^{(i)}, \dots, x_{N_T}^{(i)}] \in N \times N_{T-1} \quad (14)$$

Optimization design problem S^w for outer loop at $(i + 1)$ th iteration converges to, where

$$f_w(x_t, S_{-t}^{(i)}) = f_w(x_1^{(i)}, x_2^{(i)}, \dots, x_{t-1}^{(i)}, x_t^i, x_{t+1}^{(i)}, \dots, x_{N_T}^{(i)}) \quad (15)$$

Thus, optimized code matrix for $(i + 1)$ th iteration for optimal solution $P_{t, S^{(i)}}^w$ becomes,

$$S_t^{*(i+1)} = [x_1^{(i)}, x_2^{(i)}, \dots, x_{t-1}^{(i)}, x_t^*, x_{t+1}^{(i)}, \dots, x_{N_T}^{(i)}] \quad (16)$$

Again, for optimal code for inner loop code also that is $x_t(d)$, same procedure is followed: Pick a sub-coordinate $x_t(d)$ where d is varying from 1 to N . Set

$$x_t^{(h+1)}(d) = \arg \min_{x_t(d)} g_{w, S_{-t}^{(i)}}(x_t(d), x_{t,-d}^{(h)}) \quad (17)$$

where $x_{t,-d}^{(h)}$ is all the coordinates of x_t kept unchanged in $(h + 1)$ iteration of inner loop. By selecting t th code vector and choosing scalar $x_t(d)$ as the optimization variable. $x_{t,-d}^{(h)} \in C^{N-1}$.

$$x_{t,-d}^{(h)} = [x_t^{(h)}(1), \dots, x_t^{(h)}(d-1), x_t^{(h)}(d+1), \dots, x_t^{(h)}(N)]^T \quad (18)$$

Then, the resulting optimization must satisfy the condition given in Eq. (16)

$$P_{d, x_t^{(h)}}^w = \begin{cases} \min_{x_t^{(d)}} & g_{w, S_t^{(i)}}(x_t(d), x_t^{(h)}) \\ \text{s.t.} & x_t(d) \in \alpha_L \end{cases} \quad (19)$$

where $g_{w, S_t^{(i)}}(x_t(d), x_t^{(h)}) = w \cdot g1$. In Eq. (17), the value of $g1$ is evaluated as

$$g1 = \text{Max} \left\{ \max_{k \neq 0} |AC_{tt}(k)|, \max_{l(l \neq t)} \max_k |CC_{tl}(k)| \right\} \quad (20)$$

Hence, the optimized t th transmit pulse is represented as

$$x_t^{(h+1)} = \left[x_t^{(h)}(1), \dots, x_t^{(h)}(d-1), x_t^*(d), x_t^{(h)}(d+1), \dots, x_t^{(h)}(N) \right]^T, \\ \text{here } x_t^*(d) \quad (21)$$

which the desired solution of the given condition expressed in Eq. (16). Similarly, from the initial matrix S , the optimized matrices such as $S^{(1)}, S^{(2)}, S^{(3)}, \dots$ can be obtained after each iteration. The final optimized matrix S^* which is obtained after applying CD algorithm to outer and inner loops. The S^* is a set of complex envelope orthogonal sequences that is applied for the phase overlay. The condition for obtaining the phases of polyphase (PP) matrix S^* given by,

$$\text{polyphase matrix} = \tan^{-1} \left(\frac{\text{imag}(S^*)}{\text{Real}(S^*)} \right) \in C^{N \times N_T} \quad (22)$$

Above gives the $N \times N_T$ dimensional polyphase matrix that is used here for multiplying with the radar pulse of same dimensions.

4 Results and Discussions

The ambiguity functions of orthogonal overlay and derivative phase overlay are shown in Figs. 5 and 6, whereas Figs. 7 and 8 represent the aperiodic ACF for orthogonal and derivative phase overlay, respectively. In derivative phase, overlay has peak sidelobe level of -16.65 dB and sidelobe level in case of orthogonal overlay is -9.576 dB. One can observe that the sidelobe levels are large in case of orthogonal overlay than derivative phase overlay. Figures 3 and 4 depict the Prometheus Ortho-Normal Sets (PONS) matrix overlay auto-correlation functions for length 8 and length 16, respectively. It shows that the performance for length 8 is better than the length 16. It means PONS is not performing well compared to the derivative phase overlay when length is increased. The Hadamard matrix considered for recursion is $[1, 1; -1, 1]$.

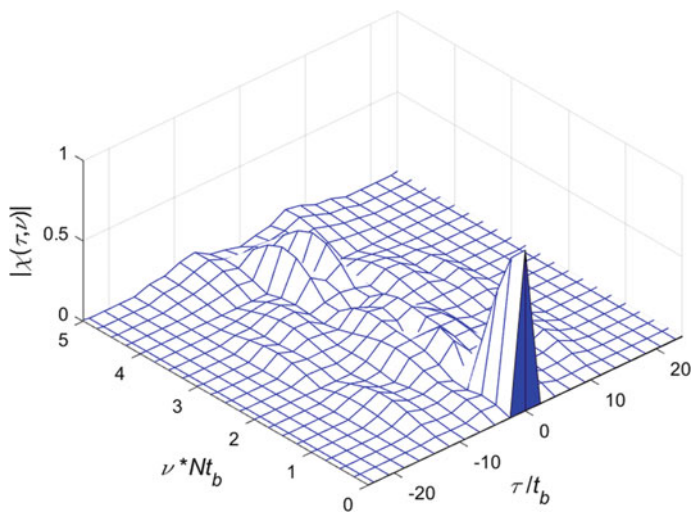


Fig. 5 AF of orthogonal phase overlay

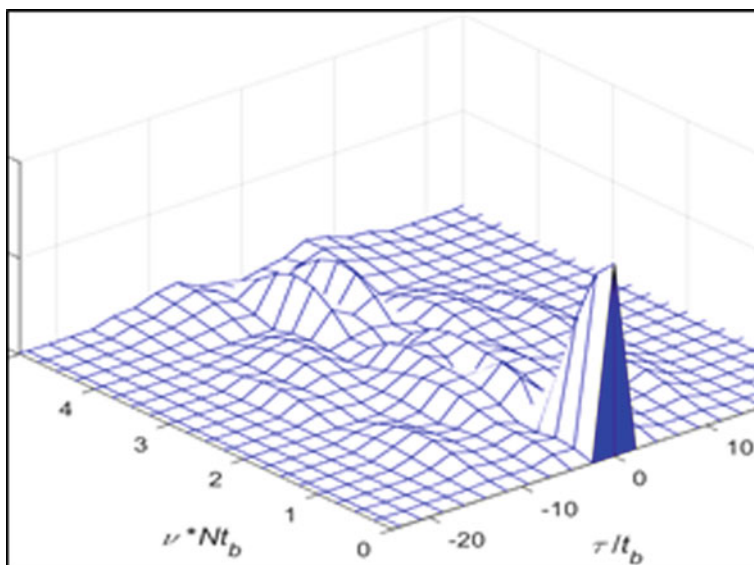


Fig. 6 AF of derivative phase overlay

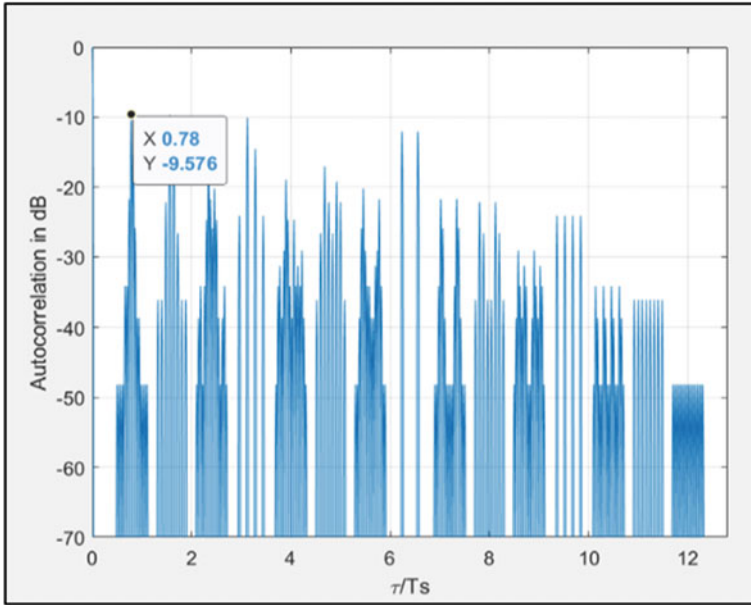


Fig. 7 ACF of derivative Phase overlay

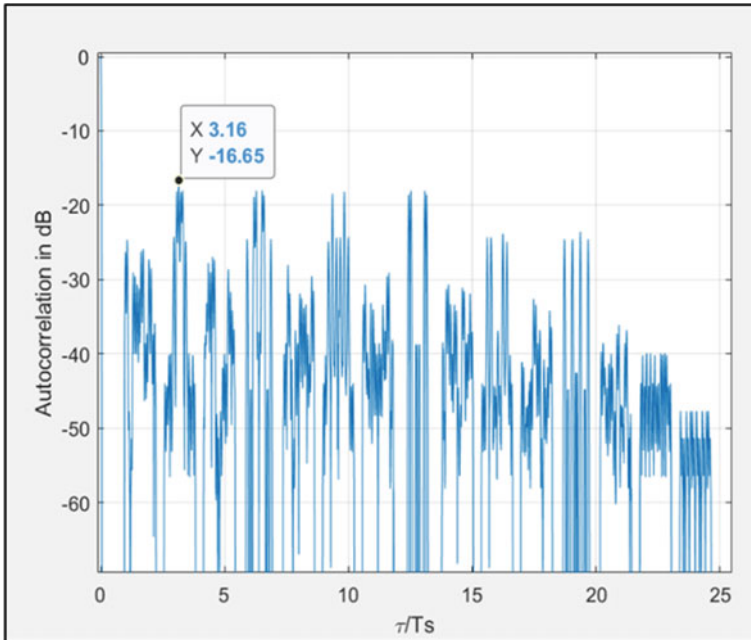


Fig. 8 ACF of orthogonal phase overlay

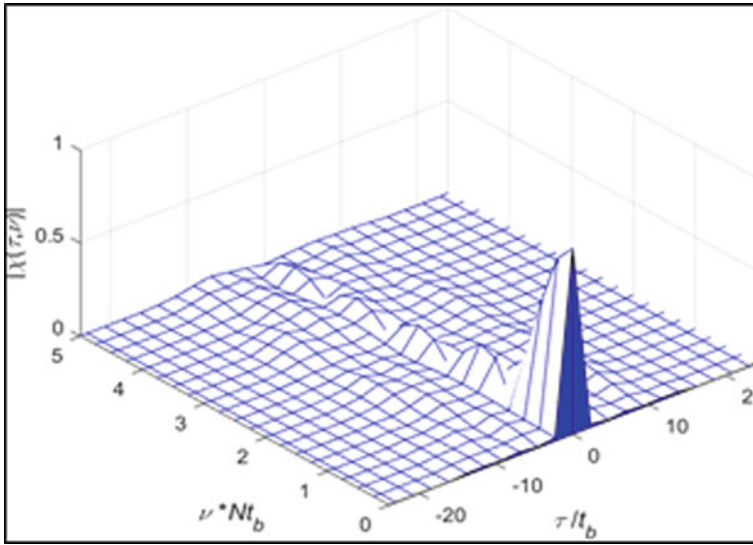


Fig. 9 AF of polyphase overlay

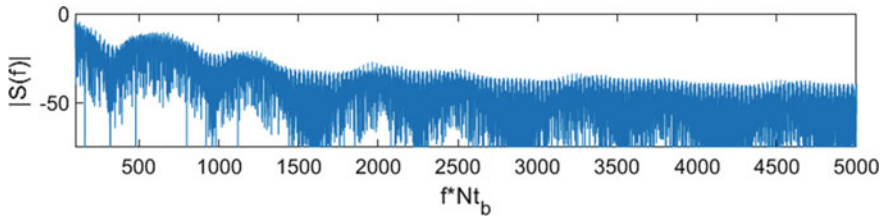


Fig. 10 Spectrum of PONS overlay

The same 16×16 orthogonal matrix as discussed above is used to generate 16×32 DP matrix with split slice method. The PONS overlay gives better ambiguity function than proposed polyphase (PP) overlay. The ambiguity function for PP overlay shown in Fig. 9. PONS matrix is generated here with the help of method described in Sect. 2.3. AF of PONS overlay is better than any above given overlay methods.

The generation of polyphase overlay matrix is described above. Coordinate descent algorithm is used for optimization of PSL of the given input orthogonal matrix.

From Figs. 10 and 11, spectrum null are more in the PONS overlay, whereas polyphase overlay spectrum is continuous and efficient. That is the phase transition among each chip duration t_b is minimized using CD algorithm. Figures 11, 12, 13 and 14 are showing the amplitude of pulse train, phase transition in radians and frequency change if each chip duration t_b , respectively.

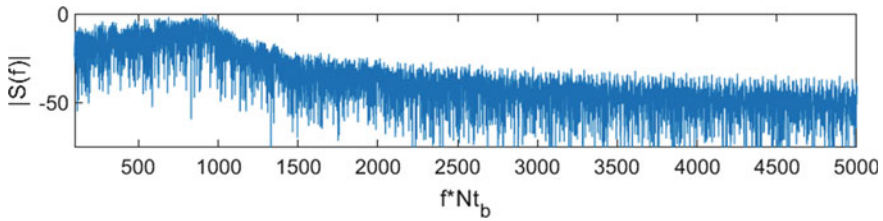


Fig. 11 Spectrum of polyphase overlay

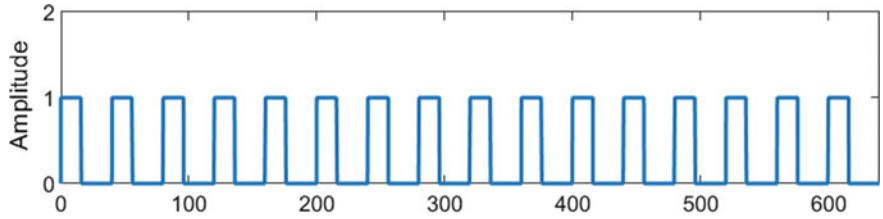


Fig. 12 Pulse train

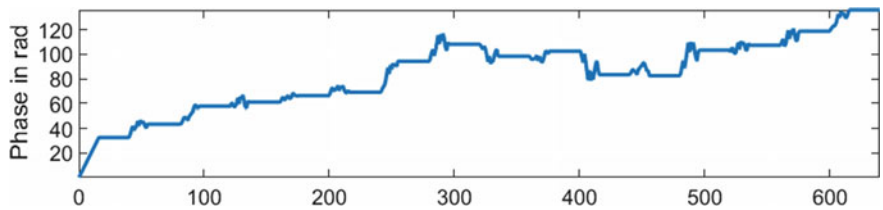


Fig. 13 Phase transition

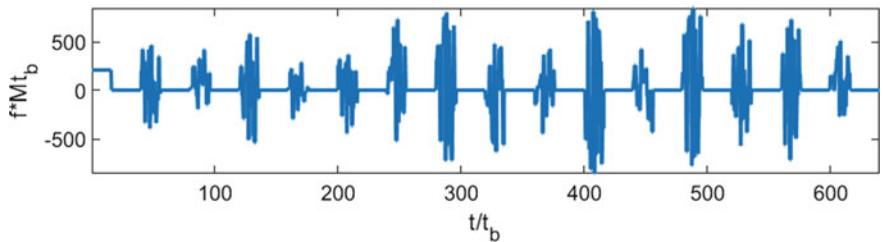


Fig. 14 Frequency changes for polyphase overlay

Aperiodic auto-correlation function of the PONS and polyphase overlay are shown in Figs. 15 and 16, respectively. In proposed PP overlay, the overall sidelobe suppression is less than -20 dB which much better than the PONS case, which is around -12 dB. The overall improvement in sidelobe suppression is nearly 8 dB. This is due to improvement in spectral efficiency.

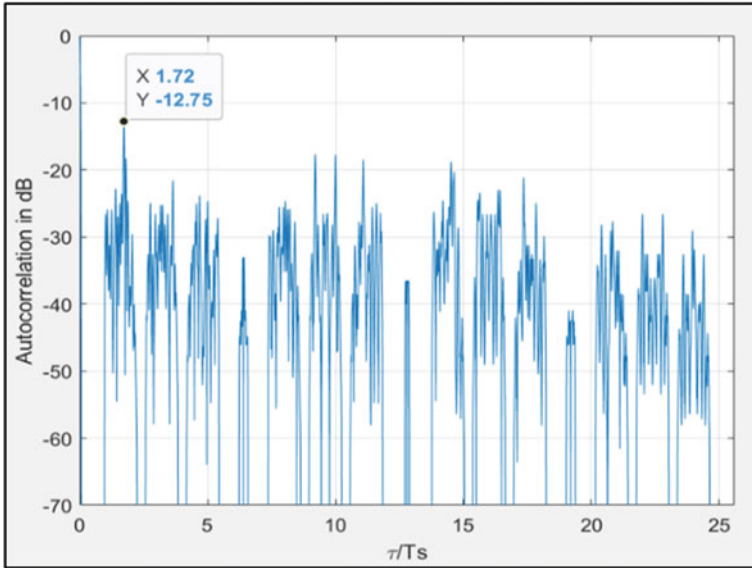


Fig. 15 ACF of PONS phase overlay for N=25

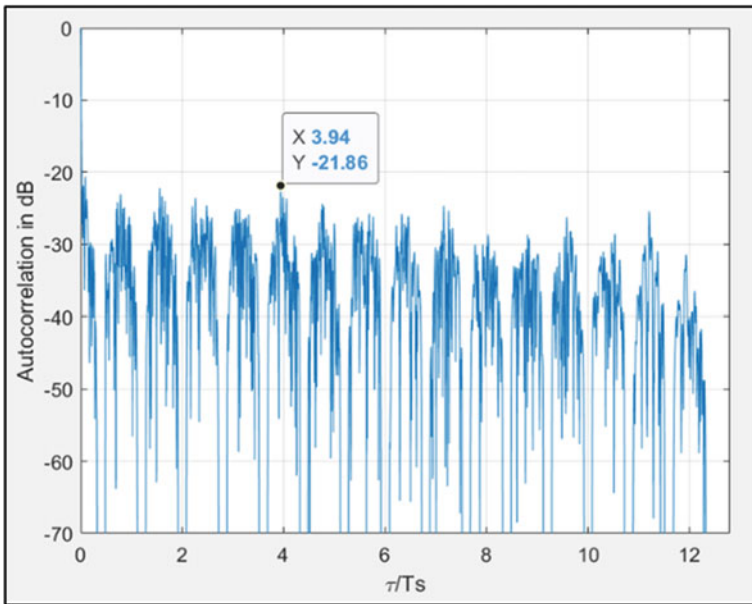


Fig. 16 ACF of polyphase overlay for N= 12

5 Conclusion

Overlay method for radar waveform design gives better optimal performance in resolution. In PONS, the performance is better when sequence length is 8 and sidelobe level increases when sequence length is increased to 16. To overcome this problem, the orthogonal matrix generated with Hadamard recursive method is used and each sequence of the recursive matrix is optimized by using CD optimization algorithm. The obtained polyphase code matrix gives better performance in range and Doppler. The overall sidelobe suppression in ACF is achieved nearly -20 dB.

References

1. Bergin J, Guerci JR (2018) MIMO radar theory and application. Artech House
2. Levanon N, Mozeson E (2004) Radar signals. Wiley, New York
3. Levanon N (2005) Implementing orthogonal binary overlay on a pulse train using frequency modulation. *IEEE Trans Aerosp Electron Syst* 41(1):372–382
4. Deb K (2001) Multi-objective optimization using evolutionary algorithms, vol 16. Wiley, Hoboken, NJ, USA
5. Wright SJ (2015) Coordinate descent algorithms. *Math Program* 151(1):3–34
6. Levanon N (2006) Cross correlation of long binary signal with longer mismatched filters. *IEEE Proc Radar Sonar Navig* 152(6):377–382. <https://doi.org/10.1049/ip-rsn:20050024>
7. Ashe JM, Nevin RL, Murrow DJ, Urkowitz H, Bucci NJ, Nesper JD (1994) Range sidelobe suppression of expanded/compressed pulses with droop. In: Proceedings of the 1994 IEEE national radar conference, Atlanta, GA, pp 116–122
8. Alaae-Kerahroodi M, Modarres-Hashemi M, Naghsh MM (2019) Designing sets of binary sequences for MIMO radar systems. *IEEE Trans Sig Process* 67(13):3347–3360. <https://doi.org/10.1109/TSP.2019.2914878>
9. Cui G, De Maio A, Farina A, Li J (2020) Radar waveform design based on optimization theory. In: The Institution of Engineering and Technology 2020, SciTech Publishing
10. Mozeson E, Levanon N (2003) Removing autocorrelation sidelobes by overlaying orthogonal coding on any train of identical pulses. *IEEE Trans Aerosp Electron Syst* 39(2), 583–603
11. Liu B (2009) Orthogonal discrete frequency-coding waveform set design with minimized autocorrelation sidelobes. *IEEE Trans Aerosp Electron Syst* 45(4):1650–1657

Design of an All Digital Phase-Locked Loop Using Cordic Algorithm



Mohd Ziauddin Jahangir , Chandra Sekhar Paidimarry , Md. Sikander, and M. V. Shrivanthi

Abstract This paper presents a design of an all digital phase-locked loop (ADPLL) using Cordic Algorithm. In an ADPLL all the components are digital in nature. ADPLL are being used in a lot of different applications specially in the communication. The ADPLL presented in this paper is built completely using all digital blocks, i.e. Digital phase detector, Digital IIR filter and a digital algorithmic VCO. A CORDIC algorithm-based phase detector and a CORDIC-based VCO is used, which alters its operating frequency depending on the output of the loop filter to lock the output signal with the input signal. The proposed ADPLL model is simulated using Simulink and then the HDL version of the same is simulated using ModelSim. It was found that the proposed system exhibit excellent locking behaviour.

Keywords CORDIC · ADPLL · DDS

1 Introduction

1.1 PLL

A phase-locked loop, PLL, is basically a control system, used to get the desired phase/frequency. A PLL consists of three blocks namely, phase detector, LPF and VCO as shown in Fig. 1.

CBIT, Hyderabad, Telangana, India

M. Z. Jahangir (✉) · Md. Sikander · M. V. Shrivanthi
Chaitanya Bharathi Institute of Technology, Hyderabad, Telangana, India
e-mail: jahangir_ece@cbit.ac.in
URL: <http://www.cbit.ac.in>

M. Z. Jahangir · C. S. Paidimarry
University College of Engineering, Osmania University, Hyderabad, India

© The Author(s), under exclusive license to Springer Nature Singapore Pte Ltd. 2022
P. Kumar Jain et al. (eds.), *Advances in Signal Processing and Communication Engineering*, Lecture Notes in Electrical Engineering 929,
https://doi.org/10.1007/978-981-19-5550-1_14

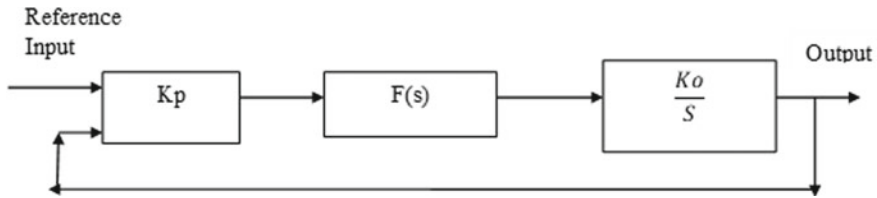


Fig. 1 A general block diagram of a PLL

1.2 Classification of PLLs

There are several variations of PLLs. They can be differentiated based on different blocks used and also based on whether these blocks are analogue or digital. Basically, the PLL can be differentiated into three types as follows:

Analogue PLL (APLL): It uses all analogue blocks.

Digital PLL (DPLL): Most of DPLL's are analogue PLL's with a digital phase detector such as EX-OR, edge-trigger JK, Phase frequency detector.

All Digital PLL (ADPLLs): It uses only digital blocks in entire design. It uses digital phase detector with Digitally controlled oscillator instead of VCO.

1.3 All Digital PLL

All Digital PLLs are being used a lot of new applications. Figure 2 shows block diagram of All Digital PLL. It includes digital phase detector and other basic digital blocks which replaces analogue blocks in Conventional PLL. One such FPGA implementable ADPLL can be found in [1]. As different circuits/blocks can be used for implementing Digital phase detector like an XOR gate, PFD, Multiplier, etc., Similarly the filter can be implemented in many ways like IIR, Moving average, etc., and DCO as well can be implemented in many ways. Therefore, there are wide varieties of ADPLLs available in the literature as in [1–3]. The phase detector and VCO implemented in this work is of CORDIC type.

1.4 CORDIC Algorithm

CORDIC stands for Coordinate Rotation Digital Computer. In the recent years it has been extensively used in calculation of phase difference between two signals. Further literature on this can be found in [4] and [5].

2 Design of CORDIC ADPLL

2.1 The Architecture of CORDIC ADPLL

The ADPLL implemented in this work uses CORDIC algorithm for phase detection and as a VCO. Figure 3 shows the block diagram of the ADPLL implemented in this work which mostly based on [2]. The block diagram of the ADPLL is as shown below.

CORDIC Phase Detector A Cordic-based phase detector is designed in this work. In the Phase detection system, the sine wave input is multiplied with the sine and cosine variant of VCO reference to generate the in-phase and quadrature phase components. Fourth order moving average filters are used for filtering the multiplied signals. The phase information is then obtained from Inphase and Quadrature component using the CORDIC.

Digital LPF The next block in the design is that of the LPF. The design of the filter is a very important and difficult step in the design of any PLL. It becomes even more complicated with ADPLLs. Bilinear transformation is the easiest method to derive a digital filter given its analogue equivalent.

CORDIC based DCO A DCO generally consists of two parts as shown in Fig. 4:

- A phase accumulator (PA), accumulates the phase phase for every clock cycle and based on the value of input word, it can either accumulate at different speed. Thereby able to generate wide range of frequencies.

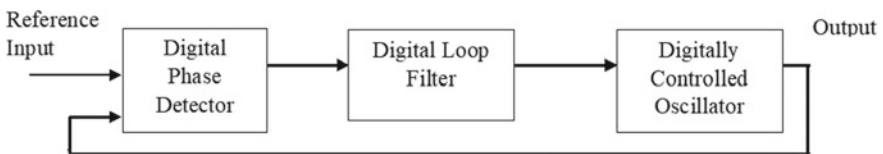


Fig. 2 Block diagram of an ADPLL

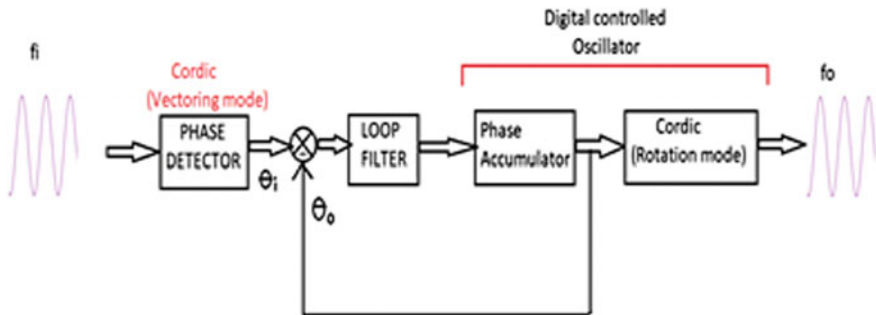


Fig. 3 Block diagram of an ADPLL

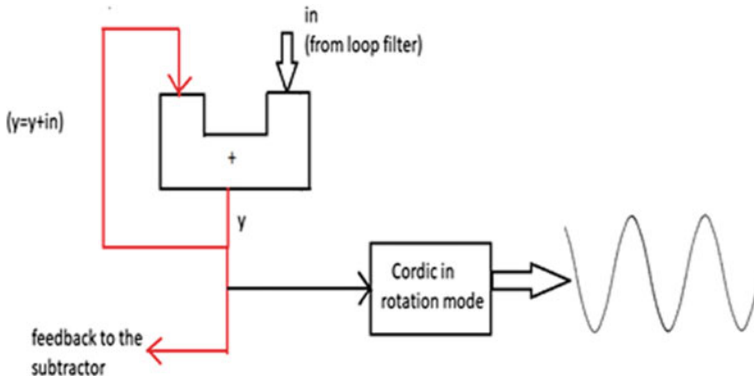


Fig. 4 Architecture of CORDIC based DCO

- **Cordic in Rotation mode:** This algorithm is used in its rotation mode to generate amplitude samples based on phase input. It takes the input angle from the phase accumulator and generates its corresponding sine value.

2.2 The CORDIC ADPLL Algorithm

As the design was implemented in MATLAB, the above design needs to be modelled as an algorithm that can be operated in sequence. An equivalent algorithm was developed to mimic ADPLL in digital domain. The algorithm is as shown in Fig. 5. The algorithm shown in Fig. 5 is simulated in MATLAB and the results obtained of this model are discussed in next section.

3 Results

In this section the results obtained after implementing the algorithm described in above section at high level and at HDL level are described. First the results from the simulation of MATLAB is presented followed by the results of HDL implementation in ModelSim.

3.1 ADPLL Implementation in MATLAB

The results of the MATLAB simulation are shown in Fig. 6. The design was tested by applying an input sine wave of frequency 7 kHz. The input is shown in Fig. 6a.

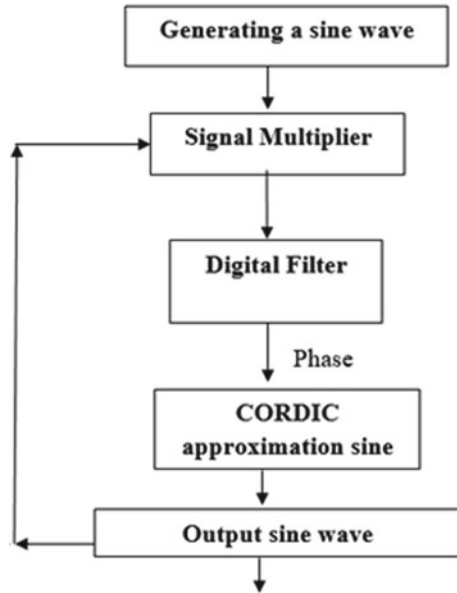


Fig. 5 CORDIC-ADPLL algorithm

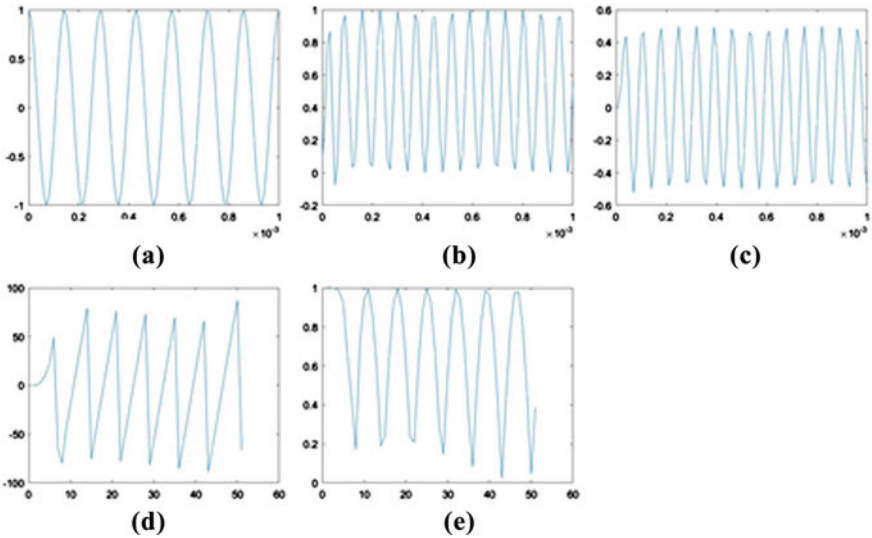


Fig. 6 The results of simulation of CORDIC-ADPLL algorithm in MATLAB

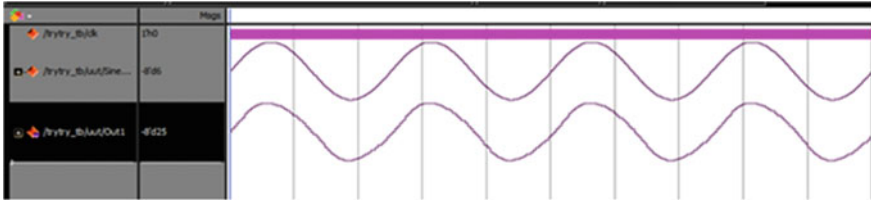


Fig. 7 The results of simulation generated HDL of CORDIC-ADPLL algorithm in ModelSim

The Inphase and quadrature components generated by the phase detector is shown in Fig. 6b, c, respectively. The phase output of the phase accumulator is shown in Fig. 6d and The output waveform generated by the CORDIC is shown in Fig. 6e. Figure 6 shows the transient behaviour of the ADPLL.

3.2 Results of HDL Implementation in ModelSim

The HDL code generated from MATLAB is simulated and tested on ModelSim. The output is viewed in analogue mode in order to view the exact shape of the signal produced by the waveform. It was observed that the designed ADPLL exhibits perfect locking behaviour (Fig. 7).

4 Conclusions

A CORDIC-based All Digital PLL that uses CORDIC for phase detection and output generation was designed and implemented using MATLAB and later the HDL obtained from MATLAB HDL generator was simulated in ModelSim. The PLL exhibits good locking behaviour.

Acknowledgements The Authors would like to thank the CBIT. We would also like to thank D. Shanthi Priya and K. Suhethaa for their support.

References

1. Kumm M, Klingbeil H, Zipf P (2010) An FPGA-based linear all-digital phase-locked loop. *IEEE Trans Circ Syst I* 57(9):2487–2497
2. Das A, Das S, Sahoo AK, Chitti Babu B (2012) Design and implementation of FPGA based linear all digital phase-locked loop. In: 2012 annual IEEE India conference (INDICON). IEEE, pp 280–285. <https://doi.org/10.1109/INDCON.2012.6420629>
3. Fiala P, Linhart R (2015) High efficient carrier phase synchronization for SDR using Cordic implemented on an FPGA. In: 23rd telecommunications forum, Nov 24–26th, 2015
4. Weedman K. Cordic design and simulation. <http://www.youtube.com>
5. Arar S. An introduction to the CORDIC algorithm. <https://www.allaboutcircuits.com/technical-articles/an-introduction-to-the-cordic-algorithm>

Analysis of Deep Learning Algorithms for Image Denoising



Nikita Choudhary and Rakesh Sharma

Abstract A deep learning-based image denoising model for removing non-additive non-gaussian noise from images is proposed in this paper. Images are considered unstructured data, and these are easily corrupted in the complex environment. Due to the noise in the digital images, poor image quality-related issues arise in the images. Image noise reduction is an issue in the realm of image processing. Learning-based algorithms for image denoising have gotten a lot of focus because of their superior denoising performance. Deep learning models are neural networks that have multi-layer structures. These structures are very helpful for extracting very complex features from input images and then remove noise. An extensive database of images is used to train and validate the model. The qualitative evaluation based on visual quality is used to assess the denoised images. The quantitative assessment with mean squared error, peak signal to noise ratio, and structural similarity index measure is used to evaluate the denoising outcomes.

Keywords Image denoising · Deep learning (DL) · Convolutional neural network (CNN) · Optimization method · Mean squared error (MSE) · Peak signal to noise ratio (PSNR) · Structural similarity index measure (SSIM)

1 Introduction

In the practical world, digital photographs may be used for a variety of purposes, including UV imaging (The earth's location is scanned using a satellite or from a very high vantage point, and then it is extensively appraised in order to obtain data about it) is considered one of the numerous use of digital photographs in the actual world, transmission and encoding (Thanks to image processing in the field of remote sensing, we may now witness live video feeds or CCTV photographs from one place

N. Choudhary · R. Sharma (✉)

Electronics and Communication Engineering Department, National Institute of Technology Hamirpur, Hamirpur, Himachal Pradesh 177005, India
e-mail: rakesh.sharma@nith.ac.in

© The Author(s), under exclusive license to Springer Nature Singapore Pte Ltd. 2022
P. Kumar Jain et al. (eds.), *Advances in Signal Processing and Communication Engineering*, Lecture Notes in Electrical Engineering 929,
https://doi.org/10.1007/978-981-19-5550-1_15

151

to another in a couple of seconds. The consciousness of this field is no longer just concerned with transmission, but also with encoding. Many distinct codecs for large and small bandwidth picture encoding and transmission have been created), vision of machines and robots (Today, one of the most important missions that a robot faces is to expand the robotic creative and prescient and make a robot that can see, discover, and detect obstacles, among other things), processing of video (video is more than a series of pictures moving at a very fast rate) the amount of frames/images in a minute and each body's quality used influence the video's quality, medical field (imaging with Gamma rays, imaging with X rays, CT scan, imaging with UV rays, and other digital image processing applications are all widespread in the clinical field) and so on.

There are typically three types of virtual pics. Binary, grays and color images are all examples of images. Image may be described as a function f where a belongs to $[p, q]$ and b to $[r, s]$, and which gives output pixel depth values ranging from maximum to minimum. As a result, it may be stated as, $f : [p, q] * [r, s] \rightarrow [\min, \max]$. Binary images, $f : [p, q] * [r, s] \rightarrow 255$ or 0 (The feature's output is either the brightest pixel 255 or the darkest pixel 0 in binary photos). Gray images, $f : [p, q] * [r, s] \rightarrow [\min, \max]$ (For gray photographs, the function returns a list of potential values ranging from brightest pixel 255 to darkest pixel zero). As a "vector valued function," for color photos three characteristics are piled together. Red, blue, and green pixel make up these characteristics:

$$f(x, y) = \begin{Bmatrix} r(x, y) \\ b(x, y) \\ g(x, y) \end{Bmatrix}$$

Most of these images affected by noise. It is an external source that's causing the picture signal to deteriorate. It affected the image during image acquisition and transmission. Noise in a picture can be mathematically represented by; $N(a, b) = O(a, b) + H(a, b)$, here $N(a, b)$ = noised image's function; $O(x, y)$ = real image's function; $H(x, y)$ = noise function. Noisy photos provide information that is not useful for applications in real-world [1]. There are many methods and filters to cast off noise from the images [2, 3] and Deep Learning technology has become widely used in numerous industries since the dawn of the artificial intelligence era, demonstrating a significant advantage in picture noise reduction [4]. CNN's success in picture denoising can be ascribed to its extensive modeling abilities and remarkable breakthroughs in network design and training [5–8]. The CNN model does not appropriately generalize the non-additive noisy pictures, and it is best successful when the noise level is within a certain range [9]. In this paper suggest an optimization technique based on an autoencoder convolutional neural network to solve the shortcomings of previous CNN-based denoising approaches.

2 Modeling and Methodology

CNN is a type of deep neural network that is most commonly accustomed to read visual image in DL. SIANN are built on the weight shared structure of kernels that moves over enter capacities to allow interpretation equivariant responses. The application of the convolutional mathematical process by the network is referred to as a “convolutional neural network.” CNN are a sort of normal network that utilizes convolution in at least one of its layers instead of the more usual matrix multiplication. Input layer, middle layers, and an output layer make up a convolutional neural network.

These CNNs have been successfully used by autoencoder to address a variety of issues (diverse problems). Encoders are made up of a variety of convolutional layers with varying amounts of filters. These layers take functions from the input picture, which is noisy, and then transfer those functions to a hidden layer. A convolution layer is included in the hidden layers, and its input is the encoder’s feature map or output. The feature maps are created as a result of the convolution process as shown in Fig. 1.

The squares or features in the supplied image retain the connection between pixels. Feature scans the original image. The method of generating the scores is known as filtering. After examine the real image, each feature produces a filtered image with top and less scores. If in the square exist a good match, it has a great score. The result is a less if there is a low or no match. With additional filters, the model may extract a greater number of characteristics. More characteristics, on the other hand, imply a lengthier training period. Padding: What factors are used to assess if two people are a good match? It is a hyper-parameter which allows you to perform one of two things:

- (i) To accommodate the feature, pad the real picture with zeros.
- (ii) Discard portion of real picture which does not accommodate and preserve portion that does.

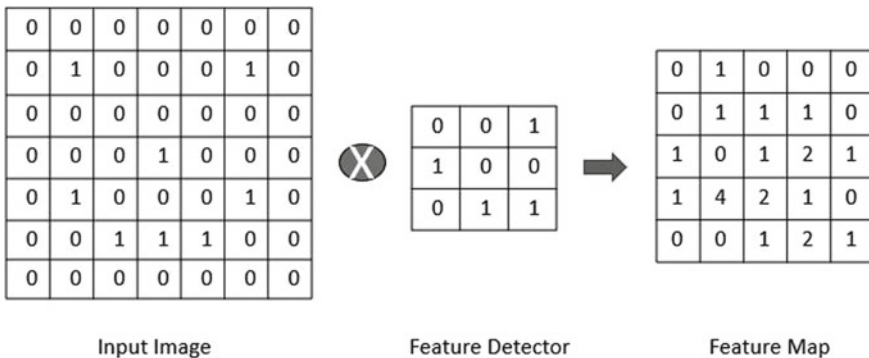


Fig. 1 Convolutional operation

ReLU: The Rectified Linear Unit is a step in a neural network that is identical to the step in a traditional neural network. It converts any negative number to a zero to ensure that the arithmetic works correctly.

The picture size is reduced through pooling. The size is a 2 by 2 window that examine the filtered pictures and set the maximum value of 2 by 2 window to a 1 by 1 square in a picture which is new one. The top score is allocated to the 1 by 1 square since the largest value in 2 by 2 window is a great score. A fresh stack of smaller filtered photos is created after pooling. Now divide and stack the smaller filtered photos into a list. The stride is the size of the input (in pixels) matrix that shift. Shift the filters pixel by pixel, stride is one. Decoding procedure is added on top of it. Because the encoder uses convolution layers, it makes sense to deconvolve to generate a picture that looks similar to the input picture. Deconvolution of pictures is accomplished by multiplying the intensity of single pixel taken from characteristic map with kernel having weights, same to a convolution layer. The pixel in the function map is replaced by this new matrix [10].

A process for identifying the entry parameters or arguments to a function that result in the least or maximum output of the characteristic is referred to as optimization. The term “optimizer” refers to a set of approaches or strategies for altering the properties of a network, as examples weights and rate of learning, to reduce losses. By minimizing function, technique is employed to address optimization issues. Optimization algorithms responsible for reducing loss and giving the most exact results. For improving denoising speed and for unexpectedly finding ultimate solution in image denoising an optimization technique with usage of a CNN turned into an effective tool. In this paper Optimization approach-based with the use of a Autoencoder CNN is modeled to measure the overall performance with some parameters as shown in Fig. 2.

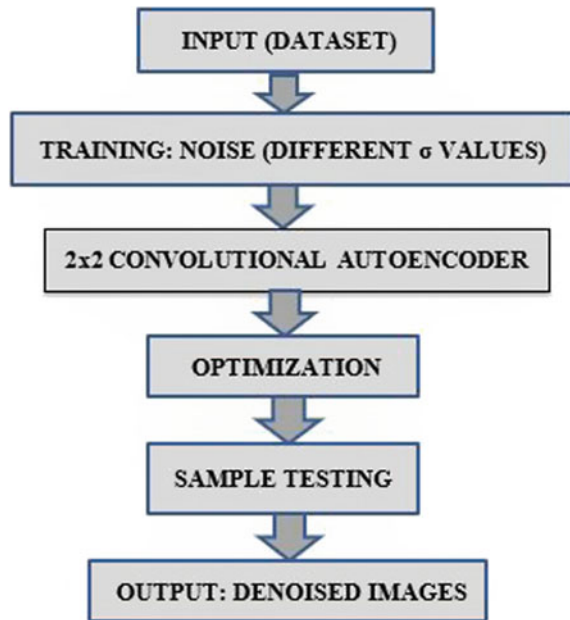
3 Modeling Results and Discussion

Training and Testing Dataset: The MNIST database is a big library containing numbers, fashion, and other information is often used to train digital picture processing algorithms. The dataset of Fashion from the Keras is used in this paper. Keras has a 60,000-record training database and a 10,000-record test database Each record has a resolution of 28 * 28 pixels [11]. Calculating the MSE, PSNR, and SSIM is a handy way to verify the performance of a deep learning system for picture denoising. The mathematical representations of MSE and PSNR are as follows:

$$\text{MSE}, \mu = \frac{1}{A \times B} \sum_{A,B} [O(a, b) - P(a, b)]^2 \quad (1)$$

$$\text{PSNR}, p = 10 \log_{10} \frac{\max^2}{\mu} \quad (2)$$

Fig. 2 Deep learning model for picture denoising



$$p = 20 \log_{10} \frac{\max}{\sqrt{\mu}} \quad (3)$$

$$p = 20 \log_{10} (\max) - 10 \log_{10} (\mu) \quad (4)$$

where A and B are number of rows and columns in an image, $O(a, b)$ are actual values and $P(a, b)$ are predicted values.

For a good quality image, the mean squared error should be as low as possible and the PSNR, it should be as large as feasible, as previously stated. The third performance metric parameter is the SSIM is a perceptual metric for determining the degradation of quality of image because of the image processing, for example loss of data transfer or compression of data. This is a thorough remark metric which requires images a remark shot and processed photo taken from the same picture. In most cases, picture after processing is compressed. It is mostly dependent on visible structures in the photo, unlike PSNR. Clearly, the alternative cannot be described by simply looking at the denoised image because human eyes are incapable of seeing such minute changes. As a result, there should be performance criteria that can tell the difference between a noisy image and a denoised image. Some machine learning models that were able to assess performance metrics are included in [4].

Figures 3 and 4 exhibit denoised pictures for additive white gaussian noise at varying amounts of noise, i.e., $\sigma = 15, 25, 35$ and 50 :

The parameters values of original and noisy pictures for AWGN at various noise levels, Table 1 shows the results.

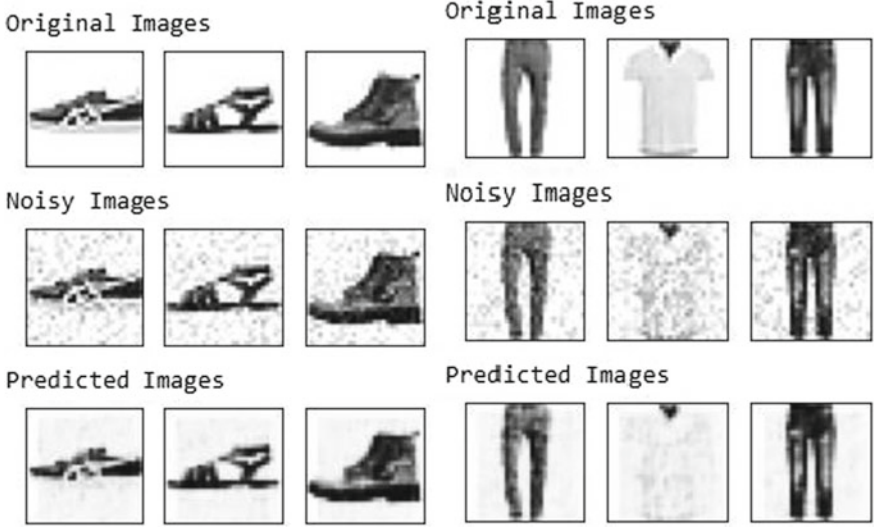


Fig. 3 Original and denoised images at noise level $\sigma = 15$ and 25 , respectively

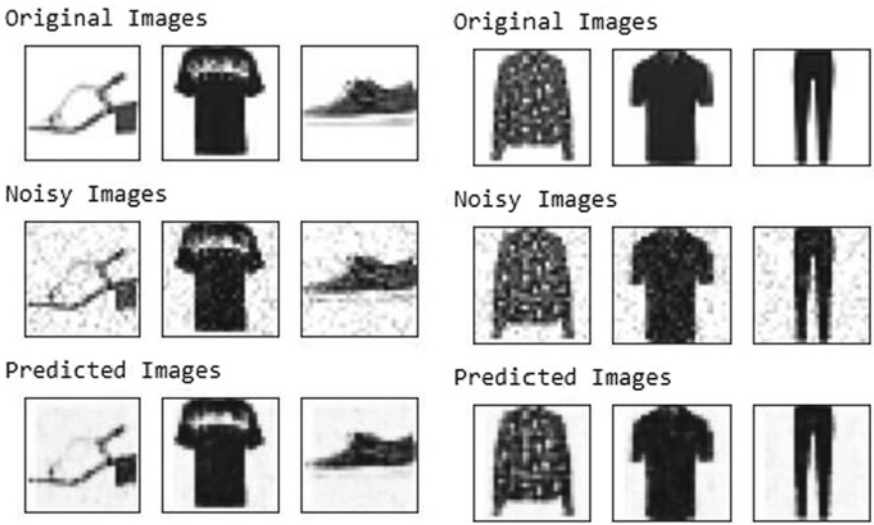


Fig. 4 Original and denoised images at noise level $\sigma = 35$ and 50 , respectively

Table 1 Parameters of actual images recovered from various levels of AWGN

Performance parameters	$\sigma = 15$	$\sigma = 25$	$\sigma = 35$	$\sigma = 50$
MSE	0.006	0.006	0.005	0.005
PSNR (dB)	22.027	21.958	22.411	22.802
SSIM (%)	99.95	99.96	99.96	99.96

Table 2 Parameters of forecasted images recovered from various levels of AWGN

Performance parameters	$\sigma = 15$	$\sigma = 25$	$\sigma = 35$	$\sigma = 50$
MSE	0.004	0.003	0.003	0.002
PSNR (dB)	23.396	24.692	24.242	26.504
SSIM (%)	99.96	99.97	99.97	99.98

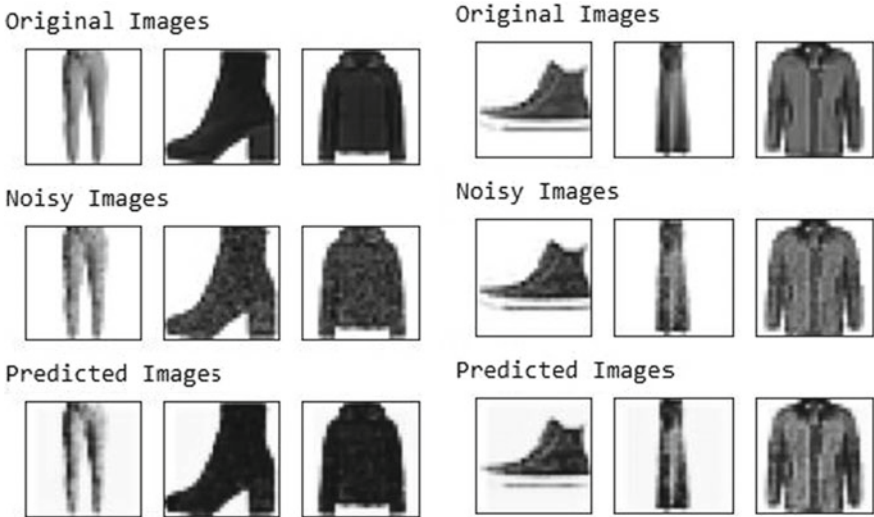


Fig. 5 Original and denoised images at noise level $\sigma = 15$ and 25 , respectively

The above discussed parameters values of actual and forecasted pictures for AWGN at varying amounts of noise, Table 2 shows the results.

Figures 5 and 6 exhibit denoised pictures for poisson noise at various levels of noise, i.e., $\sigma = 15, 25, 35$ and 50 :

Table 3 illustrates the parameter values for poisson noise original and noisy pictures at various levels of noise.

The parameter values of actual and forecasted pictures for poisson noise at varying amount of noise, Table 4 shows the results.

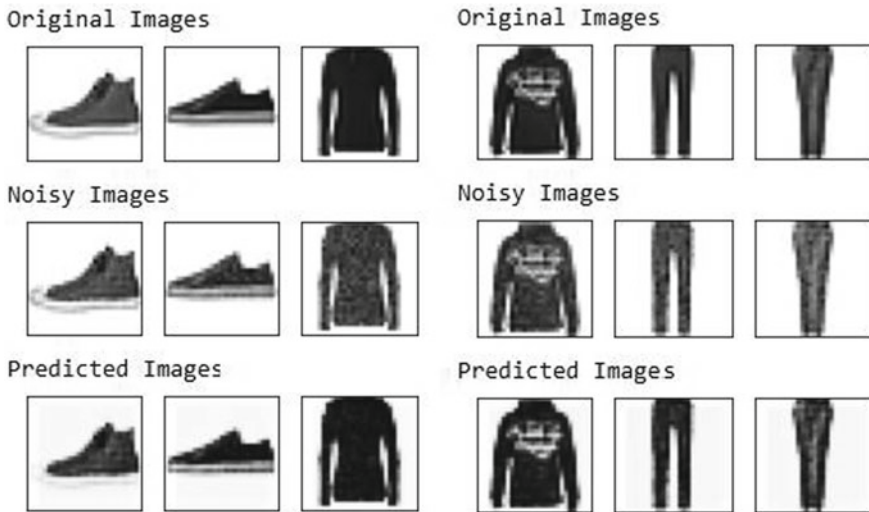


Fig. 6 Original and denoised images at noise level $\sigma = 35$ and 50 , respectively

Table 3 Parameters of actual images recovered from various levels of Poisson noise

Performance parameters	$\sigma = 15$	$\sigma = 25$	$\sigma = 35$	$\sigma = 50$
MSE	0.003	0.001	0.004	0.001
PSNR (dB)	24.450	27.985	23.982	28.645
SSIM (%)	99.98	99.99	99.98	99.99

Table 4 Parameters of forecasted images recovered from various levels of Poisson noise

Performance parameters	$\sigma = 15$	$\sigma = 25$	$\sigma = 35$	$\sigma = 50$
MSE	0.002	0.004	0.002	0.002
PSNR (dB)	25.613	23.033	26.356	25.985
SSIM (%)	99.97	99.95	99.98	99.98

Evaluation of simulation is based on both qualitative and quantitative criteria. The retrieved photos were revealed using visible figures in the qualitative evaluation. To check the denoising outcomes, the quantitative assessment employed MSE, PSNR, and SSIM data from the denoiser.

4 Conclusion

This paper suggests the significance of a version of deep networks used for image denoising. This research highlights the importance of a certain type of DL network for image denoising. It shows the importance of virtual images in real-world applications and different types of digital images and simple DL frameworks for image noise elimination. The DL methodology for blur photos is also presented. This model performs well in the situation of AWGN and Poisson noise. At dissimilar noise, the MSE values between actual and noisy photos are 0.006 or 0.005 in case of AWGN and 0.003 or 0.004 in case of Poisson noise, the PSNR values are in the range of 21 dB or 22 dB for AWGN and 23 dB or 24 dB for Poisson noise, and the SSIM values are equal to 99% in both the cases. In the other scenario, at dissimilar noise, the MSE values between the real and predicted pictures are 0.002 or 0.003 for first case and 0.002 for second case, the PSNR values are in the range of 24 dB or 26 dB for AWGN and 25 dB or 26 dB in case of Poisson, and the SSIM values are 99% for both the noises. In both situations, the model simulation produces excellent results, with MSE near to 0, PSNR increasing, and SSIM providing the similarity percentage. The qualitative outcomes also offer a clear picture.

The techniques described above may also be used to various other noises present in the practical world. After examining it, the parameter values provide a clear picture of the model's performance in terms of quantitative analysis. However, the visual picture outputs are not that impressive. As a result, different algorithms must be used to overcome this flaw and produce a satisfactory result. More effort is being made to improve the image quality and clarity. Also, for future generations, meticulous boosting of the hardware gadgets is really important to suppress the noise for shooting high-quality digital images.

References

1. Xu J et al (2018) Real-world noisy image denoising: a new benchmark. arXiv preprint [arXiv:1804.02603](https://arxiv.org/abs/1804.02603)
2. Dhruv B, Mittal N, Modi M (2017) Analysis of different filters for noise reduction in images. In: Recent developments in control, automation and power engineering (RDCAPE). IEEE
3. Suresh S et al (2018) Multispectral satellite image denoising via adaptive cuckoo search-based Wiener filter. *IEEE Trans Geosci Remote Sens* 56(8)
4. Anwar S, Barnes N (2019) Real image denoising with feature attention. In: Proceedings of the IEEE/CVF international conference on computer vision
5. Zhang K, Zuo W, Chen Y, Meng D (2017) Beyond a Gaussian denoiser: residual learning of deep CNN for image denoising. *IEEE Trans Image Process* 26(7)
6. Zhang K, Zuo W, Zhang L (2018) FFDNet: toward a fast and flexible solution for CNN-based image denoising. *IEEE Trans Image Process* 27(9)
7. Valsesia D, Fracastoro G, Magli E (2019) Image denoising with graph-convolutional neural networks. In: 2019 IEEE international conference on image processing (ICIP). IEEE
8. Guo S et al (2019) Toward convolutional blind denoising of real photographs. In: Proceedings of the IEEE/CVF conference on computer vision and pattern recognition

9. Al-Ghaib H, Adhami R (2014) On the digital image additive white Gaussian noise estimation. In: 2014 international conference on industrial automation, information and communications technology. IEEE
10. Tian C et al (2020) Deep learning on image denoising: an overview. *Neural Netw* 131:251–275
11. Xiao H, Rasul K, Vollgraf R (2017) Fashion-MNIST: a novel image dataset for benchmarking machine learning algorithms

An Extensive Survey on Assessment of Multicore Processors for Embedded Systems



P. Yasasri Uma, M. V. Kala Sindhuja, A. Kishore Reddy, N. Arun Vignesh, and Asisa Kumar Panigrahy

Abstract To boost the performance and reduce power consumption, embedded systems have lately benefited from multicore technology. The parallel benchmark using OpenMP is used to evaluate. In this research, three SMP multicore embedded processors, as well as a multicore CPU for a desktop PC, were utilized. The findings show that, despite low memory performance, programs that are highly required for future generation high-speed computing. This paper presents an extensive survey on the assessment of multicore processors for embedded systems.

Keywords Multicore processors · OpenMP · Embedded systems · Low cost · High reliable

1 Introduction

The availability of low-cost, high-reliability multi- and many-core processors has had a significant impact on embedded system architecture. These vast potentials assist the automotive industry in particular. It is possible to build powerful systems that are well-suited to the significant changes that emerging themes such as autonomous driving, sensor fusion and new powertrain technologies are bringing to the automotive industry.

Moreover, the accessibility of well-known programming languages and frameworks for parallel systems makes parallel software development very appealing. The development of new parallel software systems and the parallelization of existing software using languages like OpenMP [1] are less time-consuming and error-prone than manual parallelization procedures, resulting in performance benefits at an acceptable cost.

P. Y. Uma · M. V. K. Sindhuja · N. A. Vignesh · A. K. Panigrahy (✉)
Department of ECE, Gokaraju Rangaraju Institute of Engineering and Technology, Hyderabad,
Telangana 500090, India
e-mail: asisa@griet.ac.in

A. K. Reddy
Department of ECE, Andhra Engineering College, Nellore 524322, India

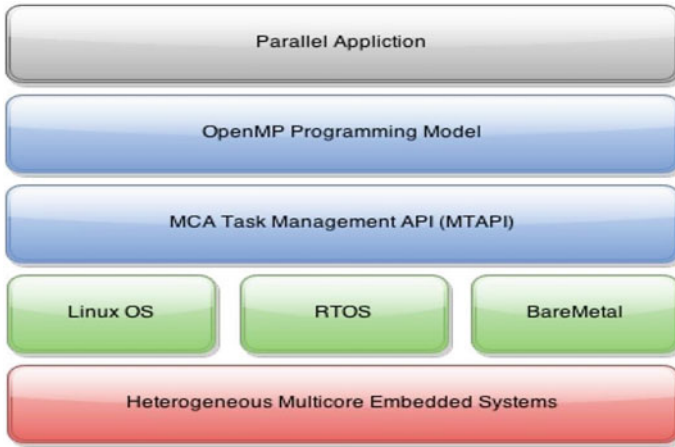


Fig. 1 Project solution stack

We use parallel benchmark programs written in OpenMP to evaluate certain integrated multicore CPUs with a shared memory mechanism in this study. We also use embedded multicore systems require a cross-compiling environment to create the OpenMP implementation as shown in Fig. 1.

Given the widespread use of embedded multicore processors, we look into the following:

- OpenMP's influence as a programming language; and
- An SMP multicore CPUs as far as memory bandwidth and synchronization performance are concerned, as well as their influence on overall system performance.

Task parallelism is commonly used by embedded software developers to improve performance. An excellent example is the automobile industry. Valve electronic controls, sensors for different types of fuel injection pieces of data and driver assistance all require cutting-edge automotive MCUs to manage a range of signals and executions [2].

Each of these activities might be considered a task. We just read about self-driving automobiles, which exacerbates the requirement for task parallelism even more. Several additional embedded domain examples might benefit from task parallelisms, such as robots and airplanes.

Asymmetric multicore processors (AMPs), which include cores with various microarchitectures or ISAs, have been proposed to satisfy the demands of a wide range of applications. However, because to the diversity of their architecture and application situations, several obstacles must be overcome in order to properly construct AMPs and maximize their potential for improving sequential and parallel performance. Several new approaches have been developed to overcome these issues. We offer an overview of architectural and system-level approaches for creating and

maintaining AMPs in this paper. We highlight the similarities and contrasts between the approaches by categorizing them based on certain important features.

2 Methodologies

- (1) Several threads are active at the same time.
- (2) The threads are sharing the same address space. This is in contrast to several processes running in parallel but each with their own address space.
- (3) Threads are in charge of coordinating the work of the other threads.
- (4) Threads are scheduled by the underlying operating system, which needs OS support.

3 Related Work

This section addresses parallel programming embedded systems models and as well as to abstract various embedded architectures, we use standards or libraries.

A. Parallel Programming Model

In the general computer area, there exist a variety of parallel programming paradigms. Some of these are well-established and widely used in industry and academia.

There are not many models for the embedded domain that are based on industry standards OpenCL is a language extension for the C programming language that intends to act as a replacement for C as a paradigm for heterogeneous data parallel programming platforms. OpenCL is mostly used for programming. On general-purpose calculations, GPUs are used; nevertheless, there are notable exceptions [3]. OpenCL was supported by the work on a variety of embedded devices, including [4] and [5]. When reusing OpenCL applications for multiple architectures, performance portability is a major issue.

MPI is the most widely used message-passing programming prototype in distributed memory computing. For embedded systems, MPI, on the other hand, is far too feature rich. Some projects adopted elements of the MPI specifications to enable embedded distributed systems; however, portability problems remain a major roadblock to MPI supporting a larger range of embedded devices. With the introduction of the OpenMP 4.0 standard, the de-facto programming prototype in common memory computing has been expanded toward assorted platforms [6, 7].

Attempts are being made to map OpenMP to the embedded domain.

Program: OpenMP task example

```

int fib(int n)
{
    int i, j;
    if (n < 2) return n;
    else {
        #pragma omp task shared (i)
        i = fib (n-1);
        #pragma omp task shared (j)
        j = fib (n-2);
        #pragma omp taskwait
        return i + j;
    }
}

int main(void) {
    #pragma omp parallel shared (n)
    {
        #pragma omp single
        printf ("fib (d) = %d\n", n, fib (n));
    }
}

```

To allow OpenMP on different freescale semiconductor power-based embedded devices, we already converted OpenMP to MCA resources management API. On a DSP MPSoC with excellent performance, we built OpenMP features software cache coherence and efficient memory management Marongiu and colleagues. On a multi-cluster MPSoC embedded scheme, OpenMP is used [4, 8–11].

On the other hand this effort is not transportable and would need considerable effort to adapt to any other device. There are numerous research initiatives aiming at mapping OpenMP onto embedded schemes and manufacture OpenMP a viable option aimed at creating parallel submissions for embedded schemes, as we can see.

“The OpenMP equal for develop” can be utilized to proficiently perform information parallelism, the assignment and errand bunch builds can be utilized to rapidly research the recently presented target develop has a ton of potential to empower different kinds of gas pedals for offloading registering and task parallelism for sporadic calculations.

However, due to lack of resources, different architectures, programming for little power, usage of OpenMP on embedded schemes, are limited.

B. Morals for Programming Multicore Embedded Schemes

Vendor-developed package for embedded systems often necessitates operations of vendor-provided APIs at a lower level, resulting in a high learning curve and no guarantee of program portability.

Business and academic experts have focused their emphasis on the relevance of industry standards in abstracting the difficulties. An alliance of driving semiconductor organizations and colleges made the Multicore Association (MCA) to give “a bunch of APIs” that “theoretical the low-level” hardships “of implanted programming” improvement and make asset simultaneousness, correspondence and assignment parallelism simpler to determine.

We are seeing increasing academic and industry activities on using MTAPI as mission correspondence organization API for embedded systems since the introduction of the MTAPI definition.

Siemens just released an open-source MTAPI implementation as depicted in Fig. 2.

The purpose of the “Embedded Multicore Building Blocks (EMBB)” project was to develop an improved software elucidation for embedded devices, and this implementation is part of that. In this post, we “build an OpenMP-MTAPI sample” runtime “library (RTL)” using Siemens’ MTAPI operation. The MTAPI implementation developed by the “European Space Agency (ESA)” was designed to make implementing SMP systems in space products as simple as feasible. For their work on exposed tiled many-core SoCs, Stefan et al. gave a basic implementation of MTAPI.

HSA is a joint effort among AMD and ARM to foster equipment and programming to diminish spasmodic memory tasks for heterogeneous models, advance GPUs as the top of the line of co-processors and permit extra installed registering gadgets. Not at all like the MCA APIs, the HSA requires framework-level equipment and programming configuration support [12, 13] (Table 1).

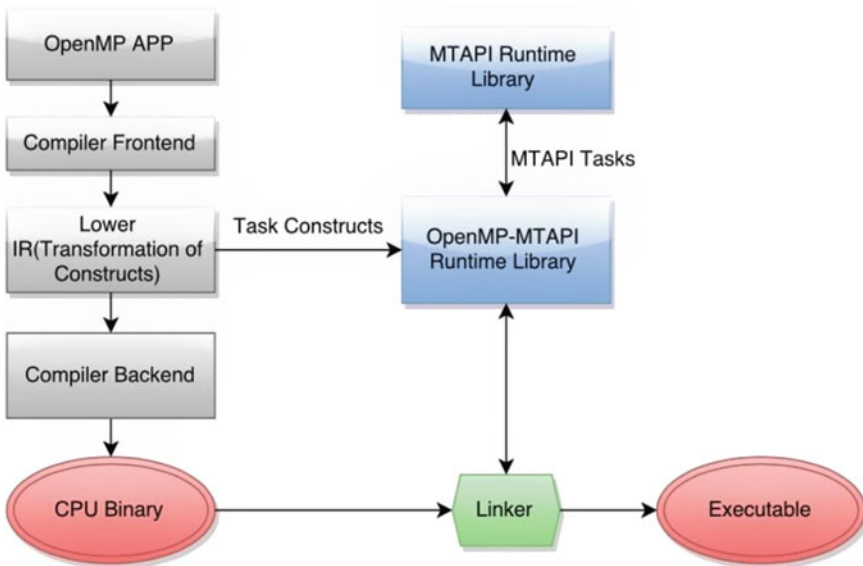


Fig. 2 OpenMP-MTAPI solution diagram

Table 1 Results of performance evaluation (units: seconds)

Processor	PU	IS	CG	Susan_s	FFT	Blowfish	Mpeg2encode
M32700	1	4.66	183.5	22.1	19.6	175.3	1143.8
	2	4.32	93.2	11.8	10.5	94.3 (90.6–102.4)	788.0
MPCore	1	11.3	31.0	21.7	3.19	138.9	–
	2	7.66	15.6	11.2	1.71	112.4 (69.8–140.6)	–
	3	7.09	10.8	7.80	1.31	79.4 (46.8–139.8)	–
	4	7.09	8.15	5.99	1.03	76.1 (34.9–139.3)	–
RPI	1	4.14	4.43	8.49	0.280	60.2	57.4
	2	2.26	2.44	4.51	0.147	33.5 (29.5–60.0)	46.6
	3	1.64	1.85	3.18	0.107	31.6 (19.9–59.8)	39.8
	4	1.41	1.56	2.52	0.085	23.5 (19.7–30.6)	35.9
Q6600	1	0.06	0.215	0.933	0.0076	6.12	5.47
	2	0.036	0.116	0.476	0.0048	3.14 (3.13–3.15)	3.69
	3	0.029	0.086	0.322	0.0065	2.59 (2.58–2.62)	2.88
	4	0.026	0.073	0.251	0.0063	1.70 (1.69–1.71)	2.48

C. Parallel Benchmarks Using OpenMP Evaluation

Parallel benchmarks are then used to assess the multicore CPUs. To begin, we will look into NAS parallel benchmarks. The increase in IS speed is seen in figure. (Class W). The exact execution timings for each of the benchmarks are also shown in Table 2. NPB IS is a memory-intensive program. Due to low memory bandwidth of embedded processors, the MPCore having four cores only gets an acceleration of 1.6 epochs, while the M32700 achieves a speedup of 1.1 times. On the other side, RPI with four cores accelerates 2.9 epochs.

The RPI has one separate bus for managing sneak caches, and findings show that the RPI’s cache-control mechanism is effective. Figure depicts the CG speedup (1, 400 1, 400, sparse matrix). The RPI and Q6600 with four cores both outperform the Q6600 by 2.8 times on this test. Because CG is a computationally expensive benchmark, this is the case. The MPCore, on the other hand, offers a 3.8-fold increase in performance speedup. Cache efficiency looks to improve since the L2 cache is collective “by four cores.” Acceleration of NPB IS and CG is shown in Figs. 3 and 4, respectively, and acceleration of Susan (leveling) and blowfish depicted in Figs. 5 and 6, respectively.

Table 2 Modification cost for OpenMP

Benchmark	Change
SS	Add 6 directives
BF	Add 9 directives and modify 12 lines
FFT	Add 4 directives

Fig. 3 Acceleration of NPB IS (CLASS = W)

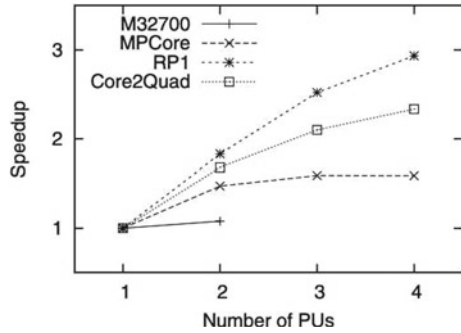


Fig. 4 Acceleration of CG

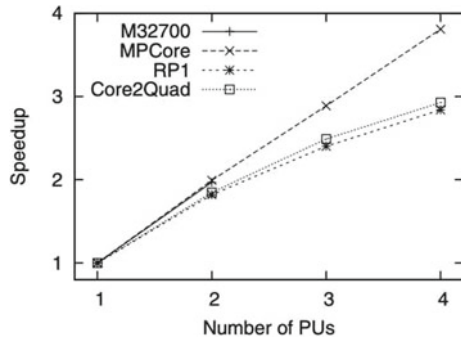
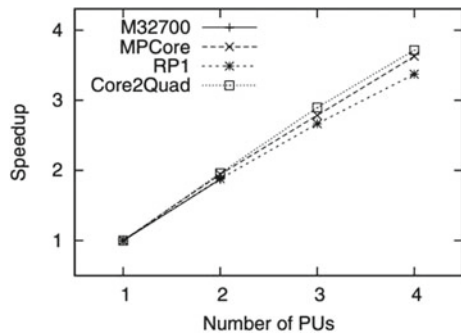


Fig. 5 Acceleration of Susan (leveling)



Then, in Mi Bench’s case, we look at the speedup. We present Mi data sets, a collection of varied workloads for Mi Bench. We use Mi Bench’s large dataset for FFT (n wave = 6, n sample = 65,536) and Mi Data Sets’ 19, PGM for SS and 4.txt for BF. Furthermore, we change BF’s algorithm from CFB64 to ECB. The SS, BF and FFT speedups are shown in Figs. 7 and 8, respectively. SS accelerates by 3.4–3.7 times thanks to its strong parallelism.

The equal form of “BF” takes “40 bytes from” the “input document,” encodes “multiple times” and “then, at that point” expresses “40 bytes to” the “yield record”

Fig. 6 Acceleration of blowfish

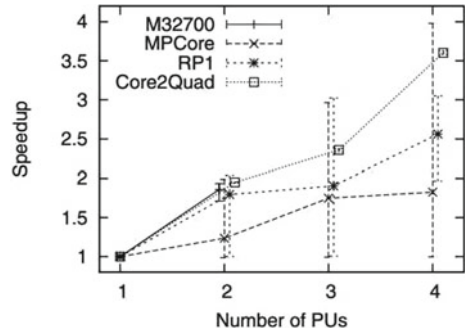


Fig. 7 Speedup of FFT

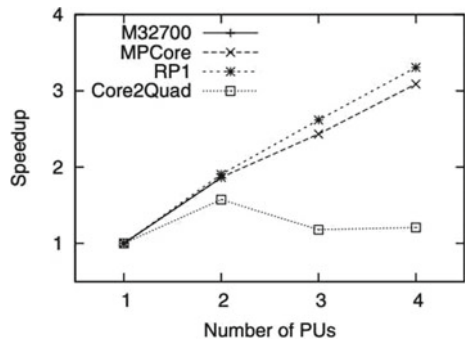
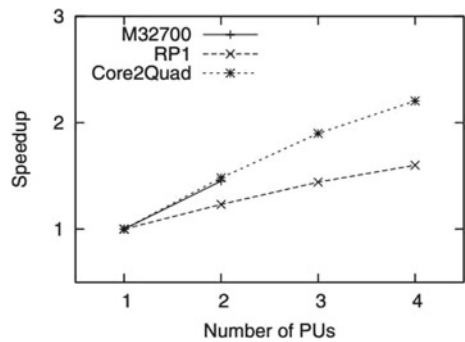


Fig. 8 Speedup of Mpeg2 encode



in a pipelined way. We add the base and greatest execution times to the normal time since BF shows that “the implementation time” is scattered. Since information for the Q6600 is predictable, the NFS seems, by all accounts, to be the explanation of scattering. Due to the insignificant “reliance among” just “8 bytes in the ECB mode,” in the finest situation of multitude of preliminaries, we could get a speedup of 4.0 occasions through four centers on the MP Core and 3.0 occasions with three centers on the RP1.

Due to strong parallelism, FFT on RP1 with four cores may be sped up by 3.3 times. Because the working set for the Q6600 is so tiny that the synchronization cost becomes dominating, the speedup is decreased when three or four cores are used instead of two.

Parallelization using OpenMP is straightforward, simply requiring the addition of a few OpenMP directives depicted in Fig. 7.

Finally, Fig. 8 depicts the Mpeg encoding speedup. A fatal error prevents us from running this benchmark on the MP Core. Even though the Q6600 with four cores has a 2.2-fold speedup, due to the transparency of file operations over NFS, the speedup on RP1 with four core is just 1.6 times. Because of software emulation of floating-point operations, the implementation time is adequately long; there is no performance decrease with the M32700.

4 Design and Specifications

Renesas Technology: M32700 ARM and NEC Electronics: MP Core Waseda Univ. and Renesas and Hitachi: RP1. Sample of a multicore processor for a desktop PC
Renesas Technology: M32700 ARM and NEC Electronics: MP Core Waseda Univ. and Renesas and Hitachi: RP1 Core2Quad Q6600 is an Intel processor.

5 Conclusion

This exploration took a gander at “the order of four multicore” processors: “the M32700,” MP Core, “and RP1 for installed frameworks,” “and the Core2Quad Q6600 for work area” PCs. “We” utilized OpenMP-parallelized “benchmarks including the NAS parallel benchmarks,” Media Bench, “and” Mi Bench in the wake of analyzing synchronization execution with the EPCC miniature benchmark’s sync seat. Later, the impact “of spinlock” on synchronization “under” many “equal responsibilities ought to be” investigated. Moreover, “most multicore processors incorporate” on-chip “quick inward” memory, which we will use to speed up synchronization. We will likewise take a gander at how each multicore CPU framework’s force utilization changes as the quantity of centers develops.

References

1. Marongiu A, Burgio P, Benini L (2011) Supporting openmp on a multicluster embedded mpsoc. *Microprocess Microsyst* 35(8):668–682
2. Siemens (2014) Embedded multicore building blocks from Siemens. <https://github.com/siemens/embb>

3. Cederman D, Hellstrom D, Sherrill J, Bloom G, Patte M, Zulianello M (2014) Rtems smp for leon3/leon4 multi-processor devices. *Data Syst Aerosp*
4. Kranthi BJ, Suhas G, Varma KB, Reddy GP (2020) A two-way communication system with Morse code medium for people with multiple disabilities. In: 2020 IEEE 7th Uttar Pradesh section international conference on electrical, electronics and computer engineering (UPCON), Prayagraj, India, pp 1–6. <https://doi.org/10.1109/UPCON50219.2020.9376479>
5. Ganapathi Raju NV, Radhanand A, Balaji Kumar KN, Pradeep Reddy G, Sampath Krishna Reddy P (2020) Machine learning based power saving mechanism for fridge: an experimental study using GISMO III board. *Mater Today Proc* 33(4819–4822). <https://doi.org/10.1016/j.matpr.2020.08.387>
6. <https://dl.acm.org/doi/10.1145/2883591.2883594>
7. Mittal S (2014) A survey of techniques for improving energy efficiency in embedded computing systems. *Int J Comput Aided Eng Technol (IJCAET)* 6(4)
8. Rogers P, Fellow AC (2013) Heterogeneous system architecture overview. In: *Hot Chips*
9. LaGrone J, Aribuki A, Chapman B (2011) A set of microbenchmarks for measuring openmp task overheads. In: *PDPTA*, vol 2, pp 594–600
10. Free Software Foundation: GCC, the GNU compiler collection. <http://gcc.gnu.org/>
11. https://link.springer.com/chapter/10.1007/978-3-642-02303-3_2
12. Javaid H, Parameswaran S (2009) A design flow for application specific heterogeneous pipelined multiprocessor systems. In: *DAC*, pp 250–253
13. <https://www.embedded.com/development-and-optimization-techniques-for-multicore-processors>

Image Segmentation Techniques and Optimization Algorithms for Lung Cancer Detection



B. Sucharitha , Damiseti Savitri Devi, and Jakku Sushmitha

Abstract The most frequent malignancy is lung cancer and it has the greatest fatality rate among all types of cancer. Early discovery and treatment of the condition can minimize the mortality rate and probability. Other imaging methods are not as good as CT. CT scan images are visually interpreted and it can be a time-consuming and error-prone endeavor, delaying lung cancer identification. Lung cancer was diagnosed using chest X-ray films but using these films, the cancer is not classified into various and accuracy obtained is not acceptable. The main goal is to develop an automated method for detecting lung cancer in scans. Image preprocessing methods such as median filtering are proposed, followed by segmentation of the lung region of interest using mathematical morphological operations and optimization algorithms such as Particle Swarm Optimization, k-means clustering and Inertia Weighted Particle Swarm Optimization. Out of all, the algorithms k-means clustering outperformed with the high (Brindha et al. in J Chem Pharm Sci, 2016) gave a highest accuracy of 90% than the other methods which has only 89.05% accuracy.

Keywords Lung cancer · Malignant · Particle swarm optimization

1 Introduction

Lung carcinoma is a type of cancer that affects the lungs. It is vital to treat this in order to prevent it from metastasizing to other parts of the body. The most common type of lung cancer is carcinoma. The two most frequent types of lung carcinoma (LC) are

B. Sucharitha
ECED, MJCET, Hyderabad, India
e-mail: sucharithanagulapally@mjcollege.ac.in

D. S. Devi (✉) · J. Sushmitha (✉)
ECE, MJCET, Hyderabad, India
e-mail: sarayudamisetti@gmail.com

J. Sushmitha
e-mail: sushmithajakka123@gmail.com

small cell LC and non-small cell LC [1]. The primary cause of most lung cancers is long-term cigarette use [2]. People who have never smoked but are exposed to second-hand smoke, asbestos, and radon gas as a result of air pollution and second-hand smoking have a small number of cases. CT-computed tomography and radiography are the two most common methods for identifying the lung cancer. A biopsy, which is frequently conducted through bronchoscopy or CT scan, confirms the diagnosis. The most common kind is lung cancer, which is the main cause of cancer-related death among men. As a result, developing a unique, reliable method for diagnosing lung cancer at an early stage is crucial [3].

Image processing methods are frequently employed in a variety of medical fields to improve image quality during the early phases of detection and therapy. Image processing is a method of transforming an image to digital form and then executing operations on it in order to improve the image or extract relevant data. It is a signal distribution method in which an image, such as a video frame or a photograph, is used as the input and the output is an image or image-related properties. Images are typically treated as two-dimensional signals that are subjected to predetermined signal processing techniques by an image processing system. The separation of the lung nodule from other parts of the CT scan pictures is known as image segmentation.

A new use of machine learning to image processing will almost certainly be beneficial to the discipline, allowing for a better understanding of complicated images. As the demand for adaptation grows, the number of image processing algorithms that contain certain learning components is projected to grow. The main goal of this special issue is to raise image processing researchers' understanding of the influence of machine learning methods. Radiologists' burden can be decreased by using automated image processing using powerful machine learning algorithms, and more accurate and faster results can be obtained. The healthcare business has already benefited from computer vision software based on machine learning algorithms.

For the purposes of this study, four algorithms were examined. The use of a median filter, adaptive histogram equalization, k-means clustering, and k-nearest neighbors found to be effective (KNN)-based algorithms which has more accurate results among others.

The paper organized as: Sect. 2 deals with previous related work. Section 3 deals with various methods used in preprocessing and segmentation stage. Section 4 deals with performance factors used for detection. Section 5 analyzes and makes inferences from the experimental results. Section 6 of the study finishes with conclusion and future scope.

2 Literature Review

To reduce the physician's interpretation of computer tomography (CT) scan images, an effort has been made to investigate an efficient image segmentation algorithm for medical imaging. In the following, the most important lung cancer detection techniques that have been proposed are revised: In a method for effectively detecting

malignant cells from CT, MRI, and ultrasound images was proposed. As input, the system receives any medical image from the three options of MRI, CT, and ultrasound. The canny filter is used for edge detection after the image has been preprocessed. The medical images were segmented using Super Pixel Segmentation, and the Gabor filter was used to de-noise them. The cancer detection system's simulation results are obtained using MATLAB, and the three medical photographs are compared. In [4], a new technique for lung cancer detection has been proposed that combines three techniques: BFO-bacterial foraging optimization algorithm, PCA-principal component analysis, and BPNN-back propagation neural network, with performance measures such as false acceptance ratio, false rejection ratio, and accuracy used to evaluate the outcomes. In the MATLAB 7.10 environment, the overall planned model was completed. According to the findings, the suggested technique based on back proposed neural network is superior to the prior SVM technique. In [5], a novel candidate group search algorithm is proposed, which is based on an evolutionary approach. This optimization system enables assistant doctors to detect pulmonary nodules in their early stages. Manual interpretations take a long time and are quite important. The genetic algorithm (GA) aids in the identification of genes that can be used to classify a patient's lung cancer status with high accuracy.

For picture preprocessing and feature extraction, histogram equalization is used, and a neural network classifier is used to evaluate if a patient's condition is normal or pathological. If lung cancer is diagnosed and anticipated early on, there are fewer treatment options available, as well as a lower risk of invasive surgery and a higher chance of survival. As a result, a system for detecting and predicting lung cancer will be proposed that is simple, cost-effective, and time-saving. This will yield excellent results in terms of lung cancer diagnosis and prediction. As a result, early detection of the diseases and prediction of lung cancer should be a key element of the diagnosis process, as well as improving the patient's survival rate. Employs an improved median filter approach for de-noising badly damaged images and edge preservation. Mean, median, and enhanced mean filters are used to detect noise. The principles of image processing are demonstrated, as well as the processes of image degradation and restoration. The images are reconstructed after being distorted with varied noise densities. There is both Gaussian and impulsive noise [6].

The PSNR and MSE are calculated using an algorithm. In very impulsive noise, the typical median filter's good performance is greatly hampered [7]. A simple and effective noise cancellation algorithm that operates across a large range of noise densities, from 10 to 98%, while preserving excellent image quality is one of the methods unique advantages.

In [8], a modified technique has been proposed that grows clusters without requiring the initial cluster representation to be specified. In the interpolated (bicubic) multispectral image, a local search single swap heuristic can initially identify the number of clusters and their centers. The findings of the previous method are then used to do normal k-means clustering on the genuine picture data set. Even when the number of clusters is not defined at the outset, the technique produces a significant speedup of the clustering process, and the classification accuracy is enhanced in a smaller number of iterations.

The study tried to find global ideal cluster centers for multispectral pictures using the enhanced genetic k-means algorithm. In pure GA, goal is to build viable clusters while reducing convergence time by avoiding costly crossover or fitness. Using pure GA in this context has the downside of requiring an expensive crossover or fitness to create valid clusters (non-empty clusters). Hybridization of GA with k-means as genetic k-means has already been proposed to address GA's limitation. The results indicate that the proposed method takes fewer generations to reach the global optimum than standard GA and uses less computational complexity than GKA. It shows to be a good grouping strategy for multispectral pictures.

In [9] this paper, to categorize the cancer stages, they used seven low-level features collected from the discovered lung cancer nodule as input to a 3-layer ANN classifier. This technology aids radiologists and clinicians by delivering more information and allowing them to make accurate decisions for lung cancer patients in a short amount of time. As a result, this procedure is low-cost and time-consuming. In [10], on CT scan images from the Data Science Bowl and Kaggle dataset, CNN architecture, one of the most successful deep learning models in medical research, was utilized to diagnose lung cancer. Furthermore, in order to assess the proposed architectures, two well-known CNN architectures were investigated, 3D-AlexNet and 3D-GoogleNet, which were modified to be compatible with 3D pictures.

3 Methods

3.1 Preprocessing

Due to the fact that medical image segmentation involves human lives, precision is paramount. Before undergoing inspection, it is critical to remove all noise and improve image quality [11]. Preprocessing is the term for this type of job. Noise reduction and contrast enhancement are the two main phases in the preprocessing stage (Fig. 1).

3.1.1 Implementation of Median Filter

The median filter reduces noise while maintaining image sharpness. Each and every pixel is changed by the median value in the surrounding region. This filter [12] employs a 3×3 window. Among the standard filters for removing speckle noise, this is one of the best. The algorithm below shows the steps that were taken to create the median filter.

- Assume $N \times K$ size of input matrix and denoted as “X”.
- By putting zeros on the input matrix's sides, create an $N + 2$ rows and $K + 2$ columns size of matrix.
- Choose a 3×3 mask.

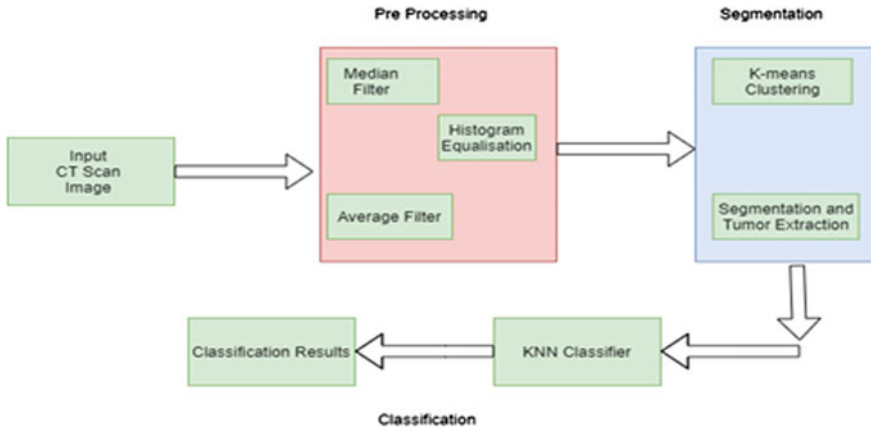


Fig. 1 Work flow of the proposed method

- Apply the mask to the first element of matrix “X.”
- All elements of the mask should be selected and sorted in ascending order.
- From the sorted array, take the median value (center element) and replace it with the median value in element $X(1, 1)$.
- Move the mask to the following element.
- Repeat steps 4–7 until the median value of each element of matrix “X” has been replaced.
- A median filter is used in spatial processing to preserve edge detail while also removing non-impulsive noise. It keeps the image’s modest structure and edges. The size of the window varies depending on the pixel.

3.1.2 Implementation of Avg Filter

This is a basic digital filter for reducing spatial noise. The data collecting procedure is primarily to blame for the occurrence of spatial noise. Each pixel’s neighborhood mean value is calculated and replaced with the appropriate mean value. For each pixel in the image, the same process is repeated [13]. Every pixel is changed when the operator is slid across the complete range of pixels. The average filter’s steps are explained in the algorithm below.

- Assume “X” is the input matrix of K columns and N rows.
- To create a matrix of $K + 2$ rows and $N + 2$ columns, add zeros to the input matrix.
- Choose a mask in the size of 3×3 .
- Apply the mask to the first element of matrix “X”.
- Calculate the average of all the elements in the mask’s list.
- Remove the element $X(1, 1)$ and replace it with median value of the sorted array.
- Move the mask to the following element.

- Repeat steps 4–7 until the mean value of all the members of matrix “X” has been replaced.

3.1.3 Histogram Equalization

Image enhancement is a technique for enhancing the quality of an image. Enhancing the contrast of medical images is required for improved interpretation and analysis. Histogram equalization is the approach utilized for this. In this technique, the intensity of picture pixels is slightly altered, and each and every pixel is assigned intensity proportionate to its rank among the pixels around it. The algorithm below shows the processes involved in histogram equalization.

- Calculate the probability mass function from the histogram of the input image.
- Determine the cumulative distributive function (CDF), and then calculate the CDF based on gray values.
- Use the following equation to find the new gray levels:
- $CDF_{new} = CDF * (\text{no of gray levels} - 1)$
- Plot the adjusted histogram after mapping the new values into a total no of pixels.

SEGMENTATION

This level entails the use of four strategies, namely.

3.2 K-means Clustering Algorithm

The most basic and well-known cluster analysis method. The given dataset is divided into two or more clusters using this approach [14]. The accuracy of this strategy is entirely dependent on the cluster center chosen. To get the best results, you must choose the best cluster center. The general measure for separating the dataset is the Euclidean distance [15]. The Euclidean distance is used to allocate pixels to separate clusters. In this algorithm, the objective function is

$$J(v) = \sum_{i=1}^C \sum_{j=1}^{C_i} (\|x_i - v_j\|)^2 \quad (1)$$

The no of points in the i th cluster is x_i , the no of cluster centers is v_j , while C_i is the no of data points for the i th cluster and C is the number of cluster centers.

$\|x_i - v_j\|$ is the distance between x_i and v_j , the number of data points for the i th cluster is C_i and C is the no of cluster centers.

The algorithm below shows the processes involved in k-means clustering.

- Choose the cluster centers at random. Let “C” be the no of cluster centers.
- Calculate the Euclidean distance between two points.

- If the distance between the pixel and the cluster is the shortest, the cluster is closest to the pixel assign each pixel to the relevant cluster.
- Recalculate the new center of cluster using the following formula once all of the pixels have been segregated:

$$v_i = (1/C_i) \sum_{j=1}^{C_i} x_i$$

- Steps 2–4 should be continued for a specified number of iterations or until a condition is met.

3.3 *K-median Clustering Algorithm*

This is a clustering algorithm that is based on the k-means algorithm with some modifications. The median value is used in centroid calculations rather than the mean value. Because the Euclidean distance is calculated without a squared operation, this method has a very low error rate. This approach produces smaller clusters. This method employs Lloyd-style iteration as an alternative. The algorithm [15] below shows the processes for k-median clustering.

- Choose the cluster centers at random. Let “C” be the no of cluster centers.
- Calculate the Euclidean distance between two points.
- If the cluster’s Euclidean distance from the pixel is the shortest, assign each pixel to the relevant cluster.
- Recalculate the new center of a cluster using the median value rather than the squared formula once all of the pixels have been separated.
- Steps 2–4 should be repeated for a given no of iterations or until a specific condition is met.

3.4 *Particle Swarm Optimization (PSO)*

PSO [16] is a metaheuristic algorithm for successfully evaluating medical pictures. It imitates the social behavior of foraging birds [17]. The basic concept of PSO is information exchange and communication. Each particle has an initial velocity and position in this method. The fitness value is used to update the both velocity and position. The following are the two relevant PSO equations for updating location and velocity [16, 17]:

$$v(t + 1) = v(t) + c_1r_1[pbest(t) - x(t)] + c_2r_2[gbest(t) - x(t)] \quad (2)$$

$$x(t + 1) = x(t) + v(t + 1) \quad (3)$$

The acceleration coefficients c_1 and c_2 , as well as the random values r_1 and r_2 , are both positive constants. The fitness function is critical to PSO's success. For this research, the following fitness function was used:

$$\text{maximize } f = \sum_{i=1}^n \frac{\text{interclusterdistance}}{\text{intraclusterdistance}} \quad (4)$$

The number of clusters is given by n . The algorithm below shows the steps that were taken for the PSO.

- Set all of the particles' velocity and position to random numbers.
- Create a fitness-related function.
- Determine each particle's fitness value.
- When comparing the value of fitness to the best fitness, it is important to remember that the former is more valuable than the latter. Set new best to the existing value if the fitness values are better.
- Steps 3–5 should be repeated for each particle.
- Using equation, update the velocity value.
- Update the position.
- gbest should be updated.
- Repeat steps 7–9 until specified conditions are met or the predetermined no of iterations is reached.

3.5 Inertia Weighted Particle Swarm Optimization (IWPSO)

The inertia weight is used to guide exploration and exploitation in PSO. Eberhart and Kennedy presented the fundamental PSO in the year of 1995, which has zero inertia weight. When Shi and Eberhart added continuous inertia weight to the equation in 1998, they created the concept of inertia weight. According to popular belief, a big inertia weight aids global lookup, whereas a lesser inertia weight aids local search. This reduces the number of iterations while increasing the rate of convergence. Having an inertia weight of less than one enhances the results in general. The method used improves the pace of convergence while minimizing the time and number of iterations needed.

$$v(t + 1) = w * v(t) + c_1 r_1 [pbest(t) - x(t)] + c_2 r_2 [gbest(t) - x(t)] \quad (5)$$

where “ w ” is the inertia weight,

With $w = 0.7$ for constant inertia and $w = 0.5 + \text{rand}() / 2$ for random inertia.

3.6 KNN Algorithm

The KNN technique saves all of the data that is accessible and identifies a new data point based on its resemblance to previously classified data. This indicates that the KNN algorithm can swiftly classify new data into a well-defined category.

- Choose the K th neighbor's number.
- Calculate the Euclidean distance between K of closest neighbors.
- Using the Euclidean distance, determine the K -nearest neighbors.
- Count the number of data points in each category among these k neighbors.
- Assign the new data points to the category with the greatest number of neighbors.
- Our model is finished.

3.7 Confusion Matrix

The outcomes of a classification task prediction are displayed in a confusion matrix, which is a table. The entire number of right and incorrect predictions is tallied together, and then divided by class using count values. The confusion matrix's key is this (Fig. 2).

When formulating predictions, the classification model becomes bewildered, as shown in the confusion matrix. It exposes not only the types of errors made by the classifier, but also the total number of errors. The disadvantage of relying only on categorization accuracy is addressed in this analysis.

The steps for creating a confusion matrix are outlined below.

- With expected outcome values, create a test or validation dataset.
- From test dataset, make a prediction for each row.
- Count the number of expected outcomes and predictions.
- Each class's total number of incorrect guesses, listed by expected class.
- The following is how these numbers are arranged in a table or matrix:
- Each row of the matrix corresponds to a predicted class, as shown on the side.
- Each column in the matrix represents a separate class, as predicted across the top.

Fig. 2 Confusion matrix

		True Class	
		Positive	Negative
Predicted Class	Positive	TP	FP
	Negative	FN	TN

The number of correct and incorrect categories is then entered into the table. In the expected row and predicted column for a class, the total number of correct predictions is reported.

Similarly, for each class value, the total no of incorrect predictions is placed into the anticipated row and predicted column.

4 Performance Measures

The results of medical picture segmentation are evaluated using a set of performance metrics.

True Positive (TP) imaging studies detect an illness when it is already present.

True Negative (TN) images show that no disease has been discovered and that no disease exists.

False Positive (FP) imaging findings are those that detect an illness when one does not present.

False Negative (FN) images are those that detect a disease while it is still in its early stages.

ACCURACY

The accuracy is the parameter specifies the percentage of valid outcomes among all the results. Formula to calculate

$$\text{Accuracy} = \frac{\text{TP} + \text{TN}}{\text{TP} + \text{TN} + \text{FP}}$$

SENSITIVITY

The sensitivity is a metric that shows the reliability of a positive result achieved when a person is diagnosed with a condition. Formula to calculate

$$\text{Sensitivity} = \frac{\text{TP}}{\text{TP} + \text{FN}}$$

SPECIFICITY

The specificity of a negative result achieved when a person has the disease is a metric that shows the veracity of the negative result.

$$\text{Specificity} = \frac{\text{TN}}{\text{TN} + \text{FP}}$$

5 Simulation Results

Results of Preprocessing stage

Figure 3 illustrates the outcome of applying a median filter to the CT scans, which reduces the speckle noise while maintaining the image's sharpness. Figure 4 is the output obtained after applying an average or mean filter to a digital image to reduce spatial noise caused primarily by the data gathering method. Sliding the operator throughout the entire pixel range affects every pixel in the digital image. Figure 5 demonstrates the outcome of histogram equalization to increase the image quality, and a modest modification of image pixel intensity is made using image enhancement technique to boost the contrast of the image, and each pixel has an intensity that is proportional to the intensity of the pixels around it (Figs. 9, 10 and Tables 1, 2).

Fig. 3 Result of median filtering

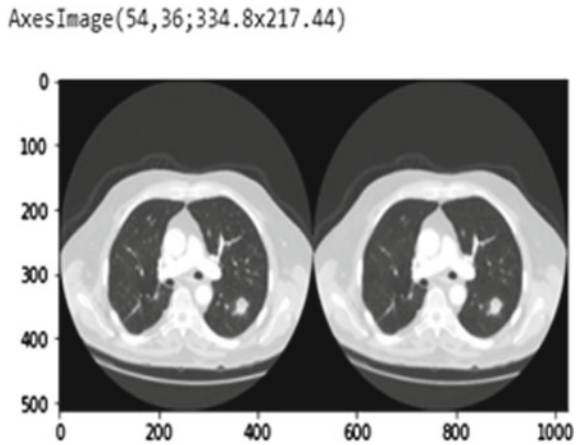


Fig. 4 Result of average filter

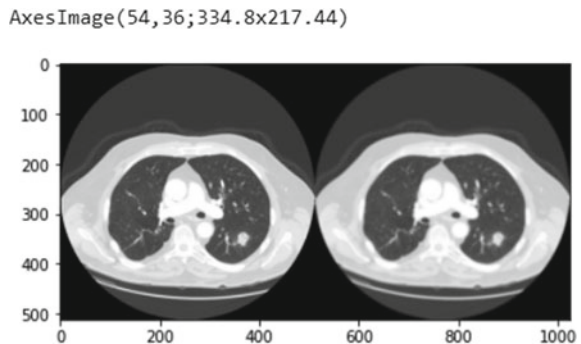


Fig. 5 Result of histogram equalization

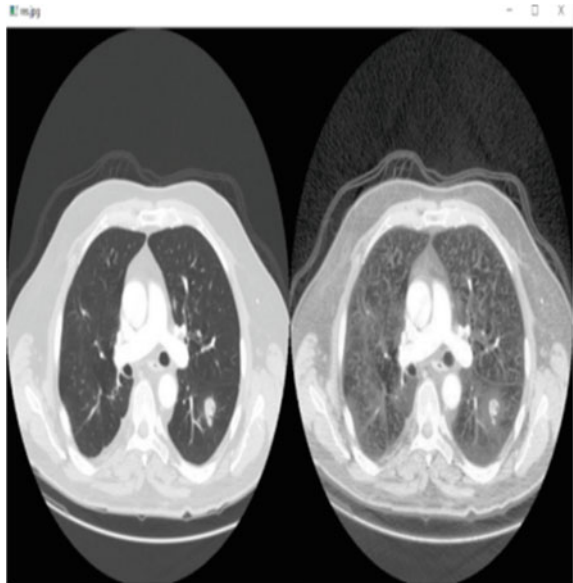


Table 1 Performance parameters obtained methods from confusion matrix

True label	Predicted label	Performance parameter	Value obtained
1	1	TP	9
1	0	FN	2
0	1	FP	0
0	0	TN	9

Table 2 Comparison of the predicted accuracy to other techniques

Methods	% Accuracy
PSO, GA, and SVM algorithm	89.50
K-nearest neighbors classification using GA	90.00

5.1 Results of Image Segmentation

Result of k-means clustering of 3 different lung images.

Figures 6, 7 and 8 shown above are the results obtained after segmentation stage, and the tumor section was retrieved from the k-means clustering algorithm’s segmented output. By measuring the Euclidean distance, this algorithm divides the dataset into two or more groups. Based on Euclidean distance, pixels are assigned to separate clusters and compared to the original CT picture.

The accuracy can be obtained from the confusion matrix as shown in Fig. 9 and Table 1 by substituting TP, TN and FP values

Fig. 6 Segmentation results of image1



Fig. 7 Segmentation results of image2

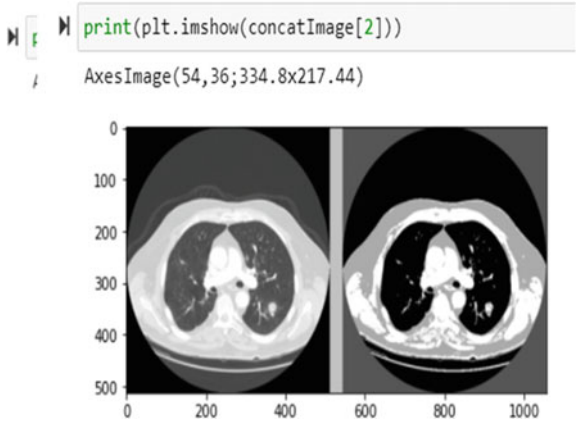


Fig. 8 Segmentation results of image3

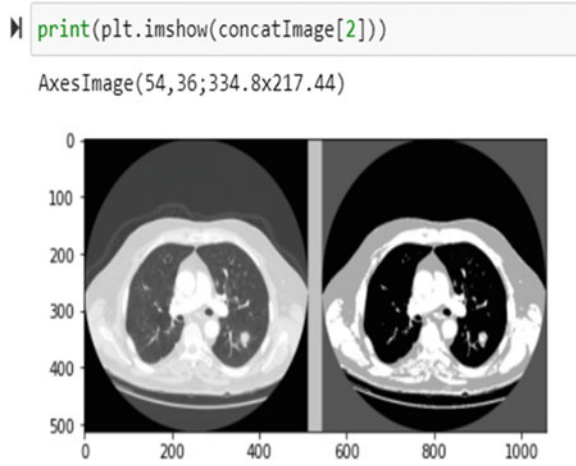


Fig. 9 Confusion matrix

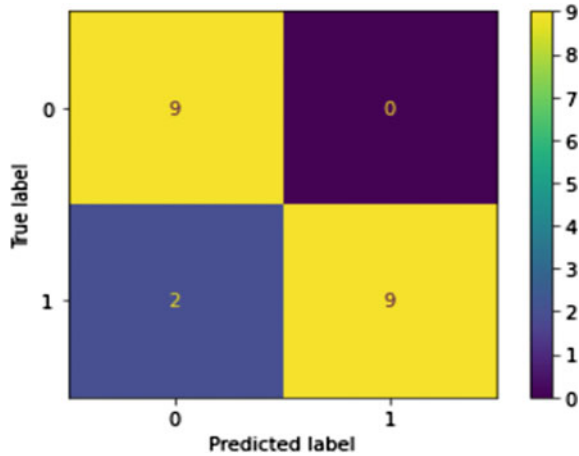
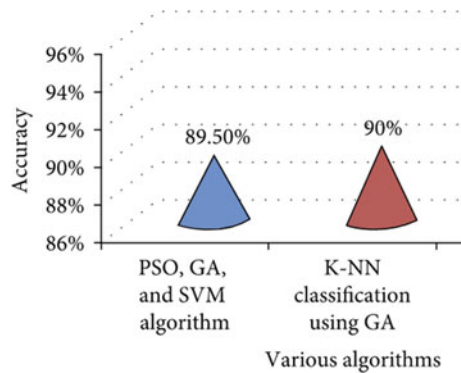


Fig. 10 A graphical representation of accuracy



$$\text{Accuracy} = \frac{\text{TP} + \text{TN}}{\text{TP} + \text{FP} + \text{TN}}$$

Accuracy obtained is 90.0% as shown Table 2 and Fig. 10.

6 Conclusion and Future Scope

In this experiment, many optimization tactics were used in order to locate the tumor. Medical images are typically preprocessed before going for statistical analysis. The median filter gives good results since its speckle suppression index, as well as the speckle and means preservation index value are lower than the mean filter’s. When all of the methods are evaluated, KNN has the best level of tumor extraction precision, with approximately 90% precision in all the images. It is much more accurate than the prior technique, which was only 89.50% accurate in four out of ten datasets. To

increase accuracy, a larger number of optimization techniques will be used in the future.

References

1. Brindha AA, Indirani S, Srinivasan A (2016) Lung cancer detection using SVM algorithm and optimization techniques. *J Chem Pharm Sci*
2. Kurkure M, Thakare A (2016) Introducing automated system for lung cancer detection using evolutionary approach. *Int J Eng Comput Sci*
3. Rani B, Goel AK, Kaur R (2016) A modified approach for lung cancer detection using bacterial foraging optimization computational and mathematical methods in medicine 15 algorithm. *Int J Sci Res Eng Technol*
4. Panpaliya N, Tadas N, Bobade S, Aglawe R, Gudadhe A (2015) A survey on early detection and prediction of lung cancer. *Int J Comput Sci Mob Comput*
5. Gupta G (2011) Algorithm for image processing using improved median filter and comparison of mean, median and improve median filter. *Int J Soft Comput Eng*
6. Venkatalakshmi K, Shalinie SM (2005) Classification of multispectral images using support vector machines based on PSO and K-means clustering. In: *IEEE international conference on intelligent sensing and information processing*
7. Venkatalakshmi K, Shalinie SM (2007) Multispectral image classification using modified k-means clustering. *Int J Neural Mass-Parallel Comput Inf Syst*
8. Venkatalakshmi K, AnishaPraisya P, Maragathavalli R, MercyShalinie S (2007) Multispectral image clustering using enhanced genetic k-means algorithm. *Inf Technol J*
9. Kyaw NN, Naing KK, Thwe PM, Htay KK, Htun H (2019) Detection and classification of lung cancer stages using image processing techniques. 6
10. Polat H, Danaei Mehr H (2019) Classification of pulmonary CT images by using hybrid 3D-deep convolutional neural network architecture. *Appl Sci* 9(5):940. <https://doi.org/10.3390/app9050940>
11. Dalatu PI (2016) Time complexity of k-means and k-medians clustering algorithms in outliers detection. *Global J Pure Appl Math*
12. Senthilkumar K, Venkatalakshmi K, Karthikeyan K, Kathirkamasundari P (2015) An efficient method for segmenting digital image using a hybrid model of particle swarm optimization and artificial bee colony algorithm. *Int J Appl Eng Res*
13. Venkatalakshmi K, Mercyshalinie S (2005) Classification of multispectral images using support vector machines based on PSO and k-means clustering. In: *IEEE international conference on intelligent sensing and information processing*
14. Venkatalakshmi K, AnishaPraisya P, Maragathavalli, Mercyshalinie S (2008) A customized particle swarm optimization for classification of multispectral imagery based on feature fusion. *Int Arab J Inf Technol*
15. Bansal JC, Singh PK (2011) Inertia weight strategies in particle swarm optimization. In: *IEEE world congress on nature and biologically inspired computing*
16. Patel PK, Sharma V, Gupta K (2013) Guaranteed convergence particle swarm optimization using personal best. *Int J Comput Appl*
17. Bhuvanewari P, Brinthatherese A (2014) Detection of cancer in lung with K-NN classification using genetic algorithm. In: *International conference on nanomaterial's and technologies*
18. Khobragade S, Tiwari A, Patil C, Narke V (2016) Automatic detection of major lung diseases using chest radiographs and classification by feed-forward artificial neural network. In: *IEEE international conference on power electronics, intelligent control and energy systems (ICPEICES)*

Handwritten to Text Document Converter



S. Aruna Deepthi, E. Sreenivasa Raol, and M. D. Shadab farhan

Abstract Handwriting recognition also recognized as handwriting Optical Character Recognition (OCR) is an OCR applied science that translates handwritten letters to analog digital text. In this paper, a software solution is provided to automatically convert the handwritten image into text. Almost every sector and all the organizations require information. Organizations like educational institutions, medical and healthcare sectors, IT organizations, banks, small-scale and large-scale industries and businesses require the customer or the client to fill out a handwritten form. This information is uploaded into the database manually which is tedious and time-consuming. In this project, CNN and bidirectional RNN by using open-source libraries like OpenCV, tensor flow and Matplotlib in Python language to perform segmentation, normalization and feature extraction are implemented. An attempt is made to use deep learning to convert the handwritten text in an offline format (e.g., on a piece of paper) into a text document. Many handwriting recognition tools have been in the market, but still, there are not many tools that give maximum accuracy as each person owns a unique style of writing, pressure and tilt. There are two ways to recognize characters: Markov model and artificial neural networks (ANN). Deep learning enables to train and test the model with huge datasets, thus leading to maximum accuracy. In this model, neural networks consisting of five convolutional neural network (CNN) layers and two recurrent neural networks (RNN) layers and connectionist temporal classification (CTC) model to decode are used. There are many methods for handwriting detection. Each method is different from the other, but the method used in this paper is CNN which uses neural networks to mimic the function of the human brain resulting in a higher accuracy rate when trained with large datasets.

Keywords CNN · RNN · ANN · CTC · OpenCV

S. A. Deepthi (✉) · E. S. Raol · M. D. S. farhan
Vasavi College of Engineering, Hyderabad, India
e-mail: sadeepthi@staff.vce.ac.in

© The Author(s), under exclusive license to Springer Nature Singapore Pte Ltd. 2022
P. Kumar Jain et al. (eds.), *Advances in Signal Processing and Communication Engineering*, Lecture Notes in Electrical Engineering 929,
https://doi.org/10.1007/978-981-19-5550-1_18

187

1 Introduction

Deep learning is a man-made function that mimics the performance of a human brain to manage information and create designs and utilize it to make decisions. The practical definition of deep learning is “It’s a sub-domain of machine learning (ML) algorithms in the type of a neural network that applies a cascade of layers of working units to derive features and make perceptive approximations about new data.” Deep learning can also be called deep neural network. A convolutional neural network is a deep learning algorithm that is capable of receiving an input image, delegate importance to different facets/entities within the image and be proficient in separating or characterizing from one to another. Filters are hand-engineered in basic approaches, with ample training.

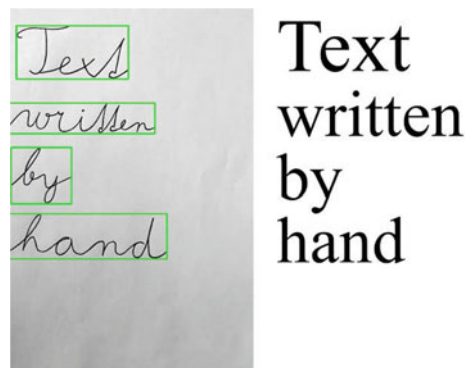
A ConvNet is capable of effectively obtaining the spatial and temporal colonies with the use of appropriate filters in a picture. The design performs a more accurate match to the picture dataset due to the decrease in the number of variables included and re-usability of weights. In alternative terms, the network can be prepared to better comprehend how the image is progressing.

Handwritten text recognition (HTR) is nothing but translating handwritten content into digital text. There are two types of handwritten text recognition, i.e., online recognition and offline recognition. Offline recognition, on the contrary, is done after the material has been written. Online recognition is said to be a less challenging problem. Presently, enormous sums of manually written reports are scattered in libraries shared via the internet. Interpreting and tabulating make these records easily available to all.

A case of HTR within the area of records is given in Fig. 1 which shows one text-line translation.

The examined classifier is based on ANN. HTR tasks are connected to hidden Markov models. Nevertheless, the proclaimed results of HTR contend to appear that artificial neural networks outperform hidden Markov models; consequently, artificial neural networks have been chosen to participate in this research. The only exemption is word-segmentation, which is since the datasets are annotated on a line-by-line

Fig. 1 Text by the HTR system



basis. Hence, one plausibility is to divide text-lines into words and segregate each word on its own, while another one is to refrain from segmentation and bolster a several lines in the classifier.

The proposed model makes use of ANNs. Classification operation is done to do training and decoding. Translating will be able to take favor of a language model: Firstly, putting the issue simpler for the classifier and data augmentation, and secondly dispatching the tilt from the text and word division are talked about as well as solutions that make things easier. The derived text can consist of spelling mistakes; hence, a text-postprocessing routine is used to account for them.

2 Literature Survey

In 1959, Grimsdale made a major endeavor in the field of character recognition research. In 1960s, a method called the analysis-by-synthesis method, proposed in the year 1968 by Eden, was at the heart of a lot of research. Crane's early work resulted in the first patent for a unique pen device in 1964. A basic technique for entering handwritten Chinese characters was released later that year.

Gaurav and Bhatia [1], discussed early approaches applied in character detection with various types of pictures, ranging from mere handwritten forms to documents with colored and complicated backgrounds and varying intensities. However, even with all of the aforementioned strategies in place, it may be impossible to attain 100% precision in a pre-processing system.

Espana-Boquera et al. [2] suggested for identifying unconstrained offline handwritten texts; a hybrid hidden Markov model (HMM) model is suggested in this paper Pal et al. [3]. It is proposed to recognize offline handwritten digits in six prominent Indian scripts using a modified quadratic classifier-based method.

Pradeep et al. [4] proposed offline character recognition for diagonal feature extraction. Arora et al. [5], Intersection, chain code histogram, shadow features and straight-line fitting features were employed as feature extraction approaches.

Som and Saha [6], for HCR, they have discussed a fuzzy membership function-based technique. Normalized character pictures are 20×10 pixels. Each character's average picture (fused picture) is made up of ten images. The test image's similarity score is compared to the fusion image's similarity score, and the characters are categorized.

For the classification [7] of Devanagari numerals, researchers used two different types of characteristics: moment features and density features. They presented a multi-classifier connectionist design to improve recognition dependability, and they achieved 89.6% accuracy.

Khedher et al. [8]. This study explains how the features utilized in character recognition play a big role. Several characteristics of handwritten Arabic characters are highlighted and examined. The significance and precision of the selected features are assessed. The detection accuracy for numerals and letters is 88% and 70%, respectively, based on selected attributes.

Patnaik and Panda [9] research suggested the use of bacterial foraging optimization and particle swarm optimization methods to achieve effective harmonic compensation by reducing the undesired losings that occur within the APF. The stroke [10] was displayed as a string of shape features using a structural or shape-based representation.

Pirlo and Impedovo [11] proposed a new class of membership functions for zoning-based classification called fuzzy membership functions. Yoshimasa Kimura et al. presented a paper on how to use a genetic algorithm to choose features for character recognition printing area which is 122 mm \times 193 mm. The text should be justified to occupy the full line width, so that the right margin is not ragged, with words hyphenated as appropriate. Please fill pages so that the length of the text is no less than 180 mm, if possible.

3 Proposed Methods and Simulation Results

a. Dataset

The dataset IAM (on-line handwriting database) is used (Table 1).

It is a 128 \times 32 pixel gray value image. Since the images in the dataset are rarely exactly this size, they are scaled until they are either 128 pixels wide or 32 pixels tall. The image is then copied into a (white) target image with a size of 12,832 pixels. Figure 3 depicts this procedure. Finally, the image's gray levels are normalized, making the task easier for the NN. By duplicating the image to irregular spots, or by randomly scaling the image, data augmentation can be simply implemented.

3.1 Convolutional Neural Network (CNN)

The CNN layers are fed into the input image. These layers have been trained to extract important information from images. There are three operations [12] in each layer. To begin, the convolution operation is completed; Fig. 2 shows the CNN code snippet, which includes all of the functions in the CNN layer, such as RELU, pooling, normalization and 2D convolution.

Table 1 Dataset details

Dataset	Training-set	Validation-set	Test-set
Iam dataset	1364	80	160


```

pool = cnn_in4d # input to first CNN layer
for i in range(num_layers):
    kernel = tf.Variable(
        tf.random.truncated_normal([kernel_vals[i], kernel_vals[i], feature_vals[i], feature_vals[i + 1]],
                                   stddev=0.1))
    conv = tf.nn.conv2d(input=pool, filters=kernel, padding='SAME', strides=(1, 1, 1, 1))
    conv_norm = tf.compat.v1.layers.batch_normalization(conv, training=self.is_train)
    relu = tf.nn.relu(conv_norm)
    pool = tf.nn.max_pool2d(input=relu, ksize=(1, pool_vals[i][0], pool_vals[i][1], 1),
                           strides=(1, stride_vals[i][0], stride_vals[i][1], 1), padding='VALID')

self.cnn_out_4d = pool

```

Fig. 2 Code snippet of CNN

```

# basic cells which is used to build RNN
num_hidden = 256
cells = [tf.compat.v1.nn.rnn_cell.LSTMCell(num_units=num_hidden, state_is_tuple=True) for _ in
         range(2)] # 2 layers

# stack basic cells
stacked = tf.compat.v1.nn.rnn_cell.MultiRNNCell(cells, state_is_tuple=True)

(fw, bw), _ = tf.compat.v1.nn.bidirectional_dynamic_rnn(cell_fw=stacked, cell_bw=stacked, inputs=rnn_in3d,
                                                         dtype=rnn_in3d.dtype)

```

Fig. 3 Code snippet of RNN

3.1.1 CNN Output

The CNN layers produce a 32-character sequence as their output. There are 256 features in each entry. Of course, the recurrent neural network layers will treat these features further, but few of them already have a strong relationship with the input image's high-level attributes:

3.2 Recurrent Neural Network

The RNN propagates important information along the feature pattern, which has about 256 features per each time step. The long short-term memory (LSTM) RNN application is utilized since it can relay information over greater distances and has more [13] strong training features than a vanilla RNN. Figure 2 is the code snippet for RNN.

Create a bidirectional RNN from it that traverses the input sequence from front to back and vice versa. As a result, two 32×256 output sequences, forward and backward, are generated.

```

# ground truth text as sparse tensor
self.gt_texts = tf.SparseTensor(tf.compat.v1.placeholder(tf.int64, shape=[None, 2]),
                                tf.compat.v1.placeholder(tf.int32, [None]),
                                tf.compat.v1.placeholder(tf.int64, [2]))

# calc loss for batch
self.seq_len = tf.compat.v1.placeholder(tf.int32, [None])
self.loss = tf.reduce_mean(
    input_tensor=tf.compat.v1.nn.ctc_loss(labels=self.gt_texts, inputs=self.ctc_in_3d_tbc,
                                          sequence_length=self.seq_len,
                                          ctc_merge_repeated=True))

```

Fig. 4 Code snippet of CTC

3.2.1 RNN Output

RNN output matrix bears the characters scores, with the CTC blank label as the final (80th) element. From top to bottom, the other matrix elements match the characters listed.

It can be observed that the characters are almost always predicted precisely where they appear in the picture. The CTC procedure does not need segmentation and is unconcerned about absolute locations.

3.3 *Connectionist Temporal Classification (CTC)*

During the training of the NN, the RNN output matrix and ground truth text are given to CTC and the loss value is calculated. The matrix to infer is handed to the CTC, which decodes it into the final text. The maximum length of both the ground truth and recognized messages is 32 characters.

Figure 4 has the code for CTC.

A sparse tensor is used to encode the ground truth text. Both CTC processes need the length of the input sequences.

3.4 *Training*

The mean of the batch element loss values is used to train the NN, which is then put into an optimizer like Adam optimizer. This is shown in the above Fig. 5.

```

self.optimizer = tf.compat.v1.train.AdamOptimizer().minimize(self.loss)

```

Fig. 5 Code snippet for training

3.5 Model Evaluation

Model evaluation is a crucial step in the creation of a model. It helps in the selection of the best model to represent our data, and the prediction of how well the chosen model will perform in the future. Both techniques employ a test set (not visible to the model) to evaluate model performance in order to avoid over fitting.

The goal of model assessment is to determine a model’s generalization accuracy on future (unseen/out-of-sample) data. The graphs of loss and accuracy against epochs are plotted here.

On the IAM dataset, a plot of the loss function for the first 4 min of training is shown in Fig. 6. The time in seconds is represented on the horizontal axis, while the CTC loss is represented on the vertical axis.

Top image batch size = 5.

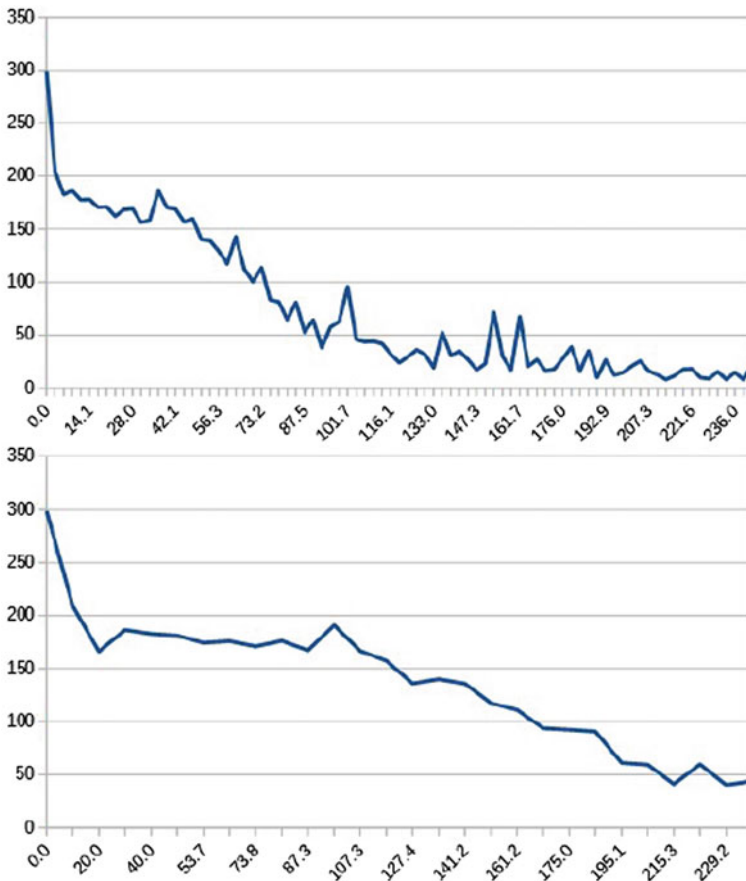







Fig. 6 Plot of loss function

Table 2 Test images

S. No.	Test image
1	 Recognized: "put down a resolution on the subject" Probability: 0.3410680
2	 Recognized: "A MOVE to stop Mr. Gaitskell from" Probability: 0.4538659006357193
3	 Recognized: "nominating any more labour life peers" Probability: 0.21466925740242
4	 Recognized: "is to be made at a meeting of labour" Probability: 0.66699731349945
5	 Recognized: "MPs tomorrow" Probability: 0.17748476564884186

Bottom image batch size = 2.

$$\text{Accuracy} = 100\% - \text{WER} \quad (1)$$

Table 2 shows the test images along with output digitalized text. In Fig. 7, graph shows the relationship between loss and Epoch. The accuracy of various test images can be calculated by above formula Eq. (1).

4 Conclusion and Future Scope

4.1 Conclusion

In this paper, the neural networks which recognizes text in images have been discussed. The document also contains an explanation of all the methods used in the model with the help of a flowchart. The NN generates a character–probability matrix and has five convolutional neural network (CNN) and two recurrent neural network (RNN) layers. This matrix is either used to calculate CTC loss or to decode

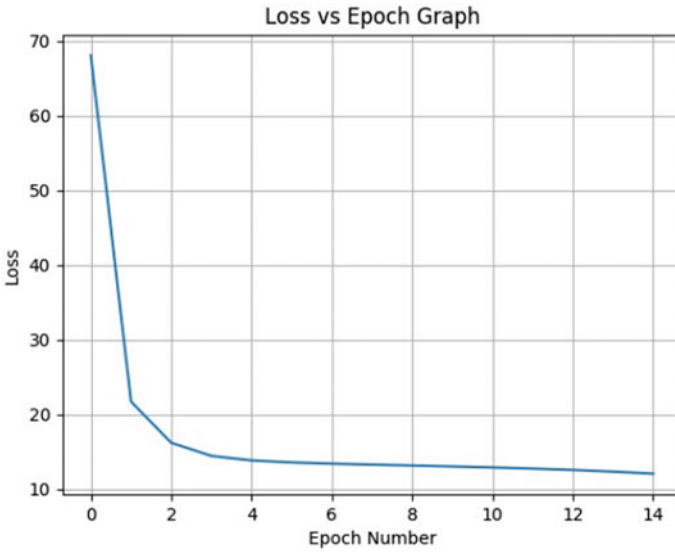


Fig. 7 Loss versus epoch graph

CTC. Some important parts of the codes are presented. The outputs of the handwritten images are tabulated. Using the model, character accuracy of 89.28% and word accuracy of 80.55% have been achieved.

4.2 Future Scope

This model can be deployed in educational institutions, IT companies, healthcare centers and hospitals, business industries to digitalize the handwritten information and directly store it in the database saving time and hard work. Also, the project can be extended by adding algorithms to identify the strokes, pressure and handwriting style. This model can be linked to any type of database like criminal database and police records to identify the trespasser, thus identifying and avoiding forgery and any such crimes. To feed a complete page, instead of line images, the input size of the neural network is increased. Also, to improve the recognition accuracy, some of the following methods like data augmentation, deslanting, decoder and text correction can be employed. Further, this paper can be improved to identify the style of writing, i.e., the vocabulary used, grammar used, repetition of words, etc., to identify the author of unknown ancient scripts. If 2D-LSTM is used instead of bidirectional LSTM in RNN layer, the word accuracy and character accuracy can be further improved. 2D-LSTM will also give further scope to interpret different handwriting styles.

Acknowledgements We are thankful to the authorities of Vasavi college of Engineering for allowing us to use the resources for the completion of this paper.

References

1. Gaurav K, Bhatia PK (2013) Analytical review of pre-processing techniques for offline handwritten character recognition. In: 2nd International conference on emerging trends in engineering and management, ICETEM
2. Espana-Boquera S, Castro-Bleda MJ, Gorbe-Moya J, Zamora-Martinez FB (2011) Improving offline handwritten text recognition with hybrid HMM/ANN models. *IEEE Trans Pattern Anal Mach Intell* 33(4)
3. Pal U, Wakabayashi T, Kimura F (2007) Handwritten numeral recognition of six popular scripts. In: Ninth international conference on document analysis and recognition ICDAR 07, vol 2, pp 749–753
4. Pradeep J, Srinivasan E, Himavathi S (2011) Diagonal based feature extraction for handwritten alphabets recognition system using neural network. *Int J Comput Sci Inf Technol (IJCSIT)* 3(1)
5. Arora S (2008) Combining multiple feature extraction techniques for handwritten Devnagari character recognition. In: IEEE region 10 Colloquium and the third ICIIIS, Kharagpur, India
6. Som T, Saha S (2011) Handwritten character recognition using fuzzy membership function. *Int J Emerg Technol Sci Eng* 5(2):11–15
7. Bajaj R, Dey L, Chaudhury S (2002) Devnagari numeral recognition by combining decision of multiple connectionist classifiers. *Sadhana* 27(1):59–72
8. Khedher MZ, Abandah GA, Al-Khawaldeh AM (2005) Optimizing feature selection for recognizing handwritten Arabic characters. In: Proceedings of world academy of science engineering and technology, vol 4, Feb 2005. ISSN: 1307-6884
9. Patnaik SS, Panda AK (2012) Particle swarm optimization and bacterial foraging optimization techniques for optimal current harmonic mitigation by employing active power filter applied computational intelligence and soft computing. 2012(897127)
10. Aparna KH, Subramanian V, Kasirajan M, Vijay Prakash G, Chakravarthy VS, Madhvanath S (2004) Online handwriting recognition for Tamil. In: IWFHR, 2004, proceedings. Ninth international workshop on frontiers in handwriting recognition, proceedings. Ninth international workshop on frontiers in handwriting recognition 2004, pp 438–443. <https://doi.org/10.1109/IWFHR.2004.80>
11. Pirlo G, Impedovo D (2011) Fuzzy zoning based classification for handwritten characters. *IEEE Trans Pattern Recognit Mach Intell* 19(04):780–785
12. Arica N, Yarman-Vural FT (2002) Optical character recognition for cursive handwriting. *IEEE Trans Pattern Anal Mach Intell* 24(6):801–113
13. Hanmandlu M, Murthy OVR (2007) Fuzzy model-based recognition of handwritten numerals. *Pattern Recognit* 40:1840–1854
14. Brakensiek A, Rottland J, Kosmala A, Rigoll G Offline handwriting recognition using various hybrid modeling techniques and character n-grams

An Efficient Energy Aware for Reliable Route Discovery Using Energy with Movement Detection Technique in MANET



Kamlesh Chandravanshi, Gaurav Soni, and Durgesh Kumar Mishra

Abstract In a growing field of network research, communication technology updated as per user demand. The mobile ad hoc network is one of the advance network architecture for availability anytime anywhere strategy without any cost. Nowadays, various research done in the field of mobile ad hoc network to improve their quality as per user needs. In this paper, proposed a technique to reduce the energy utilization and improve the network reliability on the bases of energy aware and location sensing of the mobile nodes. Node energy calculates based on per packet discharging rate and location sensing on the bases of LAR protocol. The network is designed and adopted the approach of the DSR routing protocol, which provides the route on the modified methodology of energy and location and compares the result on the basis of energy utilization, overhead, throughput and percentage of data received.

Keywords Location · Power aware · Energy uses · MANET · DSR

1 Introduction

In a communication network, lightweight, portable group of device self-form the backbone without the participation of any centralized controller it's called MANET. Mobile devices do not require existing infrastructure or a centralized service point and dynamical change their topology. Due to its ease of implementation, MANET applications span temporally form the network to provide instant needed service in remote location such as military application, disaster management and local communication. Wireless nodes are low-power devices which struggle by energy issue so our aim to develop a methodology to require low energy for communication. In the ad hoc

K. Chandravanshi (✉) · G. Soni
School of Computing Science and Engineering, VIT Bhopal University, Bhopal-Indore Highway
Kothrikalan, Sehore, Madhya Pradesh, India
e-mail: kamlesh.vjti@gmail.com

D. K. Mishra
Computer Science and Engineering, Shri Aurobindo Institute of Technology, Indore, India

© The Author(s), under exclusive license to Springer Nature Singapore Pte Ltd. 2022
P. Kumar Jain et al. (eds.), *Advances in Signal Processing and Communication Engineering*, Lecture Notes in Electrical Engineering 929,
https://doi.org/10.1007/978-981-19-5550-1_19

197

communication network topology, maintenance is a very crucial task, because route discovery depends on neighbor nodes which is moveable and low-power devices [1–3].

At the moment, there are two primary concepts in ad hoc networks concerning energy routing algorithms [4–6]. The first concept is to require low energy for data delivery to receiver, and the second concepts is to provide maximum reliability of the network. In previous research, various work was done to implement the routing protocol based on network demand. In this paper, we consider dynamic source routing (DSR) for the route discovery process.

2 Related Work

The section describes about all relevant work which minimized the network energy consumption and location sensing techniques.

Chandravanshi et al. [7] proposed an energy management approach which increases the network lifetime of mobile ad hoc network using the optimal link state routing (OLSR).

In this work [8], Zhu et al. investigate the energy efficient topology control issue using the CC model while considering the energy efficiency of routes.

“A energy model to prolong the network lifetime in ad hoc on demand distance vector (AODV) routing protocol” by Malek et al. [9]. Author presents a unique energy model which extend the network lifetime to achieve network reliability under dynamic routing protocol such as AODV that have been enhancing in this way to prolong the lifetime of MANET networks.

Tamilarasi et al. suggested a technique for altering dynamic source routing (DSR) to decrease overhead by reducing the route packets flooding in to the network their paper title “Efficient Energy Management for Mobile Ad Hoc Networks.” [10].

In their paper “MANET Energy conservation Aided Routing Protocol Use of Variable Range Location,” Joshi et al. [11] presented a device power control approach based on neighbor distance between the devices.

“Accuracy of energy level using OLSR routing in Mobile Ad Hoc Networks” has been proposed by Alhalimi et al. [12]. The underlying routing protocol they optimized is the routing strategy for optimal link state routing protocol.

The researchers are working on cross-layer node energy with network load aware relay framework such name as (DELAR) to conserve energy from multiple aspects, such as routing, transmission schedules and energy control, all examples of energy-conscious routing. Liu et al. [13], proposed a work on cross-layer node energy with network load aware relay framework such name as (DELAR) to conserve energy from multiple aspects, such as routing, transmission schedules and energy control, all examples of energy-conscious routing.

“Energy-Efficient Topology Control in Cooperative Ad Hoc Networks” proposed Zhu et al. [14]. In this article, the author presents a newer approach of topology control

with energy efficient cooperative communication to reduce the power consumption of all cooperative nodes.

In their paper “Ad Hoc Wireless Networks Power Aware Routing,” Rishiwal et al. [15] describes an effective technique that optimizes network lifespan by reducing low energy utilization in between source to destination node.

3 Approaches for Improving Energy Efficiency

Use dynamic source routing (DSR), which includes node current energy, discharging rate, and speed, and broadcast the route packet into the network, to improve network efficiency in terms of energy and network stability. While the broadcasted packets come into the intermediate node, those that participated in route call, they encapsulate their energy, discharging rate and location. Finally, the route packet reaches the destination node, which evaluates the complete route participated node and takes the decision for a reliable path between sources and destination pair.

Our strategy provides the most efficient use of energy and the highest level of dependability. However, if two paths exist, path1 and path2, and path1 have the most energy and path2 has the least amount of node mobility, we should choose path2 because path2 is more reliable than path1 since node presence is more essential than energy. In comparison with previous energy-based routing methods, our proposal provides superior energy usage, maximum data transmission and little routing overhead.

3.1 Algorithm of E-DSR Proposed Routing

In this section describe the formal description of proposed energy efficient dynamic source routing protocol which minimize the network energy consumption and more reliable for the communication.

- Input:** N: Number of Node
 T: Transmitter $\in N$
 K: Receiver node $\in N$
 DSR: Network layer protocol
 E_i : Node real-time energy
 M: Movement of node
 Ψ : radio range of node
- Output:** U_t : Utilized energy
 PDR: Percentage of data receives
 Thr: Network throughput
 Ro: Network Routing Load
- Routine:** Deploy Network $X*Y$ define by user
 Call DSR (T, K, E_t , M_t)

```

DSR form packet header broadcast route (T, K, Et, Mt)
If (N! = K & in Ψ)
    Rtablen ← N provide (En, Mn) in header
    Route packet to next N
Else if (N = K)
    K check number of path
    Create vector data structure to store respective path values
    Select path (High En, Low Mn)
    Execute LAR for location tracking
    K send Ack to N by selected path
    T Send_Data(T,K, Nn)
Else
    Path not found due to energy or Link failure
End if
End Routine
    
```

4 Simulation Architecture

The Network Simulator 2 (NS2) is the product of a continuous research and development effort led by Berkeley researchers [5].

4.1 Network Simulation Inputs

The table gives the network input parameter for analyzing the result of proposed E-DSR-Motion routing methodology (Table 1).

Table 1 Network Simulation parameter

Parameters	values
Mobile nodes in network	40
Grid structure	800 × 600
Routing protocol	DSR and energy
Simulation reset	100 s
Transport protocol	UDP and TCP
Data traffic	FTP and CBR
Size of packet (Byte)	512
Max traffic connection	8
Max speed (m/s)	Random

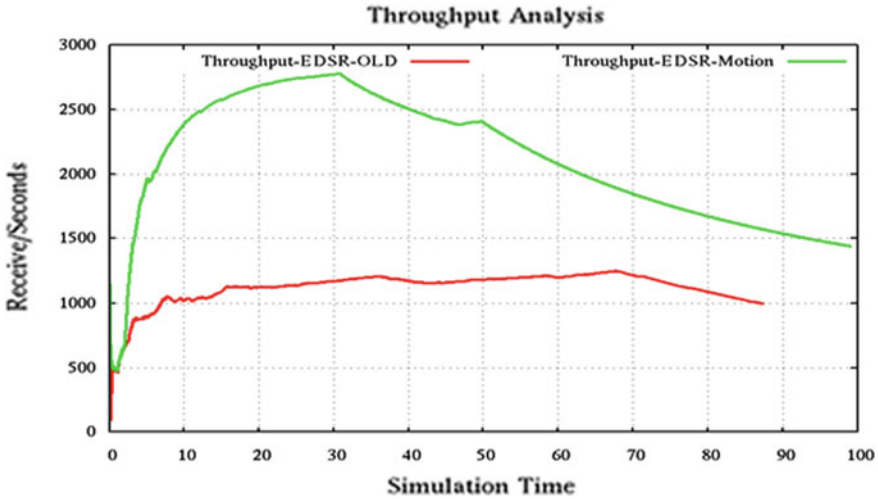


Fig. 1 Throughput analysis

4.2 Network Throughput

In the above resultant, Fig. 1 shows the network throughput during E-DSR with motion detection (Proposed) and existing E-DSR technique. The throughput performance of proposed methods is significantly superior than the traditional energy-based routing. In the proposed E-DSR with movement system, throughput is very high such range is 1500 pkt/s to 2800 pkt/s and existing E-DSR the throughput in between 1000 and 1200 pkt/s. The result concludes that proposed approach is better than the existing system.

4.3 Routing Load Analysis

Network routing load plays the important role which identifies network stability, while overhead higher it means network is unstable. Figure 2 shows the comparative analysis of existing DSR and proposed E-DSR with motion detection-based routing. Here, we observe that proposed approach provides very less routing packet nearly 500 but the existing system that overhead is very higher that is nearly 3700 packet. In the proposed system, the network is more stable as compare to existing system.

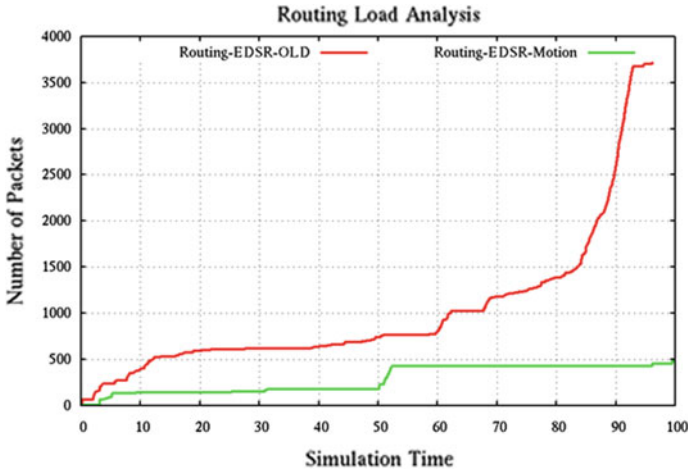


Fig. 2 Routing load analysis

4.4 Percentage of Data Receiving

Figure 3 shows that proposed E-DSR-Motion-based technique provides higher percentage of data receiving as compared to conventional energy-based DSR routing. The PDR is around 89% in this situation, but in the suggested schemes, we add the component of packet loss based on queue length estimate, which was not included in the previous scheme, thus the proposed mobility-based energy efficient system has a PDF of around 100%. It implies that the network's performance has improved as compared to the prior scheme.

4.5 Energy Utilization Analysis of Nodes

In any mobile ad hoc network, the node energy is the main concern. In Fig. 4, we analyze the energy utilization of the respective nodes in two different protocols. Through the result, it has been observed that proposed E-DSR-Motion algorithm makes utilization of low energy of the node which results in the improvement of the network lifetime.

5 Conclusion

Due to the lack of resources, it is not appropriate to recharge and charge the batteries. Energy utilization is the core challenge as all the nodes in a network are totally

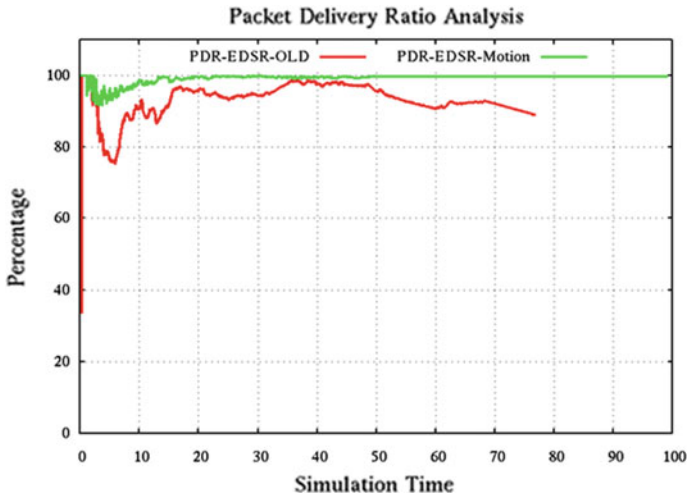


Fig. 3 Packet delivery ratio analysis

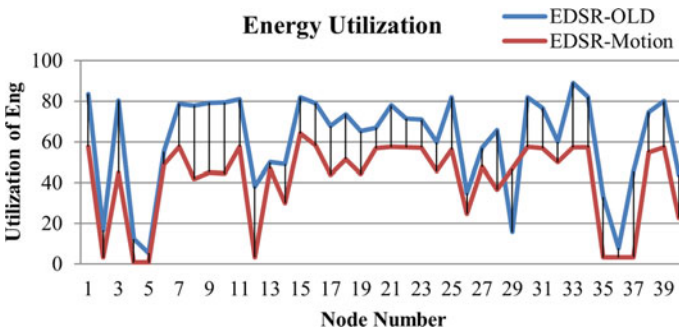


Fig. 4 Energy utilization

dependent on the energy of the relevant nodes of the network. In the ad hoc scenario, even if the node does not make communication on its own, it passes the data and routes packets to others. In this paper, we proposed the energy efficient dynamic source routing protocol which provides maximum lifetime of the network with low utilization of node energy. With the observation of the previous study of DSR routing it has been observed that our work is more efficient in terms of data receiving, throughput, energy utilization and overhead.

References

1. Li J, Zhang Y, Cordes D (2005) Power-Aware routing protocols in ad hoc wireless networks. *IEEE Wirel Commun* 69–81
2. Power Management tools Intel. <http://developer.intel.com/design/mobile/intelpower/tools/>
3. Maltz DA, Jetcheva DA, Hu Y, Johnson DB (2002) Mobile ad hoc network dynamic source routing protocol (DSR). Internet Draft of IETF
4. Vaidya N, Ko Y (1998) Location aided routing in mobile ad hoc networks. In: ACM/IEEE international conference on mobile computing and networking
<http://www.isi.edu/nsnam/ns/>
5. <http://www.isi.edu/nsnam/ns/>
6. Soni G, Chandravanshi K, Jhariya MK, Tomar D (2020) A multipath location based hybrid DMR protocol in MANET. In: 3rd International conference on emerging technologies in computer engineering: machine learning and internet of things (ICETCE-2020), 07–08 Feb 2020. IEEE
7. Chandravanshi K, Mishra DK (2018) Energy base network life time aware in mobile ad hoc networks using OLSR. *IJETAE* 8(1)
8. Huang M, Wang Y, Chen S, Zhu Y (2012) Energy efficient topology control in cooperative ad hoc network. *IEEE Trans Parallel Distrib Syst* 23(8)
9. Malek ALG, Layuan L, Li C, Bo W (2010) A new energy model prolong the network lifetime of ad hoc on demand distance vector routing protocols (AODV). IEEE
10. Tamilarasi M, Palanivelu TG, Chandramathi S, Mobile ad hoc network for , efficient energy management, electronics and communications engineering. Pondicherry Engineering College, India
11. Joshi NN, Joshi RD (2011) Mobile Ad hoc network energy conservation using the ad routing protocol of the variable range location, *Int J Wirel Mobile Netw (IJWMN)* 3(5)
12. Kunz T, Alhalimi R (2007) Mobile ad hoc networks with energy level accuracy OLSR. In: WICON 2007, Oct 22–24, 2007, Austin, Texas, USA
13. Liu W, Zhang C et al (2011) DELAR a device energy load aware relaying framework for heterogeneous mobile ad hoc networks. *IEEE* 29(8)
14. Huang M, Wang Y, Chen S, Zhu Y (2012) Energy efficient topology control in cooperative ad hoc networks. *IEEE Trans Parallel Distrib Syst* 23(8)
15. Yadav M, Bajapai SK, Verma S, Rishiwal V (2009) Power aware routing in ad hoc wireless network. *JCS&T* 9(2)

Design and Implementation of Imprecise Adders for Low-Power Applications



N. Alivelu Manga and Varala Pasula Nikhila

Abstract In modern age, the design of low-power and high-speed devices has become a major requirement. But it is getting harder to maintain a balance between these two parameters. Approximate computing is viewed as a sustainable alternative which addresses this issue by returning outputs that are slightly erroneous in exchange for improvements in performance and power consumption. In application domains like speech recognition, Web search, multimedia, graphics, and image processing, obtaining accurate results is not mandatory as they are resilient to a certain level of errors. In this paper, four approximate computing-based adders called approximate mirror adders are designed in Cadence Virtuoso tool by modifying the accurate mirror adder circuit. Then, these are used to build 8-bit adders in which the accurate computations are performed in MSB positions, and approximate computations are performed in LSB positions. These adders are then analyzed and compared in terms of power consumption and error rate. Finally, the accurate adders in image compression process are replaced with the designed approximate adders in MATLAB, and its impact on the quality of the reconstructed images is examined.

Keywords Approximate computing · Low power · Error resilience · Approximate adders · Image compression

1 Introduction

Gordon Moore has proposed Moore's law based on the observations on historical trends. According to him, the count of IC components will be doubled every 2 years [1]. But as the transistor count increased, the speed at which the transistor size was shrinking has slowed down making it difficult to develop smaller feature sizes. As the CMOS technology moves into the deep submicron regime, power consumption turned out to be a critical problem. Some new technologies or new ways of over-

N. Alivelu Manga · V. P. Nikhila (✉)

Department of Electronics and Communication Engineering, Chaitanya Bharathi Institute of Technology, Hyderabad, Telangana 500075, India
e-mail: varalanikhila@gmail.com

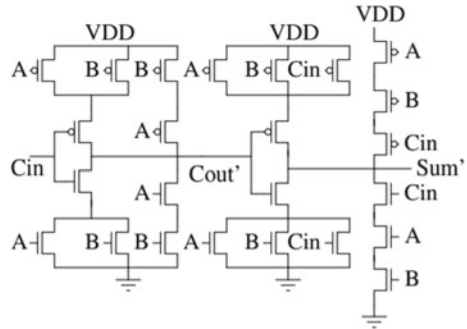
coming these problems must therefore be explored because the available and existing methods are unable to fulfill the technology needs in future. Approximate computing is one such alternative method which has been the hot topic of research in recent years [2].

Approximate computing is an approach which provides energy efficiency by relaxing the output accuracy which is done through intentional introduction of acceptable errors. This method minimizes the complexity of circuits and provides low-power area with increased speed. There are a wide variety of applications in which there is no need of highly precise calculations called as error resilient or error tolerant applications which act as a major motivational factor for approximate computing. These are the ones that are able to withstand a specific loss in precision and accept a range of values as correct outputs. Multimedia, signal processing, image processing, data mining, biometric security, data analytics, etc., come under this category. Error resilience in these applications can be caused by any one of the following factors [3]: (a) The visual perception of human beings has a limitation and cannot pick up everything they see, (b) inherently, input signals of some applications can be mixed with noise, or (c) approximate answers are accepted in the event of failure to come up with the right answer.

As adders form an important part of digital systems, they are used in the construction of numerous error tolerant applications. Ripple carry adder (RCA) and carry look-ahead adder (CLA) are the two commonly used traditional accurate adders [4]. RCA has a simple structure in which a number of single-bit adders are cascaded. But the carry has to be propagated from one adder block to the other which causes large delays resulting in this circuit having slow speed. In CLA, the delay is minimized as it produces the carry generate and propagate signals simultaneously. Here, the area required is increased due to the additional circuitry. These problems are resolved by approximating the adders in order to acquire the desired features.

Approximation of adders has generated a significant amount of research effort in recent times which has resulted in a wide diversity of adders based on approximate computing being envisaged in the literature to overcome limitations in technology. Three new approximate XOR/XNOR-based adders (AXA) have been proposed in [5]. These are based on 10-transistor exact full adder which provides area and power efficiency. Redundant transistors are removed to reduce the logic complexity, and this is achieved by implementing the multiplexer using pass transistor logic. In [6], full adder circuit is approximated at gate level to obtain three inexact/approximate adder cell (InXA) designs which have small transistor count compared to the existing accurate and other inaccurate adders. In these adders, only one of the full adder outputs is approximated, while accurate result is used for the other output. Two approximate multiplexer-based adders (TGA) are proposed in [7], in which logic complexity is reduced at gate level. The multiplexer is implemented using transmission gates which is a good alternative for pass transistors. An approximate computing-based adder called accuracy configurable adder is presented in [8] in which precision of the output may be set during run time. It can be operated in accurate mode when complete precision is needed and in inaccurate mode when approximate results are sufficient. The segmentation technique proposed in [9] divides the n -bit addition

Fig. 1 Accurate mirror adder [10]



into m subblocks, which can be overlapping blocks or separate blocks, each having bit-width of k . One bit is added at the end of each sub-block for using the concept of carry kill signal to confine the propagation of carry, delay of the critical path and to hold the actual and exact carry-out of every sub-block.

The remaining part of this paper is organized along the following lines. Section 2 describes about the accurate and approximate mirror adders. The image compression is explained in Sect. 3. Section 4 presents the comparison of AMA with respect to RCA and the output images of image compression using approximate additions. The work done in this paper is concluded in Sect. 5.

2 Accurate and Approximate Mirror Adders

Figure 1 denotes the structure of a single-bit traditional precise mirror adder which consists of 24 transistors. It is predominantly used for execution of a full adder module [10]. The PMOS and NMOS chains are symmetrical to each other. In the first part of this circuit, the carry-out is generated, whereas in the second part, the sum is generated. Four approximate versions of this adder are built by logic complexity reduction.

For obtaining the first approximated version called AMA1, a total of 8 transistors are discarded from the accurate adder such that the truth table of full adder has less errors, and the approximate version does not have short circuit or open circuit. Figure 2 shows the structure of AMA1 which is made up of 16 transistors. In this adder, the sum has two erroneous values, and carry-out has only one erroneous value out of all the eight input combinations as represented in Table 1. Here, the values with ✓ beside them indicate that they are correct whereas the values with × beside them indicate that they are wrong or erroneous. From this table, by looking at the outputs of accurate adder, it is seen that $Sum = \overline{C_{out}}$ for six cases out of eight excluding the inputs $A = 0, B = 0, C_{in} = 0$ and $A = 1, B = 1, C_{in} = 1$. AMA2 is constructed according to this observation, and its structure with 14 transistors is represented in Fig. 3. It has the carry generation unit of accurate adder followed by a buffer stage for equating the $\overline{C_{out}}$ to sum.

Table 1 Truth table for accurate and approximate mirror adders

Inputs			Accurate mirror adder		AMA1		AMA2		AMA3		AMA4	
A	B	C _{in}	Sum	C _{out}	Sum	C _{out}	Sum	C _{out}	Sum	C _{out}	Sum	C _{out}
0	0	0	0	0	0	0	1	0	1	0	0	0
0	0	1	1	0	1	0	1	0	1	0	1	0
0	1	0	1	0	0	1	1	0	0	1	0	0
0	1	1	0	1	0	1	0	1	0	1	1	0
1	0	0	1	0	0	0	1	0	1	0	0	1
1	0	1	0	1	0	1	0	1	0	1	0	1
1	1	0	0	1	0	1	0	1	0	1	0	1
1	1	1	1	1	1	1	0	1	0	1	1	1

Fig. 2 AMA1 [10]

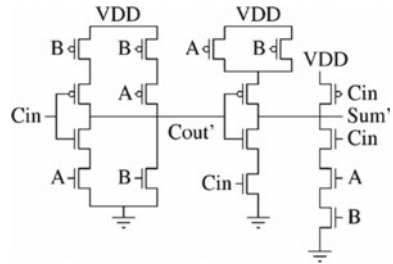
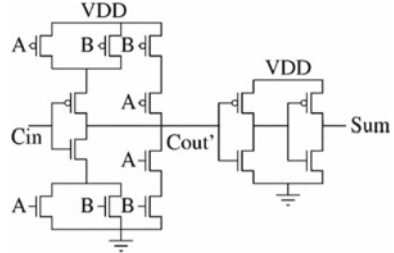


Fig. 3 AMA2 [10]



This adder has two erroneous values in sum like AMA1 and no erroneous values in carry-out according to Table 1.

Then, AMA3 is built by taking a combination of both AMA1 and AMA2. It has 11 transistors as shown in Fig. 4. Table 1 shows that there are three erroneous values in sum, whereas carry-out has only one erroneous value. For constructing AMA4, the truth table of accurate adder is considered in which $C_{out} = A$ for six combinations of inputs apart from $A = 0, B = 1, C_{in} = 1$ and $A = 1, B = 0, C_{in} = 0$. So, first carry-out is equated to A by using an inverter, and then, the sum generation unit of AMA1 is used. It has 11 transistors as shown in Fig. 5. As per the Table 1, sum has three erroneous values, and carry-out has two erroneous values.

Fig. 4 AMA3 [10]

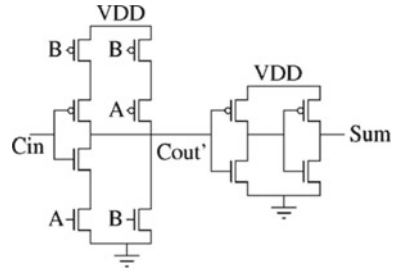
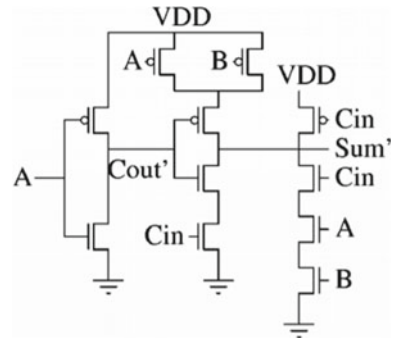


Fig. 5 AMA4 [10]



3 Image Compression

Image compression refers to the process of representing the image in a compact format by minimizing the size of image. The memory required for storing this image is also reduced which in turn results in lowered cost and time for transmitting the image [11]. The discrete cosine transform acts as an important block for image compression. A 2-dimensional DCT is expressed by Eq. 1, where the values of u, v are given in Eq. 2, $C(u, v)$ denotes the DCT coefficients, $a(u), a(v)$ represent the factors which are dependent on, respectively, as given in Eqs. 2 and 3, and $f(x, y)$ denotes the $N \times N$ input matrix. This DCT can be performed by applying 1-dimensional DCT on both rows and columns of the input matrix. The speed of system will be reduced due to huge computations involved in the conventional DCT. So, to overcome this problem, Loeffler’s algorithm is used for implementation of 1-dimensional DCT which is a fast and has a butterfly kind of a structure. The additions and subtractions in DCT will be replaced with the designed approximate adders to lower the power consumed. After this, we obtain the DCT coefficients, and image is compressed by eliminating the unwanted coefficients that do not carry significant information.

$$C(u, v) = a(u)a(v) \sum_{x=0}^{N-1} \sum_{y=0}^{N-1} f(x, y) \cos \left[\frac{(2x + 1)u\pi}{2N} \right] \cos \left[\frac{(2y + 1)v\pi}{2N} \right] \quad (1)$$

where $u, v = 0, 1, \dots, N - 1$

$$a(u) = \begin{cases} \sqrt{\frac{1}{N}}, & u = 0 \\ \sqrt{\frac{2}{N}}, & u = 1, 2, \dots, N - 1 \end{cases} \quad (2)$$

$$a(v) = \begin{cases} \sqrt{\frac{1}{N}}, & v = 0 \\ \sqrt{\frac{2}{N}}, & v = 1, 2, \dots, N - 1 \end{cases} \quad (3)$$

4 Result

The single-bit accurate and approximate adders that have been discussed in this paper have been designed and simulated in Cadence Virtuoso tool. 8-bit ripple carry adder is designed using 8 single-bit accurate mirror adder cells cascaded in series. The 8-bit approximate adder, AMA3, is built by utilizing the single-bit AMA3 cells in the least significant bit positions, while retaining the accurate versions in most significant positions to ensure that a certain level of accuracy is maintained. The error rate of single-bit approximate adders and power consumed by 8-bit approximate adders is calculated and compared to that of ripple carry adder as shown in Table 2. The error rate for a single-bit AMA ranges from 25 to 37.5% for sum and 0 to 25% for carry. The RCA consumes 551.6 nW of power, whereas the maximum power consumed by approximate adders is 468.2 nW which is still very less than that of RCA. It is observed that AMA3 consumes the least power among all which is 361.6 nW, and it is the right choice for utilization in low-power applications. The power savings are in the range 9.15–34.45%.

In the 8-bit approximate mirror adders, the number of LSBs in which AMA3 cells are used is changed between 2 LSB, 3 LSB, and 4 LSB positions, and these versions are used in image compression in MATLAB, in the place of accurate additions. Two different images have been compressed, and the simulation results for the same using approximate addition-based compression are shown in Fig. 6. From this figure, it has been observed that as the approximated bit number increases, the quality of the image is further reduced, but the image can still be identified. The same has been verified by quality assessment which is done using the peak signal to noise ratio. Table 3 shows the PSNR values of two images obtained using AMA3 along with that of the accurate adder. Here also, it is seen that as the number of LSBs which have been approximated increases, the PSNR value reduces which means the quality is minimized to an acceptable level, but there is an advantage of low-power consumption due to the use of approximate adders.

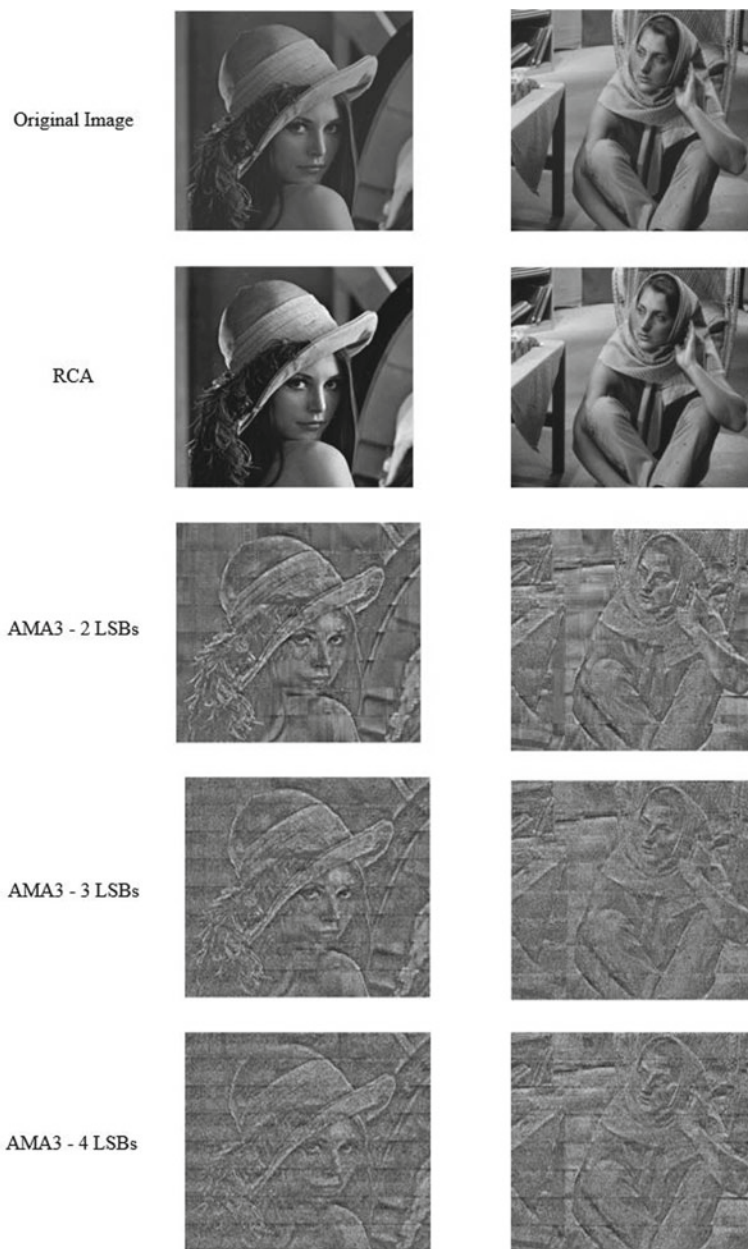


Fig. 6 Simulation results of approximate addition-based image compression

Table 2 Comparison of 8-bit AMAs with RCA

Adder	Error rate of single-bit adder (%)		Total power consumption (nW)	Improvement in power consumption (%)
	Sum	Carry		
RCA using MA	–	–	551.6	–
AMA1	25	12.5	468.2	15.12
AMA2	25	0	501.1	9.15
AMA3	37.5	12.5	361.6	34.45
AMA4	37.5	25	421.9	23.51

Table 3 Comparison of PSNR of two images

PSNR	RCA	AMA3—2 LSBs	AMA3—3 LSBs	AMA3—4 LSBs
Image 1	42.111	15.0239	14.4888	14.3991
Image 2	38.1601	15.2626	14.8175	14.7819

5 Conclusion

Approximate computing is a novel and fresh approach which has procured significance in the recent years due to the improvements provided in terms of power consumption and performance while delivering acceptable outcomes. This paper focused on designing and simulating single-bit accurate and approximate mirror adders. After comparison, it has been observed that AMA3 has the lowest power consumption, and the power savings range from 9.15 to 34.45% in approximate adders. Then, this AMA3 single-bit adder cell is used to construct 8-bit approximate adder by varying the number of positions in which the approximation is done. Two images have been compressed using RCA and AMA3. The simulation results show that the images reconstructed using approximate adders can be traced, and as the approximation increases, the image quality is reduced up to some extent which can be tolerated in exchange for reduction in power consumption in error resilient applications.

References

1. Moore GE (2006) Progress in digital integrated electronics. Reprinted from Technical Digest, International electron devices meeting. 1975 in IEEE Solid State Circuits Society Newsletter, Sept 2006, vol 11, no 3. IEEE
2. Dutt S (2018) Analysis, design and modeling of approximate adders for error-resilient applications. Ph.D. thesis, IIT Guwahati

3. Jie H, Michael O (2013) Approximate computing: an emerging paradigm for energy-efficient design. In: IEEE European test symposium (ETS). <https://doi.org/10.1109/ETS.2013.6569370>
4. Pathak R (2018) A review of approximate adders for energy-efficient digital signal processing. *Int Res J Eng Technol* 05(10)
5. Yang Z, Jain A, Liang J, Han J, Lombardi F (2013) Approximate XOR/XNOR-based adders for inexact computing. In: IEEE international conference on nanotechnology (IEEE-NANO 2013), Aug 2013. <https://doi.org/10.1109/NANO.2013.6720793>
6. Almurib HAF, Nandha Kumar T, Lombardi F (2016) Inexact designs for approximate low power addition by cell replacement. In: Design, automation and test in Europe conference and exhibition (DATE), Mar 2016
7. Yang Z, Han J, Lombardi F (2015) Transmission gate-based approximate adders for inexact computing. In: Proceedings of the 2015 IEEE/ACM international symposium on nanoscale architectures (NANOARCH-15), July 2015. <https://doi.org/10.1109/NANOARCH.2015.7180603>
8. Kahng AB, Kang S (2012) Accuracy-configurable adder for approximate arithmetic designs. In: DAC design automation conference. <https://doi.org/10.1145/2228360.2228509>
9. Al-Maaitah K, Tarawneh G, Soltan A, Qiqieh I, Yakovlev A (2017) Approximate adder segmentation technique and significance-driven error correction. In: 27th international symposium on power and timing modeling, optimization and simulation (PATMOS), Sept 2017
10. Vaibhav G, Debabrata M, Park SP, Raghunathan A, Roy K (2011) IMPACT: IMPrecise adders for low-power approximate computing. In: IEEE/ACM international symposium on low power electronics and design. <https://doi.org/10.1109/ISLPED.2011.5993675>
11. Rojatkar DV, Borkar ND, Naik BR, Peddiwar RN (2015) Image compression techniques: lossy and lossless. *Int J Eng Res Gen Sci* 3(2)

Speech Processed Public Addressing System



Vijaya Kumar Gurrala, Y. Padma Sai, Nikhitha Karennagari,
and K. Yashwanth Reddy

Abstract In the fast-emerging world today, where there are numerous ways of expressing our ideas, speech is proven to be the best. The most essential aspect of this is to have a good voice pitch level, which is the root cause for the success of expressing our intention to the audience. Grabbing the attention of the target audience is the challenging part. The advancements and improvements in the speech processing domain made our lives easier. Today we have several algorithms in the speech processing domain. Pitch shifting is one of the speech processing techniques that helps to shift the pitch level of the speaker to a proper level. This proper pitched voice can help in greatly influencing the audience. Hence, there is a need for the usage of most effective time domain/frequency domain pitch shifting algorithms. This project can be implemented by using the short-time Fourier transform (STFT) technique with improved time–frequency resolution for analysis of the input speech signal. The analysis of the speech signal can be performed using the STFT algorithm in MATLAB by creating a GUI using the MATLAB App Designer and further evaluating the results.

Keywords Short-time fourier transform (STFT) · Discrete fourier transform (DFT) · Pitch shifting

1 Introduction

Pitch is the most basic concept which is related to the lowest frequency of the sound wave, which is classically the fundamental frequency of the periodic wave. Pitch shifting can be used in real time to help people [1] with improper voice features by processing their speech through a system that further yields the proper pitched voice without any lag, i.e. the system simultaneously gives the output as soon as the input is taken with a minimal or no delay. Also, the processed signal has the

V. K. Gurrala (✉) · Y. Padma Sai · N. Karennagari · K. Yashwanth Reddy
Department of ECE, VNR Vignana Jyothi Institute of Engineering and Technology, Hyderabad,
Telangana 500090, India
e-mail: vijayakumar_g@vnrvjiet.in

same characteristics as that of the original signal with the only change in the pitch level. This effect can now be achieved in real time by using MATLAB [2], Python JAVA, and many other environments where there is a possibility of creating a GUI by implementing the algorithm by writing code. Moreover, this could be further extended by creating a real-time system by deploying the code of the algorithm into an FPGA or ASIC. With the elimination of various types of noises, the system can be made more efficient and unailing.

2 System Overview

Speech is the most natural way to express ourselves as human beings. These days we see people feeling difficult to express their views to the targeted audience due to naturally improper pitch levels which forestalls them from grabbing the attention of the audience. For this reason, we do pitch shifting to the input signal (speaker's voice). Shifting the perceived pitch of the input speech signal is most readily accomplished by altering the signal's playback speed, however, this approach alters the temporal scale and distorts some of the features of the input voice. This project aims to accurately shift the pitch of the speaker's voice while preserving its characteristics, i.e. maintaining the speed of the signal as that of the original speech and implement this entire process in real time. This thesis provides two methods of shifting the pitch, one by direct scaling of the frequency and the other by the usage of pitch shifting algorithms. The former has a restriction in terms of the output signal's speed change as compared to the input speech signal. The latter method is shown to be the best, for pitch shifting. Pitch shifting algorithms can be implemented in both the time domain and the frequency domain, although time domain methods are inefficient for polyphonic audio sources. The frequency domain algorithm provides a better time–frequency resolution. Short-time Fourier transform (STFT) is one of the frequency domain pitch shifting algorithms used here. The short-time Fourier transform is a well-known audio synthesis technique used for pitch shifting. The pitch is then shifted and transmitted through a speaker.

3 Transforms and Pitch Shifting

3.1 Transforms

Complex exponential signals are used as building blocks in the Fourier transform. The signal is compared to the sinusoid at that frequency, at each frequency of the complex exponential signal. The correlation is stronger if the signal comprises that frequency. If the signal at a given frequency does not have a spectral component, the correlation is zero or poor. Consequently, nonlinear processing techniques are

required, which are typically computationally expensive. When pitch shifting, certain computational costs are important. Fortunately, rapidly falling computing costs have opened the way for low-cost digital processing units capable of performing pitch shifting and related transforms using a variety of algorithms that can be studied.

3.1.1 Fourier Transform Shortcomings

The limitations of the Fourier transforms include in terms of time, i.e. the exponentials stretch to infinity. Moreover, the Fourier transforms will examine the signal globally rather than locally. As a result, the Fourier transform can only determine what frequencies are present throughout the stream, but not when these frequencies occur. Hence, the signal must be examined locally to get the temporal localization of the spectral components.

3.1.2 Short-Time Fourier Transform (STFT)

The working of STFT involves picking a window with a limited length and placing this window above the signal at time $t = 0$. Then, the signal is to be trimmed using the aforementioned window. The Fourier transform of the truncated signal has to be calculated and saved. Further, small amounts of a window have to be slid. The procedure has to be repeated continuously till the window signal comes to an end. We obtain a distinct Fourier transform for each location of the window. As a result, each Fourier transform offers simultaneous time and frequency information, as well as spectrum information for a given signal time scale. STFT provides the time information by computing different Fourier transformers over a series of the period and then combining them. If the window is large, then STFT becomes the normal Fourier transform. For narrow windows, there is poor time resolution for both time and frequency. Once the window has been chosen, the resolution is set to both frequency and time.

3.2 Heisenberg Uncertainty Principle

$$\Delta t \times \Delta f = 1/(4\pi)$$

The resolution of both frequency and time cannot be set arbitrarily high at the same time. We have no way of knowing exactly where a frequency component is at any given time. We can only determine which frequency intervals are present in certain time intervals.

3.3 Various Pitch Shifting Algorithms

The purpose of pitch shifting algorithms is to adjust the pitch without changing the replay rate. This may be done by replaying the sound waveform at a different speed than it was recorded at. Earlier digital processors can only modify pitch values after they have been entered, but many newer gadgets that employ computer processing technology can do it practically in real time.

3.3.1 Time Domain Versus Frequency Domain

Pitch shifting algorithms consist of time domain and frequency domain algorithms. The frequency domain representation will indicate the relative strengths of the signal's frequency components, which can be difficult to determine or detect in the time domain. Sound modulation in the frequency domain is usually achieved by splitting the signal into tiny overlapping segments (windows) and processing each segment individually. This is critical because the frequency of the signal varies with time, resulting in a massive number of observed frequencies. Before a windowed segment can be processed from the time domain to the frequency domain, it must be translated. Thus, fast Fourier transform (FFT) can be used to achieve this.

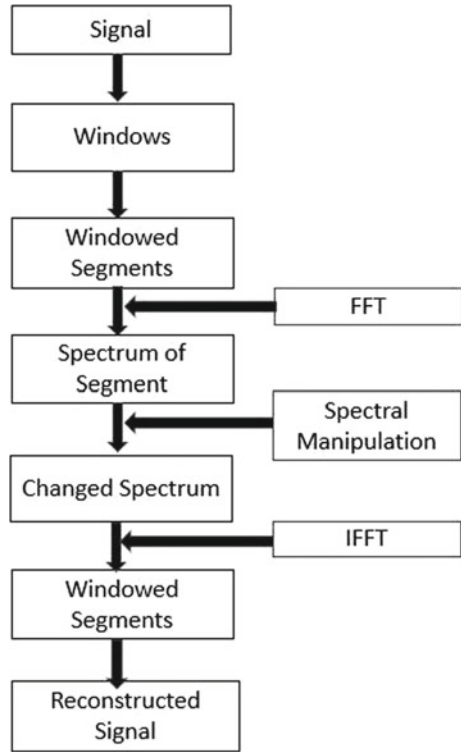
Some of the pitch shifting algorithms are constant Q transform, pitch synchronous overlap and add (PSOLA), and short-time Fourier transform). Implementation of constant Q transform is more complicated in comparison with the normal Fourier transform because the number of samples used in the calculation of each frequency bin varies which in turn varies the length of the windowing function. In the PSOLA method, the pitch marking must be exact because the quality of pitch shifting depends on the quality of pitch marking which is difficult to achieve. STFT is based on fast Fourier transform.

The fast Fourier transform generates a collection of complex quantities that can translate the complex quantity into magnitudes to reflect an average power of a specific frequency range. The frequency resolution of the fast Fourier transform can be determined by these number of bins, which is defined as the following equation [3]:

$$\text{Resolution(Hz)} = (\text{rate of sampling})/(\text{size of window})$$

High resolution is achieved through a wide window, but the drawbacks are slower processing and a higher risk of frequency instability. The windowed segment's spectrum are then spectrally changed to adjust the frequencies inside the signals, which may be accomplished with several pitch shifting algorithms. Finally, to reproduce the pitch-shifted signal, the processed windowed segments are combined and resynthesized. These measures are depicted in the Fig. 1.

Fig. 1 Procedural steps for a frequency domain pitch shifting algorithm



4 Results

4.1 Simulation Results of Frequency Scaling

The GUI in MATLAB is created using an app designer. Using various buttons, the user can interact with the application. The speech signal has been tested and verified with various inputs (Fig. 2).

This frequency scaling helps to change the pitch of the signal but also results in a change in the speed of the signal. To have control over this, short-time Fourier transform algorithm is used.

4.2 Simulation Results of Pitch Shifting Using STFT

In the GUI, the slider helps to adjust the level of the pitch. As we move towards the right side of the slider, the pitch increases, and the pitch decreases as we move towards the left side of the slider. The duration helps us to indicate the length of the

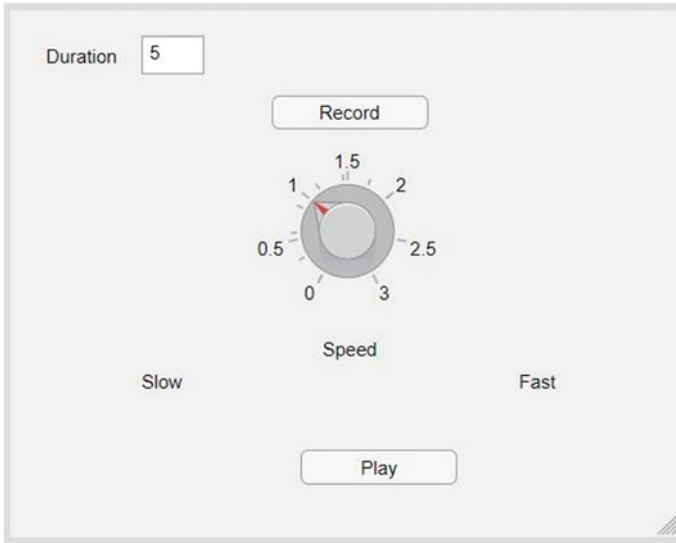


Fig. 2 GUI of frequency scaling

Fig. 3 GUI of pitch shifting using STFT



recording. The record button is used to get the input from the microphone with the specified time duration in the box (Fig. 3).

4.3 MATLAB Plots Depicting the Pitch Shifting for a Human Voice

Figures 4 and 5 shown above are the MATLAB simulated plots which show the inputted human audio and the pitch-shifted version of it. The pitch of the human voice gets shifted based on the number of semitones mentioned to achieve the desired pitch level.

Fig. 4 MATLAB plot for input audio signal

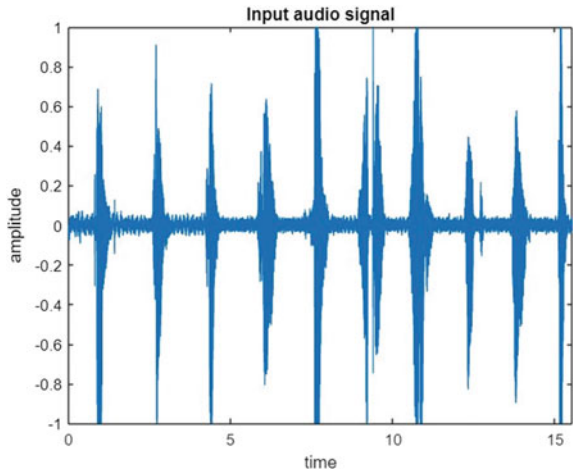
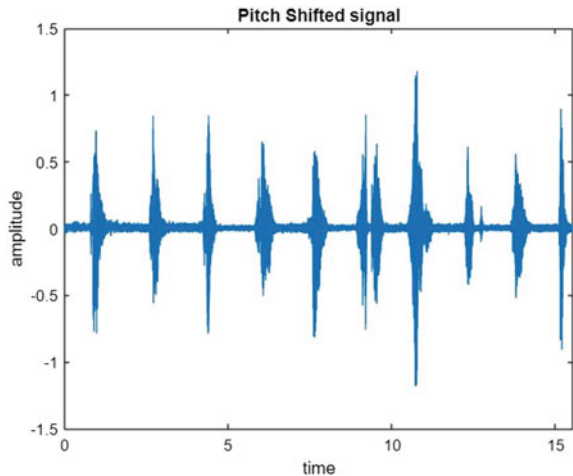


Fig. 5 MATLAB plot for output pitch-shifted signal



5 Conclusions

Based on extensive research and thorough analysis, two ways of pitch shifting, i.e. through frequency scaling and STFT algorithm have been implemented with a novel MATLAB-based GUI created using App designer. The frequency scaling-based pitch shifting led to the variation of signal speed with the pitch shift which is undesirable. The STFT-based design was found to be most suitable as it could even overcome the limitation of the varying speed of the signal with the required shift in pitch level.

6 Future Scope

The work done so far has exhibited fair outcomes, but there is still greater scope for improvement. The software code can be enhanced further to make it work in real time, where we get the output as soon as we start recording. This software developed in MATLAB using the STFT algorithm could be deployed in a hardware processor to make it work in real time and pitch levels could be adjusted dynamically based on the input speech. In the system proposed, a smart signal processor can be embedded which takes programmed instructions as per the requirement and outputs the pitch-shifted version of our voice.

References

1. Klofstad CA, Anderson RC, Peters S (2012) Sounds like a winner: voice pitch influences perception of leadership capacity in both men and women. *Proc R Soc*
2. Kim J (2013) Automatic pitch detection and shifting of musical tones in real-time
3. Schörkhuber C, Klapuri A, Sontacchi A (2012) Pitch shifting of audio signals using the constant-Q transform

An Approach Towards Data Privacy Issues in Distributed Cyber Physical System



Shubham Joshi, Radhika Joshi, and Durgesh Mishra

Abstract A cyber physical system (CPS) comprises countless geologically scattered substances, and conveyed information sharing is important to accomplish network-wide objectives. A significant concern is raised when disseminated data is shared as private data of the authorized entities might be leaked to the unofficial entities. To deploy a certain cyber physical system, we need to address priority as it has become a high priority issue. Most privacy protection methods being used only pay attention to cyberspace and ignore the real world so they alone are not sufficient to secure the cyber physical system privacy. In this paper, we sum up the ongoing examinations on the most proficient method to create control-hypothetical ways to deal with supplementing existing protection safeguarding procedures and guarantee CPS security.

Keywords Cyber physical systems · Data privacy · Distributed CPS · Privacy issues · Internet of services

1 Introduction

1.1 A Subsection Sample

Please note that the first paragraph of a section or subsection is not indented. The first paragraphs that follows a table, figure, equation, etc., do not have an indent, either.

S. Joshi (✉)

Department of Computer Engineering, SVKM's NMIMS MPSTME, Shirpur,
Maharashtra 425405, India
e-mail: shubhamjoshi@ieee.org

R. Joshi

Perception and Endeavors, Indore, Madhya Pradesh 452009, India

D. Mishra

Department of Computer Science Engineering, Sri Aurobindo Institute of Technology, Indore,
Madhya Pradesh 452011, India

Subsequent paragraphs, however, are indented.

The main aim of CPS is to monitor the actions of physical processes and activating actions for changing its nature so that it can make the physical world work better [1]. Physical process and a cyber system are two main elements of a CPS. The cyber system which is a networked system containing many small devices controls the physical process. This system contains devices having sensing, computing, and intercommunication capabilities. The physical cycle included might be a characteristic wonder or a system which is man-made or both. As CPS comprises an enormous number of topographically scattered substances and circulated information sharing is important to accomplish network-wide objectives.

In many CPS systems, security susceptibilities are found like in medical or smart transport systems, etc. So, the vulnerabilities should be considered in these systems as they are highly confident. In the field of security, most of the work aims on mapping solutions from the subsisting domains. An example of one such domain is sensor networks. This network has low capability features and it also shares networked operations with cyber physical system. The ability to interoperate among various applications is not designed by the conventional secure correspondence solutions. So while interacting with other systems, we need to make sure that system is still secure which becomes the main issue for cyber physical system. Also there are plenty other issues related to security of CPS that needs to be discussed. In this paper, we discuss some related works that are done on CPS security. Then, we give a detailed description on the general workflow of cyber physical system. We also discuss some objectives and threats faced by CPS security. Finally, we propose a security framework to solve the privacy issues faced by CPS security.

2 Related Works

2.1 A Subsection Sample

The research interests are increasing in the domain of CPS security. Here, we summarize some recent works done in this domain. Shamir's secret sharing strategy was used in the work done by Lu and Zhu in the year 2015. By using this scheme, they achieved best secrecy in the sight of semi-honest attackers. The problem of distributed optimization was solved which was based on tree topologies. Specifically, the joint calculations in an angle strategy are preoccupied as aggregate entirely calculations over the specialists' private information sources. The private input is shared to the neighbors by the agents after which iterative protocol is followed to summarize the shares from neighbors in the network. It is a fully decentralized approach and it extends the traditional shamir's scheme. Some works use homomorphic encryption to solve distributed optimization and for solving quadratic programs. Privacy preserving algorithm was proposed in some works of Lu and Zhu. This algorithm used the homomorphic scheme with a private key. Here, multiplication and addition

were implemented using different computing entities. For linear programming and optimal power flow problems, obfuscation method was applied by Borden, Wang, and Ren. Specifically crafted by Borden in 2012, it embraced confusion methods to ensure secret force system boundaries, which showed up as info lattices and vectors in the target capacity and imperatives of OPF problems. The works of Ruan likewise thought to be dynamic aggressors and utilized the method of computerized mark to empower discovery of message manufacturing or altering assaults. Other than the over two arrangements of works, all the more as of late, there arose a solitary work (Altafini 2019) utilizing an alternate strategy to accomplish similar sort of security thoughts for beginning states in normal agreement against semi-fair aggressors. Intermediate states were masked by this work as it adopted time varying output maps and is a fully decentralized approach. When the information is released, we need to check how much information of the private data is disclosed. So for this, we measure the mutual information of both private and released data. This method is used in the work of Pradhan in the year 2015, where Shannon-entropy was used to measure the equilibrium between data privacy and performance of the physical system. They also described about the stochastic control system, where data extraction and injection attacks occur. For data extraction attacks problem, an event-based common data metric was proposed by Han in 2016. In this approach, they used information entropy to measure the privacy loss. The drawback of this approach was that for source information and additional data it needed specific statistical models.

3 The General Workflow for Cyber Physical System

There are 4 main steps in the general workflow of cyber physical system as shown in Fig. 1:

- **Monitoring:** The basic role of CPS is to monitor the physical process and also the environment. Past actions of CPS also get feedback in this step. It also ensures that correct operations are performed by CPS in present and in the future.
- **Networking:** Here, data accumulation and diffusion are performed. CPS can have one or more sensors as per the requirement. Real-time data is generated by these sensors. For analyzers to operate further, the data generated is accumulated/diffused. Simultaneously, various applications interact with networking correspondence.
- **Computing:** The data accumulated during monitoring is analyzed in this step. Here, the physical process is checked on the basis of predefined criteria. So if the criteria do not match, some actions are proposed which are further executed.
- **Actuation:** Here, the actions are executed which are taken in the commuting phase. Various forms of actions are activated in this phase. The actions include altering of physical processes or rectifying the cyber nature of CPS.

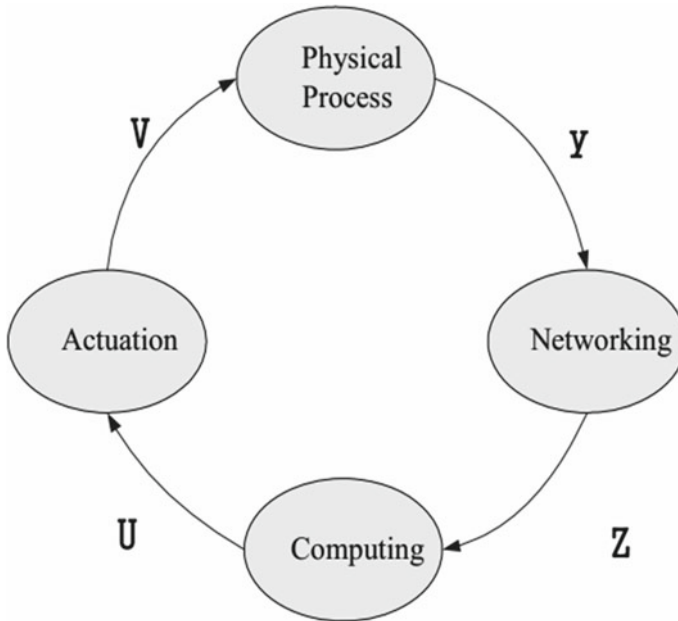


Fig. 1 Abstraction of CPS

In the following figure, ‘y’ represents the data aggregation from the sensors, ‘z’ represents the physical data aggregation in the network, ‘u’ is the computed result of the physical system states, and ‘v’ is the control commands sent to the actuators.

4 Objectives and Threats of CPS Security

The objectives include:

- **Confidentiality:** Preventing the private data from exposing in front of uncertified systems/people is known as confidentiality [2]. Like for healthcare cyber physical system, personal healthcare records are uploaded on the Internet which are sent from the record system to the doctor or the medical gadgets. So here, the system enforces confidentiality by applying encryption in the places where these records are stored like databases, etc. On the off chance that an unapproved party gets the individual medical care in any capacity, a penetration of classification has happened. Secrecy is essential (however not adequate) for keeping up the clients’ security in CPS [3]. Adversaries are prevented in cyber physical systems by using confidentiality.
- **Integrity:** Modifying the data without any authorization is known as integrity. If any adversary modifies the crucial data, then integrity gets violated. After that false

data is obtained by the receivers which they believe it to be true. Physical goals are achieved by using this objective as it prevents, detects, and blocks deception attacks on the data sent [4].

- **Availability:** Availability of service must be there when required by the system to serve its purpose. So it means that data is stored and processed by the CPS, and physical processes are performed by the physical controls. The main aim of CPS is to provide services at all times by preventing correspondence corruptions and computing which occurs due to DoS attacks, hardware/power failures, etc. [5].
- **Authenticity:** This objective aims to ensure that the correspondence, data, and transactions are genuine. It also needs to validate the parties involved are who they claim they are. It also aims to authenticate every process involved in CPS like sensing, activation, correspondence, etc.

Now, the types of security threats include

The types of attacks in CPS are as shown below in Fig. 2.

- **Eavesdropping:** Snooping alludes to the assault where a foe can capture any data imparted by the system [6]. It is considered latent assault that the aggressor does

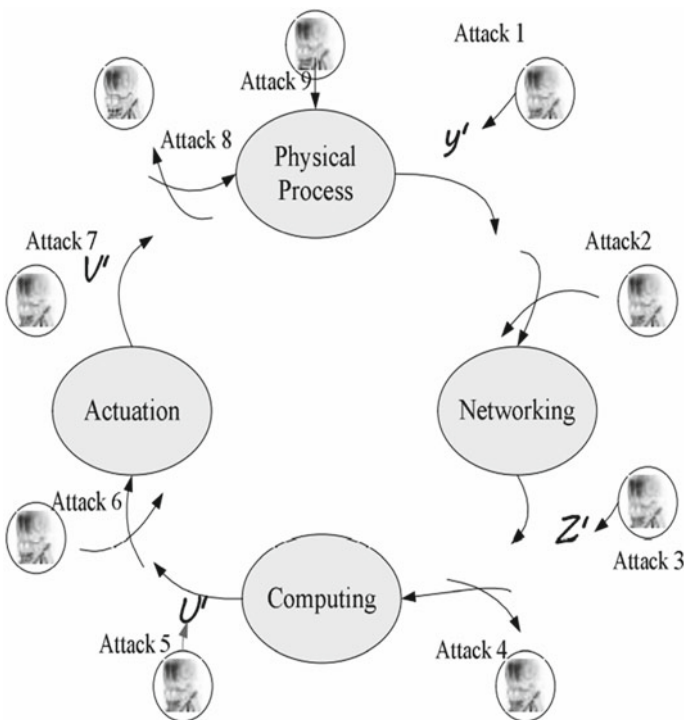


Fig. 2 Attacks

not meddle with the working of the system and just notices its activity. CPS is especially defenseless to listen in through rush hour gridlock investigation, for example, catching the checking information moved in sensor networks gathered through observing. Snooping additionally disregards the client’s protection, for example, a patient’s very own wellbeing status information moved in the system. In Fig. 2, assault 4 can address the listening in assaults on information total cycles; assault 8 can address the tapping on regulator requests.

- **Compromised key attack:** A mysterious code that is important to decipher secure data is known as a key. When an aggressor gets a key, at that point, the key is viewed as an undermined key [7]. An aggressor can access a correspondence without the view of the sender or collector by utilizing the undermined key. The aggressor can unscramble or change information by the trading off key, and attempt to utilize the undermined key to process extra keys, which could permit the assailant admittance to other got interchanges or assets. In reality, it is feasible for an aggressor to acquire a key albeit the cycle might be troublesome and asset escalation. For instance, the assailant could catch the sensors to execute a figuring out work to sort out the keys inside, which could be addressed in assault 9 appeared in Fig. 3, or the aggressor could profess to be a legitimate sensor hub to cheat to concede to keys with different sensors.
- **Man in the middle attack:** Here, bogus messages are shipped off the administrator and can appear as a bogus negative or a bogus positive [8]. This may

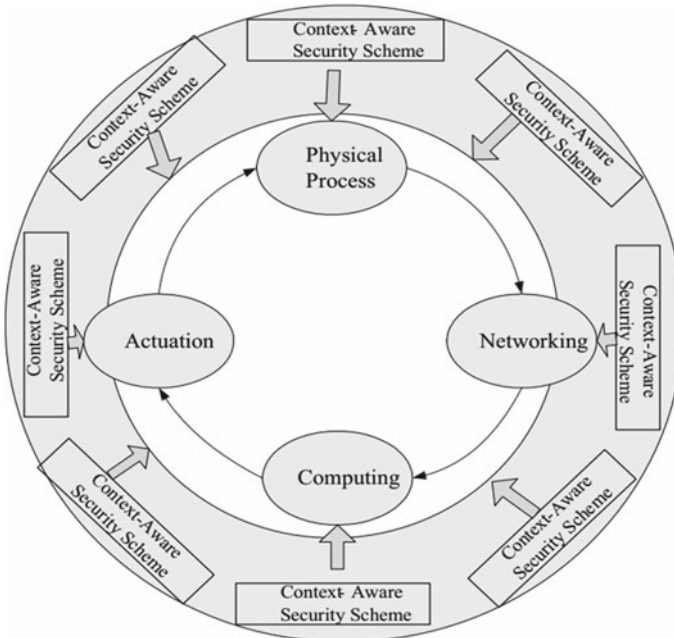


Fig. 3 The context-aware security framework

make the administrator make a move, for example, flipping a breaker, when it is not needed, or it might make the administrator think all is well and not make a move when an activity is required. For instance, in Fig. 3, assault 7 shows that the foe sends V' to demonstrate a system change, in any case, V' is not the genuine real order. At the point when the administrator follows ordinary techniques and endeavors to address the issue, the administrator's activity could cause a bothersome occasion. There are numerous varieties of the alteration and replay of control information which could affect the activities of the system. Assault 1, assault 3, and assault 5 can likewise address this sort of assault.

- **DoS Attack:** Authentic traffic is prevented by this attack and requests net resources from being progressed or retorted to by the system. Abundant amount of data is transmitted to the network by this attack so that it engages in handling the data thus denying normal services. Overall access to system resources is lost by legal entities when attacker has access to the network of CPS it can do the following:
 - Can flood the whole sensor network along with traffic
 - Send invalid information to whole network
 - Block traffic

Some characteristics of adversaries include:

- Finding vulnerabilities in software and creation of exploit code are the strengths of a skilled hacker.
- Attackers only require the understanding of the target system to gain access in the unrestricted domains to carry out cybercrimes.
- Extortion is the main motive to launch attacks on CPS for the criminal groups [9].
- Aero systems are targeted by the terrorist groups for taking down the country's cyber physical systems. They also target the power grid systems by appointing skilled coders.

5 The Proposed Framework for Security

For cyber physical system security, we propose a context aware framework for security. As shown in Fig. 3, we make context aware security schemes that are integrated into authentication, protocols, and many more security measurements. So the security mechanisms are adapted to physical domain using context coupling. This framework is called context aware security framework (CASF). A group of environmental states is known as context. It is also a setting to determine the nature of application [10]. Context is provided by different context data suppliers. There are four categories of context, namely system (like CPU, etc.), user (like location, etc.), physical environment (like temperature, etc.), and time context.

Security-based context is tackled by the proposed framework, and it contains a group of contextual attributes which are used to describe the entity's situation. It also

affects the value of the configuration of the appropriate controls that secures the data systems from uncertified access so that they cannot modify or disrupt the data as the system consists of confidentiality, availability, and integrity. So the configuration of the most appropriate controls is employed for alleviating the threats. The workflow of the proposed scheme is shown in Fig. 4. Following formula represents the proposed security framework:

$$\{\text{Security Processes}\}_{\text{Context}} \rightarrow \text{Secure Measures} \tag{1}$$

CASF is divided into 3 main parts as detailed and shown below in Fig. 5.

Sensing security: The context data should be accurate and authentic in the security configuration. So for achieving secure sensing, we use a trusted platform module (TPM) which uses a hardware component to build trusted software systems [11]. This proposed method supports trusted platform module functionality of integrating

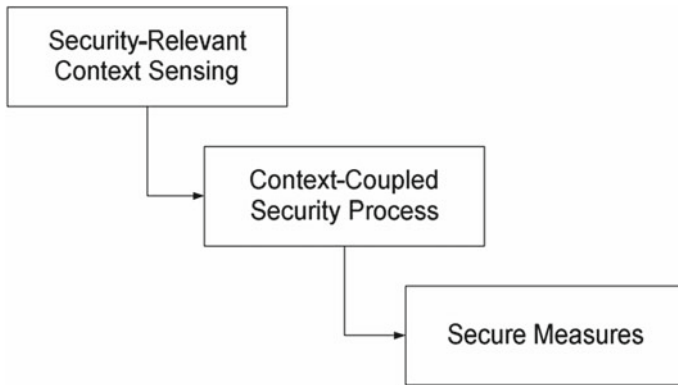


Fig. 4 Workflow of general context-aware security scheme

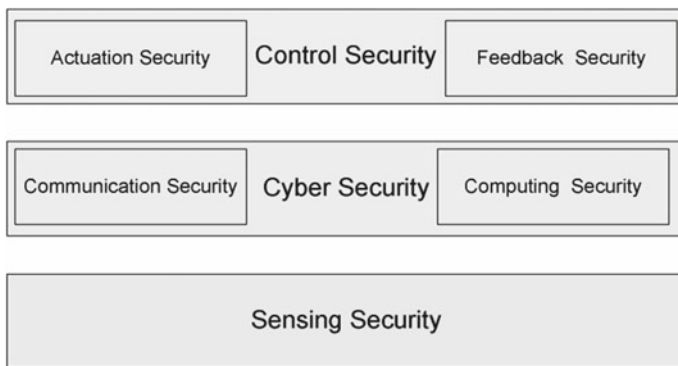


Fig. 5 Main security aspects

the remote verifier to the sensor in which the software is running. For enabling trusted boot, we use TPM. Here, every single piece of code is loaded to the boot time and is measured before loading by using cryptographic hash [12]. Security level is enhanced when we use the ARM 11 processor in which the trusted zone feature is adopted [13]. In this, the security parameters are limited to a single chip. On SoC memory is used to store the main keys and data and prevent it from the attacks. The sensor node platform consists of the following:

- External memory like SDRAM
- Transmitter
- ARM 11 chip
- Temperature sensor
- Power supply which is battery operated.

The data transmitted from the sensors to the verifiers is authenticated using secret keys. Memories and master keys along with cryptographic eliminators are embedded into the processor chip to block the possible loopholes.

Cyber Security: Both computing and control security are included in cyber security. Inter and intra cyber physical system is secured when we design context integrated correspondence protocols. This way it is secured from the active and passive adversaries.

The context aware schemes like key management, mutual authentication, and privacy protection schemes are included in it. The data accumulated and processed are stored to be accessed in the future and any tampering done to this data will lead to disruptions.

Control Security: This security is separated into 2 parts, namely actuation and feedback security. To perform activations under relevant authorization is the main aim of actuation security. As the needs of CPS change from time to time, so there are vast specifications for the authorizations. The protection of the feedbacks based on the activation effects that are provided by the control systems is ensured by the feedback security. The main focus of the security solutions is based on data security. So to defend the various attacks on cyber physical system, we need to focus more on control algorithms.

6 Conclusion

As CPS contains dispersed entities, so to achieve network-wide goals, we require distributed data sharing. Before the deployment of CPS, we need to address privacy which has become a high priority concern. So in the coming future, we need to develop more security protocols and schemes for CASF of cyber physical system. User's privacy is prevented from data stealing by privacy and encryption schemes. By using the context aware schemes, many problems are solved. For example, to solve the uncertified access problem, we use access control scheme which is context

aware. So in this paper, we talk about the data privacy issues which are faced by CPS. Then, we discuss some related works done in the field of CPS security. The general workflow of the CPS is also discussed. Then, some objectives and threats faced by the CPS security are conferred. Finally, we propose a framework to solve the issues and problems faced by CPS security.

References

1. Wan K, Man KL, Hughes D (2010) Specification, Analyzing challenges and approaches for cyber-physical systems (CPS). *Eng Lett* (3):EL_18_3_14
2. Han J, Jain A, Luk M, Perrig A (2007) Don't sweat your privacy: using humidity to detect human presence. In: *Proceedings of 5th international workshop on privacy in UbiComp (UbiPriv'07)*, Sept 2007
3. Pham N, Abdelzaher T, Nath S (2010) On bounding data stream privacy in distributed cyber-physical systems. In: *2010 IEEE international conference on sensor networks, ubiquitous, and trustworthy computing*
4. Madden J, McMillin B, Sinha A (2010) Environmental obfuscation of a cyber physical system—vehicle example. In: *Workshop on 34th annual IEEE computer software and applications conference*
5. Work D, Bayen A, Jacobson Q (2008) Automotive cyber physical systems in the context of human mobility. In: *National workshop on high-confidence automotive cyber-physical systems*, Troy, MI
6. Kao J-C, Marculescu R (2006) Eavesdropping minimization via transmission power control in ad-hoc wireless networks. In: *3rd Annual IEEE communications society on sensor and ad hoc communications and networks*
7. Chalkias K, Baldimtsi F, Hristu-Varsakelis D, Stephanides G (2009) Two types of key-compromise impersonation attacks against one-pass key establishment protocols. *Commun Comput Inf Sci* 23(Part 3):227–238
8. Saltzman R, Sharabani A (2009) Active man in the middle attacks, a security advisory. A whitepaper from IBM ration application security group
9. O'Connell K (2008) CIA report: cyber extortionists attacked foreign power grid, disrupting delivery. *Internet Bus Law Serv.* http://www.ibls.com/internet_law_news_portal_view.aspx?id=1963&s=latestnews
10. Gui F (2009) Development of a new client-server architecture for context aware mobile computing. PhD thesis, Florida International University
11. Escrypt whitepaper (2009) Trusted computing technology for embedded systems
12. Perito D, Tsudik G (2010) Secure code update for embedded devices via proofs of secure erasure. INRIA Rhône-Alpes, Technique Report
13. Yussoff YM, Hashim H (2010) Trusted wireless sensor node platform. In: *Proceedings of the world congress on engineering*, vol I. WCE 2010, June 30–July 2, London, U.K.

Classification of LPI Radar Signals Using Multilayer Perceptron (MLP) Neural Networks



Metuku Shyamsunder and Kakarla Subba Rao

Abstract LPI digital receivers play an important role in Electronics Warfare. The signals are generated for LPI radar using frequency and phase modulation techniques within the pulse. It is difficult to know the modulation parameters for ESM receivers under low signal to noise ratio conditions. Advanced signal processing algorithms are applied to extract the various modulation parameters. It is not sufficient to counter attack just by knowing the parameters. Besides modulation parameters, it is important to know the type of modulation technique. In this paper, a multilayer perceptron neural network is developed to classify the type of modulation technique under various noise conditions. The results are compared with the existing techniques.

Keywords Electronic warfare · LPI radar · Poly phase codes · Multilayer perceptron neural network

1 Introduction

The block diagram for the parameter extraction using modified S transform (MST) followed by preprocessing of the signal and then the classifier is shown in Fig. 1. Autonomous preprocessing is done based on the 2D FFT filtering. Time frequency plane obtained from MST is considered as image matrix and passed through a LPF using frequency domain filtering to remove the noise. Cropping is performed on the filtered MST TF image for the required region and to delete the no signal region. Principle component analysis (PCA) is used for reducing the dimensionality and feature extraction of the cropped MST TF image. Feature vectors are given to the classifier for the detection of modulation type.

As shown in Fig. 1, the classifier is used for the classification of five types poly phase codes frank, $P1$, $P2$, $P3$, and $P4$. Output of MST is a time frequency (TF) representation of poly phase codes. The various modulation parameters are extracted

M. Shyamsunder (✉) · K. S. Rao
University College of Engineering, Osmania University, Hyderabad, Telangana, India
e-mail: shyamsunder@osmania.ac.in

© The Author(s), under exclusive license to Springer Nature Singapore Pte Ltd. 2022
P. Kumar Jain et al. (eds.), *Advances in Signal Processing and Communication Engineering*, Lecture Notes in Electrical Engineering 929,
https://doi.org/10.1007/978-981-19-5550-1_23

233

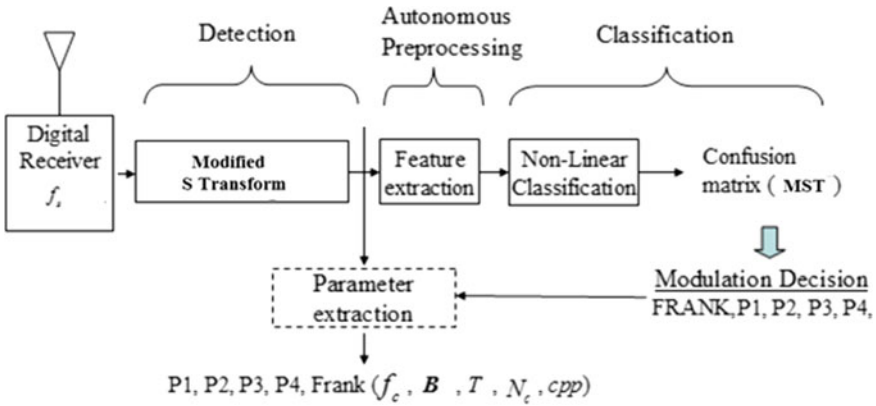


Fig. 1 Detection, parameter extraction and classification architecture

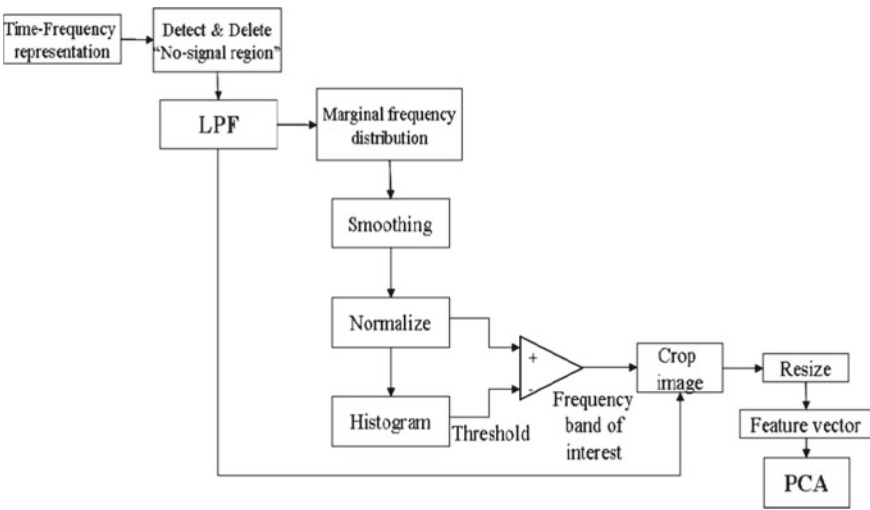


Fig. 2 T-F autonomous cropping and feature extraction algorithm

from TF plots. To classify the type of modulation, each TF plot of all the poly phase signals is assumed as images. MST images [1] under various noise conditions are preprocessed for the extraction of features. These features are used to train the neural network with multiple perceptrons and then classify the type of modulation technique.

2 Methodology

LPI signals with intra-pulse phase modulated signals are transformed into time frequency plane by using modified S transform. It is observed that energy concentration in TF plane is following different patterns for all the poly phase coded signals. To classify the type of modulation, each TF plane is assumed as image. It is also observed that energy concentration is spreading across the TF plane as noise is increased. Therefore, MST TF images need to be preprocessed to extract the features for classification.

2.1 Autonomous Preprocessing

Block diagram for preprocessing is shown in Fig. 2. The first step to crop the TF image along the frequency axis for the required bandwidth from 500 to 1500 MHz. The frequency bands of interests are shown in Fig. 3 for the TF image obtained from MST method. The selection of the region in TF image for cropping is sensitive to the noise presence. If the noise in the cropped portion of image is more, it is observed that the distortion of the signal is also more. The second step is to pass the no signal region deleted TF image through the low pass filter to reduce the noise within the required bandwidth and to get the marginal frequency distribution by accumulating the vales along the time axis.

Thresholding operation is performed on marginal frequency distribution (MFD) with minimum interference. The third step is to reduce the dimensionality of the input vector and generate a feature vector using PCA algorithm by preserving the discriminative properties. The MST TF planes are considered as images for preprocessing and classification stages. For the MST images with matrix dimensions $M \times N$ where $M = 641$ and $N = 1280$ for the signals with $f_c = 800$ MHz is taken.

2.2 Preprocessing of MST TF Images

The first step in the block diagram is to remove the no signal region or the out of interest region in both the time and frequency direction. The block diagram for removing the unwanted region is shown in Fig. 4 [2].

The MST image representation of a Frank code for $f_s = 6.4$ GHz, $f_c = 800$ MHz, $N_c = 16$, and $\text{cpp} = 2$ ($B = 400$ MHz) with a SNR of 0 dB is shown in Fig. 5. Figure 5a shows input MST image, and Fig. 5b shows removal of unwanted region.

After no signal region is deleted, the TF image is passed through a low pass filter to remove the noise component present in the high frequency regions. Assuming that energy is preserved in the low frequency regions. The filtering process is done in

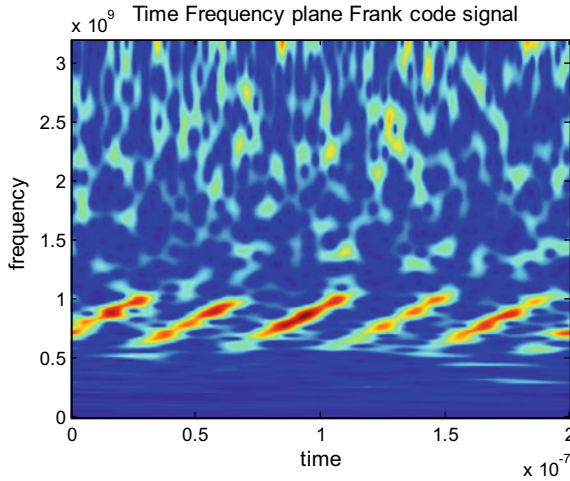


Fig. 3 The frequency bands of interests for the output of MST

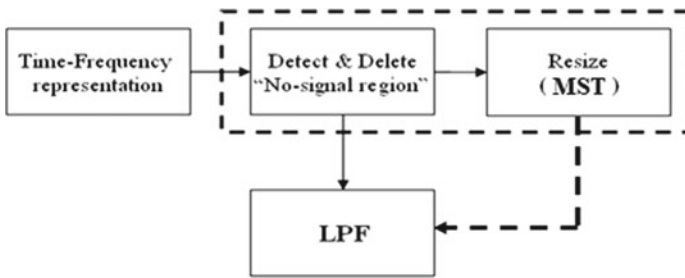


Fig. 4 Detect and delete "No-signal region" block

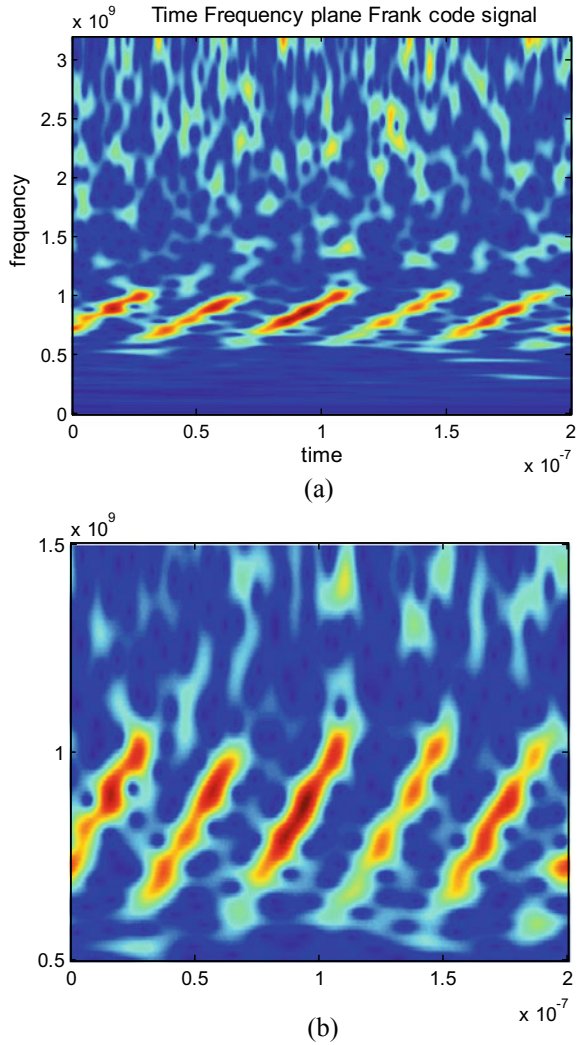
frequency domain [3] using 2D DFT. The 2D discrete Fourier transform (2D DFT) is explained briefly in the following section and frequency domain filtering. Due to small dimensions (201×1280) of MST images compared to original images, they are resized to their original size before applying to filter.

2.3 The 2D DFT and Frequency Domain Filtering

The block diagram for filtering in frequency domain is shown in Fig. 6. An ideal low pass filter has the transfer function

$$H_d(u, v) = \begin{cases} 1 & \text{if } D(u, v) \leq D_0 \\ 0 & \text{if } D(u, v) > D_0 \end{cases} \quad (1)$$

Fig. 5 **a** Input TIF image, **b** output image with unwanted region removal



where D_0 is cutoff parameter for given positive value, $D(u, v)$ is the distance from center of the filter to the point (u, v) . D_0 is defined as the normalized value of ω_1, ω_2 by π . Next, a 2D Gaussian window with standard deviation (SD) of σ is obtained

$$\sigma = N \times \frac{D_0}{8} \tag{2}$$

where N is represents the columns in image. The structure of the filter becomes adaptive to the desired frequency response variation due to σ is related to D_0 .

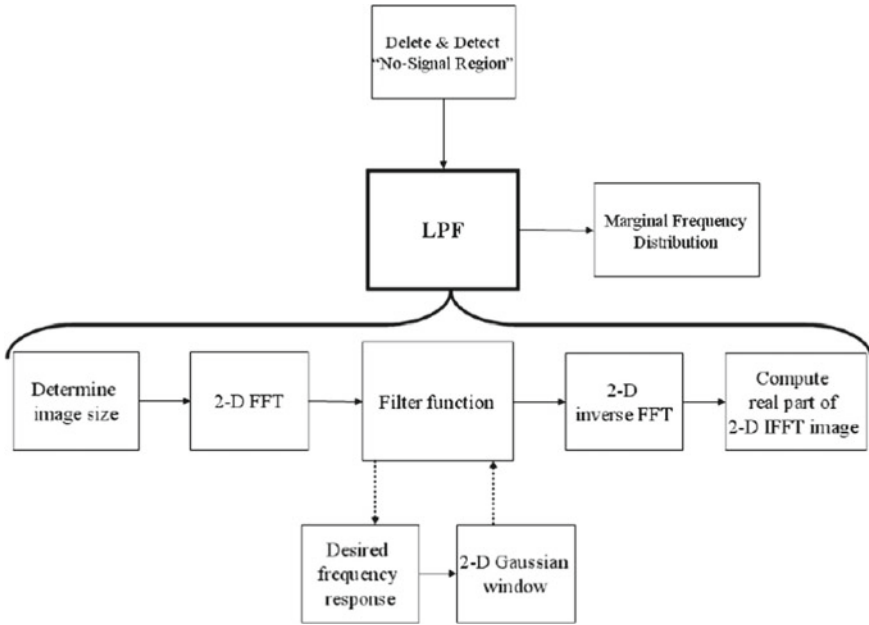


Fig. 6 Frequency domain filtering operations

Frequency response with $D_0 = 0.4696$, $\omega_1 = 0.2353\pi$, and $\omega_2 = 0.4696\pi$ is shown in Fig. 7a. Gaussian window for $\sigma = N \times \frac{D_0}{8}$ is shown in Fig. 7b. Figure 7c shows mesh plot of Gaussian low pass filter, and Fig. 7d shows top view of low pass filter.

Figure 8a shows the output of frequency domain filtering for Fig. 5b. Figure 8b shows frequency components decentering Fig. 8c 2D inverse FFT.

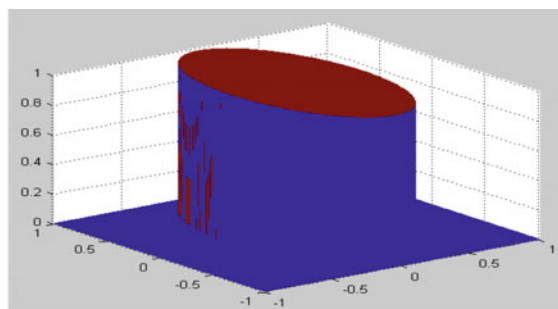
Generation of Feature Vector The method of cropping and generation of feature vector is shown in Fig. 9.

The output of LPF, image after cropping, and contour plot of signal energy shown in Fig. 10a–c, respectively.

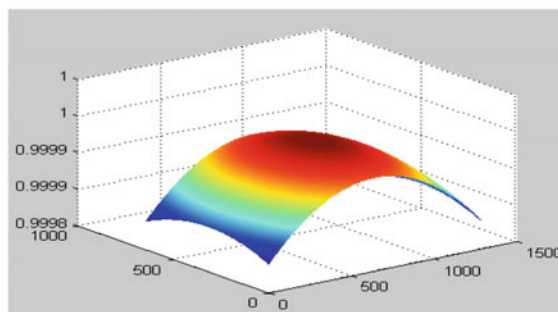
3 Principal Components Analysis

PCA is one of the dimensionality reduction algorithm used to reduce the class features. It reduces the size of the input data matrix using projection matrix to represent the data in mean square sense [4]. Eigenvectors obtained from data covariance matrix are used to represent a data in PCA. Higher dimensional vectors are projected on to dominant eigenvectors to get the lower dimensional vector [5]. The PCA algo-

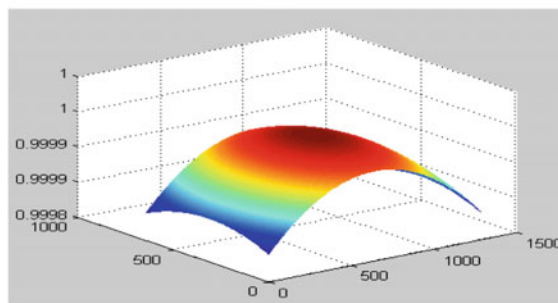
Fig. 7 Filter function implementation **a** $H_d(u, v)$, **b** Gaussian window, **c** mesh plot of Gaussian low pass filter, **d** top view of Gaussian low pass filter



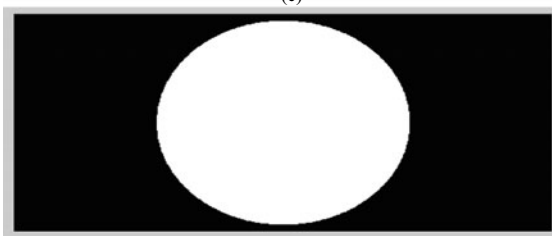
(a)



(b)



(c)



(d)

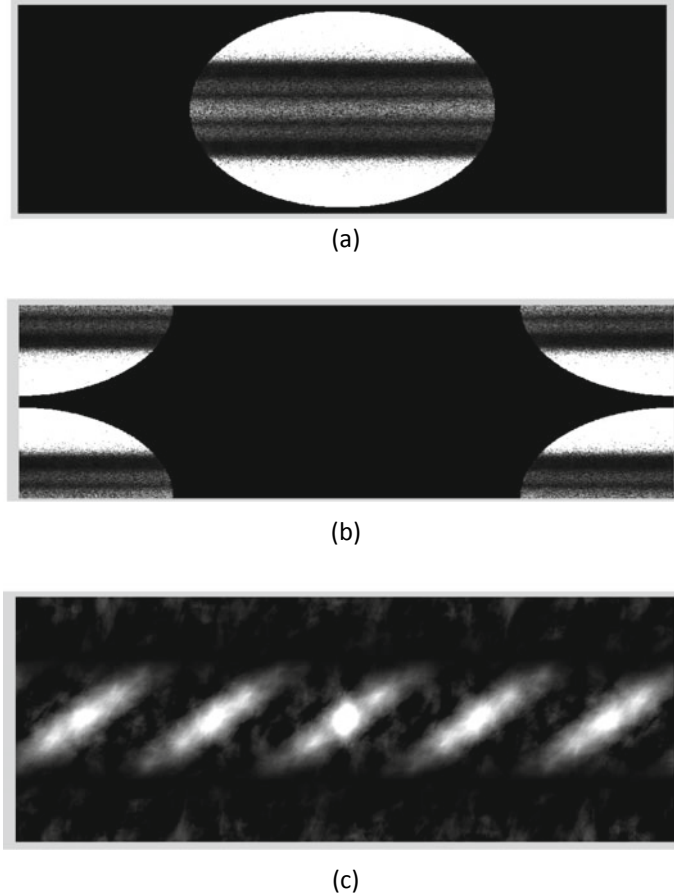


Fig. 8 **a** Filtering in frequency domain, **b** shift back of frequency response, **c** 2-D IFFT output

rithm maps P N -dimensional vectors onto the P -dimensional vectors for with linear transformation. Linear transformation is obtained by matrix A so that

$$Y = A^H X \quad (3)$$

where A has orthogonal column vectors and H is Hermitian operation. The transformed data vectors Y have uncorrelated components with a choice of transformation matrix A [5]. The PCA algorithm is applied to the training signals consists of various modulation types with different signaling condition. The cropped images are resized to a common dimension where any type of signal can be applied and processed for classification. The resized matrix columns are stacked together to get column vector to represent features of one signal. Process is repeated for all the signals in the training set and forms a feature matrix. Mean is calculated for each column and subtracted

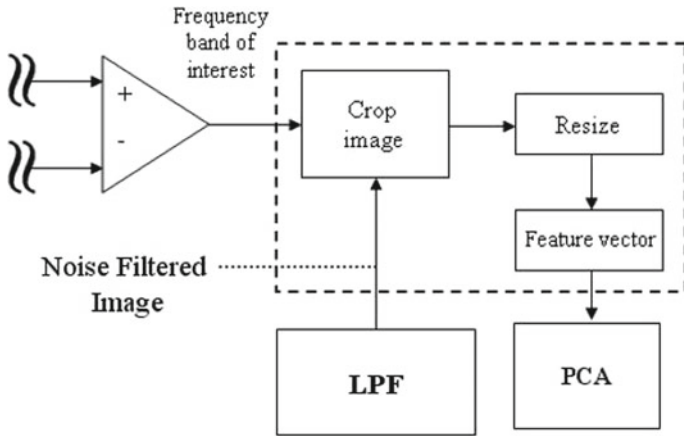


Fig. 9 Feature vector generation block set

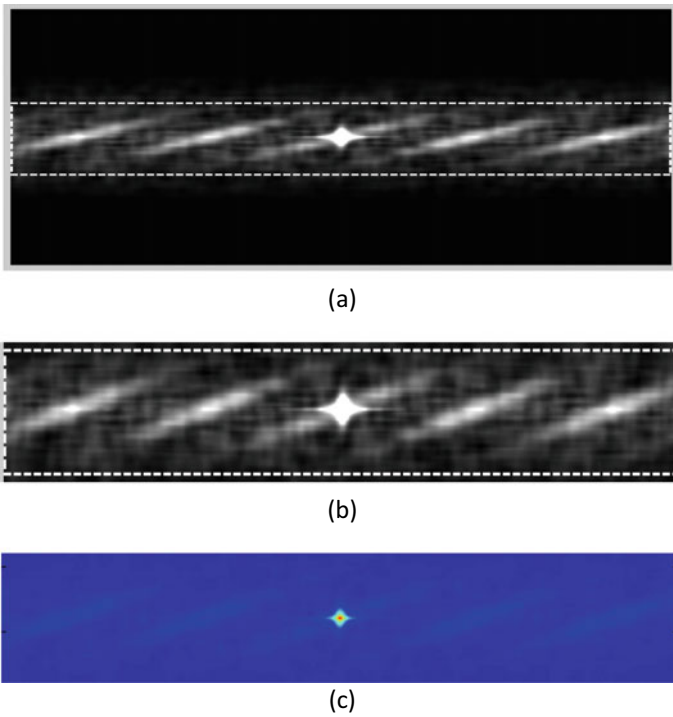


Fig. 10 a Output of LPF, b wanted region, c contour plot of required region

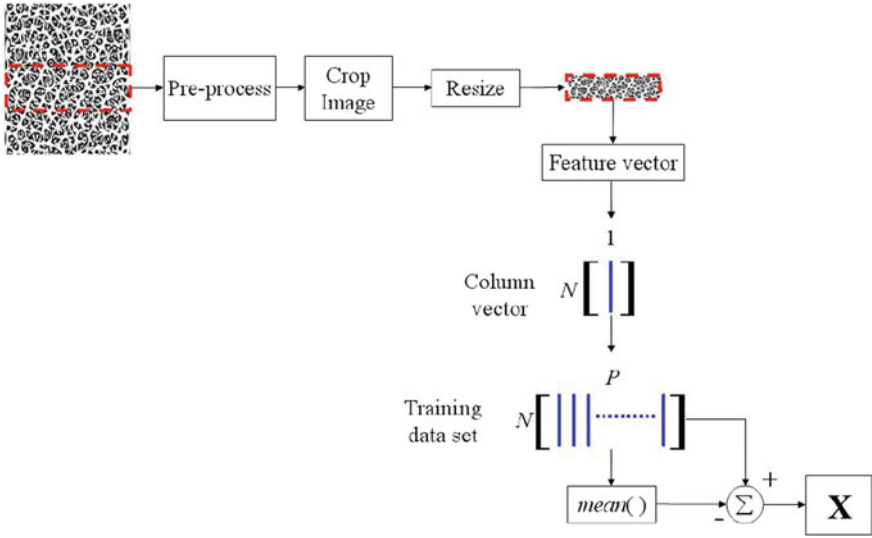


Fig. 11 Generation of training matrix (From [4])

from the data set to get X is shown in Fig. 11, where P is the size of training set and N is feature vectors length. For MST TF image, the X is of dimension 86×1280 for signals with $f_c = 800$ MHz. The method singular value decomposition (SVD) states that matrix X is decomposed as

$$X = U \sum V^H \tag{4}$$

where U and V are unitary square matrices with dimensions N, P , respectively, and \sum is non-negative real singular values matrix. Note that

$$X^H X = V \sum^H (U)^H U \sum V^H = V \left(\sum \sum \right) V^H \tag{5}$$

Equation (5) indicates the eigenvectors of $X^H X$ and XX^H are contained V, U matrices, respectively. If $p = \min(P, N)$, XX^H and $X^H X$ have same eigen values [7]. The XV product gives

$$XV = U \sum V^H V = U \sum \tag{6}$$

since V is unitary, eigenvectors associated with non-zero eigen values are obtained by

$$U = XV \sum^{-1} \tag{7}$$

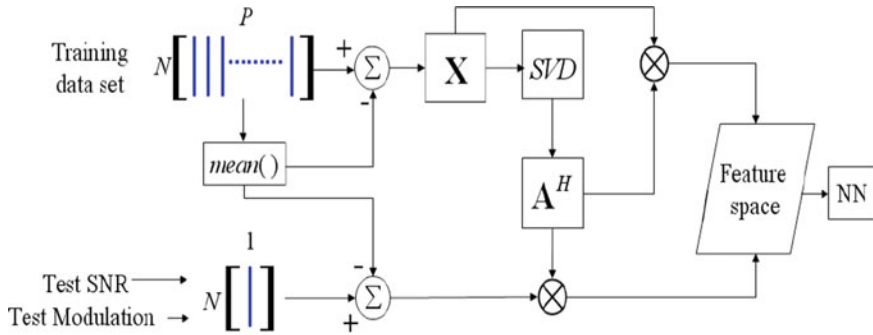


Fig. 12 PCA algorithm (From [4])

As a result, eigen values of the covariance matrix XX^H are computed by calculating SVD of the covariance matrix $X^H X$ [8]. After getting the eigenvector matrix U and eigen values from the input data matrix X using the SVD, the transformation matrix A is obtained from the U using the largest eigen values. In order to find the largest eigen values, optimum values of eigen value threshold constant Th_λ and eigenvector are chosen. Let eigenvector

V_i , with $i = 0, 1, 2$, and 3 are given as

$V_0 \rightarrow$ All eigenvectors corresponding to eigen values above Th_λ .

$V_1 \rightarrow$ All eigenvectors corresponding to eigen values above Th_λ except the eigenvectors corresponding to eigen value with highest value.

$V_2 \rightarrow$ All eigenvectors corresponding to eigen values above Th_λ except eigenvectors correspond to two eigen values.

$V_3 \rightarrow$ All eigenvectors corresponding to eigen values above Th_λ except three eigenvectors corresponding to three eigen values with highest.

Training and testing signals are projected on to matrix A to get a lower dimensional feature vectors with size $D \times 1$ for one signal. All such signals form a $D \times P$ matrix and given as input to MLP neural network for the classification.

The MATLAB functions to perform PCA [4] implemented in the classification routines. The PCA algorithm is shown in Fig. 12.

4 Classification Network

In the present work, a feed-forward neural network (NN) is considered for classification as shown in Fig. 13. The no. of neurons in the output layer depends on number of output classes. The work is focused on poly phase modulated signals with 5 types.

Multiple values of neuron numbers for hidden layer are considered. Regularization is used to improve the network generalization. The regularization performance R is measured using

$$R = gM_{SE} + (1 - g)M_{SW} \tag{8}$$

where

- g performance ratio ($g = 0.7$)
- M_{SW} mean sum of squares of network weights
- M_{SE} mean sum of squares of the network errors. For each of the training set, more training iterations are performed to find an optimum value.

5 Results and Discussion

A total of 270 signals are used with carrier frequencies 800 MHz, 1000 MHz, 1200 MHz and with SNR values from 0 to -7 dB for Frank, $P1$, $P2$, $P3$, $P4$ coded LPI signals. Out of the 270 signals, 188 signals are used for training, 41 signals for validation, and remaining 41 signals used for testing. Confusion matrices (CM) are computed for the classification test of each SNR level.

5.1 Optimization of MLPNN

To train the network, the initializations are done for following parameters of classifier.

- Epochs
- Eigenvalue selection threshold constant Th_λ
- Neurons in the hidden layer S_1
- Eigenvector selection variations V_i .

Network is trained with more number of iteration with respect to average probability of correct classifications. Once the required performance is achieved, the network is used to test the unknown modulation type signal.

For classification of MST images, the initial values taken are $TH_\lambda = 0.1$, epochs = 1000 and $S - 1 = 5$. Figure 14 shows the average probability of correct classification (Pcc) results for multiple eigen values. The hidden layer variations are shown in Table 1.

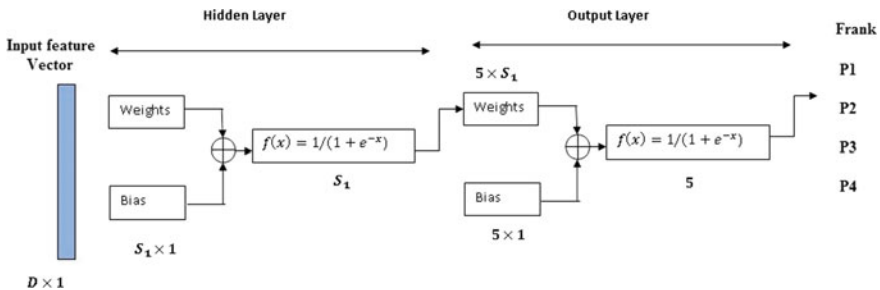


Fig. 13 Two-layer PNN

Table 1 Multiple values of neuron numbers in the hidden layers

*HLM	1	2	3	4	5	6	7	8	9	10
*S1	5	10	15	20	25	30	35	40	45	50

Table 2 Optimum values of MST image classification using MLPNN

S_1	TH_λ	V_i	Epochs
20, 25	0.1	v_1	1000

*HLM: Hidden Lauer Model, *S1: number of neurons As shown in Fig. 14, the hidden layer model 4 and 5 gave the optimum result with $S_1 = 20$ and 25, $TH_\lambda = 0.1$, and V_1 given in Table 2.

The CMs are presented in Tables 3, 4, 5, and 6 for SNR values of signal only condition, 0 dB, -4 dB, and -7 dB, respectively.

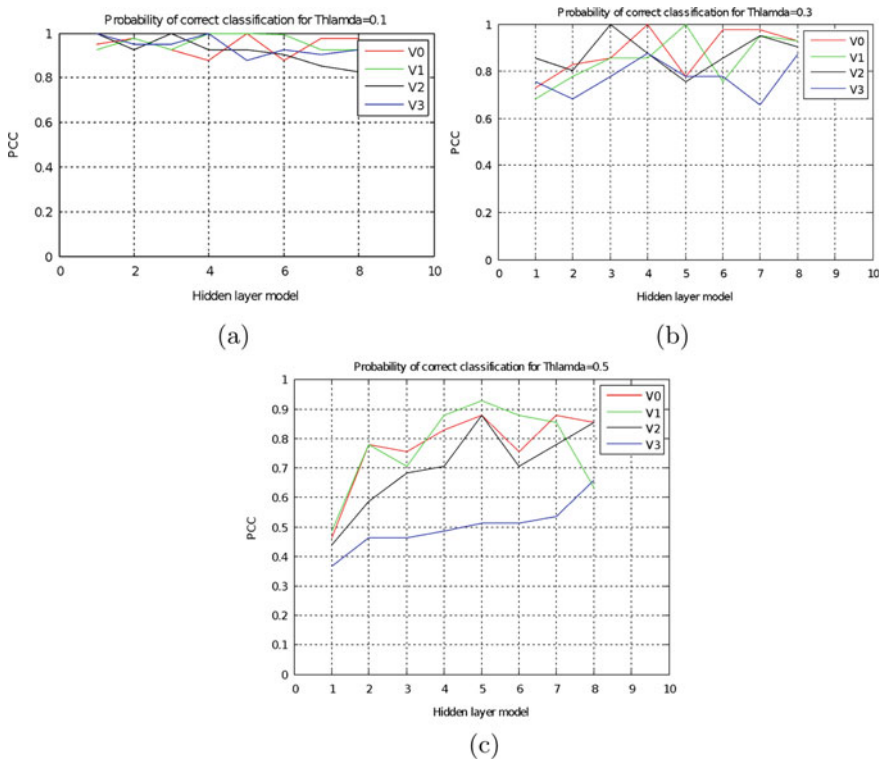


Fig. 14 Optimization of S_1 , TH_λ , and V_i for MST image classification with MLPNN

Table 3 Confusion matrix (signal only condition)

Test	$f_c = 800\text{ MHz}$				
SNR	Frank	$P1$	$P2$	$P3$	$P4$
Frank	0.99	0	0	0	0
$P1$	0	0.99	0	0	0
$P2$	0	0	0.99	0	0
$P3$	0	0	0	0.99	0
$P4$	0	0	0	0	0.99

Table 4 Confusion matrix (SNR = 0 dB)

Test	$f_c = 800\text{ MHz}$				
SNR	Frank	$P1$	$P2$	$P3$	$P4$
Frank	1.00	0	0	0	0
$P1$	0	1.00	0	0	0
$P2$	0	0	1.00	0	0
$P3$	0	0	0	0.99	0
$P4$	0	0	0	0	1.00

Table 5 Confusion matrix (SNR = -4 dB)

Test	$f_c = 800\text{ MHz}$				
SNR	Frank	$P1$	$P2$	$P3$	$P4$
Frank	0.99	0	0	0	0
$P1$	0	1.00	0	0	0
$P2$	0	0	0.99	0	0
$P3$	0	0	0	0.99	0
$P4$	0	0	0	0	0.99

From the tables, it is observed that MLP NN with the optimum value given in Tables 1 and 2, all signals with carrier frequency $f_c = 800\text{ MHz}$ are classified with 99% accuracy. The work carried out by Ravikishore et al. [9] for automatic intrapulse modulation classification using fractional Fourier transform is able to classify the poly phase signal up to signaling conditions of -2 dB SNR. The results obtained are compared in the Table 7.

Table 6 Confusion matrix (SNR = -7 dB)

Test	$f_c = 800$ MHz				
	Frank	<i>P1</i>	<i>P2</i>	<i>P3</i>	<i>P4</i>
SNR	Frank	<i>P1</i>	<i>P2</i>	<i>P3</i>	<i>P4</i>
Frank	0.99	0	0	0	0
<i>P1</i>	0	0.99	0	0	0
<i>P2</i>	0	0	0.99	0	0
<i>P3</i>	0	0	0	1.00	0
<i>P4</i>	0	0	0	0	0.99

Table 7 Comparison of performance measurement for classification using MLPNN

Modulation type	Proposed method	Existing technique	Proposed method	Existing technique
	SNR (dB)	SNR (dB)	Correct classification (%)	Correct classification (%)
Frank	-7	-2	99	95
<i>P1</i>	-7	-2	98	95
<i>P2</i>	-7	-2	99	95
<i>P3</i>	-7	-2	99	95
<i>P4</i>	-7	-2	99	95

6 Conclusion

An algorithm for image cropping and feature extraction using 2D FFT and PCA is developed. MLPNN is described as non-linear. The simulation results of the classification network are presented. MLPNN is used as the non-linear classifier for classifying the type of modulation. The results indicate that the classification success rate is 99%. Hence, this method could be used to classify the type of modulation in real time.

References

1. Shyamsunder M, Rao KS (2017) Time frequency analysis of LPI radar signals using modified S transform. Int J Electron Eng Res 9(8):1267–1283. ISSN 0975-6450
2. Gulum TO, Pace PE (2008) Time-frequency feature extraction for classification of LPI radar modulations using principal components analysis. In: 2008 IEEE international conference on acoustics, speech and signal processing
3. Zilberman ER (2006) Autonomous time-frequency cropping and feature extraction algorithms for classification of LPI radar modulations. Master’s thesis, Naval Postgraduate School, Monterey, CA
4. Fargues MP (2001) Investigation of feature dimension reduction schemes for classification applications. Naval Postgraduate School, Monterey, CA, NPS-EC-01-005, June 2001

5. Gonzales RC, Woods RE, Eddins SL (2004) Digital image processing using Matlab. Prentice Hall, Upper Saddle River, NJ
6. Therrien CW (1991) Discrete random signals and statistical signal processing. Prentice Hall, Englewood Cliffs, New Jersey
7. Lee CK (2004) Infrared face recognition. Master's thesis, Naval Postgraduate School, Monterey, California
8. Oppenheim AV, Willsky AS, Nawab SH (1997) Signals and systems. Prentice Hall, Upper Saddle River, NJ
9. Ravikishore T, Dheerga Rao K (2017) Automatic intra-pulse modulation classification of advanced LPI radar waveforms. IEEE Trans Aerosp Electron Syst 53(2)

A Systematic Review on Screening of Diabetic Retinopathy and Maculopathy Using Artificial Intelligence



Aida Jones, Thulasi Bai Vijayan, Sadasivam Subbarayan, and Sheila John

Abstract Diabetes mellitus is a condition that occurs when the glucose level in the blood goes high. The eye-related issues due to diabetes may include diabetic retinopathy and diabetic maculopathy. It also includes conditions such as Glaucoma and Cataracts. All these conditions can steer toward poor vision and blindness. Artificial intelligence (AI) is the latest methodology used for eye image analysis. It is all about intelligent programming with the help of intelligent algorithms that make intelligent machines do what a human does. Machine learning and deep learning techniques are subtypes of AI. In this paper, we have summarized the findings of studies that have detected diabetic retinopathy and diabetic maculopathy using various AI methods.

Keywords Diabetic retinopathy (DR) · Diabetic maculopathy (DM) · Diabetic macular edema (DME) · Fundus images · Teleophthalmology · Machine learning (ML) · Deep learning (DL)

1 Introduction

The retina is a tissue that is light sensitive on the inside of the eye that lines its posterior end. The retina sends light on which the lens is focused to the brain for visual perception after converting the light into neural signals [1]. The macula is the core of the retina that provides the central vision. It also gives high resolution and color vision. It is around 5.5 mm in diameter in human beings. The macula is normally yellow. It acts as a sunblock to that area. The core of the macula is called the fovea.

A. Jones (✉) · T. B. Vijayan · S. Subbarayan
Department of Electronics and Communication Engineering, KCG College of Technology,
Chennai 600097, India
e-mail: aidajones89@gmail.com

S. John
Department of Teleophthalmology, Sankara Nethralaya Eye Hospital, Chennai 600006, India

Diabetic retinopathy is a condition where the blood vasculature on the retina of diabetic patients gets blocked or damaged [2]. Diabetic macular edema is a menace for vision. A person suffering from diabetic retinopathy is at high risk to suffer from macular edema. This condition is called diabetic maculopathy. For this reason, many non-invasive tools have been developed for various eye diseases [3]. Conjunctivitis can also cause the retinal disorder. This is another such issue to be kept in mind while screening retina. A person can also become anemic due to eye disorders [4].

2 Image Analysis

The commonly used images for examination are OCT and CFP. Some of the traditional methods used for image analysis are object segmentation, classifiers for identifying objects on each segment, image classification, and so on. On using so many classifiers, the computation becomes more expensive, consumes more time, and practically requires more skilled people. This makes it clear that the traditional methods are inefficient [5].

To combat these issues, AI methods [6–8] such as artificial neural networks (ANN) and convolutional neural networks (CNN) are used.

2.1 *Artificial Neural Networks (ANN)*

Neural networks were created based on the human brain. Every neuron of a neural network layer is coupled to every other neuron. And each neuron is activated with a weight based on the training data. When one neuron is activated, it triggers another neuron. Neural networks are categorized into several types. They are feed-forward neural networks, recurrent neural networks, and propagation neural networks. And the most commonly used feed-forward network is a multilayer perceptron [9].

2.2 *Convolutional Neural Networks (CNN)*

CNN is a type of ANN used for the detection of patterns. Pattern recognition is used for the analysis of images. A CNN [10] will have non-convolutional layers also, but the main factor of CNN is convolutional layers. The convolutional layers may also be called hidden layers. The first layer of the convolutional layers will receive the input from the input layers. The received input on the convolutional layer undergoes some transformation, and this transformed information is transferred to the next layer. This transformation is nothing but a convolutional operation. CNNs are formed of a variety of filters such as edge detection filters, object detection filters, texture detection filters, circle detection filters, corner detection filters, shape

detection filters, square detection filters, etc. The number of filters used is to be mentioned during the formation of the layer. The deeper the complexity of the filters go, the more sophisticated the layers will be [11].

3 Methods to Overcome Inadequate Dataset

Instead of training a blank network, a feed-forward method is used in the lower levels to fix the weights. These levels recognize the composition found in the images. The weights of the upper level are retrained by using the back-propagation method. This model can perceive the features of the images which may be of any category. Thus, transfer learning is an algorithm that is used to process medical-related images. It can provide accuracy and prompt diagnosis of the defects found in the images. The advantages of this method are giving faster results and making use of fewer images for training, and the computational power used is less.

Another method to combat inadequate datasets is data augmentation. The different techniques of data augmentation include parallel and perpendicular tossing, spinning, reverse color, translation, and external and internal scaling. Noises such as Gaussian noise, random noise, salt and pepper noise, changes in the hue, contrast, opalescence, color, or contour, filtering, clipping, i.e., random shearing, partial concealing, i.e., cut out and random erasing, exchange background, and many more [12].

4 General Methodologies

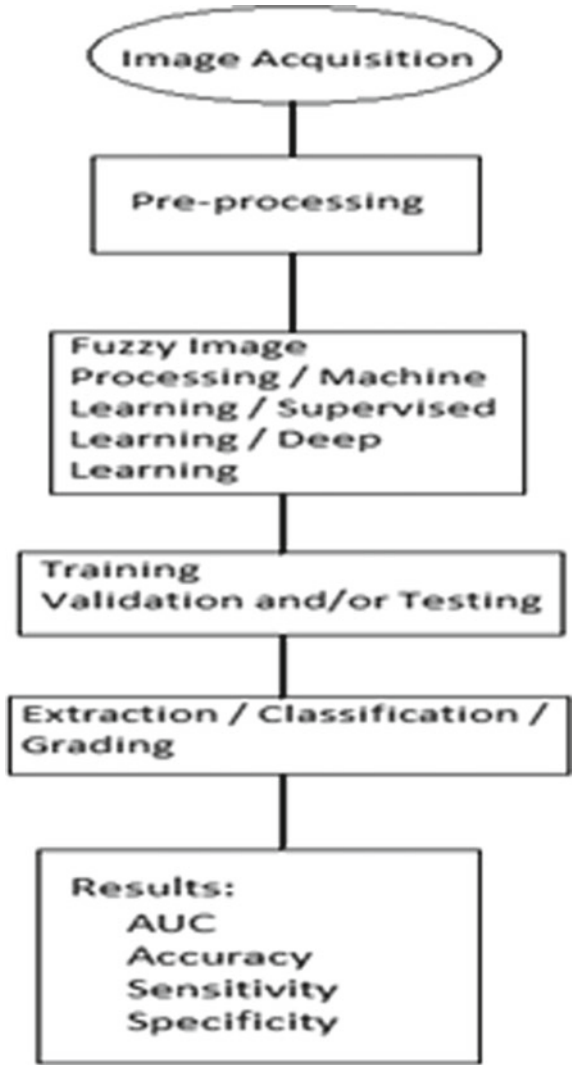
The general procedure in the existing methodologies for detecting diabetic retinopathy and diabetic maculopathy is image acquisition, preprocessing, AI algorithm-based training and testing, disease classification, and determining result efficiency as shown in Fig. 1.

In previous works, it has been discussed that deep learning is the most sought-after research area in computer algorithms and image processing. DL makes use of several neural networks where CNN has been mostly employed for image classification, object detection, and segmentation. DL techniques help in providing accuracy. It provides better sensitivity by detecting tiny vessels.

Also, it is discussed in earlier works that with the discernment of the placement of the optic disk, the fovea center can be determined. The fundus images were subdivided into several quarters of the eye. Localization has been done in several stages [13].

A paper on DME severity [14] has been proposed that deals with the spatial distribution of exudates around the macular region. The macular region has been divided into several zones. The DME is graded as per the presence of the amount of exudates in each zone. The exudates were detected based on the following methods:

Fig. 1 General procedure for disease detection



Foreground extraction, candidate detection, and exudate candidate selection. Once the optic disk is suppressed as it gave a false alarm, the DME was graded.

Certain limitations of the application of AI in the medical field have been discussed [15]. One of them is that the physicians would lose the ability of their skills by not making informed decisions and suggesting opinions. One more problem is that the psychological and the social aspects of the nature of the patients are not considered which drastically may affect the reliability of the results. Also, this technology may replace the need for a physician. However, it is to be considered that this is nothing but a technology-driven advanced tool for the assistance of the physicians.

Other than studies related to AI in detecting the diseases, there are also works considering other factors. One such important factor to be considered in the detection of DR and DM is the deficiency of Vitamin D. Generally, there is a pathological process known as vascularization of blood vessels in normal people which is a very normal thing. But in diabetic patients, a process called neovascularization occurs which is nothing but an abnormal growth in blood vessels. This abnormal presence of neovascularization occurs in diabetic patients with Vitamin D deficiency, hence will exhibit diabetic retinopathy and diabetic maculopathy in the retina and macula, respectively [16–19].

In this review, we have abstracted studies on the detection of DR and DM using image processing, ML, DL, and supervised learning techniques which are subtypes of AI in Table 1.

5 AI in Teleophthalmology

The estimated number of ophthalmologists in 194 countries around the world was 232,866 in 2015 [20]. In India, which is a developing nation, the ophthalmologist-patient ratio stands poor at 1: 10,000. About seventy percent of the citizens inhabit rural areas while seventy percent of its eye care professionals inhabit urban areas; this brings a daunting task to the medical fraternity to deliver eye care to patients in rural areas. Atul Kumar et al. [21] says that over the past years, it has been seen that there is a rapid decrease in the blindness caused. There is a vast reduction in the number of partially sighted folks in India. It is diminished to nearly 34 million compared to WHO evaluation of 62 million in 2010. In 2020 and later, it is expected to decrease even further with the help of newer research technologies. Opportunities such as remote monitoring, teleconsultation with medical providers, optometric or ophthalmologic providers, and consumer home monitoring are all the scope of Telemedicine [22]. In the USA, a retail health clinic known as CarePortMD has been started and set inside Albertsons grocery stores. CarePortMD is an AI screening method for diabetic retinopathy [23]. The aim was to provide a retail setting. Similarly, as India is a developing country, advanced technologies can be developed and implemented to serve society better.

6 Discussion

In a population where people have no knowledge about their eyes getting affected due to diabetes, teleophthalmology comes to its aid. Most of the times the patient would have been too late to be treated. We would like to suggest that with the help of AI in teleophthalmology, screening the diseases, and preventing vision loss may be possible at an early stage itself. Teleophthalmology can provide clinical accuracy at a great level for screening of DR and DM while refining patient access in an

Table 1 Studies on diabetic retinopathy and diabetic maculopathy

Reference	Dataset	Technique	Method	Results
Kuwayama et al. [12]	OCT images Normal—570 Wet AMD—136 DR—104 ERM—90 Others—19	Deep learning	Vogt-Koyanagi-Harada detected by Image augmentation in CNN training	Response to doctors decision: First candidate disease—83% of images Second candidate disease—7% of images Type Normal Wet AMD DR ERM Precision 0.85 1 0.78 0.75 Recall 0.97 0.77 1 0.75
Lee et al. [29]	1289 OCT images	CNN	Data augmentation, Smoothed dice coefficient	Detection of Intra-retinal fluid
Lee et al. [30]	EMR and OCT images Type: Normal—52,690 AMD—48,312	Deep learning technique -occlusion test to verify	<ul style="list-style-type: none"> – OCT database linked to EMR – 11 images selected from each OCT scan – DNN training to categorize normal or AMD 	Image level Macula level Patient-level Peak sensitivity Specificity AUC: 92.78% Accuracy: 87.63% AUC: 93.83% Accuracy: 88.98% AUC: 97.45% Accuracy: 93.45% 92.64% 93.69%
Ashok Kumar et al. [31]	Non dilated low contrast fundus images	Fuzzy C-means algorithm (FCM) Image processing	<ul style="list-style-type: none"> – Preprocessing – Feature extraction – GLCM Classifiers such as FCM and cascade neural network	Evaluation Specificity Sensitivity Accuracy CNN 96% 90% 97% FCM 98% 96% 99%
Zheng et al. [32]	ImageNet and Messidor 2 dataset	Deep learning, transfer learning, tenfold cross-validation	Image categorization (Grading), labeling, preprocessing (cropping, CLAHE, and de-noising)	Specificity—93.45% Sensitivity—96.93% Accuracy—93.49% AUC—0.9905

(continued)

Table 1 (continued)

Reference	Dataset	Technique	Method	Results
Ren et al. [33]	46 images from STARE and 40 images from DRIVE database	Supervised feature learning	Generalized low-rank approximation of matrices and supervised manifold regularization	Stare Specificity—97.06% Sensitivity—90.03% Accuracy—96.92% Drive Specificity—94.93% Sensitivity—87.41% Accuracy—94.81%
Gargeya et al. [34]	EyePACS, E-Ophtha, and Messidor 2 dataset	Deep learning, transfer learning, fivefold cross-validation	Preprocessing, DL layers, and gradient boosting classifier	AUC—0.97 Sensitivity—94% Specificity—98%
Nagasawa et al. [35]	378 photographic ultra-wide-field fundus images	VGG 16 deep convolutional neural network, K fold validation	Preprocessing and DL layers	AUC—0.969 Sensitivity—94.7% Specificity—97.2%
Pratt et al. [36]	80,000 images	CNN	Data augmentation and stochastic gradient descent with Nesterov momentum	Sensitivity—95% Accuracy—75%
Li et al. [37]	13,673 fundus images	Deep learning	Preprocessing, DR grading annotation, Pixel-level annotation, and Bounding-box generation	High Sensitivity and Specificity (> 90%)
Sahlsten et al. [38]	41,122 graded retinal color images	Deep learning – Inception v3	Grading, classification and Clopper–Pearson method	AUC—0.987 Sensitivity—0.896 Specificity—0.974

economical and ascendable process. It can be carried out in remote areas which can expand the figure of patients who will be screened and protecting patients' vision through timely diagnosis and therapy. Pooled results can help in comparative studies as well as maintaining statistical data. A device such as a smartphone may also be used with AI as a cost-effective method. It may be used as a handheld device or fit into a slit lamp. Thus AI-based detection through Telemedicine makes ophthalmology economical and accessible to the underprivileged [24–28].

References

1. Soomro TA, Afifi AJ, Zheng L, Soomro S, Gao J, Hellwich O, Paul M (2019) Deep learning models for retinal blood vessels segmentation: a review. *IEEE Access* 7:71696–71717
2. Interpretation of stereo ocular angiography: retinal and Choroidal Anatomy 2104 project Orbis international. archived from the original on 19 December 2014 Retrieved 11 October 2014
3. Muthalagu R, Bai VT, Gracias D, John S (2018) Developmental screening tool: accuracy and feasibility of non-invasive anaemia estimation. *Technol Health Care* 26(4):723–727
4. Kasiviswanathan S, Bai Vijayan T, Simone L, Dimauro G (2020) Semantic segmentation of conjunctiva region for Non-Invasive Anemia detection applications. *Electronics* 9(8):1309
5. Kermany DS, Goldbaum M, Cai W, Valentim CC, Liang H, Baxter SL, McKeown A, Zhang K (2018) Identifying medical diagnoses and treatable diseases by image-based deep learning. *Cell* 172(5):1122–1131
6. Russel SJ, Norvig P, *Artificial intelligence: a modern approach*, 2nd edn. Upper Saddle River, Prentice Hall, New Jersey. ISBN 0-13-790395-2
7. Szolovits P (ed) (2019) *Artificial intelligence in medicine*. Routledge
8. McCarthy J (2007) *What is artificial intelligence*. Chicago
9. Atlanta GA (2014) US department of health and human services, & centers for disease control and prevention. *National diabetes statistics report: estimates of diabetes and its burden in the United States*
10. Abramoff MD, Leng T, Ting DS, Rhee K, Horton MB, Brady CJ, Chiang MF (2020) Automated and computer-assisted detection, classification, and diagnosis of diabetic retinopathy. *Telemedicine e-Health* 26(4):544–550
11. Hassan A, Mahmood A (2017) Efficient deep learning model for text classification based on recurrent and convolutional layers. In: 16th IEEE international conference on machine learning and applications (ICMLA). IEEE, pp 1108–1113
12. Kuwayama S, Ayatsuka Y, Yanagisono D, Uta T, Usui H, Kato A, Takase N, Ogura Y, Yasukawa T (2019) Automated detection of macular diseases by optical coherence tomography and artificial intelligence machine learning of optical coherence tomography images. *J Ophthalmol*
13. Rajaput G, Reshmi B (2014) Mathematical morphology based fovea center detection using retinal fundus images. In: *Recent advances in intelligent informatics*. Springer, Cham, pp 41–52
14. Sundaresan V, Ram K, Joshi N, Sivaprakasam M, Gandhi R (2015) Computer-assisted grading of diabetic macular edema on retinal color fundus images. In: 2015 37th Annual international conference of the IEEE engineering in medicine and biology society (EMBC). IEEE, pp 4330–4333
15. Kapoor R, Walters SP, Al-Aswad LA (2019) The current state of artificial intelligence in ophthalmology. *Surv Ophthalmol* 64(2):233–240
16. Payne JF, Ray R, Watson DG, Delille C, Rimler E, Cleveland J, Lynn MJ, Tangpricha V, Srivastava, SK (2012) Vitamin D insufficiency in diabetic retinopathy. *Endocrine Practice* 18(2):185–193

17. Zhang J, Upala S, Sanguaneko A (2017) Relationship between Vitamin D deficiency and diabetic retinopathy: a meta-analysis. *Can J Ophthalmol* 52(S1):S39-S44
18. Mohan H (2018) Textbook of pathology. Jaypee Brothers Medical Publishers
19. Satyanarayana U, Chakrapani U (2006) Biochemistry, Books and Allied (P) Ltd, 3rd edn
20. Resnikoff S, Lansingh VC, Washburn L, Felch W, Gauthier TM, Taylor HR, Eckert K, Park D, Wiedemann P (2000) Estimated number of ophthalmologists worldwide (International Council of Ophthalmology update): will we meet the needs? *Br J Ophthalmol* 104(4):588–592
21. Kumar A, Vashist P (2020) Indian community eye care in 2020: achievements and challenges. *Indian J Ophthalmol* 68(2):291
22. Brady CJ, Garg S (2020) Telemedicine for age-related macular degeneration. *Telemedicine e-Health* 26(4):565–568
23. Nelson R (2021) AI screening for diabetic retinopathy moves to retail clinics, Medscape, <https://www.medscape.com/viewarticle/921828>. Last accessed 04 Aug 2021
24. Rajalakshmi R, Subashini R, Anjana RM, Mohan V (2018) Automated diabetic retinopathy detection in smartphone-based fundus photography using artificial intelligence. *Eye* 32(6):1138–1144
25. Tozer K, Woodward MA, Newman-Casey PA (2015) Telemedicine and diabetic retinopathy: review of published screening programs. *J Endocrinol Diabetes* 2(4)
26. DeTore J, Rizzolo D (2018) Telemedicine and diabetic retinopathy. *J Am Acad PAs* 31(9):1–5
27. Shi L, Wu H, Dong J, Jiang K, Lu X, Shi J (2015) Telemedicine for detecting diabetic retinopathy: a systematic review and meta-analysis. *Br J Ophthalmol* 99(6):823–831
28. Natarajan S, Jain A, Krishnan R, Rogye A, Sivaprasad S (2019) Diagnostic accuracy of community-based diabetic retinopathy screening with an offline artificial intelligence system on a smartphone. *JAMA Ophthalmol* 137(10):1182–1188
29. Lee CS, Tying AJ, Deruyter NP, Wu Y, Rokem A, Lee AY (2017) Deep-learning based, automated segmentation of macular edema in optical coherence tomography. *Biomed Opt Express* 8(7):3440–3448
30. Lee CS, Baughman DM, Lee AY (2017) Deep learning is effective for classifying normal versus age-related macular degeneration OCT images. *Ophthalmol Retina* 1(4):322–327
31. Kumar DA, Sankari A (2017) Investigations on severity level for diabetic maculopathy based on the location of lesions. In: 2017 World congress on computing and communication technologies (WCCCT). IEEE, pp 127–131
32. Li F, Liu Z, Chen H, Jiang M, Zhang X, Wu Z (2019) Automatic detection of diabetic retinopathy in retinal fundus photographs based on deep learning algorithm. *Transl Vis Sci Technol* 8(6):4–4
33. Ren X, Zheng Y, Zhao Y, Luo C, Wang H, Lian J, He Y (2017) Drusen segmentation from retinal images via supervised feature learning. *IEEE Access* 6:2952–2961
34. Gargeya R, Leng T (2017) Automated identification of diabetic retinopathy using deep learning. *Ophthalmology* 124(7):962–969
35. Nagasawa T, Tabuchi H, Masumoto H, Enno H, Niki M, Ohara Z, Mitamura Y (2019) Accuracy of ultrawide-field fundus ophthalmoscopy-assisted deep learning for detecting treatment-naïve proliferative diabetic retinopathy. *Int Ophthalmol* 39(10):2153–2159
36. Pratt H, Coenen F, Broadbent DM, Harding SP, Zheng Y (2016) Convolutional neural networks for diabetic retinopathy. *Procedia Comput Sci* 90:200–205
37. Li T, Gao Y, Wang K, Guo S, Liu H, Kang H (2019) Diagnostic assessment of deep learning algorithms for diabetic retinopathy screening. *Inf Sci* 501:511–522
38. Sahlsten J, Jaskari J, Kivinen J, Turunen L, Jaanio E, Hietala K, Kaski K (2019) Deep learning fundus image analysis for diabetic retinopathy and macular edema grading. *Sci Rep* 9(1):1–11
39. Dimauro G, Ciprandi G, Deperte F, Girardi F, Ladisa E, Latrofa S, Gelardi M (2019) Nasal cytology with deep learning techniques. *Int J Med Inform* 122:13–19
40. Dimauro G, Girardi F, Gelardi M, Bevilacqua V, Caivano D (2018) Rhino-Cyt: a system for supporting the rhinologist in the analysis of nasal cytology. In: International conference on intelligent computing. Springer, Cham, pp 619–630

Area Efficient and High-Throughput Radix-4 1024-Point FFT Processor for DSP Applications



Mohan Rao Thokala 

Abstract 1024-point FFT processor is implemented with two parallel paths using 65nm² process technology. The implemented FFT processor occupies 3.6 mm² of an area and operating at supply voltage of 0.4–1 V and 600 MHz clock frequency. Two parallel paths can be implemented with four parallel paths by taking advantage of Radix-4 FFT algorithm, which algorithm uses simple butterflies and less memory requirement. Implemented FFT processor is designed with multiple delay commutators, and feed-forward delay commutators signal can be processed one stage to another stage without any delay in processing the signal. Implemented four parallel path FFT processor requires less hardware which is 20% lesser and power consumption which reduces more than 30% when compared with two parallel paths Radix-2² FFT. Four parallel path FFT processor provides high throughput and less area requirement.

Keywords Discrete fourier transform (DFT) · Butterfly stage (BF) · Sample/clock · Twiddle factor · Multiple delay commutators (MDCs) · Counter · Read and write circuit (R/W)

1 Introduction

To compute the discrete Fourier transform, fast Fourier transform technique is widely used as it takes less multiplications and additions, and also, it is a speedy method to compute the DFT. DFT computations are required to calculate the frequency spectrum like spectrum analysis and filtering are required. FFT algorithm first explained by Cooley and Tukey, and it is opened new era in signal processing applications as it reduces order of complexity of DFT. It reduces number of order of complexity of DFT from N^2 to $N\log_2 N$. FFT is a speedy method to compute DFT, as it takes less computation time and improves performance by factor of 100 or more compared to

M. R. Thokala (✉)

Department of Electronics and Communication Engineering, Siddhartha Institute of Engineering and Technology, Hyderabad, Telangana, India

e-mail: tmohanrao2020@gmail.com

direct evaluation of DFT. In FFT, there are different algorithms to compute DFT, and these algorithms are used depending on input data vector, complexity, and specific application.

In digital signal processing and image processing applications, FFT algorithms are widely used as it takes less multiplications and additions, in turn which advantages using of less multipliers and adders. Along with FFT algorithms, pipelined architectures are preferred for computation for DFT, and this combination gives higher throughput, low latency, less area, and reducing power consumption. Single-path pipelined architectures using sequential input/output data vectors are preferred for high-speed real-time applications. On the other hand for global data interconnections, more transforms are required which leads use of parallel architectures. Parallel architectures use many arithmetic units, which lead to large power consumption and large chip area.

We propose four-path parallel paths FFT processor using Radix algorithm and MDC, which is more efficient. In terms of speed and area requirements compared to regular Radix-2² MDC and two parallel path FFT processor provides better improvement. In this algorithm, we use simple butterfly structure and simple control circuit, such that to meet Radix-4 algorithm.

2 Literature Survey

1024-Point Radix-2² Feed-Forward FFT Processor

Radix-2 algorithm is obtained by using divide-conquer approach, in this approach the DFT of any composite size N in to smaller DFT's with (N) multiplications and twiddle factors. Two parallel paths 1024-point FFT processor is designed with two parallel data paths and nine processing stages. In each processing stage, memory design input scheduler along with butterfly operation is present; during butterfly operation, it takes required twiddle values from memory. There are two types of butterfly stages: One is odd-numbered BF (BF-I) and even-numbered BF (BF-II). BBFI is a conventional Radix-2 butterfly, and BF-II is also conventional Radix-2 BF, but it requires additional circuits such as control circuit and multiplexers, for switching data between two phases. MSB bit of the n -bit counter is used as control signal, here $n = (1 + \log d)$, where d is the distance required between two BF stages. For example, in the 2nd stage, distance (d) is 128, so 8-bit counter is used for generating control signal (Fig. 1).

Size of the multiplier up to the fourth stage is 16-bit * 16-bit, then after that size of the multiplier is increased, so in this architecture, variable size multipliers are used, and also, truncation is required as the product size increases (Fig. 2).

Architecture includes nine butterfly stages; in these, we have even-numbered BFs and odd-numbered BFs; even-numbered BFs include adders and subtractors, whereas odd-numbered BFs include one more multiplier along with adders and

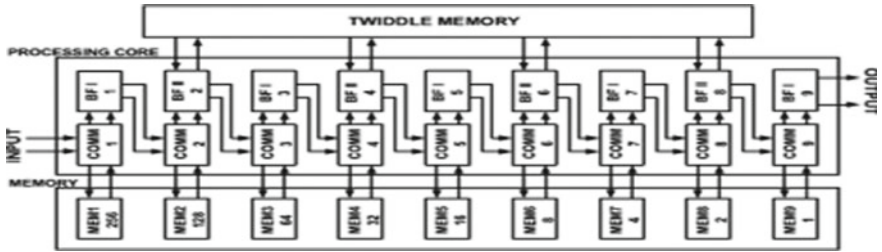


Fig. 1 1024-point Radix-2² feed-forward FFT architecture with dual path

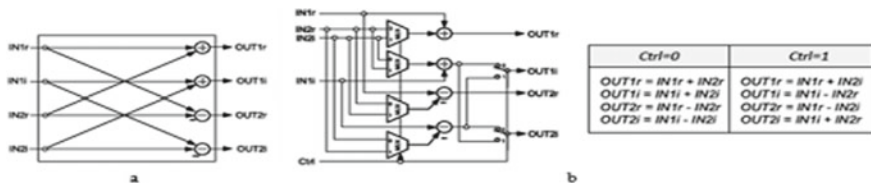


Fig. 2 Diagram of a BF-I, b BF-II

subtractors. BF-II multipliers take required twiddle factor value from twiddle factor memory; there are four multiplier butterfly stages out of nine processing stages.

Radix-4 Algorithm

To increase the speed of computation count, Radix-4 algorithm is used, which process large data for each butterfly operation. Radix-4 algorithm can process four input data samples at a time in compare with Radix-2 which takes only two samples, so whenever input data are large, it is preferred. In Radix-4 algorithm, each butterfly takes four inputs and gives four outputs. The Radix-4 FFT divides the DFT in to four quarter length DFTs, with group of every fourth sample. In Radix-4, numbers of stages are reduced and use only 75% of complex multiplications compared Radix-2 algorithm (Fig. 3).

Radix-4 algorithm features

- It has complex control structure

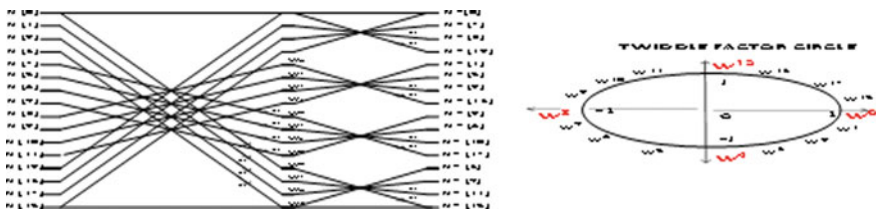


Fig. 3 16-point Radix-4 DFT Radix-4 butterfly diagram and its twiddle factor circle

- Operates on four samples, takes four input samples, and gives four output samples
- It can take twiddle factors from memory, and result can be stored in the memory at time
- Whenever data size is large, it holds good result
- It utilizes memory efficiently
- Speed of computation is more compared to the Radix-2 algorithm.

3 Four Parallel Path FFT Processor

Four parallel path architecture, where the input data is divided in to four equal size data inputs, and they are processed to the butterfly stages in parallel; memory is also divided in to four equal size parts to store four equal size data inputs at a time; input storage module takes input data and stores in four equal size memory parts, and they are given to BFs to perform algorithm operation in parallel (Fig. 4).

Input data are divided in to four equal size data values (IN [1], IN [2], IN [3] and IN [4]) and all four smaller data inputs are given to multiplexer, depending on counter MSBs signal particular input is given to particular data memory where it switches to Radix algorithm block. Memory is divided in to four equal size memories (MEM [1], MEM [2], MEM [3] and MEM [4], to store data samples of input and output. Radix algorithm is applied to the data input values by taking twiddle factor value from memory; here, it reuses the twiddle factor values efficiently to increase the speed of computation. MEMORY is divided in to four equal size memories, i.e., MEM [1], MEM [2], MEM [3], and MEMORY [4]; each memory size must be equal to half of the input data size. In each clock cycle, read operations and writes operations are performed; during positive half cycle read operation and during negative write operation is performed. Input data are divided in to four smaller data size (IN [1], IN [2], IN [3], and IN [4]), correspondingly four memory sizes namely MEM [1], MEM [2], MEM [3], and MEM [4] are arranged; four parallel data paths are used to get output result from the memory, i.e., OUT [1], OUT [2], OUT [3], and OUT [4]. In each clock cycle, four read operations and four write operations are performed, during positive half cycle read operation and during negative half cycle

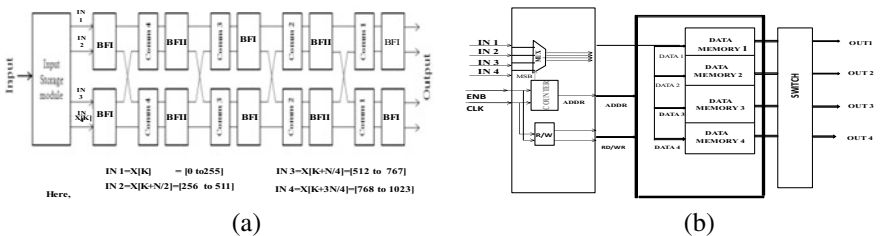
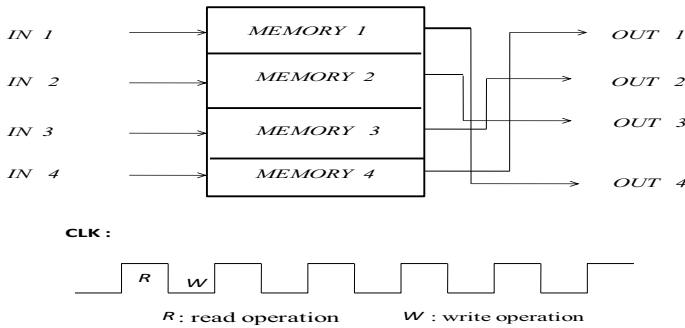


Fig. 4 **a** Four parallel path FFT processor architecture, **b** four-path FFT internal control processor architecture

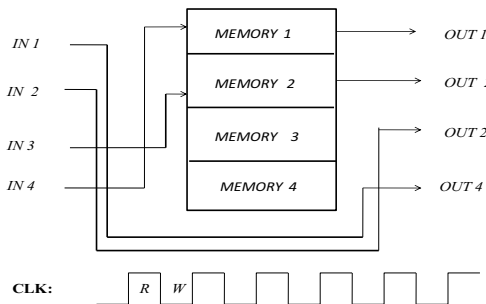
write operation is performed. R/W circuit is operated; it provides correct signals for read and writes operations. Switch is used to give four parallel path output result signal to the respected four input signals; in each clock cycle, four read operations and four write operations are performed.

Phase-1(P1) Operation: PHASE-I is activated for the first 512 clock cycles; for each clock cycle, four read operations and four write operations are performed, during positive half cycle read operation and during negative half cycle write operation is performed (Fig. 5).

During positive half cycle, read operation performed, OUT [1], OUT [2] reads data from MEM [3], MEM [4], and OUT [3]; OUT [4] reads data from MEM [1], MEM [2], so we have four read operations. During negative half cycle, input writes the data in to memory, IN [1], IN [2], IN [3], and IN [4] in to MEM [1], MEM [2], MEM [3], and MEM [4], respectively, totally four write operations. After the first 512 clock cycles, P2 is activated for second 512 clock cycles, and in each clock cycle, four read operations and four write operations are performed.



(a)



(b)

Fig. 5 a Phase-I operation, b phase-II operation

PHASE (II) Operation: During positive half cycle, OUT [1], OUT [2] read data from to MEM [1], MEM [2], and OUT [3]; OUT [4] reads data directly from IN [2] and IN [1], respectively, during negative half cycle IN [3] writes data in to MEM [2], and IN [4] writes in to MEM [1]. R/W circuit is used to provide the correct signals for read and writes operations. Switch is used to give four-path result signal to the respected four input signals; in each clock cycle, four read operations and four write operations are processed in parallel.

4 Result Analysis

Radix-4 FFT algorithm is used, whenever the input data size is more and to process the data as fast as possible using minimum area requirement, when we compare two-Path FFT using radix- 2^2 algorithm with four-path FFT using Radix-4; four-path utilizes less number of cells, and power consumption is also decreased with little bit overhead of speed. Four parallel paths are used to process the data so that whenever the input data size is large, it can give better results (Figs. 6, 7 and 8; Tables 1 and 2).

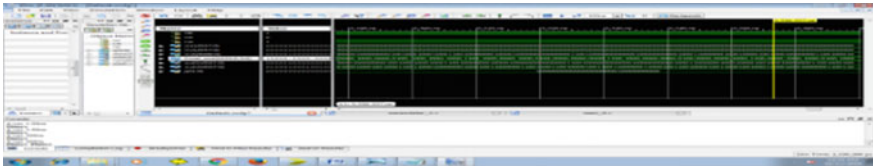


Fig. 6 Simulation output of two-path FFT processor

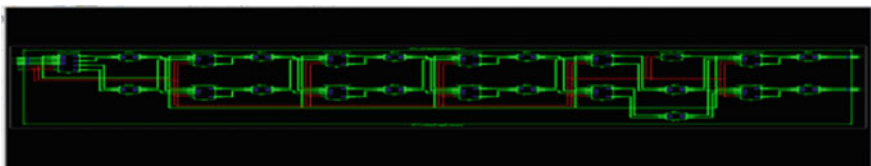


Fig. 7 RTL schematic diagram of four parallel paths FFT processor

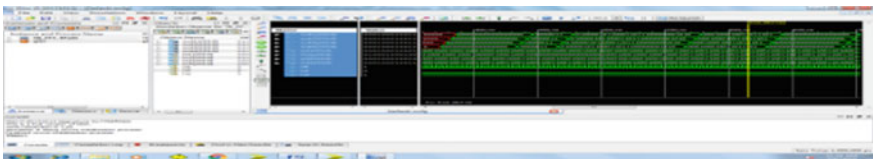


Fig. 8 Simulation output of four-path FFT processor

Table 1 Comparison between two-path and four-path FFT processor

Components	Two-path FFT	Four-path FFT
Clock period(ns)	3.405 ns	6.019 ns
Area (cells)	228,368	69,396
Delay	4995 ps	5762 ps
Power	6,862,152 nw	1,471,825 nw
Used flip-flop/LUT	26,401/60,240	11,275/13,192
Clock buffers	1	2
Min. clock period	3.405 ns	6.019 ns
Min. input arrival time before clock	2.140 ns	2.315 ns

Table 2 Device utilization comparison between two-path and four-path FFT processor

Components	Two-path FFT	Four-path FFT
Available LUT flip-flop pairs	60,730	16,368
Slice LUTs	60,600 out of 204,000	13,192 out of 1,221,600
I/O buffers	7170	2050
Fully used LUT flip-flops	26,271	8096
Used flip-flop /LUT	26,401/60240	11,275/13192

5 Conclusion

The proposed processor can process the data in four independent data streams simultaneously and thus by making it is suitable for low-power and area-efficient real-time applications. High throughput, i.e., four samples/clock can be obtained with parallel processing with same hardware as used in two parallel path FFT Radix-2² processor. Moreover, architecture provides high performance compared the two parallel path FFT processor architectures.

Area requirement is greatly reduced as it uses Radix-4 FFT algorithm with less number of cells utilized compared to two-path processor. As it uses Radix-4, less number of multipliers used which cause to reduce both area and power consumption, which is highly suitable for VLSI design environment. Four parallel path FFT processor provides high throughput, less area requirement, and lower power consumption, but all are can be obtained with increasing complex control structure and delay.

The FFT processor can be implemented with SRAM design above 500 MHz, but it challenges in low-power SRAM design. Whenever input data size is large, four parallel path architecture along with high radix algorithms gives better results for efficient signal transmission.

References

1. Konguvel E, Kannan M (2017) A survey of FFT/IFFT processors for next generation telecommunication systems. 27(03):1830001
2. Sk NM (2016) Multi-mode parallel folded VLSI architectures for ID-Fast fourier transform. Integr VLSIJ 55:43–56
3. Chen KH (2015) A low-memory-access length-adaptive architecture for $2n$ -point FFT. Circ Syst Sig Process 34(2):459–482
4. Rao KR, Kim DN, Hwang JJ (2010) Fast fourier transform algorithm and applications. Springer, Amsterdam, Netherlands
5. Jiang X, Liu CY, Zhang P (2012) A novel approach in place in order prime factor FFT algorithm. In: Proceeding of 5th international congress image signal process (CISP), Chongqing, china, pp 1500–1503
6. He S, Torkelson M (1996) A new approach to pipeline FFT processor. In: IEEE Proceeding of IPPS, pp 766–770
7. Stojanovic V (2006) Fast fourier transform VLSI A architectures course material for communication systems design, MIT open wave accessed
8. Bi G, Li G (2011) Pipelined structure based on radix- 2^2 FFT algorithm. In: Proceeding of IEEE conference industrial electron-application, pp 2230–2533



Mohan Rao Thokala Received B-TECH degree from Vaagdevi College of Engineering, Warangal, obtained M-TECH degree from Anurag Engineering College, Kodhad. Currenly working as Assistant professor in Siddhartha Institute of Engineering and Technology, Hyderabad, Telangana State, India. Published nine research papers and attended four national and international conferences.

Air Quality Monitoring System Based on Artificial Intelligence



Vattam Sowmya and Shravya Ragipani

Abstract In present-day life, quality of air is reducing day by day which leads to environmental issues and also damaging public health with harmful gases present in the air where the ecosystem is affected. The implementation of a cost-efficient system that controls the air pollutants in a large area is a challenging task. Therefore, this paper suggests a portable air quality measurement unit. Most of the harmful gases are released from industries and vehicles. Internet of things (IoT) plays an important role in the monitoring of air quality. We measure the quality of air using an mq135 sensor with also carbon oxide using mq7. Measuring the air quality is important for bringing awareness to the people for taking care of future generations for their health. Based upon the review, Government of India has taken some measures to ban single stroke and two-stroke engine motorcycles which are causing high pollution. Although New Delhi remarked as the most polluted city comparing with other cities in the world which as recorded air quality above 300 ppm. IoT is used for clouded computing where it is used for collecting data from different sensors. We are using artificial intelligence to predict the future data from the collection in the database. The data collected at the cloud application can be processed by using data analytics and artificial intelligence (AI). After knowing the future predicted data, we can be alert and take precautionary measures and keep the indoor air quality as good as possible. We have used the support vector machine algorithm which is popularly known as SVM. It is also famously known as supervised machine learning. Satisfactory alternatives based on different conditions are generated by using the proposed model. The proposed method focuses on air pollutant control with IoT and AI in combination with the SVM algorithm.

Keywords Raspberry Pi · SVM algorithm · Cloud computing · Air monitoring · Artificial intelligence

V. Sowmya (✉)

Department of Electronics and Communication Engineering, B. V. Raju Institute of Technology, Hyderabad, Telangana, India
e-mail: vattamsowmya@gmail.com

S. Ragipani

Sri Devi Women's Engineering College, Hyderabad, Telangana, India

1 Introduction

In this present days, air pollution is the main reason which is accelerated to we are concerned about climate change scientists and activists and the implications [1]. Several toxic gases released from industry are harmful not only to terrestrial but also to aquatic organisms. Health conditions will also increase as the cardiac because of some low air quality diseases, stroke, lung cancer, and respiratory diseases [2]. According to WHO statics, millions of deaths were registered world according to WHO statics, and millions of deaths were registered worldwide last year due to air pollution wide last year. So this created a need for analyzing the real-time air quality. This paper provides real-time monitoring of air quality.

In recent times, chemicals from factories, car emission gases, smoke, and dust are present anywhere, and this is the main reason why air condition is more polluted. Harmful gases like carbon monoxide, LPG gas, and methane are present in the air which cannot be dictated by a human. Level of air pollution has been increasing with a lot of factors, i.e. increasing usage of vehicles, increasing the pollution and industrialization, which results harm full effect directly or indirectly on human life. We will develop an AI-based air quality control system to track this. Air quality is monitored via the Web server, and the warning will also be triggered if air quality falls from a certain standard, where there are enough complete gas hazards available in the air such as CO₂, alcohol, smoke, benzene, and NH₃. It displays ppm air quality on and on the LCD panel so that we can conveniently measure ppm anywhere in the world using a computer or a mobile device.

Globalization is the important reason for the contamination, and there are some cases of air pollutants: – Air emissions toxic: are produced by or emitted from chemical plants by burning fossil fuels. Through inhaling this smoke, birth defects may also lead to cancer and too many other poisonous gases. – Carbon oxide: gases generated by the use of fossilized fuels are commonly emitted from cars that are not visible or detected. This causes people to feel sleepy and exhausted and can lead to headaches for some people. – Ozone: The air we breathe can have ozone which can harm our health especially at the time of hot sunny days. Most of the people are effecting by asthma in children and older adults who are moving outdoors workers. It reduces lungs and induces certain respiratory effects, such as asthma, toxin, and certain breathing difficulties. – Sulphur dioxide: It is occurred by the combination of sulphur fuel and also natural disasters like a volcano. – Nitrogen dioxide: This gas is released from vehicle fuel, wooden burring, electric affluence, and industrial boilers. This may lead to lung-related diseases (Figs. 1 and 2).

2 Previous Work

Several air quality monitoring systems have been deployed which uses few sensor values and hard-coded rules to operate. In these kinds of systems, the technology

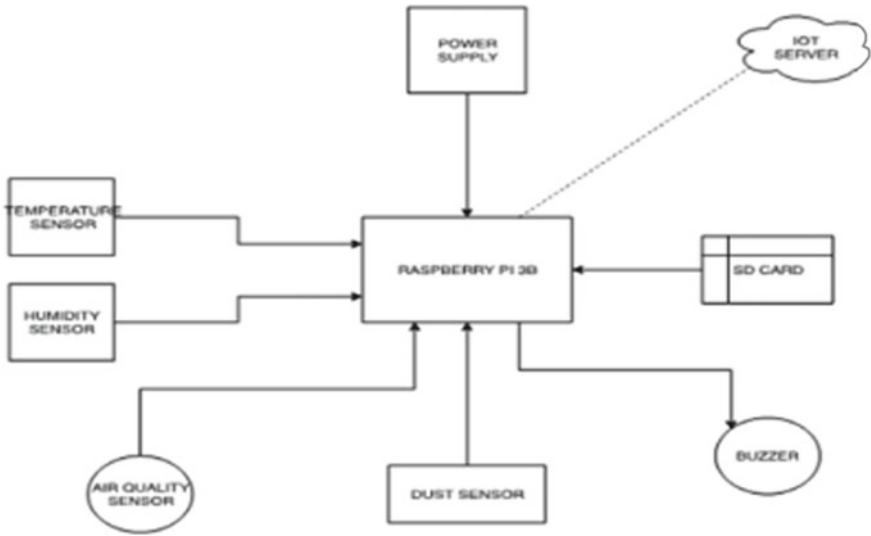


Fig. 1 System diagram of air quality monitoring system

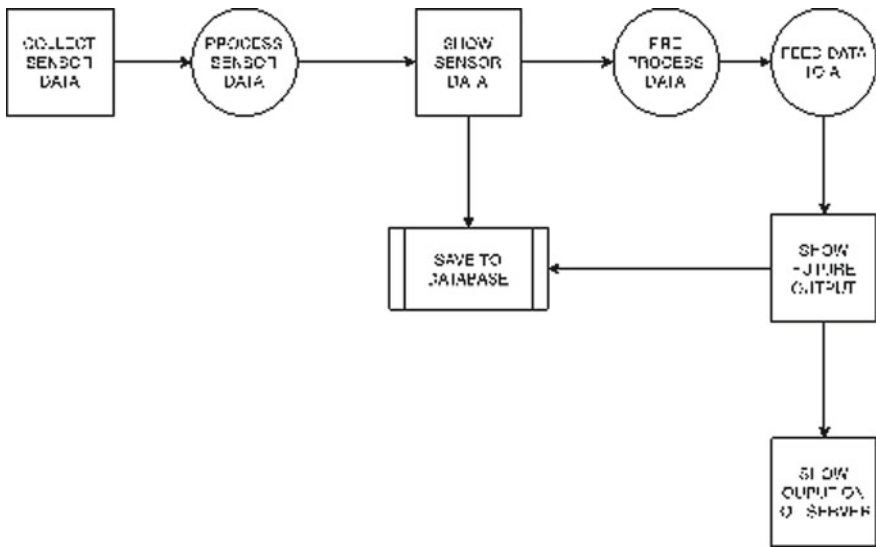


Fig. 2 Flow chart of sensing data

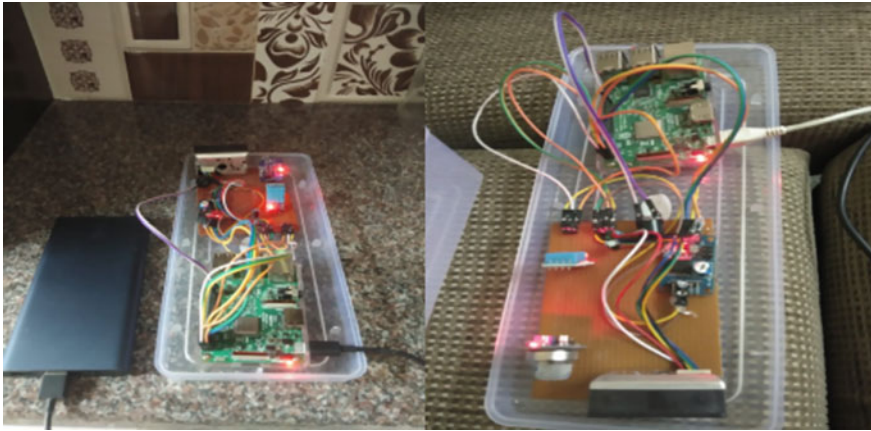


Fig. 3 Hardware implementation in different areas

used is quite old, and leveraging of new technologies is not done. Air pollution monitoring through computer-like tomography technique which is developed set of pair dimensional for pollution concentration. It has various applications for the absorption method. It consists of a cylindrical mirror for reflecting the beam at an angle. This technique has concentrated on laser energy which will increase range and monitoring for contain various pollutant gases [3].

Monitoring the quality of air through online GPRS developed and analyzed. It has only one chip microcontroller. The frame will be updated for the GPRS modem, and public data is transferred to the server through a public mobile network to store data in the database [4].

WSNs have real-time monitoring architecture, double layer network system, and an electronic grid system. The algorithm for data mining is used to collect data and the operating system for performance analysis. WSN has an important contribution to this field. It is used for detecting various gases like CO_2 , NO_2 . For and interim interfaces are used [5]. It can be present on the Internet.

Air quality control system is used to assess the air quality, which means that these approaches are very costly and low resolution sensing data; the system has a sensor gateway, and it can be controlled through the LabVIEW programme. So the system established in the cities for observing various gases is carbon monoxide concentrations. It has the benefit of easy establishment with less cost where it can provide real-time data [6].

Quality of air has attached with virtual instrument mechanism and also has frequency hopping mechanism to reach wireless data transmission. They have developed to aim spectrum hole disclosure for modifying the frequency depend upon the conclusion and based on radio spectrum if the signal is not available at the time of wireless transmission in the real-time data [7] (Fig. 3).

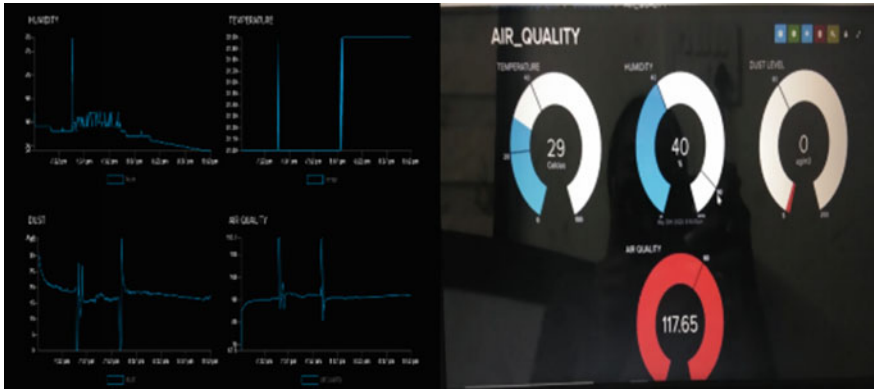


Fig. 4 Display of data onto cloud and monitoring result

3 System Design

Moreover, we are using artificial intelligence to monitor all the sensor data and take the necessary decision to keep the indoor air quality as good as possible. The AI will be responsible to raise alerts and activate actuators to keep the indoor air quality as good as possible.

The above-shown figure is the block diagram of the project. The block diagram consists of the temperature sensor, humidity sensor, air quality sensor, and dust sensor which process the data and are fed to Raspberry Pi 3B board. The device is connected with other components such as an SD card, buzzer, and IoT server. IoT server acts as a cloud for the system, SD card stores all the data of sensors which are fed to the Raspberry Pi. Whenever the sensors process the data, the IoT server checks the quality of the air. If the quality of the air decreases as per the sensor readings, the buzzer gives the indications of the components present in the air such as the decrease in temperature, humidity, air quality, or increase of dust present in the air. The buzzer helps us to find whenever there is an increase or decrease in the air. The idea behind this is not only to collect data from several sensors but also, we are using IoT technology to upload real-time data on the cloud and data collection. Also, we are implementing artificial intelligence to control actuators which will try to keep the indoor air quality as good as possible (Fig. 4).

3.1 Data Sensing

The activity diagram of this monitoring system contains the sensor data and flow of the sensor data to output on the IoT server. The data from all the sensors is collected, it is then processed so that we can see the data of the sensor, and this data is then

Timestamp	Temperature	Humidity	Air quality	Dust
30-05-2020	30	43	84.31	32.11111111
30-05-2020	30	43	84.31	32.11111111
30-05-2020	30	43	84.31	31.2283737
30-05-2020	30	43	84.31	32.11111111
30-05-2020	30	43	84.31	31.2283737
30-05-2020	30	43	84.31	31.2283737
30-05-2020	30	43	84.31	31.2283737
30-05-2020	30	44	84.71	32.11111111
30-05-2020	30	44	84.31	31.2283737
29-05-2020	31	44	84.71	31.2283737
29-05-2020	31	44	84.71	31.2283737

Fig. 5 Data collected from different parameters

stored into a database for the further use of air monitoring [3]. The pre-process of data is done so that the data of all the sensors of all days get stored, and this data is fed to AI. Now, the database present collects all the sample qualities of the air then monitor all the air qualities and averages them to give an accurate air quality for further and future implementations. The data such as temperature, weather, and air quality is shown as the output on the IoT server. In this monitoring system, we are taking qualities of present air as input to check and monitor the future air qualities as output (Fig. 5).

3.2 Algorithm for the Developed System

Supervised machine learning algorithm is widely used in classification and regression problems. Rules of the classification depend on mathematical values and the data collected from the pollutants.

3.3 Software Configuration

At the earliest, we install the library of the sensors through the git hub and downloaded the files. Import the sensor library file example MQ135>> import

Adafruit_MQ135>> ready to start then execute the code and run. The same configuration is done for another sensor.

4 Results

This chapter includes the experimental results that have been obtained as a part of our project. The image shows the setup for monitoring of air used for practical testing purposes.

5 Conclusion

In the proposed system, the Raspberry Pi microcontroller was used to collect the real-time data from the sensors and analyze it. We are using artificial intelligence to control actuators which will try to keep the indoor air quality as good as possible. In our system, the AI is responsible for all the data analysis and decision-making.

References

1. Moore F (2009) Climate change and air pollution: exploring the synergies and potential for mitigation in industrializing countries. *Sustainability* 1(1):43–54
2. Cascio W, Hong Y, Howard G, Lipsett M, Luepker R, Mittleman M, Samet J, Smith SC Jr, Tager I (2004) Air pollution and cardiovascular disease: a statement for healthcare professionals from the expert panel on population and prevention science of the American Heart Association. *Circulation* 109(21)
3. Byer RL, Shepp LA (1979) Two-dimensional remote air pollution monitoring viatometry. *Opt Lett* 4:75–77
4. Al-Ali AR, Zualkernan I, Aloul F (2010) A mobile GPRS sensors array for air pollution monitoring. *Sens J* 10(10):1666
5. Prasad RV, Baig MZ, Mishra RK, Desai UB, Merchant SN (2011) Real-time wireless air pollution monitoring system. *ICTACT J Commun Technol Spec Issue Next Gener Wirel Netw Appl* 2(2)
6. Liu JH, Chen YF, Lin TS, Lai DW, Wen TH, Sun CH, Juang JY, Jiang JA (2011) Developed urban air quality monitoring system based on wireless sensor networks
7. Wang H, Wu T, Wu G (2010) Air quality monitoring system based on frequency hopping system. In: International conference on intelligent control and information processing

An Improved Technique for Identification of Forgery Image Detection Using Clustering Method



S. Jeevetha, Deepa Jose, P. Nirmal Kumar, and H. Kareemullah

Abstract In forensics, the detection of forgery images is very important. In this method of forgery, the same image of the region can be able to copied and pasted. The keypoint-based method was advertised to reveal ineffective forgery detection against different attacks like geometric transformations because the number of keypoints is less in small regions. To overcome these problems, the following methods are involved. In the first stage, we extract many keypoints by reducing the low enhancement by the CLAHE algorithm. After extraction, there will be some keypoint matching problems to solve this problem the FANN algorithm is used. At the final stage, the tampered region is localized, and in order to overcome FPR, an iterative localization technique called the Density-based clustering algorithm and GORE method is used. By using the software MATLAB R2017a, the performance of experimental results is evaluated and accuracy of 93% by image and pixel level.

Keywords Scale-invariant feature transform · Hierarchical matching · Contrast-limited adaptive histogram equalization · Density-based clustering · Random sample consensus · Guaranteed outlier removal · Iterative localization

1 Introduction

In modern days, images are edited by software like Photoshop and Gimp; images are forgery at a cheap cost. Digital images bring trust-worth issues. These processes can be used by rotation, image compression, resizing the image, and addition of noise to make final forgery images more convincing. In the copy-move forgery image, the

S. Jeevetha (✉) · P. Nirmal Kumar
Department of ECE, CEG, Anna University, Chennai, Tamil Nadu 600025, India
e-mail: jeevetha251994@gmail.com

D. Jose
Department of ECE, KCG College of Technology, Chennai, Tamil Nadu 600097, India

H. Kareemullah
Department of EIE, B.S.A. Crescent Institute of Science and Technology, Vandalur 600048, India



Fig. 1 Pipelining stage of forgery detection

two main categories are block-based and keypoint-based methods. The pipelining structure of the forgery detection involves three steps. Figure 1 represents pipelining stage of forgery detection. In the first step is preprocessing, in this step, the image will be preprocessed depend on the image application, and then, the image will be converted into a color image into a grayscale image. The extraction of feature images will be divided into the square image or circular image of the region. After extraction, images are matched between two similar feature descriptors. If the two images are matched together, it will be clustered to reduce the false matches of the image. In the forgery detection method, the two main issues are accuracy and efficiency of the image; it will be achieved by the time and space complexity of the image size and image distortions where the number of keypoints extraction will be very less than the number of image blocks. To overcome these issues, we improve the copy-move forgery detection technique that was proposed for reducing the false alarm rate and accurate result of the image.

2 Related Work

For detecting the forgery image, there are two methods involved: block-based method and keypoint-based method in the literature review of forgery image detection, block-based method has such transforms are found: discrete cosine transformations (DCTs), discrete wavelet transforms (DWTs), single value decomposition (SVD), and histogram of orientation gradient (HOG). These transforms are improved for forgery image detection techniques Christlein et al. [1]. Out of all block-based techniques, DCT transform is one of the great extended methods for forgery image detection method to locate forgery areas Nazari et al. [2]. In the preprocessing level operations of geometric transformation of blurring, rotation, scaling, DCT method was introduced truncating the feature vector Huang et al. [3]. In real-time application purpose, block-based method is not suitable for high false-positive rate. To overcome the post-processing operations, keypoint-based technique is involved; the most popular keypoint feature image technique in forgery detection is scale invariant feature transform (SIFT) Bakiah et al. [4]. The hierarchical feature matching is applied to the input image of the forged region to extract the multiple levels of dense feature Li et al. [5]. The author Abdel-Basset et al. [6] introduced the SIFT-based method is applied to density-based spatial clustering of application with noise (DBSCAN) in the spatial domain, and random sample consensus (RANSAC) algorithm is used for frequency domain. This will handle high false-positive rate results in the clustering method.

3 Existing Method

In the existing method, the keypoint-based method was revealed to ineffective forgery detection against different attacks like geometric transformations because the number of keypoints is less in small regions. To handle this problem, the SIFT algorithm is used to extract the image by lowering the contrast threshold level and resizing the image. In order to solve a large number of key points, the group matching technique is used and the image is iterated finally. It is then followed by the localization technique that is used to identify the result of the tampered region in the image [6–8].

SIFT algorithm is used to identify the multiple features of images in the same location and is used for detecting the feature of images. SIFT keypoints are extracted from the reference image and stored in a database.

A. Sift Feature Generation

The SIFT algorithm contains the below four phases are as follows:

- Keypoint identification by using scale-space extrema detection.
- Keypoints are eliminated by contrast and edge thresholds.
- Each keypoint is assigned by dominant orientation.
- Generation of feature descriptor.

- **Detection of Scale-Space**

Identify the location and at the different scales by achieving the scale-space extreme is used by the formula.

$$L(x, y, \sigma) = G(x, y, \sigma) * I(x, y) \quad (1)$$

Input image $I(x, y)$ is convoluted with the operator of a blurred image of Gaussian $G(x, y, \sigma)$.

DoG operation is used for locating the extrema in between the difference of both images. $D(x, y, \sigma)$ function is represented by:

$$D(x, y, \sigma) = L(x, y, k\sigma) - L(x, y, \sigma) \quad (2)$$

A function of DoG points of invariant scale-space and orientation can be detected by local maxima and minima. The representation of scale-space extrema is shown in Fig. 2.

- **Keypoint Localisation**

Based on each candidate, keypoints are resolving the scaling and location of the region and selected by the stability value.

- **Orientation Assignment**

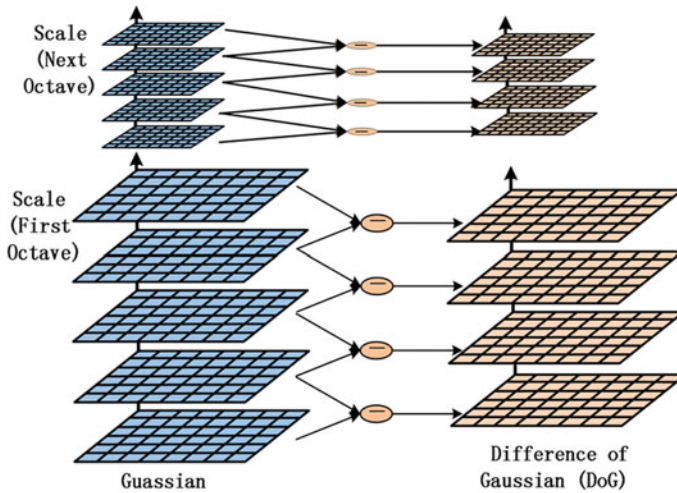


Fig. 2 Representation of scale-space

Each keypoint of assignment orientation is allocated by the location and slope directions of the image. The performance of an operation on image data will assign the orientation by local image and scaling.

- **Keypoint Descriptor**

Keypoint descriptors are used to create local gradient data. The information of the gradient is rotated with the orientation of keypoints. Each keypoint region is measured by a selected scale of the local image gradient. These transformations allow a significant level of distortion in local space and illumination change.

- **Sift Feature Matching**

Keypoints are used to identify by analyzing the magnitude and direction of intensity changes in local image neighbors to detect the high contrast corner and edges. The matching process is used for finding the correct orientation and approximate position of the image. From the feature detection image, green color box indicates octaves; red color lines indicate the edge ratio of the image; the blue color box indicates the blob, and the green color (+) indicates the threshold value (Fig. 3).

4 Feature Extraction

Due to noise and according to the method of geometric transformation, here, SIFT algorithm is used to extract the feature image. As discussed previously, the keypoints-based method cannot generate the number of sufficient keypoints in plain regions.

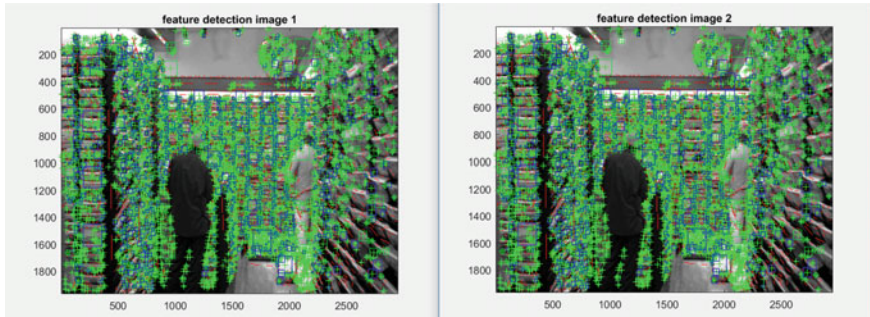


Fig. 3 Feature detection of original and tampered image

In this section, for increasing the keypoints in the image, the contrast value of the threshold will be lowered and resizing the given image.

A. Lowering the Contrast Threshold

Based on the SIFT algorithm, we can able to reduce the threshold values. So, we set the contrast threshold value by 4; only, fewer keypoints can be identified. If we lowering the contrast threshold value from 4 to 0.1, more keypoints are identified as shown in Fig. 4a.

B. Resizing the Input Image

It cannot fully solve the sufficient number of keypoint problems by lowering the contrast threshold. The scale factor S corresponds to the SIFT keypoints to resize the input image for producing the keypoints. Here, we set the scale factor from 1 to 2 to a good trade-off as mentioned in Fig. 4b.

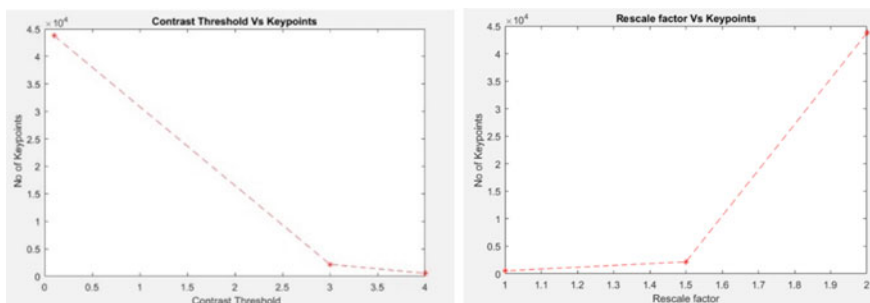
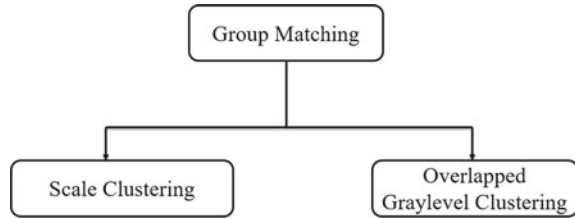


Fig. 4 a Contrast threshold vs no of keypoints; b rescale factor vs no of keypoints

Fig. 5 Classification of group matching



5 Group Matching

The group matching of a hierarchical algorithm is to detect the same location of the images (Fig. 5).

A. Scale Clustering

At different scale spaces of keypoints will be tightly clustered. For the first octaves and second octaves, every single octave will apply the matching procedure separately. Grouped multiple octaves value in the higher octaves. Clusters are separated into different keypoints through scale clustering. For low scale & medium scale ranges from (0 to 60), it will be matched within a single octave. The high scale ranges from (200 to 255); it will match the higher octaves.

B. Overlapped Gray-Level Clustering

In our method, the matching algorithm becomes more essential for both the first octaves and, then, the second octaves. In the feature extraction, more keypoints are produced. We propose group matching through the overlapped clustering of gray levels to speed up the process of group matching. Both image 1 and image 2 are matched by the inlier points by the gray-level clustering (Fig. 6).

The disadvantage of the existing work in a keypoint-based method is described as below:

1. In this case of a smooth or small region, a sufficient number of keypoints are generating to be more.
2. In this case, it is difficult to identify the clustering and segmentation for all images because it can be any shape/textures and sizes.
3. Absence of reliability in the validation of affine matrix and inliers selection.
4. The probability of false alarm rate will be high compare to the proposed method

6 Proposed Method

The keypoint of forgery detection was proposed to reduce the false alarm rate, and the requirement of time and space complexity will be improved by a technique of density-based clustering and the GORE method. In the DSCAN, it will be clustered into a group and identify the accurate result by reducing time and space complexity



Fig. 6 Matched inlier points

Then, false matches will be reduced effectively using the GORE algorithm and are employed with the RANSAC algorithm for better result.

A. Preprocessing Using CLAHE Algorithm

In the pre-processing stage, Contrast-limited adaptive histogram equalization method is used for enhancing the low contrast image. Contrast clipping limit is initiate for reducing the amplification of noise problem. In our proposed method, the clip limit will set to 0.01, and the tile size is (4*4) (Fig. 7).

B. FANN Algorithm

Keypoints are extracted from preprocessing images by using SIFT algorithm, and the images of the matching points are matched by the algorithm of fast approximate nearest neighbor (FANN). This algorithm will provide a fast nearest neighbor search

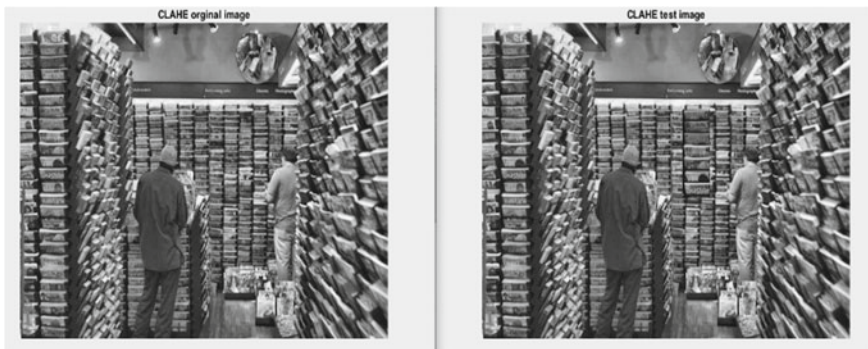


Fig. 7 Preprocessing image using CLAHE



Fig. 8 Feature matching process

of the data points in the view of high dimensional. The threshold value will set to $T = 0.5$ for a good trade-off (Fig. 8).

C. DBSCAN Algorithm

After the feature matching pairs, clustering is applied to the spatial regions and detects the cloned regions to identify the keypoints of the image. The density-based spatial clustering algorithm is divided into two separate density clusters of high and low. Clusters can be varying by shapes that contain outliers and noise of an image.

Two main parameters of the DBSCAN algorithm:

Epsilon: It represents a data point of the clusters around the neighborhood of the region.

Minimum points: Data points occur within the radius value of epsilon (Fig. 9).

In this algorithm, the following data points are as follows:

- **Core Points:** A point more than minimum points within the radius value of epsilon.
- **Border Points:** A point that has fewer than minimum points within the radius value of epsilon.
- **Outlier:** It doesn't exist in core or border point (Fig. 10).

D. Two-Stage Process of Outlier Removal

In this process, after the clustering process, the images are cluster into groups; then, the GORE algorithm is applied to the group-matched pairs of clusters. Green lines indicate inliers, and red lines are outliers. GORE was able to remove almost all the outliers. Finally, to estimate the affine transformation, RANSAC algorithm is used in between the original and duplicate image (Fig. 11).

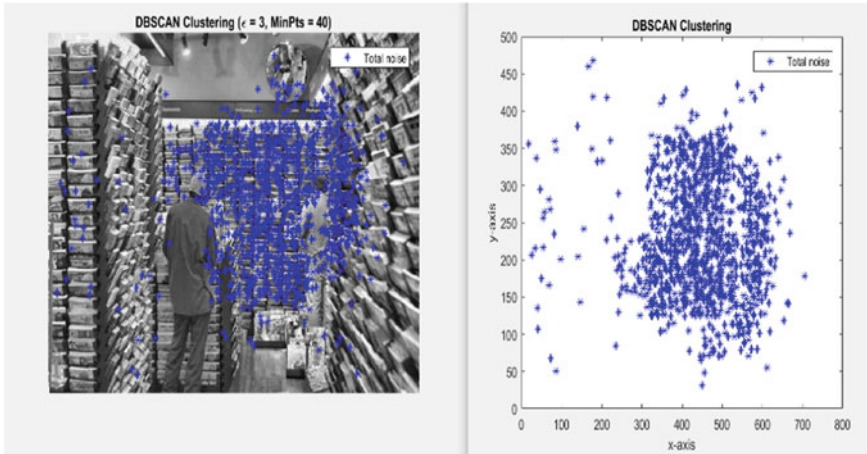


Fig. 9 DBSCAN clustering

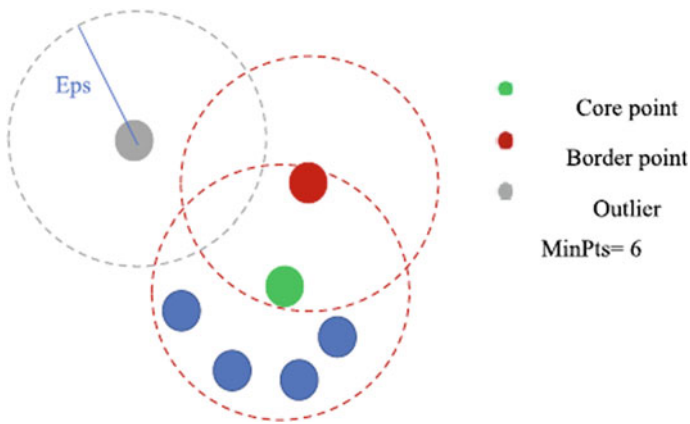


Fig. 10 Data points of DBSCAN clustering

7 Forgery Localization

Forgery localization is used to locate the identical regions of an image in a dense area.

A. Isolated Matched Pairs Removal

In this removal of matched pairs, it cannot be isolated the correct matched keypoints properly because the forgery image is in appendant shape for that in the forgery localization method is used for reducing the false alarm rate.

B. Homography Estimation

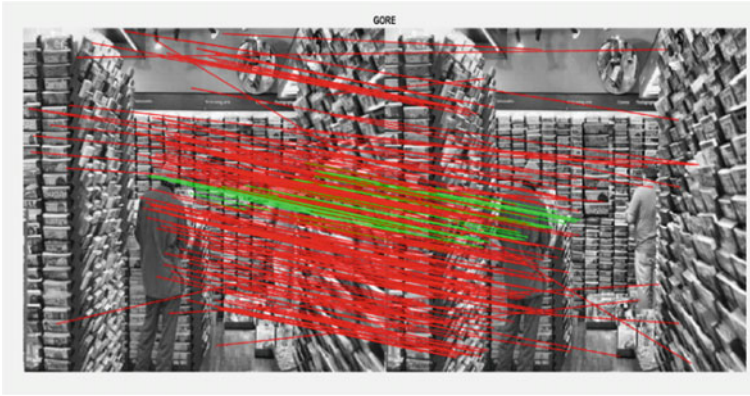


Fig. 11 Outliers removal by GORE

Estimation of the local homography method is a part of an affine matrix to evaluate a pair of matching from two appendant regions of an image. We choose the matched pairs and record them. After that need to construct all closed matched pairs and generate from the two appendant local regions. To oppose these problems, we apply the RANSAC algorithm in between equivalents of the matched pairs for estimating homography.

C. Homography Validation and Inliers Selection

In our method, validation of local homography and selecting inlier points using the dominant orientation is used to discard the inaccurate estimation because of cannot trust fully the result of the RANSAC algorithm. Orientation is a major part of the rotation invariance in SIFT algorithm.

D. Forgery Localization in Dense Field

The forgery localization in a dense field of new algorithm comprises of below two phases:

The scale information of each inlier is used to construct the suspicious regions present in a forged image. The fineness and texture of the colour information is validated to refine the suspicious region (Fig. 12).

8 Evaluation Performance

Evaluation metrics are measured by image and pixel level. In the image-level, a genuine image can be distinguished clearly from a forged one whereas in the pixel-level, the accuracy level of a forged image can be identified from that of a genuine one (Table 1).



Fig. 12 Forgery localization

Table 1 Classification of evaluation metrics

Evaluation measure	Explanation
True Positive (TP)	Correctly detected the images as tampered
False Positive (FP)	Falsely detected the images as tampered
False Negative (FN)	Falsely undetected the images as forged
True Negative (TN)	Correctly detected the images are not forged

Performance of the evaluation metrics of true-positive rate (TPR) and false-positive rate (FPR), which are defined by the following manners.

$$TPR = \frac{TP}{TP + FN} \tag{3}$$

$$FPR = \frac{FP}{TN + FP} \tag{4}$$

Mathematically, the F_1 -score is represented by.

$$F_1 = \frac{2TP}{2TP + FP + FN} \tag{5}$$

Accuracy is defined as a ratio of observed by true predicated value by the total value of observation (Table 2).

$$Accuracy = \frac{TP + TN}{TP + FP + FN + TN} \tag{6}$$

Table 2 Comparison evaluation on MICC-F220 to filtering method in terms of (%)

Method	TPR	FPR	F_1	Accuracy
RANSAC	81	9.97	93	90
GORE-RANSAC	97	4.44	97	93

9 Conclusion

In this paper, by studying the (SIFT) keypoint extraction algorithm, a sufficient number of keypoints in the soft or fewer region of the images are generated, by minimizing the value of the contrast threshold, and the image is resized. After that density-based clustering algorithm is clustered into a group and reduces false matches effectively by GORE, and tampered region is localized accurately by iterative localization technique. Finally, better performance of evaluation metrics and experimental results is demonstrated. The least false matches of multiple forgeries images can be handled.

References

1. Christlein V, Riess C, Angelopoulou E (2010) A study on features for the detection of copy-move forgeries. *Sicherheit* 105–116
2. Nazari M, Sharif A, Mollaeefar M (2016) An improved method for digital image fragile watermarking based on chaotic maps. *Multimed Tools Appl* 1–17
3. Huang Y, Lu W, Sun W, Long D (2011) Improved DCT-based detection of copy-move forgery in images. *Forensic Sci Int* 206(1–3):178–184
4. , Abd Warif NB, Wahab, AWA, Idris, MYI, Ramli R, Salleh R, Shamshirband S (2016) Copy-move forgery detection: survey, challenges and future directions. *J Netw Comput*
5. Li Y, Zhou J (2016) Image copy-move forgery detection using hierarchical feature point matching. In: *Proceeding of Asia–Pacific signal information processing association annual summit conference*, pp 1–4
6. Abdel-Basset M, Manogaran G, Fakhry AE, El-Henawy I (2018) 2-Levels of clustering strategy to detect and locate copy-move forgery in digital images. *Multimedia Tools Appl* 1–19
7. Joe IRP, Varalakshmi P (2019) A multilayered clustering framework to build a service portfolio using swarm-based algorithms. *Automatika* 60(3):294–304
8. Indumathi V, Ganesan R, Amuthadevi C, Prabakeran S (2018) In-depth survey to perceiving the effect of kidney dialysis parameters using clustering framework. *J Comput Theor Nanosci* 15(7):2233–2237

EEG Signal Analysis During Stroop Task for Checking the Effect of Sleep Deprivation



Bhagyashree Narkhede, Sai Kate, Vaishnavi Malkapure, and Revati Shriram

Abstract Studies suggest that eight hours of sleep is important for the brain to function properly. Sleep deprivation may affect individual's health and cognitive ability. In this project, we studied how cognitive ability is affected by sleep deprivation. For this, the Stroop test was used which is based on the color word incongruency. Congruent word is word written in same color ink, and incongruent word is word written in different color ink. For our project, three different Stroop test, namely English, Hindi, and Animal, are used. The animal Stroop task is a picture Stroop task. Here, two animals will be displayed on the screen. Congruent is when the animal bigger in real life is shown bigger and incongruent is when animal smaller in real life is shown bigger on the screen. All three tests had eleven stages with the incongruency increasing with each stage. To analyze the difference in the brain functioning and the performance of the Stroop test both sleep deprived and non-sleep deprived individuals were considered in this study. A base EEG in relaxed stage was also taken before the test to compare each subjects signal with his/her relaxed state reading. To analyze the results, detrended fluctuation analysis, Higuchi fractal dimension, entropy, Kolmogorov complexity, and Lyapunov exponent of the EEG signal were studied using MATLAB. Using these features, we were able to analyze the difference in brain functioning of sleep deprived and non-sleep deprived individuals. The reaction time of the test was used to comment on whether sleep deprivation affects cognitive performance. For this project, equal contribution was made by all the contributing authors.

Keywords EEG · Stroop test · Congruent · Incongruent · Sleep deprivation · Reaction time · Kolmogorov complexity · Detrended fluctuation analysis

B. Narkhede (✉) · S. Kate · V. Malkapure · R. Shriram
MKSSS's Cummins College of Engineering for Women, Karvenagar,
Pune, Maharashtra 411052, India
e-mail: bhagyashree.narkhede@cumminscollege.in

© The Author(s), under exclusive license to Springer Nature Singapore Pte Ltd. 2022
P. Kumar Jain et al. (eds.), *Advances in Signal Processing and Communication Engineering*, Lecture Notes in Electrical Engineering 929,
https://doi.org/10.1007/978-981-19-5550-1_28

287

1 Introduction

Cognition refers to all the mental processes responsible for an individual's perception, reasoning ability, working memory, etc. One such cognitive function is attention. This function helps individuals focus on relevant stimuli despite increase in interference or stress. Sleep deprivation affects cognition mainly attention and working memory. There are two main hypothesis theories explaining the impairment in cognition due to sleep loss: (1) The wake state instability hypothesis in which the impairment in cognition is attributed to the attentional lapses and increased reaction times and (2) Sleep-based neuro-psychological perspective which states that the impairment of cognition is due to the deprivation weakening the functionality of specific brain regions. Various studies have been based mainly on these two hypothesis. Some studies suggest that acute sleep deprivation does not affect the overall psychometric performance [1]. However, recent studies have found out that sleep deprivation does have a negative impact on overall psychometric test performance with increased reaction time and errors [2, 3]. Changes were also observed in alpha asymmetry, beta power of the brain, and the frontoparietal control (FPC) [4]. All of these studies have used different psychometric tests such as verbal tasks, questionnaires, and Stroop test. The studies on effect of sleep deprivation on cognition have contrasting results due to the varied tests, different sleep deprivation periods, and limited parameters explored. In this research, the psychometric test used is the Stroop test. This test is based on the color word reading interference and used for assessing the workload during cognitive task [5, 6]. Not much work has been done which comments on the interference effect but only on the increased reaction time. This may be due to the mode of conduction and recording of results for the test. Also, other parameters related to the psychometric test like the emotional response are less explored.

Thus, the aim of this research was to be able to comment on the interference effect induced using Stroop test, analyze whether sleep deprivation has a negative impact on the Stroop test results and analyze whether there exists a difference in neural dynamics of sleep deprived individuals, how it impacts their performance as compared to non-sleep deprived subjects.

2 Methodology

Three types of Stroop tests were developed, namely English Stroop test, Marathi Stroop test, and animal Stroop test [7]. These tests were built using GUI, MATLAB, and were developed such that reaction time and answer were automatically saved in Matlab. The subjects were asked to come sleep deprived and non-sleep deprived (after 2–5 h of sleep) to perform the Stroop task during which his/her EEG was recorded. EEG signals were recorded while performing three different Stroop tasks using a data acquisition system named POWERLAB (Fig. 1).



Fig. 1 Sample slides of Stroop task

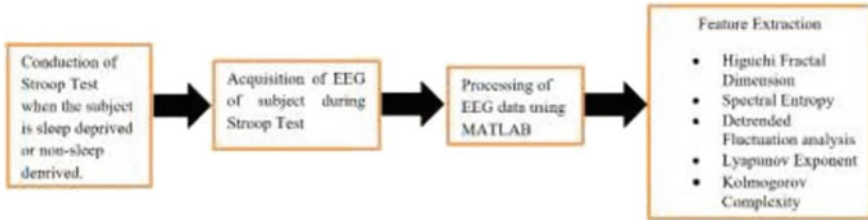


Fig. 2 System block diagram

The eyeblink and muscle artifact removal was done by empirical mode decomposition (EMD) of the EEG and line noise by using notch filter. The SNR and PSD was observed. EEG signal analysis was carried out using features: Higuchi fractal dimension, spectral entropy, detrended fluctuation analysis (DFA), Lyapunov exponent, and Kolmogorov complexity. Figure 2 shows system block diagram which describes the flow of the process.

2.1 Spectral Entropy

The concept of spectral entropy is based on information theory and was developed by Claude Shannon. It is obtained by finding the probability of the PSD of the signal. Finding the entropy in frequency domain uses the power spectral density (PSD) of the signal. Here, P_{norm} is the probability of PSD. It is computed using the following formula:

$$SE = - \sum P_{norm} \log(P_{norm}) \tag{1}$$

2.2 Lyapunov Exponent

Lyapunov exponent is used to study the nonlinear behavior of the system. This is done by first converting the time series system into a phase-space system. For measuring the exponent, a point on the trajectory is selected. Then, its distance with

nearest neighbors is measured. This process is repeated once the threshold is reached. Lyapunov exponent is obtained as follows:

$$\lambda_1 = \frac{1}{N\Delta t} \sum_1^{M-1} \log_2 \frac{L'_i}{L_i} \tag{2}$$

Here, L'_i is the point selected for measuring trajectories, and L_i is when the process is terminated due to exceeding threshold. Lyapunov exponent is used to study the dynamic nature of a system.

2.3 Detrended Fluctuation Analysis

This technique of fractal analysis is applied only to nonlinear signals. In this technique, the signal of length N is integrated and then divided into boxes of size N ; then, for each of these boxes, a local trend is obtained. The detrending is done by subtracting each point in the box with the trend value.

$$F(n) = \sqrt{\frac{1}{N} \sum_{k=1}^N [y(k) - y_n(k)]^2} \tag{3}$$

This gives the variance. The average of all these variances should be such that: $F(n) \propto L^H$, where H is the Hurst exponent. $y(k)$ are the individual boxes/series, and $y_n(k)$ are the trends. Fractal analysis helps identify if the signal is a random or non-random signal [8].

2.4 Higuchi Fractal Analysis

In this, the time series is first split into K_{max} individual time series. The length of curve of each of these time series is obtained; the length of the main time series is the average of these lengths. If this length is: $k \propto k^{-D}$, the fractal dimension of the time series exists [9]. Length of the curve is given by

$$L_m(k) = \left\{ \left(\sum_{i=1}^{\lfloor \frac{N-m}{k} \rfloor} |X(m+ik) - X(m+(i-1)k)| \right) \frac{N-1}{\frac{N-m}{k} \cdot k} \right\} / k \tag{4}$$

2.5 Kolmogorov Complexity

EEG signal dynamics can be studied by quantifying complexity of EEG signal. Kolmogorov complexity is introduced by Andrey Kolomogorov which is a statistical property used to measure complexity of signal. Normalized measure of complexity, $h(n)$ is calculated by, $h(n) = c(n)/b(n)$ where, $c(n)$ is the Kolmogorov complexity and $b(n)$ is ratio of n by $\log n$. Here, n is the length of the EEG signal.

3 Database Collection

Database was captured in Cummins College of Engineering for Women, Pune. We have included the data of 15 participants in our study. Their reaction time, acquired EEG was saved. Also, the database of sleep deprived and non-sleep deprived individuals were saved separately. All the participants were healthy individuals. Written consent was given by all the volunteers before recording EEG data and its use in the research.

4 Results

For all subjects, reaction time increased with increase in incognition. With increase in incognition, the interference effect was also observed for some subjects. The reaction time was in the same range for both sleep deprived and non-sleep deprived subjects. The reaction time for English Stroop task was the highest followed by Marathi and animal Stroop task. Subjects that were not fluent with Marathi language had a higher reaction time for Marathi Stroop task than those who were fluent in Marathi. No significant difference was observed in the reaction time of sleep deprived and non-sleep deprived individuals. Both sleep deprived and non-sleep deprived subjects had similar performance in the English, Marathi, and animal Stroop task.

Figure 3a shows original EEG and first three intrinsic mode functions (IMFs) obtained after empirical mode decomposition of EEG signal. Figure 3b shows remaining four intrinsic mode functions of the same EEG. It is observed that, first 2–3 signals had most noise, and the remaining IMFs contain most of the useful information. Figure 3c shows spectral entropy of EEG, and entropy of signal is plotted against time (minutes). Figure 4a and b shows detrended fluctuation analysis and Higuchi fractal analysis plots. The fractal dimension of a signal gives the extent of irregularity of the signal. Fractal analysis also helps identify if the signal is a random or non-random signal. Figure 4c shows Lyapunov exponent plot of EEG. A positive Lyapunov exponent shows the system is more dynamic, and a negative Lyapunov exponent means that the system is linear.

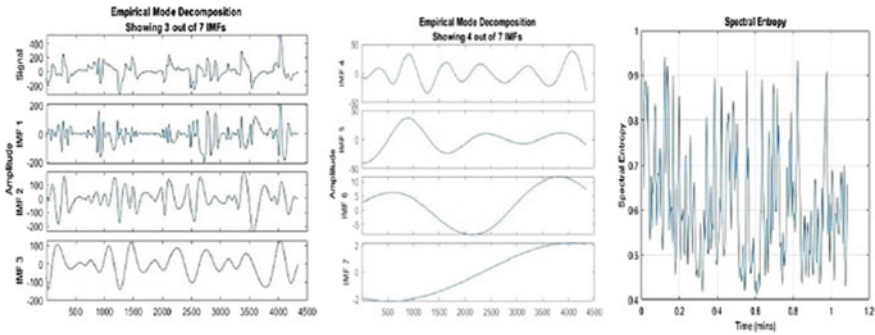


Fig. 3 a Shows original EEG and first three intrinsic mode functions (IMFs) obtained after empirical mode decomposition of EEG signal. b Shows remaining four

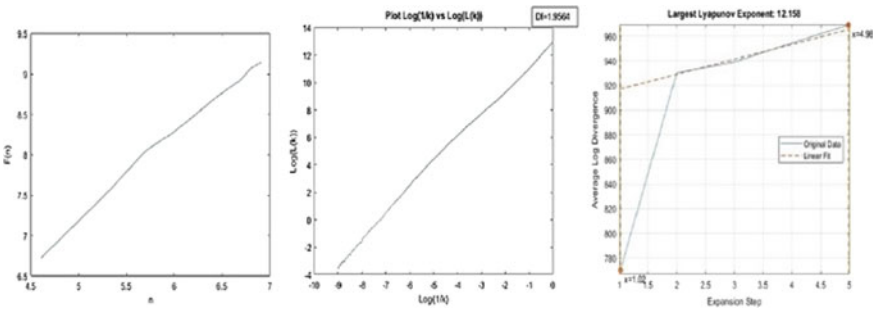


Fig. 4 Detrended fluctuation analysis, Higuchi fractal analysis, and Lyapunov exponent plot

Comparing the results of the three Stroop tasks, it was observed that two features, detrended fluctuation analysis and Lyapunov exponent have shown change with respect to the sleep deprivation. The detrended fluctuation had a higher value for sleep deprived subjects than for non-sleep deprived subjects. The difference in the Lyapunov exponent of EEG measured from the two electrodes was higher for sleep deprived subjects than non-sleep deprived subjects. Detrended fluctuation analysis indicates cognitive functioning. Higher value thus indicates higher cognition. Lyapunov exponent is used to estimate sleep deprivation.

The features of Kolmogorov complexity, entropy, and Higuchi Fractal Analysis helped us compare the performance of the three Stroop Tasks: English, Marathi and Animal. The Kolmogorov Complexity value was symmetric across the two EEG's. For all subjects the Kolmogorov Complexity was highest for the English Stroop task as it was the first task that was conducted followed by Marathi and Animal Stroop task. Subjects not fluent with reading Marathi language also showed a high complexity value for Marathi Stroop Task as well. These subjects were mostly those whose medium of education was English. The entropy value was also greater than 0.5 for maximum subjects. Kolmogorov and entropy helped analyze each subject's

alertness. The Higuchi Fractal Analysis value was on the higher side (1.8–2.0) for some subjects. This value indicates the emotional response of individual to the Stroop task.

5 Discussion

On the basis of work done previously, we hypothesized that the frontal region of the brain is most active during cognition and hence used fronto-polar electrodes to obtain the EEG signal [10]. Most of the studies done previously on cognition consider EEG features which assume that the EEG is a stationary signal [11]. However, the EEG is a non-stationary and nonlinear, inherently complex signal. This nature of the EEG is taken into consideration widely in studies related to schizophrenia, epilepsy, depression, etc. Hence, for this research, features that considered the fractal nature and complex behavior of the EEG were considered. These features help determine the effect of the physiological stress, i.e., sleep on the cognition during a psychometric task. The task used here was the Stroop task which induced a psychological stress on the subject with increase in difficulty level.

Detrended fluctuation analysis has been previously used to assess the cognitive ability of individuals [12]. Higuchi fractal analysis has been widely used in studies related to depression to quantify the amount of emotional stress. But recent studies have found that Higuchi Fractal Analysis does not indicate about a person's depression but rather his or her anxiousness [13]. Since with increase in stress, the anxiety of a person may increase; this feature was used to observe the emotional response of subjects involved in this study. Consciousness of the brain is measured by observing the apparent complexity by entropy and algorithmic complexity of the brain by observing the Kolmogorov complexity [14]. How conscious an individual is will affect his response to a particular task, and hence, it was measured during our research. Lyapunov exponent is used to monitor the different sleep stages in epilepsy and schizophrenia studies [15]. The Lyapunov exponent value significantly changes for sleep deprived individuals. This helps us understand that neural oscillations do change when a person is sleep deprived. Considering the nonlinear and complex nature of the EEG not only gives us information about the cognitive functioning of the brain but also about the emotional stress and awareness of the brain which affects an individual's cognitive performance.

6 Conclusion

These are the result interpretation for all three Stroop tasks: Sleep deprivation does not negatively affect cognition. However, the neural dynamics do change when a person is sleep deprived. A higher cognitive functioning is required to perform the same task when an individual is sleep deprived. Thus, it can be concluded that

though individuals may have same results, every brain functions differently based on the individuals stress response toward physiological, psychological and emotional stress. The work conducted during this research considered acute sleep deprivation only, and no difference in the performance output was observed. However, further work could be done on subjects with chronic sleep deprivation as it is known that chronic sleep deprivation is detrimental to health and thus could negatively impact cognition as well.

References

1. Patrick Y, Lee A, Raha O, Pillai K, Gupta S, Sethi S, Mukeshimana F, Gerard L, Moghal MU, Saleh SN, Smith SF, Morrell MJ, Moss J (2017) Effects of sleep deprivation on cognitive and physical performance in university student. *Sleep Biol Rhythms* 217–225. <https://doi.org/10.1016/j.sleep.2017.11.533>
2. Cain SW, Silva EJ, Chang AM, Ronda JM, Duffy JF (2011) One night of sleep deprivation affects reaction time, but not interference or facilitation in a Stroop task. *NIH Public Access* 76(1):37–42
3. Morales J, Yañez A, Gonzzlez LF, Magraner LM, Ahullò AM, Tramunt MS, Calvete E (2019) Stress and autonomic response to sleep deprivation in medical residents: a comparative cross-sectional stud. *PLoS ONE* 14(4)
4. Peng Z, Dai C, Ba Y, Zhang L, Shao Y, Tian J (2020) Effect of sleep deprivation on the working memory-related N2-P3 components of the event-related potential waveform. *Front Neurosci* 14
5. Deoskar V, Kulkarni P, Dhengade T, Shriram R, Bhat M (2020) Workload assessment based on physiological parameters. AISC series. Springer. ISBN: 978-981-15-1479-1
6. Shriram R, Sundhararajan M, Daimiwal N (2013) EEG based cognitive workload assessment for maximum efficiency. *IOSR J Electron Commun Eng (IOSR-JECE)* 7:34–38. ISSN: 2278-2834. ISBN: 2278-8735
7. Vanitha L, Suresh G, Chandrasekar M, Punita P (2017) Development of four stress levels in group Stroop colour word test using HRV analysis. *Biomed Res* 28(1):98–105
8. Hardstone R, Poil S-S, Schiavone G, Jansen R, Nikulin VV, Mansvelder HD, Hansen KL (2012) Detrended fluctuation analysis: a scale-free view on neuronal oscillations. *Front Physiol*
9. Higuchi T (1988) Approach to an irregular time series on the basis of the fractal theory. *Physica D* 31:277–283
10. Kate S, Malkapure V, Narkhede B, Shriram R (2020) Analysis of electroencephalogram during coloured word reading interference. In: *CISCON 2020*, 30–31 Oct 2020, Manipal. LNEE series. Springer. ISBN: 978-981-16-0335-8
11. Unde S, Shriram R (2014) PSD based coherence analysis of EEG signals for Stroop task. *Int J Comput Appl (IJCA)* 95:50–55. ISSN: 0975-8887
12. Seleznov I, Zyma I, Kiyono K, Tukaev S, Popov A, Chernykh M, Shpenkov O (2019) Detrended fluctuation, coherence, and spectral power analysis of activation rearrangement in EEG dynamics during cognitive workload. *Front Hum Neurosci* 13
13. Kawe TNJ, Shadli SM, McNaughton (2019) Higuchi's fractal dimension, but not frontal or posterior alpha asymmetry, predicts PID-5 anxiousness more than depressivity. *Sci Rep* 9(1)
14. Ruffini G (2017) An algorithmic information theory of consciousness. *Neurosci Consciousness* nix019. <https://doi.org/10.1093/nc/nix019>
15. Kutepov Vitaliy I, Dobriyan Maxim V, Zhigalov Mikhail V, Stepanov Anton F, Krysko Tatyana V, Yakovleva V, Krysko VA (2020) EEG analysis in patients with schizophrenia based on Lyapunov exponents. *Informatics in medicine unlocked*, vol 18, p 100289

UWB Localization Procedures with Range Control Methods—A Review



Y. VenkataLakshmi and Parulpreet Singh

Abstract The indoor positioning of many finished, including military, civil, disaster relief and missions for peace and security, has emerged in recent years as a key feature. The detection of location information in indoor environments needs more precision compared to outdoor environments, partially because different objects represent and transmit signals. The ultra-wideband (UWB) has demonstrated improved indoor positioning technology compared to the others. Several error management and identification codes are used to maintain a safe and stable system that develops a minimum system affected by defects. Convolution code is a way to detect and correct errors in long distance communication. A system to detect, avoid and resolve errors should be developed. Deep space networking, cellular protocols, voice-band modems, submarines, digital communication, satellite communications and many more are the application areas. Present review discussing about the localization techniques and its approaches implementing with UWB.

Keywords Localization · Soft computing · UWB

1 Introduction

A communication network should be able to transmit data with reasonable accuracy from one end to some other. Data/message is corrupted in the channel when transmitted. The network may be connection to the microwave, fibre optic and co-axial cables subject to different noise, distortion and interference [1]. Error occurrence is spontaneous in nature, due either to external interference or to physical defects. This disruption leads to signal form changes (original data). These changes can be single-bit or multiple-bit for digital communication. This change results in losses in two categories. First of all, single-bit error, only one bit of 0 is modified or 1 is changed to 0. So, noise period is higher [2]. It happens least in analyse data. Secondly, burst

Y. VenkataLakshmi (✉) · P. Singh
Lovely Professional University, 144402 Punjab, India
e-mail: venkatlaki@gmail.com

© The Author(s), under exclusive license to Springer Nature Singapore Pte Ltd. 2022
P. Kumar Jain et al. (eds.), *Advances in Signal Processing and Communication Engineering*, Lecture Notes in Electrical Engineering 929,
https://doi.org/10.1007/978-981-19-5550-1_29

295

is the most probable serial communication error. More than one bit is modified in this situation. The burst is calculated from the first bit to the last bit corrupted, but in the meantime, it is not corrupted. So, noise is more than one bit longer. In long distance communications, such a noise is most likely to happen.

Ultra-Wideband (UWB): UWB is characterized as an RF signal that includes portions of frequency bandwidth over 20% or greater than 500MHz by the Federal Communications Department. UWB is a network that distributes data across a wide selection of ranges. With minimum energy consumption, UWB transmitter can transfer large amounts of data [3]. UWB is used to locate the RF signal by using the arrival time difference (TDOA) in order to identify between the reference point and the purpose.

Communication Systems: Use of UWB techniques and the broad RF bandwidths available has enabled UWB communication links. For a short-range wireless local network with data speeds of up to one second, the extremely wide bandwidth is available. This bandwidth is low-frequency available. Therefore, the attenuation of building material for UWB transmissions is significantly smaller than for high-bandwidth wave applications. Path consumption was reduced, and the power needed is decreased to improve performance by working with low frequencies. Mobility is important, and in addition to UWB peripherals, many wireless devices are used in a common area. The wireless network is complete with one mouse, one keyboard, a printer, display, a sound speaker, a microphone, joystick and PDA [4]. UWB is also used in a network sensor as a communication channel. The wired sensor tangle is produced by the patient network of UWB sensors. In medical conditions, pulse speed, temperature and other essential signals are detected using sensors. UWB is used for the transmission of sensor-free information but also for the use of a remote controller, heart beat and for medical images. UWB pulses are used to ensure a very high data rate efficiency in multi-user network applications. These short-run waving types are relatively resistant in the mobile and in-house setting to multi-way cancellation effects. Moreover, time division multiple access (TDMA) for multi-user communications is easily implemented due to extremely short waveforms of time, packet burst and time division.

1.1 Implementing Localization Algorithms

The capability to machine wireless sensor networks is a very necessary function. Measuring data without knowing, where the data is being collected in environmental monitoring applications such as fire monitoring, water quality monitoring and precision processing, is useless. In addition, localization evaluation can include multiple applications such as inventory management, network security, road transport analysis, health monitoring, identification and security. By using the sensor network, the position of sensors with unknown location data was evaluated in order to be aware of the absolute positions of a few sensors and to observe inter-sensor distance and

bearing scales. The anchors are considered to be sensors with knowledgeable location information and can be accessed by a GPS or anchors deployed at coordinated device points.

In this basis of the observation that the air sonic velocity is significantly less than that in air (RF) [5], a uniform promoting time measuring technology has been developed which solves this synchronization problem. The RF and ultrasound equipment are used in combination. An RF signal and an ultrasound pulse are simultaneously transmitted on each broadcast. The RF signal will enter the receiver before the ultrasonic wave. If the receiver receives the RF signal, the ultrasonic receiver is enabled to hear the pulsed ultrasonic. The time difference between the RF signal transmission and the ultrasonic signal receipt is used to estimate the one-way acoustic propagation time. Their approach has provided a fairly accurate measurement of the distance at the costs of additional equipment and system complexity since ultrasonic reception suffers from the extreme effects of the reflections on walls and surfaces. The use of ultra-wideband (UWB) signal is a new development in the analysis of time propagation [6, 7]. A signal UWB is a signal whose ratio of bandwidth to the centre of a frequency is greater than 0.2 or the bandwidth of a signal over 500 MHz in the UWB can be more specific, as its bandwidth and pulse are very wide, and therefore very small. This feature enables UWB signals to be resolved in good times and multi-way separation is easy.

Various algorithms and methodologies for localization have been recommended in different applications to deal with various problem areas. A combination of different techniques known as hybrid location is a well-known method of location with adequate precision and coverage [8]. In the study, on the other hand, hop distance and hop counting location algorithms are widely known as connectivity-based or range-free algorithms. The algorithms without this range are categorized according to the method used for evaluating the intermediate distance between nodes into two categories: heuristic and analytic [3, 5–7, 9–25].

In general, range-free algorithms in location are defined in the implementation scenarios. The separation into four categories is: (1) static sensor and anchor actually knows that are statically compatible [26, 27]; (2) mobile and mobile sensor connections [28, 29] mobile sensor and anchor static nodes [30, 31]. Although different optimization technology can be used to overcome positioning problems in WSNs, these combinations and the minimum number of anchor nodes are almost limited and can be used for this type of scenario. For example, in some cases, the sensors to be developed can only communicate with one or two anchor nodes. New positioning techniques focused on hybrid data fusion and/or heterogeneous access are therefore suggested and evaluated [32]. The clustered system suggested with improvements to conventional GA LEACH. The function of CH is energy, total number of nodes and HCs and the distance from each sink node to CH and BS. Reducing energy consumption, less CHs and a shorter transmission distance contribute to a high fitness value. The proposed clustering process improves network life and reliability. The protocol has been proposed to optimize the energy-efficient clustering of adaptive TEENs and GA routing systems. In GA, network decisions based on the following criteria, average minimum time, transmission distance, energy-left per node, energy dissipation

transmission energy, cluster distance are used. A variation of these parameters is the fitness function. The community centre is responsible for implementing CH, improving the life and energy quality of the WSN network. Shashi et al. KGA for KGA configurations for WSN (K-means clustering and GA) based on K-means and GA clusters. The proposed clustering population protocol is seeded in GA with K-means for better clustering performance. Fitness must count the number of ani modes, the distance between applications and interfaces. The proposed approach operates on a theory that maximizes the energy consumption of the network. The results of the simulation demonstrate that the KGP performs better in comparison with ERP, IHCR and SEP, taking residual capacity, network life and performance into consideration.

The three key areas for the UWB application are: (1) contact and sensors; (2) placement and monitoring and (3) radar. UWB positioning techniques are also capable of providing indoor accuracy monitoring for many applications in real time, such as mobile inventory and emergency locator beacons, indoor navigation for persons with blind and visually impaired vision, human and instrument tracking and military detection. UWB signals provide correct indoor position and place estimation.

WSN implementation for localization: Small, economical sensor node networks are WSNs. The sensor nodes comprise an or more sensors to monitor the phenomenon, an ADC to translate monitor data into digital formats, a small memory unit, a Bluetooth module for data processing, a battery power supply and an information exchange transmitter and receiver [33]. Data transmission detection also includes sensor nodes. Nodes transfer the monitored data to a gateway node or wireless device through single-hop or multi-hop routings [34, 35]. The gateway node is a functioning node, which process data and functions [8]. Sensor nodes are located based on input data and other inputs based on localization steps, as described in Fig. 1.

Accuracy and Precision: Precision and accuracy are the relevant criterion for positioning. Precision implies a similarity to the actual location of the expected position. The accuracy refers to the consistency and reliability of the location measured. Scalability: It is defined as how promptly the localization technique provides the location information. This is also known as responsiveness. Self-organization: Ability of the system to supervise, monitor and manage element activities without the support of an external agency. Power: Power is a necessary parameter in wireless sensor network. Each sensor node has power which is driven from battery. Node Density: Performance of algorithms also depends on node density. Some algorithms such as hop-count-based require high node density for accurate results. Mobile Nodes: Wireless sensor networks consist a few numbers of GPS-enabled mobile nodes that are

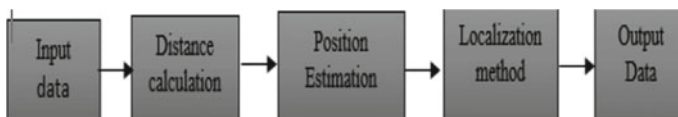


Fig. 1 Localization procedure

homogeneous in nature. Mobile nodes have more battery power and coverage than the static nodes. Also, the mobile nodes are more energy efficient.

Issues in localization procedures: The localization of the sensor network is problematic [16] so the research community still has a wider range of experience. Some of the issues are:

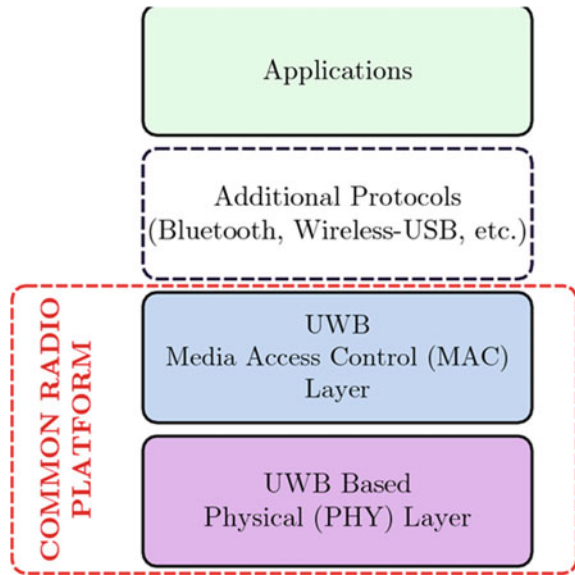
- **Cost-effective algorithms:** The costs incurred in hardware and implementation must be taken into account in the design of the localization algorithm. Due to its cost and hardware size, GPS is not suitable. The use of GPS devices is not recommended due to higher hardware price and size.
- **Robust algorithms for mobile sensor networks:** Due to the accessibility and coverage facility, mobile sensors are useful in many conditions. New algorithms must therefore be created to enhance mobility.
- **Algorithms for three-dimensional spaces:** Accurate location information is essential for many WSN applications. The more the algorithms proposed for 2D space are applicable. Some of the applications require 3D WSN positioning.
- **Accuracy:** If the node location is improperly estimated, the precision of the localization decreases. Accuracy in sensor localization is very necessary.
- **Scalability:** The monitoring area and sensor nodes could increase their size in large-scale deployment. It requires constant observation for the scalability of the localization techniques.

UWB Technology for WSN: The very good time-domain resolution makes it possible to precisely locate, to track, live together with existing narrower band systems (due to the extremely low power spectral density), to install low power and to install low price on the chip technology, a viable technology for wireless sensor networks (WSNs). Sensor nodes (SN), which form the basis of these networks, are typically mobile-based devices. As batteries, these nodes are usually powered by relatively small, limited processing capabilities. This has resulted in the creation of a range of UWB sensing network concepts in both the industry and government. In terms of UWB systems, three separate loops are available: the sub gigahertz (250–750 MHz), the low (3.1–5 GHz) and the top (6–10.6 GHz). Each UWB band has a single compulsory channel and devices which work independently of each other. In this case, priority is given to UWB' (3.244–4.742 GHz) low band based on WSN applications' propagating spectrum technology (Fig. 2).

The system's main feature is the flexibility of design, based on a basic binary manipulation and a non-coherent detail-oriented. The results of the simulation show that the vibrating duplicate code has a major impact on accuracy, data rate control and reliable reception. Furthermore, the data is retrieved with a method of detecting that makes the recipient design easier and ensures that higher flow syncing and consistent detection are avoided. We also analysed a pulse repetition coding to allow robust and powerless transmission devices in accordance with the methodology for the wireless communication.

A WSN is really just known as a wide array of sensors. There is a sensor, processor and radio transceiver for every node. These networks have a broad data acquisition

Fig. 2 Overview of UWB technology for WSN

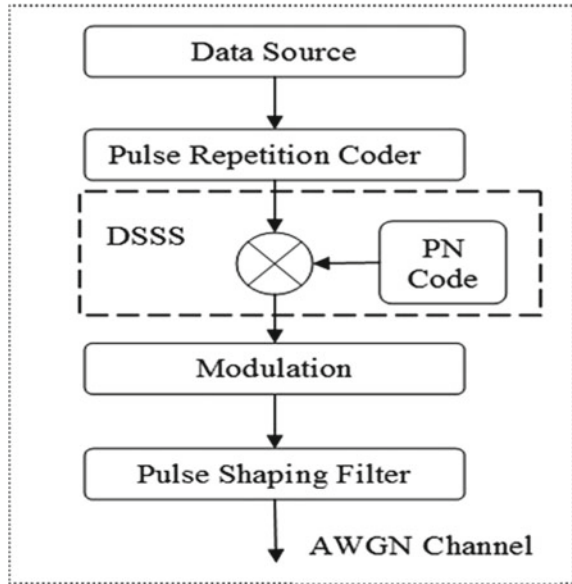


and treatment capability to monitor environmental phenomena in particular throughout the region. Communication nodes are connected to a multi-hop network of sensors via wireless networks the selected media must be available worldwide to allow these networks to operate globally. The communications device is used between nodes to access data. For most of WSN applications, radio frequency (RF) communications are widely used. It needs a reasonably long range of high data rate communications at low-energy costs at fair mistake rates without the power grid. The transmitter and receptor are essential for actual communication in the sensor node but can, as suggested by ZigBee, be optimized for a complete or reduced function system. In general, each WSN node has a transceiver that communicates through the wireless network with other nodes. The main objective is to process a small stream from and to the radio waves in a processor. Recent developments have contributed to the growth of low-cost wireless and electronic sensor networks.

System Architecture Modelling of a UWB: WSN is a principle related to Wireless Personal Area Networks (WPANs). This range of networks has many different uses, such as surveillance, military applications, home automation and civil network hardware. In considering these applications, it can be easily concluded that WSN has some intrinsic constraints: low costs, low power, simplicity and small nodes. No network will also be viable WSN without these features. We therefore consider this context in this article, so that we can design and compare UWB receivers in a suitable way. The FCC determines a UWB radio system whether the -10 dB signal range is 500 MHz or more or the fractional bandwidth of the signal is greater than 20%.

UWB system design: In recent years, various implementation activities have occurred in UWB schemes, including pulse amplitude modulation (PPM) for impulsive radio

Fig. 3 Digital data transmission

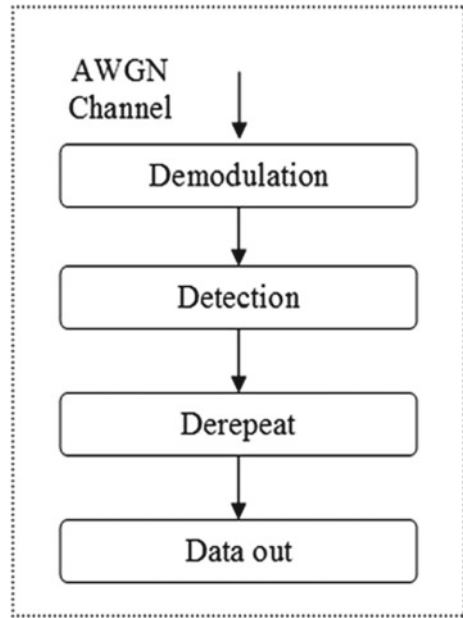


methods, binary phase-shift modulation (BPSK), pulse orthogonal frequency modulation (OFDM) approaches and frequency-based challenges. Due to the extreme lack of amplification, the UWB system is less optimal, although normal narrow band and wideband systems use RFs to transfer the signal from the system software to the real frequency where the system is working. In comparison with traditional RF radio, data transmission as digital pulse simplifies the transceiver system (Figs. 3 and 4).

UWB bandwidth:In this, bandwidth is the bandwidth constrained by the points of 10 dB below the maximum radiated pollutants, or by 5.944–10.234 GHz. **Centre frequency:** The centre frequency, f_C , equals $(f_H + f_L)/2$. **Fractional bandwidth:**The bandwidth of the band is $2(f_H - f_L)/(f_H + f_L)$ and the bandwidth of the bandwidth equal to or greater than 0.20.

2 Literature Review

Wireless sensor networks (WSNs) are one of the major wireless communications applications that have drawn attention from many researchers to multiple applications such as environmental monitoring, health care, security, tracking and military applications. WSNs are developed in the field of interest by implementing sensor nodes. Efficient design maximizes network coverage, connectivity and network life-cycle performance [9, 10]. As shown in Fig. 2, nodes of the sensor can be used algorithmically or statistically. The position of each sensor node is described for a deterministic deployment. A minimum number and their location can be calculated

Fig. 4 Digital data reception

in order to achieve the required coverage and linkage level by knowing the field geometry and the pattern of the RF nodes [11, 12].

However, this approach is not normally appropriate for large networks involving hundreds to thousands of knots, since they require the installation of a large number of knots at predefined locations. Random uniform application is better suited for networks comprised of a large number of sensor nodes [13, 14]. The downside to such a system is that it does not ensure full coverage and connectivity because it requires randomness. Coverage and connectivity may be lacking in some areas of the field. Wireless UWB short-range communication is not the same as a conventional carrier wave system. UWB waveforms are short-term and have very special features. The UWB principle is particularly appealing because it spreads signals through very large bandwidths because it allows an excellent bandwidth to be shared among various systems and applications. Rapid technological advances using UWB signals have been tested in recent years. In three wireless applications: networking, radar and positions and ranges, UWB technology provides significant enhancements.

Although there is a literature survey available under on localization techniques, although a few reports concentrate on standalone localizing techniques without reflecting on new and emerging technologies and uses. Therefore, the survey is inaccurate, while concentrates only on ultrasonic. The work in [36] describes comparatively modern proposed technique but only concentrates on the indoor localization techniques and addresses the free location briefly. The research reviews various technologies used for indoor positioning, such as Wireless Local Areas Network (WLAN). But they do not address placement in recent applications, including envi-

ronmental assistance and health live applications, either from an energy efficiency or demand perspective. The survey in gives a significant category of different outdoor placement approaches based on fingerprints and describes how each approach works.

3 WSN with Various Soft Computing Approaches

Dynamic, distributed, highly constrained organized networks are the wireless sensor networks (WSNs). It is a high computing environment with a small and regulated transmission, processing and limited source of energy. The severe force constraints have a significant impact on the nature of active nodes and thus network life in WSN's distributed autonomous devices is sensed, computed and wireless. Though WSN is widely used, it has still resolved a number of challenges. The major issue in WSN is how the power supply is preserved and the energy of the network is preserved to enhance the life of the network. In order to solve WSN problems, researchers' attention has been drawn to the concept of using WSN's embedded computing techniques in order to overcome soft computing paradigm in order to treat the complexity and uncertainty of data in a complex environment. Furthermore, some assessment factors were used to validate new suggested approaches or compare various real-time techniques to find the best for a particular application. More advanced algorithms are required to overcome these challenges. All these activities would certainly significantly increase the advancement of the WSN technology for large-scale application systems (Fig. 5).

Soft computing technologies show great analogy and compatibility through wireless sensor networks, particularly with regard to approaches in power management and self-decision.

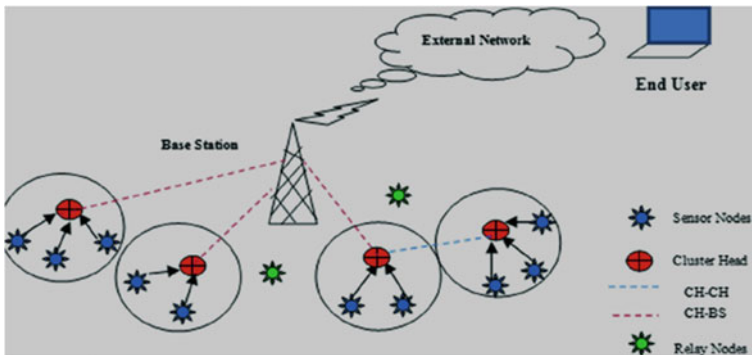


Fig. 5 Proposed system

3.1 Localization for UWB in WSN

Each sensor node is compared to an electrical signal transducer, analogue-to-digital converter (ADC) transducer, data computing and storage, radio system and electrical device the main part of electricity consumed is referred to as the WSN contact unit [1]. Usually, the nodes are a wireless transceiver and powered by recycling batteries, which create nodes as long as it lives until the battery is destroyed. In other things, WSN is inherently a resource constraint and a limited speed of information processing, bandwidth and data capacity. WSNs will be responsible for the self-organization of the infrastructure network, leading to a creation which in a specific environment may detect and respond to a phenomenon. During the application of the node, it is necessary to control the energy consumption knowingly and to manage it effectively [2]. To allow user observation and analysis, WSN must transmit their data to main location or sink via a network. WSNs are hundreds of thousands of sensor nodes linked to each other via a network of communication. The network may not always be secure, because there is a node failure that causes the network to be reconfigured and the routing path recomputed to delay the selection of long routes leading to network life [37]. WSNs designer's main aim is to create a protocol for energy-efficient routing. If each node begins transmitting its own data to a fixed or mobile base station directly or through a set of nodes on the network containing a high proportion of nodes. The routing at WSNs is very important, most each of its characteristic's changes from each other. In [4], the authors talk for wireless routing algorithms to increase the existence of the network and the node. Numbers of routing protocols have been previously suggested, based on a network structure that can be divided into 3 primary, flat, location-based and hierarchical categories [38]. Due to the results in energy saving, the later type brought great attention and decreased the dissipation of energy into a WSN. The hierarchy of low-energy adaptive clustering (LEACH) [39] is one of the popular hierarchical network routing systems. A routing protocol based on clusters minimizes worldwide use of energy by spreading charge to all nodes in various times. The concept is to use clustering to transfer data on the cluster head (CH) chosen to lower transmission distances for most nodes to the base station and to rotate CH to spread the device energy demand over all the nodes.

Homogeneous network: This network calculates the overall dissipation of energy throughout the network by assuming that the network divides in cluster types. Based on the measured distance, WSN optimization algorithms can be divided into two categories: centralized and distributed. In a centralized standardization, all the inter-sensor determined distances are then sent to the central place to measure the location of and sensor node. On the other hand, with other anchor nodes, the different sensor nodes use distance calculations to determine its own position. The key approaches to clustered algorithm design include multidimensional (MDS), linear programming and stochastic optimized algorithms. The algorithms of the distributed location are DV-Hop, DV-distance [10] and several others based on these two algorithms [13, 14].

Method	Additional Hardware Required	Synchronization between Nodes	Effect of Speed of sound
RF- RF	No	Required	No
RF-Ultrasonic	Yes	Not Required	Yes
Ultrasonic – Ultrasonic	Yes	Required	No

Fig. 6 Comparison of TDOA Methods

Type of Measurement		Accuracy		Overhead	
		Line of Sight	Non Line of Sight	Hardware	Computational
Angle	AOA	High	Very Low	High	Low
Distance	Hop Count	Low	Very Low	Low	Low
	RSSI	Low	Very Low	Low	Low
	TDOA	Very High	High	High	Low
	TOA	High	High	Low	Low

Fig. 7 Measurement techniques comparison

3.2 Comparison of TDOA Methods

See Fig. 6.

3.3 Measurement Techniques Comparison

See Fig. 7.

4 Simulation Results and Discussions

Field variations may be due to natural boundaries that result in reflections, diffraction, absorption and spread of radio from nodes. This results in NLOS node coordination, characterized by an estimated NLOS error to various distributions, such as Gaussian distribution, uniform distribution and exponential distribution, under varying conditions (Figs. 8 and 9).

Irrespective of the substantial advancement of research in this direction, some unresolved problems remain. At the end, we focused on solving those problems.

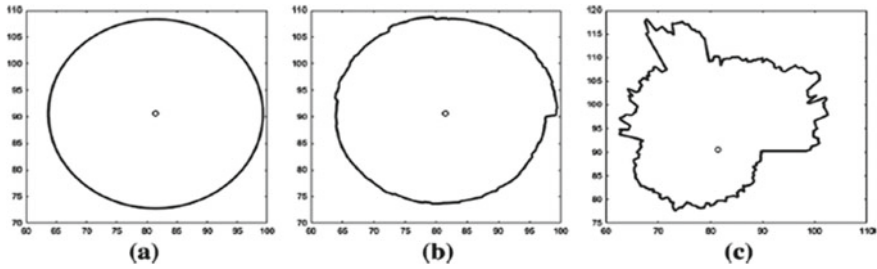


Fig. 8 Various distributions used in the experimentation

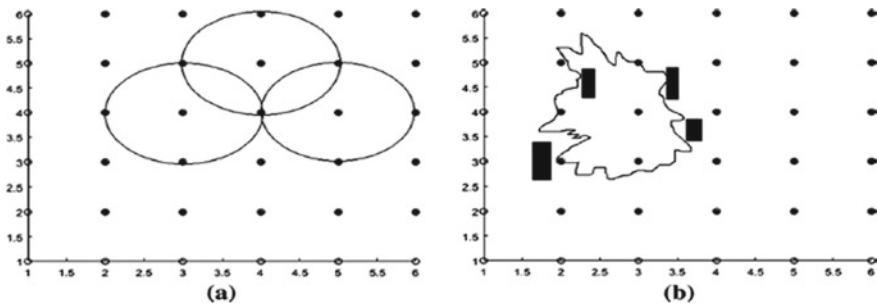


Fig. 9 NLOS node coordination

This paper is very useful to those who are interested in standardization growth, modification and optimization techniques.

Evaluation of the Localization Algorithms: The performance of our system is better than that of our DS-UWB and TH-UWB, in the figure, but both the BER and variance of error bits are increasing as the user population increases.

Random Deployment: As shown in Fig. a, 100 nodes in a 100m/100m square region where points represent nodes and borders represent connections between neighbouring nodes were deployed at random. The interaction is 12 m and the interconnection is average 4.6 m. Between .00 and .025, the STRESS value was set. Figure(b) represents each NMDS-MLE node's relative coordination. It indicates that the relative coordinates are different from the original Fig network (a). This is because the relative coordinate is dependent only on the distance between all nodes in the network. In Fig. b, the relative information of 4 random anchor nodes to which the ŠER refers changes their relative coordinates. The points are the actual node codes and the triangle lines show mistakes from nearby locations; the average place error is about 5385 per cent. The average location error is 18 4746 per cent, even though the MDS-MAP algorithm is used.

Grid Deployment: There were 100 nodes in a 45m-to-45m square grid deployment area (a). The contact range is 12 m, and the average link is 16.8 m. The value of the STRESS was between .00 and .025. The relative map with NMDSMLE algorithm

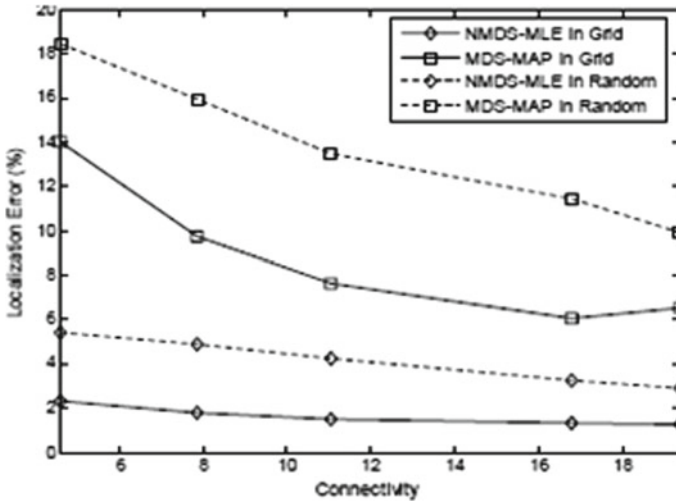


Fig. 10 Comparison of Localization Accuracy

with the same secondary structure is represented in Fig. b, and the absolute map is shown by the change based on 4 random anchor nodes in Fig. c. The average location error for the grid is around 1.2876

Performance analysis: In different scenarios under different levels of connectivity, NMDS-location MLE’s output is tested with the same test settings compared to MDS-MAP. From the figure, it can be observed that NMDS-MLE algorithm’s location error in various scenarios is much less reliable and stable than MDS-MAP. In addition, when NMDS-RSS and MDS-MAP are implemented in a grid of various connectivity variations, it shows that in the grid layout, NMDS-RSS achieves higher localization accuracy than in the random layout with a same level of connectivity (Fig. 10).

Figure. 11 shows the correlation between localization error and N in NMDS-MLE algorithm. Since the precision of the range is enhanced by MLE, using the RSS data given by our U-BOTH systems, it is apparent that the localization problem declines drastically when the levels of random and grid deployments increase significantly (Figs. 11, 12 and 13).

4.1 Implementation of UWB Network Simulation

Tags distribute UWB signals in slots for specified times. The time differential of the receiving signal is reached after the signal is intercepted with each positioning anchor. The time difference will then be transferred wirelessly via LoRa technology to the solar collector. The data collector is sent to the position server via data transfer. The

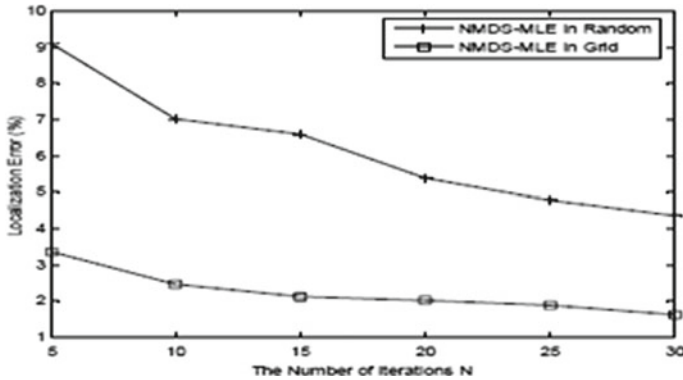


Fig. 11 Localization accuracy vs iterations

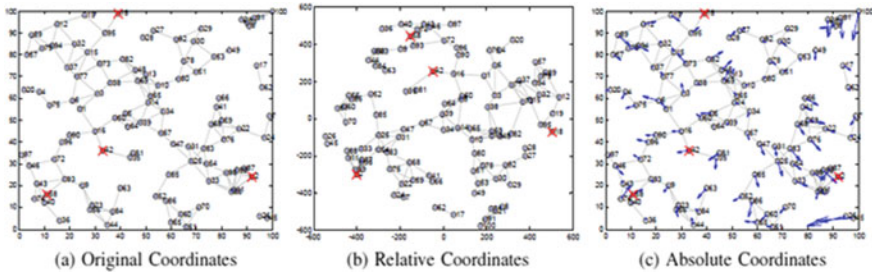


Fig. 12 NLOS Node coordination comparison

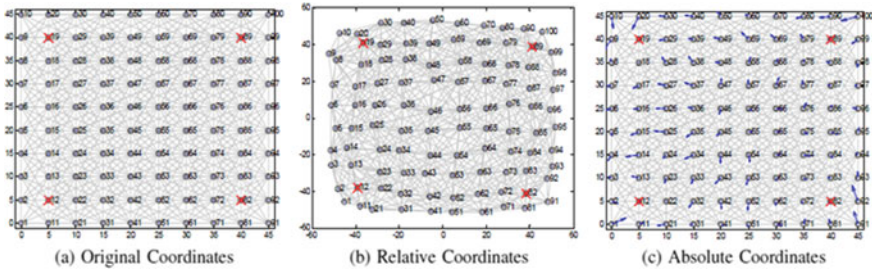


Fig. 13 TDOA Node coordination comparison

server uses the optimized TDOA positioning algorithm to locate the tag accurately (Figs. 14 and 15).

Under the condition of no external interference, the data is processed by the differential the weighted average method of correction and movement. The error in the tag is between 11 and 18 cm and 13 cm on average. The error in placing the sign. Under external interference, the positioning error on the positioning system tag is considerably higher. The error of positioning at the moment is 14–25 cm and the

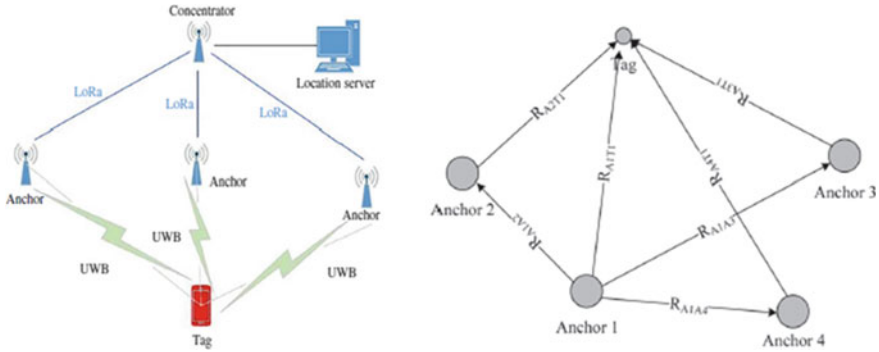


Fig. 14 Proposed UWB network structure

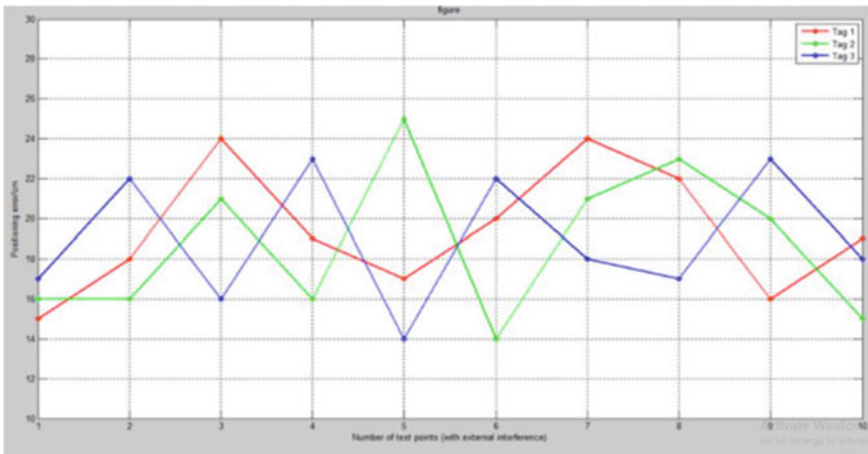


Fig. 15 Test points with external interference

average error of positioning is about 19 cm. The interference source can be seen with a certain effect on indoor positioning accuracy. For study, ten standard locations have been selected and the findings are given in Table 1. There are no major differences or locations during the test procedure that indicate that the process is working (Figs. 16, 17 and 18).

5 Conclusion

In the review, it concluded that network localization that uses the measuring UWB range to estimate the node positions and the measurement distribution parameters simultaneously, while in addition to several more characteristics, UWB provides a

Table 1 Methods in the literature

Authors name	Study	Methods	Remarks
[17] Abdulrahman Alarif (2016)	To analyse the present state of UWB positioning technologies	Hybrid approaches are more tolerant of the external pressure of interference and reflection, and so appear to be successful	The environment can improve positioning efficiency, while node cooperation can improve performance if exploited carefully
[18] Rajan Kadel (2019)	The development and implementation of error correction systems in WBAN are challenging	The WBAN norm is a bottom two layers OSI error correction in WBAN communication	The energy restricted existence of nodes and computer complexity for WBAN
[19] Kexin Guo (2016)	Cooperative ultra-wide-screen related localization algorithm and GPS neutralized environment experiments for many unmanned aerial vehicles	Indirect cooperative method of relative location to evaluate aerial vehicles uncontrolled	The current 3D case result will be investigated and checked under more general restrictions and a UWB specific training flight
[20] Carmelo Di Franco	Study the path of calibration-free network using ultra-wideband non-line-of-sight parameters	We introduce a method of calibration-free, infrastructure-free sensor network area	We compare our approach to the alternative implementation, using simple Gaussian error models, of our coordinate decent algorithm and thus do not capture multimodality of the error distributions
[3] Xuezhi Zeng (2020)	A compact and accessible ultra large band noise sensor for medical diagnoses has been developed	The sensor functions for respiration and pulse control have been demonstrated	Pre-hospital care has technical solution over the last few decades, becoming an integrated part of the health system
[21] J. K. Ravan (2013)	In this scheme, the data is distributed across high-rate sequences over a few GHz bandwidth	This approach enables solving this problem while preserving scalable participant complexity UWB technology plays a major role in the modern wireless network	It allows the device range to be enlarged by very significant amounts in particular at high bit rates

(continued)

Table 1 (continued)

Authors name	Study	Methods	Remarks
[22] Adrienn Dineva (2019)	This article presents the state of the art of soft computing techniques and their applications,	the simulation and evaluation processes were performed by employing MATLAB/Simulink software	Design problems of machines smart way complicated and defined optimization algorithms, which are multi-objective
[5] Ioannis (2020)	Study the advantages and possible limitations of revised AI techniques for multiple DR tasks	Machine learning is a multidisciplinary field that focuses on concepts from different areas, ranging from computer science, statistics, mathematics and engineering	In reality, many of the solutions suggested require testing and evaluation through large-scale real life research studies
[6] Dinesh Kuma (2012)	To study the optimization-based approach for class responsibility assignment problem	To reassign methods and class attributes in a diagram of the method. This helps designers of the object-oriented applications	In each phase, the solution was then transferred to these equations within the search area in an effort to reach the best value. These are used due to particle convergence into optimal method
[7]Hyongdoo Jang (2020)	An description of the SC applications published in various industrial areas	The MMS target is the most desirable mining method among the possible alternatives for a mineral deposit	Their mutual dynamics make the issues more challenging. However, mining engineers also face many global problems
[23] Irene Ndanu (2016)	Study detection approach and maintenance for cyclic and hamming protocols	Data communication is able to recognize and correcting channel errors	The theory of coding concerns data transmission across noisy networks and the analysis of corrupted messages
[24]Marwa Sharawi (2014)	To improve the network's life time, we have overcome the economic contraction and keep the sensor node processing as late as necessary	WSN size depends primarily on the size and coverage for a particular application of the deployed network geographical area	The efficient use of energy in WSN is a problem of congestion that affects network performance and life time

(continued)

Table 1 (continued)

Authors name	Study	Methods	Remarks
[25] Anup Kumar Paul (2017)	We evaluate different measuring techniques and methods in respect of range- and range-free location with specific attention on, respectively	The role in WSNs to determine physical sensor node coordinates is called the position or positioning	Moreover, a central and distributed localization scheme is divided into range- and variation
[26] Ali Yassin (2016)	To study the recent advances in indoor localization: a survey on theoretical approaches and applications	Both are based upon evolutionary algorithms searches, with the objective of reducing positioning errors during wireless preparation	Cluster co-operation enhances position estimation and is most beneficial if traditional localization technology, like indoor scenarios, fail to produce accurate evaluation
[27] S. Sand (2010)	Hybrid data fusion (HDF) observed that the power accurate location information for communications networks. We will present the scenarios and radio technologies assessed by the WHERE wireless placement consortium in this study	Accuracy and reliability of the position may still not be sufficient to enhance communication systems, we are looking for a new cooperative position system	Current multiple specific HDF algorithms based on the path that either track a direction parameter or directly place the signal received
[28] Junlin Yan (2014)	The relevant aspects of these algorithms are related and correlated. The direct (non-iterative) algorithms are extremely significant and often used for indoor positioning	In this section, we will research ID methods which include the most suitable method, the method of Newton, the sensitive area, the approach of Gauss Newton and the method of logistic regression	The purpose of this work is to provide a systematic and thorough analysis of the previously mentioned LS positioning procedures and pay particular attention to the traditional approaches
[29] Jaron fontaine (2020)	To address this, we propose (i) a novel semi-supervised autoencoder-based machine learning approach for improving ranging	This approach approaches the existing algorithms in machine learning though achieving restricted complexity	We suggest an inferior architecture for UWB localization systems with minimal response times and large bandwidth savings in attempt to overcome the functional limitations of cloud computing such as low bandwidth requirements

(continued)

Table 1 (continued)

Authors name	Study	Methods	Remarks
[40] Angelo Coluccia (2018)	To this aim, the positioning of mobile devices operating in the network becomes crucial	The field of wireless positioning with focus on cooperation, mobility and advanced array processing, which are key enablers for the design of novel localization solutions for crowdsensing WSNs	The obtained performance demonstrated that mm Wave and MISO are enabling technologies for designing accurate positioning systems that can be readily implemented in the near future
[41] Guenther Retscher (2019)	Obtained from a robotic total station. This approach is validated in both static and kinematic tests. The calibration range has been established	The calibration range has been established as one component of an indoor laboratory to undertake a more diverse research agenda into robust indoor positioning systems	Implementation of D Wi-Fi and extraction point identification, the so-called iCPs, in the UWB range measurements are discussed for user pathway navigation
[30] Sunil K. (2019)	The range limitation is evaluated and corrected using uncertainties of parameters to improve performance under these conditions	Parameters are collected in two different conditions in real-time experimental installations. A proposed fluid inference model uses these uncertainty and relationships to estimate errors of range	The experimental and simulation results show that the proposed model reduces the range of errors and the calculation burden effectively. In addition, because of the non-statistical approach, the model does not cause any delay in estimating a range error

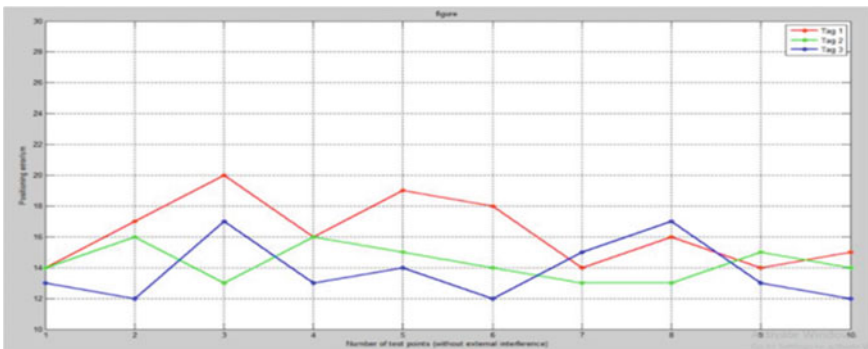


Fig. 16 Test points without external interference

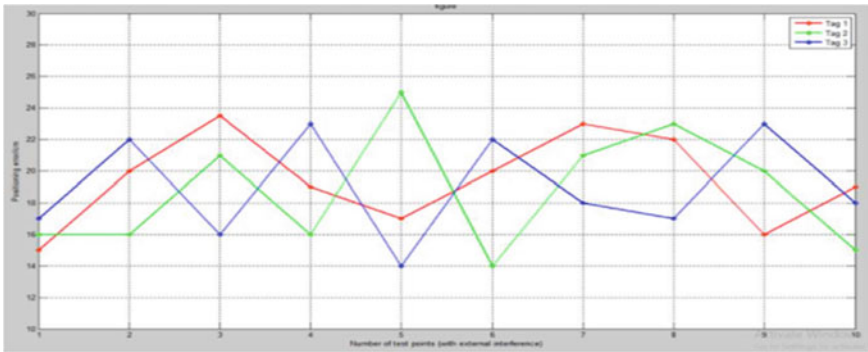


Fig. 17 Simulation results with and without external interference

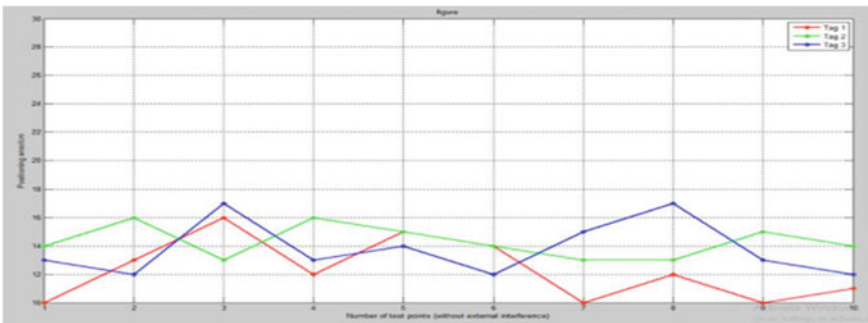


Fig. 18 Test points with and without external interference

high degree of accuracy (e.g. licence-free and low power consumption, does not affect most existing radio systems, high multi-path resolution level, etc.). UWB systems are one of the leading indoor positioning technologies and were used in much more applications than before as compared to other systems. Various factors can improve the positioning efficiency. In addition, we have implemented UWB technology, which focuses primarily on positioning and recognizes both internally (strength or weakness) and actively (chances and threats) influencing this technology. For UWB and WSN, a few examples were discussed in detail, and the results were implemented in simulations tested for future architecture.

References

1. Bhargava VK, Yang Q, Peterson DJ (1993) Coding theory and its applications in communication systems. *Defence Sci Journal* 43(1):59–69
2. Neha, Rather GhM (2015) Convolution error control coding—a review. *Int J Electr Electron Data Commun* 3(3). ISSN: 2320-2084
3. Zeng X, Robakowski J (2020) Investigation of an ultra-wideband noise sensor for health monitoring. *Sensors* 20:1034. <https://doi.org/10.3390/s20041034>

4. Gomez JM, Lopez O, Montes M, Bota SA, Juvells I, Herms A (1996) Implementation and design of new model of neural network with application on typographical character recognition. In: IEEE international conference on image processing, 1996
5. Antonopoulos I (2020) Artificial intelligence and machine learning approaches to energy demand-side response: a systematic review. *Renew Sustain Energy Rev* 130:109899
6. Saini DK, Sharma Y (2012) Soft computing particle swarm optimization based approach for class responsibility assignment problem. *Int J Comput Appl* (0975-8887) 40(12)
7. Jang H, Topal E (2020) A review of soft computing technology applications in several mining problems. *Appl Soft Comput*. <https://doi.org/10.1016/j.asoc.2020.05.019>
8. Gruber T, Cammerer S, Hoydis J, Brink S (2017) On deep learning-based channel decoding. In: 51st annual conference on information sciences and systems (CISS), Mar 2017, pp 1–6
9. Kumawat HL, Sharma S (2012) An implementation of a forward error correction using convolution encoding with Viterbi decoding. *IJSCE* 2(5):95–99. ISSN: 2231-2307
10. Vikrama Narasimha Reddy S et al (2013) Design of convolutional codes for varying constraint lengths. *Int J Eng Trends Technol* 4(1):61–66
11. Mago VK, Devi MS, Bhatia A, Mehta R (2010) Using probabilistic neural network to select a medical specialist agent. In: Multi-agent systems for healthcare simulation and modeling: applications for system improvement, p 164
12. Mahasantipiya P, Yeasarapat U, Suriyadet T, Sricharoen J, Dumrongwanich A, Thaiupathump T (2011) Bite mark identification using neural networks: a preliminary study. In: Proceedings of the international multiconference of engineers and computer scientists, vol 1
13. Shankarapillai R, Mathur LK, Nair MA, George R (2012) Periodontitis risk assessment using two artificial neural network algorithms—a comparative study. *Int J Dental Clin* 4(1)
14. Sumathi B, Santhakumaran A (2011) Pre-diagnosis of hypertension using artificial neural network. *Glob J Comput Sci Technol* 11(2)
15. Patil SM, Mudholkar R (2012) An osteoarthritis classifier using back propagation neural network. *Int J Adv Eng Technol* 4(2)
16. Letchner J, Fox D, LaMarca A (2005) Large-scale localization from wireless signal strength. In: National conference on artificial intelligence, vol 1. AAAI Press, pp 15–20
17. Arifi A, Al-Salman A, Alsaleh M (2016) Ultra-wideband indoor positioning technologies: analysis and recent advances. *Sensors* 16:707. <https://doi.org/10.3390/s16050707>
18. Kadel R, Islam N (2019) Opportunities and challenges for error correction scheme for wireless body area network—a survey. *J Sens Actuator Netw* 8:1. <https://doi.org/10.3390/jsan8010001>
19. Guo K, Qiu Z, Meng W (2017) Ultra-wideband based cooperative relative localization algorithm and experiments for multiple unmanned aerial vehicles in GPS denied environments. *Int J Micro Air Veh* 9(3)
20. Di Franco C, Prorok A (2017) Calibration-free network localization using non-line-of-sight ultra-wideband measurements. In: IPSN 2017, Pittsburgh, PA, USA, April 2017
21. Ravan JK, Chougule SR (2013) High data rate UWB system design using multi code approach. *Int J Eng Res Technol (IJERT)* 2(12). ISSN: 2278-0181
22. Dineva A, Mosavi A (2019) Review of soft computing models in design and control of rotating electrical machines. *Energies* 12:1049. <https://doi.org/10.3390/en12061049>
23. John IN, Kamaku PW (2016) Error detection and correction using hamming and cyclic codes in a communication channel. *Pure Appl Math J* 5(6):220–231
24. Sharawi M, Soriet I, El-Mahdy H, Emary E (2013) Routing wireless sensor networks based on soft computing paradigms: survey. See discussions, stats, and author profiles for this publication at: <https://www.researchgate.net/publication/255754336>
25. Paul AK, Sato T (2017) Localization in wireless sensor networks: a survey on algorithms, measurement techniques, applications and challenges *J Sens Actuator Netw* 6:24. <https://doi.org/10.3390/jsan6040024>
26. Yassin A, Nasser Y (2016) Recent advances in indoor localization: a survey on theoretical approaches and applications. Engineering Product Development, Singapore University of Technology and Design, Singapore plus German Aero Space Center (DLR), Oberpfaffenhofen, Germany

27. Sand S, Mensing C, Ma Y, Tafazolli R (2010) Hybrid data fusion and cooperative schemes for wireless positioning. Authorized licensed use limited to University of Surrey. Downloaded on 23 April 2010 from IEEE Xplore
28. Yan J (2013) Review of range-based positioning algorithms. *IEEE Aerospace Electron Syst Mag.* <https://doi.org/10.1109/MAES.2013.6575420>
29. Fontaine J, Ridolfi M (2020) Edge inference for UWB ranging error correction using autoencoders. Received 3 July 2020. Accepted 17 July 2020. Date of publication 29 July 2020. Date of current version 10 Aug 2020
30. Meghani SK, Asif M (2019) Empirical based ranging error mitigation in IR-UWB: a fuzzy approach. Received 11 Feb 2019. Accepted 28 Feb 2019. Date of publication 11 March 2019. Date of current version 29 March 2019
31. Prorok A, Martinoli A (2014) Accurate indoor localization with ultra-wideband using spatial models and collaboration. *Int J Robot Res* 33(4):547–568
32. Kar S, Moura JMF, Ramanan K (2012) Distributed parameter estimation in sensor networks: nonlinear observation models and imperfect communication. *Trans Inf Theory* 58(6):3575–3605
33. Shanthi D, Sahoo G, Saravanan N (2009) Designing an artificial neural network model for the prediction of thrombo-embolic stroke. *Int J Biom Bioinform (IJBB)* 3(1):10–18
34. Schrch C (2016) A partial order for the synthesized channels of a polar code. In: *IEEE international symposium on information theory*, July 2016, pp 1C-5
35. Zhang M, Huang Q, Wang S, Wang Z (2018) Construction of LDPC codes based on deep reinforcement learning. In: *IEEE international conference on wireless communications and signal processing*, Oct 2018, pp 1–6
36. Karabatak M, Ince MC (2009) An expert system for detection of breast cancer based on association rules and neural network. *Expert Syst Appl* 36(2):3465–3469
37. Berrou C, Glavieux A, Thitimasjshima P (1993) Near Shannon limit error-correcting coding and decoding: turbocodes(1). In: *Proceedings of the IEEE international conference on communication (Geneva, Switzerland)*, May 1993, pp 1064–1070
38. Arikan E (2009) Channel polarization: a method for constructing capacity achieving codes for symmetric binary-input memoryless channels. *IEEE Trans Inf Theory* 55(7):3051–3073
39. Orr RK (1997) Use of a probabilistic neural network to estimate the risk of mortality after cardiac surgery. *Med Decis Mak* 17(2):178–185
40. Coluccia A, Fascista A (2019) A review of advanced localization techniques for crowdsensing wireless sensor networks. *Sensors* 19:988. <https://doi.org/10.3390/s19050988>
41. Retscher G, Gikas V, Hofer H (2019) Range validation of UWB and Wi-Fi for integrated indoor positioning. *Appl Geomat.* <https://doi.org/10.1007/s12518-018-00252-5>

Multilevel Authentication to Wireless Sensor Networks Against Malicious Attacks Using Butterfly Method



Ishrath Unissa, Ch. Raja, and Syed Jalal Ahmad

Abstract Wireless sensor networks (WSN) are the arrangement of the group of sensor nodes used to communicate information between end nodes. WSN's are autonomous, hence node entry or node exit is common to the network structure, which results in security threats. This burning and challenging issues deflect the research community to provide much focus on this field. Most of the researches done in this era enhance the security of such networks by providing key distribution methods. However, this type of security may not be optimum due to the autonomous structure of the network. To overcome this challenge few researchers proposed zero-knowledge algorithms, but due to huge mathematical calculations and extra hardware requirements, the complexity increases. Hence delay is increased and paves way for the attacker node. In this paper, vulnerable technique without key distribution is being presented that not only enhances the security against malicious attacks but also reduces the complexity. The presented approach is validated by a network simulator.

Keywords WSN · Malicious attack · Butterfly method · Code word · Network simulator

1 Introduction

A wireless sensor network is the arrangement of sensor nodes grouped in a particular geographical area to transfer information between end nodes. This network provides the solution where cellular networks do not work. Initially, this network was dedicated

I. Unissa (✉)
CMR Technical Campus, Hyderabad 501401, India
e-mail: ishrath.ece@cmrtc.ac.in

Ch. Raja
Mahatma Gandhi Institute of Technology, Hyderabad 500075, India
e-mail: chraja@mgit.ac.in

S. J. Ahmad
Malla Reddy Engineering College (Main Campus), Hyderabad 500043, India

to the military for collecting environmental information in terms of temperature, pressure, and pollution. Latter due to its vast application, the industrial sector also chooses this network to sense the data, monitor the activity, for communication, and so on. As the network does not require any pre-defined infrastructure, i.e., one can form a sensor network anywhere in any period by placing a group of sensor nodes in any geographical area. However, due to node mobility, any node can move and any node can enter into the network, this particular issue of node mobility gives birth to security threats, there are several security threats in wireless sensor networks Jalal et al. [1]. So security became a necessary parameter to address. Several types of research provide the solution against these security threats by providing the key distribution and by measuring the energy parameter of the node. The key distribution technique will not work in wireless sensor networks because of its autonomous structure. Initially, the energy parameter can be used to judge the attacker nodes very easily by comparing the energy of the anchoring node to the active nodes. However, once the energy parameter matches by entering attacker nodes into the network with multiple energies, then the security using energy may not be the optimum solution. To overcome this drawback, researchers provide another type of solution against these attacks using zero-knowledge algorithms. But all these approaches are complex and required additional hardware to fulfill the security. As a result, the complexity and additional hardware increase both processing and transmission delay. This issue of increasing delay allows malicious nodes into the network and corrupts the information from the active node.

In this paper, a simple and dynamic approach is being presented using the Butterfly method that does not require any key distribution and energy to authenticate the active node within the network. Also, the proposed approach minimizes the complexity and additional hardware of the node hence can optimize the total nodal delay.

The rest organization of the paper is as follows. Section 2 presented the survey of the literature, Sect. 3 shows the proposed approach, and in Sect. 4, simulation results have been presented, and the conclusion of the paper is given in Sect. 5.

2 Survey of Literature

Wireless sensor networks have numerous attacks [1] at various layers (i.e., at network, transport, and application layers). Ankur and Amit [2] come with a meticulous survey about security approaches that can avoid the various attacks in the network Nagar et al. [3] proposed an algorithm to avoid denial of service attacks. The authors authenticate some nodes in the network as service provider nodes, which may be always possible in sensor networks due to their autonomous structure. Furtak et al. [4] discussed an approach in which the authentication of nodes is done locally. Again this is not feasible in sensor networks, as node entry and node exit is always possible due to network autonomous structure. Yang et al. [5] designed an algorithm based on the blockchain and reinforcement learning technique to guarantee the security of wireless sensor networks. The designed algorithm adds the nodal delay between source and

destination. The algorithm is complex and reduces the efficiency of the network. Ahmad et al. [6] proposed a solution to black hole attacks by designing a simple binary code for the hop count. However, the authentication process is done only at a single level so may not be the optimum solution. Rangeetha et al. [7] designed a security algorithm in which the security to the network is provided by key distribution with the help of zero-knowledge algorithms. However, the distribution of keys is not possible in wireless sensor networks because of their autonomous structure in nature. Shyam and Munesh [8] presented a technique to secure the network using a zone routing protocol. However, creating a code at every node in the network is complicated particularly when the arrangement of the network is multi-hop, and node entry and exit are possible between the end nodes. Ahmed et al. [9] presented a security model based on energy parameters. However, this model may not give the optimum solution when the attacker nodes enter into the network with different energies and becomes difficult to identify them.

In this paper, main focus was given to avoid malicious attacks in the network, as this is a very common attack of wireless sensor networks. In this approach, a simple multilevel and efficient security solution is being provided to the sensor network using the Butterfly method.

3 Proposed Approach

Here we are presenting our proposed approach. In this model, we initially use decimal numbers of equal-weighted hex code as input to Butterfly structure. The decimal numbers of equal-weighted hex code can be calculated as

$$y = \prod_{i=1}^4 3i \quad i = 1, 2, 3, 4 \quad (1)$$

and the remaining decimal numbers of the series of equal-weighted hex code can be calculated as

$$X_0 = \frac{p+q}{2}, \quad X_1 = 2X_0 \quad (2)$$

where ‘ p ’ and ‘ q ’ are the first and last decimal numbers of Eq. (1), respectively

From the above two equations, we get

$$x = \{X_0, X_1\} = \{5, 10\} \quad (3)$$

$$y = \{3, 6, 9, 12\} \quad (4)$$

Fig. 1 2-point butterfly structure for 'x' series

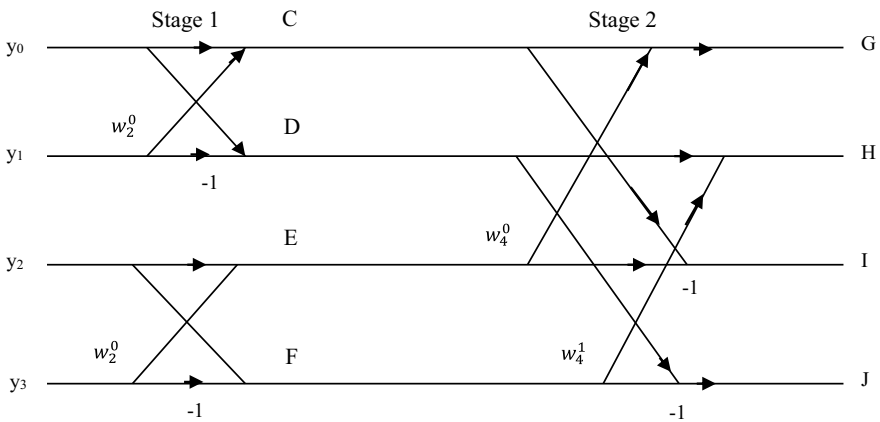
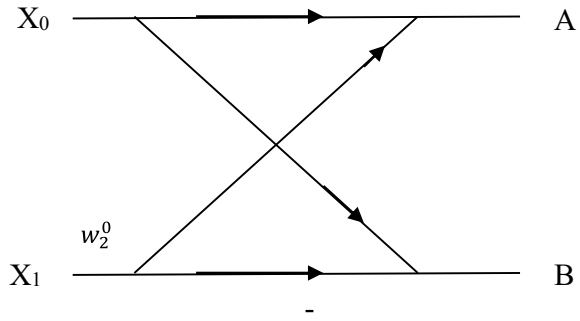


Fig. 2 4-point butterfly structure for 'y' series

The series of x and y are given as input to 2-point and 4-point Butterfly structure as represented in Figs. 1 and 2, respectively.

The output A and B can be calculated by the equations represented as

$$A = X_0 + w_2^0(X_1) \tag{5}$$

$$B = X_0 - w_2^0(X_1) \tag{6}$$

where $w_2^0 =$ twiddle factor $= 1$.

The general twiddle factor can be represented as

$$w_N^k = e^{\frac{j2\pi k}{N}} \tag{7}$$

The inputs of Fig. 3 are taken in the bit reversal manner of the sequence as given in Eq. (4). Where $y(0) = 3, y(1) = 6, y(2) = 9, y(3) = 12, w_4^0 = 1,$ and $w_4^1 = -j$.

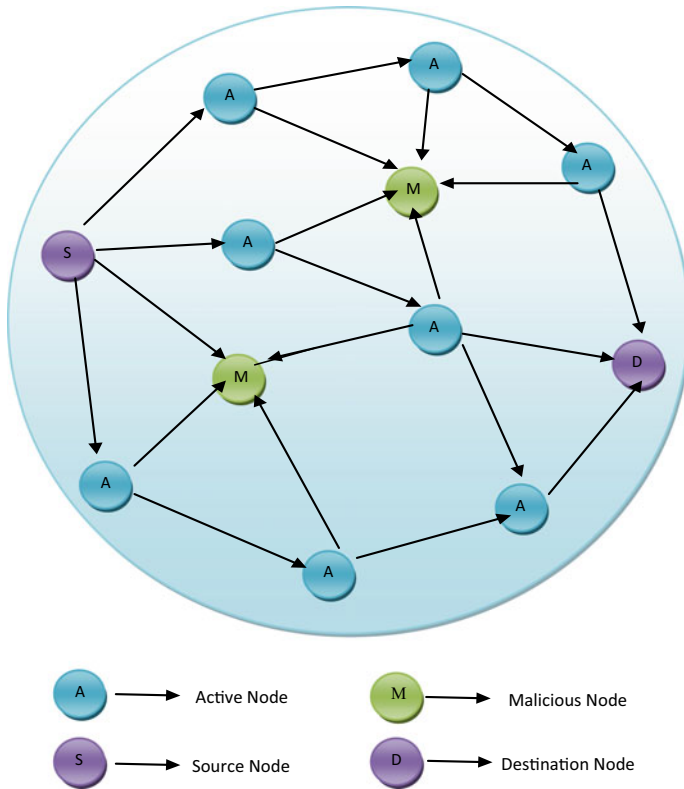


Fig. 3 Wireless sensor network of any geographical area

Figure 3 has two stages, the output of stage 1 is $C, D, E,$ and $F,$ and the output of stage two $G, H, I,$ and $J.$

The equations for the output at stage 1 can be represented as

$$\begin{aligned}
 C &= y(0) + w_2^0 y(2), \\
 D &= y(0) - w_2^0 y(2), \\
 E &= y(1) + w_2^0 y(3) \quad \text{and} \\
 F &= y(1) - w_2^0 y(3)
 \end{aligned} \tag{8}$$

And the equations for the output at stage 2 can be represented as

$$\begin{aligned}
 G &= C + w_4^0 E, \\
 H &= D + w_4^1 F, \\
 I &= C - w_4^0 E \quad \text{and}
 \end{aligned}$$

$$J = D - w_4^1 F \quad (9)$$

In the proposed approach, the security at various layers, i.e., network, transport, and application layers is provided. At all levels of security, the proposed approach avoids the number of malicious attacks. (e.g., wormhole at the network layer, session hijacking at the transport layer, and repudiation at the application layer). At level one, we are given the security generated by 2-point Butterfly structure output, stage 1 output of 4-point butterfly structure is used at level two securities, and stage 2 output of 4-point butterfly structure is used at level three securities. All the outputs are represented in the binary system and final security codes are obtained.

In the proposed technique, minus sign (−) is considered as a compliment. For example, the output of any stage is −6 then the final binary code is 1 0 0 1 (i.e., complement of 0 1 1 0). The symbol ‘j’ can be considered as −1.

3.1 Node Matching Process

Let us consider a wireless sensor network in a certain geographical area as represented in Fig. 3. Let the source node wants to communicate with the destination node through intermediate nodes. Initially at hop1, the source node sends a request for data transmission to all its neighboring nodes, so the neighboring nodes that satisfy the proposed security will be considered as active nodes, and the nodes that will not satisfy the given security model will be treated as attacker nodes. The security codes that need to satisfy at different layers (i.e., at network, transport, and application layers) can be represented in the next section.

3.1.1 First Level Security (Network Layer Security)

At this level, the node should generate the binary hex code of the output value of 2-point Butterfly structure to satisfy the security, i.e., value of A and B .

So from Eqs. (5) and (6), we have

$$A = 15 = 1111(\text{hex value})$$

$$B = -5 = -(0101) = 1010$$

(to remove −ve sign we compliment).

Hence, the final code that needs to satisfy at level one can be represented as

$$SC1 = \{AB\} = \{11111010\}$$

So the nodes that satisfy this code a level 1 (i.e., at the network layer) will be allowed to do the next security check.

3.1.2 The Second Level of Security (Transport Layer Security)

At this level, the node should generate the output of stage 1 of 4-point Butterfly structure to satisfy the security (i.e., C , D , E , and F) and the values of these outputs can be calculated using Eq. (8)

$$\begin{aligned} C &= 12 = \{1100\} \\ D &= -6 = -\{0110\} = \{1001\} \\ E &= 18 = \{00011000\} \\ F &= -6 = -\{0110\} = \{1001\} \end{aligned}$$

Hence, the final code that needs to satisfy at level two can be represented as

$$SC2 = \{CDEF\} = \{11001001000110001001\}$$

So the nodes that satisfy this code at level 2 (i.e., at the transport layer) will be allowed to do the next security check.

3.1.3 The Third Level of Security (Application Layer Security)

At this level, the node should generate the output of stage 2 of 4-point Butterfly structure to satisfy the structure (i.e., G , H , I , and J) and the values of these outputs can be calculated using Eq. (9)

$$\begin{aligned} G &= 30 = \{00110000\} \\ H &= -6 + j6\{-6 + (-1)(6)\} \\ &= \{-6 - 6\} = -12 = \{11101101\} \\ I &= -6 = \{1001\} \\ J &= -6 - j6 \\ &= \{6 - (-1)(6)\} = 0 = \{0000\} \end{aligned}$$

Hence, the final code that needs to satisfy at level three can be represented as

$$SC3 = \{GHIJ\} = \{001100001110110110010000\}$$

So the nodes that satisfy this code at level 3 (i.e., at the application layer) will be allowed to access the data and transmit it to the next anchoring node, and this process will continue at all intermediate nodes till it reaches the destination. Here all the active nodes can generate the desired security code for the desired layers as they know the security operation. However, the attacker nodes cannot understand the security operation and can be easily detected and at the same time can be avoided.

4 Simulation Results

Table 1 represents the simulation parameters used to analyze the network. In this section, simulation results have been and compared with the art of work.

Here we have seen Fig. 4 represents the variation of packet delivery ratio concerning simulation time, it has been observed from the figure that the packet delivery ratio is more when compared to the other approaches.

Figure 5 represents the variation of packet loss rate concerning the packets sent. It is observed from the figure the loss rate of the proposed approach is less when compared with the other approaches as given in Fig. 3. Because the proposed

Table 1 Simulation parameters

S. No	Parameters	Values
1	Simulation time	65 s
2	Node count	0–265
3	Hop count	7
4	Propagation model	(ground) Two ray
5	Type of queue	Drop tail
6	Antenna type	Omni type
7	Type of routing	LAEERP
8	Type of traffic	Video (VBR)
9	Experimental network area	1500 m × 1500 m
10	Speed of node mobility	1, 2, 3, 4, 8.10 m/s
11	Pause time	0, 30, 60.120, 150, 190 ms
12	Size of packet	1 kb

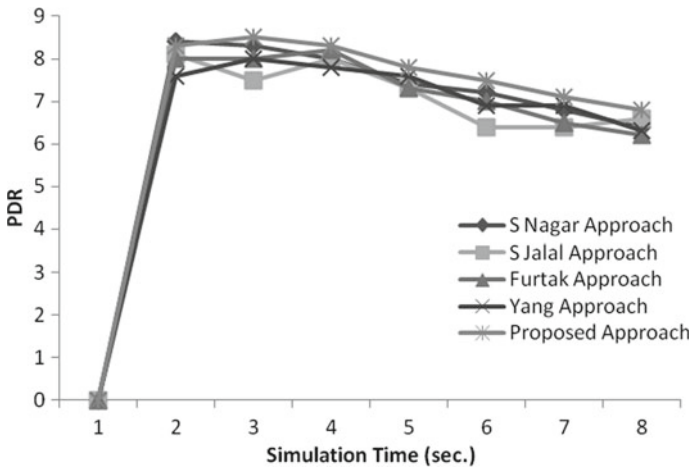


Fig. 4 Variation of PDR versus simulation time

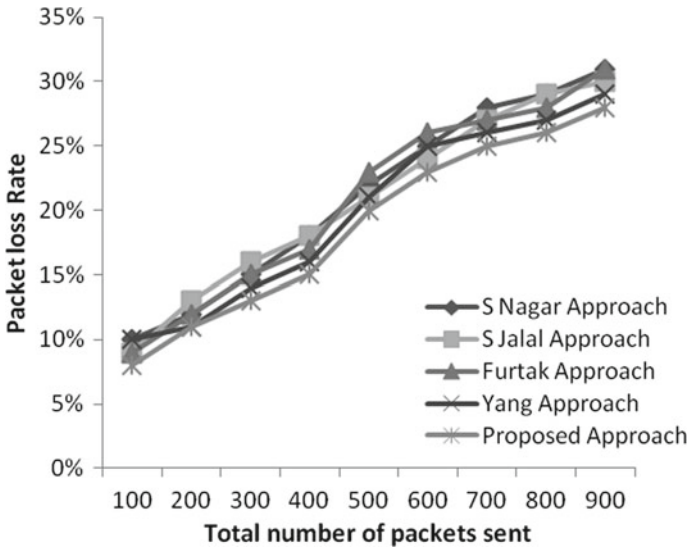


Fig. 5 Total packets sent versus packet loss rate

approach does not allow the attacker nodes to interact with the active nodes, hence may not be able to drop the packets and shows better results with compared with the given approaches.

5 Conclusion

This paper presents a simple and very effective method using to authenticate malicious attacks in wireless sensor networks. This method not only improves the detection process of malicious nodes easily but also enhances the packet delivery ratio as well. The proposed approach also reduces the energy consumption between end nodes by reducing the mathematical complexity. The proposed approach also helps the research community to guide for further improvement in this field.

References

1. Jalal Ahmad S, Unissa I, Shoukat Ali M (2018) Enhanced multi-level security support for MANETs. *Int J Res Anal Rev* 5(4):948–957
2. Sirohi A, Agarwal AK (2020) Security in wireless sensor network (WSN): a detailed survey. *Int J Adv Sci Technol* 29(5s)
3. Nagar S, Rajput SS, Gupta A, Trivedi MC (2017) Secure routing against DDoS attack in wireless sensor network. In: 3rd IEEE international conference on computational intelligence and communication technology (CICT), pp 1–6

4. Furtak J, Zieliński Z, Chudzikiewicz J (2019) A framework for constructing a secure domain of sensor nodes. *Sensors* 19(2797)
5. Yang J, He S, Xu Y, Chen L, Ren J (2019) A trusted routing scheme using blockchain and reinforcement learning for wireless sensor networks. *Sensors* 19:970
6. Jalal Ahmad S, Reddy VSK, Damodaram A, Radha Krishna P (2015) Detection of black hole attack using code division security method (CDSM). In: *Advances in intelligent systems and computing*, vol 2. Springer Publication, pp 307–314
7. Ranjeetha S, Renuga N, Sharmila R (2017) Secure zone routing protocol for MANET. In: *International conference on emerging trends in engineering, science and sustainable technology (ICETSST-2017)*, pp 67–76
8. Rajput SS, Trivedi MC (2014) Securing zone routing protocol in MANET using authentication technique. In: *International conference on computational intelligence and communication networks*, pp 872–877
9. Ahmed A, Bakar KA, Channa MI, Haseeb K, Khan AW (2016) A trust aware routing protocol for energy constraint wireless sensor networks. *Telecommun Syst* 61(1):123–140. 24

Advanced 18 nm FinFET Node-Based Energy Efficient and High-Speed Data Comparator Using SR Latch



M. Lavanya , Malla Jyothsna Priya, Ponukumatla Janet, Kavuluri Pavan Kalyan, and Vijay Vallabhuni 

Abstract Comparators are predominantly employed in data converters. In this paper, the primary SR latch-based comparator circuit using 180 nm standard CMOS is altered using 18 nm FinFET for even more significant speed in data comparison. The 18 nm FinFET technology produces energy-efficient conversion. 18 nm FinFET nodes have superior control over the channel, and they have quick switching speed and high current compared to CMOS. Cadence Virtuoso tool is utilized to design and simulate the circuit. The circuit works for high frequencies, even as much as 1 GHz. When compared to the original design, the speed in data conversion is escalated, providing better results.

Keywords CMOS · Dynamic comparator · FinFET · SR latch · Switching speed

1 Introduction

Comparators are an integral part of transforming information from one form to other. In electronics, they are used to convert analog data toward digital data. The primary operation is to give an output signal by juxtaposing a pair of input signals. Currents or voltages are compared by a comparator yielding a 0 or 1. High-gain differential amplifiers are present in comparators [1–4]. Relaxation oscillators, successive approximation ADC's digitize the analog signal to do that, and comparators are used. Dynamic comparators are comparators with a clock. After the alteration in the clock, the output is brought forth in dynamic comparators. Clocked comparators are of high-speed and low-power dissipation. Dynamic comparators consist of regenerative feedback. Dynamic comparators with various applications are developed every year with added attributes to overcome the limitations and extend their application in the circuits. High-speed ADC's is the main application of clocked comparators

M. Lavanya · M. J. Priya · P. Janet · K. P. Kalyan · V. Vallabhuni (✉)
Department of Electronics and Communication Engineering, Institute of Aeronautical Engineering, Dundigal, Hyderabad 500043, India
e-mail: v.vijay@iare.ac.in

© The Author(s), under exclusive license to Springer Nature Singapore Pte Ltd. 2022
P. Kumar Jain et al. (eds.), *Advances in Signal Processing and Communication Engineering*, Lecture Notes in Electrical Engineering 929,
https://doi.org/10.1007/978-981-19-5550-1_31

327

(Dynamic comparators) [5]. Apart from the primary dynamic comparator, the other type of comparator uses positive feedback for its functioning and is known as a conventional comparator. Full-scale digital output in conventional dynamic latched comparators is due to slight variation in input voltages which pull up to 0 or 1. Rapid settling time and high rise data rates are assisted by a comparator when the time frame is brief [1].

Nevertheless, the fabrication process faults the variable results, imprecision [2–4, 6]. In the conventional comparator, the regenerative stage is prepended with a separate preamplifier to subdue the weaknesses [7]. Kickback noises are minimized by modifying the conventional comparator by including a separate preamplifier. However, minimized kickback noise made the design ineffective for low-power circuits, creating a drawback in designing high-speed ADC [8]. Switching power supplies and error detection are other applications of comparators, along with data conversions. Chip area, speed, and power dissipation are reproving limitations in switching power supplies and error detection. Pre-amplifier-based dynamic latch comparator has superior accuracy but has static power issues. However, this problem can be solved using a new and improvized technique that uses low power. That technique is known as the dynamic latch comparator, which uses the charge sharing mechanism (CSDLC). CSDLC employs two dynamic latch comparators. One is a resistive dividing comparator, and the other is a differential current sensing comparator [9].

However, a pair of clock cycles is not enough to pull off a full-scale swing and needs excessive average power, which fails to make it a perfect solution [10]. A high offset and low-speed technique, i.e., dynamic latch comparator, which uses strong-arm mechanism (SADLC), is employed to conquer all hindrances of CSDLC [11]. However, to increase the steadiness of the circuit, another improvized technique was to append an SR latch to the SADLC [1]. Appending the SR latch to the SADLC yields better results, but the issue is that 18nm CMOS usage in the circuit has some disadvantages.

Metal oxide silicon field-effect transistor (MOSFET), going by the name IGFET (Insulated Gate Field effect transistor), has some drawbacks. One is that they have a short life [12]. The other is that they are susceptible to the overload voltage, so handling them with great care is needed. The most crucial disadvantage in MOSFET is that additional transistors are used, which raise the size of the chip to enhance the computational power. However, the chip size should be minimized to enhance the computational power. MOSFET unveil short-channel effects, which makes its usage impossible. Thus FinFETs heaved into sight [13–17].

FinFET is the same as MOSFET; it is just that the direction is switched, and instead of keeping it flat, it is established straight on edge. This way of installing it is demonstrated to be more effective in controlling the progression of electrons from source to drain. Thus, it provides the FinFET with high transconductance, fast switching speed, and low power consumption.

The SR latch is a unique sort of nonsynchronous device which turns out independently for control signals. A latch is a device that stores the data. The latch speeds up the comparisons in this design because it is connected to a comparator [1].

This paper is an improvement to the SR latch-based dynamic comparator which uses standard 18 nm CMOS. As mentioned above, the FinFET is more advantageous when compared to the MOSFET, which yields better results. The paper’s organization is planned as proposed circuit details are in Sect. 2. Results of the simulation are in Sect. 3, and conclusions are drawn out in Sect. 4.

2 Designing Process of Comparator by Using FINFET

2.1 The Primary Functioning of Dynamic Comparator

The fundamental working principle of the comparator circuit is to compare the two input voltage signals and give output has as either 1 (if the voltage is high) or 0 (if the voltage is low). The schematic of a comparator with SR latch is shown in Fig. 1. The comparator has synchronous data link control (SDLC), which is accompanied by an SR latch. Regenerative latch with positive feedback is a part of the comparator. The SR latch speeds up the comparison at the output stage by detecting a slight variance at the transitional nodes, O_1 and O_2 .

2.2 Construction of Dynamic Comparator-Based SR Latch Using FINFET

Dynamic comparator-based SR latch using FINFET proposed diagram is appeared in Fig. 2. The distinguishing input contains semiconductors set Q_1 and Q_4 . The semiconductors Q_2 and Q_3 , associated with the distinguishing input set Q_1 and Q_4 individually, given positive criticism, empowers the detecting of little distinction between the input voltages V_{in} and V_{ref} , bringing about the quicker dynamic of halfway yield nodes O_1 and O_2 . Two different p-FINFET semiconductors Q_{12} and Q_{13} , are utilized at O_1 and O_2 for quicker pre-charge. The positive input at the yield phase comprising

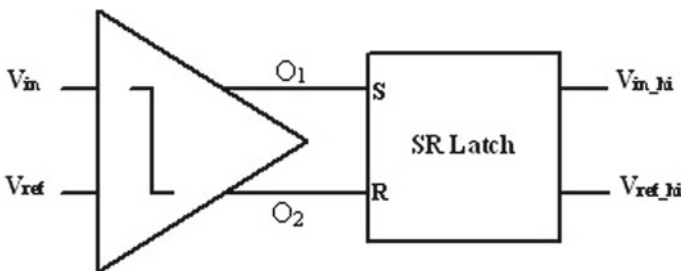


Fig. 1 Basic block diagram of dynamic comparator-based SR latch

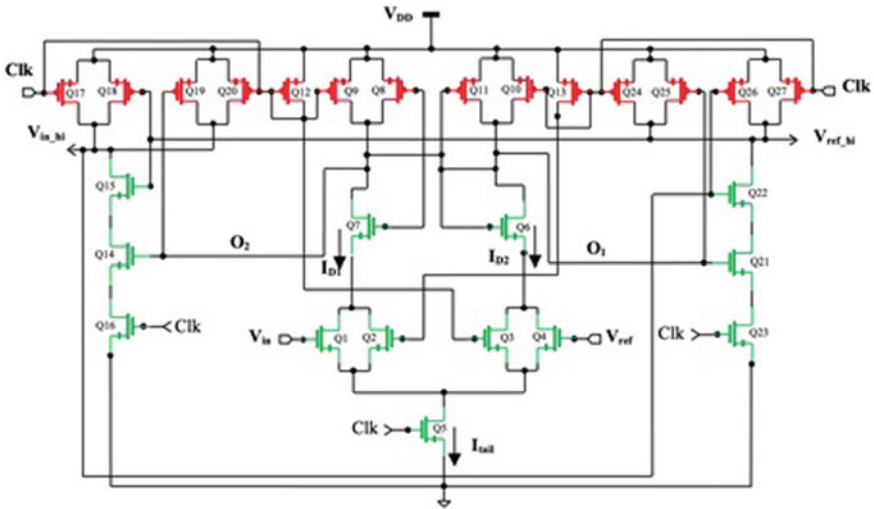


Fig. 2 Dynamic comparator based on SR latch using FINFET circuit diagram

of SR latch framed based NAND by using the semiconductors Q22, Q21, Q25, Q26 and Q14, Q15, Q18, Q19, regeneratively enhance the distinction between the outputs O₁ and O₂ to offer rail-to-rail swing with diminished reaction time.

2.3 Operation of Proposed Design

Working Principle of SR Latch Dynamic Comparator Using FINFET. The two vital phenomena’s of the proposed module is explained by splitting the SR latch into the evaluation phase followed by the reset phase, as given in Fig. 2.

Evaluation Phase. When the signal appears high, the tail n-FINFET semiconductors Q5 at the distinct phase and Q16 and Q23 at the yield phase are turned ON. In contrast, any remaining p-FINFET clocked semiconductors turn OFF. At this stage, the positive feedback activity of n-FINFET semiconductors Q₂ and Q₃ can be clarified: on the off chance that $V_{in} > V_{ref}$, the channel voltage of Q₁ will fall at a quicker rate than Q₄. Presently, as the positive criticism activity of Q₂ and Q₃ drive-in, the channel voltage of Q₁ will drop considerably quicker. Accordingly, releasing the node O₂ to the ground and simultaneously rapidly charging the hub O₁ to V_{DD} [1, 11, 12]. Subsequently, a minor distinction somewhere in the range of O₁ and O₂ is adequate to move the SR latch yields V_{in_ht} to V_{DD} and V_{ref_ht} to GND, regeneratively.

Reset Phase. The n-FinFET semiconductor Q5 goes OFF when the wave moves to logic 0 from logic 1. Terminating the current stream and restricting static power occurs when the present way to the ground goes off with it [1]. The clocked p-

Table 1 Design parameters of proposed circuit shown in Fig. 2

Transistor	L (nm)	W (nm)
Q ₁ to Q ₇ , Q ₁₅ and Q ₂₂	18	72
Q ₈ to Q ₁₁	18	113
Q ₁₂ and Q ₁₃	18	170
Q ₁₇ to Q ₂₀ , Q ₂₄ to Q ₂₇	18	97
Q ₁₄ and Q ₂₁	18	36
Q ₁₆ and Q ₂₃	18	144

FINFET semiconductors, Q₉, Q₁₂, and Q₁₀, Q₁₃, go ON to rapidly pre-charge the distinguishing yield nodes, O₁, and O₂, to V_{DD} . Additionally, the p-FinFET clocked semiconductors of the last phase. To be specific, Q₁₇, Q₂₀, Q₂₄, and Q₂₇, resetting the separate nodes V_{in_ht} and V_{ref_ht} to V_{DD} are ON as the n-FinFET semiconductors Q₁₆ and Q₂₃ are OFF at that time. Removing the present way to the ground stops the SR latch's positive input activity [1].

Aspect Ratio of Transistor. The semiconductor sizes are maintained as little as possible for the circuit to own high-velocity activity and low parasitic execution. This is additionally done while planning the other up-and-comer geographies for practical examination. The ‘‘Advanced estimating methods’’ for streamlined semiconductor sizes for the designed configuration are utilized, which are similar to that used in SADLC [10] and CSDL [9], which are contrasted and the designed plan. In Table 1, the dimensions from the library with 18 nm type are recorded for ideal semiconductor.

Power Analyses. The average power dissipation for one complete cycle from the supply voltage is represented by

$$P_{avg} = \frac{1}{T} \int_0^T V_{DD} I_D dt = f_{clk} V_{DD} \int_0^T I_D dt \quad (1)$$

In the above equation, the following notations are I_D , and f_{clk} represent the clock's comparator frequency and V_{DD} , respectively. I_D transient parts are given in Fig. 2, and I_D close by flows of semiconductors Q₈ and Q₁₁. In one clock cycle, the estimations are done. The activity is consequently clarified: (1) in the course of $clk = 0$, V_{DD} provides flow through I_{D1} , I_{D2} and the last, respectively, yielding charge nodes O₁ and O₂ to supply voltage. During assessment ($clk = V_{DD}$), semiconductors Q₈ and Q₁₁ go off first. At that point, as any of the yields is released and is cut down adequately beneath edge voltage to turn on the relating p-FINFET semiconductor (Q₈/Q₁₁), recovery begins.

Consequently, a slight distinction (somewhere in the range of O₁ and O₂) changes the progress to excite V_{in_ht} to V_{DD} and V_{ref_ht} to GND (SR latch outputs) because of

positive criticism activity. Thus, the circuit is named a dynamic comparator. Here, the force utilization happens just at transitions and is appropriately estimated.

Analysis of Offset: The most significant information contrast that a comparator cannot distinguish is offset, which is estimated as input fault [2]. Speed is influenced by restricting the target [16, 17].

The designed configuration excludes any methods to limit balance. A trade-off between precision and speed is in this way seen because of gadget befuddle (FinFET). The offset cannot be invalidated. In any case, methods like auto-focusing and chopper adjustment at the expense of expanded circuit intricacy are decreased. A component of edge voltage-confuse ($|\Delta V_T$) is balance, load-obstruction criss-cross (ΔR_L), and semiconductor befuddle ($\Delta\beta$). The overall condition that presents these conditions for $V_T R_L$ and β can be communicated as:

$$V_{GS} = \Delta V_T + \frac{V_{gs} - V_T}{2} \left(\frac{\Delta R_L}{R} + \frac{\Delta\beta}{\beta} \right) \Delta\beta \quad (2)$$

The above equation factor is an after effect of bungle in semiconductor measurements rule (2). Additionally, the feature is that a solid capacity of the overdrive voltage ($V_{GS} - V_T$) is β . It is confirmed that the counterbalance voltage brings down with the regular mode voltage.

3 Results of Simulation and Proposed Work Experimental Findings

The dynamic latch comparator simulation is done on the Cadence Virtuoso software using advanced 18 nm FinFET technology with a V_{DD} ranging from 0.1 to 1 V to compare the overall performance of the proposed comparator to previous works. The clock frequency is tested at various frequencies, from 50 MHz to 1 GHz. The same software is used to simulate all three parameters using the transistor dimensions specified in Table 1. Table 2 contains the kickback noise, offset clock-feed, the average dynamic power, the power delay product (PDP), energy delay product (EDP), offset voltage, and the average delay for the proposed and reference designs. Figure 3 illustrates a typical screen capture that depicts the proposed design's time-domain waveform.

As shown above, during the evaluation process ($CLK = 1$), only V_{in_ht} transitions, whereas V_{ref_ht} stays at V_{DD} . Thus, it helps explain the proposed design's low power dissipation compared to the CSDL simulation [10]; both V_{in_ht} and V_{ref_ht} make the transition. For the input differences at the lowest 3 mV, the design concept is further reported rail-to-rail swing. Table 2 contains a list of specific enhancements.

As the average delay decreases compared to previous works [9, 10], it is observed here that the speed is increased. Additionally, a decrease in the offset voltage is also observed.

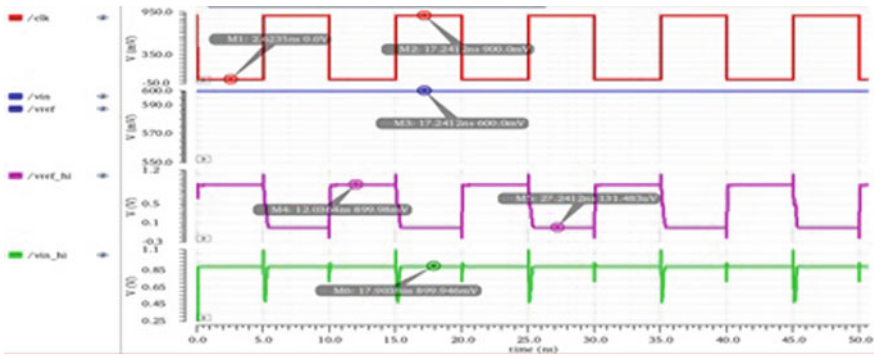


Fig. 3 SR latch shown in Fig. 2 experimental graph at $f_{clk} = 100\text{MHz}$, $V_{ref} = 900\text{mV}$, $V_{in} = 600\text{mV}$, and $V_{DD} = 0.9\text{V}$

Table 2 Comparative performance of comparators

Topology	Average delay (ps)	Average dynamic power (μW)	PDP (fJ)	EDP ($\times 10^{-27}\text{Js}$)	Offset voltage (mV)	Clock-feed (beyond 1V) (V)	Kickback noise (beyond 1V) (V)
CSDLC	177.14	17.56	3.21	571.82	63	0.04	0.213
SADLC	93.42	4.69	0.48	44.84	6	0.061	0.182
CMOS	72.01	18	1.29	92.89	3.04	0.053	0.108
Proposed	57.6	6.3	0.362	20.85	1.836	0.036	0.055

4 Conclusion

Here, in this paper, design of the dynamic latch comparator is developed by adding an SR latch. This dynamic comparator circuit diagram is designed by using 18 nm FINFET. The postponement of the comparator is tucked with SR latch, making activity quick even though the power dissemination increments hardly. This extra latch drastically decreases the minuscule yield needed to begin recovery. Thus, it offers a rail-to-rail swing. It also minimizes the kickback noise. Designed configuration is carried out on 18 nm quality FinFET measure at 1.8 V. There is an improvement in speed by 70%, and the balance voltage is seen to decrease by half. The PDP is barely expanded when contrasted with [3] although it is 59.5% less when contrasted with [2]. It is observed that the impact of payoff commotion and clock-feed through is diminished by 40.2% and 11%, separately. Thus, the designed configuration is strong. It likewise creates steadier yield when contrasted with those of [2, 3] even at supplies is low. Along these lines, a plan of decision for information blocks the converter, among others. The recurrence of activity is expanded up to 2 GHz. The striking force can be additionally diminished by decreasing the swing of the volt-

age at transitional yield nodes O_1 and O_2 . Consequently, when worked at least, the designed circuit can be viewed as economic friendly, supporting philanthropic reason by utilizing suitable innovation.

References

1. Satapathy B, Amandeep K (2021) A high speed, low energy comparator based on current recycling approach. In: 2021 IEEE international symposium on circuits and systems. IEEE, pp 1–5
2. Mehra K, Tripti S, Simran S (2021) Performance analysis on low-power, low-offset, high-speed comparator for high-speed ADCA review. In: Intelligent communication and automation systems. CRC Press, pp 99–112
3. Hu B et al (2021) Sampling and comparator speed-enhancement techniques for near-threshold SAR ADCs. IEEE Open J Circ Syst 2:304–310
4. Nagyt L et al (2021) EKV MOS transistor model for ultra low-voltage bulk-driven IC design. In: 2021 24th international symposium on design and diagnostics of electronic circuits & systems, pp 6–10
5. Rony MW et al (2021) A system level modeling approach for simulating radiation effects in successive-approximation analog-to-digital converters. IEEE Trans Nucl Sci
6. Liang J et al (2021) An offset-cancelling discrete-time analog computer for solving 1-D wave equations. IEEE J Solid-State Circuits
7. Hima Bindu K, Sadulla S, Vijay V (2020) FINFET technology in biomedical-cochlear implant application. In: International web conference on innovations in communication and computing, ICICC'20, 5 Oct 2020, India
8. Talukdar J et al (2021) Impact of temperature counting the effect of back gate bias on the performance of extended source tunnel FET (ESTFET) with δp + SiGe pocket layer. Appl Phys A 127(1):1–14
9. Solis F et al (2021) 4GS/s 8-bit time-interleaved SAR ADC with an energy-efficient architecture in 130 nm CMOS. Int J Circuit Theory Appl
10. Rahman LF et al (2021) Design topologies of a CMOS charge pump circuit for low power applications. Electronics 10
11. Perez AJ et al (2021) VLSI design and comparative analysis of several types of fixed and simple precision floating point multipliers. Cult Ciec Tecnol 18
12. Shakibae F et al (2021) Design of a high-speed and low power CMOS comparator for A/D converters. J Electr Comput Eng Innov 9:153–160
13. Sotoudeh M, Farzan R (2021) A new dual-network bootstrapped switch for high-speed high-resolution applications. Comput Electr Eng 91:107125
14. Vendelin GD et al (2021) Microwave circuit design using linear and nonlinear techniques. Wiley
15. Ray MK et al (2021) Design of 4-bit multiplexer-based encoder for analog to digital converter. In: Proceedings of the fourth international conference on microelectronics, computing and communication systems. Springer, Singapore, pp 959–966
16. Vallabhuni V, Pittala CS, Shaik S, Putta M, Rallabhandy A, Merugu R, Nakka N (2021) Design and performance evaluation of energy efficient 8-bit ALU at ultra low supply voltages using FinFET with 20nm technology. In: Nandan D, Mohanty BK, Kumar S, Arya RK (eds) VLSI architecture for signal, speech, and image processing. CRC Press
17. Krishna GM et al (2021) Design of dynamic comparator for low-power and high-speed applications. In: ICCCE 2020. Springer, Singapore, pp 1187–1197

A Novel Fault Diagnosis and Recovery Mechanism Based on Events Prediction in Distributed Network



M. Srinivasa Rao, D. Nagendra Rao, P. Chandrashekhar Reddy,
and V. Usha Shree

Abstract In current growth, the detection of faults in computer networks has fascinated wide attention due to its significance in network administration. Most existing problem-solving techniques depend on dynamic search methods that are quickly and accurately diagnose the occurrence of faults. However, these techniques undergo traffic constraints, particularly on highly scalable networks. Fault-tolerant distributed system components have to be able to perfectly identify which system elements are defective and which are normal. This paper intends to propose a novel fault diagnosis and recovery mechanism (FDRM) for distributed networks based on events logs identification at nodes in completely linked networks. The observation of events of a node can define the status of the node as standard or vice versa. The novel FDRM algorithm can achieve the diagnosis of execution events till the node remains in a certain condition for long enough to allow all required estimation to detect a node status. The experimental evaluation was performed considering a hierarchical evaluation strategy where all nodes are normal in the form of the hypercube. The simulation results have a significant reduction in average latency and false alarm rate with high detection accuracy and when evaluated to other related approaches to enhance the fault diagnosis.

Keywords Fault diagnosis · Recovery · Events identification · Distributed network

M. Srinivasa Rao (✉) · P. Chandrashekhar Reddy
Department of Electronics and Communication Engineering, JNTUH, Hyderabad, India
e-mail: asivadu@gmail.com

D. Nagendra Rao
Department of Electronics and Communication Engineering, AHTC, Hyderabad, India

V. Usha Shree
Department of Electronics and Communication Engineering, JBREC, Hyderabad, India

1 Introduction

Today a computer network participates in many essential activities such as controlling and implementing many services in the modern industry and communication. Like various other systems, network devices can undergo overhead due to environmental factors or element failures. Therefore, there is a desperate need for an efficient and accurate network fault diagnosis method having minimum diagnosis latency. It seems to be highly important that fault diagnosis must ensure the consistency and survival of the systems. In the past years, the researcher has explored the various limitations and problems of the systems that lead to network and service failure [1, 2]. Related numerous fault detections are being utilized in various domains to satisfy the QoS [3, 4]. The application of these technologies in computer networks is important hypothetically and practically.

The process for diagnosing faults for computer networks involves two steps: detecting and locating the faults [5, 6]. Fault detection search is to establish if a fault has to take place or not. At this stage, diagnostic methods are taken to identify network crashes. If there is a defect, the cause of the fault is determined to find out the cause and place. Therefore, fault detection is the primary resolution step to troubleshooting a computer network. A fast and precise fault recognition method is required to ensure the normal procedure of the network [7].

In general, the fault detection tools are often not flexible enough to consider all kinds of events for detection. These methods utilize alerts transmitted by faulty elements to supervise network function status and faults in the event of faults [8]. If a fault is detected, then more locations search is required according to the fault observation [9]. Due to its non-persistent and passive, detection method has been extensively utilized [10, 11]. The foremost constraint of the passive method is that it requires the support of network component responses. To use these passive methods, it needs to be alerted when all network components fail. However, many real-time network devices do not have this feature, and the alarm may perhaps be disrupted or missed during communication [12]. In simultaneously, the complexities of modern networks disrupt the relationship among the misobservation and actual fault making it difficult to identify where the problem generally occurs [13].

Research on the detection of past failures based on active discovery has mainly focused on optimization algorithms that select a group of detectors to analyze the entire system [14]. If this network is undersized or this topology is straightforward, then these methods are able to function effectively. However, as networks become larger and more complex, these methods are computationally impractical [15] and can consume too much network bandwidth. Barford et al. [15] and Zhao et al. [16] offer various strategies to monitor network performance to eliminate the shortcomings of these existing methods. At each discovery stage, they accepted a straightforward algorithm to opt for a collection of experiments to reduce traffic flow and close a network segment that could be closed to all nodes. They also looked at traffic patterns planned at several levels and network connections were partially monitored in each

phase. These two mechanisms offer a novel approach to erroneously identify large networks.

In reviewing, a system containing a potentially faulty or normal N node in a distributed network, the reliability of the node is determined. Suppose the system is entirely connected, that is, there is a connection among several groups of nodes and the connection without any faulty nodes. This technique is frequently utilized to represent local systems where every node distributes in a connected environment. The system-level distributed detection algorithm supports the normal nodes in this structure to determine the status of every node, taking into account the ability to reliably evaluate and report the test results of trusted nodes [2, 4]. This algorithm is called adaptation when determining the subsequent evaluation depends on the outcomes of the earlier evaluation of the node [6].

This paper presents a novel fault diagnosis and recovery mechanism (FDRM) based on event log (*ELog*) observation. Every one node that executes the algorithm holds an *ELog* of the status of the other nodes in the network. This *ELog* value acts as an incremental and increases each instance the node transforms its status [7]. Thus, each assessment does not cause any conflict, i.e. it does not take the previous situation for a new situation, and observation regarding a particular node in the network is taken from an additional than individual evaluated node. In such a case, a normal node evaluation gets diagnostic observation for the $N/2$ node to obtain the diagnosis information.

The node that runs the algorithm can detect runtime events until the nodes are in a certain state, allowing all evaluations to determine that state. Despite the advantages of storing and dispatching, *ELogs* the FDRM will considerably decrease the standard delay of other substitutes and offer a new alternative for real diagnostics.

In the below sections, we discussed the related works in Sect. 2, the proposed FDRM is discussed in Sect. 3, it presents fault diagnosis and recovery mechanism. Section 4 presents the experiment evaluation, and the conclusion of the paper is present in Sect. 5.

2 Related Works

Many types of research have conducted mainly since the 1980s to identify and diagnose faults in physical conveniences. These mechanisms are being inadequate to certain circumstances and environments. Due to the complexity of the system, it seems to be difficult to establish several representations of constraints. Recently, with the advent of artificial intelligence (AI) practices [17], modern data-based mechanisms such as machine learning (ML) being utilized extensively for fault detection [18]. For example, Haedong et al. [19] present fault diagnosis, and identification of machine systems was studied using a model-based approach. Wasim et al. [20] present a predictive technology for machines using retrospective methods of machine learning. However, faults are common in sensors and can have serious consequences.

Therefore, it is important to identify and detect network sensor faults promptly to ensure improved data quality, prolong network life and shorten response time [21].

The fault detection in the distributed environment is majorly utilized in the sensor network for various data monitoring and it always has the potential to drift toward fault occurrences. Distributed fault detection (DFD) algorithm [7] is discussed to identify the most common faults in networks. It computes the information obtained by the nearby nodes to establish the primary status of the node. The status of the adjacent nodes checks every former for the presence of a defective node or spread the detection result to the next node, but the DFD technique requires the node to interact employing the adjacent node three periods and then establish the overall communication condition of the node. Therefore, this algorithm requires a lot of effort to optimally detect fault prediction.

In current years, a lot of scientists have recommended numerous methods to determine distributed defects depend on the DFD algorithm [22–24]. Previous work in [25–27] shows that while the various adjacent nodes are low, and the possibility of node malfunction is high, the performance of this algorithm determines to be significantly reduced since the DFD procedure makes a very strong judgment if the node is normal. This algorithm has been enhanced and the final situations of the algorithm have been changed [28]. Distribution adaptation based on the DFD algorithm suggested a mechanism for detecting sensor network failure [5]. They introduced the concept of trust depend on the reliability of the neighboring node, which opts for a believed cross and evaluates the observation at the local node to identify the condition of the node. The debugging algorithm is utilized to determine the status of networked network nodes on nodes that are still unknown.

Mengjie et al. [6] introduced other “self-management” functions and proposed a hierarchical structure for the proper distribution of troubleshooting between sensor nodes. Additionally, they believe an alternative explanation to the identity-assembly functionality of sensor nodes that adapt to diverse scheme necessities, such as faulty system alternative. However, the effect of debugging (such as late responses) is diminished.

Huang et al. [29] depend on the probability distribution of the network nodes and the fault distribution observation in the sensor nets (according to the Pareto principle) proposed an algorithm to identify faults based on the probability of selecting the sensor nodes as a test site. The simulation shows that algorithms and regulation can extend the life of the distributed network, dedicating merely the speed at which the fault is found. The Pareto principle, which covers many of the shortcomings of a small group, was also demonstrated, and this principle was used in the selection of research principles effectiveness.

Babaie et al. [30] present a new method of fault management that was proposed to identify and recover faults in a decentralized manner. This mechanism detects a fault in a decentralized manner and corrects the fault. However, for distributed controls, the size of the network increases to detect, detect, and restore traffic.

In [31], it provides a “hierarchically adapted distributed structure-level diagnostic” (Hi-ADSD) algorithm for distributed networks. The Hi-ADSD diagnosis delay

is at most $\log^2 N$ evaluation for the N -node system. Along with neighborhood assistance techniques, the precision of the fault recognition algorithm is advanced, and problems caused by regular interaction between the nodes are eliminated. Therefore, the qualities of distributed networks are rarely utilized to progress the accuracy of fault recognition and the creation of algorithms to increase the convenience for wireless node networks with rare nodes and high sensor faults.

One goal of system-wide diagnostics is to allow conventional nodes to diagnose as quickly as possible. Node activation and the number of evaluations should be reduced by the system-level diagnostic algorithm. In addition, the diagnostic observation substituted among the nodes has to be reserved to a least.

3 Proposed Fault Diagnosis and Recovery Mechanism (FDRM)

The previous hierarchical adaptive distribution algorithm assumed static fault conditions for system-level diagnosis. In other words, a new event can happen simply if the earlier event was found in all normal nodes after the event in the system. This situation does not always coincide with reality. This is because it is impossible to conclude when an event, in reality, occurs in a virtual system.

This section shows that FDRM with *ELog* can detect certain actions while performing events, that is, events that occurred before the previous event was completely detected. The recovery process is first described so that the node recovered from the failure can be connected to a node that is already performing the algorithm.

3.1 *Faults Diagnosis with Events Assessment*

In any network system, all nodes are good at first, but their status varies depending on the activity performed. In this case, when the node goes into a faulty state, it goes through a recovery mechanism to recover it. Therefore, there are always two types of nodes in a network. One is the node that has already been repaired, and the other is normal. The event cannot be detected in the delay of the algorithm still the entire faulty nodes are revamped and the confined diagnostic event is updated. During that time, the repaired nodes will need to restart the algorithm and log intervals to update the local diagnostic observation.

In general, when an event occurs, it is said that when the recovery procedure is completed, and all normal nodes in a normal state are informed of the event, it is fully diagnosed. In terms of events, we say that these normal nodes are stable. This definition indicates that the nodes must remain normal until they can diagnose events. Since there are numerous faulty nodes in the network and they are renovated in

sequence and then previous nodes are faulty and corrected and so on, it is important to check which nodes are analyzed for which occurrences. If every component is faulty and continues to recover rapidly, it will not be able to identify any events in the network.

The fault detection (FD) mechanism provides the conditions necessary to fully identify the event. Therefore, when the system detects an event and makes it fully known, all the stable and normal nodes in the network must maintain the observation for a longer period of instant because all the reviews are sufficient to receive that information.

Let's say a given node, e.g. node x goes through several repeated sets of events. Few of these events are recognizable but some are not from this set of events. Node z sends diagnostic observation to node x and y on the connected network, new diagnostic observation. If node z is normally sufficient to overtake fresh diagnostic observation simply for a single assessment for node x , however, if that observation is not sent to node y , the corresponding *ELog* of node x is diverse from the equivalent *ELog* of node y . Node x 's *ELog* has been updated, and node y is not receiving incident observation. In such a case if the evaluation result of node z , node x and node y receives a fresh observation of diagnosis, then it can be concluded that all the nodes are completely diagnosed and identified their status.

Although some events do not occur and dissimilar events occur in diverse nodes, in the end, all the nodes in the overall node system reach a long-term agreement on the current situation. In other words, in the end, every one node retains the identical value at the border counter of every node affected by changed events.

3.2 *Recovery Mechanism*

In the case of a node recovered from its faulty state, it does not have any observation of diagnosis performed by the system. During the period when a node is faulty, it records different events that occurred. It updates its diagnostic observation when it performs node evaluation and receives diagnostic observation from another normal node. To display uptodate diagnostic data and information, it needs to identify the process that allows for a modified normal node. Otherwise, false diagnostic observations can propagate throughout the system.

In considering with the observation of diagnostic, which every node is expecting from the next available nodes in the system. The *ELog* table maintains the state of each node in a data structure which is utilized to identify the status recovery or faulty. Each item must include a field representing that the item has been reorganized because of the last time the node was recovered. This environment can be applied to an instance and is assigned to 1 if the observation is updated or otherwise 0. The status is defined in a term as *log-bit* for updating the event log of the nodes.

Initially, all the log-bits are assigned to 0 when the algorithm initializes in a node. When the node starts to perform the diagnostic algorithm, it examines other nodes and receives observation of diagnostic from the normal node. As each evaluation

improves the location information, the corresponding log-bit is assigned to 1. For every observation of diagnostic from the estimated node, the evaluation *ELog* must be checked to see if the observation is uptodate at the estimated node. In other words, the evaluation confirms if the log-bit is 1, if so, then the evaluation will update the local observation of diagnosis.

Now let's find out what occurs when a node is now restored, and there are previous nodes that execute the procedure for a while. An illustration of the event log of the system is shown in Fig. 1. Suppose a node *N2* has just been restore and we haven't received any observation of diagnosis of the system yet. So, when *N1* evaluates *N2* and detects that it is normal, it sends diagnostic observation for the *N2* in the group, that is, *N3*. By inspecting the corresponding *log-bit*, *N1* determines that *N2* has not yet updated these observation bits and therefore cannot be used to update local assessment diagnostic observation.

At present, let's considered the *N2* updates and their local diagnostic observation. If *N3* evaluates to be faulty, *N2* updates the observation of diagnostic for the evaluated faulty node by configuring the *ELog* to 1. However, *N2* not able to assign its log-bit to 1 till it acquires observation about *N3* from a different normal node. In the example, the *ELog* of *N1* to *N3* is 3, which is greater than 1. At the next interval, if *N2* evaluates *N1* as normal, *N2* acquires observation concerning the entire system from *N1*, and then *N2* updates the *ELog* for *N3*.

Nevertheless, if the evaluation has just been repaired and all nodes have been evaluated as defective, then the log-bit of all evaluated nodes should be set to 1. If there are other normal nodes in the system after the *logN* evaluation interval, then it also does the evaluation tests of them. So, if after the *logN* evaluation interval the

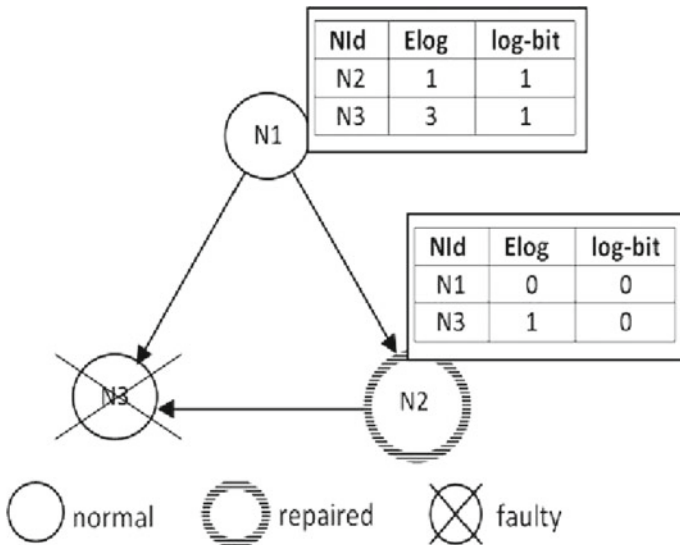


Fig. 1 Event log status for different state of nodes

node finds no other normal node, it able to steadily assign the log-bit of the evaluated faulty node to 1. It is similar to an algorithm function initialization during execution. Nevertheless, it may find other normal nodes in the evaluation during that phase, but there may be no updated information about the specific faulty nodes that were evaluated. In this case, after the $\log N$ interval, the evaluation checks whether the log-bit of each evaluated faulty node can be assigned to 1.

3.3 FDRM with ELog Assessment

Let's assume a completely connected network consisting of N nodes having both faulty and normal forms of state. The interconnection between the pair of nodes provides a stable link among all types of nodes. Here a normal node presents reliable diagnosis results for iterations of evaluation.

The distribution of the node is represented in a directional graph for S nodes named Diagnosis Graph, $D(S)$. The diagnosis is directed between the edges nodes of the $D(S)$. Here, if a node g has to diagnose node h , then it assessed each connected edges nodes of g to reach h in a particular assessment interval. The process of diagnostic assessment in $D(S)$ moves in the form of a hypercube till all nodes of the system are diagnosed and brings it to a normal state. An illustration of a $D(S)$ having six nodes is shown in Fig. 2.

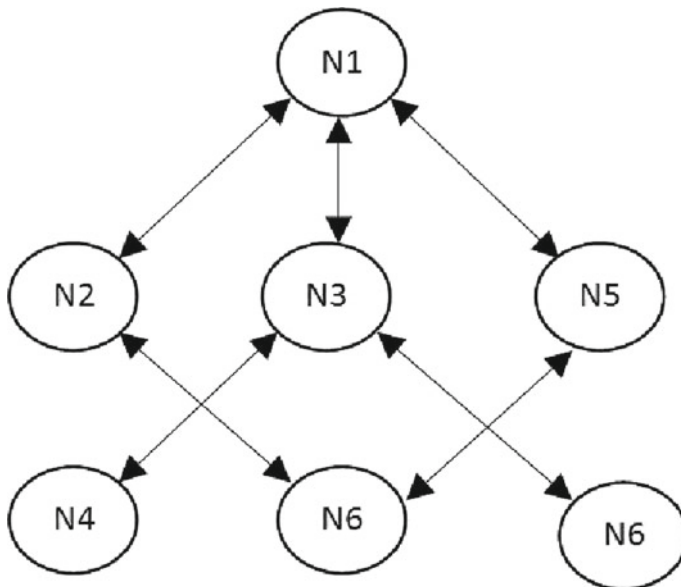


Fig. 2 Illustration of six nodes $D(S)$ for a system

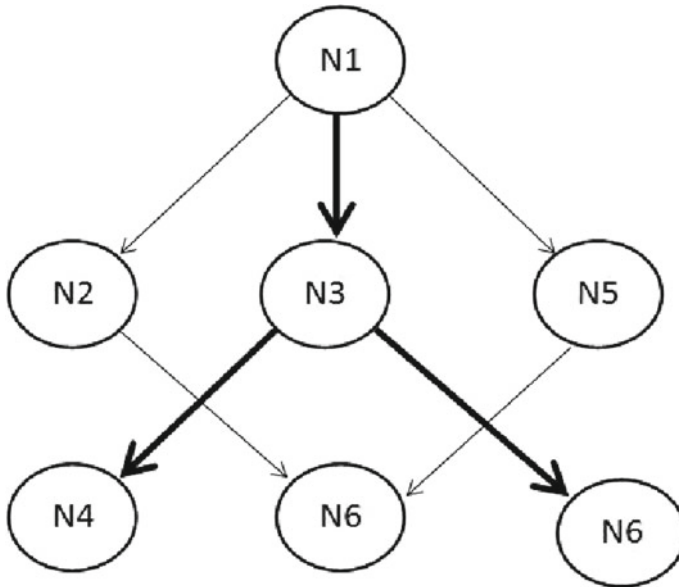


Fig. 3 Illustration of diagnosis $w_{x,u,v}$ as $x = N1$, $u = N4$, and $v = N6$

To minimize the diagnosis latency, it needs to diagnose in the least possible time interval and prefer the shortest distance between the edges of nodes. According to Fig. 2, the minimum diagnosis hops between $N1$ and $N6$ is 2. So, to assess a node x in $D(S)$ defined as AG_x utilized the shortest distance in the directed graph between the edged nodes.

Let $N_{x,u,v}$ represents the node that is supposed to reach node v via node u having the number of diagnostic hops which will be equal to be $u - 1$. So, in such case, the nodes in AG_x have the majority u edges in the path to reach the target node and they belong to belongs $N_{x,u,v}$ as shown in Fig. 3.

In FDRM with $ELog$, node x can obtain observation of diagnosis regarding node y from more than two normal nodes (like between node v and v'). So, it must be ensured that node x can conclude the latest observation regarding the condition of node y . As shown in Fig. 3, since $N6$ belongs to $N_{1,\log N,2}$ and $N_{1,\log N,4}$, $N1$ will obtain diagnostic observation about $N6$ through $N2$ and $N5$. Therefore, it is necessary to ensure that $N1$ only gets the latest observation about $N6$.

The latest observation regarding the state changes of node x will ensure concerning the state of node y , in turn, we utilize the approach of the system-level diagnostic algorithm to implement in an all-purpose topology network [7]. The scheme includes the utilization of $ELog$ method that allows timestamp updates of the observation of diagnostic changes. Here, this update is considered as a counter for the state of event changes by a node. The counter should be increased each time the test is performed, and the evaluation node realizes that the estimated node has transformed.

To guarantee that node x constantly remains the latest observation regarding node y 's condition, whenever node x evaluates node v , node x has to refer its *ELog* with node v 's *ELog* concerning the node y . If node x 's *ELog* is identical to or larger than node v 's *ELog*, i.e. node x is attained an expired observation concerning node y , x then it's necessary to remain its *ELog* as it remains. However, if node x 's *ELog* is not as much of node v 's *ELog*, i.e. node x is attaining the latest observation concerning node y , x then it should update the observation regarding node y 's event condition in its *ELog*. The mechanism of FDRM with *ELog* is described in Algorithm 1.

Algorithm 1 FDRM with *ELog* for a Node x

```

for ( N: = 1; till logN)
{
  Diagnosing-Node: = NextNode  $\rightarrow N(x, u, v)$ ;
  NStatus = FDAssessment (Diagnosing-Node);
  if (NStatus == "Normal").
  {
    for (y: = 1 to N/2).
    {
      if(new.ELog[y] > current.ELog[j])
      {
        Update FD observation of y;
        Update ELog ( y );
      }
    }
  }
  else if (NStatus == "Faulty").
  {
    Update FD observation of Node-to-Assess;
    Update ELog(Node-to-Assess);
  }
}

```

FDRM ensures that as the numerous fault nodes enhance with the *ELog* evaluation function, and the number of evaluations performed in the system decreases.

4 Experiment Evaluation

In this segment, we discuss the FDRM with *ELog* simulation diagnostics on a large network and also discuss the resulting outcome of the method in comparison with others. We have considered three different events for a node, "faulty", "recovered" and "normal". The outcome measures are compared with detection accuracy (DA) and fault positive rate (FPR) of the proposed FDRM in comparison with Hi-ADSD [31] and the DFD algorithm [7]. All experiments are repeated for analysis, usually

giving statistical significance to the test. Random fault nodes are added to random nodes with the probability of failure.

The algorithm DA and FPR are calculated using the Eqs. (1) and (2) as given below. The DA is mathematically defined as

$$DA = \frac{\sum \text{Faulty Nodes Identified}}{\sum \text{Faulty Nodes in network}} \quad (1)$$

FPR is the standard ratio of nodes accounted as faulty, as well recognized as FAR. It measures the proportion of the non-faulty along with the sum of the normal nodes that exist in the network. It is mathematically specified as,

$$FPR = \frac{\sum \text{Non-Faulty Nodes Identified as Faulty}}{\sum \text{Normal Nodes in network}} \quad (2)$$

4.1 Result Analysis

Here we discuss the proposed FDRM and the analysis of results between Hi-ADSD and DFD. Figure 4 shows the DA comparison, and Fig. 5 shows the FPR comparison. The purpose of this experiment is to show the effect of diagnosing faults and recovering to normal in various circumstances. To generate this situation, it gradually enhances the count of faulty nodes in the network at a rate of 25% as the count of nodes enhances.

Figure 4 shows that FDRM has improved significantly over others, where Hi-ADSD shows the lowest DA as the count of nodes enhances. FDRM illustrates an average of 30% better fault accuracy with low latency. The utilization *ELog* accurately identifies node state changes. If the number of nodes is small, all methods will show more than 90% of the DA, but if it exceeds 300, the repetitive load for predicting faults will also be high. This creates another way to lose DA with a large number of nodes. FDRM reduces diagnostic latency by receiving diagnostic observations from different paths to predict DA accuracy. Even the results obtained by simulation show that FDRM with *ELog* is 4 times faster in DA prediction than Hi-ADSD and DFD.

Figure 5 shows a comparative analysis of FPR as the count of nodes enhances. The improvement of DA by FDRM reduces FPR compared to others. FDRM is the lowest because it regularly updates diagnostic observation in the *ELog*. With the help of *ELog* FDRM, it effectively predicts faulty nodes and supports recovery. Regular log-bit updates provide the correct prominence of the node to predict the correct status of the node's FDRM and reduce the FPR. The DFD algorithm primary establishes the first condition of a node by evaluating its neighbors' data with itself. The node's state is then determined by the preliminary status of the node and its neighbors. This can happen since the DFD has a high false-positive rate while the failure state is increased, and the different neighbors are immense. FDRM constructs

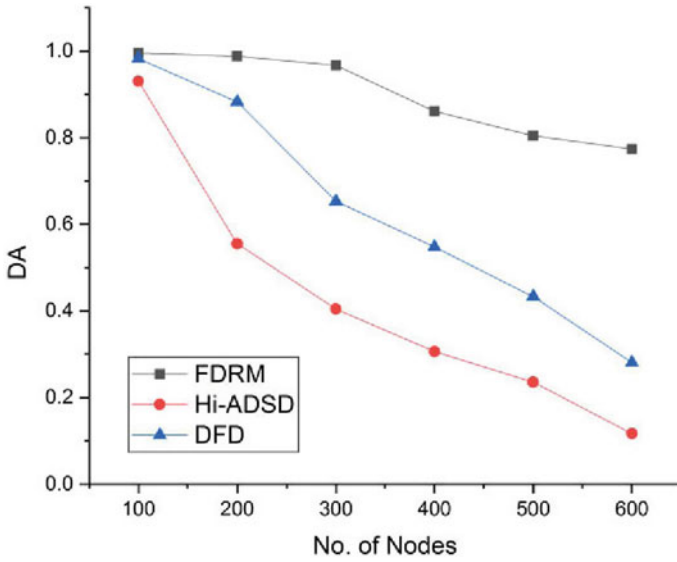


Fig. 4 Detection accuracy comparison analysis

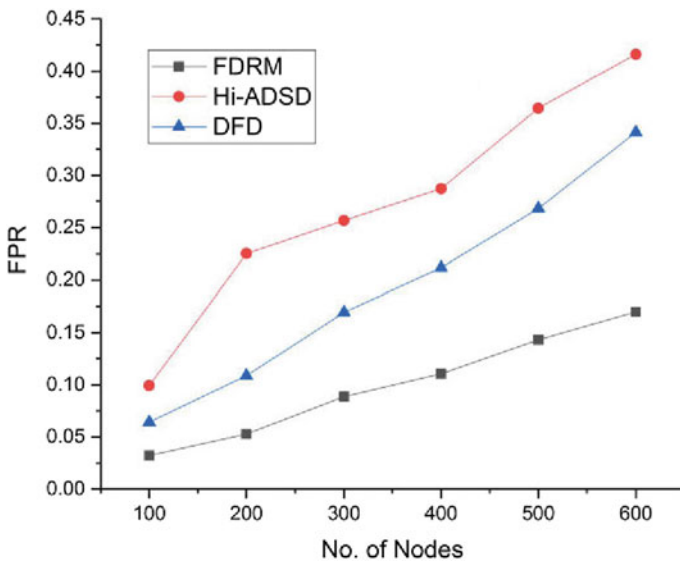


Fig. 5 False positive rate comparison analysis

the *ELog* with chronological data and precisely concludes the faulty node. FDRM reduces dependence on neighboring nodes by adding suggestion entities as per the association among nodes, and the standard processing latency of this algorithm is lower in comparison with other similar algorithms.

So, the results of this experiment validate that FDRM nodes working among the *ELog* can investigate specific run-time events, events that occurred before the previous event was completely investigated.

5 Conclusion

Network-level diagnostic algorithms preferably are utilized to construct a consistent network in various environments of application. This paper introduces a novel hierarchical and adaptive distributed network-level diagnosis algorithm, namely FDRM along with *ELog*. This algorithm allows all normal nodes in the network to comprehensive the diagnosis in a short occasion on average and has Better DA and lower FPR than other similar algorithms. To reduce waiting time, FDRM adopts an evaluation strategy that allows obtaining observation about another node in the system from multiple nodes. The strategy includes the use of *ELog*, a mechanism that allows data updates to diagnostic observation. We have shown that if a normal node remains in a normal state long enough to evaluate it to obtain new event observation, the algorithm can ensure that multiple simultaneous events are diagnosed. The simulation outcomes demonstrate that in expressions of DA and FPR, satisfactory impromptu improvement (average delay) is about four times faster than existing methods.

References

1. Minji Y, Taejin K, Taek YJ, Yunhan K, Soho K, Byeng Y (2020) A resilience measure formulation that considers sensor faults. *Reliable Eng Syst Safety* 199:106393
2. Ranjan SR, Mohan KP, Kumar BS (2020) Underlying and persistence fault diagnosis in wireless sensor networks using majority neighbors co-ordination approach. *Wireless Pers Commun* 111(2):763–798
3. Zeyu Z, Amjad M, Lei S, Zhiqiang H, Yu Z, Mithun M (2018) A survey on fault diagnosis in wireless sensor networks. *IEEE Access* 6:11349–11364
4. Abbasi AA, Younis MF, Baroudi UA (2013) Recovering from a node failure in wireless sensor-actor networks with minimal topology changes. *IEEE Trans Veh Technol* 62(1):256–271
5. Sharma KP, Sharma TP (2017) rDFD: reactive distributed fault detection in wireless sensor networks. *Wireless Netw* 23(4):1145–1160
6. Mengjie Y, Mokhtar H, Merabti M (2008) Self-managed fault management in wireless sensor networks. In: *Mobile ubiquitous computing, systems, services and technologies, UBICOMM'08*, pp 13–18
7. Chen J, Kher S, Somani A (2006) Distributed fault detection of wireless sensor networks. In: *Proceedings of dependability issues in wireless ad hoc networks and sensor networks*, pp 65–72
8. Thaha M, Ahmed SR (2017) An analysis of fault detection strategies in wireless sensor networks. *J Netw Comput Appl* 78:267–287

9. Abduljalil M, Otman B (2010) Fusion based approach for distributed alarm correlation in computer networks. In: Second international conference on communication software and networks, pp 318–324
10. Jyrki K (2013) Detection, identification, and quantification of sensor fault in a sensor network. *Mech Syst Signal Process* 40(1):208–221
11. Yongning T, Ehab A-S (2009) Overlay fault diagnosis based on evidential reasoning. In: Proceedings of the IEEE INFOCOM, pp 2596–600
12. Lu C, Xuesong Q, Luoming M, Yan Q, Raouf B (2010) Efficient active probing for fault diagnosis in large scale and noisy networks. In: Proceedings of the IEEE INFOCOM, pp 1–9
13. Nancy S, Ahmed K (2008) Network anomaly diagnosis via statistical analysis and evidential reasoning. *IEEE Trans Netw Serv Manage* 5(2):65–77
14. Chu LW, Zou S, Cheng S, Wang W, Tian CQ (2009) Internet service fault management using active probing in the uncertain and noisy environment. In: 4th International conference in communications and networking, pp 1–5
15. Paul B, Nick D, Amos R, Joel S (2009) Network performance anomaly detection and localization. In: Proceedings of the IEEE INFOCOM, pp 1377–1385
16. Yao Z, Zhaosheng Z, Yan C, Dan P, Jia W (2009) Towards efficient large-scale VPN monitoring and diagnosis under operational constraints. In: Proceedings of the IEEE INFOCOM, pp 531–539
17. Samanta B, Al-Balushi KR (2003) Artificial neural network-based fault diagnostics of rolling element bearings using time-domain features. *Mech Syst Signal Process* 17(2):317–328
18. Jing T, Carlos M, Michael HA, Michael P (2015) Motor bearing fault detection using spectral kurtosis-based feature extraction coupled with K-nearest neighbor distance analysis. *IEEE Trans Ind Electron* 63(3):1793–803
19. Haedong J, Bumsoo P, Seungtae P, Hyungcheol M, Seungchul L (2019) Fault detection and identification method using observer-based residuals. *Reliable Eng Syst Safety* 184:27–40
20. Wasim A, Ali KS, Manjurul IMM, Myon KJ (2019) A reliable technique for remaining useful life estimation of rolling element bearings using dynamic regression models. *Reliable Eng Syst Safety* 184:67–76
21. Ullah JS, Doo LY, Jungpil S, Insoo K (2017) Sensor fault classification based on support vector machine and statistical time-domain features. *IEEE Access* 5:8682–8690
22. Munir A, Antoon J, Gordon-Ross A (2015) Modeling and analysis of fault detection and fault tolerance in wireless sensor networks. *ACM Trans Embed Comput Syst* 14(1):3
23. Ould-Ahmed-Vall E, Ferri BH, Riley GF (2012) Distributed fault-tolerance for event detection using heterogeneous wireless sensor networks. *IEEE Trans Mob Comput* 11(12):1994–2007
24. Chan SC, Wu HC, Tsui KM (2012) Robust recursive Eigen decomposition and subspace-based algorithms with application to fault detection in wireless sensor networks. *IEEE Trans Instrum Meas* 61(6):1703–1718
25. Muhammed T, Shaikh RA (2017) An analysis of fault detection strategies in wireless sensor networks. *J Netw Comput Appl* 78:267–287
26. Artail H, Ajami A, Saouma T, Charaf M (2016) A faulty node detection scheme for wireless sensor networks that use data aggregation for transport. *Wirel Commun Mob Comput* 16(14):1956–1971
27. Panda M, Khilar PM (2015) Distributed Byzantine fault detection technique in wireless sensor networks based on hypothesis testing. *Comput Electr Eng* 48:270–285
28. Jiang P (2009) A new method for node fault detection in wireless sensor networks. *Sensors* 9(2):1282–1294
29. Huang R, Qiu X, Ye L (2010) Probability-based fault detection in wireless sensor networks. In: International conference on network and service management (CNSM), pp 218–221
30. Babaie S, Shojaiy MG (2010) Improving fault management using a voting mechanism in wireless sensor networks. In: International conference on IEEE computational intelligence and communication networks (CICN), pp 359–362
31. Duarte EP, Nanya T (1998) Hierarchical adaptive: distributed system-level diagnosis algorithm. *IEEE Trans Comput* 47(1):34–45

Medical Image Fusion by Using Different Wavelet Transforms



M. N. Narsaiah, D. Venkat Reddy, and T. Bhaskar

Abstract Combining two or more images from different sensors in to a single image is called image fusion. The resultant image contains the complementary information of the both source images. Stationary wavelet transform, discrete wavelet transform, etc., are commonly used techniques to fuse medical images like CT and MRI. In this article, by using the duel filter algorithm and different wavelets are considered to fuse the images. The quantitative and qualitative analysis of various wavelets is measured in terms of evaluation parameters like entropy, $Q_p^{(AB/F)}$ and mean value; by comparative analysis, one can chose a particular wavelet that provides better results for a specific metric.

Keywords DWT · CT · MRI · Image fusion · $Q_p^{(AB/F)}$ · Mean value · Entropy

1 Introduction

Image fusion is a method in which multiple images are combined into one image which contains the significant data of the various input images. Image fusion is required for images obtained from various modalities and strategy of capture of a similar object, for example, multi-focus, multi-sensor, and multimodal images. For example, in multi-focus imaging, more than one object might be in focus in specific range where as different objects in a similar scene might be in the other range.

M. N. Narsaiah (✉)

Department of Electronics and Communication Engineering, KG Reddy College of Engineering and Technology, Hyderabad, Telangana 501504, India
e-mail: narsaiahmanthena@gmail.com

D. Venkat Reddy

Department of Electronics and Communication Engineering, Mahatma Gandhi Institute of Technology, Hyderabad, Telangana 500075, India

T. Bhaskar

CMR College of Engineering and Technology, Hyderabad, Telangana 501401, India

Examples for the images which are detected abstractedly have great spectral data when compared with other images that have higher geometric resolution.

In medical imaging [1], the most frequently utilized modalities are MRI and CT; the CT scan does not provide everything related to brain structure indistinctly, and it is suitable for hard tissues imaging such as bone structure; MRI scan gives substantially more point by point data about the delicate or soft tissues, for example, brain in recognizing the diseases related with the skull, and these two images complementary in practically all the ways; data provided by either CT or MRI images [2] are absolutely not enough to detect the diseases. The main advantages of source images is that we can completely exploited by combining the corresponding features observed in various images by techniques of image fusion which produces a composite image that contains the best features detected in source images.

2 Related Work

Image fusion is a method in which the data from various sensors or modalities are combined into single image, which incorporates the applicable data of the more than one source images [3].

Medical image fusion algorithm is proposed primarily used two filters; they are one is laplacian filter, and the second one is guided filter; based on the experimental results, it is concluded that the proposed algorithm provided better results with the help of performances metrics like as entropy, $Q_p^{(AB/F)}$ and mean value using Haar wavelet transform compared to the existing algorithms [4].

Shifali M Patil proposed an algorithm to fuse the images which ensured the edges and uniform intensity of source images are included in resultant image; in this article, gradient criteria present the edge information where as smoothness criteria ensure the region of uniform intensity in resultant image; hence, the noise in the fused image is minimized [5].

Li et al. have promoted image fusion using multisensory with the aid of the use of the wavelet transform; in the process of image fusion, a cascade sequence of forward and reverse transforms on the multimodal images produces a resultant image [6, 7].

Hill et al. demonstrated a process of image fusion in which multiple images are combined by directionally selective DTCWT [8–10]. The different wavelets are used in this paper to fuse the images are, db2, haar, sym2, coif1, dmey, dmey, fk4, bior1.1, and rbio1.1.

3 Proposed Work and Parameters Computation

The functional block diagram of proposed algorithm is shown in Fig. 1; after the registration of source images, wavelet transform is employed to decompose the images

in to low- and high-frequency components. Laplacian filter is used to de-noise the high-frequency components as they have more noise.

By comparing the pixel values of not only low-frequency components but also high-frequency components weight maps $W1$ and $W2$ are calculated that are applied as the input to the guided filter and the low-frequency components as guided image. Guided filter is used to smooth the weight maps and generate the new weight maps $M1$ and $M2$ which are called as refined weight maps. For the guided filter, the default parameters are $r_1 = 45$, $\epsilon_1 = 0.3$ and $r_2 = 7$, $\epsilon_2 = 10 - 6$ where r is the filter size and ϵ is the blur degree of the guided filter.

By using weighted fusion algorithm, a resultant low-frequency component is obtained by fusing two low-frequency components and refined weight maps; similarly, three resultant high-frequency components are determined by fusing the six high-frequency components and refined weight maps.

At the end, with the help of fused low- and high-frequency components and by the application of inverse wavelet transform, the resultant image is obtained.

3.1 Entropy

Data content of the fused image is measured by the entropy which is denoted by the H ; if the value of entropy is high, it indicates that the fused image has better information content. In probability theory, entropy represents the uncertainty

$$H = - \sum_{k=0}^{N-1} P_k \log_2 P_k \tag{1}$$

3.2 Petrovic’s Metric

$Q_p^{(AB/F)}$ is basically an algorithm which transfers the source gradient data into the fused image precisely. It is generally called the gradient based the objective image fusion performance evaluation metric. Consider input images A and B , and F is the fused image.

$$Q_p^{(AB/F)} = \frac{\sum_{n=1}^N \sum_{m=1}^M Q^{AB}(n, m)w^A(n, m) + Q^{BF}(n, m)w^B(n, m)}{\sum_{i=1}^N \sum_{j=1}^M (w^A(i, j) + w^B(i, j))} \tag{2}$$

The range of $Q_p^{(AB/F)}$ is from 0 to 1, where 0 indicates the complete loss of source information and 1 represents ideal fusion process.

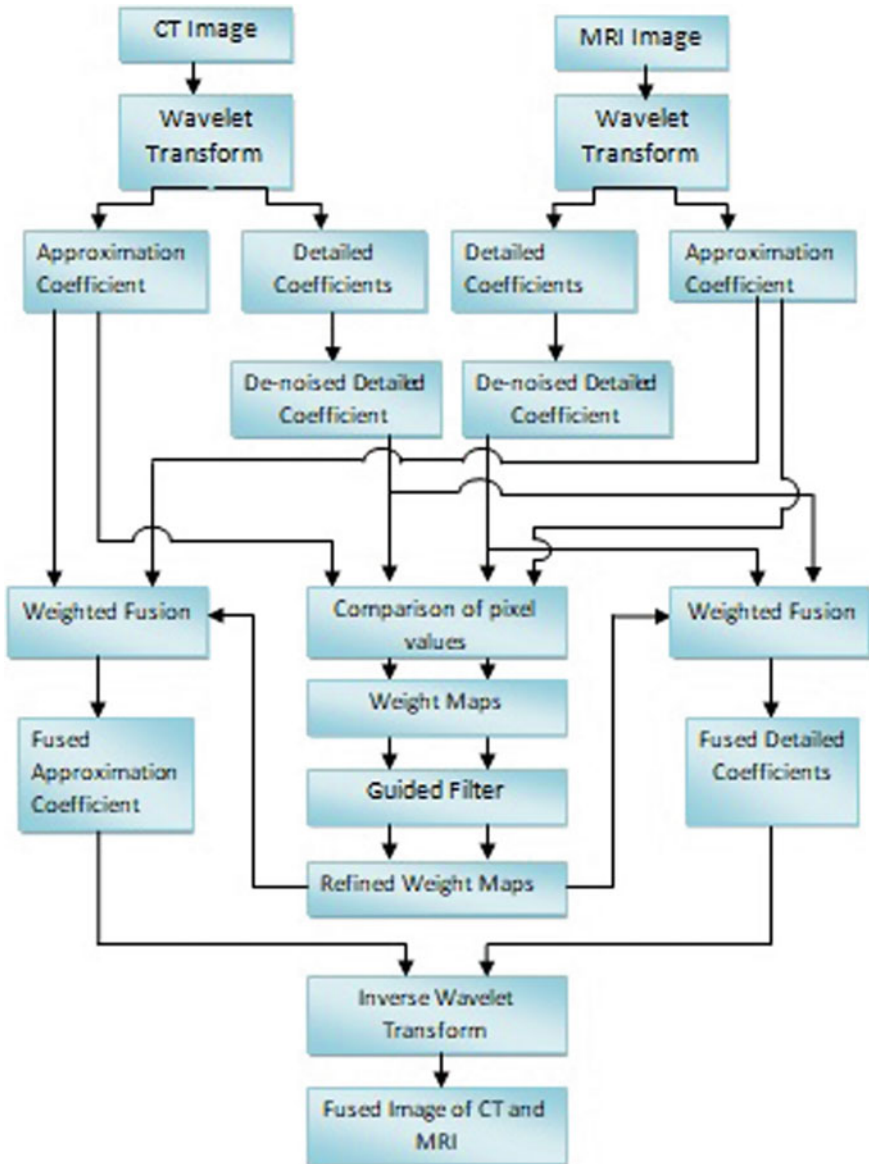


Fig. 1 Functional block diagram of proposed algorithm

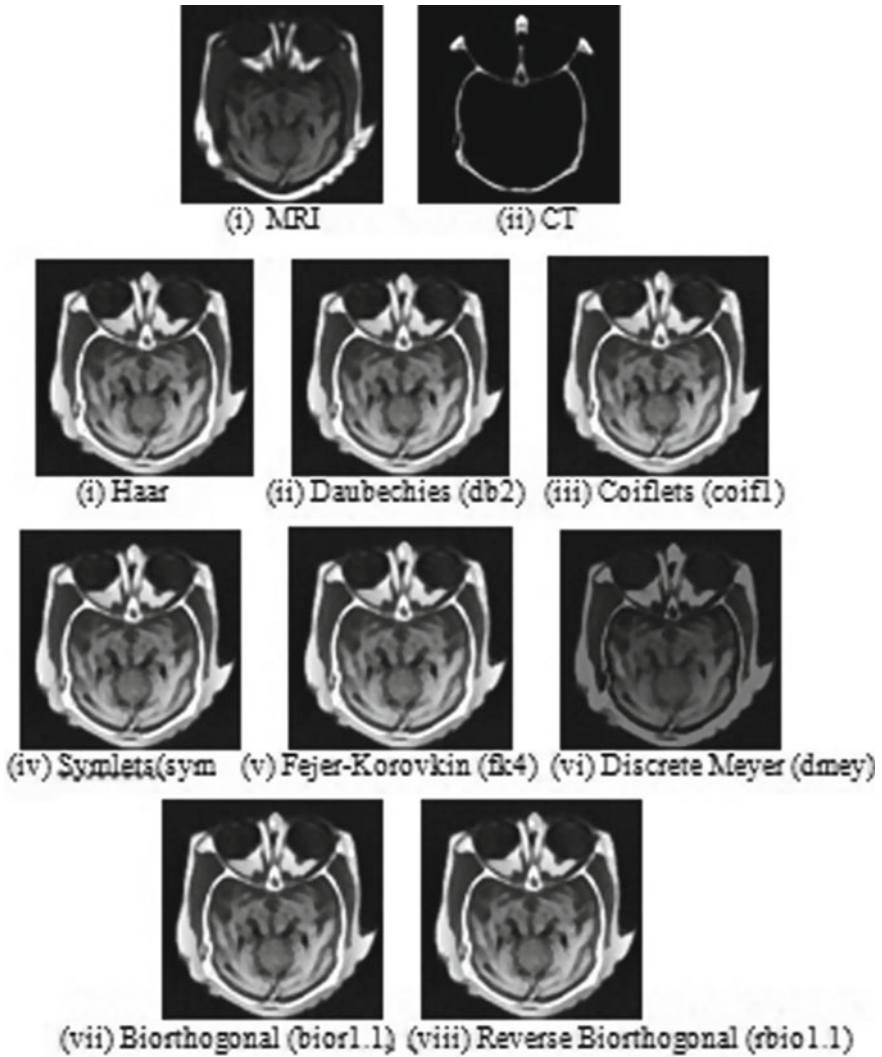


Fig. 2 Resultant images of different wavelets

3.3 Mean Value

Average intensity of a resultant image is denoted by the mean value. If the value of mean is high, it denotes the intensity of the image is high. Mean value mathematical expression is given by

$$\hat{\mu} = \frac{1}{n \times n} \sum_{i=1}^m \sum_{j=1}^n x_{ij} \tag{3}$$

4 Experimental Results

The source images used in this paper are CT and MRI images (Fig. 1); these images are fused by using the different wavelet transforms, and resultant images of all the wavelets are represented in Fig. 2.

4.1 Quantitative Analysis of Wavelet Transforms

CT and MRI images are fused using various wavelet transforms. The performance of the all the wavelet is measured by the evaluation metrics like mean value, entropy, and $Q_p^{(AB/F)}$ that is shown in Table 1. The graphical representation of evaluation metrics like entropy, $Q_p^{(AB/F)}$ and mean value for different wavelets shown in the following figures.

We can note from Fig. 3 that the wavelet transforms Haar, bior1.1, and rbio1.1 outperforms than other wavelets. In order to obtain the better entropy of fused image, the Haar, bior1.1, and rbio1.1 wavelets are used. The wavelet Dmey provides very poor entropy compared to the other wavelets.

We can note from Fig. 4 that the wavelet transforms Haar, bior1.1, and rbio1.1 outperform than other wavelets. In order to obtain the $Q_p^{(AB/F)}$ of fused image, the Haar, bior1.1, and rbio1.1 wavelets are used. The wavelet Dmey is not recommended because its provides poor results compared to the other wavelets.

Table 1 Objective analysis of various wavelets using evaluation metrics

Evaluation metrics/wavelets	Entropy		Mean value
haar (existing)	7.436653	0.714457	0.330038
db2	7.407697	0.714392	0.324988
coif1	7.368849	0.711696	0.320118
sym2	7.407697	0.714392	0.324988
fk4	7.409459	0.713794	0.325484
Dmey	6.973368	0.683785	0.271127
bior1.1	7.436653	0.714457	0.330038
rbio1.1	7.436653	0.714457	0.330038

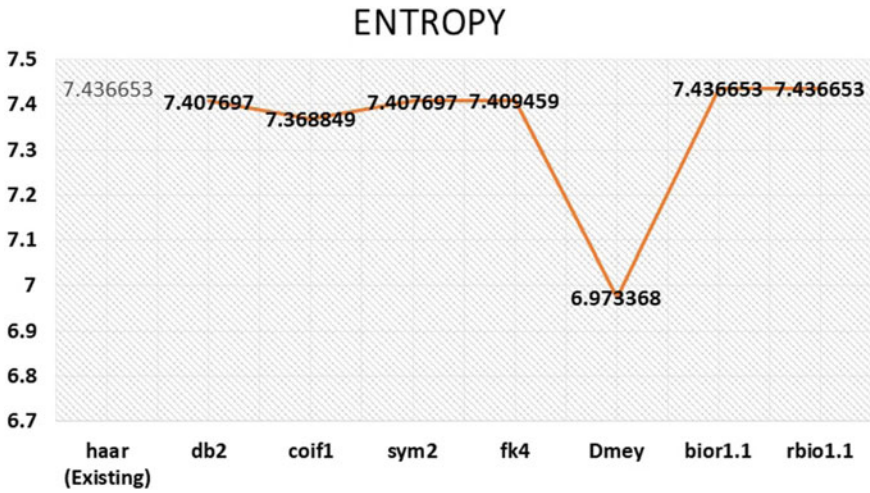


Fig. 3 Different wavelet performance for entropy

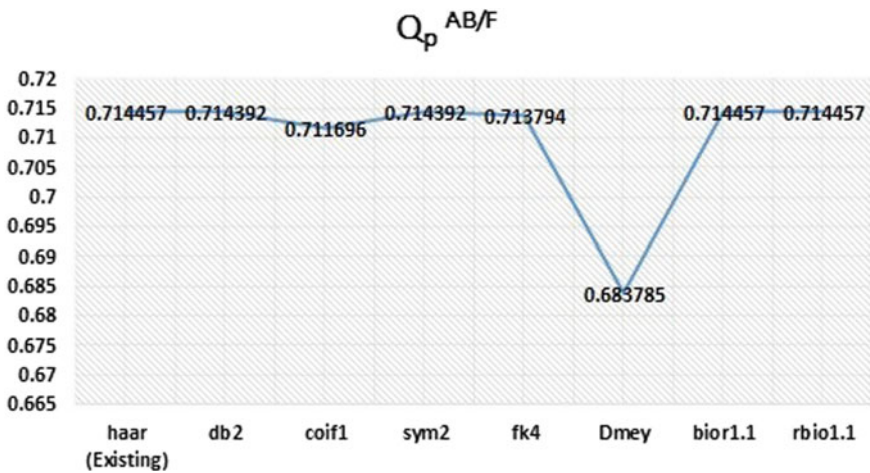


Fig. 4 Different wavelet performance for $Q_p^{(AB/F)}$

We can note from Fig.5 that the wavelet transforms Haar, bior1.1, and rbio1.1 outperforms than other wavelets. In order to obtain the better mean value of fused image, the Haar, bior1.1, and rbio1.1 wavelets are used. The wavelet Dmey is not recommended because its provides moderate results compared to the other wavelets5.

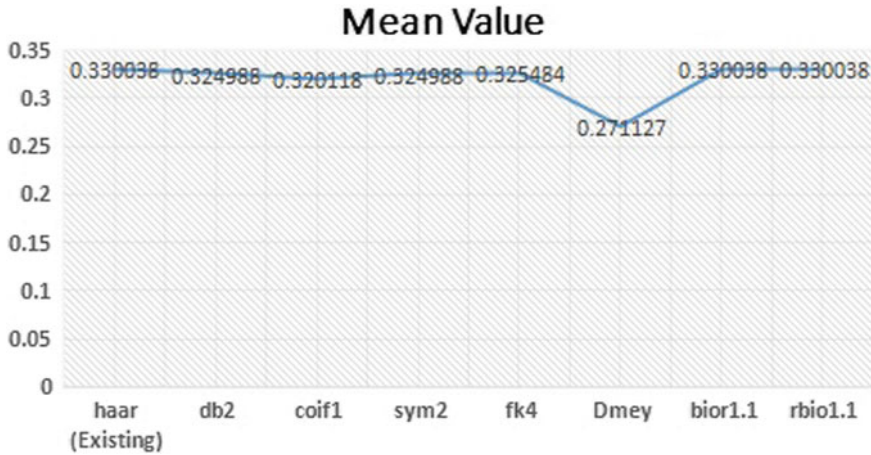


Fig. 5 Different wavelet performance for mean

5 Conclusion

CT and MRI images are fused with different wavelets using the dual filter algorithm. Based on the resultant image, it is found that both the sources images and fused image have the same qualities. By the quantitative analysis of fused image in terms of evaluation metrics such as entropy, $Q_p^{(AB/F)}$ and mean value provided information in selecting the appropriate wavelet along with evaluation metric which provided better results compared to the remaining wavelet transforms. Shown that the wavelets Haar, bior1.1 and rbio1.1 provided better results for the all the three evaluation metrics.

References

1. Yelampalli PK, Nayak J, Gaidhane VH (2018) Daubechies wavelet-based local feature descriptor for multimodal medical image registration. *IET Image Process* 12(10):1692–1702
2. Gaidhane VH, Hote YV, Singh V (2012) An efficient similarity measure technique for medical image registration. *Sadhana* 37(6):709–721
3. Malviya A, Bhirud SG (2009) Image fusion of digital images. *Int J Recent Trends Eng* 2(3):146
4. Narsaiah MN, Vathsal S, Venkat Reddy D (2019) Dual filter based images fusion algorithm for CT and MRI medical images. *Int J Innov Technol Expl Eng (IJITEE)* 8(9). ISSN: 2278-3075
5. Patil SM (2016) Image fusion using wavelet transform. *Int J Eng Adv Technol (IJEAT)* 5(4). ISSN: 2249-8958
6. Li H, Manjunath BS, Mitra SK (1995) Multisensor image fusion using the wavelet transform. *GMIP: Graph Models Image Process* 57(3):235–245
7. Yocky R (1996) Multiresolution wavelet decomposition image merger of Landsat thematic mapper and SPOT panchromatic data. *Photogr Eng Remote Sens* 62:1067–1074
8. Hill PR, Canagarajah CN, Bull DR (2002) Image fusion using complex wavelets. *BVMC*

9. Garguet-Duport B, Girel J, Chassery J, Pautou G (1996) The use of multiresolution analysis and wavelets transform for merging panchromatic and multispectral image data. *Photogr Eng Remote Sens* 62:1057–1066
10. Wang L, Liu B, Hu J, Zhang B (1998) Low light level dual spectrum images fusion based on wavelet transform. *Proc SPIE* 3561:393–397

Two-State Hybrid Learning Approaches for Energy Reduction Estimation on Wireless Sensor Networks



V. Sivasankara Reddy and G. Sundari

Abstract Wireless Sensor Networks (WSNs) with current technologic advances have been improvised with prime development scenarios that would impact the different areas of research in computer science. Several researchers have been providing real-time solutions with data-mining strategies in wireless environments where these sensor models tend to implement the lifetime of the network and also to reduce energy usage. This paper presents a design model for the WSN network based on optimized link states modeling to identify the specific nodes where the energy minimum has been established. The generated energy estimations where each set of established relay points ensures the energy minimum improvising the parametric criteria on energy will be dealt with the design factors that govern the learning model. The LEACH-A and LEACH-D are implemented with a Fuzzy logic model for the energy reduction criteria. The LSR-MSR protocol where node identification is classified, and the reduction of energy levels is estimated using an ensemble approach on WSN. The proposed DEEC with Link state-machine learning (LS-ML) approach has improvised the design parameters such as energy, entropy, and packet loss for each data transmission with 8 percent values observed for the improved factors.

Keywords Link state-machine learning · Fuzzy logic system · Wireless Sensor Networks · Energy-efficient classification · and Whale optimization algorithm

1 Introduction

WSNs are set up with minimal power [1], memory, electricity dealing with, and transmission potential for small trade and radio variety [2]. Abound within the literature primarily with the factors that govern the different set of design conditions. Considering that the sensing devices must accomplish under immoderate strength constraints, it might not be possible to ship the noticed data to go away from the

V. Sivasankara Reddy (✉) · G. Sundari

Electronics and Communication, Sathyabama Institute of Science and Technology (Deemed to be University), Chennai, India

e-mail: tejapav05@gmail.com

© The Author(s), under exclusive license to Springer Nature Singapore Pte Ltd. 2022

359

P. Kumar Jain et al. (eds.), *Advances in Signal Processing and Communication Engineering*, Lecture Notes in Electrical Engineering 929,

https://doi.org/10.1007/978-981-19-5550-1_34

station. It uses clustering formulation to search for sources that percentage statistics to some degree within the most effective of the personal Internet links. The safety and protection devices utilized for tough networks aren't being moved right away to Wi-Fi sensing unit networks because of the decreased computational efficiencies and electricity resources of the sensing unit nodes. Thus the protection frameworks deliberate for sensing unit networks ought to be evolved with the undertaking of wireless sensor, power systems, memory, further to the confined battery life of the sensing unit nodes in guidelines, network protection services may be identified into crucial agencies: approaches based totally in big element on prevention and detection primarily based improvements. Detection-based enhancements [3, 4] goal is to implement an integral security mechanism, a new hybrid intrusion detection system (HIDS) for to decrease energy consumption.

With technological advantages, nodes turn out to be being smaller, but WSNs are extensive. Consequently, dealing with a terrific deal of documents created via those networks is an extreme adventure that is managed realistically using information mining strategies. Information extracting [5] is a gadget that examines large amounts of facts for styles that permit information to be eliminated. For WSN, the kind may be made use of for assignment discovery [6], outdoor detection [7], invasion detection [8], and so forth. Several studies research has in reality been attended to wireless sensing unit community safety and safety problems. In [9], the authors checked out the law WSN safety and safety, and moreover supported for threat versions and also security fashions directing in Wi-Fi sensor networks. They confirmed new instructions for formerly undocumented assaults as opposed to sensing unit networks, which are sink assaults HELLO flooding [10], supplied important specific protection to analyze all big directing and moreover electricity protocols. They have been keeping geography algorithms for sensor networks. The crossbreed Wi-Fi sensor community-based totally breach detection system end up supplied in [11] proper right here, the authors maintain the invasion discovery plan that taken to apply a cluster-based totally approach to develop a pecking order area and sneak sight of both anomalies and also misuse techniques. Disclose the effectiveness of the endorsed scheme, in comparison with the chosen commands Advice excursions. Onat and also Miri in [12] have provided anomaly invasion detection structures for massive sensor networks that control the steadiness of region data.

The clustering formula [13] has been completed to element the same nodes and maintain the specified lost strength in sending the data observed at each sensor for each cluster head formation. In [14], they have got genuinely supplied cordless sensing unit networks for a singular hierarchical directing process. It is primarily based totally on the important clustering technique recommended by way of the adequate approach technique to contain sensor networks right into collections and obtain a much performance parameter. This paper proposes a whale optimization formula based totally higher KNN classifier to discovering the exquisite placement of a solitary sink node with decreasing strength consumption to enhance the network lifetime inside the wireless sensing unit community ecosystem. Better, complying with organizing the position of sink node inside the network unearths best of close by subsequent-door neighbor's hyperlinks. Lastly, the performance of the recom-

mended whale optimization-based stepped forward KNN (IKNN) is as compared with a specific set of regulations which consist of K-technique and traditional KNN formulas.

2 Existing Model and Implementation

2.1 *LEACH-A,B Implementation*

Wendi B. Heinzelman, Anantha P. Chandrakasan, and Hari Balakrishna introduced a hierarchy model termed as LEACH Low-Energy Adaptive Clustering Hierarchy [15–17] which was the first and prominent case on the WSN energy reduction scheme. This protocol would impart the different assumptions on the power transmission and its related formulation model with precise transmit power to reach BS. This node ensures the control capability for each set of conditions adjusted to withhold the transmission power and will be addressed with the computation power observed at each node while providing the MAC protocols to ensure the signal processing functions are modeled. Each round for the design of LEACH protocol would improvise with timing scenario on states of clusters as setup, steady-state, framing and rounding the data. Ensure the clusters are generated with an effective solution based on the threshold equation for each node would perform the CH. Considering the different values chosen for the nodes where the threshold < number chosen, then the sensor node becomes the CH for the current round either wise it will iterate till it satisfies the below equation.

Once all the cluster heads are selected, the member nodes in the cluster transmit the data to the cluster head. The cluster head collects the received data and transmits it with its own data to the base station.

2.2 *Fuzzy Logic for LEACH Protocol*

The structure of Fuzzy logic system [18–21] is mentioned in Fig. 1 depicts the importance of different requirement scenario of parametric criteria considered where each set of the block are justifying the importance of implementing the different aspects of the WSN features where each specific values on the energy and network lifetime are modeled using the prediction values observed while calculating the different case studies observed for each set of the node selected from the WSN network. The design factors with blocks in considered with distance and communication model where these would provide the real-time values for each set of iterations considered on the design platform for each set of fuzzification for predicting the different input criteria mentioned on the different nodes which are estimated with minimized prediction values.

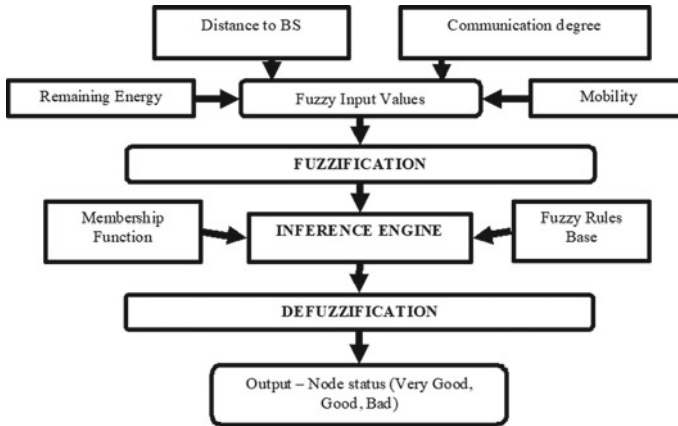


Fig. 1 Representing the flow diagram of Fuzzy logic

The fuzzification and defuzzification generates the fitness values of each parametric criteria considered where rules of each prediction criteria are implemented with aggregator function on each parameter. A map function is utilized with consideration on the single set of input values from the fuzzy model and it's estimated with each output values observed from the desired functional operation as an aggregator. The weights calculated for each parametric criteria on the deterministic functional changes with criteria of values are fed to defuzzification process where each of the functional values is estimated with its weight and classified.

2.3 Genetic Algorithm Phase

The criteria on the current algorithms for the design features would improvise on the different scenarios on each set of parametric criteria that ensure the correct and predicted outcome. Here we establish different sections of modeling the problem solution depending upon the different states utilized.

1. Population: Solution set on each subset of problems that assigned for specific criteria on specifications such as node estimation and characterizing the node value states.
2. Chromosomes: The single solution set on each set of iterated outcomes observed on a single phase.
3. Gene: Elemental values on each position changes observed when a chromosome is generated.
4. Genotype: Computation model for each set of problem solution criteria considered. Encoding and Decoding: Spatial changes on variables and their position values observed.

2.4 WSN with Genetic Algorithm

Genetic Algorithm (GA) [22–26] is utilized in several regions in Wireless Sensor Networks (WSN) like to create a plan for which network to utilize, to send the data either for the network or the user, direct the different signal data with the established model, bunching of a different set of clusters which have to be energy minimization, etc. Data groups and its functional values have become a serious scenario for utilization of genetic algorithm in Wireless Sensor Network, seeing that it buildings bunches this are most vitality effective and stable. GA is utilized uniquely for integrated grouping calculations in execution greater impressive hubs like the BS. Generally, a first-rate in the chromosomes speaks to a sensor hub. Here, the length established when created the network model represents the features aspects of the design parametric criteria ensuring the different sensor hubs which either communicates on clusters.

3 Research Method

The research method improvises on the link state modeling with a decision threshold algorithm which ensures the different set of sensor nodes are active and passive with each set of MPR's selected. This MPR's formation is achieved by considering the different sensors and its relative position model utilized using Dijkstra's algorithm. The proposed design imparts the design feature with a machine learning approach to ensure better outcomes on each set of parameters such as energy, network lifetime, packet drops, alive and dead scenarios. These criteria for each parametric scenario would be observed and estimated with an aspect of developing a novel scenario on each functional model as mentioned below. The research method with LS-DT is modeled and implemented using the specific optimized decision tree with AdaBoost algorithm. The features that we have considered on the AdaBoost algorithm would be entropy and gain values observed from each node and its selected MPR's which are explained in Eq. (1).

3.1 Problem Statement

1. Analyzing the current design optimizers with machine learning models ensuring with best performance characteristics observed.
2. Our proposed design implicates on the factors of decision thresholding algorithm which provides the entropy calculations on each selected nodes for the link state algorithm.
3. Reduction of values such as energy, range of transmission, rate of packets established and loss and load on network would emphasize on the mathematical estimation model as mentioned in Eq. (4).

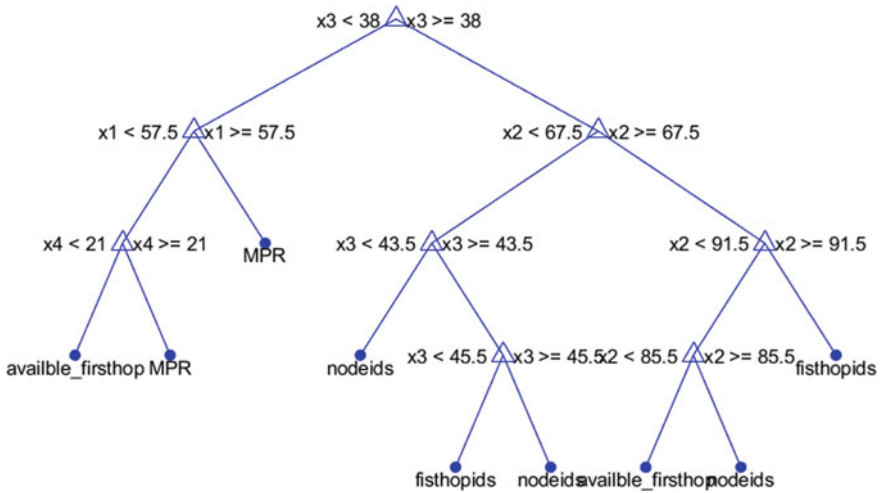


Fig. 2 Representing the hopping, node-IDs and MPR’s branched with decision tree algorithm

3.2 Link State Decision Tree with Thresholding Algorithm

1. Initialize the design with flag and graph where each node is utilized with maximum value.
2. Estimation on each tree graph is generated with a selection of different MPR’s based on Dijkstra’s distance. We initiate the different scenario on the model where optimization is observed with minimum distance between each node estimated for selection of MPR’s.
3. Optimizing the threshold values for each selected MPR is generated with Eq. (1).
4. Hopping on iterations changes would suffice the selection of MPR’s selection onto minimum energy model is applied for given criteria.

3.3 Link State Model for Multipoint Relays in WSN

The current design on the links stages would improvise a switching node for forwarding packets which are labeled with routers. As from Fig. 2, we have utilized two scenarios on learning models improvising the design accuracy and energy reduction capabilities. Decision tree and ensemble approach are implemented ensuring the improved scenario where nodes are identified with MPR’s where each such selection MPR’s are clustered to create a link state maps decision tree maps. The best logical path is estimated from the selected MPR’s to every possible destination of the designed LS-DT link state decision tree.

Figure 2 represents the initial analysis model on the link state algorithm with probability distances estimation for each set of nodes considered for MPR selection ensuring the minimum energy.

3.4 Link State Prediction with Energy Clustering

The hybrid protocol intends with multiple point relays combined with threshold attempts. To initiate multipoint sections with specified hops, the prime considerations are generated flags and exit flag conditions. The cluster node with MPR's dedicated with update and existing verification of each node user.

3.5 Formulation for Energy Efficient

We improvise a decision threshold for each set of nodes and selected MPR as:

$$F(i > k) = \sum_{i=1}^N (n_i * MPr(i) + W_i * D_i) + E(i) + G_i * W_i \quad (1)$$

The function for value 'k' threshold would provide entropy and weighted distance with gain on each selected MPR's ensuring the less energy factor at each selection. The generalized clusters with the characteristic nodes where energy transmitted over the network is estimated with F as each value of clusters and its head occupancy on the WSN would provide minimum energy. Here $E(i)$ represents the entropy of each selected MPR. Hence, the total network energy estimated is:

$$PE_{cluster_MPR's} = \rho * F(i > k) \quad (2)$$

$$PE_{Head_cluster} = \omega * W_i * D_{min} + \alpha MPr(i) + E(i) \quad (3)$$

$$PE_T = PE_{Head_cluster} + PE_{cluster_MPR's} \quad (4)$$

3.6 DEEC Model with Ensemble Approach

Distributed energy efficient algorithm is utilized to initiate the network model creation for operational features estimation and prediction of the data as observed from the LS-DT algorithm. Our proposed design with two-state procedural model on the

implication on the node selection and energy minimization on the selected nodes are two states for which the ensemble learning model is applied. With criteria on this model, we improvised on the learning model where each set of observed energy values with two states 0, 1 are initiated with the probability values observed for each node on the energy values which are either active or passive. Random values of the active and passive are mentioned when considering the different outcome on basis of Eq. (4).

4 Results and Discussions

Figure 3 representing the WSN structure on the design platform considering the links states and its hopping iterations for each selected MPR's (Fig. 4)

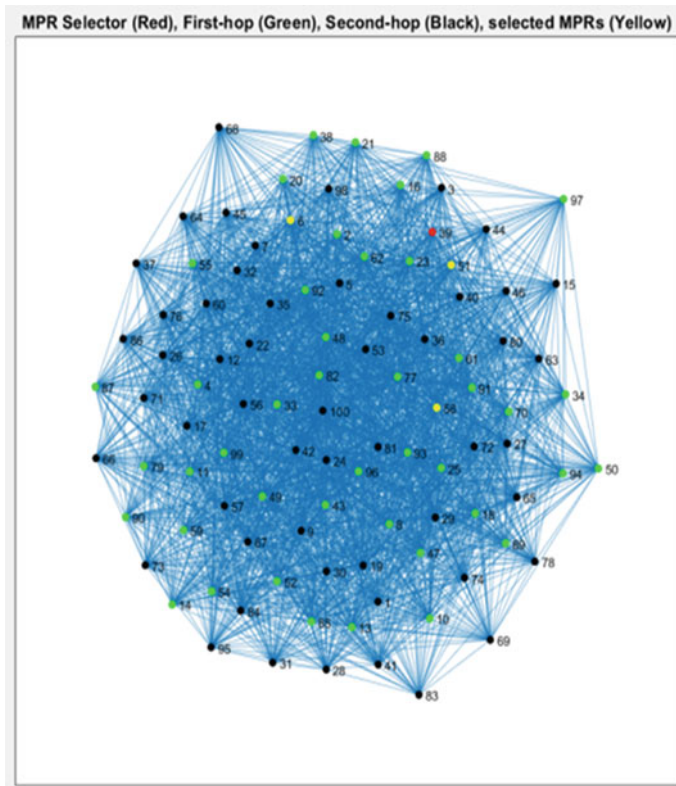


Fig. 3 Representing WSN structure on LS-DT algorithm model for MPR selection

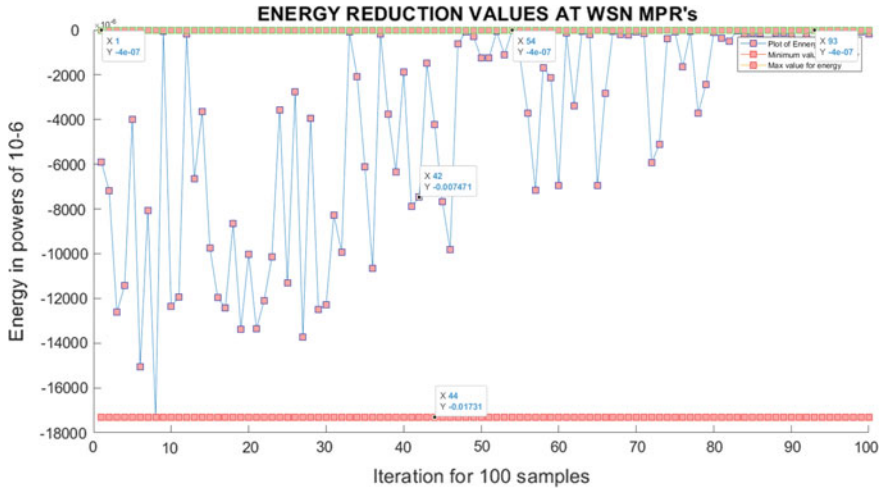


Fig. 4 Representing the minimum energy values for the MPR-node at each iteration length of 5000

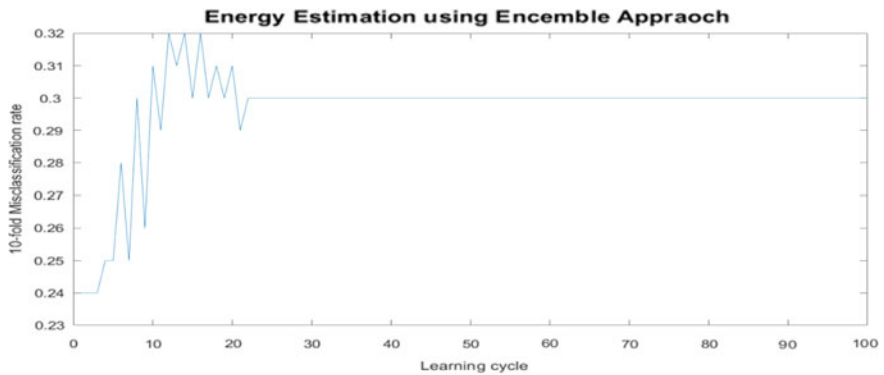


Fig. 5 Representing the energy minimization using ensemble approach

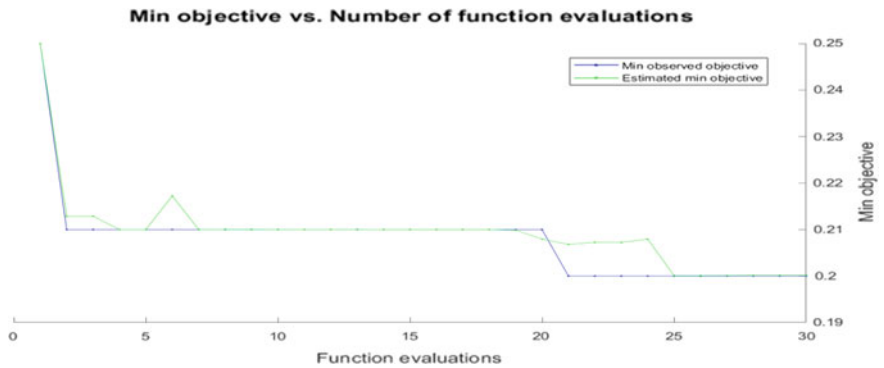


Fig. 6 Representing the minimum objective function values for energy optimized from ensemble algorithm

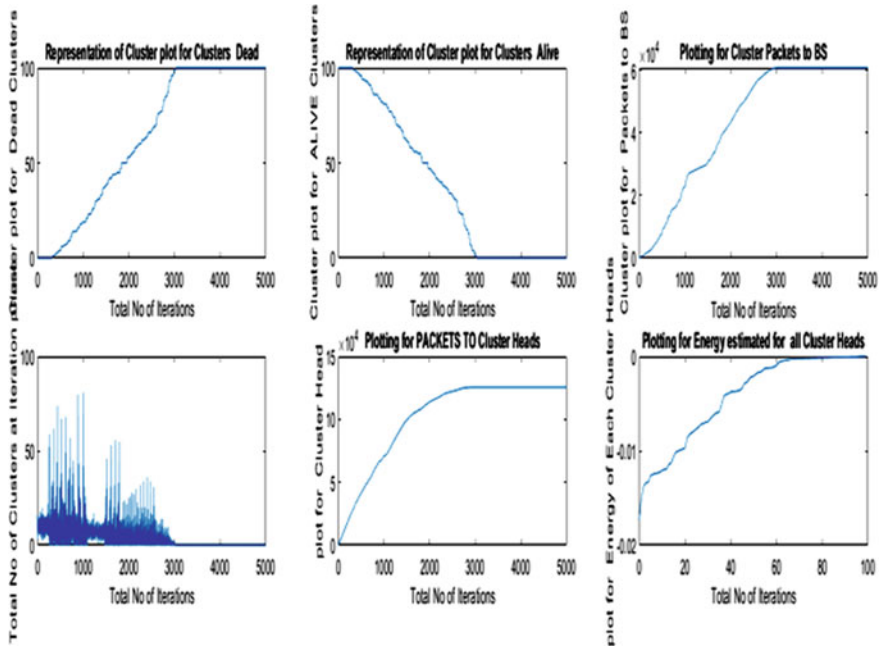


Fig. 7 Representing the cumulative representation of the DEEC model with 5000 iterations on each parametric criteria

Figures 5 and 6 represent the utilization of ensemble approach for ensuring the objective functionalities and accuracies are observed from the design optimization such as the ADABOOST algorithm.

Figure 7 represents DEEC model implementation with energy cluster and cluster head scenario for all iteration of 5K providing alive and dead clusters. Dead clusters are identified with values 468 and 4306 value is observed for the alive clusters with the total iterations.

The network size with 100×100 nodes have been estimated where each set of nodes are modeled with selected MPR and its energy minimization using ensemble approach with optimized function as LGBS, AdaBoost algorithm which is plotted in Fig. 8. The estimation of the different functional algorithms are utilized with the feature of an ensemble where Random forest, extra-tree classifier, optimizers with LGBS and AdaBoost algorithms are modeled as callback functions. According to the ensemble approach, multiple algorithms with multiple optimizers are estimated using the function fit ensemble ($x, y, options$) (Fig. 9).

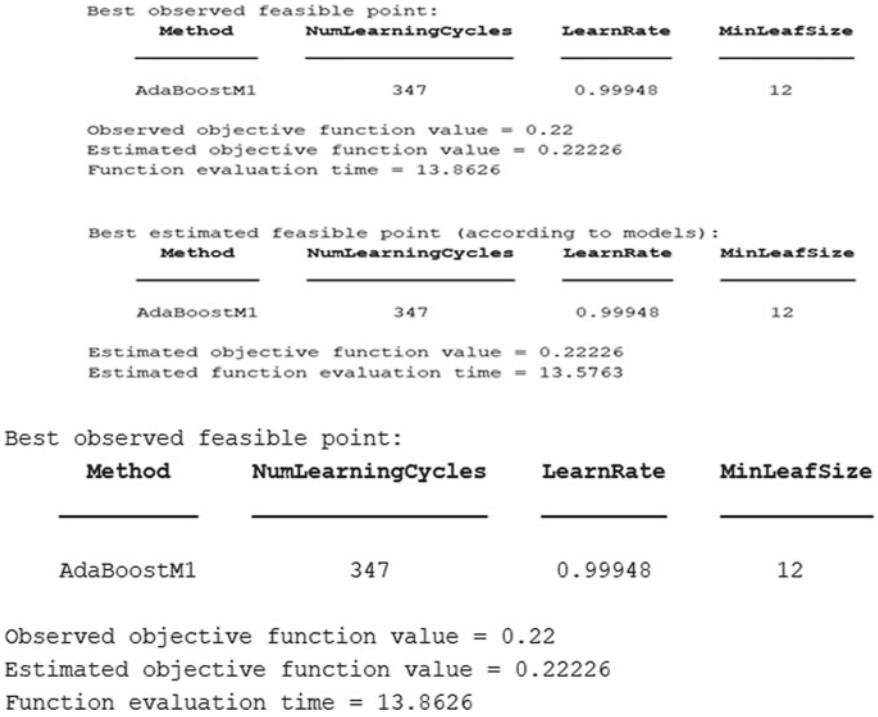


Fig. 8 Representing objective functionality on the energy optimization using AdaBoost algorithm

Table 1 Representing the proposed and existing model comparison with parametric design criteria

S. No.	Parameters	Existing LEACH-A,B and GA	Proposed LS-DT, DEEC-Ensemble two state
1	Minimum energy	-2.2×10^{-4} J	-4×10^{-7} J
2	Maximum energy	-0.0705J	-1.731×10^{-2} J
3	Active nodes	1986	4306
4	Passive nodes	468	468
5	Minimum energy node node 93	-2.2×10^{-4} J	-4×10^{-7} J
6	Minimum energy node node 54	-2.2×10^{-4} J	-4×10^{-7} J
7	Accuracy of prediction nodes with minimum energy	73%	90%
8	Minimum energy in dB	-73.15	-127.95
9	Maximum energy in dB	-23.03	-35.23

Iter	Eval	Objective	Objective	BestSoFar	BestSoFar	Method	NumLearningC-	LearnRate	MinLeafSize
result			runtime	(observed)	(estim.)		ycles		
1	Best	0.29	13.442	0.29	0.29	RUSBoost	329	0.0063563	1
2	Best	0.27	0.76315	0.27	0.27104	RUSBoost	17	0.0035315	25
3	Best	0.25	1.8311	0.25	0.25132	LogitBoost	40	0.49191	2
4	Accept	0.25	18.995	0.25	0.25	LogitBoost	481	0.065379	22
5	Accept	0.29	2.3734	0.25	0.25	GentleBoost	47	0.67085	7
6	Accept	0.29	1.1597	0.25	0.25	LogitBoost	25	0.0010196	7
7	Accept	0.26	5.7634	0.25	0.25634	LogitBoost	137	0.247	14
8	Accept	0.26	19.221	0.25	0.25	LogitBoost	488	0.14391	2
9	Best	0.24	0.61257	0.24	0.24001	LogitBoost	11	0.83329	10
10	Accept	0.26	0.48714	0.24	0.24001	LogitBoost	10	0.036532	21
11	Accept	0.27	0.59241	0.24	0.25271	LogitBoost	12	0.98187	32
12	Accept	0.27	3.1917	0.24	0.24	LogitBoost	70	0.93246	5
13	Accept	0.26	2.6152	0.24	0.24219	LogitBoost	61	0.92644	9
14	Accept	0.25	3.2052	0.24	0.25642	LogitBoost	78	0.29356	10
15	Accept	0.5	14.867	0.24	0.25594	Bag	492	-	50
16	Accept	0.3	2.1066	0.24	0.25593	AdaBoostM1	61	0.014483	22
17	Accept	0.27	0.60817	0.24	0.25654	GentleBoost	13	0.0010004	7
18	Accept	0.25	6.5407	0.24	0.25697	RUSBoost	160	0.99889	12
19	Accept	0.29	0.73364	0.24	0.25757	RUSBoost	19	0.9863	24
20	Accept	0.25	1.2901	0.24	0.2572	AdaBoostM1	33	0.99701	4

Iter	Eval	Objective	Objective	BestSoFar	BestSoFar	Method	NumLearningC-	LearnRate	MinLeafSize
result			runtime	(observed)	(estim.)		ycles		
21	Accept	0.28	0.6671	0.24	0.25708	RUSBoost	18	0.0010035	2
22	Accept	0.29	8.9791	0.24	0.25658	AdaBoostM1	228	0.0010019	2
23	Accept	0.25	1.6106	0.24	0.25724	AdaBoostM1	37	0.99992	2
24	Best	0.22	13.863	0.22	0.24622	AdaBoostM1	347	0.99948	12
25	Accept	0.25	4.0516	0.22	0.247	AdaBoostM1	96	0.99668	1
26	Accept	0.25	17.912	0.22	0.24694	GentleBoost	372	0.021772	20
27	Accept	0.26	15.965	0.22	0.2468	AdaBoostM1	495	0.17829	19
28	Accept	0.5	0.15321	0.22	0.21895	AdaBoostM1	33	0.99785	43
29	Accept	0.25	9.2747	0.22	0.2188	GentleBoost	246	0.0038986	50
30	Accept	0.28	2.9506	0.22	0.22226	AdaBoostM1	91	0.0012569	11

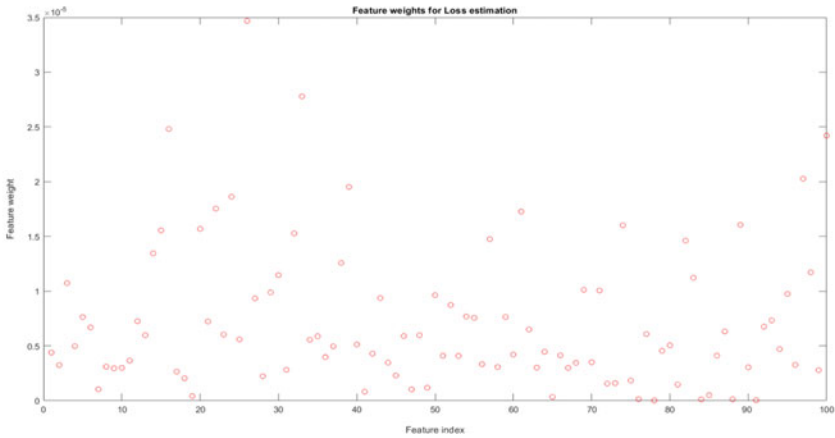


Fig. 9 Representing the optimization with 30 iterations in different algorithm schemes ensuring the multi-objective functional analysis

5 Conclusion

The design depicts the two-state models with features of link state analysis and its importance on the decision threshold analysis for the different distances observed for each set of application on the design factors on energy reduction capabilities as formulated in Sect. 3.5. The minimum energy with increased active nodes are

tabulated with factors considering the equation on energy which improvised with Eq. (1) in Sect. 3. These formulas representations on each set of nodes are estimated with the current energy Eq. (4) which improves the active nodes where the minimum energy is observed with 4.6×10^{-5} J. The average energy estimation with DEEC and LEACH-A, B is justified with tabulated results in Table 1, which imparts on the different parametric behavior observed while calculating and estimating the different energy minimization at each set of active nodes. Since LS-DT algorithm is utilized with a factor of selection of different random nodes on existing network, the accuracy of the design system is observed with an improved the factor of 17%.

References

1. Nithya B (2020) Cluster based key management schemes in wireless sensor networks: a survey. *Procedia Comput Sci* 171:2684–2693
2. Wang J, Gao Y, Liu W, Sangaiah AK, Kim H-J (2019) Energy efficient routing algorithm with mobile sink support for wireless sensor networks. *Sensors* 19(7):1494
3. Moulad L, Belhadaoui H, Rifi M (2017) Implementation of a hierarchical hybrid intrusion detection mechanism in wireless sensors network. *Int J Adv Comput Sci Appl* 8(10):270–278
4. Sikarwar H, Das D (2020) A lightweight and secure authentication protocol for WSN. In: 2020 international wireless communications and mobile computing (IWCMC). IEEE, pp 475–480
5. Fouad MM, Oweis NE, Gaber T, Ahmed M, Snasel V (2015) Data mining and fusion techniques for WSNs as a source of the big data. *Procedia Comput Sci* 65:778–786
6. Carlos-Mancilla MA, Lopez-Mellado E, Siller M (2018) Distributed methods for multi-sink wireless sensor networks formation. In: *Encyclopedia of information science and technology*, 4th edn. IGI Global, pp 6522–6535
7. Shia HH, Tawfeeq MA, Mahmoud SM (2019) High rate outlier detection in wireless sensor networks: a comparative study. *Int J Mod Educ Comput Sci* 11(4)
8. Butun I, Morgera SD, Sankar R (2013) A survey of intrusion detection systems in wireless sensor networks. *IEEE Commun Surv Tutor* 16(1):266–282
9. Shi Q, Qin L, Ding Y, Xie B, Zheng J, Song L (2020) Information-aware secure routing in wireless sensor networks. *Sensors* 20(1):165
10. Lee D, Rhee Eugene (2019) Attacks, detection, and countermeasures in WSN network layer. *J IKEEE* 23(2):413–418
11. Revathi GK, Anjana S (2019) Hybrid intrusion detection using machine learning for wireless sensor networks. *Int J Innov Technol Expl Eng* 8(12):4867–4871
12. Ioannou C, Vassiliou V, Sergiou C (2017) An intrusion detection system for wireless sensor networks. In: 2017 24th international conference on telecommunications (ICT). IEEE, pp 1–5
13. Norozpour S, Darbandi M (2020) Proposing new method for clustering and optimizing energy consumption in WSN. *Talent Dev Excell* 12
14. Hanzalek Z, Jurcik Petr (2010) Energy efficient scheduling for cluster-tree wireless sensor networks with time-bounded data flows: application to IEEE 802.15.4/ZigBee. *IEEE Trans Ind Inform* 6(3):438–450
15. Ch RR, Harinadha Reddy K (2018) An efficient passive islanding detection method for integrated DG system with zero NDZ. *Int J Renew Energy Res (IJRER)* 8(4):1994–2002
16. Fu C, Jiang Z, Wei WEI, Wei A (2013) An energy balanced algorithm of LEACH protocol in WSN. *Int J Comput Sci Issues (IJCSI)* 10(1):354
17. Arumugam GS, Ponnuchamy T (2015) EE-LEACH: development of energy-efficient LEACH Protocol for data gathering in WSN. *EURASIP J Wirel Commun Netw* 2015(1):1–9

18. Maryem M, Belkassem T (2020) Routing in wireless sensor networks using fuzzy logic: a survey. In: 2020 international conference on intelligent systems and computer vision (ISCV). IEEE, pp 1–6
19. Jha AK, Kaur S (2021) Multi layer fuzzy logic based optimization algorithm to improve energy efficiency for hierarchical protocol in WSN
20. Kousar A, Mittal N, Singh P (2020) An improved hierarchical clustering method for mobile wireless sensor network using type-2 fuzzy logic. In: Proceedings of ICETIT 2019. Springer, Cham, pp 128–140
21. Tan H-Y, Yap W-S, Goi B-M (2019) Performance analysis of an fuzzy logic based LEACH protocol. In: Proceedings of the 2019 8th international conference on software and computer applications, pp 33–37
22. Alwafi AAW, Rahebi J, Farzammia A (2021) A new approach in energy consumption based on genetic algorithm and fuzzy logic for WSN. In: Proceedings of the 11th national technical seminar on unmanned system technology 2019. Springer, Singapore, pp 1007–1019
23. Radhika M, Sivakumar P (2021) Energy optimized micro genetic algorithm based LEACH protocol for WSN. *Wirel Netw* 27(1):27–40
24. Yuan X, Elhoseny M, El-Minir HK, Riad AM (2017) A genetic algorithm-based, dynamic clustering method towards improved WSN longevity. *J Netw Syst Manag* 25(1):21–46
25. Hamidouche R, Aliouat Z, Gueroui AM (2018) Genetic algorithm for improving the lifetime and QoS of wireless sensor networks. *Wirel Pers Commun* 101(4):2313–2348
26. Dhami M, Garg V, Randhawa NS (2018) Enhanced lifetime with less energy consumption in WSN using genetic algorithm based approach. In: 2018 IEEE 9th annual information technology, electronics and mobile communication conference (IEMCON). IEEE, pp 865–870

Design of IoT-Based Transmission Line Fault Monitoring System



N. Dhanalakshmi, Chanikya Mamindlapalli, Dinesh Reddy Sunkari,
and Rohith Reddy Salguti

Abstract Power is transmitted from the generation plants to end users at distant locations through the transmission lines. Due to various environmental conditions, faults may occur causing power interruption to end users and damage to the power system. The operators cannot know information about fault immediately. To classify the faults, various methods have been developed such as transient analysis, phasor measurement units and artificial neural networks based approaches. The purpose of this project is to detect and classify the faults in transmission lines using IoT in addition with fuzzy logic for fault classification. In this project, we are designing a system to collect data from the transmission lines to detect and classify the faults, and then, data is transmitted to the cloud and SMS alert is sent to the operator. The project used MATLAB Simulink to simulate generally occurring faults and detecting them.

Keywords IoT · MATLAB Simulink · Fuzzy logic

1 Introduction

The transmission line serves as a critical link between the electrical power generation plants and all electricity users. Transmission lines with a length of several kilometers would be affected, and service continuity is disturbed as there is a possibility that a fault will occur. Faults should be cleared at regular intervals to ensure stability. Transmission line faults cause equipment damage and instability [1]. As a result, fault protection for the electric power system is needed. Transient faults last for a short period of time, while permanent faults last for a longer period of time. Faults should be identified quickly for immediate isolation of the defective line from the device for effective defense [1]. Following that, fault classification and position must be carried out in order to restore and speed up the system's recovery. Faulty current and voltage signals are used in transmission networks to locate, detect and classify

N. Dhanalakshmi · C. Mamindlapalli · D. R. Sunkari (✉) · R. R. Salguti
Chaitanya Bharathi Institute of Technology, Hyderabad, Telangana, India
e-mail: ugs17032_ece.dinesh@cbit.ac.in

© The Author(s), under exclusive license to Springer Nature Singapore Pte Ltd. 2022
P. Kumar Jain et al. (eds.), *Advances in Signal Processing and Communication Engineering*, Lecture Notes in Electrical Engineering 929,
https://doi.org/10.1007/978-981-19-5550-1_35

373

faults [2]. The circuit breaker is used to disconnect the part of the transmission line where fault occurred from the remaining part after the relay detects an irregular signal [3].

These faults may be either open circuit or short circuit. Wearing of insulators on transmission lines and opening of conductor due to wearing are examples of open-circuit faults. A short circuit occurs when two or more lines carrying different voltages are connected to the ground or getting in contact with each other either inadvertently or deliberately, due to environmental effects such as tree falling on the lines or because of birds sitting on lines. Three-phase faults (three phases of the lines touching ground or three phases short circuited) are symmetrical short-circuit faults, while the rest are unsymmetrical faults. These are the most common and extreme types of faults that cause abnormally high currents to flow via the transmission lines or facilities [4]. If the faults are not resolved for a long period of time, it contributes to significant equipment damage in a limited period of time. In addition to safeguarding the environment, finding the fault site protects power system equipment from damage caused by a fault. It is crucial.

There are many benefits to accurate fault determination, including reduced time to restore electricity, lower maintenance costs and less exhausting work for the crew searching for fault locations in difficult terrain. Many fault classification and location estimation techniques are available, including impedance techniques, traveling wave techniques, wavelet analysis and artificial neural network-based approaches, etc.

2 Related Work

Transmission line fault classification using various fault analysis techniques are being done, and it is also very important to develop newer techniques for overcoming current systems limitations and meet the emerging needs. It is also necessary to understand the working of various existing systems and work with this project as it uses one of these techniques in addition with IoT.

2.1 Existing Systems for Fault Classification

The electric power grid is highly vulnerable to a variety of natural actions, which can have a considerable effect on power system operation. To detect and locate faults on transmission lines, several methodologies have been developed and are still being developed today. Here, some of the best methods of fault classification are discussed.

2.1.1 Wavelet Transform

In [2], the voltage and current signals are decomposed into smaller and higher frequency components, and then the high-frequency components are removed, and if the high-frequency component exceeds a threshold level, a fault is detected.

2.1.2 Phasor Measurement Unit

PMU is a system that synchronizes the measurements of voltages and currents with GPS, and thus, the phasors of these quantities can be calculated [5]. The measurements done through PMUs have real-time synchronization, and hence, monitoring of power system spread in large area can be done accurately [6]. Many algorithms have been developed that use data collected from the best PMU locations to distinguish between various types of transmission line events using positive and negative sequence of voltages and currents [7].

2.1.3 Artificial Neural Networks

Voltages and currents of the three are taken as inputs to the training model of fault classification which is trained with large data sets of voltage and current inputs and output is whether fault occurred or not [8].

These are the techniques used mostly in fault classification and can be used reliably [7–9]. The transmission of fault information to the operators can be done by deploying voltage, current and fire sensors as explained in [10–12]. This project combines both the fault classification techniques and also uses ThingSpeak cloud to send alerts to the operator about the faults.

3 Proposed Methodology

This project on transmission line fault detection and classification is done by using the symmetrical component analysis of three-phase transmission line. The faults on transmission lines cause unbalance in the system which can be observed from the voltage and current values on three phases during the fault. To classify the faults, the project uses symmetrical component variations on the three phases and also fuzzy logic technique. The symmetrical components are calculated and are given to the fuzzy logic to classify the faults. The analysis is done in MATLAB Simulink, and the information about the fault is sent to the ThingSpeak cloud, and alerts are given to the operators.

3.1 Fuzzy Logic for Fault Classification

The most immediate and effective starting point for fault classification by means of fuzzy logic approach is the elaboration with fuzzy techniques of the symmetrical components of the line signals. The symmetrical components negative and zero sequences increase in magnitude when the fault occurs. The symmetrical component analysis of faults shows that during the faults involving the ground-zero sequence rises, negative sequence components are present during all the unsymmetrical faults [4]. So, these variations are modeled using fuzzy logic.

3.2 Determination of the Fuzzy Variables

The different kinds of faults reflect on a different amount of the fault current symmetrical components. As the presence of zero sequence indicates, fault involving ground has occurred and negative sequence indicates all unsymmetrical faults; we can also estimate which fault has occurred among all the unsymmetrical faults by analyzing the magnitudes of the sequence components. But using alone the negative sequence components of currents can lead to ambiguity in the faults, and the ratio of positive sequence and the rated current gives additional information of faults. The use of deterministic algorithm to obtain information about the type of fault from the above sequence components during different faults is difficult and complex. In this situation, fuzzy logic proves to be effective to some extent in classifying line to ground fault and line–line ground faults. So, we can also consider actual values of positive, negative sequence and zero sequence components of fault currents. So, the ratios of the sequence components which consider all these observations can be used as variable to the fuzzy logic are negative current to positive sequence currents (I_n/I_p), zero sequence current to positive sequence current (I_o/I_p), positive sequence current to rated current (I_p/I).

3.3 Simulink Block Diagram

Figure 1 shows the Simulink block diagram of the proposed model. A three phase, 50 Hz AC source with grounded neutral is considered. The total transmission line is divided into two parts, and at the middle of the transmission line, different faults are introduced. The three-phase currents are then measured and converted into the sequence components. Using these components, the ratios I_o/I_p , I_n/I_p and I_p/I rated are calculated and then fed to the fuzzy logic controller. The output of the fuzzy controller is displayed. The faults are introduced at 0.1 s and cleared at 0.5 s. The transient time is 0.1 s. Since the supply frequency is 50 Hz.

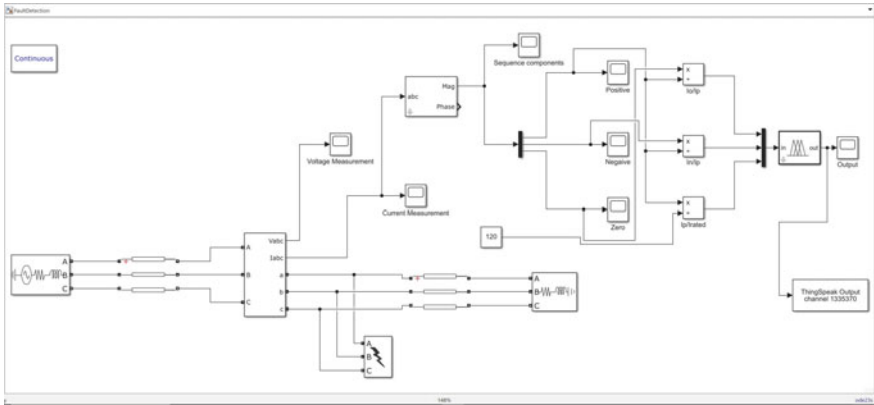


Fig. 1 Simulink block diagram for transmission line fault classification

3.4 Proposed Model

Power system element	Parameters
Three-phase source	Line to line voltage = 25 kV
	Frequency = 50 Hz
	Internal connection = Y_g
	Source resistance = 0.08 Ω
	Source inductance = 1 mH
Three-phase transformer	Rated power = 100 MVA
	Connection = $\Delta - Y_g$
	Voltage = 25 kV
	R_1, L_1, R_2 and $L_2 = 0.002, 0.008, 0.002$ and 0.008 pu
Transmission line	Resistance = 1 Ω
	Inductance = 1 mH
	Capacitance = infinite
Three-phase load	Active power = 10,000 W
	Inductive reactive power = 100 VAR
	Capacitive reactive power = 0
	Fault resistance = 0.01 Ω
	Ground resistance = 0.001

3.5 Fuzzy Logic in Fault Classification

The input and output fuzzy variables have been defined below, and the membership functions for the input variables must be defined together with the rules that give the fuzzy relationship between the input and output variables. Basically, two procedures can be followed to attain this result and optimize the membership functions tuning and the rules: a manual procedure or an automatic procedure. The manual procedure is effective when the number of input variables is high and the relationship between output and input variables is not as evident; as in the case, several tools are available to automatically tune the membership functions and write the rules. The fuzzy logic designer for defining membership functions is shown in Fig. 2.

The following four fuzzy sets have been defined for the fuzzy input variables:

- Low (L)
- Medium low (ML)
- Medium high (MH)
- High (H).

The following five fuzzy sets have been defined for the fuzzy output variables.

- Normal
- Single line to ground fault (SLG)
- Line to line fault (LL)
- Double line to ground fault (DLG)

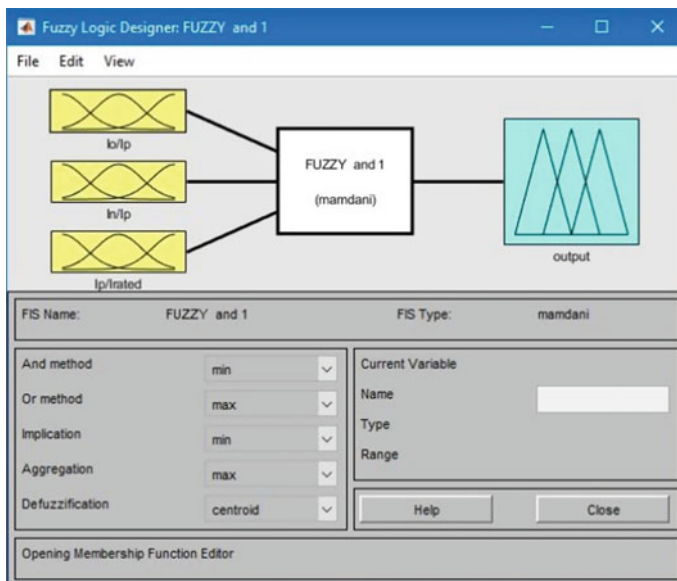


Fig. 2 Fuzzy logic designer

- Triple line to ground fault (TLG).

The membership function curves are drawn for the linguistic variables defined earlier for the three input ratios of sequence components using the triangular and ramp functions selected from type selector option in the limits of 0 and 1 on y-axis.

The fuzzy rules are those which govern the output variable for a given input variable, depending upon the range to which it belongs.

The membership functions are defined approximately to reach the magnitude of the symmetrical components changes for different faults. Fuzzy rules are framed with the defined variables, i.e., sequence component ratios, so that behavior of the power system during faults is modeled.

4 Transmission of Fault Information Using IoT

In Simulink, ThingSpeak output block is used to send the fuzzy output of fault classification to ThingSpeak channel. The values of the fuzzy output are uploaded to the ThingSpeak channel every 15 s interval with the initially configured ThingSpeak channel and use these channel id, API key.

4.1 Steps in Using ThingSpeak

1. **Creating a channel:** In the channels, my channels option is used to create a new channel by entering the desired values in the name of the channel and other fields in the channel and then the channel can be saved.
2. **Uploading values to channel:** Data can be uploaded to ThingSpeak channel from the devices with sensors, from the PC, or from a web page using the channel details available from previous steps with the help of ThingSpeak functions in MATLAB.
3. **Analyzing the data:** Fuzzy output values for faults are in the range [1, 8], and these may not be integers all the time. In React, alert can be triggered only when the channel data meets certain conditions like equality, less than, or greater than the specified value. Therefore, rounding off the fuzzy values is done by writing a code in MATLAB analysis app and these values are stored in a new channel.
4. In ThingSpeak, ThingHTTP and React apps are created for each of the fault to trigger the rounding off the numbers which in turn triggers the Zapier web server from which the SMS alerts are sent to the operators.

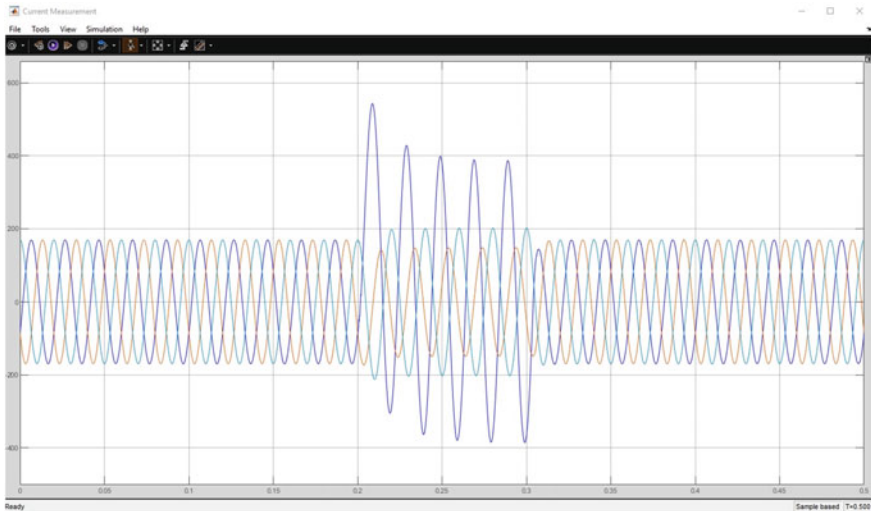


Fig. 3 Current during single line to ground fault

5 Results and Discussion

Different faults can be known from the fuzzy output values with each value specifying the certain fault occurred. This output value is obtained by evaluating the fuzzy rules and defuzzification of the output of fuzzy rules. The faults are classified as follows (Figs. 3, 4, 5, 6, 7, 8, 9 and 10; Table 1).

6 Conclusions and Future Scope

The faults occurring on the power transmission lines should be resolved as they can damage the power system and also interrupt the power supply to users. There are various power system protection techniques from fundamental circuit breaking of transmission line to remotely monitoring the power system. This project is useful in the monitoring of transmission lines to detect and classify the faults occurring on them. This project used the symmetrical component analysis and fuzzy logic technique to classify the faults and also sends the alerts to the operator about the type of fault occurred on the line. The classification of faults was successfully performed by using the fuzzy logic technique. The symmetrical components during the faults are modeled using fuzzy logic to classify the faults.

The project classified the faults by defining fuzzy rules based on symmetrical component analysis, and the output fuzzy sets for different faults are produced by evaluating the rules, and the fault classification is done by indicating each fault with a numerical value. Transmission of this information as alerts to the operators

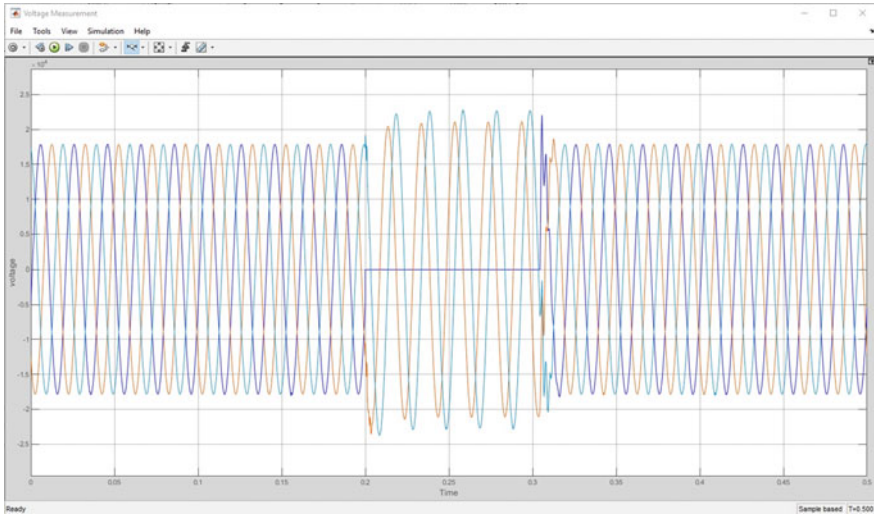


Fig. 4 Voltages during single line to ground fault

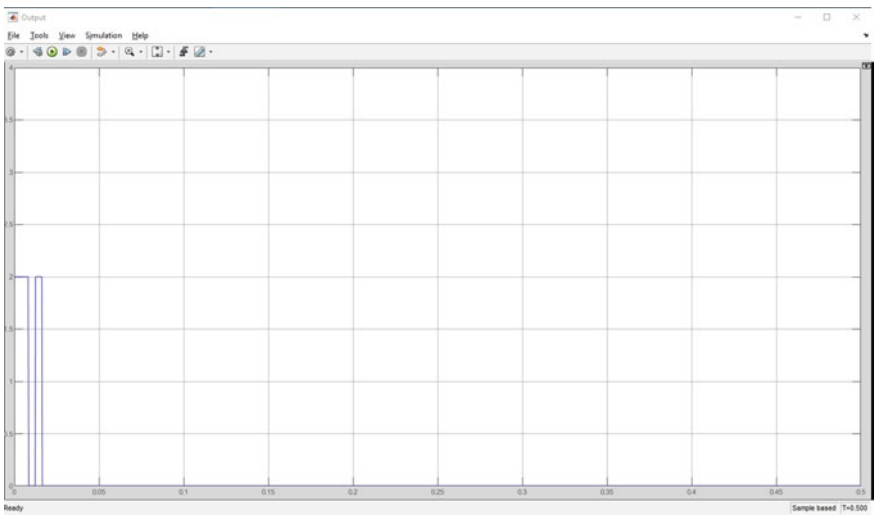


Fig. 5 Fuzzy output during normal condition

using ThingSpeak cloud is also achieved to help the operator in resolving the faults immediately when they occur.

The fuzzy logic technique is reliable for fault classification on transmission lines and can be implemented in real-time power systems. This technique can be made much effective if the membership functions are designed with care. This can help achieve the best performance of power system.

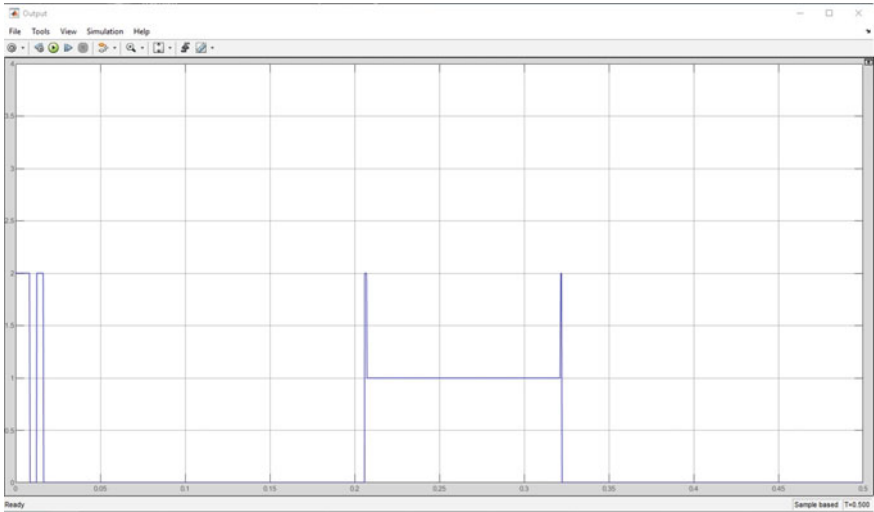


Fig. 6 Fuzzy output during single line to ground fault

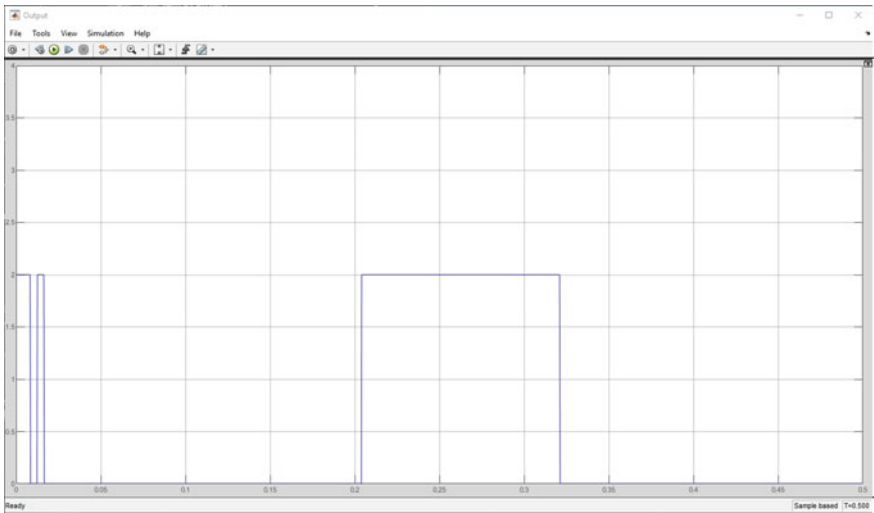


Fig. 7 Fuzzy output during line to line fault

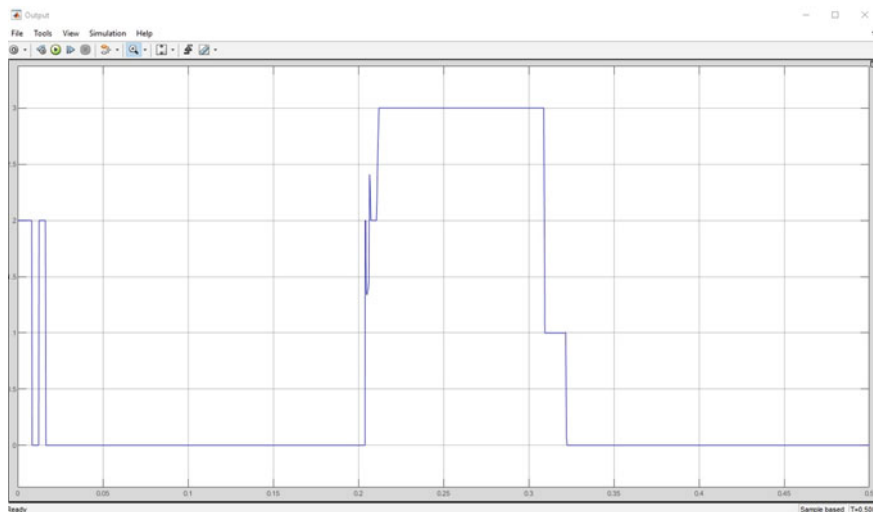


Fig. 8 Fuzzy output during double line to ground fault

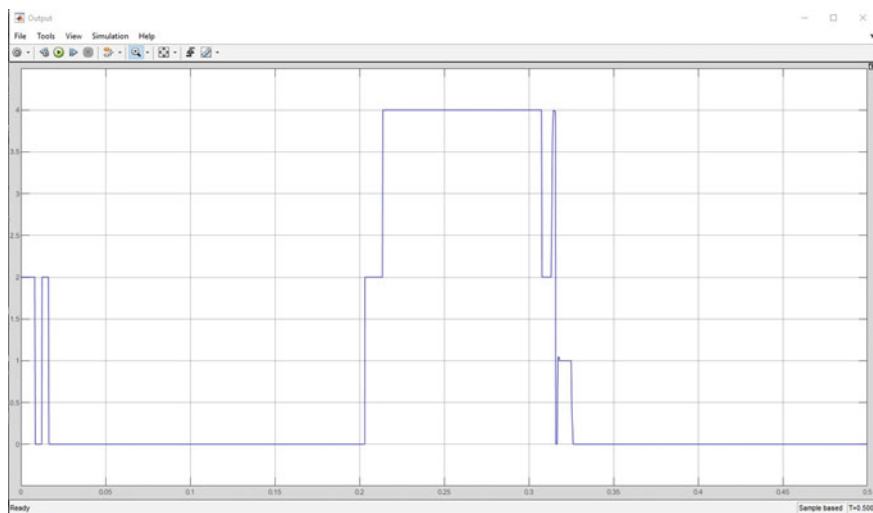


Fig. 9 Fuzzy output during three-phase fault

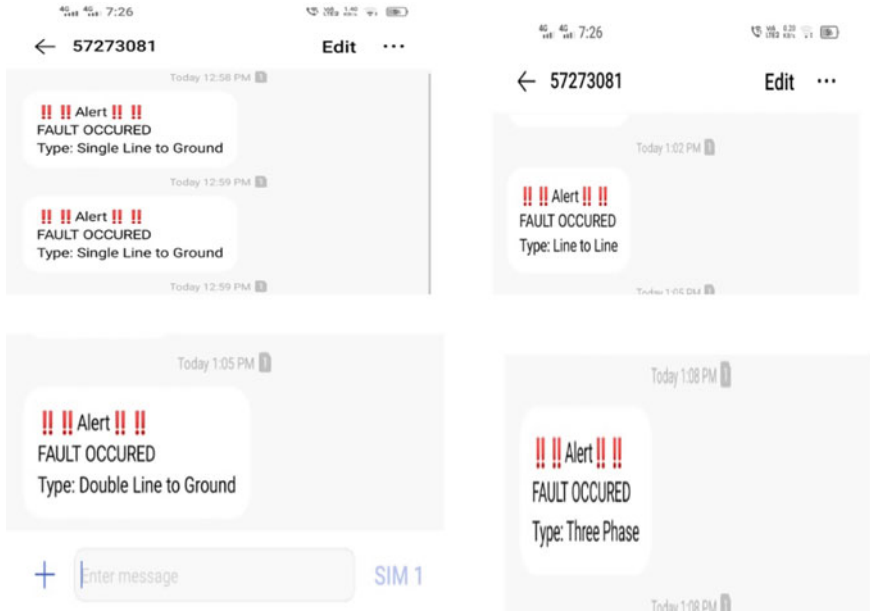


Fig. 10 SMS alerts during the faults

Table 1 Fault classification output of fuzzy logic controller

Fuzzy output value	Type of fault
0	No fault
1	Line to ground fault
2	Line to line fault
3	Double line ground fault
4	Three-phase fault

References

- Jana S, De A (2013) Transmission line fault detection and classification using wavelet analysis. In: Annual IEEE India conference (INDICON). IEEE, pp 1–6
- Saravanababu K, Balakrishnan P, Sathiyasekar K (2013) Transmission line faults detection, classification, and location using discrete wavelet transform. In: International conference on power, energy and control (ICPEC). IEEE, pp 233–238
- Mishra DP, Ray P (2018) Fault detection, location and classification of a transmission line. *Neural Comput Appl* 30(5):1377–1424
- Wadhwa CL (2006) *Electrical power systems*. New Age International
- https://en.wikipedia.org/wiki/Phasor_measurement_unit
- Rahmatian M, Dunford WG, Moshref A PMU based system protection scheme. In: IEEE electrical power and energy conference. IEEE, pp 35–40
- Jain A, Archana TC, Sahoo MBK (2018) A methodology for fault detection and classification using PMU measurements. In: 20th national power systems conference (NPSC). IEEE

8. Jamil M, Sharma SK, Singh R (2015) Fault detection and classification in electrical power transmission system using artificial neural network, vol 4. Springer, p 334
9. Prasad A, Edward JB, Ravi K (2018) A review on fault classification methodologies in power transmission systems: part—I. *J Electr Syst Inf Technol* 5(1):48–60
10. Jothimani A, Sourabh S, Sahu D, Mishra M (2020) Transmission line falling detection using IOT. *IJSEC* 10(4):25388–25390
11. Krishna RN, Niranjana L, Shyamsundar N, Venkatesan C (2020) IoT based transmission line fault monitoring system. *IJRAR* 7(3)
12. Karalkar M, Adlok S, Ramteke A, Parchake S, Tawade R, Manwar S, Wankhade S (2019) Transmission line fault detection using IoT. *Int J Res Eng Sci Manage* 2(3)

Optimized VLSI Design of Squaring Multiplier Using Yavadunam Sutra Through Deficiency Bits Reduction



J. Sravana , K. S. Indrani , Sankeerth Mahurkar, M. Pranathi, D. Rakesh Reddy, and Vijay Vallabhuni 

Abstract In this digital era, digital multipliers are used in high-speed digital circuits. Many optimized algorithms exist to implement digital multipliers. One of the operations of these multipliers is squaring a number. Squaring has a wide range of applications in digital systems. But, this operation is time-consuming. In Indian Philosophy, a Veda named Atharvaveda provides a set of methods to carry out arithmetic operations. These methods are fast and straightforward to perform. One method in this Veda is Yavadunam Sutra. It is a method used to carry out squaring operations of the numbers close to the power of 10, such as 8, 99, 991, and 10,002. This paper implements a digital squaring circuit based on the Yavadunam Sutra's logic to perform squaring operations. The proposed digital circuit is modeled and analyzed using the Xilinx Vivado tool.

Keywords Squaring multiplier · Vedic mathematics · VLSI design · Yavadunam Sutra

1 Introduction

Digital circuits are the core systems of modern electronics. One of the primary jobs of these digital circuits is to perform arithmetic operations. Optimization of these primitive operations is a critical workaround. Many algorithms and optimization techniques have been proposed from time to time. Multiplication is the most common operation that has innumerable use cases. Many multipliers have been proposed since the evolution of digital systems. Some examples of digital multipliers are Wallace tree multiplier, Booth multiplier, sequential multiplier, array multiplier, and combinational multiplier [1]. The squarer circuit is one most used components in digital system processing. In general, Booth's multiplier is commonly used as squarer

J. Sravana · K. S. Indrani · S. Mahurkar · M. Pranathi · D. Rakesh Reddy · V. Vallabhuni (✉)
Department of Electronics and Communication Engineering, Institute of Aeronautical
Engineering, Dundigal, Hyderabad 500043, India
e-mail: v.vijay@iare.ac.in

in DSP. The delay caused by Booth's multiplier can be reduced by using a dedicated squarer circuit.

Risojević et al. [2] proposed a squarer circuit based on the characteristic number of the most significant bit. The design also uses approximation and error principles. Their depicted method uses the simple combinational logic for the first approximation and correction terms. The approximate squaring is performed in a simple way resulting in the desired accuracy.

Hoda et al. [3] proposed a squarer circuit based on the approximate squaring function. It uses combinational logic to compute the square of the number. The hardware design consists of a controller, MUXes, and modifier circuits.

These proposed methods have a significant amount of efficiency over DSP applications. There is also an ancient Indian methodology called Vedic Mathematics to carry out arithmetic operations.

Vedic Mathematics is an ancient way of solving arithmetic problems. It is an old mathematical system developed by ancient Indian saints in 1200–500 BCE. Vedic Mathematics was brought back into the light in 1965 by an Indian monk named “Bharthi Krishna Tirthaji” [4]. According to him, these techniques are present in Atharva Veda. These methods are composed of 16 sutras (formulas) and 13 sub-sutras [5]. These methods make solving arithmetic, algebraic, and conic problems much more effortless. The reasoning, creativity, and analytical skills can be improved by practicing Vedic Mathematics. It involves the person thinking analytically to get the answer. Vedic Mathematics helps solve complex multiplications and squaring operations ten to fifteen times faster than conventional mathematics. It is efficient in terms of speed, accuracy, simplicity, and acquiring its concept. It involves the one to think analytically and to concentrate more to get the answer. Vedic Mathematics helps solve complex multiplications and squaring operations ten to fifteen times faster than conventional mathematics. The concept of one Vedic sutra applies to performing more than one mathematical operation. Vedic sutras in Vedic Mathematics related to multiplication are Ekadhikena purvena, Nikhilam navatascaramam Dasatah, Urdhva-Tribhagya (vertically and crosswise), Ekanyunena Purvena, Anurupyena, Adyamadyenantya—mantyena, Antyayor Dasakepi, Yavadunam sutra.

Sethi and Panda [6] proposed the multiplier architecture based on “Urdhva Tiryagbhyam.” It includes using a 2-bit squaring circuit, a 2×2 Vedic multiplier, a CSA, and a binary adder. This design used 6 LUTs and showed significantly reduced delay.

Khan et al. [7] proposed another design based on the “Urdhva Tiryabhayam.” It uses some fundamental digital components like two AND gates and two half adder for designing a multiplier to perform the squaring operation of 2-bit binary numbers. The designed multiplier has two input ports as multiplication operation requires multiplicand and multiplier and has four output ports representing the resultant product. The squaring circuit has been simulated successfully by Xilinx ISE software. The number of slices used is 1 out of 4656. The number of 4 input LUTs used is 2 out of 9312. The number of bounded IOBs used is six out of 232. It is a quick and most uncomplicated design. It has less complexity, occupies less area, and delay is also minor. There is has a restriction over its input bit size. This design could be only

for 2-bit binary numbers. However, this has design showed a significant reduction in device utilization. It used only 1 slice and 4 LUTs.

Akhter et al. [8] proposed the design squaring circuit based on another Vedic technique called Yavadunam Sutra. In this design, the half adder is replaced with NOT and AND gates, respectively. This change gives rise to a new scope to increase the input bit size. As the input bit size increases, the digital components also increase, leading to complexity and increased delay. The number of LUTs used are 6, and the delay is measured as 18.67 ns.

Yavadunam Sutra is a squaring technique used to square the numbers close to powers of 10 such as 98, 102, 1004, and 9998. This paper provides an optimized implementation of a 4-bit square multiplier using this technique.

The procedure of squaring goes as follows:

Step 1. Consider a number 97

Step 2. This number is close to 10^2 , i.e., 100

Step 3. This number is three steps away from 100. It is known as deficiency. The formula to calculate deficiency is $D = \text{Given Number} - \text{closest power of 10}$. Here the deficiency, $D = -3$

Step 4. Calculate the square of 3; it is 9. Now, RHS is 09. (Append 0 s to this square product to make its digit the same as the given number)

Step 5. Now, calculate a sum as $S = \text{Closest power of 10} + D$. Here, the Sum is $S = 100 + (-3) = 97$. Moreover, this sum is LHS

Step 6. Combine LHS and RHS to get the result. That is 9403

This implementation is designed and simulated using Xilinx Vivado Software and Zync 7000 toolkit.

Some proposals of square multipliers that already exist were discussed above. However, these proposals have some drawbacks associated with them.

Deepa and Marimuthu [9] have proposed the most efficient square multiplier based on Yavadunam Sutra to date, which is the work's current state. This algorithm produces a 4-bit deficiency for 4-bit input. It results in the use of a 4×4 multiplier embedded within the circuit.

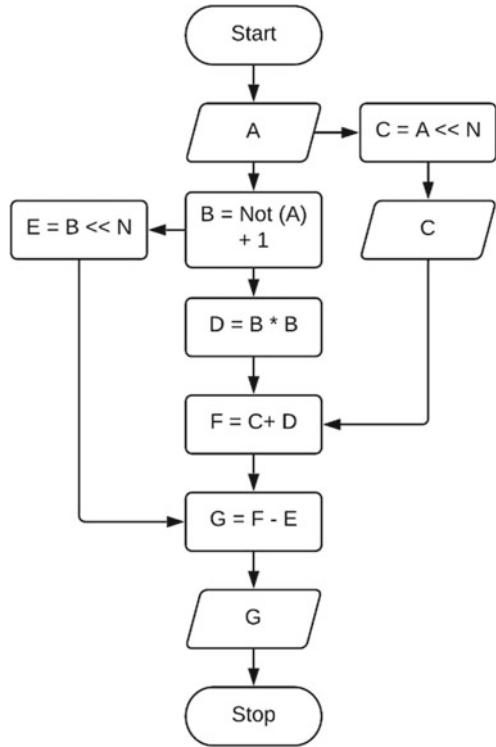
This paper proposes the architecture based on Yavadunam Sutra. The algorithm proposed in this paper defines the boundary on the input. Because of the constrained input range, the deficiency bits get reduced. Due to the reduction in deficiency bits, the size of the internal multiplier reduces. These changes lead to the better and optimized performance of the circuit. When the circuit is extended for the big input sizes, it helps in computing the square of big numbers.

The paper is further organized as follows. Section 2 contains the design proposal for a 4-bit squaring circuit and describes its implementation through a flowchart and block diagram.

Detailed implementation analysis done in the Xilinx tool is provided in Sect. 4. This section also compares device utilization and overall delay with the design proposed in the paper [9].

Section 4 concludes the research work and discusses the major drawback of using the Yavadunam Sutra.

Fig. 1 Flowchart to find the square of binary number using Yavadunam Sutra



2 The Proposed Design and Implementation of a 4-bit Squaring Multiplier

Yavadunam Sutra is an algebraic technique used to calculate the square of a natural number. One of the crucial requirements for this technique is that the number should be close to the base number. In terms of digital logic, if the input size is 4-bits, then deficiency could be represented in 2-bits. This consideration eliminates the need for an internal 4×4 multiplier. According to Deepa and Marimuthu [9], the mathematical representation of square of number A can be logically expressed in Eq. 1.

The algorithm to design the circuit is as follows.

$$G = (A \ll N) + (B * B) - (B \ll N) \tag{1}$$

The flowchart of the below algorithm is provided in Fig. 1.

Step 1. Find the deficiency using 2's complement of A. That is, deficiency $B = \text{not}(A) + 1$

Step 2. Left shift A by four bits. Let $C = A \ll 4$

(continued)

(continued)

Step 3. *Compute Square of Deficiency. Let $D = B * B$*

Step 4. *Left shift B by four Bits. Let $E = B \ll 4$*

Step 5. *Compute the sum of C and D. Let $F = C + D$*

Step 6. *Subtract E from F. This gives the square of A. Let $G = F - E = A^2$*

For the design of a 4-bit square multiplier using the above-described algorithm, we require the following components. As it could be observed, two 4-bit shifters are required, an 8-bit ripple carry adder and an 8-bit ripple carry subtractor. A 2×2 square multiplier is also required to square the deficiency. These required components are summarized in Table 2.

The block diagram of the overall design is shown in Fig. 2. First, the input is given to block one and block two. Block one is modified 4-bit RCA and outputs 2-bit deficiency B . Block two left shifts A by 4-bits. The result of block one is then fed to blocks three and four. Block three squares the deficiency and outputs the 4-bit number. Block four left shifts the deficiency by 4-bits. The outputs of blocks two and three are fed to block five, which is 8-bit RCA and outputs an 8-bit sum. This sum and output of block four are fed to block six. This block is an 8-bit ripple carry subtractor and outputs the final result, the square of A .

A detailed description of each block is provided below.

2.1 Block 1 (Two's Complement of A)

This block computes the deficiency by calculating 2's complement of A . It takes 4-bit input A , whose allowed values are 1101, 1110, 1111, and outputs 2-bit output B . The truth table of this block is shown in Table 1.

2.2 Block 2 (Left Shift of A by 4 Bits)

This block left shifts the input A by 4-bits. 4 LSBs are given from A , and the remaining 4 MSBs are set 0 s. This block outputs eight bits output C .

2.3 Block 3 (2-Bits Square Multiplier)

This block is a two-bit square multiplier that accepts 2-bit input and outputs a 4-bit result. This block squares the deficiency. The truth table is shown in Table 2.

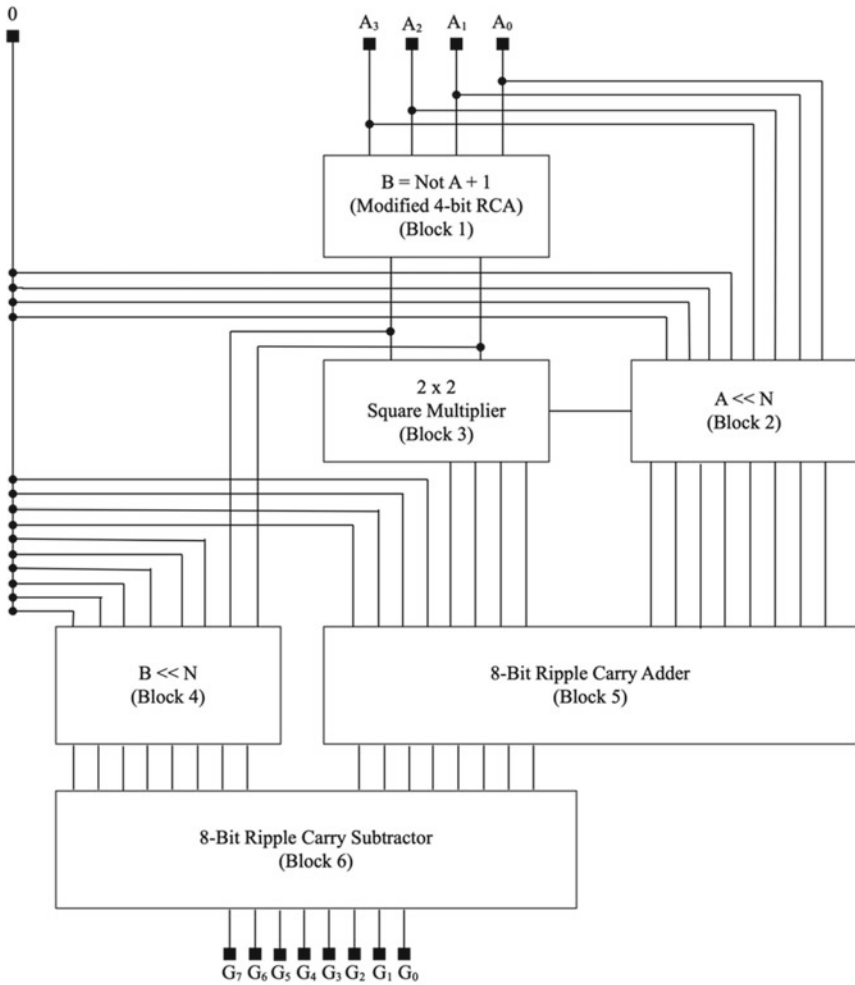


Fig. 2 Proposed block diagram to find the square of 4-bit binary number using Yavadunam Sutra

Table 1 Truth table for block 1

Input (A)				Output (B)	
A ₃	A ₂	A ₁	A ₀	B ₁	B ₀
1	1	0	1	1	1
1	1	1	0	0	1
1	1	1	1	1	1

Table 2 Truth table for block 3

Input (A)		Output (B)			
B_1	B_0	D_3	D_2	D_1	D_0
0	0	0	0	0	0
0	1	0	0	0	1
1	0	0	1	0	0
1	1	1	0	0	1

2.4 Block 4 (Left Shift B by 4 Bits)

This block left shifts the deficiency B by 4-bits. 4 LSBs are given from B , and the remaining 4 MSBs are set 0 s. This block outputs eight bits output E .

2.5 Block 5 (8-Bit Ripple Carry Adder)

This block takes two 8-bits inputs $A1$ and $A2$ and outputs an 8-bit sum. Here, the carry is always zero since one is input is only 4-bits. One input is from block two, and the other is from block three, with the remaining input bits set zero. Truth table for this block is given in Table 3.

2.6 Block 6 (8-bit Ripple Carry Subtractor)

This block is the final block of the design that takes two inputs: block four and block five. It outputs the final output G , the square of A . The truth table of this block is shown in Table 4.

3 Design Simulation and Analysis

The proposed design was modeled in VHDL using the Xilinx vivado tool and was simulated using Zync 7000 FGPA.

Table 3 Truth table for block 5

Input 1 (C)								Input 2 (D)								Output (F)							
C_7	C_6	C_5	C_4	C_3	C_2	C_1	C_0	D_7	D_6	D_5	D_4	D_3	D_2	D_1	D_0	F_7	F_6	F_5	F_4	F_3	F_2	F_1	F_0
1	1	0	1	0	0	0	0	0	0	0	0	1	0	0	1	1	1	0	1	1	0	0	1
1	1	1	0	0	0	0	0	0	0	0	0	0	1	0	0	1	1	1	0	0	1	0	0
1	1	1	1	0	0	0	0	0	0	0	0	0	0	0	1	1	1	1	1	0	0	0	1

Table 4 Truth table for block 6

Input 1 (F)								Input 2 (E)								Output (G)							
F ₇	F ₆	F ₅	F ₄	F ₃	F ₂	F ₁	F ₀	E ₇	E ₆	E ₅	E ₄	E ₃	E ₂	E ₁	E ₀	G ₇	G ₆	G ₅	G ₄	G ₃	G ₂	G ₁	G ₀
1	1	0	1	1	0	0	1	0	0	1	1	0	0	0	0	1	0	1	0	1	0	0	1
1	1	1	0	0	1	0	0	0	0	1	0	0	0	0	0	1	1	0	0	0	1	0	0
1	1	1	1	0	0	0	1	0	0	0	1	0	0	0	0	1	1	1	0	0	0	0	1

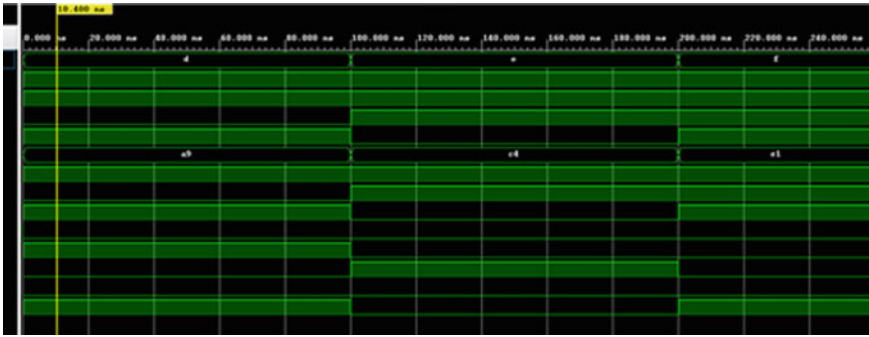


Fig. 3 Timing diagram output of proposed design for the input 13 ($0 \times D$), 14 ($0 \times E$), and 15 ($0 \times E$), respectively

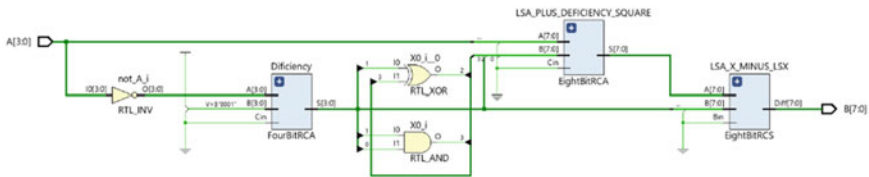


Fig. 4 RTL schematic diagram of the proposed design

3.1 Simulation Results

The timing diagram of the simulation is shown in Fig. 3. The simulation produced the correct outputs for all the acceptable input numbers 13 ($0 \times D$), 14 ($0 \times E$), 15 ($0 \times F$) as 169 ($0 \times A9$), 196 ($0 \times C4$), and 225 ($0 \times E1$).

3.2 RTL Analysis

The RTL schematic of the design is shown in Fig. 4. The schematic is composed of 6 cells, 12 I/O ports, and 32 nets.

3.3 Synthesis Analysis

The overall device utilization results of the design post-synthesis are summarized in Table 5. Only, 1 slice was utilized out of 17,600 available slices. 11 out of 100 bonded IOBs were utilized. Total on-chip power consumption was 1.553 W margin

Table 5 Design synthesis utilization report

Component	Utilization	Utilization %
Slice LUTs	1 of 17,600	<0.01
Bonded IOB	11 of 100	11
OBUF	8	–

Table 6 Proposed model and standard design comparison

Component	Existing design [9]	Proposed design
Slices	2	1
Slice LUTs	4	1
Bonded IOB	12	11
OBUF	8	8
IBUF	4	3
LUT4	2	–
LUT3	2	–
LUT2	2	2
Internal multiplier	4 × 4	2 × 2
Total power on-chip	2.207 W	1.553 W
Total delay	15.076	11.025

(1.461 W Dynamic + 0.093 W Static). Furthermore, the total delay was observed to be 11.025.

3.4 Implementation Result

Table 6 gives the typical parameters for both the existing design [9] and the proposed model.

The design proposed in this paper utilized only one slice, whereas in existing design [9] utilized 2. The usage of slice LUTs has significantly reduced from 4 to 1. Since deficiency bits can exceed 2-bits in length, internal 4 × 4 square is needed more. The implementation device schematic is shown in Fig. 5.

4 Conclusion

The algorithm provided in [9] is optimized further by removing the 4 × 4 internal multiplier. The reduction of deficiency has shown a considerable amount of optimization. The propagational delay was almost reduced to 40% compared to the existing hardware implementation.

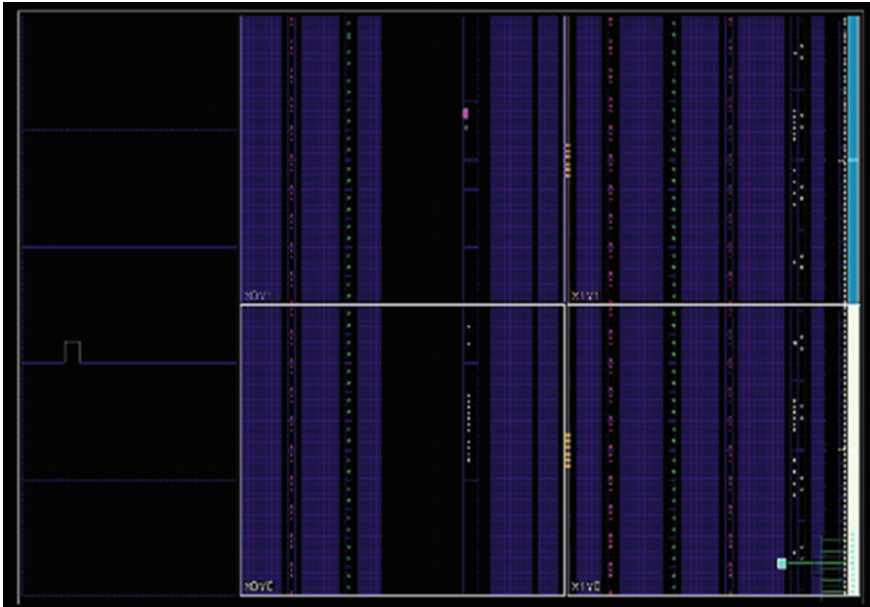


Fig. 5 Implementation layout of the proposed design

Though it has shown excellent optimization, not all numbers can be squared using this method. Only, the numbers that are close to base numbers are eligible to be operated with it.

The design implemented here can be extended to 64-bits input numbers. A recursive design approach could be applied to calculate the square of deficiency in each level.

References

1. Sabeetha S et al (2015) A study of performance comparison of digital multipliers using 22nm strained silicon technology. In: 2nd international conference on electronics and communication systems (ICECS), pp 180–184
2. Risojevic V et al (2011) A simple pipelined squaring circuit for DSP. In: IEEE 29th international conference on computer design (ICCD), pp 162–167
3. Abdel-Aty-Zohdy HS, Hiasat AA (2002) VLSI design and implementation of an improved squaring circuit by combinational logic. In: Conference record of the thirty-first Asilomar conference on signals, systems and computers, pp 426–429
4. Vedic Mathematics. [Online]. Available: Accessed: 15 Apr 2021. https://en.wikipedia.org/w/index.php?title=Vedic_Mathematics&oldid=1023124798
5. Rani DU (2011) Vedic mathematics—a controversial origin but a wonderful discovery. *Indian J Appl Res* 4:342–343
6. Sethi K, Panda R (2012) An improved squaring circuit for binary numbers. *Int J Adv Comput Sci Appl* 3

7. Khan A et al (2017) Robust high speed ASIC design of a vedic square calculator using ancient Vedic mathematics. In: 8th IEEE annual information technology, electronics and mobile communication conference (IEMCON), pp 710–713
8. Akhter S et al (2020) A distinctive approach for Vedic-based squaring circuit. In: 7th international conference on signal processing and integrated networks (SPIN), pp 27–30
9. Deepa A, Marimuthu CN (2020) VLSI design of a squaring architecture based on yavadunam sutra of Vedic mathematics. In: International conference on electronics and sustainable communication systems (ICESC), pp 1162–1167

Design and Simulation of High Performance Hybrid Full Adder Using CMOS 45 nm Technology



S. Jayamangala, T. Pullaiah, J. Sunilkumar, and M. Sivakumar

Abstract The new blended model is mostly utilized in the designing process of an arithmetic circuitry. The efficiency of a full adder with the factors of holding time, potential charge utility and the strength of the circuit is highly based on how efficiently the circuit will work. From this project, a large speed, low power consuming count of ten transistors logic circuit is designed, and it generates effective fluctuations at the same time with effective delay at output. The performance efficiency of the designed circuit is calculated by simulating it in a tanner software using 45 nm technology. The established circuit decreases the PDP factor at least by 15% than already existing XOR–XNOR models. In this project we are introducing two different designs of full adders those are designed in this article by using the already designed XOR–XNOR circuitry and existed sum and carry generating blocks. The designed full adders provides 10–40% betterment in words of power fluctuation product in the comparison of other models. To calculating the driving capacities the proposed full adders are fixed in multistage full adder circuits. Outputs show that two of the designed full adders generate the better results for a larger count of data bits in all the full adders.

Keywords Multistage adder · High fluctuation · Blended full adder · Logic circuit

S. Jayamangala (✉)

ECE Department, Santhiram Engineering College, Nandyal, Andrapradesh, India
e-mail: jayamangala.1987@gmail.com

T. Pullaiah · J. Sunilkumar

ECE Department, Vignan's Institute of Management and Technology for Women, Hyderabad, India

M. Sivakumar

ECE Department, B I T Institute of Technology, Hindupur, India

1 Introduction

Present days the people are showing interest to do smart work to manage their regular activities without any time inconsistency. So the people are attracted by the technological circuits. People not only concentrating on the designing process they are also thinking about to do the work in fast and efficient way. To design those type of electronic systems the designers will concentrate on size of the circuit and speed and energy efficient related designs [1]. The electronic systems highly containing the arithmetic circuits to calculate the efficiency of output. Basically the summer is a main building block for the different logical blocks. These circuits are mostly utilized to transfer the data in related designs [2]. They are also used in 1/3 of power utilized microprocessors. To improve the working of the adders along with the whole design at the same time.

To design a full adder we required a few static CMOS logic models to be presented. These logics can be mainly differentiated in 2 different ways: unblended and blended model of designing. In classical model of designing process the full adder is manufactured in a unic block using transistors [3]. The terminated adder is an example of this designing model. For this circuit we are using 24 active elements to build a above and below parts of a full adder. It is generates effective fluctuating results. The main demerit that the circuit is having a large forward capacitor and is connected to a pair of N&P type transistors these can decreases the performance efficiency of the circuit. Other design for the unblended model of designing process is inverting moving transistor logic related adder [4, 5]. This circuit generates high speed and high swing output with an excellent driving capacity due to large speed multi stage, coupled transistor model and reversing at the output. It has high potential loss because of more number of inner connections in the design. We are able to design a full adder by using differential transistors [5]. The differential transistors having a demerit is that high threshold voltage drop. When the inputs are given as “10” through the pair of N&P transistors. We did not get the same output at the full adder These XOR–XNOR signals must have highly effective input and output signals.

2 Literature Survey

New technology is coming in to the VLSI designing process. As technology is changing as well as the specification designs of the system is also changing. The advanced technology is mostly concentrating on less area occupation and low power consumption and also it is concentrating on high accessing speed. These Styles are trying to have a reduced fluctuations [6, 7]. With this designing process may using 0.18 um technology and we are testing the testbench setup that measures the power consumption at full adder inputs. In this project we also concentrate on energy efficiency by reducing the size of the design. We are using different technologies to

calculate the power consumption, Energy efficiency and how much area was occupied by the design of the system on chip (SOP).

In the process of working on digital signal processing we are using digital circuits like microprocessors, microcontrollers, and full adders. Which all are works on the processing the images in digital way [7]. To get the accurate designing process of a full adder we mostly concentrate on circuitry speed, area and power utilization of the circuit. To minimize the potential utility we are using different techniques like GDI design and blended transistor logic model here we are designing ripple carry adder for the wide range of applications. To design adder we are eliminating the usage of XOR/XNOR logic gates. Normally addition is the most common arithmetic operation that has to be performed using adder to design full adder we are using CMOS transistor designing process. From this paper we designed an adder by utilizing the blended CMOS logic model. It divides the entire circuit into three modules. In the first stage we can observe XOR XNOR logic circuitry [8] which generates the effective outputs and it also have good driving capacity. The second stage contains the sum circuitry which gets the input from the first stage and which produces the effective sum as output. First stage which takes the inputs from the input circuit elements which feeds its outputs to the second stage and to the third stage [9]. From the second stage we are getting sum as output and from the third stage we are getting carry as output. We proposed this hybrid CMOS multistage adder block to reduce the utilization of the potential, fluctuation between the carry input and output. In conventionally we are designing the complementary pass transistor logic (CPL) to get an effective output by reducing the transistor count [10].

3 Existing Techniques

For Fig. 1 we are giving the inputs ABC as 110, i.e., $A = 1$, $B = 1$, $C_{in} = 0$. For the XOR circuitry we are giving the inputs A&B as 11 so that both the PMOS transistors P1&P2 will become off and will generate the output as 0(zero) [10, 11]. The NMOS transistors N3 and N4 are fed with 1 and 1 so that the transistors are getting on so that the entire input is getting connected with GND so that the output becomes 0 which will store in X. The $X = 0$ is given as input to the N5 transistor and it becomes off, so the final output of XOR circuitry is 0, i.e., $XOR = 0$. For the XNOR circuit we are giving 1, 1 as input to the NMOS transistor those are N1&N2 so that the transistors are getting on it will generates the output as 1 [12, 13]. A&B is given to the PMOS transistors P3&P4 which become off so that which generates the output as 0 which output is giving as input to the transistor P5. Hence, it's become on. The final output through the XNOR circuitry is 1 (Fig. 2).

The author proposed a circuit of 6 T XOR XNOR logic block to design a conventional full adder. This design showed two complementary feedback boosters utilized to reuse the low performance signal in differential mode when the two inputs have unique logic. This circuit has high delay for the inputs of the same pair of logic values; outputs of this final circuit get their last voltage levels in two stages. This problem is

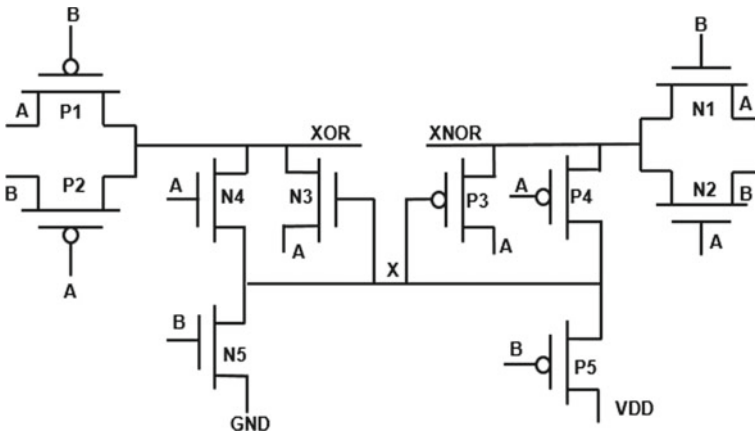


Fig. 1 Existing schematic of XOR XNOR circuit

solved by Chang. This proposed circuit generates better driving capacity, full swing at output [13]. The X-coupled diagram attaches an excess parasitic element to the XOR XNOR circuit at results. Table 1 shows the comparison table for XOR and XNOR gates at Full Swing and at partial swing. In the change method there are some defaults that are improved by Naseri and Timarchi which are designed for 12 T [14]. This circuit can take less power, produces a better delay. The XOR XNOR circuit has further changes to its better way of implementation. Even in the final circuitry we also find some mistakes when we are simulating that design by using the tanner 13 tool. In this project we are taking these drawbacks as a challenge and we are working on this project to overcome these demerits [14, 15].

4 Proposed Techniques

For the we are Fig. 3a giving the inputs ABC as 110, i.e., $A = 1, B = 1, C_{in} = 0$. For the XOR circuitry we are giving the inputs A&B as 11 so that both the PMOS transistors P1&P2 will become off and will generate the output as 0(zero). The NMOS transistors N3 and N4 are fed with 1 and 1 so that the transistors are getting on so that the entire input is getting connected with GND so that the output becomes 0 which will store in X. The $X = 0$ is given as input to the N5 transistor, so the final output of XOR circuitry is 0, i.e., $XOR = 0$ [16]. For the XNOR circuit we are giving 1, 1 as input to the NMOS transistor those are N1&N2 so that the transistors are getting on it will generates the output as 1. A&B is given to the PMOS transistors P3&P4 which become off so that which generates the output as 0 which output is giving as input to the transistor P5. Hence, it is become on. The final output through the XNOR circuitry is 1 [17].

We are giving inputs as 110 through N8, P8 and C_{in} and XNOR so that the transistors become on and will generate the carry as output, i.e., $C_{out} = 1$. For the transistors P9, N9 fed with the inputs as XOR, C_{in}' and XNOR so that both the transistors will become on and which will generate carry as 1. We are giving C_{in} , XOR and XNOR inputs as transistors P6&N6 which will turn off the transistors will generate the output as 0 that is SUM. XOR, XNOR and C_{in} as inputs to the transistors P7&N7 and which turns off the transistors and will generates the SUM as 0. For the design 1 we are giving the inputs ABC as 110, i.e., $A = 1, B = 1, C_{in} = 0$ [18]. For the XOR circuitry we are giving the inputs A&B as 11 so that both the PMOS transistors P1&P2 will become off and will generate the output as 0(zero). The NMOS transistors N3 and N4 are fed with 1 and 1 so that the transistors are getting on so that the entire input is getting connected with GND so that the output becomes 0 which will store in X [19–21]. The $X = 0$ is given as input to the N5 transistor, so the final output of XOR circuitry is 0, i.e., XOR = 0. For the XNOR

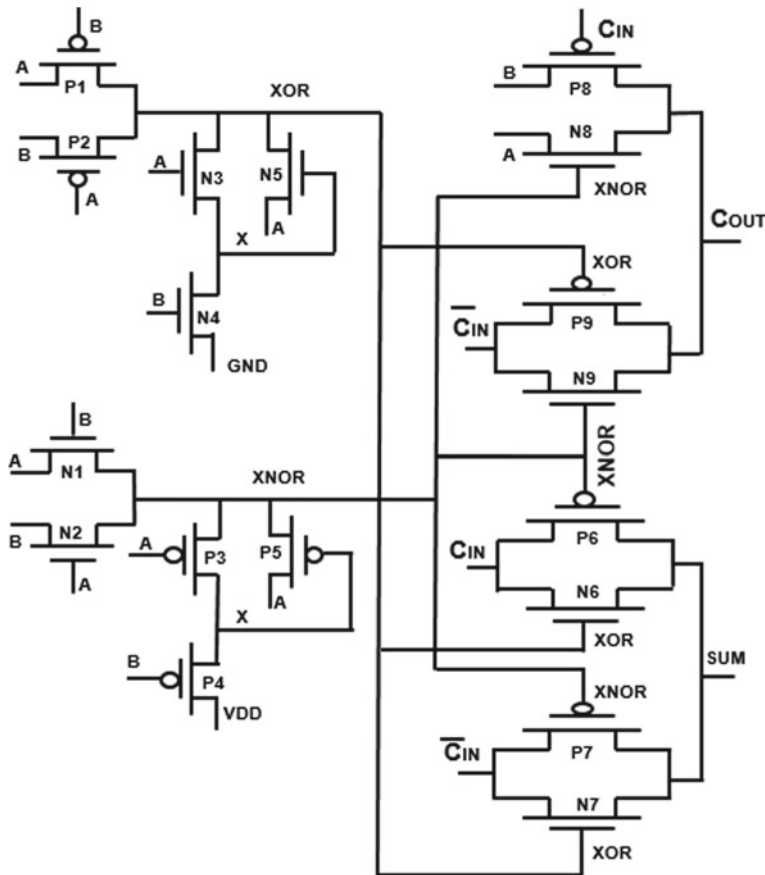


Fig. 2 a, b Existed conventional full adder schematic

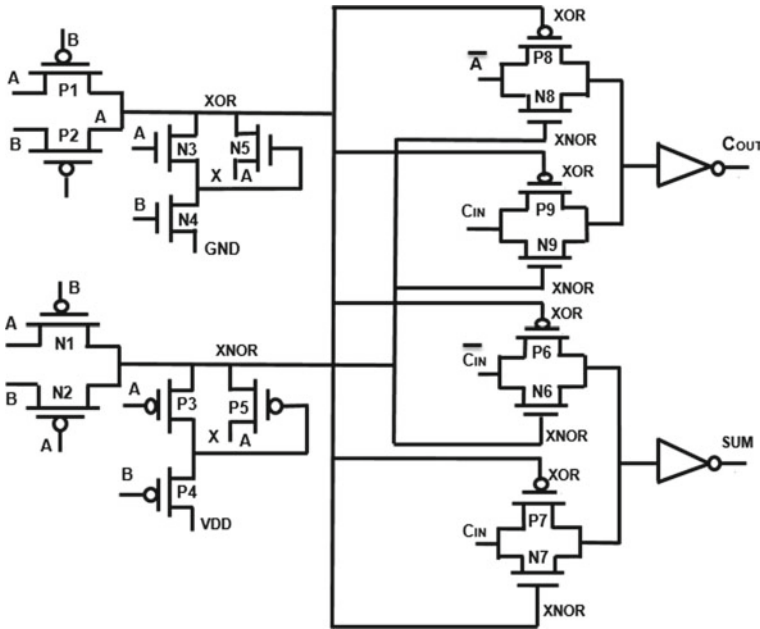


Fig. 2 (continued)

Table 1 Performance of the inputs of a XOR & XNOR circuit in different paths

Inputs A, B	Path		Path	
	XOR (full swing)	XOR (partial swing)	XNOR (full swing)	XNOR (partial swing)
00	N3	P1, P2	P4, P5	–
01	P2	–	N1	P4, P3
10	P1	N4, N3	N2	–
11	N4, N5	–	P3	N1, N2

circuit we are giving 1, 1 as input to the NMOS transistor those are N1&N2 so that the transistors are getting on it will generates the output as 1. A&B is given to the PMOS transistors P3&P4 which become off so that which generates the output as 0 which output is giving as input to the transistor P5 [21]. Hence, it's become on. The final output through the XNOR circuitry is 1. We are feeding the XOR XNOR circuit results as inputs to the sum and carry circuitry. For the transistors P8&N8 we are giving inputs as A', XNOR and XOR so that the transistors become on and will generates the output as 1 and for the transistors P9&N9 as C_{in} and XNOR and XOR so that the transistors become on will generates the output as 1. As a theoretical calculation for the input 110 we need to get carry as 1 so that we are placing the inverter at output of the carry circuit [22]. Hence, we are getting C_{out} as 0. For the

sum circuit we are giving inputs as C_{in} , XNOR, XOR to the transistors P6&N6 so that the transistors become off will generates the output as 0 and C_{in} and XOR and XNOR to the transistors P7&N7 so that the transistors becomes off so that the sum circuit will generates output as 0.

5 Result

The conventional full adder proposed by the authors was scrutinized and found some drawbacks were taken as a challenge and we overcame those issues. The simulation results of the previous techniques and present techniques was represented in Table 2 for the comparison factors of Power, delay, PDP. In the older IEEE papers the authors was used the 180 nm technology and 90 nm technologies [23]. In this paper we are using 45 nm technology and we are simulating our proposed conventional full adder and we are on the inputs as '110' for this input we are getting effective results. From the comparison table we plotting the graphs for voltage V_s power and Voltage V_s delay and along with Voltage V_s PDP as shown in Figs. 3 and 4.

The output plot of the proposed technology is shown in below simulated Fig. 5.

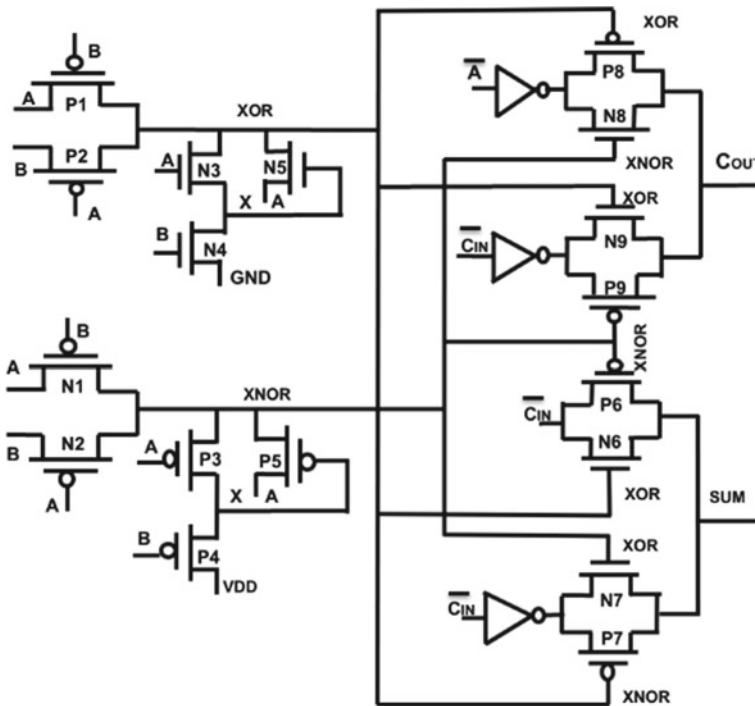


Fig. 3 a, b Proposed full adder schematic

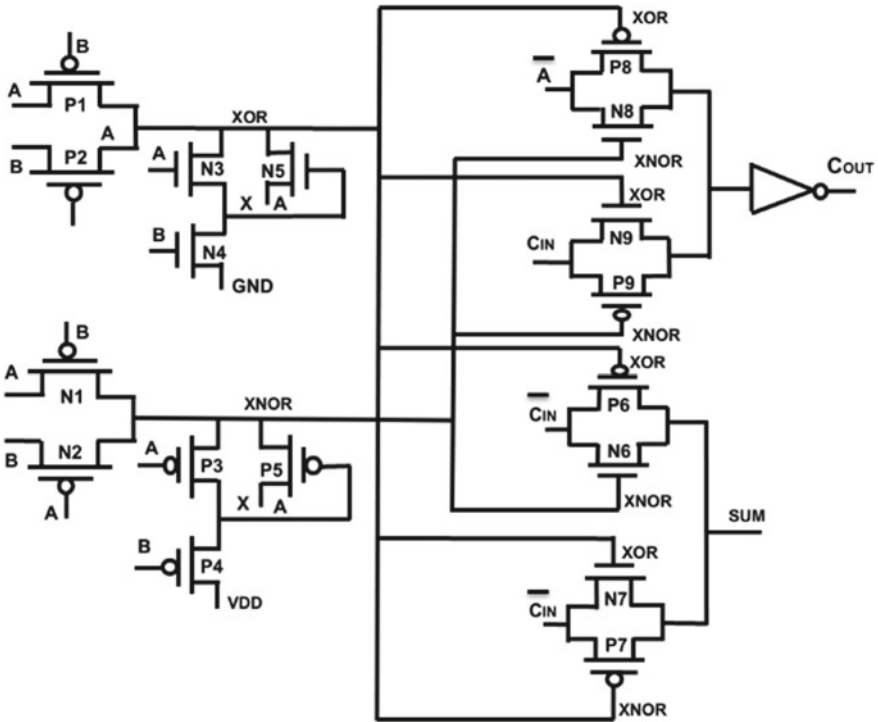


Fig. 3 (continued)

Table 2 Comparison table for existed technology and proposed technology

Conventional full adders	No of transistors	Existed technologies (90 nm)			Proposed technologies (45 nm)		
		Power (uW)	Delay (ps)	PDP (10^{-18})	Power (W)	Delay (ns)	PDP (10^{-18})
ZAVAREI [18]	26	72.3	27	1952.1	72.3	27	1952.1
VALSHANI [17]	18	71.3	25	1782.5	71.3	25	1782.5
BHATTACHARYYA [12]	16	65.59	22.6	1482.33	65.59	22.6	1482.33
H.NASERI [15]	22	55.8	26.7	1489.86	55.8	26.7	1489.86
Schematic-1	20	52.3	27.09	1459.17	9.88	150.02	1482.19
Schematic-2	26	71.8	30.4	2182.72	10.7	149.69	1601.68

6 Conclusion

In this project, a new model conventional multistage adder was established by using XOR XNOR circuit by taking reference from few of previous papers proposed

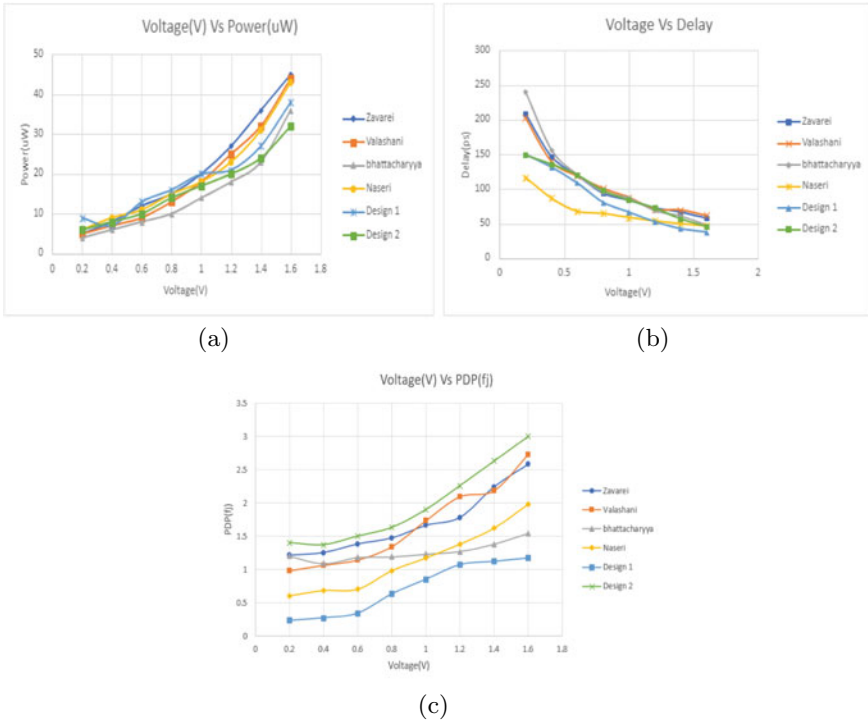


Fig. 4 Proposed design graph **a** voltage versus power, **b** voltage versus delay, **c** voltage versus PDP

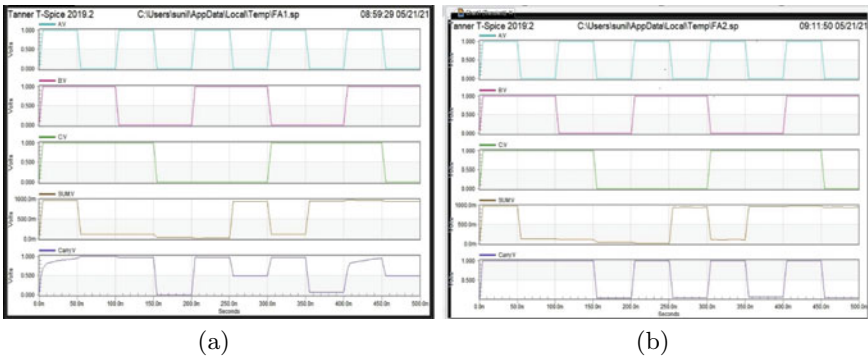


Fig. 5 Simulated output results **a** design 1, **b** design 2

by authors which generates the full swing outputs continuously. By utilizing this proposed XOR–XNOR circuit we designed 2 discrete types of adder circuits with effective outputs. The simulation results of the present XOR XNOR circuitry and the adder circuitry was verified by using mentor graphics 45 nm technology tool.

The present XOR XNOR block represents decrease in words of fluctuations, Delay up to 58%, 60% and power up to 60%, PDP up to 75%, 78.02%, respectively. Then comparing with other models.

References

1. Amini-Valashani M, Ayat M, Mirzakuchaki S (2018) Design and analysis of a novel low-power and energy-efficient 18T hybrid full adder. *Microelectron J* 74:49–59
2. Naseri H, Timarchi S (2018) Low-power and fast full adder by exploring new XOR and XNOR gates. *IEEE Trans Very Large Scale Integr (VLSI) Syst* 26(8):1481–1493
3. Nigam A, Singh R (2016) Comparative analysis of 28T full adder with 14T full adder using 180nm. *Int J Engg Sci Adv Res* 2(1):27–32
4. Valashani MA, Mirzakuchaki S (2016) A novel fast, low-power and high-performance XOR-XNOR cell. In: *Proceedings of the IEEE international symposium on circuits and systems (ISCAS)*, pp 694–697
5. Kumar A, Singh K (2015) A low-power 12 transistor full adder design using 3 transistor XOR gates. *Int J Electron Electr Comput Syst* 4
6. Bhattacharyya P, Kundu B, Ghosh S, Kumar V, Dandapat A (2015) Performance analysis of a low-power high-speed hybrid 1-bit full adder circuit. *IEEE Trans Very Large Scale Integr (VLSI) Syst* 23(10):2001–2008
7. Foroutan V, Taheri M, Navi K, Mazraeh AA (2014) Design of two low-power full adder cells using GDI structure and hybrid CMOS logic style. *Integration* 47(1):48–61
8. Agarwal M, Agrawal N, Alam MA (2014) A new design of low power high speed hybrid CMOS full adder. In: *Proceedings of the international conference on signal processing and integrated networks (SPIN)*, pp 448–452
9. Tung C-K, Shieh S-H, Cheng C-H (2013) Low-power high-speed full adder for portable electronic applications. *Electron Lett* 49(17):1063–1064
10. Lin J, Hwang Y, Shew M (2012) Low power 10-T full adder design based on degenerate pass transistor logic. *ISCAS, IEEE*
11. Ramkumar B, Kittur HM (2012) Low-power and area efficient carry select adder. *IEEE Trans Very Large Scale Integr (VLSI) Syst* 20(2)
12. Kumar M, Arya SK, Pandey S (2012) Low power CMOS full adder design with 12 transistors. *Int J Inf Technol Convergence Serv (IJITCS)* 2(6)
13. Aguirre-Hernandez M, Linares-Aranda M (2011) CMOS full-adders for energy-efficient arithmetic applications. *IEEE Trans Very Large Scale Integr (VLSI) Syst* 19(4):718–721
14. Zavarei MJ, Baghban Manesh MR, Kargaran E, Nabovati H, Golmakani A (2011) Design of new full adder cell using hybrid-CMOS logic style. In *Proceedings of the 18th IEEE international conference on electronics, circuits, and systems*, pp 451–454
15. Goel S, Kumar A, Bayoumi MA (2006) Design of robust, energy efficient full adders for deep-submicrometer design using hybrid-CMOS logic style. *IEEE Trans Very Large Scale Integr (VLSI) Syst* 14(12):1309–1321
16. Chang C-H, Gu J, Zhang M (2005) A review of 0.18- μm full adder performances for tree structured arithmetic circuits. *IEEE Trans Very Large Scale Integr (VLSI) Syst* 13(6):686–695
17. Zhang M, Gu J, Chang C-H (2003) A novel hybrid pass logic with static CMOS output drive full-adder cell. In: *Proceedings of the international symposium on circuits systems (ISCAS)*, vol 5. p 5
18. Tien Bui H, Wang Y, Jiang Y (2002) Design and analysis of low-power 10-transistor full adders using novel XOR-XNOR gates. *IEEE Trans Circ Syst II, Analog Digit Signal Process* 49(1):25–30
19. Radhakrishnan D (2001) Low-voltage low-power CMOS full adder. *IEE Proc-Circ Dev Syst* 148(1):19–24

20. Vesterbacka M (1999) A 14-transistor CMOS full adder with full voltage swing nodes. In: Proceedings of the IEEE workshop on signal processing systems. SiPS 99. Design and implementation (SiPS), pp 713–722
21. Zimmermann R, Fichtner W (1997) Low-power logic styles: CMOS versus pass-transistor logic. *IEEE J Solid-State Circuits* 32(7):1079–1090
22. Chandrakasan AP, Sheng S, Brodersen RW (1992) Low-power CMOS digital design. *IEICE Trans Electron* 75(4):371–382
23. Zhuang N, Wu H (1992) A new design of the CMOS full adder. *IEEE J Solid-State Circuits* 27(5):840–844
24. Kandpal J, Tomar A, Agarwal M, Sharma KK (2020) High-speed hybrid-logic full adder using high-performance 10-T XOR–XNOR Cell. *IEEE Trans Very Large Scale Integr (VLSI) Syst* 28(6):1413–1422. <https://doi.org/10.1109/TVLSI.2020.2983850>

Techniques for Designing Efficient ELINT Digital Receiver



A. K. Singh

Abstract Technologies in the radar domain are changing rapidly due to the advances in digital processing techniques. The advancement in radar technology poses a challenging task for the ELINT receiver—to intercept and analyze the radar signals. Today, radar operations are LPI in nature with various modes of operation and with different added antenna scan patterns including phased array radars. Present radars also employ various digital modulation techniques (Fan et al. in A new method for polyphase pulse compression codes modulation recognition based on IQPF and FRFT, pp 1172–1176 [1]) to achieve high processing gain and intercept the long distance target with minimum RF power. Currently, various electronic warfare receivers are being employed for intercepting the radar signals; however, ELINT digital receiver provides the best solution for modern radar signals, because digital receiver also employs various digital signal processing techniques to enhance the processing gain and provides improved sensitivity to intercept low-power radar. In this paper, various design techniques of ELINT digital receiver have been discussed such that they will provide very high sensitivity without compromising the accuracy of radar pulse parameters measurement

Keywords EW—electronic warfare · ELINT—electronic intelligence · ADC—analogue to digital converter · DR—digital receiver · FFT—fast Fourier transform · FPGA—field programmable gate array

1 Introduction

The availability of latest electronics components and advanced signal processing techniques made the radar very sophisticated with higher performance. The target tracking accuracy has increased, and very precisely, the target can be tracked. Various modulation techniques being employed by radar to transmit low power and advance signal processing techniques used for the echo signal received from target. This

A. K. Singh (✉)
Defence Electronics Research Laboratory, Hyderabad 500005, India
e-mail: singh.ak.dlrl@gov.in

© The Author(s), under exclusive license to Springer Nature Singapore Pte Ltd. 2022
P. Kumar Jain et al. (eds.), *Advances in Signal Processing and Communication Engineering*, Lecture Notes in Electrical Engineering 929,
https://doi.org/10.1007/978-981-19-5550-1_38

413

results in a low probability of intercept of radar, which is very difficult to intercept by Electronics Warfare receiver. However, similar advanced components and signal processing techniques are available to ELINT receivers also to handle this type of situation. The radar transmitting frequency and modulations are known so that they can apply the matched technique, however, the ESM or ELINT receiver has to scan the entire spectrum [2] to intercept signals in any frequency band. To design ELINT digital receiver, we have high analog ADC with GHz sampling frequency and by using channelization and parallel processing the entire spectrum can be scanned in very less time, which provides a very high probability of intercept. In this paper, the design aspect has been discussed from ADC to processing elements like FPGA and also the signal processing. The major thrust given for the improvement of sensitivity and the parameters accuracy. The higher sensitivity will help to intercept the LPI nature [3] of radar, and the precise parameters accuracy measurement will help to distinguish multiple close by radars. Under the parameters measurement, the various frequency measurement techniques are discussed and also which technique is suitable for which type of application. Also techniques are explained on how to improve the frequency measurement accuracy.

2 ELINT Digital Receiver Architecture

The main building block of digital receiver consists of ADC and FPGA, where ADC used for converting analog signal, i.e., RF or IF signal to digital signal and FPGA used for processing the digital signal. The selection of ADC and FPGA is very important, because sampling frequency and analog bandwidth of ADC will decide the bandwidth of input signal can be processed. Presently, ADC very high analog bandwidth up to 12 GHz is available, which can directly convert the RF into the digital signal [4]. As the signal processing is concerned, FPGA has enough number of DSP slices along with the digital logic so that the real-time signal processing can be achieved.

2.1 ADC Sampling

Selection of ADC is important for designing the ELINT digital receiver, and it is to ensure that the spectrum should be used in an optimized way. To achieve this requirement, the proper sampling technique to be adopted. Generally, for signal processing application, Nyquist sampling frequency is used, which is twice the highest frequency components, but when the signal is band limited, i.e., signal ranging non-zero value to another non-zero value, then proper choice is band pass sampling instead of Nyquist sampling. However, the following conditions given in Eqs. 1 and 2 to be satisfied to achieve the band pass sampling.

$$f_s \geq 2 \times BW \quad (1)$$

$$(2f_c - BW)/m \geq f_s \geq (2 \times f_c + BW)/(m + 1) \quad (2)$$

where f_c : center frequency (1 GHz), BW: bandwidth (500 MHz), f_s : sampling frequency, m : integer (say 1). Now, taking a bandwidth of signal say 750–1250 MHz and the above condition satisfies for sampling frequency $1250 \text{ MHz} \leq f_s \leq 1500 \text{ MHz}$. We can take 1350 MHz, which will provide electrically equal guard bands on both the side and provide effective spectrum utilization. However, today, ADC is available with a higher sampling rate, and we can do oversampling say 5400 MHz instead of the required 1350 MHz. The required sampling data of 1350 MHz can be obtained by decimating the 5400 MHz sampling by a factor of 4. This technique improves the jitter performance of ADC, and there will be improvement of 3–4 dB in SNR, which will result in improvement in sensitivity of the ELINT receiver.

2.2 Sensitivity of ELINT Receiver

Sensitivity of a receiver plays a major role for designing the ELINT receiver architecture [5]. We always try to reduce the ELINT receiver bandwidth to increase the receiver sensitivity. But reducing the bandwidth to get higher sensitivity also reduces the probability of intercept (PoI), which is undesirable for EW application. The ELINT digital receiver is designed in such a way that keeping IF frequency and reducing the resolution bandwidth by changing the higher number of points FFT, this will provide the higher signal processing gain and enable it to intercept a low-power radar and provide the range advantage factor (RAF) over radar. Equation 3 shows the factor on which the sensitivity of the ELINT receiver decides.

$$\text{sensitivity} = -114 + 10 \log(\text{sqrt}(2Br Bv) + NF + \text{SNR}) \quad (3)$$

where

- Br bandwidth of IF signals
- Bv resolution bandwidth
- NF noise figure of ELINT receiver
- SNR processing SNR of receiver.

A typical case can be considered, and we can see how the sensitivity can be enhanced. IF bandwidth (Br) can be taken 750–1250 MHz, which is internationally accepted bandwidth for any ELINT receiver, $Bv = f_s/N$, where f_s can be taken 1350 MHz and $N = 2048$, i.e., no. of point FFT, thus Bv results 0.6 MHz. Noise figure of 5 dB can be achieved for a RF band of 0.5–18 GHz converted to IF of 500 MHz bandwidth, it is possible due to high performance RF components available and also using the suitable LNA at the input of the receiver. The 5dB SNR at the output of FFT is sufficient to detect the radar signal without the false alarm, because the FFT spectrum is very

stable as 2048 samples are taken for processing and averaging provides a very stable output. Now replacing the above value in the sensitivity equation.

$$\text{sensitivity} = -114 + 10 \log(\text{sqrt}(2 \times 500 \times 0.6)) + 5 + 5 \quad (4)$$

The achieved figure is even below the noise floor of 500 MHz, which is -87 dBm, it means we can process even effectively negative SNR signals without compromising the IF bandwidth. Further, a gain of 10 – 15 dB in antenna, which is very common for a ELINT directional antenna, will take the ELINT sensitivity above -100 dBm for 500 MHz bandwidth.

3 Radar Pulse Measurement

ELINT receiver's paramount task is to measure intercepted radar signals with high accuracy. The sensitivity of ELINT digital receivers is very high, and it is able to intercept many radars of similar characteristics. It becomes a challenging task to differentiate these radar emitters from each other so that effective order of battle (EOB) can be generated and required countermeasures can be initiated. In this paper, each important parameters of radar emitter are discussed, and how its measurement accuracy can be improved is presented, so that it will be very useful to distinguish very fine variation of radar having similar characteristics [6]. The main parameters like intercepted frequency, pulse width, amplitude, and time of arrival (ToA) are discussed. Though the angle of arrival (AoA) is not a radar parameter, but it becomes very important for EW receivers because the knowledge of AoA will help to understand the threat of adversary. Also, AoA becomes very important for ELINT receivers because the radar cannot change its position instantly, whereas all other parameters can be changed very fast.

3.1 Frequency Measurement

The most important intercepted parameter is frequency which determines the type of radar and its possible threats. Today's radars are very complex, and it is able to generate various frequency modulations and agility, which poses challenges to EW receivers to intercept and analyze. One hand EW receiver requires higher instantaneous bandwidth for operation, and other hand frequency measurement accuracy [7] is also very important. To address these issues, mainly three important and practical frequency receivers have been discussed.

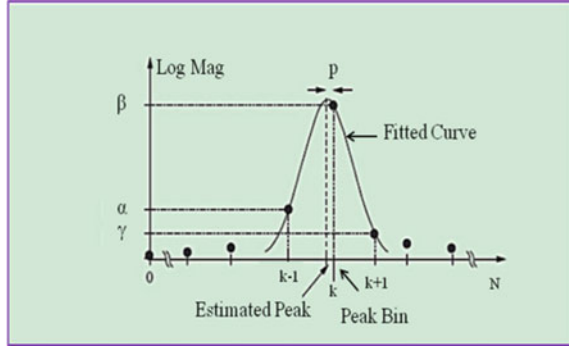
DIFM Receiver Technique Digital instantaneous frequency measurement receiver is being widely used as an EW receiver due to its instantaneous wideband coverage. DIFM receiver can be designed for 2 – 18 GHz bandwidth ESM receiver or for

500MHz bandwidth ELINT receiver. The basic principle is based on calculating phase difference between delayed signal with the un-delayed signal using a phase correlator. The delay time (τ) is decided based on the bandwidth requirement, and τ should always be less than $1/\text{bandwidth}$. This gives un-ambiguous bandwidth, but measuring accuracy is limited due to noise and to achieve the higher accuracy, prime multiple of higher length delay line to be used. Designing the delay line and selecting the proper ratio are an art for DIFM receiver design. The ratio of delay line 1:3 for 2–18 GHz bandwidth and 1:4 for 500 MHz bandwidth is very common. The higher ratio gives lesser phase margin and resolving ambiguity becomes challenging, however, precision design control and improved components allow us to go for higher ratio and achieve better frequency accuracy [8]. DIFM is still being used in an improved way for the latest EW system but suffers a limitation of handling multiple simultaneous signals. Many techniques have been discussed by various authors, but total success is not possible due to inherent limitations of design.

I-Q Technique of Frequency Measurement The I-Q method used for the frequency method is a modified method of DIFM technique. Both the measurement techniques are based on phase measurement, but I-Q technique has distinct advantages over DIFM technique. The DIFM used physical delay line to extract phase difference between un-delayed and delayed signal using the analog phase correlator, whereas I-Q technique uses the digital delay line, i.e., ADC's sample and successive ADC's sample for un-delayed and delayed samples, respectively. The measurement of DIFM is triggered based and every successive trigger should maintain a gap of processing time of the previous trigger. The I-Q technique is pure digital and continuously collects say 512 or 1024 samples for processing without any trigger. The phase delay collected based on the successive sample or the prime multiple of successive sample. The phase difference collected is based on model filter technique based on all the sample differences, which provides enhanced sensitivity compared over DIFM. As far frequency accuracy is concern, the required sample difference from same ADC's can be collected, whereas DIFM requires appropriate length of physical delay lines. The performance of digital delay lines in the I-Q method will be maintained for longer duration so many years, whereas performance will degrade in DIFM due to aging and temperature variation. Though there are many advantages of I-Q technique over DIFM, however, I-Q technique also does not provide solution for time coincidence signals like DIFM. Still, I-Q technique has been used in the space program, where FFT-based measurement technique could not be implement due to non-availability of required processing FPGA devices, and DIFM will be limited in sensitivity. Presently, I-Q technique only got implemented in the ELINT system of space program.

FFT Technique of Frequency Measurement Among all the techniques available for the frequency measurement, FFT technique is the best for ELINT receivers. The ELINT digital receiver based on FFT employs generic hardware where high-speed ADCs and FPGAs are the main building block. In FFT-based technique, sampling frequency and number of points used for FFT processing [9] decide the frequency measurement accuracy and also the sensitivity. This can be explained with the exam-

Fig. 1 Interpolation using three maximum bin amplitude samples



ple, say the sampling frequency assumed is 1350 MHz, and nos. of point 2048 is taken for FFT processing. The resolution bandwidth is $f_s/N = 1350/2048 = 0.6$ MHz. The frequency accuracy can be achieved around 300 kHz. The achieved frequency is quite good for ELINT receivers but still distinguishing multiple radar operating very close frequency may face some challenge. The further improvement in frequency can be achieved using the frequency interpolation technique on the FFT spectrum. The frequency interpolation [10] uses the FFT spectrum, where the main bin which crosses the threshold is compared with the both side bins, and frequency deviation is calculated based on the frequency interpolation equation given in Eq. 4. Where α , β , and γ are the amplitude of three successive bins, and p is the offset frequency which is being used for frequency correction (Fig. 1).

$$p = \frac{(\alpha - \gamma)}{2 * (\alpha - 2 * \beta + \gamma)} \tag{5}$$

$$\text{Estimated Freq} = (K \pm p) * (f_s/N) \tag{6}$$

The calculated frequency deviation Eq. 4 is used to correct the measured frequency value Eq. 5, and achieved accuracy can be obtained around 100 kHz, which can be used for distinguishing two or multiple radar emitters separated by 100 kHz in frequency. Figure 2 shows the frequency using FFT and frequency estimation using interpolation Plot. Figure 2a shows the input frequency versus measured frequency, and Fig. 2b shows the input frequency versus root-mean-square error (RMSE). The result is generated using 2048 point FFT, and interpolation is applied to compute the estimated frequency. These results are compared for band of 1200–1210 MHz. This band is chosen due to visibility purpose.

Angle of Arrival (AOA) Measurement AOA is a very important measurement of the ELINT receiver, because without AOA, it will be difficult to ascertain the possible threats. Though the radar can change its intra- and inter-pulse parameters easily due advances in digital technologies but cannot change its position instantly. This

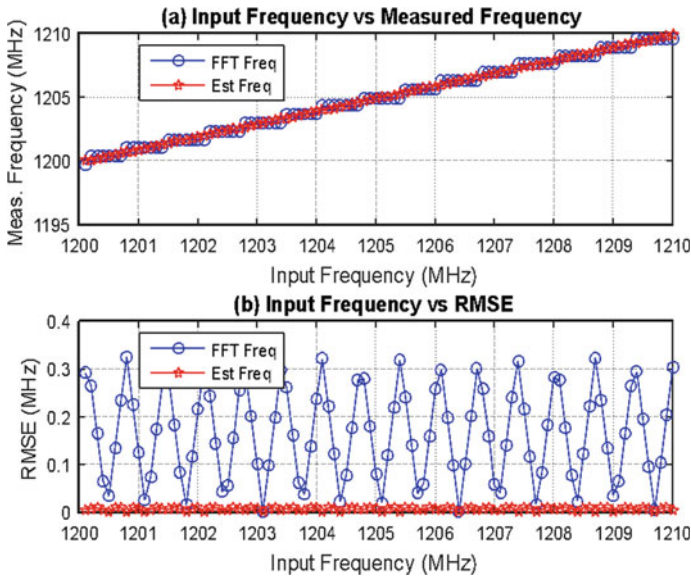


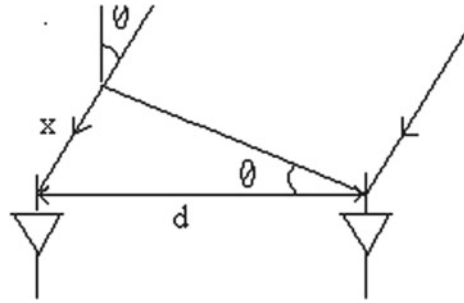
Fig. 2 Frequency using FFT and frequency estimation using interpolation plot

can be taken as an advantage for ELINT receivers, and various AoA measurement techniques can be used to know the emitter direction and initiate its counter action if required. In this paper, the three important techniques, i.e., amplitude, rotary, and phase have been discussed for AoA measurement based on digital receiver. Also explained which AoA technique will be suitable for a particular platform.

Amplitude Direction Measurement It is simple but very effective angle of arrival technique. In this AoA technique, multiple directional antennas are being used, which cover 360° in a space domain. For a simple design, where sensitivity requirement is limited, four directional cavity backed spiral (CBS) can be used, and for higher sensitivity and accuracy, 6–12 horn antennas can be used. The direction is calculated by comparing opposite antenna amplitudes, which will enable to select sector. When the sector is selected, then the adjacent antenna of that sector is being used to calculate angle of arrival. The accuracy obtained using amplitude technique is ranging from 2° to 5° depending on the number of antennas used in configuration. The airborne platform like aircraft, helicopter 4 antennas can be used for 360° coverage, whereas for ground, vehicle or ship even 6–12 antenna can be used.

Rotary Direction Finding Technique In this direction finding technique, one directional antenna is rotated azimuthally 360° with different rpm or sector scan with a varied speed. The intercepted pulses amplitude pattern will precisely indicate the AoA of the radar emitter. One channel digital receiver is used for processing the intercepted signal. Rotary direction finding technique is more suitable for higher

Fig. 3 Principle of BLI algorithm



frequency say 18–40GHz, because path loss is high, and received signal should be intercepted with a very high gain antenna like parabolic reflector of gain 25–30dB. RDF technique generally used for stationary, vehicle or ship platform, where parabolic antenna is rotated or sector scan in the probable band of radar signals.

Baseline Interferometry (BLI) Baseline interferometry (BLI) is one of the computationally efficient AoA techniques for getting higher direction finding accuracy and sensitivity of ELINT systems. The BLI technique is based on the phase difference measurement between two antennas given in Eq. 6 (Fig. 3).

$$\phi = 2\pi d \sin(\theta)/\lambda \tag{7}$$

where ϕ is the phase difference between two antennas, d is the distance between two antennas, λ is the wavelength of frequency whose DF measurement is required, and θ is the angle which is required to be measured. Signal is intercepted always along with the noise, and the phase measurement for 360° will be limited by certain degree of accuracy. The DF accuracy can be enhanced by utilizing multiple antennas in baseline and the first and the last antenna will provide the precise accuracy required by the system, because the phase measurement is modulo 360° , and the measurement phase difference is one reminder phase. This is an ambiguous phase because actual phase is given in Eq. 7

$$\phi_a = 2\pi m + 2\pi d \sin(\theta)/\lambda \tag{8}$$

The design of BLI is such that the first two antennas will provide the un-ambiguous phase [11] with less DF accuracy, and the first antenna with the last antenna will provide the ambiguous phase with high degree of DF accuracy. The Chinese Remainder Theorem (CRT) is used for resolving the ambiguous phase in a systematic manner. After resolving the ambiguity, the required accuracy can be achieved from the first and last antenna. The BLI technique generally provides AoA accuracy of 0.5° by proper selecting no. of antenna and their spacing ratio. Generally, 1:2 or 1:3 is the common spacing ratio used, however, different prime ratios also like 1:5 can be selected for getting accuracy of 0.1° . The antenna spacing ratio also decides the how much phase margin available to resolve the phase ambiguity. Higher the phase margin

indicates that the phase resolving algorithm is more robust, and it will not break for large phase tracking error. However, if the phase tracking error among channels are not corrected properly, then not only the resolving algorithm will break some conditions but also DF measurement error also will be more, because this phase error will propagate to the last phase difference, where final angle of arrival is calculated.

As the BLI algorithm is based on phase difference measurement among the antenna and any phase error introduced by the system itself will lead to the measurement error [12]. This error to be corrected before using the measured phase difference in the algorithm, and this process is called phase calibration. The phase correction becomes easy in the digital receiver because phase measurement by FFT output and its correction is part of the same hardware. The phase tracking or error starts from antenna followed by superhet receiver and digital receiver along with the connecting RF cables. The enough care is being taken for phase tracking in each of the sub-system, however, there will be phase tracking errors that will remain among channels and that need to be corrected. There are two types of errors, i.e., static or systematic error and random error. The systematic error can be corrected by feeding same phase signal at the input of ELINT system, i.e., superhet receiver and measuring at the digital receiver output using the FFT phase measurement technique.

Ideally, there should not be any error because equal phase signal was fed to the input of the superhet receiver, however, as explained earlier that there will be phase tracking error for the same batch components due to its tolerance. This error can be collected for the entire frequency range, say 0.5–18 GHz at a small equal interval. The collected phase tracking error values are stored in EPROM and used in phase correction of channels before using the resolving phase ambiguity algorithm. The random phase error cannot be corrected but we ensure that it should never cross the phase margin of the algorithm. Also antenna should not be used in phase correction as antenna phase only can be corrected in radiation mode and alignment of antennas with transmitting antenna cannot be made precise at 0 degree and small alignment error will result in system error which will be always there in operation, hence antenna tracking error to be minimize by design and still remaining error can be tolerated by phase margin of resolving algorithm.

The result is simulated for four antenna BLI and shown in Fig. 4. Figure 4a shows the set AOA versus error, and Fig. 4b shows the frequency versus RMSE. Results are generated for total 0.5–18 GHz with $\pm 45^\circ$ field-of-view (FOV).

3.2 Pulse Width and Time of Arrival Measurement

The pulse width (PW) and time of arrival (ToA) are envelop of intercepted RF signal and where is the leading edge of intercepted signal respectively. The measurement of pulse width and ToA is based on FFT processing. The frequency and time resolution are a factor of no. of point FFT used in processing. If with a sampling rate of 1350 MHz, we want to improve frequency resolution of 0.6 MHz by taking 2048

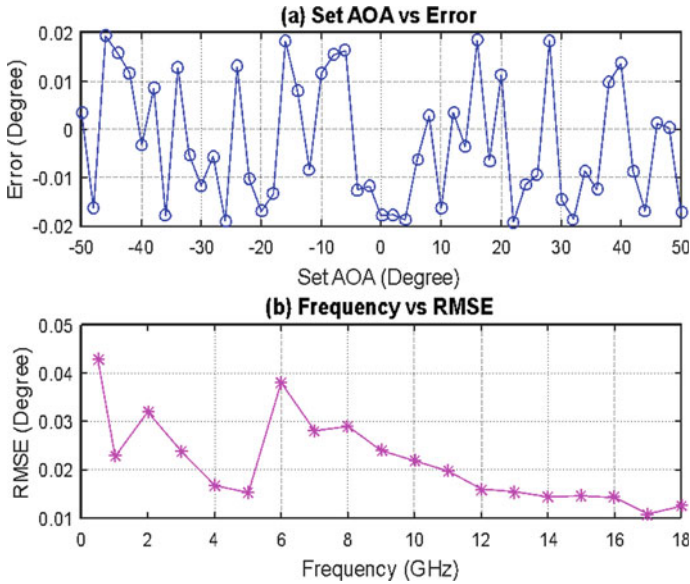


Fig. 4 Four antenna BLI AOA result

points FFT, then the time resolution will be approximately 1600 ns, which is very poor. Now, the challenge is to improve time resolution without disturbing the frequency resolution. To achieve this requirement without disturbing the rule of physics, overlapping FFT technique is used, where 50% overlapping improves time resolution upto 800 ns and so increasing overlapping till 50 ns time resolution is achieved. Theoretically, the overlapping can go up to the sampling time interval, but it becomes over design and implementing into FPGA will become difficult in real time. Hence, overlapping can be stopped up to 50 ns, which is the requirement of the ELINT system for pulse width and time of arrival.

3.3 Pulse Amplitude Measurement

The pulse amplitude is the power of intercepted RF pulse and represented in dB scale. The pulse amplitude measurement provides the estimate of distance of radar emitter for the intercept receiver if the type of radar is known. The pulse amplitude is taken from the FFT spectrum, say 2048 point FFT, and the FFT spectrum is an average effect of 2048 ADC samples. Due to averaging effect, the bin who crosses the threshold is very stable, and even 5 dB SNR is enough to declare the interception of radar emitters. Dual threshold is useful to suppress the pulse break or false alarm, signal gets detected when signal crosses the higher threshold and signal ceases to detect after first frame detection only when FFT spectrum output goes below the

lower threshold. All the pulses whose FFT power spectrum crosses higher threshold can be quantized in terms of dB, and resolution of 0.25 dB can be achieved for 2048 point FFT.

4 Intra-pulse Modulation Measurements

The modern or advanced radar has intra-pulse modulation [13] to enhance its performance in terms of detection range or reduce the probability of intercept. Generally, complete analysis of intercepted signals is being done by radar finger printing system (RFPS) in directed mode or off line. However, along with the main pulse parameter measurement, it is desirable to have limited intra-pulse modulation measurement in real time [14]. This can be achieved in ELINT digital receivers, because DSP technique is used to extract basic pulse parameters on ADC samples, and similar DSP technique is required for modulation extraction also. Many time-frequency algorithms like short-time Fourier transform (STFT), joint time Fourier transform (JTFT), Wigner Ville distribution (WVD), cyclostationary, all-phase FFT, etc., are employed to extract frequency or digital phase modulation like Barker, Frank, $P1$, $P2$, $P3$, $P4$, etc. Each time-frequency algorithm cannot detect all types of modulation and may be more suitable for a particular type of modulation. Offline processing can use all the T-F algorithms to extract the intra-pulse modulation with precision and accuracy, however, in real-time implementation, all-phase FFT [15] is explained, which can be implemented in FPGA and limited intra-modulation of pulse can be extracted. All-phase FFT can be explained with a pictorial diagram, Fig. 3. The input data is first windowed with $(2N - 1)$ length window, i.e., convolution of forward hamming and reverse Henning window, subsequently every two samples with the space between N intervals are summed up and thus a new data vector of N -length $y = [y(0), y(1), \dots, y(N - 1)]$ generated. Finally, FFT implementation on the new vector will generate the apFFT series [4] (Fig. 5).

$$w(n) = f(n) * b(n) \quad (9)$$

where $f(n)$ is forward Hamming window and $b(n)$ is reverse Henning window.

The amplitude spectrum of ap-FFT is shown in equation

$$|X_{AP}| = \frac{1}{N} \left| \frac{\pi N \left(\frac{f_0}{f_s} - \frac{k}{N} \right)}{\pi \left(\frac{f_0}{f_s} - \frac{k}{N} \right)} \right| \quad (10)$$

This is similar to the square of the traditionally FFT frequency spectrum amplitude. The phase-spectrum of ap-FFT is shown in Eqs. 10 and 11.

$$X(k) = F_{g[(k-\beta)\Delta w]} e^{j \left[\theta_0 - \frac{(N-1)(k-\beta)\Delta w}{2} (\beta-k)\pi \right]} \quad (11)$$

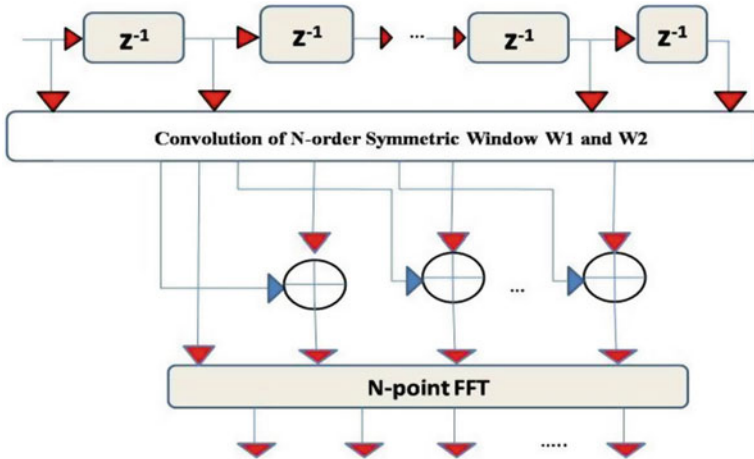


Fig. 5 All-phase FFT pictorial representation of algorithm

Table 1 Measured phase pattern using ap-FFT on Barker and Frank code

Type of signal	Actual phase pattern				Achieved phase pattern			
Barker 7	+ + + - - + -				0 0 0 180 180 0 180			
Frank 4	0	0	0	0	0	0	0	0
	0	90	180	270	0	89	180	270
	0	180	0	180	0	180	0	179
	0	270	180	90	0	267	180	87

$$Y(k) = F_{g[(k-\beta)\Delta w]} e^{j\theta_0} \tag{12}$$

where $\Delta w = \frac{2\pi}{N}$, $k \in [0, N - 1]$.

The ap-FFT is tested against 7 bit Barker and 4 bit Frank code, and the result is shown in Table 1. The Barker and Frank codes have defined phase patterns, and if measured phase has small variation over actual phase, it could be easily identified and phase pattern can be extracted.

5 Conclusion

ELINT digital receiver design can be made efficient if its configuration can be thought as per the platform requirements considering weight, size, and power available. Digital receivers can be configured for single channel or multiple channels, and different algorithms also can be implemented as per the accuracy requirement. The efficient receiver design is essential to have an edge over the advanced radar system. The

latest technologies are available for both EW and radar; however, efficient design of systems will determine the superiority. Only a thoughtful consideration of design in ELINT system can meet the requirement of tri-services.

Contributor

Dr. A. K. Singh, did ME in Digital System (ECE) and Ph.D. from Osmania University, in 2003 and 2015, respectively. Currently working as Scientist ‘G’ at DRDO-Defense Electronics Research Laboratory. He was the instrumental in design and development of digital receiver. His area of interest includes high-speed board design, time-frequency signal processing, and EW Receiver design. Presently, he is working for space systems design.

Acknowledgements It is great pleasure to thank Director DLRL, Associate Director and Group Director for their continuous guidance and support toward this activity. The author is also would like to thanks to anonymous reviewers for making valuable suggestions and comments.

References

1. Fan X, Li L, Li T, Chen T (2017) A new method for polyphase pulse compression codes modulation recognition based on IQPF and FRFT. In: Proceedings of the advanced information technology, electronic and automation control conference (IAEAC), Chongqing. IEEE, pp 1172–1176. <https://doi.org/10.1109/IAEAC.2017.8054198>
2. Dudeczyk J, Kawalec A (2015) Specific emitter identification based on graphical representation of the distribution of radar signal parameters. Bull Pol Acad Sci Tech Sci 63(2):391–396. <https://doi.org/10.1515/bpasts-2015-0044>
3. Pace PE (2008) Detecting and classifying LPI radar, 2nd edn. Artech House
4. Zheng S, Xu D, Jin X (2005) ADC limitation on the dynamic range of a digital receiver. In: International symposium on microwave, antenna, propagation and EMC technologies for wireless communications proceedings. IEEE, pp 79–82. <https://doi.org/10.1109/MAPE.2005.1617852>
5. Pekau H, Haslett JW (2005) A comparison of analog front end architectures for digital receivers. In: Proceeding of the IEEE CCECE/CCGEL, Saskatoon. <https://doi.org/10.1109/CCECE.2005.1557162>
6. Ramachandran R, Sharma R, Varughese S (2019) Graceful degradation: an airborne surveillance radar perspective. Def Sci J 69(4):389–395. <https://doi.org/10.14429/dsj.69.12135>
7. Niranjana RK, Singh AK, Chunduri BR (2020) High accuracy parameter estimation for advanced radar identification of electronic intelligence system. Def Sci J 70(3):278–284. <https://doi.org/10.14429/dsj.70.15105>
8. Zhang Q, Cheng L, Yin C. Design of multi-channel dual-frequency digital receiver based on FPGA. ICSP 2014 proceedings. IEEE, pp 403–407. <https://doi.org/10.1109/ICOSP.2014.7015037>
9. James T (2010) Special design topics in wideband digital receivers. Artech House Inc., Norwood, Massachusetts
10. Singh AK, Rao SK (2013) Implementation of interpolation algorithm in FPGA for fine frequency accuracy. IJRSET J 2(11):6424–6430

11. Ly PQC, Elton SD, Gray DA, Li J (2012) Unambiguous AOA estimation using SODA interferometry for electronic surveillance. In: 2012 IEEE 7th sensor array multi channel signal processing work shop (SAM), pp 277–280. <https://doi.org/10.1109/SAM.2012.6250488>
12. Singh AK, Rao SK (2014) Digital receiver-based electronic intelligence system configuration for the detection and identification of intrapulse modulated radar signals. *Defence Sci J* 64(2):152–158. <https://doi.org/10.14429/dsj.64.5091>
13. Park B, Ahn JM (2017) Intra-pulse modulation recognition using pulse description words and complex waveforms. In: International conference on information and communication technology convergence (ICTC), Jeju, pp 555–560. <https://doi.org/10.1109/ICTC.2017.8191039>
14. Yar E, Kocamis MB, Orduyilmaz A, Serin M, Efe M (2019) A complete framework of radar pulse detection and modulation classification for cognitive EW. In: 27th European signal processing conference (EUSIPCO), A Coruna, Spain, pp 1–5. <https://doi.org/10.23919/EuSIPCO.2019.8903045>
15. Huang X, Wang Z (2011) Phase difference correcting spectrum method based on all-phase spectrum analysis. *J Electron and Inf Technol* 30(2):293–297. <https://doi.org/10.3724/SPJ.1146.2006.00804>

Robust Deep Learning Approach for Brain Tumor Classification and Detection



J. Hima Bindu, Appidi Meghana, Sravani Kommula,
and Jagu Abhishek Varma

Abstract The human brain is the humanoid system's primary controller. A brain tumor is a consequence of abnormal cell growth and division in the brain, and the progression of brain tumors leads to brain cancer. The introduction of new technology into health care can be seen as a means of improving human judgment in diagnosis. The use of computer vision in diagnostics might reduce human judgment errors. Magnetic resonance imaging (MRI) is the most dependable and secure method among the numerous medical imaging technologies. The goal of this project is to employ a robust approach that specifically identifies minor abnormalities in MRIs and predicts the presence of a tumor with high accuracy for brain cancer detection. In this paper, we demonstrate the use of deep learning techniques through convolutional neural networks (CNN) for reliable tumor detection, followed by image segmentation through a marker-based watershed segmentation algorithm to view the tumor zone. A user-friendly GUI is built to assist medical professionals in achieving the above objectives without any complications. This system can be used as a support tool by doctors and radiologists for early detection of tumors. The results can be used as a second opinion and reviewed using several performance-assessed parameters to determine whether the patient has a brain tumor or not.

Keywords Brain tumor detection · Medical resonance imaging · Medical image processing · Deep learning · Convolutional neural network

J. Hima Bindu (✉) · A. Meghana · S. Kommula · J. A. Varma
Department of Information Technology, MGIT, Hyderabad 500075, India
e-mail: jhimabindu_it@mgit.ac.in

A. Meghana
e-mail: ameghana_it171207@mgit.ac.in

S. Kommula
e-mail: ssatyasravanikommula_it171252@mgit.ac.in

J. A. Varma
e-mail: jabhishekvarma_it171227@mgit.ac.in

1 Introduction

Medical imaging plays a significant role in the current realm of clinical practice and medical research. The manual inspection of tumors is time consuming, especially when there are a large number of images [1]. As a result, medical image segmentation and anomaly detection have garnered considerable attention for clinical analysis, and several algorithms have been introduced for this purpose. Researchers have used brain magnetic resonance imaging (MRI) as one of the best imaging modalities for diagnosing brain cancers and modeling tumor progression at both the detection and treatment stages. In the field of medical image analysis, CNNs have had a lot of success [2]. CNNs, unlike standard machine learning techniques, do not require manually retrieved features for categorization. The structure of deep models contains additional layers, which complicate learning parameters, especially on restricted datasets, according to a wide range of research publications on deep learning used to detect malignancies from brain MRI. As the model complexity grows and the simulation duration grows, it needs high-end computational tools for program executions. As a result, we have developed a solution to the complexity problem for smaller datasets [3]. Layers are reduced in proposed model to avoid the use of highly configured tools. Furthermore, the proposed CNN model outperforms the test dataset across the board in terms of all assessment parameters. As a result, the primary goal of this study is to develop a reliable CNN model that can categorize and predict whether or not a person has a tumor from brain MRI scans with a high enough level of accuracy for clinical use.

2 Proposed Methodology

2.1 Data Acquisition

In this paper, MRI dataset is used which is freely available open-source dataset. This dataset contains images with tumor (Yes) and non-tumor (No) categories. There are 198 training images and 58 testing images of brain MR in the collection, which vary in shape and size. The dataset's shape is non-uniform, and the backbone is non-uniform as well [1]. The MRI dataset is displayed in Fig. 1 according to their labels, with tumors in one category (labeled "no") and without tumors in the other (labeled "yes").

2.2 Image Input and Preprocessing

The first and most essential stage in improving the quality of a brain MRI image is image preprocessing. Image acquisition in image processing is achieved by retrieving

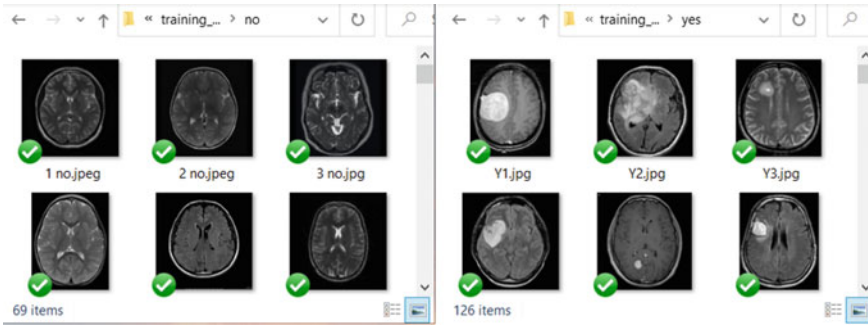


Fig. 1 Training and testing dataset

an input image for processing. The elimination of impulsive noises and image resizing are crucial steps in preprocessing [4]. This enhances the accuracy of the classification as well as the diagnosis. We transform the input image to a grayscale image in our work. Then, filters are applied to suppress the high frequencies. The images in the dataset are having different sizes, widths and heights. It is endorsed that they be resized to the same height and width for the best results [5]. It is also a good idea to resize the photographs so that important details do not get lost or the quality suffers. In this work, the MR pictures are scaled to (240×240) .

2.3 Image Segmentation

There are multiple unwanted regions and gaps in practically every image, which may lead the suggested classifier to perform poorly. As a result, the photographs must be cropped such that just the most important information is retained and the unwanted area is deleted. Image segmentation is the process of dividing an image into many areas. The steps for cropping photos using extreme point calculation are as follows:

- Step 1: Load the 240 240 3 shape's original scaled picture input.
- Step 2: Convert RGB photos to grayscale images in step two.
- Step 3: To convert grayscale photos to binary images, thresholding is used.
- Step 4: Choose the largest contour from the contours of the threshold images.
- Step 5: From the photos, find the extreme spots.
- Step 6: By combining extreme points and then crop the image.

Figure 2 depicts the process of cropping.

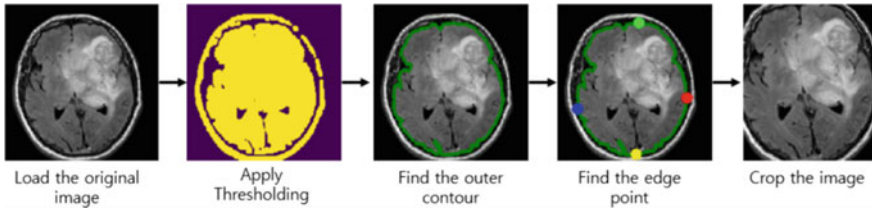


Fig. 2 Step-by-step process of cropping an image

2.4 Display of the Tumor Region

Image processing methods are applied through OpenCV to view the tumor area by employing image segmentation with a marker-based watershed segmentation algorithm. We use one color (or intensity) to mark the region that we are sure is the foreground or object, the background with another color, and mark the region we are uncertain of with 0. After that, the watershed algorithm is applied [6]. The boundaries of objects will have a value of -1 , and the marker will be updated with the labels we assigned.

3 CNN Model Architecture

3.1 Classification and Detection

Classification is one of the most effective methods for identifying images, such as medical imaging. Convolutional neural network (CNN) will be utilized as an automated and reliable classification and detection method since its structure is stable and assists in recognizing even the smallest features. A convolutional neural network (CNN) is a deep learning system that can take an image as input, assign priority to various features of the image, and differentiate between them. CNN requires significantly less preprocessing than other classification approaches [7]. In the case of supervised learning, we do not need to provide the features explicitly. Images are loaded into the CNN architecture with their class as a label to extract computational properties (tumor or no tumor). Filters and their weights are characteristics used to assess models during testing.

3.2 CNN Parameters

Layer of convolution: The input to the convolutional layer is “ l ” feature maps, while the output is “ k ” feature maps. “ $n * m$ ” is the filter size. For each feature map, there is a word called bias. As a result, there are a total of “ $(n * m * l + 1) * k$ ” parameters.

Pooling Layer: There are no parameters in the pooling layer that you can learn. This layer’s sole purpose is to shrink the image’s dimensions.

Flattening Layer: Because the flattening layer is used as an input for a fully linked network, no parameters are learned here.

Fully connected Layer: All input units have a separate weight for each output unit in this layer. The number of weights is “ $n * m$ ” for “ n ” inputs and “ m ” outputs. This layer also contains the bias for each output node, resulting in “ $(n + 1) * m$ ” parameters.

Output Layer: This layer is fully connected; hence, the parameters are “ $(n + 1)m$,” where “ n ” is the number of inputs and “ m ” is the number of outputs.

The convolutional neural network (CNN) is a type of neural network that uses convolutional layers (Fig. 3).

In our suggested architecture, the convolutional neural network (CNN) is made up of two types of layers: convolutional layers and pooling layers. In the classification phase, the flattened weighted feature map obtained from the last pooling layer is used as an input for the fully connected network [8]. These are layered after preprocessing. As is customary, the ultimate output of the last layer is tumor or non-tumor based on the probability score value (0 or 1). When comparing the likelihood score values of normal and tumor brain images, the tumor brain image has the higher value. For development and deployment, the Python programming language is used.

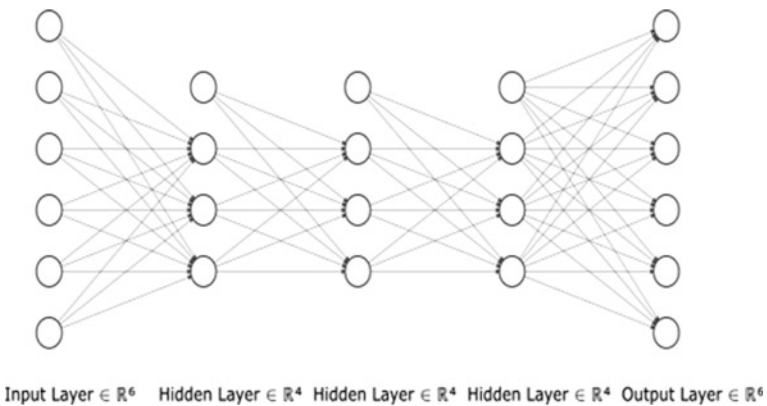


Fig. 3 Basic convolutional neural network architecture

4 Lines of Code

```
# Using the four extreme points, crop a new image from the original (left, right,
top, bottom)
image[extTop[1]:extBot[1], extLeft[0]:extRight[0]] new image =
image[extTop[1]:extBot[1], extLeft[0]:extRight[0]]
cv.resize(new image, dsize = (240, 240), interpolation = cv.INTER_CUBIC)
image = cv.resize(new image, dsize = (240, 240), interpolation = cv.INTER_CUBIC)
picture/255 = image
image = image.reshape((1, 240, 240, 3))
res = model.predict(image)
return res
def check(self):
global mriImage
# print(mriImage)
if (self.val.get() == 1):
res = predictTumor(mriImage)
if res > 0.5:
resLabel = tkinter.Label(self.FirstFrame.getFrames(), text = "Tumor Detected")
else:
res = predictTumor(mriImage)
```

5 Performance Assessment Metrics

The performance can be analyzed from the metrics such as accuracy and loss displayed for the input MR image undergoing detection for the presence of brain tumor [9]. Accuracy and loss plot curves of training and validation obtained during the training process are displayed in Fig. 4, respectively. Accuracy increases with the number of epochs and eventually saturates, indicating that the designed network's training on the dataset is complete. Furthermore, because the validation and training accuracy curves are comparable in distribution, an important conclusion from this graph is that the network is trained without underfitting or overfitting features.

6 Results and Discussion

For this system, we obtained a degree of precision and accuracy that was better than many state-of-the-art experimental setups. This method is particularly advantageous since the system is automated, and any user may test a new image simply by picking it from our GUI-based implementation. Using this robust approach, it is possible to

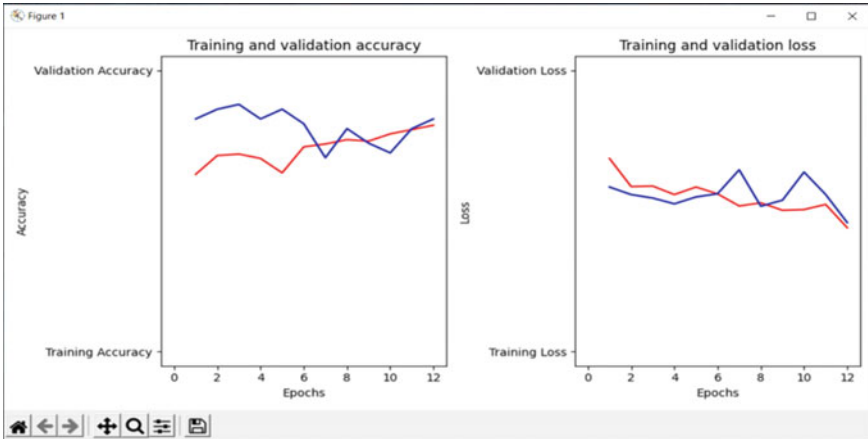


Fig. 4 Accuracy and loss graph curves of training and validation obtained during the training process

identify cancer in its early stages at a low cost, potentially increasing the survival rate of brain cancer patients (Figs. 5, 6, 7 and 8).

7 Performance of the Proposed Model

The proposed methodology for our system gives noteworthy results for the detection of tumor. The proposed CNN model consists of convolution, pooling, flattening, full connection and output layer. The performance is evaluated based on splitting the dataset. We obtain 78.98% of accuracy for 70:30 splitting ratio, and we obtain 82.87 of accuracy for 80:20 splitting ratio. Table 1 represents the performance of the proposed methodology.

When compared to other models, our proposed model has a moderate–high accuracy. The validation performance of three models (SVM, LeNet and CNN) is displayed in Fig. 9 by comparing the training and testing accuracy for all three.

8 Conclusion

The proposed system is a practical application that offers a robust deep learning computerized approach for the identification of a brain tumor using the convolutional neural network. The proposed system is a practical application that offers a robust deep learning computerized approach for the identification of a brain tumor using the convolutional neural network. The application has a 70–80% accuracy rate and produces good results with no major errors and a shorter computing time. This can

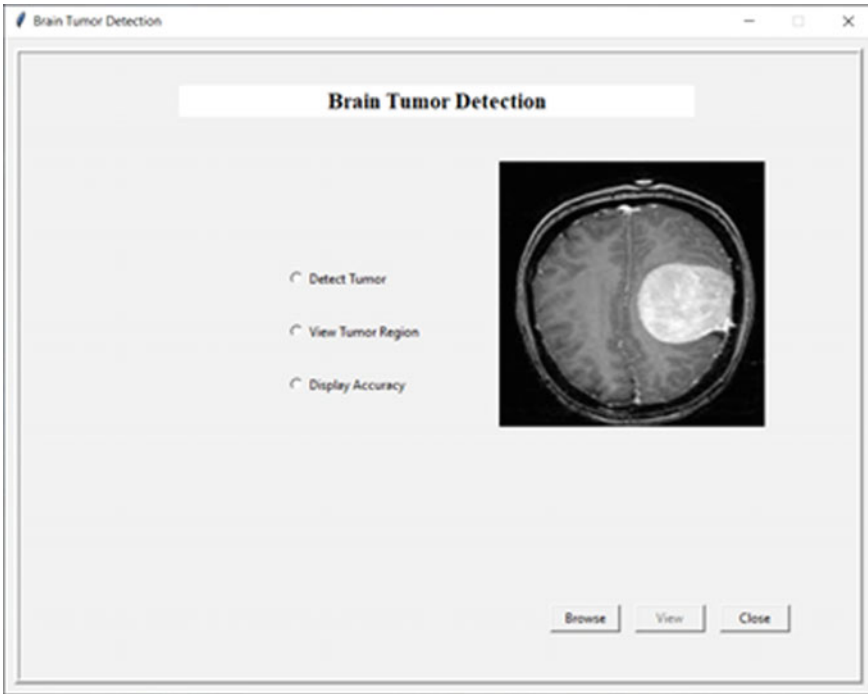


Fig. 5 Brain tumor detection GUI application platform

be utilized as a supplementary system to aid physicians and radiologists in the early detection of tumors while also assisting in decision-making and reducing obstacles.

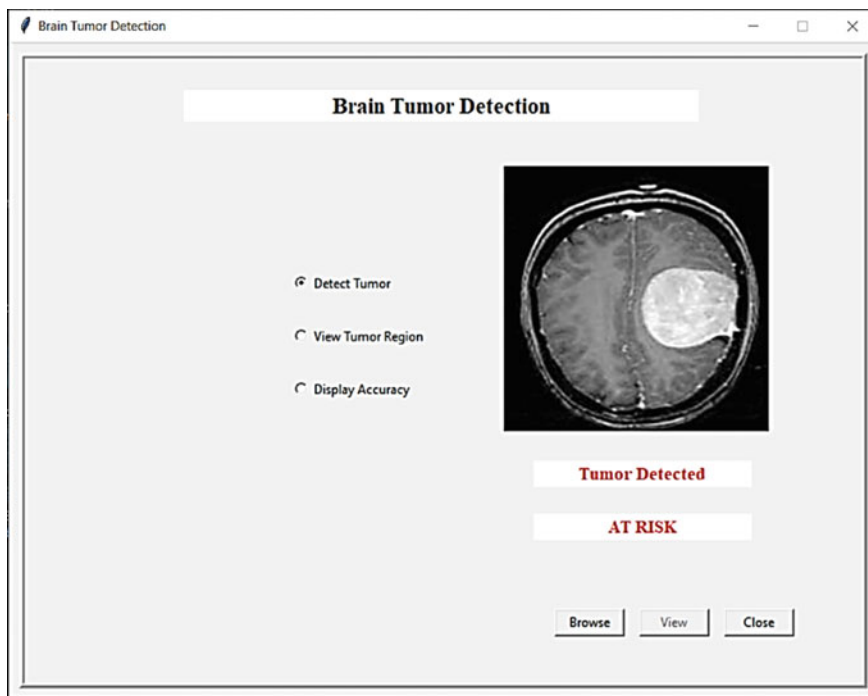


Fig. 6 Detect tumor checks for the presence of tumor and prints appropriate message

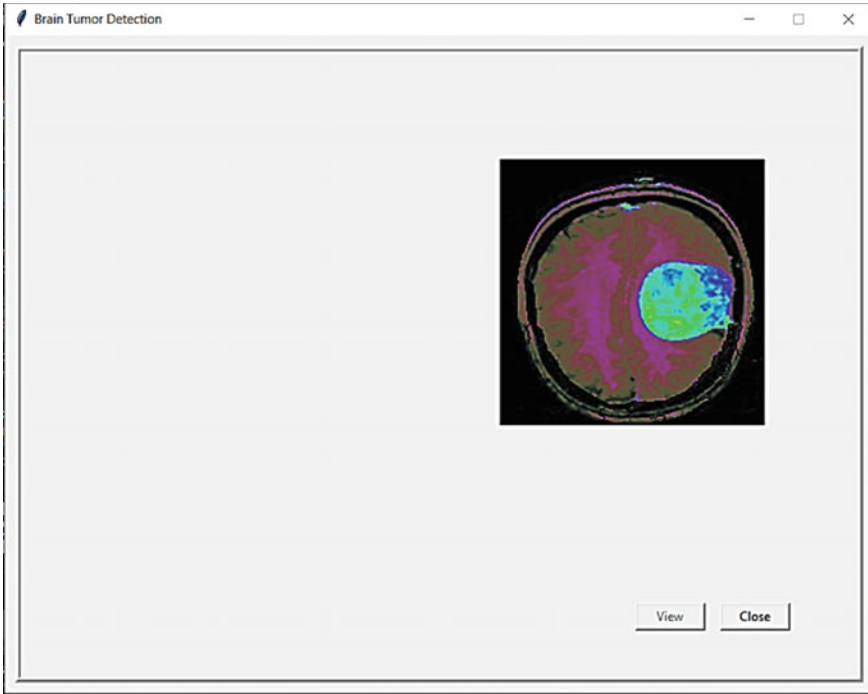


Fig. 7 Display tumor region displays the region of tumor

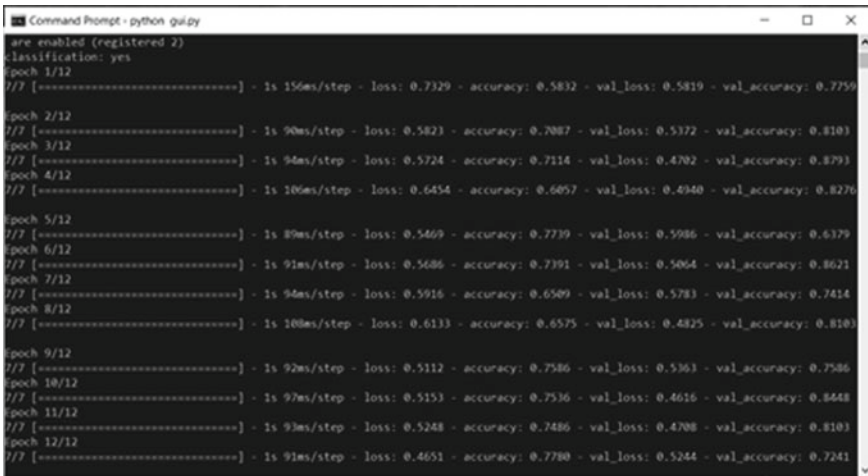


Fig. 8 Display accuracy displays accuracy and loss of training and validation

Table 1 Performance of the proposed model

Training set	Testing set	Splitting ratio	Accuracy
198	58	70:30	78.98
214	47	80:20	82.87

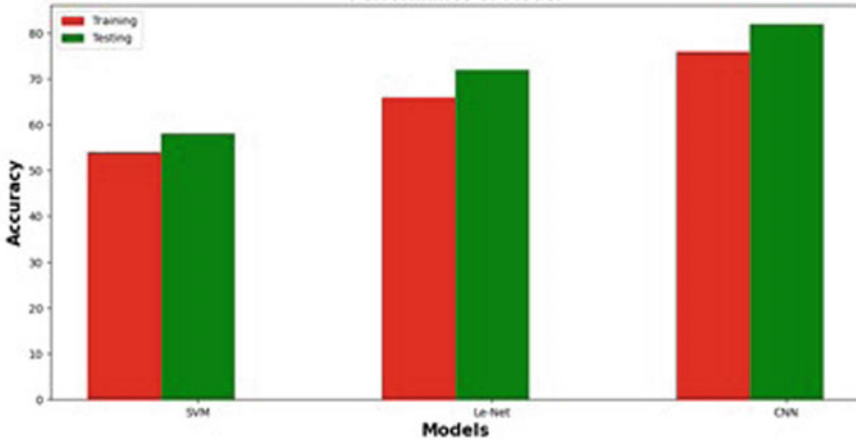


Fig. 9 Validation performance of three models (SVM, LeNet and CNN)

References

- Rai HM, Chatterjee K (2020) Detection of brain abnormality by a novel Lu-Net deep neural CNN model from MR images. *Mach Learn Appl* 2:100004
- Yousef R, Gupta G, Vanipriya CH, Yousef N (2021) A comparative study of different machine learning techniques for brain tumor analysis. *Mater Today: Proc*
- Khan P et al (2021) Machine learning and deep learning approaches for brain disease diagnosis: principles and recent advances. *IEEE Access* 9:37622–37655. <https://doi.org/10.1109/ACCESS.2021.3062484>
- Abd-Ellah MK, Awad AI, Khalaf AAM, Hamed HFA (2019) A review on brain tumor diagnosis from MRI images: practical implications, key achievements, and lessons learned. *Magn Reson Imaging* 61
- Seetha J, Raja SS (2018) Brain tumor classification using convolutional neural networks. *Biomed Pharmacol J*
- Lather M, Singh P (2020) Investigating brain tumor segmentation and detection techniques. *Procedia Comput Sci* 167
- Mittal M, Goyal LM, Kaur S, Kaur I, Verma A, Hemanth DJ (2019) Deep learning based enhanced tumor segmentation approach for MR brain images. *Appl Soft Comput* 78
- Abiwinanda N, Hanif M, Hesaputra ST, Handayani A, Mengko TR (2019) Brain tumor classification using convolutional neural network. In: Lhotska L, Sukupova L, Lacković I, Ibbott G (eds) *World congress on medical physics and biomedical engineering. IFMBE proceedings*, vol 68/1. Springer, Singapore. https://doi.org/10.1007/978-981-10-9035-6_33
- Chakrabarty N (2019) Brain MRI images for brain tumor detection, Kaggle. <https://www.kaggle.com/navoneel/brain-mri-images-for-brain-tumor-detection>

Impact of Distance Measure on Kriging Interpolation on Natural Images Corrupted by Drop-Out Noise



J. Sridevi, Ch. Raghava Prasad, and K. Vasanth

Abstract An impact of distance measurement using the Kriging interpolation technique is implemented on natural images for the removal of drop-out noise. The data drop-out can cause pointed unforeseen disturbances in the image signal. A technique of approximation known as kriging may be used to anticipate values that have not yet been seen based on observations of the value at adjacent places. Kriging assigns weights to each point based on how far it is from the unknown values at the time of calculation. The thoroughgoing testing was on natural images of a standard database. In this study, the application of Kriging interpolation depending on a distance metric between the suggested drop-out noise pictures and non-noisy images resulted in a more significant improvement in the performance of the method. Pixels that are not impacted by the effect always stay unaltered. The amount of noise is often expressed as a percentage of the total number of distorted pixels.

Keywords Kriging interpolation · Drop-out noise · Semi-variogram · Distance measures

1 Introduction

Kriging fortifies Geo-statistics and has sheer phenomenal significance. Kriging is the method of interpolation based on Gaussian processes governed by prior covariance. With best suitable expectations, this method can yield best linear unbiased predictions, particularly at unsampled areas of images. However, smoothness is a challenging task during spatial computations.

J. Sridevi (✉) · Ch. Raghava Prasad
Electronics and Communication Engineering, Koneru Lakshmaiah Education Foundation,
Guntur, Andhra Pradesh, India
e-mail: sridevi.jalakam1@gmail.com

K. Vasanth
Electronics and Communication Engineering, Vidya Jyothi Institute of Technology,
Hyderabad, Telangana, India

© The Author(s), under exclusive license to Springer Nature Singapore Pte Ltd. 2022
P. Kumar Jain et al. (eds.), *Advances in Signal Processing and Communication Engineering*, Lecture Notes in Electrical Engineering 929,
https://doi.org/10.1007/978-981-19-5550-1_40

Noise is evident as grains in the image, which is an otherwise variation of intensities in the image. Disturbances due to scenery of light and/or thermal liveliness causing brightness and heat inside the image capturing apparatus develop during the image capture. Even, noise is described as pixel intensities grabbed wrongly by the devices.

Image reconstruction is an important task in the fields of medical, geospatial, criminal and other important studies of biology. Kriging is considered a best alternative method used in image restoration and reconstruction using interpolation methods. Producing new predictions of unobserved values from the observations in the neighborhood and supply weights for the new predictions based on the distances is the most used of operations.

2 Related Work

Impulse noise, also known as salt and pepper noise, data-drop-out noise, or spike noise, is a kind of noise that occurs during the transmission of pictures or videos. Most of the time, Drop-Out Noise is generated by defective camera sensors, transmission problems, and timing issues in the A/D conversion process. Over the years different methods have been introduced to eliminate the drop-out noise.

2.1 *Drop-Out Noise*

2.1.1 Linear and Median Filters

Natural Images are prone to degradation of quality due to drop-out noise. The images are denoised using filters, linear smoothing filters are used to remove impulsive noise and contribute to estimation of latent form of original image, which is accomplished through CNN [1]. Similarly, median filters are used to remove impulsive noise in the magnetic-resonance images, and are believed to maintain edge retention. As each denoising filter has a specific advantages and disadvantages, they need to be applied carefully, otherwise the images experience blurriness [2]. Median filters shall employ continuous enlargement of window size and continue the process of increasing the maximum and lowest values of two consecutive windows until they are equal. A corrupted pixel value is replace by a minimum value or the weighted mean value of the window, otherwise unchanged [3].

A ‘decision-based trimmed media filter’ combined with mathematical morphology evolves into a hybrid filter for suppression and cancelation of noise [3]. High densities of salt and pepper noise can be eliminated by means of this filter. In cases of high rates of striking, fading and smudging is carried by ‘decision-based asymmetrical trimmed modified Winsorized mean filter’ [4].

2.1.2 Neural Network-Based Filters

If we consider denoising to be a learning issue, a feed forward conventional neural network may be used to remove salt and pepper noise from the signal. Trimmed medial numbers are used to substitute noisy pixels values such as 0 and 255 in the chosen window with values that are less noisy [4]. If the values of all the elements in the chosen window are between 0 and 255, then noisy pixels are substituted by a mean value derived from all of the elements in the window.

In an 8-bit gray-level picture, a three-values-weighted technique combined with a variable-size window that contains pixels with values other than zero and one hundred fifty-five is used for the re-establishment of a central pixel with intense values, that is, either zero or one hundred fifty-five. In a local window, the fundamental three-values are regarded to be the greatest, the lowest, and the central pixel values, respectively. To begin, each noisy pixel is assessed using a variable-size local window, which includes either the greatest or least pixel value at the window's center, depending on the situation. It is necessary to extend the window size until all of the pixels with values other than 0 or 255 are included in it if the local window's pixel values are zero or one hundred and fifty-five.

When the value of a pixel is very high or extremely low, a pixel may be considered noisy (0 or 255 for an 8-bit gray-level image). During the consideration of rebuilding the center pixel, the noisy pixel is eliminated from consideration. Based on the distance between the pixels having values other than 0 and 255, the pixels are divided into two groups: maximum and minimum groups.

As a result, we divide the number of pixels in each of these two categories by the number of weighting factors in each group. Using the weighting factors and the highest pixel value and the lowest pixel value, a medium value may be produced by multiplying them together. In order to improve the quality of noise reduction, each non-severe pixel is re-classified into one of three groups in the window: the maximum, the medium, and the minimum. A combination of the weighting factors from these three categories is used to weight the non-extreme pixels with respect to the maximum, middle, and lowest pixel values, respectively. The weighted value is substituted for the extreme value in the central pixel, allowing the noise-corrupted pixels to be recovered [5].

2.1.3 Winsorized Mean Filter (WMF)

An neutral weighted mean filter performs noise detection, spatial bias reduction, and noise reduction in a sequential successive process by fluctuation a window over a contaminated picture [6], which is accomplished by convolving a window over a contaminated image. To replace the noisy pixels depending on the present processing window values, a mean of neighbor four pixels, based on the genre of the data handling window values, a non-symmetric chopped median, a non-symmetric trimmed midpoint, or a global trimmed mean is generated [7].

A Decision-based Asymmetrical Trimmed Modified Winsorized Mean Filter (DATMWMF) first identifies noisy pixels based on their pixel values, which may be either 0 or 255, and then replaces them with the asymmetrically trimmed median value calculated from the pixel values. Pixels with values other than 0 or 255 are regarded to be non-noisy pixels since they do not have any noise. When applied to individual frames of video, the DATMWMF algorithm brings back the original picture [8], which is then combined.

2.1.4 City-Block Distance Method

Comparisons are made between the concepts of diverse distance measures on Interpolation algorithms implemented to natural pictures affected by drop-out noise. Based on the findings generated by the method utilizing City block distance (L1 norm), it was discovered that the technique produced extremely excellent results when compared to other Pythagorean measurements. When interpolating data inside a restricted neighborhood, the method requires a minimum of three pixels to be used. The rationale for utilizing three pixels is primarily to avoid the blurring of edges as much as possible. Even in the face of very excessive noise, information is retained [9].

2.1.5 Spline Method

The cardinal B-splines method is one of the strategies that may be used to remove impulsive noise from a given picture, and it is described below. It was necessary to extract each and every pixel from the picture that was not damaged by noise, such as the pixels that were not either 0 or 255. Initially, we choose a window size that is proportional to the amount of noise present. It is necessary to use four-pixel values for the interpolation of the damaged pixel in this case. If the number of noise-free pixels in a kernel is fewer than four, we affect the volume of the kernel to meet the requirements of the situation. It is recommended that when we expand the scale factor, we retain the data that were present in the original window [10].

2.1.6 Adaptive Weighted Mean Filter (AMWF)

Following the detection of noise, the Adaptive Weighted Mean Filter technique replaces the noisy pixel with the weighted mean value of the existing window, whereas the noise-free pixel is kept unaltered (see Fig. 1). It is preferable to use the weighted mean in AMWF rather than the median in AMF when replacing a noise-prone candidate, particularly when there is a lot of noise. There are two main reasons why we chose the weighted mean over the other options. For starters, the weighted mean in AMWF eliminates the impact of potentially noisy pixels, while the output median in AMF includes the consequence of such pixels. Second, we conducted investigational comparison between the weight mean and the weighted

median under the identical circumstances as in Algorithm 2 and found that the weight mean was superior to the weighted median. The PSNR of the image in which noise pixels are replace by weighted mean values is greater than the PSNR of the image in which noise pixels are not supplied by weighted mean values, according to the comparisons [11].

2.1.7 Adaptive Read Median Filter (ARMF)

An Adaptive Read Median Filter (ARMF) is a new adaptive method for salt and pepper noise removal. In this method, a Noise Image Matrices is considered to obtain a binary matrix. After that, t-symmetric pad matrices of these matrices are constructed. If an entry of the binary matrix is equal to zero and its 1-approximate matrix differs from zero matrices, then Strictly Increasing Regular Entry Matrix SIREM of the 1-approximate matrix is obtained, and the right median is evaluated. Afterward, this right median is overwritten to the entry. If an entry of the binary matrix is equal to zero and its 1-estimated matrix is zero matrices, but the 2-approximate matrix of this entry differs from zero matrices, then SIREM of 2-approximate matrix is obtained, and the right median is evaluated. Afterward, this right median is overwritten to the entry. Similarly, if an entry of the binary matrix is equal to zero and its (1)-approximate matrix is zero matrix but the k-approximate matrix of this entry differs from zero matrix, then SIREM of the -approximate matrix is obtained, and the right median is evaluated. Afterward, this right median is overwritten to the entry [12].

This paper aims to study about the impact of distance-based measures on Kriging interpolation. The remaining sections of the paper are arranged as follow. In Sect. 2, the suggested approach is explained in detail. Section 3 shows the simulation results produced by the suggested approach, together with a short analysis of the findings, and offers a comparison of the results with those achieved by current methods. Finally, in Sect. 4, the paper comes to a close.

2.2 Kriging Interpolation

The Kriging interpolation is a Geo-statistical method that generates and predicts unknown values from a known set of points. It is an interpolation method based on statistical relationships and the distance among measured points. Kriging uses the variogram and covariance to estimate the statistical relationships between measured points. Interpolation using Kriging for the exclusion of salt and pepper noise from images Isolates pixels that are not affected by noise. Only noisy pixels are processed by this algorithm. Damaged pixels are replaced with a value interpolated using weights based on the semi-variance between damaged pixels and non-noisy pixels in a small area around the affected pixels as relative to other distance metrics, large noise densities.

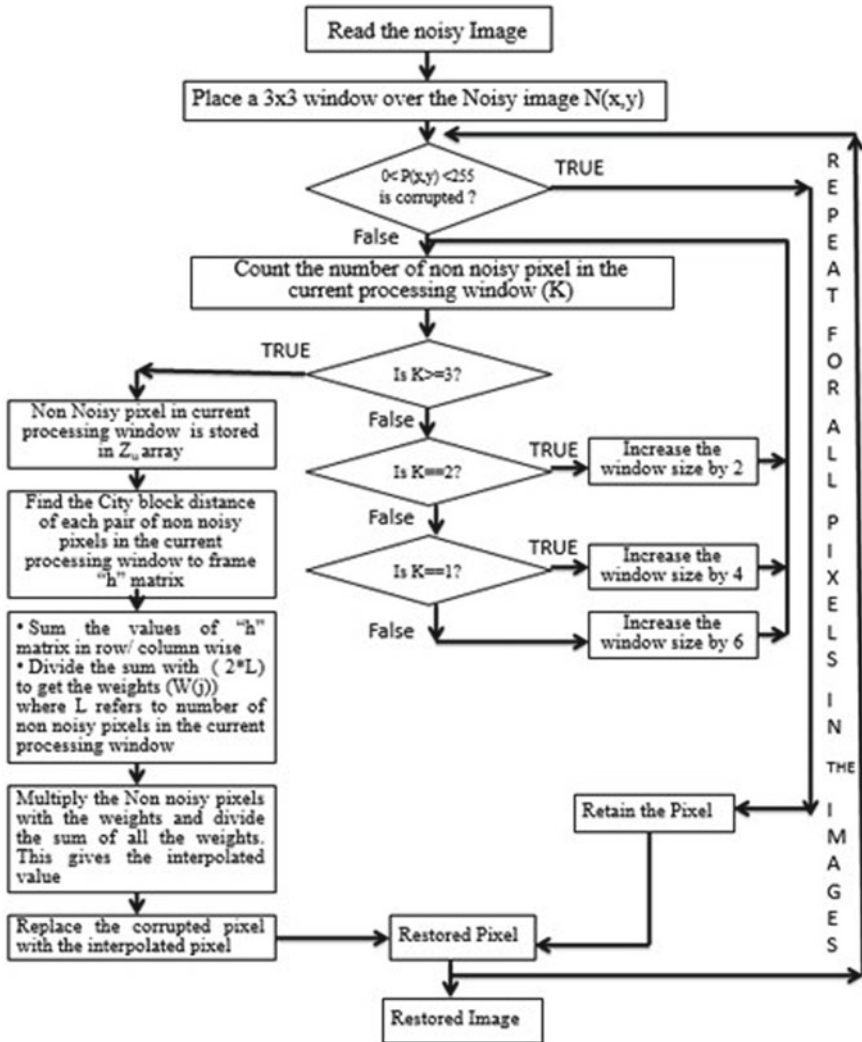


Fig. 1 Flowchart of the adaptive kriging interpolation algorithm using city block distance

2.3 Proposed Method

The planned filter is designed by varying the distance between non-noisy pixels existing adaptive Kriging Interpolation filter based on L1 norm or L2 Norm.

3 Results and Discussion

The Adaptive Kriging interpolation algorithm was proposed by Vasanth et al. The Result of the use of different distance measures is investigated in the paper. The paper initially used a Distance measure which was designed based on first, second third, and fourth-order moments. The power of the distance measure is obtained from a trial and error-based method done on different images of the database. The problem statement addressed in this work is that for a natural image we do not need to use complex distance measures to compute the distance between two non-noisy pixels as the pixels lie in closer proximity. To test our hypothesis, we run tests on a variety of natural pictures from the Image database, which we obtained from the signal and image processing institute maintained at the University of South California.

The proposed algorithm's distance measure was diverse and the algorithm was applied to images degraded by drop-out noise. The results were plotted for noise densities ranging from 10 to 90% in terms of Mean Square Error (MSE), Structural Similarity Index Metric (SSIM), and Cumulative Probability Blur detection Metric (CPBD). The value of the Mean square error indicates the amount of deviation the distance measure offers while applying the proposed algorithm. The structural correspondence index metric indicates the edge preservation competence of the proposed algorithm using different distance-based measures. The no reference metric CPBD indicates the amount of perceivable blur caused by the low pass filter by different distance measures. Table 1 indicates the error obtained when different distance measures are applied on Adaptive Kriging Interpolation Algorithm on a walk bridge image corrupted by drop-out noise.

Table 2 indicates the structural similarity index metric of different distance measures is applied on Adaptive Kriging interpolation Algorithm on a walk bridge image

Table 1 Mean square values of adaptive kriging interpolation algorithm using various distance measures on walk bridge image corrupted by drop-out noise

ND	Squared Euclidian distance	Chess board distance	City block distance	Canberra distance
0.1	21.7897	21.9566	20.9497	21.0532
0.2	44.3298	43.5364	43.2465	43.676
0.3	67.7314	69.4442	68.7202	69.9579
0.4	98.2536	99.4556	99.1289	101.905
0.5	134.7089	137.9789	134.7488	138.3903
0.6	180.7331	191.0931	181.8307	193.3193
0.7	248.037	259.615	250.193	268.8124
0.8	368.0865	387.0095	365.0073	390.3282
0.9	629.9875	651.0517	639.3513	669.6858

Table 2 Structural similarity index metric (SSIM) values of adaptive kriging interpolation algorithm using various distance measures on walk bridge image corrupted by drop-out noise

ND	Squared Euclidian distance	Chess board distance	City block distance	Canberra distance
0.1	0.9785	0.9792	0.9794	0.98
0.2	0.9555	0.9567	0.957	0.9575
0.3	0.9301	0.9294	0.9308	0.9308
0.4	0.8987	0.8983	0.8994	0.898
0.5	0.859	0.857	0.862	0.859
0.6	0.811	0.808	0.8122	0.8055
0.7	0.7469	0.7354	0.7429	0.7315
0.8	0.6427	0.6339	0.6429	0.6305
0.9	0.4865	0.4714	0.4805	0.4661

Table 3 Cumulative probability blur detection metric (CPBD) values of adaptive kriging interpolation algorithm using various distance measures on walk bridge image corrupted by drop-out noise

ND	Squared Euclidian distance	Chess board distance	City block distance	Canberra distance
0.1	0.6859	0.6864	0.6854	0.6855
0.2	0.6689	0.6689	0.6701	0.6664
0.3	0.6485	0.6514	0.6467	0.6438
0.4	0.6252	0.6208	0.6218	0.6234
0.5	0.5881	0.5907	0.5878	0.5978
0.6	0.5471	0.5526	0.5474	0.5596
0.7	0.4965	0.5016	0.499	0.5147
0.8	0.4332	0.4454	0.4403	0.4576
0.9	0.3263	0.3504	0.3422	0.3836

corrupted by drop-out the noise. Table 3 indicates the Cumulative Probability Blur detection Metric (CPBD) of different distance measures is applied on the Adaptive Kriging interpolation Algorithm on a walk bridge image corrupted by drop-out noise. Figure 2 indicates the error obtained on different distance measures on adaptive Kriging interpolation on walk bridge image corrupted by drop-out noise. Figure 3 illustrates structure preservation by different distance measures on adaptive Kriging interpolation on walk bridge image corrupted by drop-out noise. Figure 4 degree of blur by different distance measures on adaptive Kriging interpolation on walk bridge image corrupted by drop-out the noise.

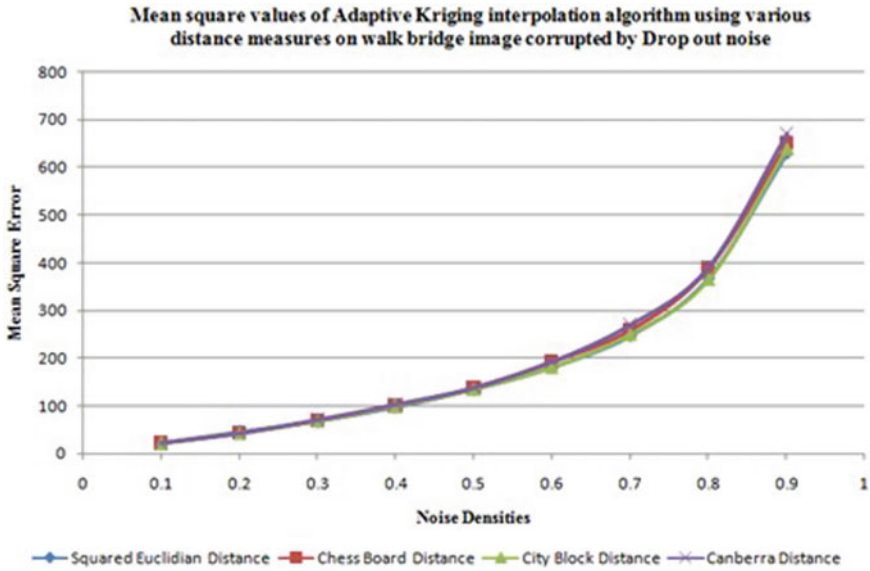


Fig. 2 Error obtained on different distance measures on adaptive kriging interpolation on walk bridge image corrupted by drop-out noise

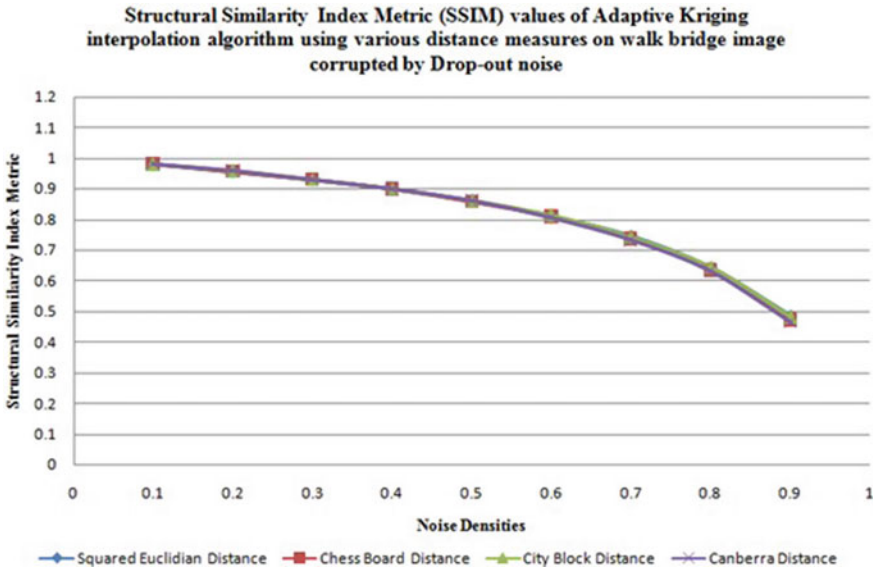


Fig. 3 Structure preservation by different distance measures on adaptive kriging interpolation on walk bridge image corrupted by drop-out noise

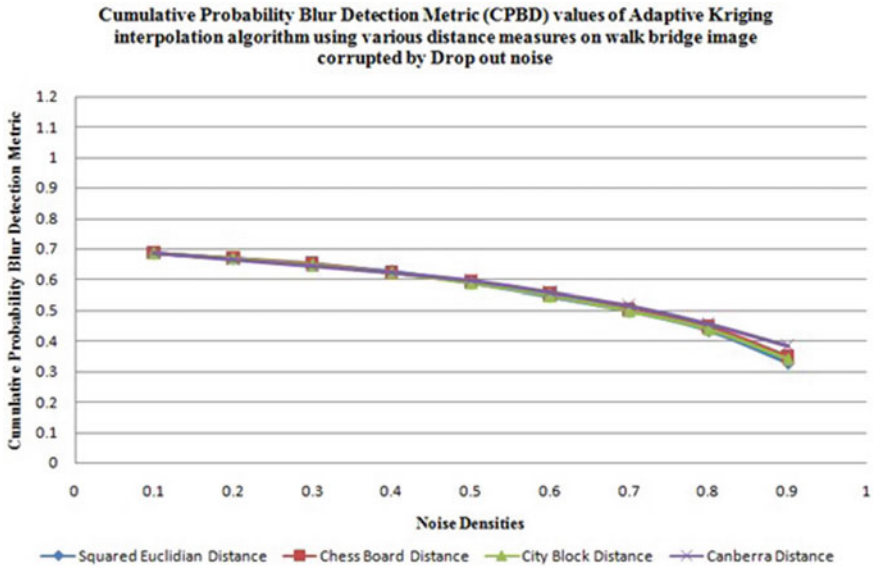


Fig. 4 Degree of blur by different distance measures on adaptive kriging interpolation on walk bridge image corrupted by drop-out noise

It was observed from Table 1 and Fig. 2 that city block distance offers very less error on walk bridge image when compared to other distance measure applied on Adaptive Kriging interpolation. Table 2 and Fig. 3 show city block distance gives higher values of SSIM after 70% on natural images. The City block distance shows a high degree of structural preservation at as relative to other distance metrics, large noise densities. Table 3 and Fig. 4 indicate the squared Euclidean distance offers less blurring at elevated noise density when compared to another distance measure. Figure 5 indicates the presentation of the proposed distance measure on natural images hosted in the university database. It is vivid that the proposed algorithm with the city block distance fairs well in all the images of the database. The City block distance act as a good replacement of Euclidean distance measure on natural images as the latter amplifies the noise due to the squaring nature of the measure and the former has reduced effect. But the degree of blurring is less in Euclidean distance. So In a natural image due to pixel values occur at closer proximity we rather use first-order distance rather than second-order distance. This reduces the complexity with enhanced noise elimination capability with good information preservation.



Fig. 5 Visual output of proposed algorithm corrupted by 90% drop-out noise on standard database images

4 Conclusion

An Adaptive Kriging Interpolation algorithm using city block distance is proposed. The use of first-order measures offers reduced error and preserves the structure of the image. The use of city block distance reduces the complexity of the algorithm while hardware implementation. The algorithm eliminates noise at high noise densities with excellent information capability in the presence of dropout noise. The algorithm is adaptive but still, the blur is compromised to a superior coverage making the algorithm a noticeable choice for the elimination of drop-out noise.

References

1. Mafi M, Izquierdo W, Adjouadi M (2020) High impulse noise removal in natural images using conventional neural networks. National Science Foundation (NSF), Dissertation Year Fellowship (DYF). IEEE, pp 0673–0677. ISBN: 978-1-7281-3783-4/20
2. Ali H (2016) A new method to remove sap noise in magnetic resonance images. IEEE, pp 155–160. ISBN: 978-1-5090-3267-9/16
3. IsmaIrum MS, Raza M, Mohsin S (2015) A nonlinear hybrid filter for sap noise removal for color images. *J Appl Res Technol* 13:79–86
4. Lu CT, Chen YY, Wang LL, Chang CF (2016) Removal of salt-and-pepper noise in the corrupted image using a three-values-weighted approach with variable-size window. *Pattern Recognit Lett* 80:188–199
5. Qistina A, Taha Md, Ibrahim H (2020) In: Jamaluddin Z, Ali Mokhtar MN (eds) Reduction of salt-and-pepper noise from digital grayscale image by using recursive switching adaptive median filter. *Sympo SIMM 2019. LNME*, pp 32–47
6. Kandemir C, Kalyoncu C, Toygar Ö, Gusa G (2015) A-weighted mean filter with spatial bias elimination for impulse noise removal. *Digit Signal Process* 46:164–174. <https://doi.org/10.1016/j.dsp.2015.08.012>
7. Vasanth K, Senthilkumar J (2015) Decision-based good-neighborliness unsymmetrical trimmed variants filter for the removal of high-density salt and pepper noise in images and videos. *Signal image and video processing. IViP*, vol 9. Springer, London, pp 1833–1841
8. Christo MS, Vasanth K, Varatharajan R (2019) A decision based asymmetrically trimmed modified winsorized median filter for the removal of salt and pepper noise in images and videos. *Multimed Tools Appl*. <https://doi.org/10.1007/s11042-019-08124-9>
9. Vasanth K (2021) Impact of distance measures in Shepards interpolation algorithm on natural images corrupted by outliers. In: *ICICV conference paper, proceedings of the third international conference on intelligent communication technologies and virtual mobile networks (ICICV 2021)*, pp 1046–1050
10. Kishorebabu V et al (2017) An adaptive decision-based interpolation scheme for the removal of high-density salt and pepper noise in images. *EURASIP J Image Video Process* 2017:67
11. Zhang P, Li F (2014) A new adaptive weighted mean filter for removing salt and pepper noise. *IEEE Signal Process Lett* 21(10):1280–1283
12. Erkan U, Gökrem L, Enginoğlu S (2019) Adaptive right median filter for salt and pepper noise removal. *Int J Eng Res Dev UMAGD* 11(2):542–550. <https://doi.org/10.29137/umagd.495904>

Implementation of Reed–Solomon Coder and Decoder Using Raspberry PI for Image Applications



Kallepalli Bapayya and Bagadi Kesava Rao

Abstract The Reed–Solomon codes are multilevel forward error-correcting block codes in which the encoder operates on byte stream data. Reed–Solomon codes are represented as RS ($n = 23$, $k = 17$) block codes. The encoder takes input symbol data ($k = 17$) and adds ' $n - k$ ' ($t = 6$) redundant information. The parity bits/symbols contribute an ' n ' (23) symbol code word. A Reed–Solomon decoder capacity of correction is up to ' t ' (3) symbols of the code word, where $2t = n - k$ (6). The output of the encoder is n symbols comprising of ' $n - k$ ' parity symbols and k information symbols. The burst error is the condition due to noise interference in the digital data due to reasons such as thunder, white noise, and scratch on a DVD which can be handled optimistically by the proposed block codes. The proposed RS coder and decoder will be able to detect the error and recover the original data from redundant information during encoding. The algorithm is being developed and implemented using Raspberry Pi using Python programming; various test sequences are given as input to the system with and without error to evaluate the error-correcting capability of the system.

Keywords Redundant · Reed–Solomon · Raspberry Pi · Python · Burst error

1 Introduction

Digital transmission and storage management are associated with the high availability of data to avoid retransmit the failed packet and backing up the critical data. Error detecting and correcting codes play a major role to recover the data from the fault. In digital communication, errors are of two types: random error and burst error. The errors which happen randomly in variable locations of the byte stream sequence are

K. Bapayya (✉) · B. K. Rao
Department of ECE, MGIT, Hyderabad 500075, India
e-mail: kbapayya_ece@mgit.ac.in

K. Bapayya
KL Univeristy, Guntur, Andhra Pradesh, India

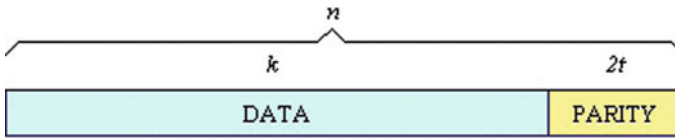


Fig. 1 RS data frame representation

a random error for which algorithms such as Viterbi, convolutional codes can be deployed. On other hands, the errors are sometimes burst in nature where continuous bits got affected due to noise and very side-by-side bits got affected, for an instance in a byte stream of 92-bits, 20 bits got inverted ‘0’s to ‘1’s and vice-versa. Especially, block codes such as Reed–Solomon are linear block codes where the encoder adds redundant information using linear-feedback shift registers (LFSRs) [1], and the code word is generated. The advantage of such codes is to retrieve the information upon error with the capability to correct up to $(n - k)/2$ symbols.

RS (255, 247) is used in Digital Video Broadcasting (DVB) [2], RS (255, 245), RS (252, 224), RS (240, 200), RS (360, 280), RS (246, 164), RS (400, 240), RS (32, 28), RS (255, 251), RS (7, 3) are available as per complexity of the application [3]. (204, 188) for Digital Video Broadcasting—Terrestrial application. RS codes are suitable for high-speed applications in HDTV, optical communications, and ATM.

RS (255, 223) is used in deep space applications in Voyagers. RS (32,28) for DVDs to retrieve data loss. An optimistic RS (23, 17) encoder [1], **as well as decoder**, is proposed which can be also used to design RS (225, 223) and RS (204, 188) [2]. RS (23, 17) takes 17 symbols as an input code words, adds 6-symbols to input to form a 23-symbol encoded data. These 6-symbols are generated using an LFSR’s which has a multiplexer to merge input with the code word. For an instance, if the received codeword, $r = [1\ 0 \dots 0\ 1\ 1\ 138\ 127\ 40\ 232\ 79\ 206]$, then the corresponding syndromes are $[222\ 172\ 13\ 191\ 219\ 186]$ [1] available for demand applications such as (255, 245), (252, 224), (240, 200), (360, 280), (246, 164), (400, 240), (32, 28), (255, 251), and (7, 3) shift registers have been introduced have turned bit ‘1’ to bit- ‘0’ few have change in the pattern where the ‘0’-bit got replaced with ‘1’ and vice-versa. s and ‘1’ is the case where the bits: this type (Fig. 1).

The paper is structured as follows. Section 2 focuses on the basic details of Reed–Solomon codes; Sect. 3 describes the methodology used, the experimental setup and result in analysis shows in Sect. 4; finally, Sect. 5 gives the conclusion and followed by the feature scope of this work.

2 Reed–Solomon Codes

The communication channel is open and prone to errors, and noise is entered into the data stream due to aging of the circuit, components, white noise, or occurrence

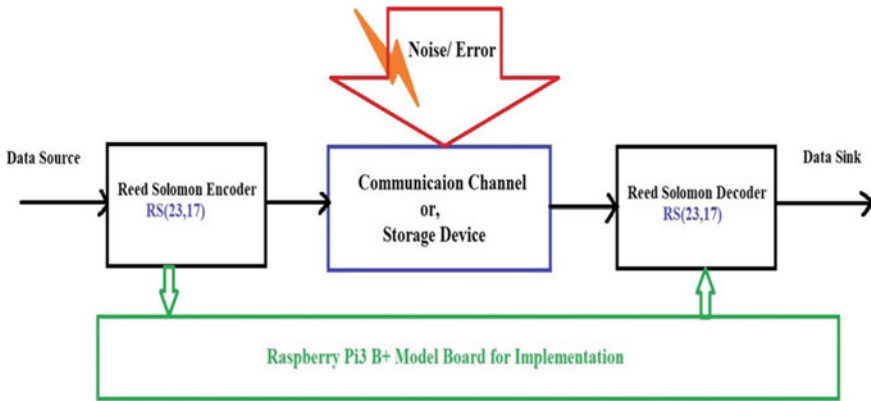


Fig. 2 Typical communication channel

of thunder during electromagnetic wave propagation. The errors may also be due to tampering of the portion of the hard-disk drive as shown in Fig. 2

2.1 RS (23, 17) Encoding

Reed–Solomon encoding that is RS (23, 17) is constructed with series of LFSR’s arranged cyclically with feedback [4]. The input data are divided into symbols (17 symbols), and these symbols, usually, 8-bits per symbol are passed through various stages (Six-stages) of the circuit. Each stage has an XOR/ADDER, a MULTIPLIER, a REGISTER [2] and which will operate respectively to give an 8-bit encoded data-1 which is accumulated using the switch at the endpoint.

The next turn is for symbol-2 which will gain propagate through the same stages to give newly encoded data-2. The iteration is performed unless whole input symbols have been processed. At the end of this iteration, the accumulated data which were encoded are final redundant data and are added to the input raw data to give the final codeword of 23 symbols. The detailed encoder diagram with LFSR is shown below in Fig. 3.

Following are the steps necessary to operate RS (23, 17) Encoder.

1. Switch-1 is ‘CLOSED’ to transfer message symbols into the (n-k) shift register.
2. The switch-2 position is ‘DOWN’ to accumulate raw data as it is to output register.
3. Switch-1 = ‘OPEN’, switch-2 = ‘UP’ to accumulate encoded symbol to the output register.
4. Repeat Step-2, Step-3, respectively, for (n-k) cycles to accumulate remaining symbols to accumulate in output register as CODEWORD.

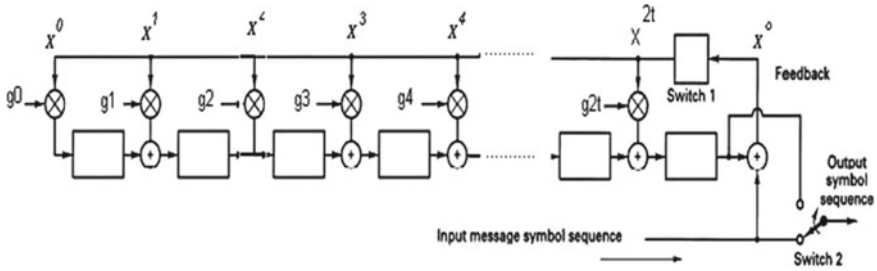


Fig. 3 Detailed RS (23, 17) encoder

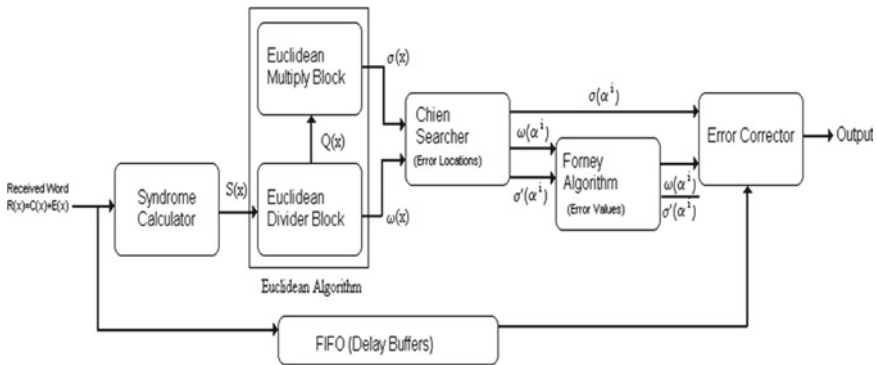


Fig. 4 General RS decoder system

2.2 RS (23, 17) Decoding

Reed–Solomon decoder has basic 5-stages through which the received signal is propagated, namely (a) Syndrome calculator, (b) Euclidean algorithm, (c) Chen searcher, (d) Forney algorithm, and (e) Error corrector by the position which is shown in Fig. 4.

2.2.1 Syndrome Calculator

The received signal $R(x)$ is combination of $C(x)$ and $E(x)$

$$R(x) = C(x) + E(x) \tag{1}$$

where if $E(x) = 0$, data are not affected by noise else the noise in the channel has affected the data [5]. Syndrome operation is part of decoding which is basic verification of occurrence of error or not. The above figure shows the syndrome calculation, where if the result after the multiplication of unity elements is non-zero, then it is said to be an error has occurred. If the result is zero, then the error-free

result occurs. Syndrome calculation, $S(x)$ depends on $E(x)$ [2]

$$S(x) = r(x) \bmod g(x) \tag{2}$$

$$\begin{aligned} R(x)/g(x) &= q(x) + S(x)/g(x) \\ &= [e(x) + c(x)]/g(x) \\ &= q(x) + S(x)/g(x) \end{aligned} \tag{3}$$

Since $C(x)$ divisible by $g(x)$ and $e(x)/g(x) = q_e(x) + S(x)/g(x)$. For the $e(x)$, ‘ $n - k$ ’ are symbols limit the search. No errors gives the syndrome polynomial $S(x) = 0$.

$$r(x) = m(x) + e(x) \tag{4}$$

$$s(x) = r(x)/g(x) \tag{5}$$

where m : original message, r : received signal, e : error signal, g : generator polynomial

aa: for i in 1 to n generate
 $r_i \leq m_i \text{ xor } e_i$;
 $s_i \leq r_i \bmod g_i$;

end generate;

$S(x) = \sum_{i=0}^{2^i-1} S_i \cdot X^i$ with $S_i = \sum_{j=0}^{n-1} r_j \cdot \alpha^{ij}$, where α is a root of the primitive polynomial and therefore a primitive element in $GF(2^8)$. The internal schematic of syndrome calculator shown in Fig. 5.

$$p(x) = x^8 + x^4 + x^3 + x^2 + 1 \tag{6}$$

The syndrome received data are shown in Table 1.

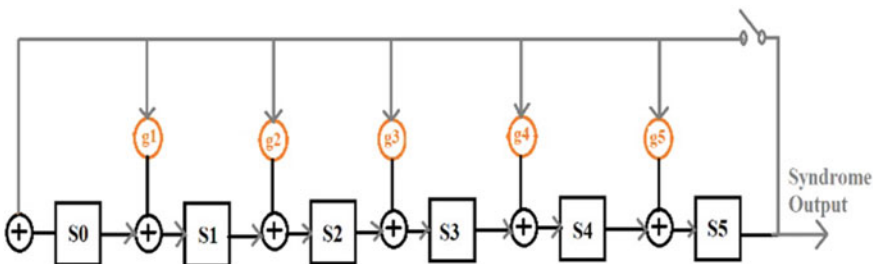


Fig. 5 Syndrome calculator

Table 1 Syndrome for received data

Received Bits	Shift Register					
	S0	S1	S2	S3	S4	S5
1 0 0 1 1 1 1	0	1	1	0	0	0
1 0 1 1 1 1 1	1	0	0	0	0	0
1 0 1 0 1 0 1	0	1	1	0	0	0
1 0 0 0 0 0 0	1	0	0	0	0	0
1 0 1 1 1 1 1	0	0	1	0	0	0
1 1 0 0 1 1 0	0	1	0	0	0	0

2.2.2 Euclidean Distance

Error locator polynomial = $\sigma(x)$ and an error magnitude polynomial = $\omega(x)$ are next attempt in decoder. This is done by applying

$$S(x)\sigma(x) = \omega(x) \text{ mod } x^{2t} \tag{7}$$

$$S(x) * B_i = R_i \text{ mod } x^{2t} \tag{8}$$

$$R_{-1} = x^{2t}, R_0 = S(x), \tag{9}$$

$$B_{-1} = 0, \text{ and } B_0 = 1. \tag{11}$$

Euclidean divider block is as shown below.

$$R_{-1}(x) = x^{20}, \tag{12}$$

$$R_0(x) = S(x) = ax^{19} + x^{18} + 1 \tag{13}$$

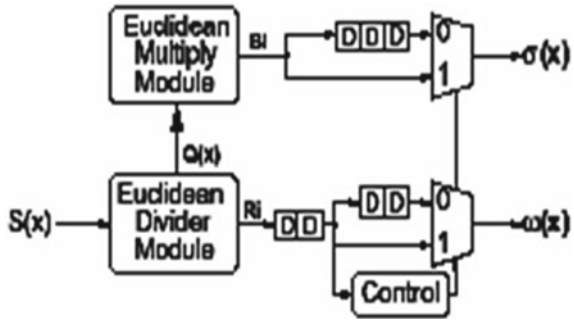
$R_i = R_{i-2} - R_{i-1}Q_{i-1}$ and $B_i = B_{i-1} - Q_{i-1}B_{i-1}$ [1]. The Euclidean algorithm has (a) multiply block, (b) divider block as shown in Fig. 6. The divider module divides, R_{i-2}/R_{i-1} , in each iteration to generate the quotient Q_{i-1} remainder R_i . Once k -iterations are over, the divider becomes $\omega(x)$. Multiply module can be generated $\sigma(x)$, error locator polynomial.

2.2.3 Chien Search/Forney Algorithm

An infinite-degree syndrome polynomial S can be represented by

$$S(x) = S_1x + S_2x^2 + \dots + S_{2t}x^{2t} + S_{2t+1}x^{2t+1} + \dots \tag{14}$$

Fig. 6 Euclidean multiply and divider module



The polynomial for error magnitude is given by

$$\Omega(x) = [1 + S(x)]\Lambda(x) \tag{15}$$

$$\Lambda(x)[1 + S(x)] \equiv \Omega(x) \pmod{x^{2t+1}}$$

$$e_{ik} = \frac{-X_k}{\Lambda'(X_k^{-1})} \tag{16}$$

where ‘ e_{ik} ’ represents error magnitude

2.2.4 FIFO Memory, Delay Buffers

It is used to sequence the data in order of received symbols following the latency. The FIFO is very useful to maintain synchronous between the incoming data and outgoing data. Shift registers are used in this process in which each shift register will handle the series of bits that further undergo the operation according to the algorithm well known as FIFO.

2.2.5 Performance of RS Codes Against Burst Noise

Consider RS $(n, k) = (23, 17)$, where each symbol is an 8-bit representation that is a byte. Since $(n - k) = 6$, this code can correct any three symbols which are 24-bits in a burst as indicated in Fig. 7 (Errors in code word block of 23 symbols). Assume the noise burst lasting for 20-bit continuously has entered the system in Fig. 8 as:

H.264-based systems can be realized using the proposed system. The overhead information increases the bandwidth which is the drawback. The asynchronous communication systems need handshaking signals which can be avoided as we can easily decode the lost packet upon previously received packet information, and acknowledgment can be avoided which is mandatory during packet.

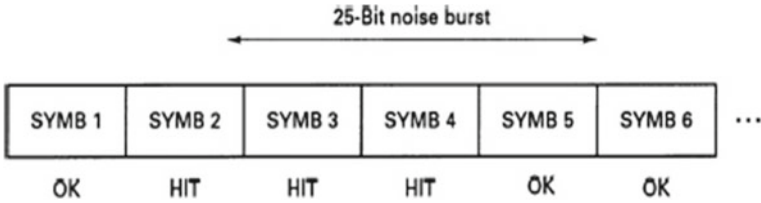


Fig. 7 Noise burst in a system

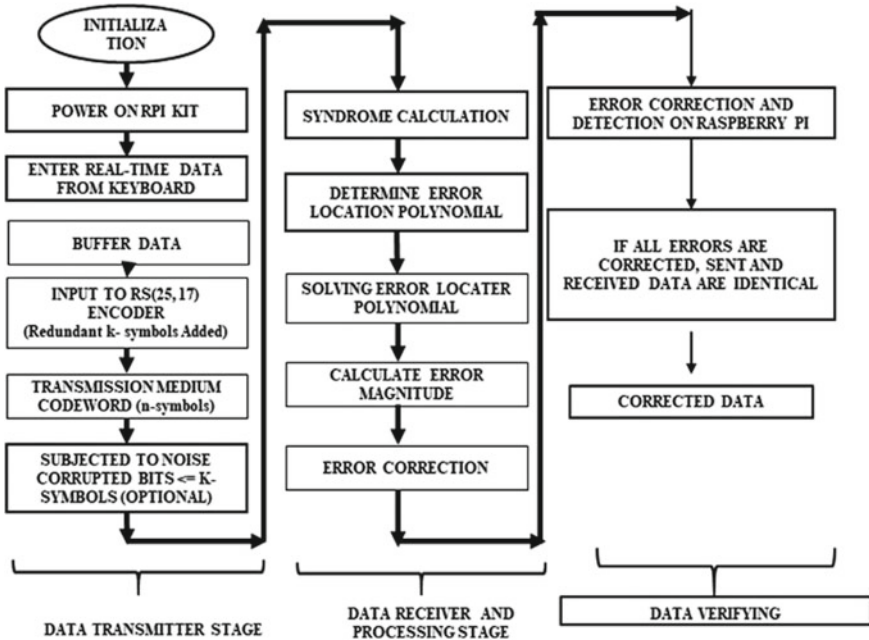


Fig. 8 Methodology for the proposed framework to Reed–Solomon codes

2.2.6 Galois Field Arithmetic

Reed–Solomon codes belong to mathematics, where the finite field has the property that arithmetic operations (+, −, ×, / etc.) are applied on-field elements [6] and always have a result in the field.

2.2.7 Generator Polynomial

The proposed system codeword uses special polynomial given:

$$g(x) = (x - \alpha)^i(x - \alpha^{i+1}) \dots (x - \alpha^{i+2t}) \tag{17}$$

The valid codeword is exactly divisible by the generator polynomial as shown below [7],

$$c(x) = g(x), i(x) \tag{18}$$

where, $g(x)$ = generator polynomial, $i(x)$ = information block, $c(x)$ = valid code word and α = primitive element.

3 Methodology

Reed–Solomon codes are forward error-correcting codes where the redundant information is used to retrieve the original data though subjected to noise in the channel. Its error-correcting capability is $n - k/2$ symbols. The RS codes can be realized using a state-of-art board like Raspberry Pi whose operating frequency is up to 2.14 GHz. Embedded systems have been always an important technology in the field of system security, the Internet of Things, and distributed intelligence. The implementation of Reed–Solomon codes on state-of-art boards like Raspberry Pi is always preferable for the embedded engineer as an embedded solution. The applications such as Digital Video Broadcasting, image processing in IoT, and algorithm development can be easily realizable using Raspberry Pi compared to FPGA. FPGA technology may optimize the power and area, but as far as multitasking is concerned with scheduling of tasks and low-cost hardware, Raspberry Pi plays a key role. Raspberry Pi gives a huge response for cheap and easy solutions for multithreading and image processing algorithms. The program development environment and multi-language support are an added advantage for Raspberry Pi.

In the proposed system, user gives real-time data serially through a GPIO pin. There is a provision to input byte stream data through the keyboard. One more way to give image data is through RPi camera, IMG_IN. The input data are buffered and provided as input to RS (23, 17) encoder block. The code is written to encode the serial data with redundant information in cyclic codes. The error-correcting capability of RS (23, 17) is $t = (n - k)/2$, $t = 3$ —symbol errors may only be corrected in units of single symbols (typically 8 data bits); Reed–Solomon coders work best for correcting burst errors. The decoder has various stages: Stage-1 is syndrome calculation to notify whether the error has occurred or not. Here, the input received symbols are divided by the generator polynomial. The result should be zero.

The parity is placed in the codeword to ensure that code is exactly divisible by the generator polynomial. If there is a remainder, then there are errors. The remainder is called the syndrome. Python-based code is written for syndrome calculation. Stage-2 is error locator polynomial to calculate the error values and their respective locations Stage-3: Perform the Chien search to find the roots of $\sigma(x)$. Stage-4 is to find the magnitude of the error values using the Forney ‘s algorithm. Stage-5 is to correct the received word $c(x) = e(x) + r(x)$ to generate IMG_OP image. All the stages were implemented using Python code and the necessary libraries in Python code.

The code can handle low-resolution images and was tested, but can also process high-resolution images too by dividing these HD images into multiple blocks of byte stream data. The low-resolution images are subjected to test by giving it to an encoder, and then, the noise is added as shown in figures. It is seen that the errors were rectified upon decoding, and reformation of the image was successfully performed.

4 Experimental Setup and Result Analysis

The main of this work is to implement Reed–Solomon codes for image applications using Raspberry Pi device which is low cost compared to the FPGA system. Another advantage is to verify the coding and decoding implemented using Python programming. As per the methodology discussed in Sect. 3, initially, the byte stream data are encoded in the form variables such as:

```
SECRET_DATA = text to be encoded
BINARY_DATA = converted data
LENGTH_DATA = length of data
ENCODED_DATA = final encoded data with redundant information which is
stored in a temporary file named 'encoded.bin'. At the receiver side, the RS
decoder decodes the data and removes redundant information, and finally gener-
ates original data. The experimental setup is shown in Fig. 9 and is evident that, if
the errorless data are transmitted during communication, the green LED always
blinking.
```

Initially started, verified the same codes for text-based input, and the output is shown in Fig. 10. It is also seen that the byte stream upon changing of information (positional errors) got retrieved successfully as mentioned in Fig. 11.

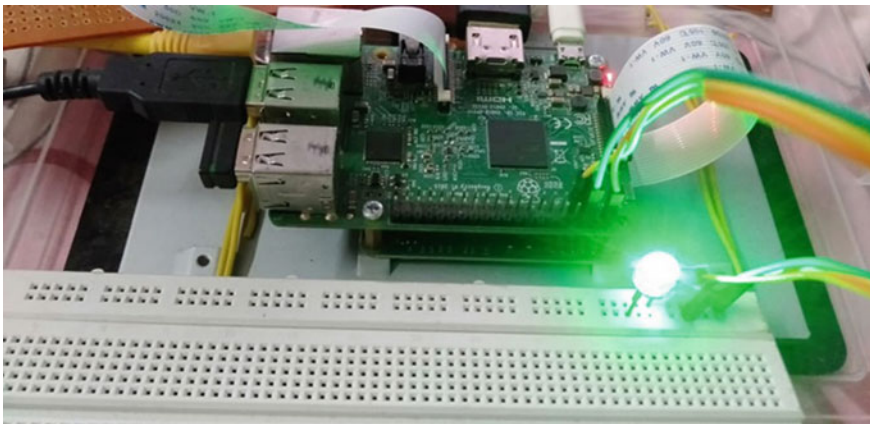


Fig. 9 Raspberry *Pi*-based setup for Reed–Solomon codes

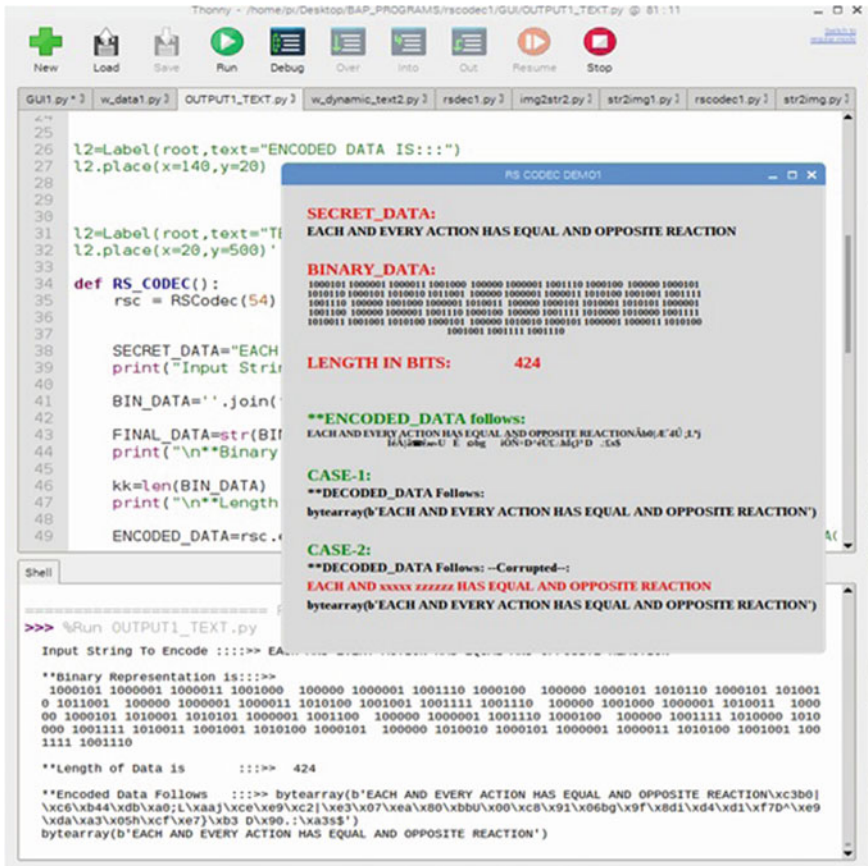


Fig. 10 RS codec for text-based data

After applying the above byte stream, the Python IDE window showing the output of error position and error-correcting capability of the given byte stream. This was shown in Fig. 12.

For validation of the algorithm, we tested the same codec using some images which were corrupted and send to the transmitter and receiver pins of Raspberry Pi. Here, the images are given as input to the RS codec then tested the errors. RS (23, 17) can be corrected up to 3-symbols among 23 symbol data. If the error exceeds this limit of 3-symbols in burst or in random in 23 symbol, the algorithm fails to correct. The output of Python IDE is shown in Fig. 14 (Fig. 13).

Some of the experimental results for various corrupted images shown in Figs. 15 and 16 give the noise removal of the image using RS codec. If the transmitted data and the received data are the same, can be compared, and upon errorless communication can be indicated by blinking LED connected to Pin-4 of Raspberry Pi as shown in Fig. 9.

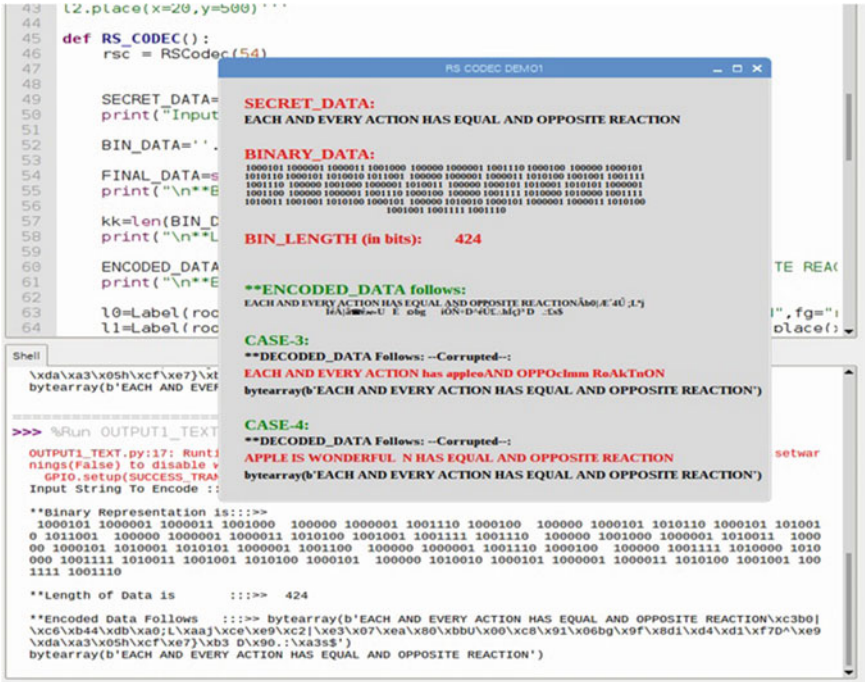


Fig. 11 Codec for burst, random, positional o/p

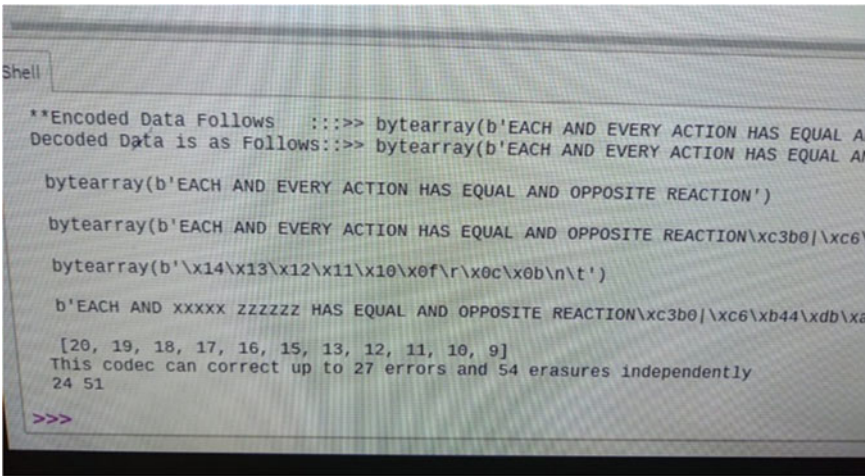


Fig. 12 IDE window showing error position and error-correcting capability



Fig. 13 Image-based input to RS codec

Another way attempted with interfacing keyboard with RPi to test the proposed method for real-time data streaming. Figure 17 gives how to interface keyboard with RPi and some LED also connected to test the byte streaming using RS codec. Real-time data streaming is realized and data verification and indication byte-by-byte through LED pattern for decoded data verification. The real-time signaling can also be observed by sending data through the keyboard to the RPi board as shown in Fig. 17. The data streaming is shown in Fig. 18

5 Conclusion

Reed–Solomon codes, RS (23, 17), can correct burst errors with $(n - k)/2$ symbols. The cyclic codes generate a unique code which is redundant information. The overhead information is successfully retrieving original data upon errors. High-resolution images are crucial in satellite-based images where a certain portion of the image may

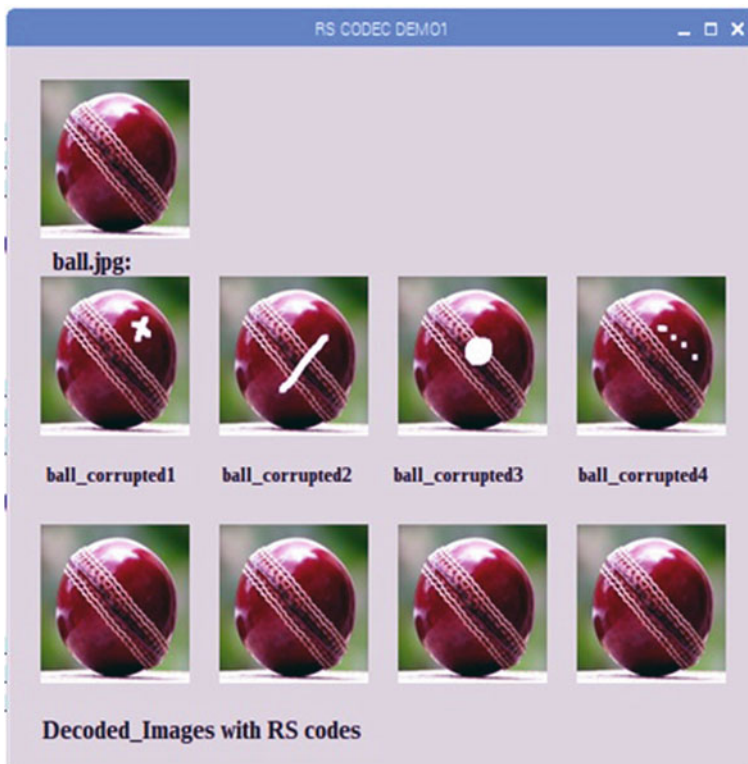


Fig. 15 IRS codec for ball_corrupted'n

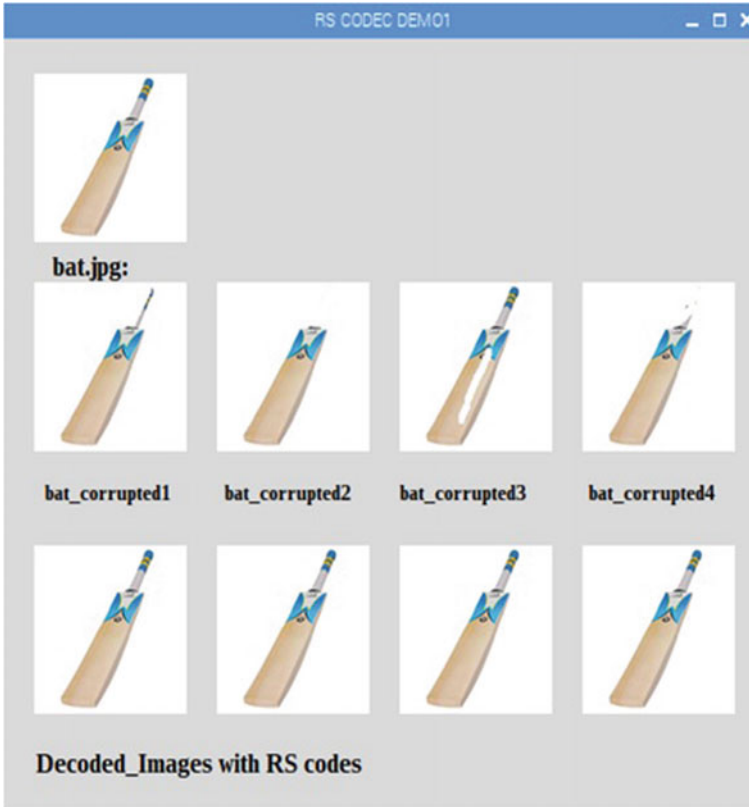
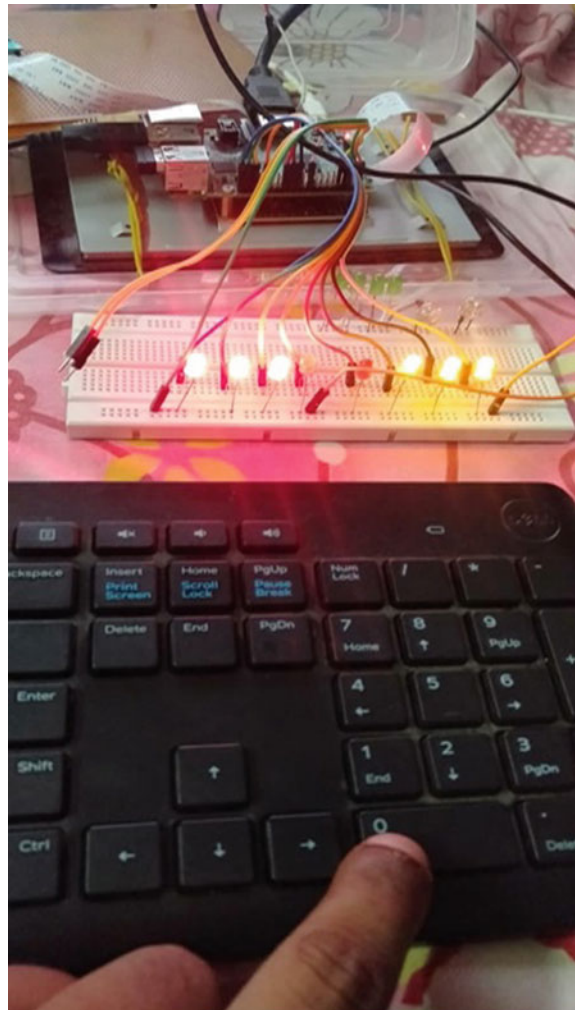
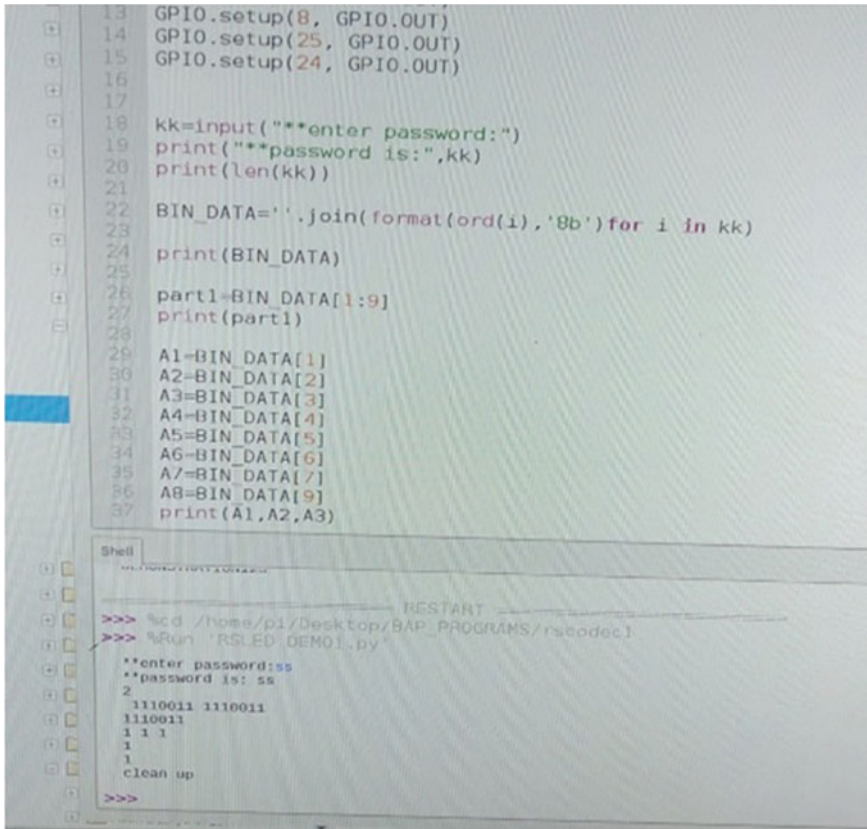


Fig. 16 IRS codec for bat_corrupted'n

Fig. 17 Interfacing keyboard for real-time data





```
13 GPIO.setup(8, GPIO.OUT)
14 GPIO.setup(25, GPIO.OUT)
15 GPIO.setup(24, GPIO.OUT)
16
17
18 kk=input("**enter password:")
19 print("**password is:",kk)
20 print(len(kk))
21
22 BIN_DATA=''.join(format(ord(i),'0b') for i in kk)
23
24 print(BIN_DATA)
25
26 part1=BIN_DATA[1:9]
27 print(part1)
28
29 A1=BIN_DATA[1]
30 A2=BIN_DATA[2]
31 A3=BIN_DATA[3]
32 A4=BIN_DATA[4]
33 A5=BIN_DATA[5]
34 A6=BIN_DATA[6]
35 A7=BIN_DATA[7]
36 A8=BIN_DATA[9]
37 print(A1,A2,A3)
```

```
Shell
-----
RESTART
>>> %cd /home/pi/Desktop/BAP_PROGRAMS/rscodec1
>>> %Run 'RSLED_DEMO1.py'
**enter password:ss
**password is: ss
2
 1110011 1110011
1110011
 1 1 1
 1
 1
clean up
>>>
```

Fig. 18 Snapshot of Streaming

Acknowledgements The heading should be treated as a 3rd-level heading and should not be assigned a number.

References

1. FPGA-based area-efficient RS (23, 17) codec (2015). Accepted: 29 June 2016 © Springer, Berlin Heidelberg
2. Holzbaur L, Polyanskaya R, Polyanskii N, Vorobyev I (2020) Lifted Reed-Solomon codes with application to batch codes. arXiv preprint [arXiv:2001.11981](https://arxiv.org/abs/2001.11981)
3. Jinzhou Z, Xianfeng L, Zhugang W, Weiming X (2012) The design of a RS encoder. In: Future computing, communication, control and management, vol 144. Lecture Notes in Electrical Engineering, pp 87–91
4. Polyanskaya R, Polyanskii N (2019) Batch codes based on lifted multiplicity codes. In: Proceeding IEEE XVI international symposium problems redundancy information and control systems

5. Kumar A, Sawitzki S (2006) High throughput and low power Reed–Solomon decoder for ultra wide band. In: Proceeding of intelligent algorithms in ambient and biomedical computing, vol 7. Springer, pp 299–316
6. Choi SW, Choi SS, Lee H (2006) A FEC architecture for UWB system. In: Proceeding of IEEE 64th vehicular technology conference, pp 1–5
7. Hsu IS, Reed IS, Truong TK, Wang T, Yeh CS, Deutsch LJ (1982) The VLSI implementation of a Reed–Solomon encoder using Berlekamp’s multiplier algorithm. TDA Progress Report, pp 72–86
8. Chien RT (1964) Cyclic decoding procedure for the bose-chaudhurihocquenghem codes. *IEEE Trans Inf Theory* 10(4):357–363
9. Skachek V (2018) Batch and PIR codes and their connections to locally repairable codes. In: Network coding and subspace designs. Springer, pp 427–442
10. Samanta J, Bhaumik J, Barman S (2015) Compact RS (32, 28) encoder. In: Proceeding of 1st international conference on intelligent computing and applications (ICICA 2014) advances in intelligent systems and computing, NIT DGP, Dec 2014, vol 343, pp 89–95
11. Wu X, Shen X, Zeng Z (2012) An improved RS encoding algorithm. In: Proceedings of 2nd IEEE consumer electronics communications and networks, pp 1648–1652
12. Kumar S, Gupta (2011) Bit error rate analysis of Reed–Solomon code for efficient communication system. *Int J Comput Appl* 30(12):0975–8887

Software Defined Radio-Based ELINT System for Geolocation of RF Emitters



D. Mallikarjuna Reddy, S. Rani Surender, and Nikhitha Karennagari

Abstract A Software Defined Radio (SDR) is a radio where digitizing the signal allows circuitry previously implemented in dedicated hardware to be moved in to the digital domain. After the signal is digitized, software can control the channel frequency, bandwidth and modulation format. The combination of wideband front ends and powerful processors makes software radios an ideal platform for ELINT, COMINT, SIGINT applications. This paper aims at introducing SDR-based ELINT system for geolocation of RF emitters from space and airborne platforms. The ELINT system proposed consists of three receivers placed in a defined configuration to receive the signal from the RF emitter simultaneously. For precise geo location of the RF emitters, it is required to time synchronize the three receivers to an accuracy of < 5 ns. A novel method of relative time synchronization based on Time to Digital Conversion (TDC) technology is discussed to enable the SDR receiver to time stamp the received RF pulse data precisely to get its Time of Arrival (TOA) information. The Time of Arrival information of the received RF pulse at each receiver is used to extract the Time Difference of Arrival (TDOA) and hence used in geolocation of RF emitters by solving the hyperbolic equations.

Keywords Software defined radio · ELINT · COMINT · SIGINT · Time to digital conversion · Time of arrival · GPS disciplined oscillator · Time difference of arrival

1 Introduction

Geolocation of RF emitters on the earth enables important applications in both military and civilian domains. For accessing the remote areas, it is often advantageous to mount these ELINT receivers on UAV's and Satellites. Passive geolocation using Time Difference of Arrival (TDOA) is best suited for high bandwidth emitters like radars. Knowing the time difference of arrival between the emitter and two sensors geolocalizes emitter to the points of a hyperbola. Having a third sensor (second

D. Mallikarjuna Reddy (✉) · S. Rani Surender · N. Karennagari
DRDO, Hyderabad, Telangana, India
e-mail: mallikarjuna.reddy@dsp.drdo.in

© The Author(s), under exclusive license to Springer Nature Singapore Pte Ltd. 2022
P. Kumar Jain et al. (eds.), *Advances in Signal Processing and Communication Engineering*, Lecture Notes in Electrical Engineering 929,
https://doi.org/10.1007/978-981-19-5550-1_42

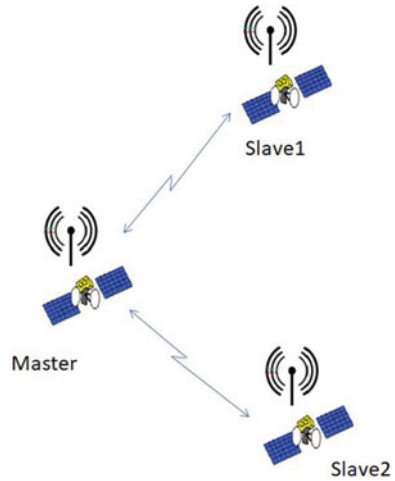
471

TDOA measurement) helps in location fixing the emitter at the intersection of the two hyperbolae. TDOA technique is effective for emitter localization because it requires the transmission time only without increasing the computational load [1, 2]. But it needs time synchronization among the three ELINT receivers for precise geolocation of the RF emitter. Time synchronization is required because it uses time difference of arrival at each of the receivers. However, each receiver that consists of hardware holds the different response characteristic each other. This response characteristic needs to be exactly the same at each receiver to collect the RF emitter data. If the response is not characterized exactly, it increases the error of TDOA measurement. In order to get higher precision of time difference, it uses the sampling data from multi receiver to perform correlation algorithm [3]. Therefore, experimental data collected by high precision synchronization system is very important. This paper proposes SDR-based hardware configuration for ELINT receivers using TDOA technique for geolocation of RF emitter and a novel time synchronization method using Time to Digital Conversion technique to synchronize them. The scope of this paper is limited up to the RF emitter data acquisition and generation of time tagged IQ samples and Pulse Descriptor Word (PDW) for the received RF pulse. Time synchronization hardware and software details are discussed in Sect. 2.1, SDR-based RF Transceiver is detailed in Sect. 2.2, Integration of ELINT Receiver with Time synchronization, Logic device FPGA Zynq Zynq Ultra Scale MPSoC used for data acquisition and processing with internal processor is discussed in Sect. 2.3. Integration of ELINT sub systems hardware and software including Time Synchronization with communication links constituting the ELINT System is presented in Sect. 3. Results of the tests conducted on the individual sub systems and their performance details are presented in Sect. 4.

2 Hardware Architecture

ELINT system for geolocation requires three ELINT receivers with integrated time synchronization modules for precise time synchronization. GPS Disciplined Oscillator is used as the input source of 1 PPS and 10 MHz signals to the TDC unit for measuring the 10 MHz cycles precisely. The three ELINT receivers are configured in Master-Slave configuration and the precisely measured time information is transmitted by the Master to the two Slaves in RF mode for time synchronization at every 1 PPS event. The RF communication for time synchronization among the ELINT receivers is in S Band with a transmit power of 1 W enabling to place the ELINT receivers in the distance range of 50–100 km. On receiving the RF emitter signal at the ELINT receiver, it time stamps the TOA of the RF Pulse using the time information provided by the Time Synchronization unit. The time tagged RF pulse data from all the three ELINT receivers is processed at a centralized station for extracting the precise location of corresponding RF emitter using TDOA hyperbolic solutions.

Fig. 1 ELINT receivers on a satellite platform in master-slave configuration



2.1 Time Synchronization—Time to Digital Conversion (TDC)

The absolute time stamp accuracy using UTC for the received signal is one of the most important factors for a TDOA system. In order to achieve the best location fix accuracies of the emitters, all the ELINT receivers clock times should be synchronized to an accuracy of better than 5 ns. In the configuration shown in Fig. 1, satellites are in master-slave configuration and any satellite can act as master with other two in slave configuration. The GPS receiver in each satellite generates 1 PPS pulse based on absolute time reference of 1.0s from the GPS satellites. Depending on the view from the GPS satellites and due to internal clock operation, the 1 PPS pulse will have a jitter, which may vary from -30 to $+30$ ns.

The satellites for geolocation accommodate GPS receivers, each in the field of view of GPS satellites where the 1 PPS pulse of each will differ by a jitter varying from -30 to 30 ns. Master measures the 1 PPS time pulse with accurate measurement down to ± 100 ps. Similarly let us say, the slaves also measure their 1 PPS with the same level of accuracy down to ± 100 ps (Fig. 2).

Assume Master has recorded the 1 pps measurement as $1.00\text{ s} \pm X\text{ ps}$. Similarly let us say the slaves 1 and 2 have recorded the 1 PPS measurement as $1.00\text{ s} \pm Y\text{ ps}$ and $1.00\text{ s} \pm Z\text{ ps}$. The absolute time is 1 s. Master measures it as $X\text{ ps}$ and the Slave1 and 2 measures it as $Y\text{ ps}$ and $Z\text{ ps}$. With reference to Master, Slave1 has an error of $X \pm Y$ and the Slave2 has an error of $X \pm Z$. Time will be measured using 64-bit counter, where 32 bits represent seconds and remaining 32 bits represent $1/2^{32}\text{ s}$. The Master, Slave1 and Slave2 all will run counters C1, C2, and C3, respectively. Start signal will come from Master. After Start command, the measurement starts from next 1 PPS. After 1 PPS, the master sends the X value and slaves 1 and 2 will adjust its counter with the error with respect to Master X. The Master and

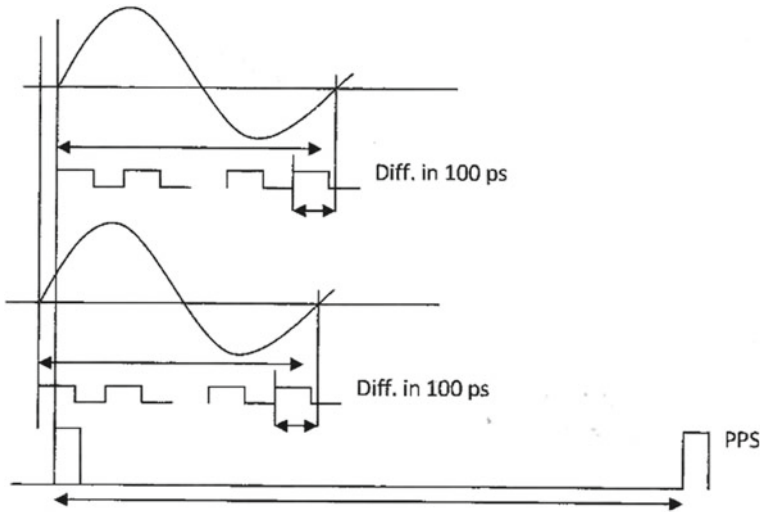


Fig. 2 Time offset measurement using TDC in ps

Slaves measure a count for 100 ms (precisely) w.r.t. to last 1 PPS edge received and create a counter D1, D2, D3. The Master will communicate the D1 to Slaves and the slaves will find the difference between D1:D2, D1:D3 and adjust their counter C2 and C3, respectively. Every 100 ms the Master sends the D1 value for adjustment. Here the slaves synchronize the time to Master, though master has error w.r.t to absolute time. Over several periods of 1 PPS, based on statistics, the Master will adjust the 1 PPS error and will communicate the same to slaves. Over a time of few milli-seconds, the C1, C2, C3 will be running concurrently with less than 1 ns error. The Peak error can be 1 ns just after 1 pps and will slowly reduce. When 1 PPS is not available, the time measurement continues every 100 ms and adjusted every 100 ms from master. The 10 MHz sine wave is used as reference clock from the GPS Disciplined Oscillator (GPSDO) and its time is precisely measured using TDC and a time base of $100\text{ms} < \pm 100\text{ps}$ is created. Every 100 ms time base counter value is D1 for master and D2 and D3 for slaves1 and 2. In absence of 1 PPS, D2 and D3 adjust against D1. The time information is communicated from Master to Slaves through communication Link (Fig. 3).

Master and slaves will exchange time information for synchronization using communication link in S Band using Code Division Multiple Access (DSSS) technique. The time information is transmitted at a data rate of 9.6 Kbps. Code length of 1023 is used for spreading.

The communication receiver sensitivity is around -116 dBm and hence requires S Band transmit power of 1 W having sufficient fade margin for the distance of 100 km. The Data to be transmitted is only 64-bit C1 counter value; 32-bit X and 32-bit D1 value. The C1 value is always w.r.t 1 PPS edge. In case Slaves miss the communication, they can re-sync to C1 value from 1 pps edge.

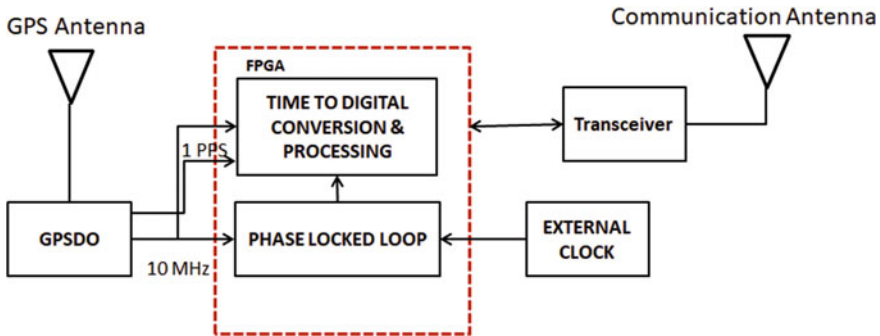


Fig. 3 Configuration of TDC unit with communication link

The time packet may need 32 bytes maximum for transmission (some reserved for other usage). HDLC format will be used with 7E header, bit stuffing and CCITT 16-bit CRC. The communication link works in TDM mode, Master sends packet and TX is switched OFF. It waits for ACK from Slave1 and Slave2. The time update interval can be around 100 ms in which the 100 ms time cycle is divided into 50 ms for TX, 25 ms for Slave1 and 25 ms for Slave2.

2.2 Software Defined Radio—AD9371

Using the AD9371 RF transceiver, ELINT receiver has been realized in a compact size. It is selected for this application as it is designed to have high performance radios across a wideband frequency range with low power consumption levels. It is a highly integrated 12 mm × 12 mm SoC covering 300-MHz to 6-GHz frequency range and supports receive and transmit functions with signal instantaneous bandwidths up to 100 MHz, fully integrated LO and clocking functions and highly advanced on-chip calibration and correction algorithms [4]. The transceiver consists of a 12-bit ADC and DAC supporting sampling rates of 245.76 Msps and 983.04 Msps, respectively. The receiver bandwidth is programmable from 8 to 100 MHz.

The high speed JESD204B interface supports lane rates up to 6144 Mbps. The fully integrated phase-locked loops (PLLs) provide high performance, low power fractional-N frequency synthesis for the transmitter, the receiver, the observation receiver, and the clock sections. All voltage-controlled oscillator (VCO) and loop filter components are integrated to minimize the external component count (Fig. 4).

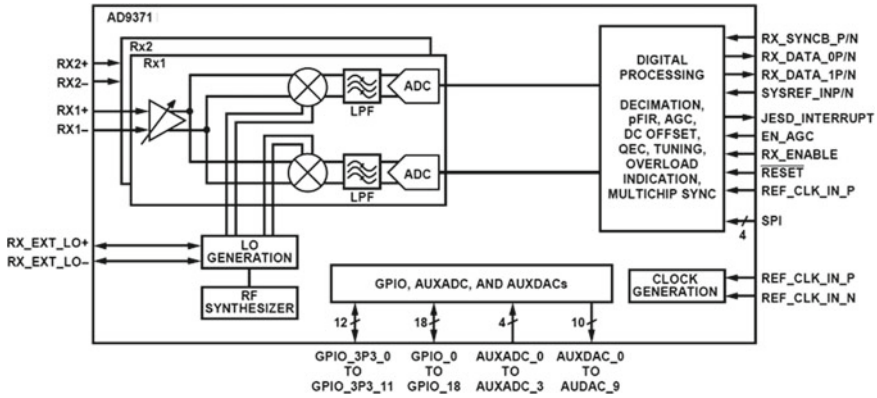


Fig. 4 Internal block diagram of AD9371

2.3 FPGA Sub System—Zynq Ultra Scale MPSoC

Zynq UltraScale+ MPSoC is the Xilinx second-generation Zynq platform, combining a powerful processing system (PS) and user-programmable logic (PL) into the same device. The processing system features the Arm® flagship Cortex®-A53 64-bit quad-core or dual-core processor and Cortex-R5F dual-core real time processor. PS acts as one standalone SoC and is able to boot and support all the features of the processing system. Hence the Cortex®-A53 processor is programmed for configuring the AD9371. The Zynq®UltraScale+™MPSoC includes a pair of Cortex®-R5F processors for real time processing based on the Cortex-R5F MP processor core from Arm [5]. Cortex-R5F MP processor is used for ELINT data acquisition and processing in real time. The PL size (DSP Slices) required for processing the RF emitter signal is adequate enough in this FPGA making it a suitable candidate for this application.

3 ELINT System with Communication Links for Time Synchronization

SDR based ELINT Receiver is developed using the Analog Devices Transceiver AD9371 with a programmable instantaneous bandwidth from 8 to 100MHz. The frequency of the SDR ELINT Receiver can be tuned in steps of 1 KHz in the frequency range of 0.3–6 GHz and the system can dwell in that frequency band for the chosen time interval. The time information is available from the TDC and communication link Unit as discussed in Sect. 2.1 with the required accuracy and defined format to the SDR ELINT receiver to use it for time stamping the TOA of the signal received.

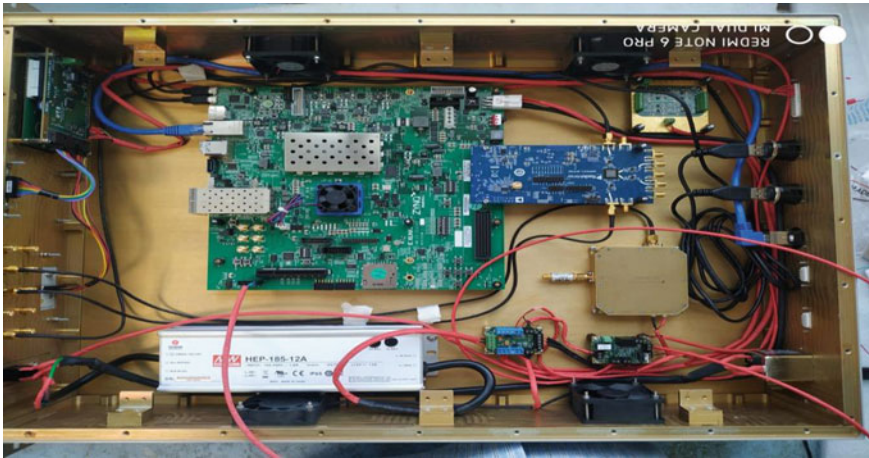


Fig. 5 SDR-based ELINT receiver with Zynq ultra scale MPSoC

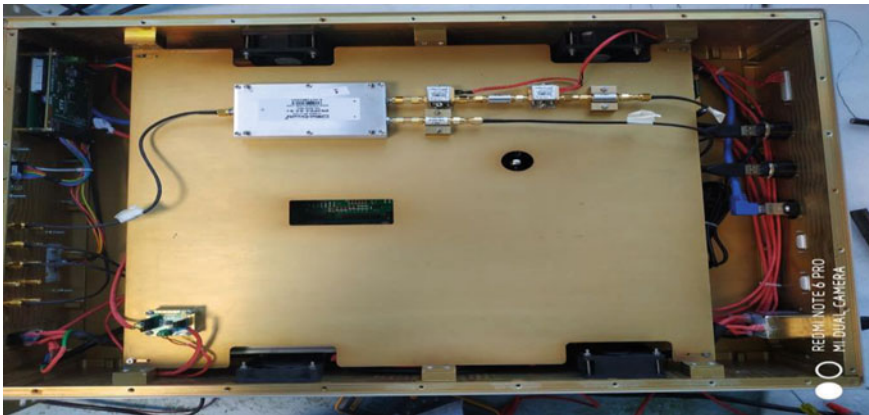


Fig. 6 External LNA in the RX chain of AD9371 with attenuators

The entire 6 GHz band can be scanned in steps of 100 MHz instantaneous bandwidth (Figs. 5 and 6).

To achieve the receiver sensitivity of -90 dBm for an instantaneous bandwidth of 100 MHz, LNA has been introduced in the receive chain. AD9371 has two receive channels and are configured with the required attenuators to get the dynamic range of 70 dB. The three SDR ELINT receivers are placed in a suitable configuration to receive the RF emitter signal simultaneously and also to have the LOS for the communication link used for time synchronization. TDC units require a few minutes (< 5 min) at cold start for them to get time synchronized. Hence before starting the ELINT signal acquisition, the TDC units need to be switched ON and allowed for synchronizing among themselves. SDR ELINT receiver generates an event trigger on receiving the RF emitter signal to the TDC unit on Rs 422 interface. TDC unit in turn

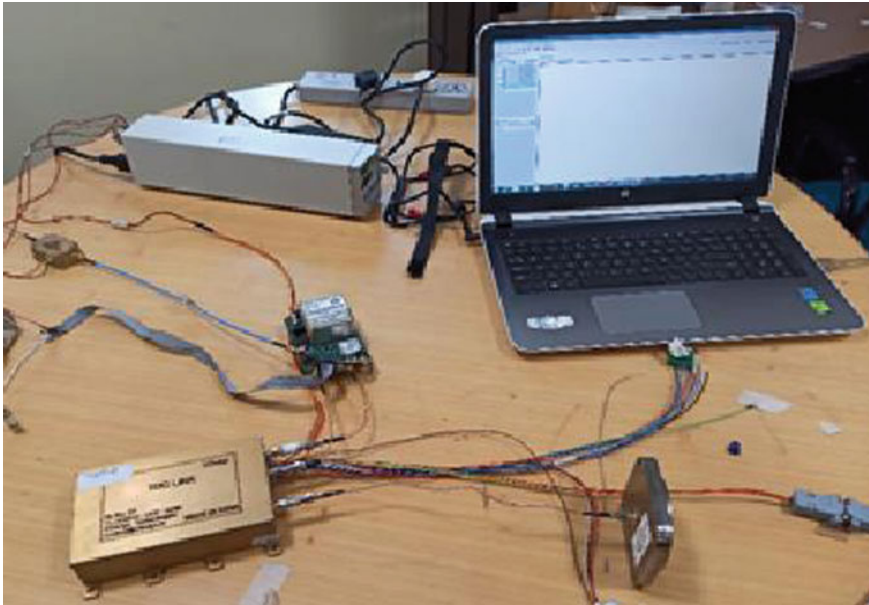


Fig. 7 TDC hardware with GPSDO Receiver and communication antenna

sends the precise time information to the SDR ELINT receiver for time stamping the received signal. Further the receiver performs real time FFT to detect the Radar pulses and processes the RF emitter signal received to compute the signal characteristics and formats the extracted information into a Pulse Descriptor Word (PDW) giving the parameters like Frequency, Pulse Width, rise time, fall time, TOA, etc., IQ data of the received RF pulse signal is also stored with time tag for precise estimation of Time Difference of Arrival of the signal between Master-Slave1 and Master-Slave2 using correlation (Fig. 7).

The IQ data from each SDR ELINT receiver is acquired by the respective computer used to configure it and is stored in the hard disk memory and streamed over Giga bit Ethernet based on command from Centralized Server. Upon request over LAN from the centralized server, the stored files with time stamps are transferred. After preprocessing the data for its validity, LF computation on the data sets which has synchronous reception from three SDR ELINT receivers will be carried out.

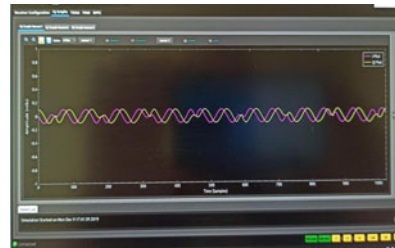
4 Experimental Results

The SDR ELINT receiver and TDC units are integrated in to a single mechanical enclosure to make it convenient for lab and field testing. The TDC unit along with GPSDO receiver is housed in the upper section of the 2 U box and the SDR ELINT

MASTER				SLAVE1				SLAVE2			
00 00 00 00 00 00 00 00	0	00 00 00 00 00 00 00 00	0	00 00 80 65 6A 34 CE	813450278094						
00 00 06 08 04 A5 10 5B	10000000000091	00 00 06 08 04 A5 0E FF	999999999743	00 00 06 08 04 A5 0F EF	999999999977	114					
00 00 01 01 A9 4A 20 EB	20000000000235	00 00 01 01 A9 4A 1F 83	1999999999875	00 00 01 01 A9 4A 1F A6	1999999999910	325					
00 00 02 0A 70 EF 30 7C	30000000000124	00 00 02 0A 70 EF 2F CE	2999999999950	00 00 02 0A 70 EF 2E F1	2999999999729	395					
00 00 03 03 A3 52 94 3F 88	3999999999928	00 00 03 03 A3 52 94 3F 8D	3999999999872	00 00 03 03 A3 52 94 3F 28	3999999999787	141					
00 00 04 04 8C 27 39 50 45	5000000000069	00 00 04 04 8C 27 39 4F 8C	4999999999932	00 00 04 04 8C 27 39 4E DC	4999999999708	361					
00 00 05 05 74 0E 5F FD	5999999999997	00 00 05 05 74 0E 5F 8B	5999999999931	00 00 05 05 74 0E 5F 82	5999999999966	11					
00 00 06 06 5D 00 83 70 AD	70000000000173	00 00 06 06 5D 00 83 6F 8E	6999999999886	00 00 06 06 5D 00 83 6F DF	6999999999967	206					
00 00 07 07 46 A5 28 7F DF	7999999999967	00 00 07 07 46 A5 28 7F C9	7999999999945	00 00 07 07 46 A5 28 7F 7C	7999999999868	99					
00 00 09 18 4E 72 AD 1A	10000000000026	00 00 09 18 4E 72 AD 1C	10000000000028	00 00 09 18 4E 72 8F 8A	9999999999882	144					
00 00 0A 01 23 17 80 BA	110000000000186	00 00 0A 01 23 17 AE EA	10999999999722	00 00 0A 01 23 17 AE F7	10999999999735	451					
00 00 0A 09 F7 8C BF BA	11999999999994	00 00 0A 09 F7 8C CD 5B	120000000000027	00 00 0A 09 F7 8C BF 5B	11999999999835	159					
00 00 0B 02 CC 61 D1 11	130000000000273	00 00 0B 02 CC 61 CF 5D	12999999999837	00 00 0B 02 CC 61 CF 14	12999999999764	509					
00 00 0C 08 A1 06 0D 09	140000000000009	00 00 0C 08 A1 06 DF D9	13999999999961	00 00 0C 08 A1 06 0D 18	140000000000024	-15					
00 00 0D 0A 75 AB FD 45	150000000000069	00 00 0D 0A 75 AB EF CA	14999999999946	00 00 0D 0A 75 AB EE FD	14999999999741	328					
00 00 0E 8D 4A 51 00 3E	160000000000062	00 00 0E 8D 4A 50 FF AB	15999999999915	00 00 0E 8D 4A 50 FF 72	15999999999858	204					
00 00 0F 76 1E FE 10 CA	1700000000000196	00 00 0F 76 1E FE 0F CA	16999999999946	00 00 0F 76 1E FE 0E FB	16999999999739	457					
00 00 10 5E F3 98 20 6A	1800000000000106	00 00 10 5E F3 98 1E 9C	17999999999644	00 00 10 5E F3 98 1E F5	17999999999733	373					
00 00 11 47 C8 40 30 09	1900000000000009	00 00 11 47 C8 40 2E 83	18999999999667	00 00 11 47 C8 40 2F 85	18999999999925	84					
00 00 12 30 9C 05 A0 44	200000000000068	00 00 12 30 9C 05 3E F1	19999999999729	00 00 12 30 9C 05 3F 3A	19999999999802	266					
00 00 13 19 71 BA 4F 4F	20999999999823	00 00 13 19 71 BA 4F 82	20999999999890	00 00 13 19 71 BA 4E 98	20999999999640	183					
00 00 14 02 46 2F 60 8D	2200000000000189	00 00 14 02 46 2F 5F 86	21999999999926	00 00 14 02 46 2F 5F 69	21999999999894	295					
00 00 14 0B 1A 04 70 C4	2300000000000196	00 00 14 0B 1A 04 6F 01	22999999999745	00 00 14 0B 1A 04 6F 69	22999999999777	219					
00 00 15 03 0F 79 80 0F	2400000000000239	00 00 15 03 0F 79 7E 0D	23999999999709	00 00 15 03 0F 79 7F 64	23999999999844	395					

Fig. 8 Measured time differences between master and slaves

Fig. 9 IQ plot with frequency offset of 2 MHz



receiver in the lower section. The debug port is made available on the front panel with LED display and Key board. All the RF connectors and Ethernet port is provided on the rear panel to be connected to the GPS antenna and ELINT antennae (a) Cavity Backed Spiral antenna covering the frequency range 0.5–2 GHz and (b) Horn antenna covering the range 2–6 GHz. These two antennae are connected to the SDR receiver input using a power combiner.

Figure 8 provides the time measurements of the Master, Slave 1 and Slave 2. With reference to the Master, the corrected offsets of Slave 1 and Slave 2 are tabulated which shows that the time synchronization accuracy of < 600ps.

The SDR ELINT receivers are tested in the Lab environment by placing the receivers at a distance of 3m. Figure 9 shows the IQ plot of the signal captured during the test.

The simulated RF emitter signal using R&S signal generator with programmable RF pulse parameters are fed to the SDR ELINT receiver and validated for different combinations (Fig. 10).

	Time Of Arrival(ms)	Pulse Width (us)	Center Frequency(MHz)	Amplitude(dBm)
1	1173.382807	0.993446	2099.96	-10.15
2	1173.387807	1.99503	2099.96	-10.3
3	1173.392807	0.993446	2099.96	-10.6
4	1173.397807	1.99503	2099.96	-11.2
5	1173.402807	0.993446	2099.96	-10.13
6	1173.407806	1.99503	2099.96	-10.26
7	1173.412806	0.993446	2099.96	-10.52
8	1173.417806	1.99503	2099.96	-11.04
9	1173.427806	0.993446	2099.96	-11.08

Fig. 10 Pulse descriptor word parameters

SDR-based ELINT Receiver testing is carried out in the field. The ELINT receiver is tuned to the central frequency of 2800MHz with a bandwidth of 100MHz (± 50 MHz). It has captured test Radar in real time. Actual Parameters of the operated Test radar were provided below (a) Frequency of operation: 2775 and 2825 MHz (b) PW 10, 100, 96 μ s and (c) PRI: 1 ms. The parameter values computed by the SDR ELINT receiver is provided in the table below and are in agreement with the actual parameters (Fig. 11).

5 Conclusions and Future Work

SDR-based ELINT receiver with a novel method of time synchronization using Time to Digital Conversion technique is discussed in this paper. The hardware is realized and tested in the lab as well as on the field. The scope of this paper is only up to the generation of time tagged IQ data and the PDW of the RF emitter signal. However, the algorithms for geolocation of the RF emitter using Complex Ambiguity Function for estimating the time delay and Doppler followed by location estimation using Maximum Likelihood Estimates are under testing. The scope of the work can be extended by studying different algorithms with Digital Terrain Elevation Data at different levels for precise estimation of the location of the RF emitters.

Receiver Configuration					IQ Graphs					TDOA					PDW					RFPS				
	Time Of Arrival				Pulse Width (us)				Center Frequency(MHz)				Amplitude(dBm)											
91	0:20:29:565:992:4				11.5956				2824.46				-52.7737											
92	0:20:29:566:133:118				98.1964				2774.58				-47.9888											
93	0:20:29:567:161:41				11.6852				2824.46				-51.1014											
94	0:20:29:567:303:16				98.4082				2775.06				-46.6959											
95	0:20:29:568:330:84				11.7096				2824.46				-49.8464											
96	0:20:29:568:472:54				98.4814				2775.54				-70.4576											
97	0:20:29:569:500:6				11.7341				2775.54				-49.165											
98	0:20:29:569:641:93				98.5384				2775.06				-58.1816											

Fig. 11 Real time display of test radar parameters

The implementation of this SDR-based ELINT receiver with a capability for recording IQ data on a small satellite using Software Defined Radio devices is feasible with low power consumption, small size and low weight.

References

1. Cho SH, Yeo SR, Choi HH, Park C, Lee SJ (2012) A design of synchronization method for TDOA-based positioning system. In: International conference on control, automation and systems , 17–21 Oct 2012 in ICC, Jeju Island, Korea
2. Fokin G (2019) Passive geolocation with unmanned aerial vehicles using TDOA-AOA measurement processing. In: International conference on advanced communication technology (ICACT), 17–20 Feb 2019
3. Li Q, Xia W, Zhang Y, Jing X, He Z (2013) Hardware design for time delay estimation of TDOA. IEEE. ISBN: 978-1-4799-1027-4/13
4. AD9371 data sheet
5. Zynq Ultra Scale MPSoC data sheet

Performance Analysis of TDOA Localization Algorithm Based on PSO with Formation Flying



Amar Singh, P. Naveen Kumar, and Anupam Sharma

Abstract This research paper focuses on the localization of RF target based on time difference of arrival (TDOA) technique from space-based platforms flying in formation. Localization from space-based platforms offers a unique advantage of covering more area of interest compared to any ground, airborne, or sea-based platforms. In this paper, results of two algorithms, viz., Earth spherical model (ESM) and particle swarm optimization (PSO), are compared by carrying out extensive simulation studies.

Keywords LEO—low Earth orbit · TDOA—time difference of arrival · ESM—Earth spherical model · PSO—particle swarm optimization · DEM—digital elevation model · WGS—world geodetic system

1 Introduction

The localization of RF targets from space-based platforms plays vital role in national security. It offers unique advantage of global coverage by reporting RF targets from deep areas that cannot be accessed by ground, airborne, or ship-based platform.

Various RF localization techniques based on angle of arrival (AOA), time difference of arrival (TDOA), frequency difference of arrival (FDOA) exist in the literature. TDOA offers quite significant localization accuracies as compared to AOA. In this paper, we focus our attention on the algorithms used for localization based on TDOA principle. We have considered three satellite configurations and compared the localization performance of ESM algorithm [1] with PSO algorithm. The limitations and advantages offered by each algorithm are also presented.

This paper is organized as follows. Section 2 describes the mathematical description of the problem statement. In this section, hyperbolic model of TDOA is described; the Earth spherical model (ESM) localization algorithm equations and

A. Singh (✉) · P. N. Kumar · A. Sharma
DRDO, Hyderabad, Telangana, India
e-mail: amar.singh@dsplab.in

the fitness function for PSO are explained. Satellite mission management and formation details are covered in Sect. 3. Section 4 describes the PSO algorithm and the steps that are required for PSO computation. Section 6 covers about system constraints and the assumptions. The simulations, analysis of results, and performance details are covered as a part of Sect. 7. Conclusion and future works are given in Sect. 7.

2 Mathematical Description

Considering three satellite formation, the ECEF (Earth Center Earth Fixed) coordinates for 3 satellites are given by

$$(x_i, y_i, z_i), \quad i = 1, 2, 3 \quad (1)$$

The location of the emitter is (x_0, y_0, z_0) . The distance from satellite i to emitter is r_i . The TDOA's are measured as range difference equation and are given as assuming satellite 1 as the reference as

$$r_2 - r_1 = \Delta r_{2,1} = c \Delta t_{2,1} \quad (2)$$

$$r_3 - r_1 = \Delta r_{3,1} = c \Delta t_{3,1} \quad (3)$$

where c denotes radio signal propagation speed, and $\Delta t_{2,1}$, $\Delta t_{3,1}$ indicate time difference of arrival measurement. Solving Eqs. (2) and (3) with regular Earth sphere model of radius R

$$x^2 + y^2 + z^2 = R^2 \quad (4)$$

results in the Earth spherical model (ESM) solution to localization problem as described in [1]. The solution so obtained can be further improved by using the WGS84 Earth ellipsoid model instead of regular sphere model.

If we closely examine Eqs. (2) and (3), we find that there are uncertainties involved in the measurements in satellite positions as well as time synchronization between the satellites. These uncertainties can be modeled in Eqs. (2) and (3) and can be rewritten as

$$r_2 - r_1 + cn_{2,1} = \Delta r_{2,1} = c \Delta t_{2,1} \quad (5)$$

$$r_3 - r_1 + cn_{3,1} = \Delta r_{3,1} = c \Delta t_{3,1} \quad (6)$$

as described in [2]. The uncertainties modeled as $n_{2,1}$ and $n_{3,1}$ can be considered as independent and identically distributed (i.i.d.) Gaussian random variables with mean zero and σ_n^2 as its variance.

Equations (5) and (6) are complex nonlinear equations. In the presence of Gaussian noise, optimization techniques such as particle swarm optimization (PSO) are very effective in accurately estimating the location of the emitter. The likelihood function

described in [2] for evaluating the estimate of the emitter location in a 3-satellite configuration is described as

$$L = \prod_{k=2}^3 \left[\frac{1}{\sqrt{2\pi\sigma^2}} \exp \left(-\frac{(\Delta r_{k,1} - r_k + r_1)^2}{2\sigma^2} \right) \right] \quad (7)$$

Analytical solution for determining the emitter positions using the likelihood function is complex as well as computationally intensive. Solving the function is akin to obtaining the emitter co-ordinates by solving the objective function defined by

$$(x_0, y_0, z_0) = \arg\{\min [((\Delta r_{2,1} - r_2 + r_1)^2 + (\Delta r_{3,1} - r_3 + r_1)^2)]\} \quad (8)$$

This fitness function is passed to PSO algorithm for determining the emitter co-ordinates.

3 Mission Management

Formation flying is a group of satellites that will fly within close range of each other. In order for localization solution to be calculated, all satellites in a formation should be in view of transmitter beam width. Planning and scheduling of satellites considers the accessing window of area of interest, simultaneous interceptions at all satellites, and GDOP of formation with respect to RF emitter at all instances. As shown in Fig. 1, three satellites are flying in formation to intercept RF emissions in given area of interest. Satellite formation moving along track makes different elevation angles to the emitter in forward and reverse directions. The geometry of formation in forward direction and reverse direction results different localization accuracies for similar elevation angles. We considered three satellite formation in LEO orbit and tested geometry of each satellite with twelve different types of emitters. The location of RF emitter with reference to formation is also considered such as along track, at the edges of swath and mid of the foot print. We considered the emitters at different terrain conditions (altitudes from mean sea level).

The formation geometry is not fixed while mission is in execution. This made us to consider any of the satellite as reference for estimation of TDOA. We studied algorithm performance with the consideration of three configurations. This analysis made us to understand the behavior of algorithm for identification of best reference satellite at that instance.

4 Particle Swarm Optimization

PSO algorithm has been applied successfully in many application areas. The objective is to optimize a given fitness function, be it maximization or minimization. PSO is used for emitter localization in a given search space. It starts with the initialization of a group of random particles in the search space; each particle representing a potential solution to emitter location. Each particle has a fitness value defined by the fitness function. These particles move in the search space by iteratively improving the candidate solution based on their personal best position and the global best position of the swarm.

The movement of particles toward the optimal solution is guided by iteratively updating its velocity and position based on its personal best position vector, p_{best} and global best position vector of the swarm, g_{best} . The velocity and position of i th particle at times $t + 1$ and t is given as

$$V_i^{t+1} = w * V_i^t + c_1 * r_1 (P_{\text{best}(i)}^t - P_i^t) + c_2 * r_2 (G_{\text{best}(i)}^t - P_i^t) \quad (9)$$

$P_i^{t+1} = P_i^t + V_i^{t+1}$, where w represents the inertia weight, c_1 and c_2 are learning factors, r_1 and r_2 are uniform distributions between 0 and 1. V and P respectively denote the velocity and position vectors.

5 System Description, Constraints, and Assumptions

5.1 Description

3-satellite configuration is taken for the evaluation of localization performance of ESM and PSO algorithms. Satellite path over the Indian sub-continent region is chosen as shown in Fig. 1. Different RF emitters are taken and scattered across the satellite path with varying terrain covering sea level to mountainous regions. Emitters E1, E3, E9, E10, E11 are high-altitude emitters located on either side of the satellite path, while emitters E2, E4, E6, E7, and E8 are medium altitude emitter. The emitters E5 and E12 are considered near MSL.

5.2 Requirements and Constraints

(A) ESM and PSO localization algorithm

1. Inputs required for the algorithms
 - (a) Time of Arrival of RF pulse at each satellite platform ($\text{TOA}_i, i = 1, 2, 3$)
 - (b) ECEF (Earth Center Earth Fixed) positions of satellite platforms

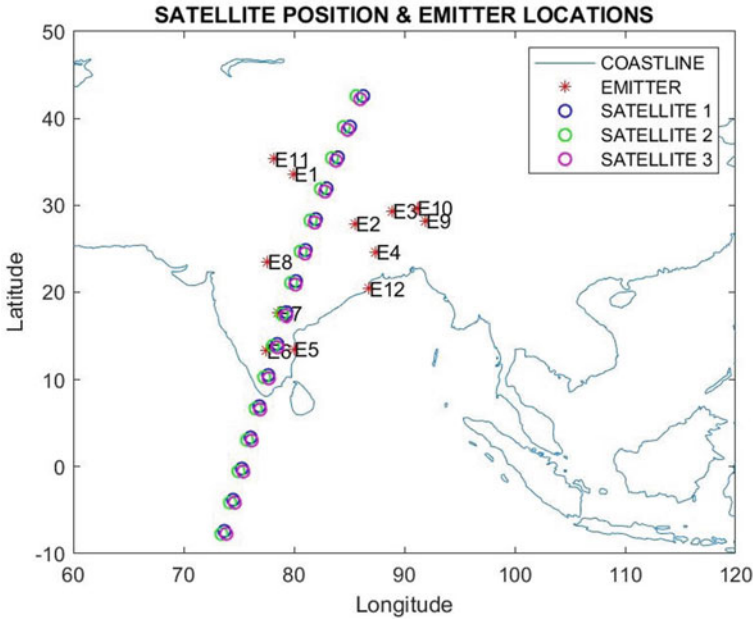


Fig. 1 TDOA scenario

- (c) Digital Elevation Model (DEM) of Region of Interest (ROI) or Average Radii of Curvature of Region of Interest
- 2. Outputs generated from the algorithms
 - (a) ECEF/Latitude-Longitude of RF emitter
 - (b) Error ellipse/ellipsoid
- 3. Optimizations parameters for PSO Algorithm
 - (a) Swarm size
 - (b) Search area
 - (c) Inertia weight factor, w
 - (d) Learning coefficients, c_1 and c_2 .

5.3 Assumptions

- 1. Satellite altitude is taken in LEO orbit and inter-satellite separation about 30 km approximately.
- 2. RF emitters are chosen along the satellite path as well as on either side of the satellite path with varying terrain covering sea level to mountainous regions.

3. ESM computation uses WGS84 standard for Earth's radius value.
4. PSO algorithm uses height information for search volume based on WGS84 standard and the average radii of curvature of RF emitter location.
5. Linearly decreasing inertia weight factor, w is chosen for PSO to avoid local minima during initial stages of iteration and later made smaller for improved convergence of the algorithm.

$$w = w_{\max} - (t) * \frac{(w_{\max} - w_{\min})}{M}$$
 w_{\max} —maximum weight factor, w_{\min} —minimum weight factor, t is current iteration and M is number of iterations.
6. The following error conditions are inserted during calculations to study and compare the performance of ESM and PSO algorithms.
 - (a) No time sync and no position error
 - (b) Time sync error (A random error between ± 5 ns is considered)
 - (c) Time sync error (A static time sync error of 1, 2, 5 and 10 ns are considered)
 - (d) Time sync (A random error between ± 5 ns) and Gaussian error distribution with variance of 10 m in satellite positioning is considered.

6 Simulation Results

The localization accuracies of ESM and PSO algorithms are evaluated for different emitter locations. The effect of satellite formation geometry related to emitters on location fix is demonstrated. The effect of choosing different reference satellites with accuracies is also shown. Finally, the variation in accuracy with time sync errors is brought out.

6.1 Simulation 1

Regular spherical Earth model is used in ESM algorithm for emitter localization. PSO parameters chosen are as follows: $c_1 = c_2 = 2$, $w_{\max} = 0.8$, $w_{\min} = 0.2$, swarm size $N = 500$, maximum number of iterations $M = 50$. Figures 2 and 3 are plots of the error magnitude in emitter localization with respect to elevation angle the emitter makes with the satellite formation. Time sync (random error between ± 5 ns) and position error (variance = 10 m) is inserted.

Figures 2 and 3 are plots of error magnitude for emitter E7 and E10 as shown in Fig. 1: TDOA Scenario. From the plots, it is inferred that PSO gives more accuracy as compared to ESM when elevation angles are low, while for higher elevation angles, ESM outperforms PSO. The effect of geometry of satellite formation with respect to emitters is also evident; E7 lies on the satellite formation trajectory, while E10 is quite distant from the trajectory, and they have different terrains. Tables 1 and 2 show

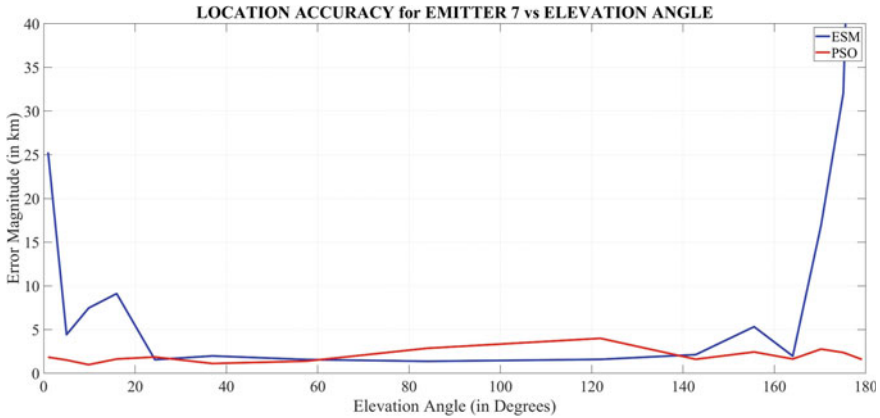


Fig. 2 Location accuracy of emitter E7

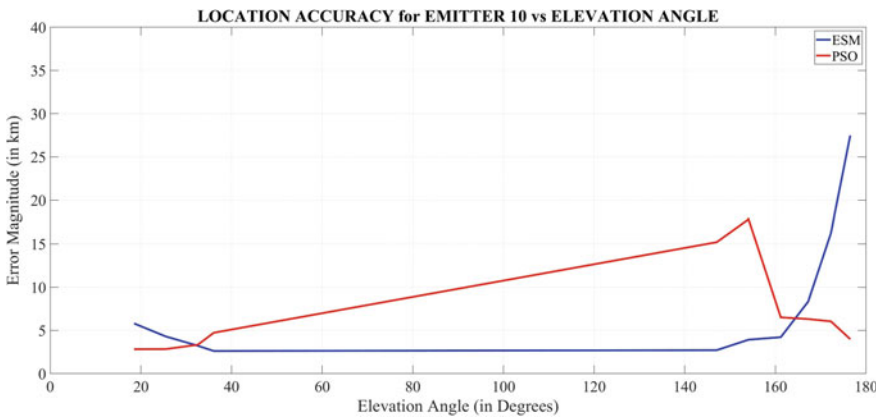


Fig. 3 Location accuracy of emitter E10

the localization error in emitter estimate with respect to elevation angle for emitter E7 and E10.

6.2 Simulation 2

Looking closely at Fig. 1, it is clear that the satellite formation orientation changes with respect to emitters as satellites traverse their orbits. Simulation 2 considers the time sync (random error between ± 5 ns) and position error (GDOP = 10m). The effect of choosing the reference satellite (for TDOA measurement) on localization accuracy is depicted in Fig. 4.

Table 1 Localization error for emitter 7, ESM, and PSO with respect to elevation angle

Elevation angle (degrees)		ESM (error in km)	PSO (error in km)
Forward	0.95	25.278	1.844
	9.84	7.467	0.986
	84.01	1.369	2.866
Reverse	-31.91	1.591	3.998
	-80.21	16.915	2.768
	-85.08	32.043	2.377

Table 2 Localization error for emitter 10, ESM and PSO wrt elevation angle

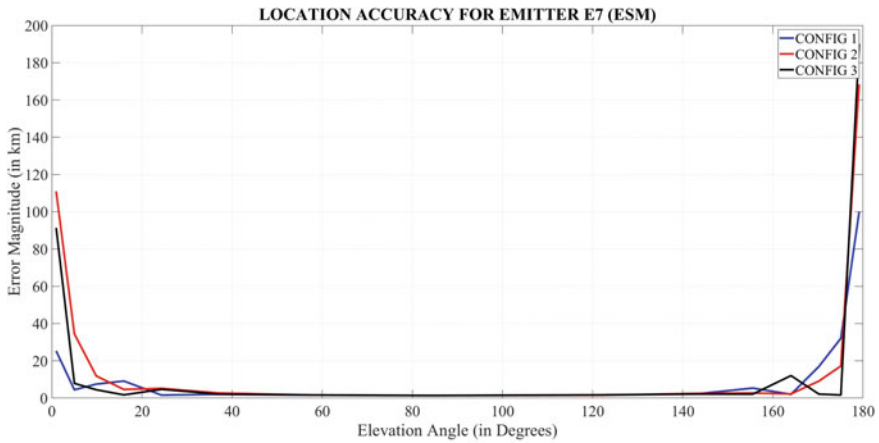
Elevation angle (degrees)		ESM (error in km)	PSO (error in km)
Forward	18.5	5.806	2.823
	25.5	4.301	2.84
	36.1	2.615	4.733
Reverse	-57.05	2.716	15.204
	-82.24	16.248	6.046
	-86.5	27.473	3.99

Figure 4a and b corresponds to ESM and PSO algorithm, respectively. The choice of a given satellite as reference can give good localization at a certain elevation, but the same satellite if chosen reference at any other elevation may give poor accuracies as depicted in Table 3. The choice of reference satellite is an important parameter in TDOA measurement since the satellite formation geometry varies over the orbital path.

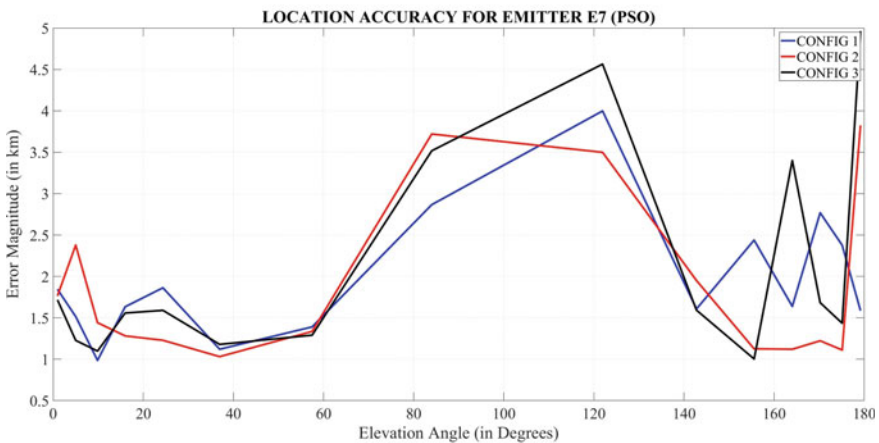
6.3 Simulation 3

The effect of time synchronization error between satellites on the localization error is simulated. Static time synchronization errors of 1, 2, 5, and 10 ns are inserted to observe the localization accuracy error trend. Figures 5 and 6 show the effect of time sync error for ESM and PSO algorithms.

Examining Fig. 5 and Table 4, it can be observed that localization error for ESM algorithm is dependent on the look angle the emitter makes with satellite formation, the time sync error, and also the choice of reference satellite. In the forward look direction, the localization error increases with an increase in time sync error when satellite 1 is reference for TDOA measurements, while in reverse look direction, the emitter estimate error decreases with increase in time sync error. An exact opposite trend is observed when satellite 2 is used as reference for TDOA computations.



(a)



(b)

Fig. 4 **a** Location accuracy with respect to satellite reference (ESM), **b** location accuracy with respect to satellite reference (PSO)

PSO algorithm (Fig. 6 and Table 5) similarly demonstrates, opposing trends in localization error with time sync error for different choices of satellite reference. However, the magnitude of variation in localization error with time sync error is far less as compared with ESM algorithm.

This clearly shows the impact of choice of reference satellite for TDOA measurements, and the role satellite formation geometry plays at different time instants in the orbital path toward emitter localization accuracies.

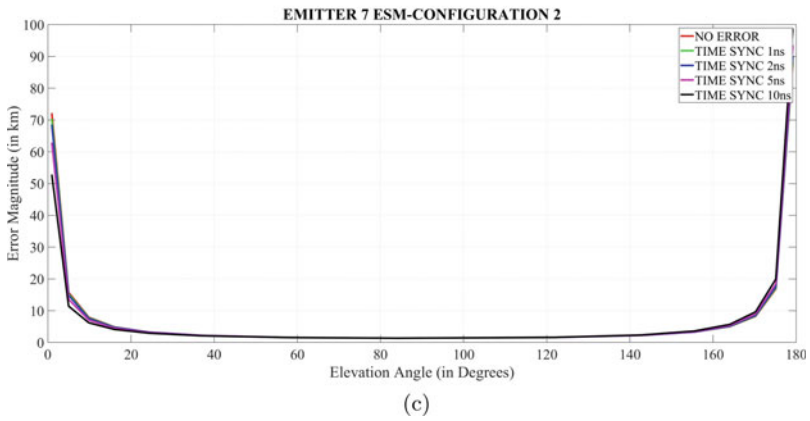
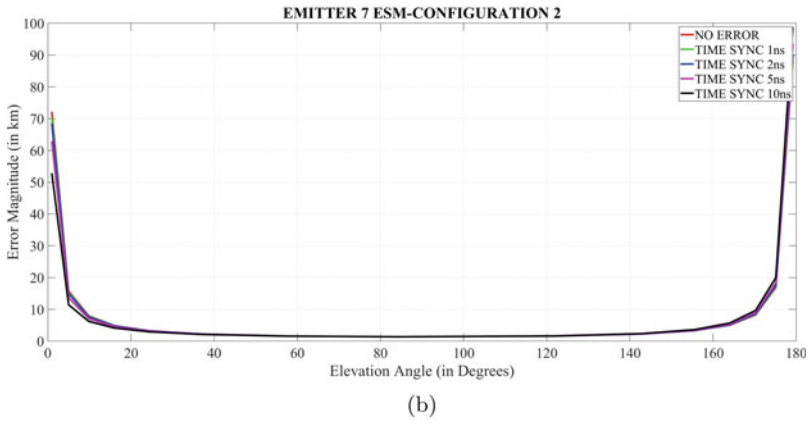
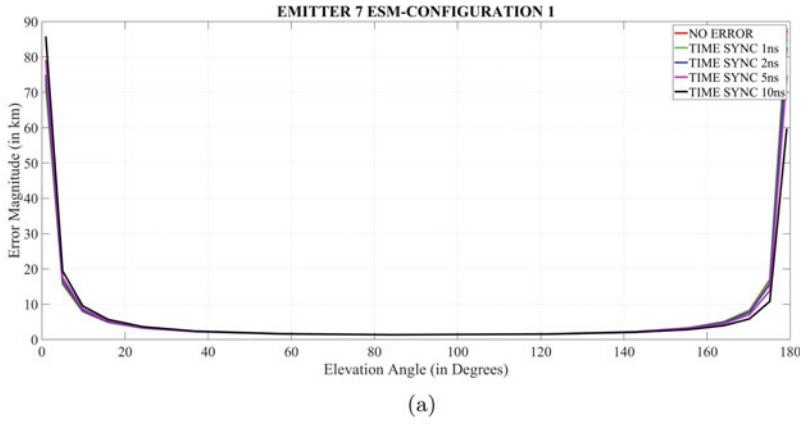
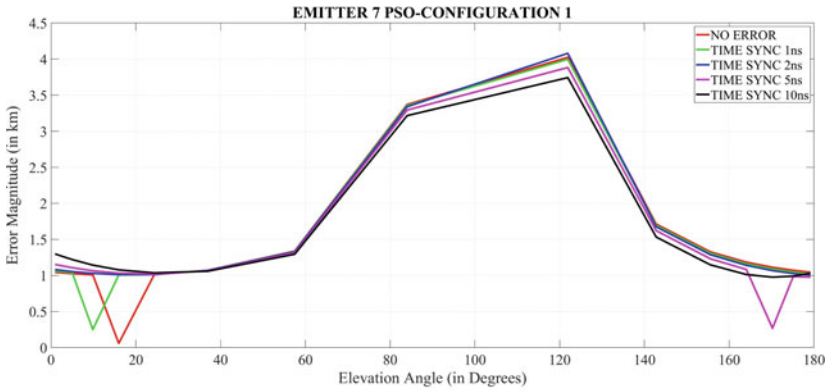
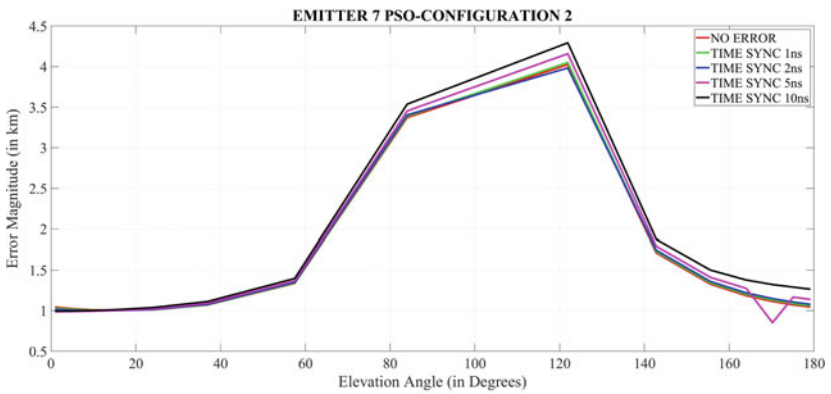


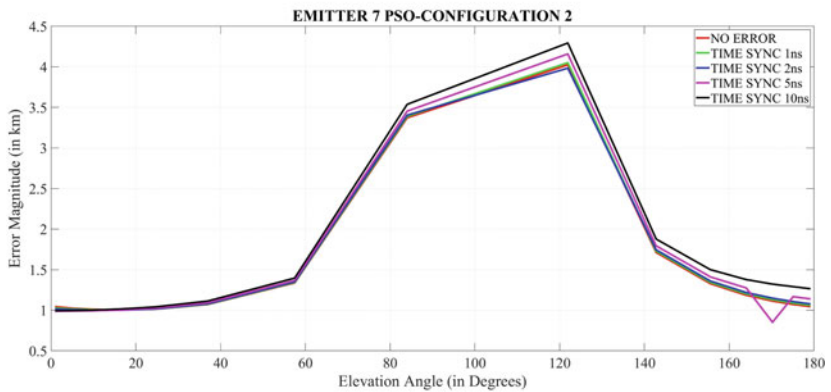
Fig. 5 Time sync error, emitter E7 **a** configuration 1 (ESM), **b** configuration 2 (ESM), **c** configuration 3 (ESM)



(a)



(b)



(c)

Fig. 6 Time sync error, emitter E7 a configuration 1 (PSO), b configuration 2 (PSO), c configuration 3 (PSO)

Table 3 Effect on localization error (emitter E7) for choice of reference satellite

Elevation angle (degrees)	ESM (error in km)			PSO (error in km)		
	Reference satellite			Reference satellite		
	1	2	3	1	2	3
0.95	25.22	110.9	91.37	1.84	1.76	1.71
9.84	7.46	11.85	4.45	0.98	1.44	1.09
84.01	1.36	1.38	1.35	2.86	3.71	3.51
-31.91	1.59	1.51	1.67	3.99	3.49	4.56
-80.21	16.91	9.07	2.11	2.76	1.22	1.68
-85.08	32.04	17.16	1.6	2.37	1.11	1.43

7 Conclusion and Future Work

A comparative conclusion based on the simulation results on the localization performance of ESM and PSO algorithm is summarized as

- i. PSO gives better localization accuracies at lower elevation look angles whereas, ESM performs better localization at higher elevation look angles.
- ii. Localization accuracies are influenced by the satellite flying formation geometry with RF emitters and the choice of reference satellite for computing TDOA measurements in both the algorithms.
- iii. The magnitude of localization error variation with time synchronization error between satellites is much lower in PSO algorithm as compared to ESM.
- iv. The absence of digital elevation model (DEM) for high-altitude emitters (E1, E3, E9, E10, and E11) has considerable influence on the localization accuracies for both the algorithms; however, the effect is less pronounced for PSO algorithm as compared to ESM.

It is also important to note that the accuracies in both the algorithms are highly influenced by the knowledge of emitter terrain. Computing a coarse location fix and then with the knowledge of digital elevation model (DEM), we can compute average radii of curvature of the area of interest. This information is passed to the algorithm iteratively resulting in improved localization accuracies. For future work, the location fix of the emitter arrived at using ESM and PSO algorithms may be passed onto iterative Newton–Raphson method to further increase localization accuracies. However, the issue of singularity during computation should be taken care of.

Table 4 Effect on localization error (ESM) with time sync error between satellites

Elevation angle (degrees)		ESM (error in km)			
		Time sync error	Reference satellite		
			1	2	3
Forward look	0.95	No error	72.15	72.15	72.15
		1 ns	73.58	70.34	72.52
		2 ns	74.99	68.51	72.88
		5 ns	79.15	62.85	73.96
		10 ns	85.83	52.84	75.75
	9.84	No error	7.92	7.92	7.92
		1 ns	8.08	7.75	7.94
		2 ns	8.24	7.58	7.95
		5 ns	8.71	7.06	7.99
		10 ns	9.51	6.2	8.06
	84.01	No error	1.36	1.36	1.36
		1 ns	1.36	1.36	1.36
		2 ns	1.36	1.36	1.36
		5 ns	1.36	1.36	1.36
		10 ns	1.36	1.36	1.36
Reverse look	-31.91	No error	1.58	1.58	1.58
		1 ns	1.58	1.59	1.59
		2 ns	1.58	1.59	1.59
		5 ns	1.56	1.6	1.59
		10 ns	1.54	1.62	1.59
	-80.21	No error	8.26	8.26	8.26
		1 ns	8.02	8.4	8.3
		2 ns	7.78	8.54	8.47
		5 ns	7.06	8.95	8.78
		10 ns	5.87	9.61	9.3
	-85.08	No error	16.9	16.9	16
		1 ns	16.29	17.2	17.19
		2 ns	15.69	17.51	17.49
		5 ns	13.87	18.43	18.38
		10 ns	10.82	19.96	19.85

Table 5 Effect of localization error (PSO) with time sync error between satellites

Elevation angle (degrees)		ESM (error in km)			
		Time sync error	Reference satellite		
			1	2	3
Forward look	0.95	No error	1.04	1.04	1.04
		1 ns	1.06	1.02	1.04
		2 ns	1.08	1.01	1.04
		5 ns	1.15	0.98	1.04
		10 ns	1.29	0.99	1.05
	9.84	No error	1.01	1.01	1.01
		1 ns	0.25	1	1
		2 ns	1.02	1	1.02
		5 ns	1.06	0.99	1
		10 ns	1.14	1	0.99
	84.01	No error	3.37	3.37	3.37
		1 ns	3.35	3.38	3.37
		2 ns	3.34	3.4	3.36
		5 ns	3.29	3.45	3.36
		10 ns	3.21	3.53	3.36
Reverse look	-31.91	No error	4.02	4.02	4.02
		1 ns	3.99	4.05	4.02
		2 ns	4.07	3.98	4.02
		5 ns	3.88	4.15	4.03
		10 ns	3.74	4.29	4.03
	-80.21	No error	1.11	1.11	1.11
		1 ns	1.08	1.13	1.12
		2 ns	1.06	1.14	1.13
		5 ns	0.27	0.85	1.15
		10 ns	0.97	1.32	1.2
	-85.08	No error	1.07	1.07	1.07
		1 ns	1.04	1.08	1.08
		2 ns	1.02	1.1	1.09
		5 ns	0.98	1.16	1.12
		10 ns	0.99	1.29	1.19

References

1. Guo F, Fan Y, Zhou Y, Zhou C, Li Q (2014) Space electronic reconnaissance localization theories and methods. Wiley
2. Gao L-p, Sun H, Liu M-n, Jiang Y-l (2016) TDOA collaborative localization algorithm based on PSO and Newton iteration in WGS-84 coordinate system. In: ICSP 2016

Intruder Detection and Tracking Using Computer Vision and IoT



Devarakonda Abhinay, Krishna Chaitanya, and Prakki Sathwik Ram

Abstract According to FBI Uniform Crime Reporting (UCR) statistics per year, there are roughly 2.5 million property-related burglaries, and out of which, the police solved only 13% of these reports due to the lack of a witness. Traditional methods such as using a CCTV surveillance system require a person to constantly monitor those cameras. This may be an effective way in locations such as offices and other public places. However, it cannot be used in houses as it would not only breach the privacy of the home owners but also not an effective way to detect an intrusion. In this paper, we propose eliminating the human aspect of monitoring cameras by implementing an autonomous intruder detection and tracking system. This system contains an indoor unit and an outdoor unit, and these two units communicate with each other using TCP/IP sockets. The indoor units contain a single camera present inside the house which uses face recognition to detect intruder. When the intruder leaves the house, the outdoor unit which contains multiple cameras located outside the house uses the image of the intruder taken by the indoor unit to look for the intruder. These two units use SMTP protocol to send email alerts when the intruder is detected. The indoor unit autonomously detects the intruder, while the outdoor unit autonomously locates the intruder. The salient feature is that by implementing this system, we can offset the lack of presence of a physical witness and aid the police in catching the intruder.

Keywords Computer vision · IoT · Face recognition · Siamese architecture · Convolutional neural network · Face embeddings · SMTP protocol · TCP/IP sockets

D. Abhinay (✉) · K. Chaitanya · P. S. Ram
Department of Electronics and Communication Engineering, M.V.S.R. Engineering College,
Hyderabad, Telangana 501510, India
e-mail: ojaabhinay@gmail.com

© The Author(s), under exclusive license to Springer Nature Singapore Pte Ltd. 2022
P. Kumar Jain et al. (eds.), *Advances in Signal Processing and Communication Engineering*, Lecture Notes in Electrical Engineering 929,
https://doi.org/10.1007/978-981-19-5550-1_44

499

1 Introduction

Over the last decade, all the major mobile manufacturers have moved from using a password as its major authenticator to using face recognition as its primary authentication. This shift has happened in the backdrop of increase in popularity of artificial intelligence and its application in face recognition to provide near perfect accuracy.

In this paper, we report herein a new protocol has been developed for an autonomous intruder detection, and tracking system is developed. The proposed system contains two units an indoor unit and an outdoor unit. The indoor unit contains a single camera inside the house of the family. We take the outputted frames from the camera and apply face recognition to detect if there are any individuals in the frame that are not part of a predefined database of family members. If any such individual is detected, we alert the family members by sending them an email with the intruder's image. This image is simultaneously sent to our outdoor unit which contains a bunch of outdoor cameras located at different locations far from the house. These cameras use face recognition to detect the intruder based on the received image from the indoor unit. When detected, we send an email with the intruder's location based on the known location of the camera that detected the intruder hence ultimately tracking the intruder. With this information, we can aid the law enforcement officials to catch the intruder.

The rest of the paper is illustrated as follows in Sect. 2 we discuss existing methodologies and compare them to our proposed methodology, followed by that in Sect. 3, we discuss the design of individual modules of the proposed framework as well as see these modules come together using a flow diagram. Section 4 illustrates the obtained results, and finally, conclusion and acknowledgements are mentioned in Sect. 5.

2 Related Work

There are existing techniques to detect home intrusion such as using a PIR sensors as reported by [1] and using image processing to perform background subtraction to detect intruder as carried out by [2]; these two methodologies essentially detect motion in a static environment and classify the reason for that motion as an intruder. This methodology cannot be applied in areas where there is a constant activity going on. Although [2] is streamlined to identify a person, however, there is no way to know if that person is friendly or an intruder. This information is not comprehensive enough to provide any assistance to the police.

We need a way to distinguish between friendly people and intruders. We propose an approach to create a database of family members faces and compare detected faces to the ones in the database then to classify them as an intruder if their face is not recognized. References [3, 4] propose a similar approach where they implement face recognition to differentiate between friendly people and intruders both [3, 4] after detecting the intruder provides an alert to the end user and stop there.

In this paper, we have used two CNN architectures pretrained for face detection and extracting feature vectors of detected faces. Facial feature vectors also known as face embeddings require only a single image of the individual to create a listing in the database. We have proposed notifying of the intrusion by sending an alert email with an attachment of intruder’s image to the house owners; this alert when received by law enforcement officials may help in catching the thief. In order to speed up the process of catching the thief, we have proposed a method to provide assistance to the police by using outdoor surveillance cameras to create a network of security cameras to track the intruder autonomously.

3 Framework Architecture and Design

The block diagram for the system we designed and implemented is depicted in Fig. 1. In this chapter, we discuss individual concepts that are used to implement the proposed system. In Sect. 3.1, we have a brief overview of the proposed architecture. In Sect. 3.2, we discuss how we implement face recognition, and in Sect. 3.3, we utilize face recognition for detecting intruders and then tracking them while simultaneously sending an alert email concerning the two activities. Finally, in Sect. 3.4, we discuss the entire workflow of the proposed system that combines all the individual concepts that we discussed.

3.1 System Architecture

In this paper, we propose detection of house intruders and then tracking them from a group outside the house given an input of video frames of the region $F(t)$, $t = 1, 2, \dots, T$. Here, t is a frame, and T is the total number of frames in an observed

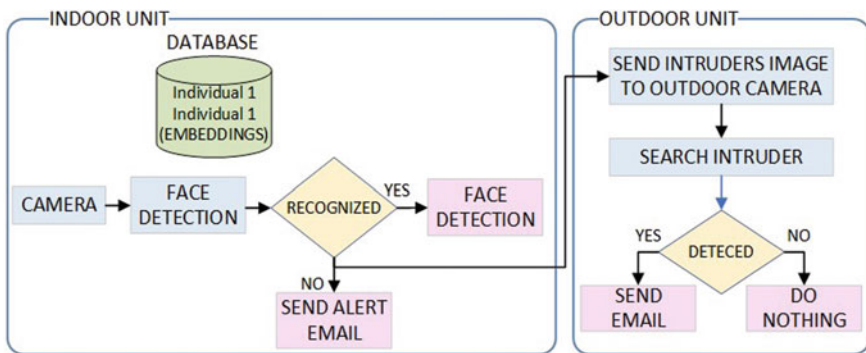


Fig. 1 Block diagram for intruder detection and tracking system

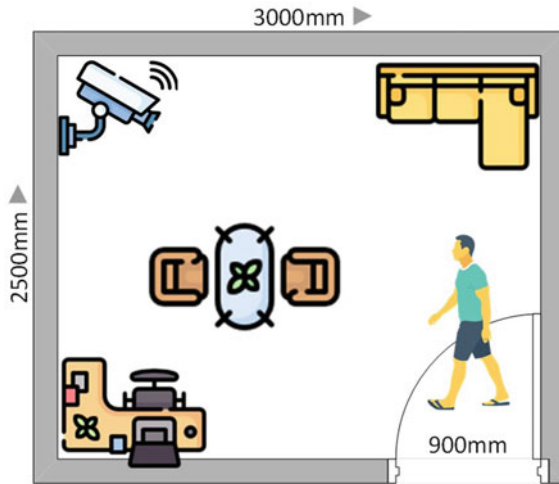


Fig. 2 Indoor unit



Fig. 3 Outdoor unit

video; the block diagram for our implementation can be found in Fig. 1. First, we detect the individual when they enter the house by using an indoor camera unit as shown in Fig. 2; we then use face recognition to identify the individual from members of the family, if failed to identify then, we send an alert regarding the presence of the intruder by sending an email to members of the family. When the intruder leaves the house, we send the intruders image taken by the indoor camera to the outdoor unit as shown in Fig. 3. Using this image, we track the intruder, and when detected, we again send an email with the location of the intruder. The indoor unit contains

a single camera, while the outdoor unit contains multiple cameras on the street. These two units communicate with each other through the Internet using TCP/IP protocol.

3.2 Face Detection and Recognition

In the proposed framework, the main methodology we use to detect intruders is through face detection and recognition; hence, this is the most important part of the framework. Face detection means identifying a human face from given input images. Face recognition, however, is the ability to confirm the identity of the face. In order to perform face recognition, the first step is to perform face detection.

Face Detection

For face detection, we use a convolutional neural network-based (CNN) [5] face detector instead of training our own neural network since the latter requires a lot of data and computational power [6]. A convolutional neural network is a type of neural network that is prominently used in image recognition systems. We use transfer learning which is a way to utilize a pretrained model and customize it with our own data. This way we don't have to re-invent the wheel every time. We use a model available in the Dlib library named as `cnn_face_detection_model_v1` [7, 8]. This pretrained model takes an input image and returns the location of one or multiple faces. With the location data, we can use OpenCV library [9], which is an open-source computer vision library developed by intel to plot a rectangular bounding box to highlight the facial region of the image. This process is illustrated in Fig. 4.

Face Recognition

Now, we have the location of the face; the next step is to identify the face. The way we identify the face is by feeding in the features of a known face and comparing it with the features of the detected face. If the features are similar, then the face is of the same person and hence has been identified. There are two ways in which we can compare facial features, first one is by training a classifier like [10] did by using support vector

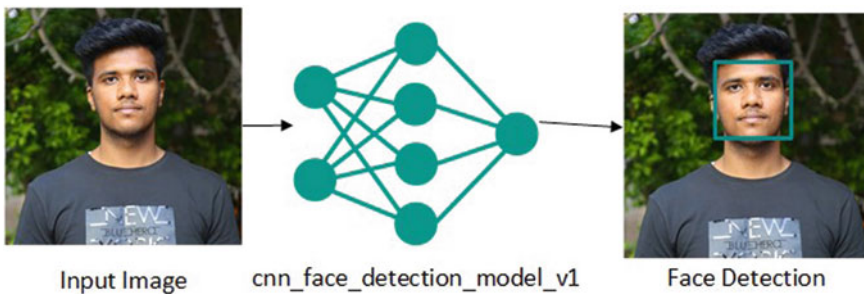
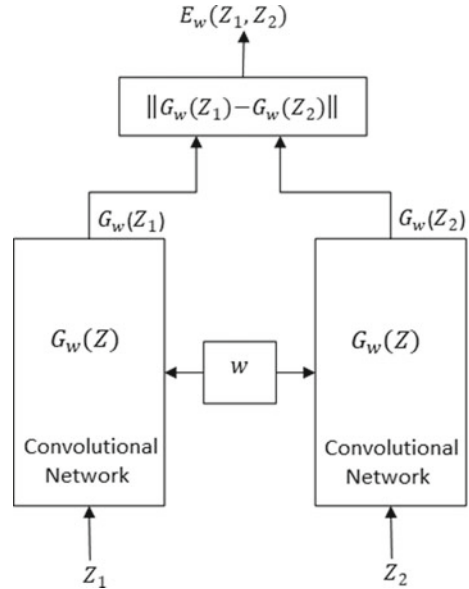


Fig. 4 Face detection implementation

Fig. 5 Siamese architecture [11]



machines (SVMs). However, for training a classifier, we require a lot of images and a high computational power, and the output of the classifier is class probabilities. In this case, the classes are the names of the individual family members upon whose images the classifier was trained on. For our application, we need to recognize the family members. Let's say we trained a classifier with images of family members and then deployed it, if in future, there is an addition to the family, we need to retrain the classifier again which is a time-consuming and computationally tedious process.

The second way, which is also the one we decided to implement, is by using similarity learning [11]. Here, instead of classifying the input, we measure the similarity of two inputs. We can do this by implementing a Siamese network similar to [11]. A Siamese network, as shown in Fig. 5, contains two identical neural networks $G_w(Z)$ to which a pair of images Z_1 and Z_2 (for which face detection has already been performed) are given as input. The output of the two networks is 128-dimensional embedding vectors $G_w(Z_1)$, $G_w(Z_2)$. These functions contain the data regarding facial features and are parameterized by w . The Euclidean distance $E_w(Z_1, Z_2)$ between these two vectors is calculated as follows.

$$E_w(Z_1, Z_2) = \|G_w(Z_1) - G_w(Z_2)\|^2 \quad \text{if } E_w(Z_1, Z_2) \leq \tau \quad (1)$$

where τ is a distance threshold value, then the two images Z_1 and Z_2 are of the same person. If $E_w(Z_1, Z_2) > \tau$, then the two images are of different people. We are essentially plotting the 128D face embeddings of Z_1 and Z_2 images; then, we calculate the distance between them. If the distance is below a threshold, then these are the images of the same person otherwise, they are of different people.

The CNN used in the Siamese architecture $G_w(Z)$ must be designed in such a way that similar images have closer embeddings and dissimilar images have embeddings that are distinct. This is done by using contrastive loss function first introduced in [12]. The general form of loss function is given below.

$$L(W, (Y, Z_1, Z_2)^i) = (1_Y)L_S(E_w^i) + YL_D(E_w^i) \tag{2}$$

where L_S and L_D are designed in such a way that minimizing L with respect to w would result in low values of E_w for similar pairs and high value of E_w for dissimilar pairs. L_S stands for the loss function that should be applied if the inputs are similar and L_D if the inputs are dissimilar. $Y = 0$ if Z_1, Z_2 are deemed similar and $Y = 1$ if Z_1, Z_2 are deemed dissimilar. The actual loss function looks as follows

$$L(W, (Y, Z_1, Z_2)^i) = (1 - Y)^{1/2}(E_w)^2 + Y^{1/2}\{\max(0, m - E_w)\}^2 \tag{3}$$

Using the above loss function, we can create a CNN that outputs face embeddings for an input face such that the values of embeddings are closer for similar images and distant for dissimilar images. Here, m stands for a margin value which is greater than 0 this indicates that dissimilar pairs which are beyond the margin will not contribute to the loss. Instead of building this network from scratch, we have used a pretrained model `face_recognition_model_v1` [13] that outputs embeddings based on contrastive loss; this process is illustrated in Fig. 6. We have used distance threshold value $\tau = 0.6$ because this value renders an accuracy of 99.38% [13].

The process until now only constitutes face verification. We are comparing two face images (Z_1, Z_2) and answering the question of whether these two faces are similar or not. To perform face recognition, we have to compare the input face with a database of face embeddings which in our case are the face embeddings of the members of the family.

To perform face recognition, we modify the Siamese network shown in Fig. 5 by replacing the second half with a database. The way it works is that instead of inputting two images and parallelly generating their embedding vectors at the same time, we calculate the embedding vectors beforehand and store it in a database. For

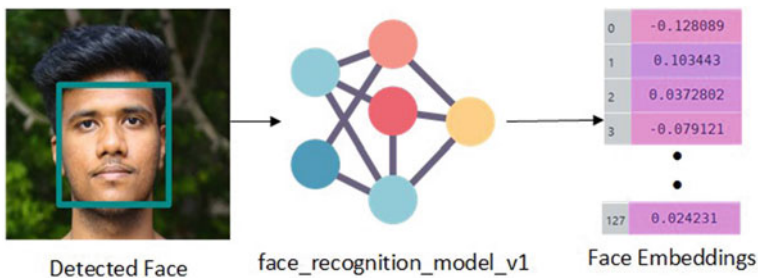


Fig. 6 Generating face embeddings

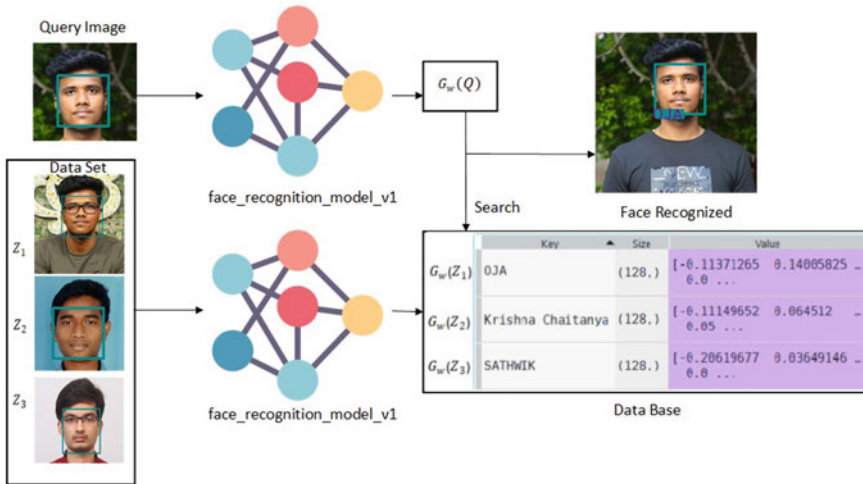


Fig. 7 Face recognition

our purpose, we want to recognize the members of the family, so we calculate their face embeddings and store them in a database as shown in Fig. 7. The database is nothing more than a dictionary data type in Python. The first half of the Siamese architecture remains the same as we input a query image the face region of the query image is detected as shown in Fig. 4. Then, the face embeddings $G_w(Q)$ are calculated as shown in Fig. 6. We then calculate the distance between this embedding and the ones stored in the database; Fig. 8 shows 3D representation of 128D embeddings values of database and query faces. This is done by using tsne [14] and matplotlib [15] libraries. We can see that the query image embeddings are closer to the embeddings with label Oja. When we calculate the distance between them it is under threshold, hence, we have recognized that the face in the query image is of the family member Oja. The whole process of face recognition after face detection is shown in Fig. 7.

3.3 Intruder Detection and Tracking

Intruder Detection

In the present paper, we propose that by creating a database of family members and an application that can recognize them as we discussed in Sect. 3.2. We can identify the individual as a possible intruder and an alert email is sent to the family members. We, however, do not send an alert if there are one or more recognized individuals along with the unrecognized person; we then assume that there is a guest in the house.

Email Notification

After classifying the individual as an intruder, the easiest way to notify the house owner is to send an alert email with the image of the intruder. This is done by using

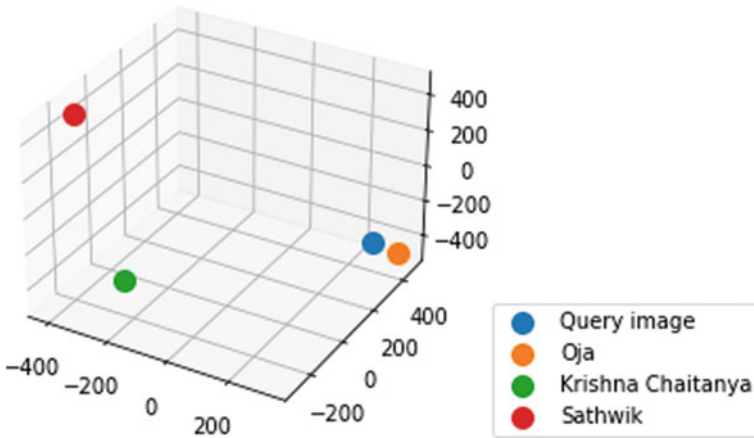


Fig. 8 3D representation of 128D face embeddings

an email transfer protocol SMTP (Simple Mail Transfer Protocol). It is a transportation protocol used to transfer messages over the Internet. The SMTP protocol is a client/server procedure which starts when a client in the local network wants to send a message to a host that is outside the local network using the local email server or when a message is exchanged between two hosts in the same network. This procedure starts with establishing a TCP connection between the email client and email server on port 25. Then, it executes a set of commands till the message is transferred to the sender’s email address [16].

Intruder Tracking

When the intruder leaves the house, in order to autonomously track the intruder, we have to make the outdoor cameras, as shown in Fig. 3, look for the intruder, and when detected, we can find out the location of the intruder based on the location of that outdoor camera.

The outdoor camera unit runs the same face recognition application we discussed in Sect. 3.2 for the indoor camera unit. The only difference is that instead of having a database of family members, here, we have a database of possible intruders. To create this database, we need the image of the intruder. When we send the alert email, we parallelly send the intruders image from indoor camera unit to the outdoor camera units. This image transfer is done through the Internet using sockets. A socket can be described as an endpoint of a connection between two computers, in this case the indoor and outdoor camera units identified by an IP address and a port number. It is essentially used to send and receive data which are images in our case. We use TCP/IP sockets for image transfer TCP/IP is a communication protocol which is used to interconnect devices on the Internet. This protocol specifies how data are exchanged over the Internet [17, 18]. TCP/IP is reliable because when a TCP client sends data to the server it requires an acknowledgement in return else it automatically retransmits data. To put it simply, TCP connection is a virtual pipe between client

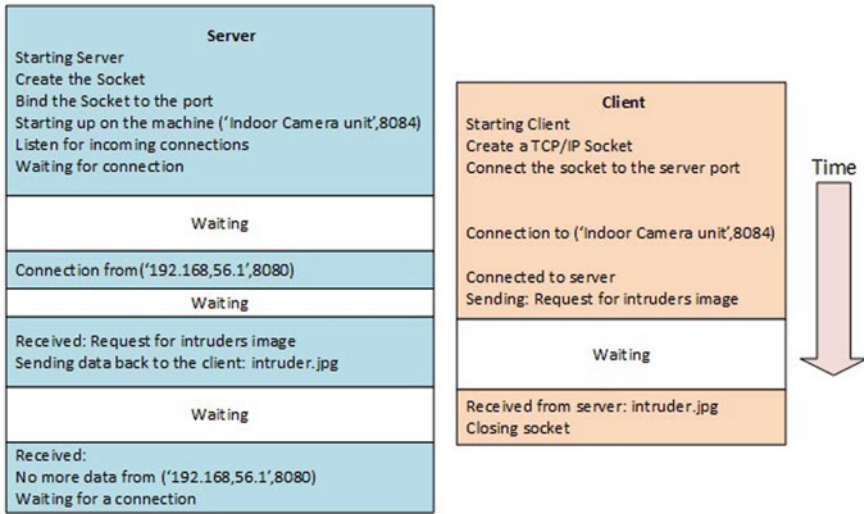


Fig. 9 Client–server communication [17]

sockets and server sockets. The server sends data to its sockets and TCP guarantees that client will receive the data as sent. The whole process of sending an image through sockets is shown in Fig. 9.

The indoor and outdoor units are connected to the Internet. The indoor unit acts like a server, and the outdoor units act as clients to that server, and using TCP/IP sockets, image transfer is done from server to client. With the received image, the outdoor unit creates the database with the label intruder_x where x is the camera ID. If an outdoor camera with ID = 1 detects the intruder, then the intruder is labeled as intruder.1, and then, we start tracking by comparing the detected faces to the intruder’s face. When a camera detects the intruder, an email is sent to the home owners with the outdoor camera ID; using this ID, we can find the location of the intruder as we know the location of the cameras.

3.4 Functional Flow of the Proposed System

Figure 10 shows the workflow of the proposed system. The indoor unit utilizes the indoor camera to look for faces and compare them with the ones in the database. If an unrecognized face is detected and provided that there is no other recognized person in the frame, we classify that unrecognized person as a possible intruder, and we send an email alert along with the image of that person. The image of this person is also sent to an outdoor unit which contains multiple cameras. Using this image, these cameras look for the intruder, and when detected an email is sent with the intruder’s

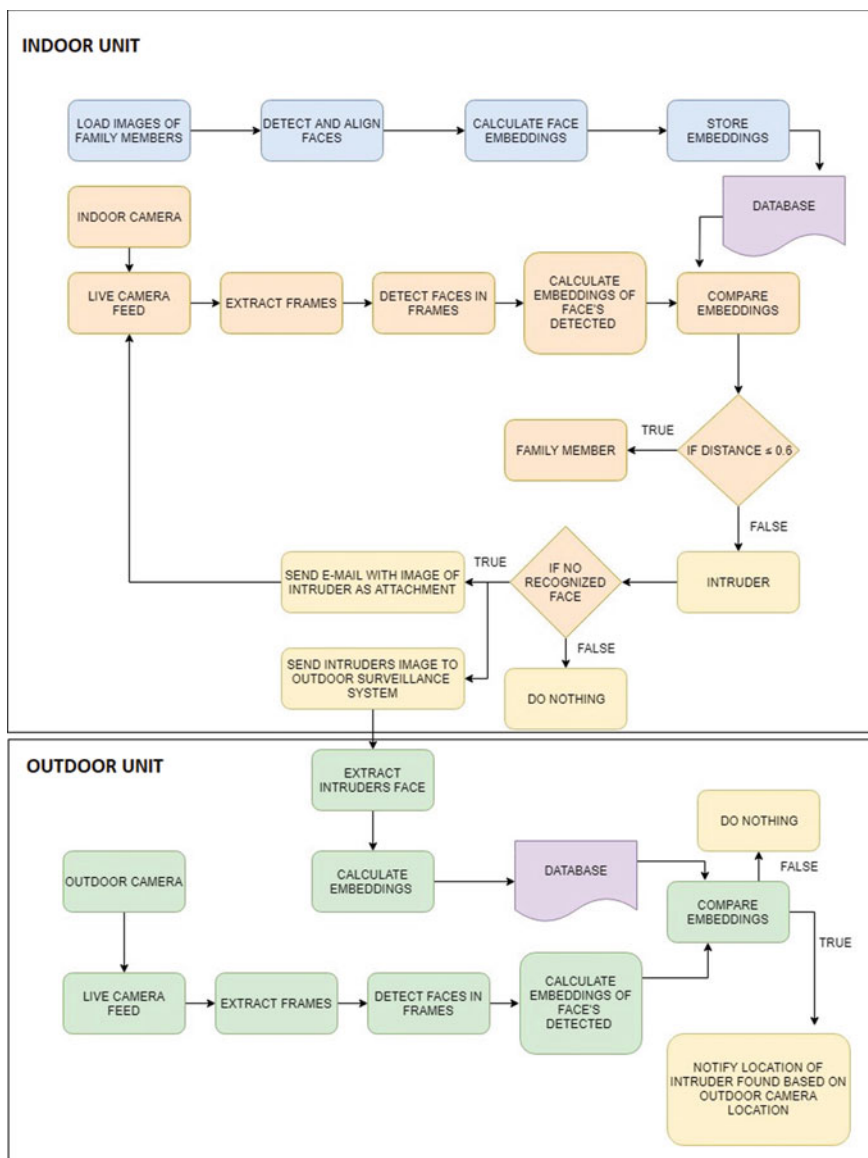


Fig. 10 Flow diagram of the proposed system

location with this information, we can provide aid to the concerned authorities to expedite the catching of the intruder.

4 Results

In this simulation, we use a laptop with Intel(R) Core (TM) i7-8750H CPU as our indoor unit and another laptop with Intel(R) Core (TM) i7-6560U CPU as our outdoor unit. In this simulation, we only use one outdoor camera. We run our intruder detection and tracking program in an Anaconda environment. We used Python language to code our program. This program is run on CPU. The simulation results can be found below.

Figure 11a shows the indoor unit able to recognize family members present in the database. Figure 11b shows when an unrecognized individual enters the frame, we classify them as a possible intruder, but there is also a recognized individual in the frame, so we assume that the unrecognized individual is a non-threatening guest, and an email alert is not sent.

Figure 12a shows an unrecognized face, and there are no other recognized faces in the frame; hence, we classify them as a possible intruder, and an email alert is sent to the family members. That email can be seen in Fig. 12b.

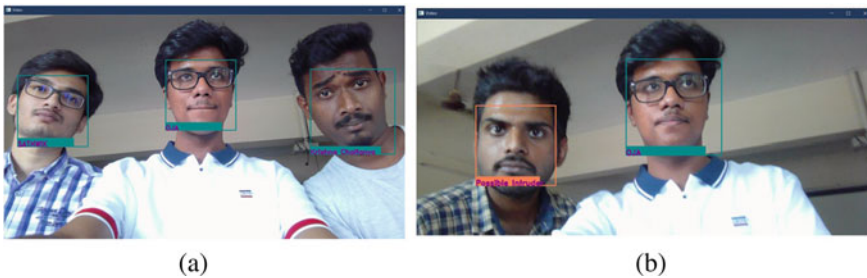


Fig. 11 a Face recognition of family members face. b Recognized face with unrecognized face

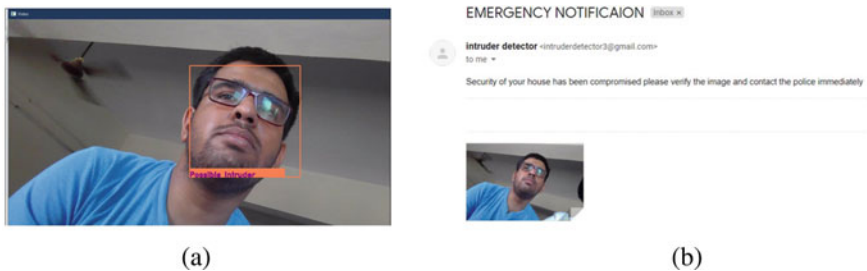


Fig. 12 a Un-recognized face. b Email notification

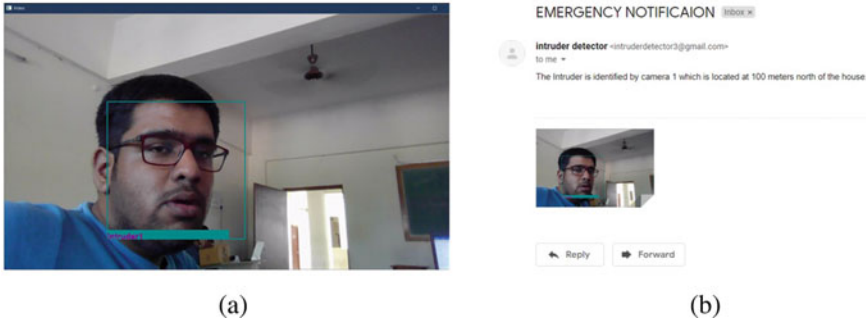


Fig. 13 a Outdoor camera detecting the intruder. b Email notification of the intruder’s location

Now, the outdoor camera looks for the intruder when detected as shown in Fig. 13a an email is sent with the intruder’s location as shown in Fig. 13b. The outdoor camera, based on our testing, was able to accurately detect the intruder when the intruder was about 12–15 ft away from the camera.

5 Conclusion

In summary, we have presented an autonomous way to detect and track intruders by using an indoor unit and outdoor units, which are both connected to the Internet and by implementing a face recognition algorithm that is essentially a Siamese architecture with dlib’s pretrained models then notifying of the intrusion, by using SMTP protocol to send email alerts. We have used TCP/IP sockets to send intruders images from indoor unit to outdoor unit; these images also serve as evidence of theft by essentially acting as a virtual witness. The outdoor unit uses face recognition to identify the intruder in public places based on the received image, and when detected, it sends an email alert hence ultimately tracking the intruder. By using the images taken by the indoor system and by utilizing the outdoor system to track the intruder, we can provide an edge to the law enforcement officials in catching the intruders.

References

1. Khan SA, Ahmad I, Shifian A, Ahmed MS (2019) A smart intruder alert system based on microprocessor and motion detection. In: 2019 international conference on robotics, electrical, and signal processing techniques (ICREST), 2019, pp 335–339
2. Shahid A et al (2017) Computer vision based intruder detection framework. In: 2017 2nd international conference on computer and communication systems, 2017, pp 41–45
3. Shaikh MU, Vora D, Anurag A (2021) Surveillance system for intruder detection using facial recognition. In: Balas VE, Semwal VB, Khandare A, Patil M (eds) Intelligent computing and

- networking. Lecture notes in networks and systems, vol 146. Springer, Singapore. https://doi.org/10.1007/978-981-15-7421-4_18
4. Uday BK, Vattikuti A, Gogineni K, Natarajan P (2019) Machine learning techniques for automatic intruder identification and alerting. In Saini H, Sayal R, Govardhan A, Buyya R (eds) Innovations in computer science and engineering. Lecture notes in networks and systems, vol 74, Springer, Singapore
 5. Albawi S, Mohammed TA, Al-Zawi S (2017) Understanding of convolutional neural network. In: 2017 international conference on engineering and technology (ICET), 2017, pp 1–6
 6. Sharma S, Shanmugasundaram K, Ramasamy SK (2016) FAREC-CNN based efficient face recognition technique using Dlib. In: International conference on advanced communication control and computing technologies (ICACCCT), 2016, pp 192–195. <https://doi.org/10.1109/ICACCCT.2016.7831628>
 7. https://devdoc.net/c/dlib-19.7/python/ddlib.cnn_face_detection_model_v1
 8. Boyko N, Basystiuk O, Shakhovska N (2018) Performance evaluation and comparison of software for face recognition, based on Dlib and OpenCV library. In: IEEE second international conference on data stream mining & processing (DSMP), 2018, pp 478–482. <https://doi.org/10.1109/DSMP.2018.8478556>
 9. <https://opencv.org/>
 10. Cahyono F, Wirawan W, Fuad Rachmadi R (2020) Face recognition system using Facenet algorithm for employee presence. In: 2020 4th international conference on vocational education and training (ICOVET), 2020, pp 57–62. <https://doi.org/10.1109/ICOVET50258.2020.9229888>
 11. Chopra S, Hadsell R, LeCun Y (2005) Learning a similarity metric discriminatively, with application to face verification. In: 2005 IEEE Computer Society conference on computer vision and pattern recognition (CVPR'05), vol 1, pp 539–546. <https://doi.org/10.1109/CVPR.2005.202>
 12. Hadsell R, Chopra S, LeCun Y (2006) Dimensionality reduction by learning an invariant mapping. In: 2006 IEEE Computer Society conference on computer vision and pattern recognition (CVPR'06), 2006, pp 1735–1742. <https://doi.org/10.1109/CVPR.2006.100>
 13. http://dlib.net/face_recognition.py.html
 14. <https://scikit-learn.org/stable/modules/generated/sklearn.manifold.TSNE.html>
 15. <https://matplotlib.org/>
 16. Sureswaran R, Bazar HA, Abouabdalla O, Manasrah AM (2009) Active E-mail system protocols monitoring algorithm. In: TENCON 2009—2009 IEEE region 10 conference, 2009, pp 1–6. <https://doi.org/10.1109/TENCON.2009.5396120>
 17. Hunt J (2019) Sockets in Python. In: Advanced guide to Python 3 programming. Undergraduate topics in computer science. Springer, Cham. https://doi.org/10.1007/978-3-030-25943-3_39
 18. Arora P, Dumka A (2018) Review of sockets for transfer of files between systems. In: Singh R, Choudhury S, Gehlot A (eds) Intelligent communication, control and devices. Advances in intelligent systems and computing, vol 624. Springer, Singapore. https://doi.org/10.1007/978-981-10-5903-2_152